

A fluorescence microscopy image of a brain section. The image shows a complex network of neurons and synapses. The neurons are stained with a green fluorescent marker, and the synapses are stained with a purple fluorescent marker. The background is dark, making the bright green and purple spots stand out. The overall appearance is that of a highly detailed and interconnected neural network.

# **Illuminating the Brain**

Dissecting synaptic architecture through genome editing

**Jelmer Willems**

# **Illuminating the Brain**

Dissecting synaptic architecture  
through genome editing

Jelmer Willems

ISBN: 978-94-6458-514-8

The studies described in this thesis were performed at the department of Cell Biology, Neurobiology and Biophysics at the Faculty of Science of Utrecht University in Utrecht, the Netherlands.

This work is supported by the European Research Council (ERC).

Cover and layout: Jelmer Willems  
Printing: Ridderprint

Copyright © Jelmer Willems, 2022  
All rights reserved

# **Illuminating the Brain**

Dissecting synaptic architecture  
through genome editing

## **Verlichten van het brein**

Het blootleggen van de synaptische architectuur  
met behulp van genoom manipulatie  
(met Nederlandse samenvatting)

## **Proefschrift**

ter verkrijging van de graad van doctor aan de Universiteit Utrecht  
op gezag van de rector magnificus, prof. dr. H.R.B.M. Kummeling,  
ingevolge het besluit van het college voor promoties in het openbaar te  
verdedigen op

woensdag 19 oktober  
des middags te 12.15 uur

door

**Jelmer Willems**

geboren op 18 november 1993 te Holten

Promotor: Prof. dr. L.C. Kapitein  
Copromotor: Dr. H.D. MacGillavry

## TABLE OF CONTENTS

<b>Chapter 1</b>	General introduction	7
<b>Chapter 2</b>	ORANGE: A CRISPR/Cas9-based genome editing toolbox for epitope tagging of endogenous proteins in neurons	25
<b>Chapter 3</b>	Duplex labeling and manipulation of neuronal proteins using sequential CRISPR/Cas9 gene editing	81
<b>Chapter 4</b>	Single-molecule localization microscopy of subcellular protein distribution in neurons	119
<b>Chapter 5</b>	A coordinate-based co-localization index to quantify and visualize spatial associations in SMLM	135
<b>Chapter 6</b>	Mapping and manipulating the synaptic distribution of endogenous AMPAR - auxiliary protein complexes	159
<b>Chapter 7</b>	Anchoring of AMPA receptors through their N-terminal domain	193
<b>Chapter 8</b>	General discussion	209
<b>Addendum</b>		223



# 1

---

## General Introduction

Jelmer Willems

---

Cell Biology, Neurobiology and Biophysics, Department of Biology, Faculty of Science, Utrecht University, Utrecht, the Netherlands



---

In the brain, billions of specialized cells including neurons and microglia together make the complex neuronal connections fundamental to our ability to direct physical, sensory, social and emotional responses. The existence and formation of the brain, its neuronal connections and functioning has fascinated many generations of scientists over the last centuries. From the first descriptions of nerves (Descartes, 1664; van Leeuwenhoek, 1695), the famous frog experiments that suggested neuronal activity to involve electricity (Du Bois-Reymond, 1848; Galvani, 1792), the first drawings of ‘nerve cells’ (although containing errors) (Deiters, 1865), and their identification as single entities that make a complex network (Cajal, 1888; Golgi, 1885), science has come far in resolving the mysteries of the brain. But still, in the twenty-first century, we have many questions remaining to be addressed and resolved, showing that the brain is even more complex than our current understanding. Advancement in the fundamental understanding of the brain, but more broadly in every aspect of scientific progress, comes with the development of new novel analytical techniques and methodologies. In this thesis, we focus our study on developing and applying novel tools to investigate neuronal architecture at the level of protein organization. This introduction aims to provide the basis on which this thesis is build, laying the groundwork for the individual chapters to come.

## NEURONS

Over the course of brain development, the formation of the different brain regions and the interplay between different neuronal cell types is an incredible piece of engineering. Neurons have a very distinct cell autonomy, with an elaborately branched network of dendrites via which signals are received and a single axon via which the neuron can send signals to other neurons. Both morphologically and functionally, neurons can differ significantly throughout the brain, but also within brain regions. The correct interplay between these different neuronal cell types and the formation of neuronal networks as such are critical for its functioning on the levels of a full brain (Sporns, 2016; Suarez et al., 2020). The formation and proper functioning of the brain goes hand in hand with communication between individual neurons, and to understand how these neurons communicate, we also have to study neuronal signaling all the way down to the molecular scale.

Briefly, neuronal communication starts with the generation of an action potential (Du Bois-Reymond, 1848) at the base of the axon, close to the soma of the cell, a region known as the axon initial segment (AIS) (Huang and Rasband, 2018; Leterrier, 2018) (Figure 1). This signal propagates along the axon via the depolarization of the membrane, mediated by ion channels controlling the flow of calcium, potassium and sodium through the membrane (Rama et al., 2018). When an action potential reaches a so-called presynaptic terminal, this electrical signal is converted into a chemical signal that can be transmitted to the postsynaptic terminal of another neuron opposing the presynaptic terminal (Katz, 1969). Together, these structures together form the chemical synapse.

## THE CHEMICAL SYNAPSE

First described as ‘nervous articulations’ (Cajal, 1888) and later referred to as synapse (derived from the word ‘syndesm’ meaning connection (Sherrington, 1897)), are the sites of contact and communication between the axon and dendrites of two neurons (Figure 1). A massive boost to investigating the synaptic architecture was initiated by the development of the electron microscope, allowing the visualization of membrane structures like the neuronal synapse with nanometer resolution (Gray, 1959; Palay, 1958). These studies identified a densely packed structure (around 1 micrometer in size) containing numerous vesicles (on

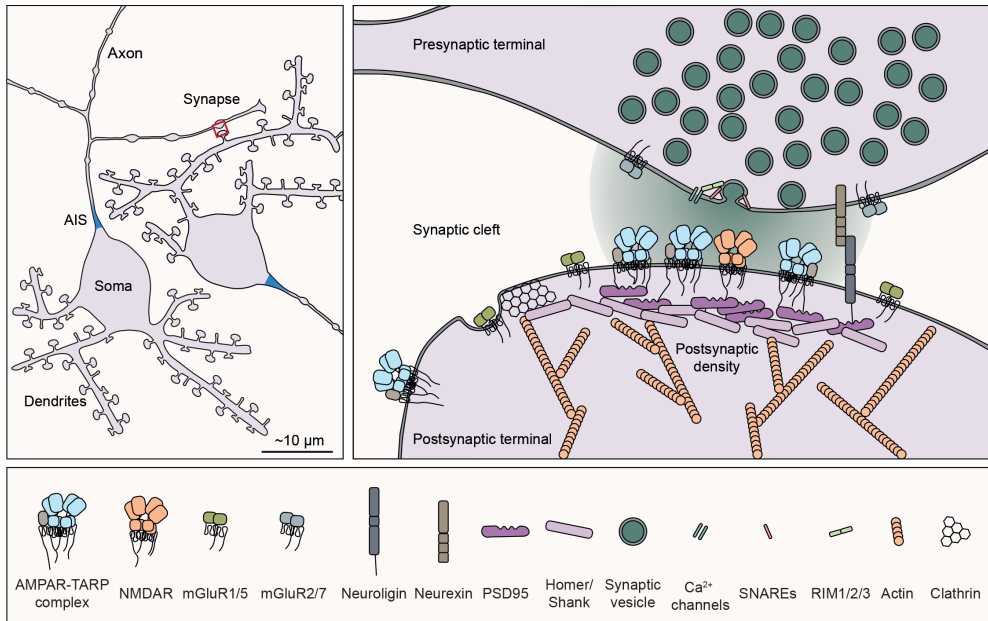


**Figure 1. Neuronal connections and synaptic architecture**

Shown is an illustration of neuronal communication between two neurons (on the left). Neurons have a very distinct morphology, with a long and narrow axon, and multiple dendrites, with protruding dendritic spines. Neuronal communication starts in the axon initial segment where an action potential is generated. This electrical signal travels along the axonal membrane to the synapse. At the synapse (on the right), the electrical signal induces the fusion of a synaptic vesicle with the membrane of the presynaptic terminal. Glutamate diffuses into the synaptic cleft, activating receptors located in the postsynaptic density. Here, a magnitude of scaffolding proteins and a highly branched actin cytoskeleton hold the receptors in place. In addition, transsynaptic adhesion molecules bridge the synaptic cleft, physically aligning the presynaptic and postsynaptic compartments. The process of synaptic plasticity can actively strengthen the synapse, which from a receptor standpoint, includes lateral diffusion, exocytosis and (local) endocytosis.

the presynaptic side) and a highly electron-dense structure on the receiving postsynapse, conveniently calling it the postsynaptic density or in short: the PSD. Together, these distinct elements make neuronal communication possible.

### *Postsynaptic architecture*

There are roughly speaking two types of synapses, being excitatory and inhibitory, depending on the type of chemical involved in signal transmission and the collection of proteins involved in this process. As a single neuron has hundreds of synapses, many excitatory and inhibitory signals together regulate both at a local (dendritic) and cellular scale whether the signals received result in the firing of an action potential from that neuron, passing on the signal (Herstel and Wierenga, 2021; van Vreeswijk and Sompolinsky, 1996). Not surprisingly, an imbalance in excitation and inhibition has been associated with various brain disorders (Lopatina et al., 2019; Sohal and Rubenstein, 2019).

The molecules that make up the PSD are so densely packed that without stain, the PSD can be observed with electron microscopy. Structurally, the PSD is held together by numerous protein-protein and protein-lipid interactions (Ziff, 1997). In addition, recent studies have

---

made interesting observations that suggest the PSD to be a protein condensate, its formation referred to as liquid-liquid phase separation (LLPS) (Hayashi et al., 2021). These condensates allow for proteins to reach local concentrations hundreds of times that of their surroundings, but still allowing for protein exchange/turnover. Several proteins at both the pre- and postsynapse have been shown to form these phase-separated condensates (McDonald et al., 2020; Wu et al., 2019; Zeng et al., 2018; Zeng et al., 2016). Moreover, *in vitro* experiments suggest that the induction of LLPS can be potentially regulated by synaptic activity mediated through CaMKII activation (Hosokawa et al., 2021). Together, these findings have opened a whole new view on how synapses are formed and maintained, and further research in this direction might thus be of great value in understanding these mechanisms.

It is remarkable to consider the number of different proteins that hold residence at the synapse (both pre- and postsynaptic) (Lowenthal et al., 2015; Sheng and Hoogenraad, 2007). Hundreds of different proteins, all with widely varying (and largely unknown) copy numbers and turnover rates that have to work in harmony to effectively support synaptic communication (Helm et al., 2021). Perturbations in synaptic protein abundance, functioning or trafficking for example due to genomic mutations are linked to many neurodevelopmental disorders such as autism spectrum disorder (Lepeta et al., 2016; Zieger and Choquet, 2021). Investigating the role of each of these proteins, whether it be receptors, scaffolding molecules, signaling factors like kinases or components of the cytoskeleton, requires techniques that allow us to visualize and study individual protein species in their native environment. In **chapter 2 and 3**, we aimed to develop and apply a novel toolbox allowing us to endogenously label proteins of interest and study their dynamic sub-cellular localization in neurons.

### *Synaptic transmission*

As mentioned earlier, synaptic communication is mediated by the transfer of a chemical signal (Dale and Gaddum, 1930; Loewi, 1922). These chemicals (i.e. neurotransmitters), are stored in numerous vesicles located at the presynaptic terminal. A few of the vesicles (30-50 nm in diameter) were found to be very closely associated with the synaptic plasma membrane in a region titled the ‘active zone’ (Couteaux and Pecot-Dechavassine, 1970; Gray, 1963). Upon the arrival of an action potential at the presynaptic terminal, these vesicles can fuse with the synaptic membrane through the process of exocytosis (Figure 1). The sequence of events that lead to the fusion of a synaptic vesicle with the membrane are complex and since the exact mechanism of action goes beyond the scope of this chapter, I would like to refer to a series of excellent reviews describing these processes in more detail (Brunger et al., 2019; Emperador-Melero and Kaeser, 2020; Rizalar et al., 2021; Sudhof, 2012). Here, I will briefly highlight several steps in synaptic communication, relevant for the further understanding of the work described in this thesis.

Neurotransmitters, released from a synaptic vesicle diffuse into the extracellular space between the pre- and postsynaptic terminals: the synaptic cleft. Being only around 30 nm apart, the pre- and postsynaptic membranes are held at close proximity by various families of adhesion molecules, that can reach deep into the synaptic cleft (Chamma and Thoumine, 2018). Many recent studies have shown adhesion molecules to play critical roles in properly aligning the pre- and postsynaptic terminals, at both the levels of synapse formation and maintenance (de Wit and Ghosh, 2016; Jang et al., 2017; Sudhof, 2021).

Activation of the postsynaptic terminal by neurotransmitters is mediated by receptors. These receptors, mostly ionotropic or metabotropic receptors, are highly enriched at the postsynaptic terminal by intracellular scaffolding molecules (Scheefhals and MacGillavry,

2018). Ionotropic receptors act as an ion channel that opens upon activation by neurotransmitters. The main type being glutamate, that can bind to  $\alpha$ -amino-3-hydroxy-5-methyl-4-isoxazolepropionic acid (AMPA) and N-methyl-D-aspartic acid (NMDA) receptors. The ion flow (mainly  $\text{Ca}^{2+}$  and  $\text{Na}^{2+}$ ) into the postsynaptic terminal results in depolarization of the membrane, forming an electrical signal that can be propagated back to the cell body (Traynelis et al., 2010). In contrast, metabotropic glutamate receptors are G protein-coupled receptors, thus directly activating downstream signaling pathways (Crupi et al., 2019; Suh et al., 2018). The positioning of these receptors in the synapse, and relative to the presynaptic release site, is important for effective signal transmission. Thus, the trafficking of receptors to and their anchoring at the synapse has to be strictly controlled.

### *AMPA receptors*

AMPA receptors carry most of the basal activity in synaptic transmission. In contrast to NMDA receptors, which are almost exclusively localized at synaptic sites, AMPA receptors, in addition to being strongly enriched in synapses, also express extrasynaptically. The extrasynaptic receptors can be recruited into the synapse on demand, and is mostly driven by synaptic activity (Figure 1). The properties of AMPA receptor diffusion over the neuronal membrane have been extensively studied (Borgdorff and Choquet, 2002; Groc and Choquet, 2020; Obashi et al., 2021). In addition, intracellular AMPA receptors can undergo endocytosis and subsequently recycle back to the synaptic membrane (Catsburg and MacGillavry, 2020; Moretto and Passafaro, 2018). On a functional level, these receptors undergo cycles of activation and desensitization, the kinetics of which are important features of the AMPA receptor, which thus have to be precisely fine-tuned (Coombs and Cull-Candy, 2021).

Important to mention is that many properties of the AMPA receptor are mediated by so-called auxiliary proteins (Bissen et al., 2019; Kamalova and Nakagawa, 2021; Schwenk et al., 2012). These proteins interact with the AMPA receptor acting as ‘minions’ in almost every aspect of AMPA receptor functioning, being it the assembly of the receptor in the endoplasmic reticulum (ER), its trafficking to and recycling from the membrane, and even the synaptic anchoring and gating properties (Jacobi and von Engelhardt, 2021; Matthews et al., 2021; Schwenk et al., 2019). Moreover, regional diversity of these auxiliary proteins throughout the brain allows for functional specialization of AMPA receptors in different neuronal subtypes (Schwenk et al., 2014). In **chapter 6 and 7**, we studied the synaptic anchoring properties of the AMPA receptors and their ‘minions’ in hippocampal neurons.

### *Synaptic plasticity and sub-synaptic clustering*

Receptor trafficking and positioning in the synapse are fundamental to our ability to form associations and store information (Takeuchi et al., 2014). At a molecular level, this ‘plasticity’ of the brain can be translated back to the so-called processes of long-term potentiation (LTP) and long-term depression (LTD), known as forms of Hebbian plasticity (Fernandes and Carvalho, 2016). Initiated by changes in synaptic activity, the processes of LTP and LTD mediate a long-lasting increase and decrease in synaptic strength respectively. In case of LTP, increased synaptic activity causes the opening of NMDA receptors, resulting in the influx of  $\text{Ca}^{2+}$  into the dendritic spine. These ions bind  $\text{Ca}^{2+}$ -dependent kinases like CaMKII that can trigger intracellular signaling pathways that results in synapse strengthening (Herring and Nicoll, 2016; Kim et al., 2016). This includes the recruitment of more receptors, synaptic scaffolding proteins, but also reorganization of the actin cytoskeleton that supports the synapse, and leads to an increase in the size of dendritic spine (Diaz-Alonso and Nicoll,

---

2021; Harris, 2020; Sun et al., 2021).

Based on the rules that underlie synaptic plasticity, one would reason that a bigger synapse with more receptors is also a stronger synapse, which is correct to some extent (Holler et al., 2021). However, knowing the approximate number of receptors in an average synapse to be ~50-100 (Nusser et al., 1998), electrophysiology measurements have shown that upon presynaptic release (under basal conditions), by far not all AMPA receptors in the synapse become activated (Frerking and Wilson, 1996; Liu et al., 1999; McAllister and Stevens, 2000). Thus, this implies that just the recruitment of receptors to the synapse is not sufficient for full contribution to synaptic activity. First of all, upon the arrival of an action potential at the synapse, usually only a single vesicle with neurotransmitter fuses with the membrane (Lisman et al., 2007; Malagon et al., 2016). Secondly, the neurotransmitters released from the site of vesicle fusion diffuse in the synaptic cleft, where its effective concentration reduces significantly over distance (Raghavachari and Lisman, 2004)(Figure 1). Third, the AMPA and NMDA (but also mGluR receptors) are quite insensitive to glutamate, with affinities in the millimolar range (Franks et al., 2003; Traynelis et al., 2010). Together, these established features fit well with an early model in which the positioning of AMPA receptors relative to the presynaptic release site was suggested to be important for the probability of receptor activation (Xie et al., 1997). Moreover, it was reasoned that synaptic plasticity can be partially regulated by reorganization of the synaptic content on a submicron scale, aligning more or less receptors with the presynaptic release site and thus modifying synaptic strength (Lisman and Raghavachari, 2006). For a more comprehensive review on this matter, I would like to refer to (MacGillavry et al., 2011).

Since then, new technical innovations, most important being the development of super-resolution microscopy techniques (more on this in the next section), have enabled researchers to investigate this hypothesis (Betzig, 2015; Sahl et al., 2017). It was revealed that synaptic scaffolding molecules as well as AMPA receptors form subsynaptic clusters called nanodomains (MacGillavry et al., 2013; Nair et al., 2013), and that these are closely aligned with nanodomains formed presynaptically as part of the vesicle release machinery forming so-called ‘nanocolumns’ (Tang et al., 2016). Hereafter, scientists have sought to identify the molecular mechanism that underlies this alignment. Although many questions remain, several recent studies have shown the involvement of synaptic adhesion molecules in this process (Fukata et al., 2021; Haas et al., 2018; Ramsey et al., 2021). In addition, the receptors themselves have the potential to interact with presynaptic membrane proteins as for example the AMPA and NMDA receptors reach into the synaptic cleft by as far as 50-70% of the total distance to the presynaptic membrane (Fossati and Charrier, 2021; Martinez-Sanchez et al., 2021; Watson et al., 2021).

Taken together, basal transmission as well as synaptic plasticity rely on a combination of dynamic receptor trafficking into and out of the synapse, as well as their local confinement into nanodomains and close alignment with presynaptic release sites (Chen et al., 2018; Scheefhals and MacGillavry, 2018). While the underlying mechanisms of synaptic protein clustering are under investigation, dissecting the role of individual proteins using increasingly advanced imaging techniques, is more and more limited by our ability to reliably label and visualize proteins of interest. For this reason, a major part of the work described in this thesis is devoted to establishing methods that enable us to overcome these challenges. Thus, in the remainder of this chapter, I will introduce some crucial developments in imaging and labeling strategies and their limitations prior to this study.

## RESOLVING THE NANOSCALE PROTEIN ORGANIZATION AT SYNAPSES

Understanding how synaptic communication (or any other cellular process) works requires us to study the proteins that are fundamental to these processes. As mentioned in the start of this introduction, scientific progress, or the ongoing paradigm of more questions than answers, drives researchers to develop novel methods and technologies. Thus, not surprisingly, newly developed methods are often key milestones that open uncountable options for addressing research questions (including raising new ones). A few historical examples in (neuronal) cell biology being the early discoveries made using microscopes by Antoni van Leeuwenhoek (van Leeuwenhoek, 1695), the use of fixatives (Rolando, 1829), and staining techniques such as the first silver nitrate staining (Golgi, 1873).

Light microscopy itself, but also its extension to fluorescence microscopy have been instrumental for many decades in investigating individual proteins in cells. Light microscopy is however limited in its ability to resolve individual structures smaller than  $\sim 250$  nm due to the diffraction limit (Vangindertael et al., 2018). For years, the main alternative to circumvent this is the use of EM. EM has been, and still is a highly respected method in studying cellular architecture including synapse organization at a resolution up to 10 nm (Liu et al., 2019). However, labeling and visualization of single protein species has remained difficult and EM relies on extensive (and careful) sample preparation, which eliminates the possibility of live-cell imaging and forcing scientist to look for alternatives.

### *Super-resolution microscopy*

Around 10-15 years ago (and after many years of development), several new so called super-resolution microscopy techniques were first applied to overcome the diffraction limit (Betzig, 2015; Hell, 2007; Sahl et al., 2017). The importance of this breakthrough is illustrated by the Nobel prize in chemistry awarded for its development in 2014. There are roughly two types of super-resolution microscopy techniques. At one hand, we have various so called ‘single-molecule localization microscopy’ (SMLM) techniques that rely on the imaging of individual light emitting molecules. These diffraction limited spots can be computationally fitted to determine the precise localization of the molecule, and plotted to create a super-resolved reconstructed image (Lelek et al., 2021). In chapter 4, we dive deeper into the principles behind SMLM and described an extensive protocol for the imaging of proteins at neuronal synapses at submicron resolution. Techniques other than SMLM rely on advanced illumination techniques including stimulated emission depletion (STED) microscopy (Hell and Wichmann, 1994; Klar et al., 2000), and structured illumination microscopy (SIM) (Heintzmann and Huser, 2017). Together, these techniques now allow for imaging of subcellular structures at a resolution of only tens of nanometers. Within a few years, these technological advancements have led to many new biological insights. Most famous is the discovery of actin rings that hold the structure of axons and dendrites (Xu et al., 2013), but also the subsynaptic clustering of receptor as discussed earlier in this introduction.

SMLM techniques in particular, are fundamentally different from regular pixel-based images in that the final image is reconstructed from the coordinates of individual localizations. Thus, these new developments also require new analytical tools to extract biological insights (Khater et al., 2020; Wu et al., 2020). For example, if we want to study the subsynaptic co-clustering of proteins, we cannot use co-localization analyses developed for pixel-based images. In **chapter 5**, we developed a new coordinate-based method for measuring relative densities and co-localization in dual-color SMLM datasets.

---

### *Common strategies for protein labeling and their struggles*

Studying proteins at endogenous levels in their native cellular environment can be challenging. In particular, most studies rely on antibodies or recombinant expression of tagged proteins to study their localization in neurons. While both have their advantages, there can be major limitations and disadvantages. Alternatively, genome editing tools allow for endogenous tagging of proteins, holding great potential for applications in neurons.

The development and usage of antibodies has been (and still is) the major method for specifically labeling proteins of interest. However, antibodies can generally only be used on fixed cells, but more importantly, obtaining specific antibodies for immunohistochemistry applications often is difficult. For many proteins, including many of the synaptic receptors discussed above, specific and reliable antibodies are not commonly available. Recombinant expression of proteins fused to epitope tags or fluorescent proteins have partially resolved these problems. It became possible to study individual protein species at high resolution in live cells, and study effect of for example protein truncations or mutations. Also, recombinant expression allows for sparse labeling of cells, a major advantage over direct antibody labeling. The main disadvantage of recombinant expression is that the expression levels of the protein are no longer under control of the endogenous transcription and translation machinery, often resulting in substantial overexpression of the protein. Artifacts like altered protein localization, and consequential effect on cellular morphology and function are therefore quite common (Sahl et al., 2017).

Efficient labeling strategies and the selection of proper tags are critical for any fluorescent microscopy application. In particular, super-resolution imaging is prone to severe artifacts, introduced by sample preparation (Jimenez et al., 2020). These artifacts can range from overexpression artifacts, linkage errors due to the size of antibodies, insufficient signal amplification and non-compatible dyes. Fluorescent proteins have the main advantage that they directly visualize the protein of interest and thus are great for live-cell imaging approaches. However, they are often not that bright and photostable, and are not suitable for most super-resolution imaging methods. Alternatives to this are the use of enzymatic self-labeling tags such as SNAP-, CLIP- and Halo-tags that can bind exogenous ligands, fused to organic dyes (Keppler et al., 2003; Los et al., 2008). While labeling of these tags does not require antibodies, the level of signal amplification is often limited. They are however a good alternative for fluorescent proteins. Ongoing debates about the influence of tag size on protein localization and function also pushes scientists to search for alternatives. Small epitope tags are therefore often used, which are usually around 10-20 amino acids in size and can be visualized by additional labeling with specific antibodies or nanobodies. Famous are the HA, FLAG and Myc tags (for an overview, see: (Brizzard, 2008)). Recently, specific de novo engineering of tags with certain properties such as a neutral charge or hydrophobicity have yielded new tags such as ALFAtag (Gotzke et al., 2019).

Taken together, the selection of the labeling strategy and tag, whether it be a fluorescent protein or organic dye is extremely important (more on this in **chapter 4**). Especially in view of the new developments in super-resolution imaging techniques, there is an increasing demand for more specific and reliable labeling strategies. In the next section, I will introduce targeted genome editing, that has the potential of revolutionizing the way we label proteins in mammalian cells, overcoming many of the challenges mentioned above.

## GENOME EDITING AS TOOL TO VISUALIZE PROTEINS IN THE BRAIN

Genome editing as a method to endogenously tag proteins of interest is considered as one of the major leaps forward in scientific progress over the last years. While CRISPR/Cas9 is currently the ‘gold standard’ in genome editing, other approaches for directed genome editing have been around for many years. Since the eighties, DNA templates with homology arms could be integrated into the genome of immortal cell lines relying on the process of homology dependent recombination (HDR) (Capecchi, 2005). Applying this strategy in embryonic stem cells also enabled the generation of genetically modified knock-in and knock-out mice (Doetschman et al., 1987; Thomas and Capecchi, 1987). Many years later, the development of techniques that applied Zinc-finger nucleases (Carroll, 2011) and Transcription activator-like effector nucleases (TALEN) (Boch et al., 2009; Moscou and Bogdanove, 2009; Romer et al., 2007) enabled researchers to make double stranded DNA breaks directed at a specific locus (Geurts et al., 2009; Miller et al., 2011). These studies showed that the generation of a double stranded DNA break at the intended site for integration, greatly enhanced efficiency of knock-in. However, TALEN and Zinc-finger are extremely laborious to work with, requiring an extensive skill set in molecular biology as both require the cloning of new multi-domain fusion protein acting as nuclease for each DNA target. Their future potential became soon largely obsolete by the development of CRISPR/Cas technology.

### *CRISPR/Cas mediated genome editing*

CRISPR, or ‘Clustered Regularly Interspaced Short Palindromic Repeats’ refers to small repeating sequences identified in bacteria and archaea (Ishino et al., 1987; Jansen et al., 2002; Mojica et al., 1993). Cas stands for ‘CRISPR-associated gene’, and together with CRISPR was associated with bacterial immunity (Jansen et al., 2002; Makarova et al., 2002). The CRISPR sequences were found to be interspaced by DNA sequences for phages (Mojica et al., 2005; Pourcel et al., 2005) and studies on the Cas genes showed that they might code for proteins with DNA restriction domains. In the years from then, the CRISPR and Cas genes were shown to work as a defense mechanism against viruses (Barrangou et al., 2007), and soon the mechanism of action was resolved. While many different CRISPR families have been identified, the mechanisms of action of CRISPR/Cas9 are by far the best described and studied (Makarova et al., 2015). After transcription, the CRISPR sequences are processed into smaller crRNAs (crRNA) that each contain the repeat sequence and viral sequence (Brouns et al., 2008). These crRNA bind to a universal tracrRNA (trans-activating RNA) (Deltcheva et al., 2011). The resulting RNA complex binds to Cas9 and guides it (hence the name guideRNA given to the RNA complex) to its target: the complementary viral DNA. Cas9 then generates a blunt-end double stranded DNA break, three base pairs upstream of a so called protospacer adjacent motif (PAM) (Bolotin et al., 2005; Deveau et al., 2008; Garneau et al., 2010; Mojica et al., 2009).

Having established the mechanism, several laboratories came to the realization that this system could potentially be programmed to direct targeted cleavage of DNA in mammalian cells. The first major breakthrough that opened the doors for CRISPR/Cas9 based genome editing technologies, came with the in vitro biochemical characterization of the mechanism and simplification of the system designing a chimera of the crRNA and tracrRNA (Jinek et al., 2012). Soon after, several labs showed that this system can be used for genome editing in mammalian cells (Cong et al., 2013; Mali et al., 2013). In the following years, a broad range of novel applications were developed (Zhang et al., 2021), which include the generation of knockouts, knock-ins, active control over gene expression using cleavage



---

defective Cas9 variants (dCas9) (Gilbert et al., 2013; Qi et al., 2013), single nucleotide base editing (Komor et al., 2016), and RNA cleavage (Abudayyeh et al., 2016), across many animal and plant species (Knott and Doudna, 2018).

### *Genome editing in neurons*

While the issue of efficient targeted cleavage of DNA was resolved, another one, that also applies to genome editing in neurons was not. The integration of DNA templates that contain homology arms relies on the cells to use homologous recombination as mechanism of DNA repair. In this process, a donor DNA contains arms that contain sequences homologous to the site of integration that is used. These arms can recombine with the cleaved DNA site via DNA repair. However, this system is mostly active during cell division and thus, generating knock-ins in post-mitotic cells remained extremely hard, if not impossible. So far, only a few studies have tried to use CRISPR/Cas9 together with HDR mediated integration, with some success (Mikuni et al., 2016; Nishiyama et al., 2017; Uemura et al., 2016). The main alternative would be to generate a transgenic knock-in mouse, but besides being expensive, time consuming and requiring the unnecessary use of animals, this will also result in global expression of the integrated tag in all cells, which due to the density of neuronal tissue and cultures, can be a severe limitation for imaging. In contrast to HDR, the DNA-damage repair process of non-homologous end joining (NHEJ) is active throughout the cell cycle and thus the main pathway for DNA-damage repair in neurons. While considered error-prone, making use of this pathway in the presence of a NHEJ-suited donor should allow for efficient and precise integration of donor tags (Betermier et al., 2014; Suzuki et al., 2016). This has been the foundation on which we developed a toolbox for efficient generation of such knock-ins in neurons (**chapter 2 and 3**).

### **SCOPE OF THIS THESIS**

Our ability to study individual protein species and understand their role in synaptic functioning is strongly dependent on available technologies and methodologies. The general aim of this thesis was to develop novel methodologies to study the localization and dynamics of endogenous proteins at neuronal synapses.

First, we aimed to develop new labeling strategies to visualize endogenous proteins in neurons. **Chapter 2**, focusses on the development of a CRISPR/Cas9 based toolbox (ORANGE), for endogenous tagging of proteins in neurons. We generated an extensive knock-in library, and show its utility with multiple delivery methods for applications in vitro and in vivo, and finally combine this with (live-cell) superresolution microscopy to reveal the nanoscale organization of NMDA receptors. In **chapter 3**, we expand on the ORANGE toolbox establishing a robust method for duplex labeling using conditional activation of knock-in expression (CAKE). This powerful combination now enables the localization and manipulation of multiple endogenous proteins in neurons.

Second, in order to investigate neuronal architecture at sub-micron resolution, there is the need for superresolution microscopy methods such as SMLM. In **chapter 4**, we described a step-by-step protocol for imaging of endogenous proteins in neurons using SMLM. We extensively discussed important experimental parameters, labeling considerations and optimization steps. In **chapter 5**, we established a new coordinate-based analysis for quantifying co-localization in SMLM datasets that is parameter-free and acts as a powerful tool to measure spatial association between two protein species.

Third, we used the methods as developed in the preceding chapters to investigate

the synaptic anchoring of AMPARs. In **chapter 6**, we dive deeper into the mechanisms underlying receptor trafficking at synapses by studying the localization of AMPAR auxiliary proteins. More specifically, we mapped the localization of multiple auxiliary protein families and studied their localization at excitatory synapses. Furthermore, we found TARP and Shisa protein expression at synapses is dependent on that of the AMPA core subunits, and that their PDZ ligand is important for synaptic targeting, but not sub-synaptic organization. In **chapter 7**, we focused our study on the AMPAR itself and aimed to investigate the importance of the AMPAR N-terminal domain (NTD) in synaptic anchoring. We found that the localization and synaptic anchoring of AMPARs is strongly dependent on their NTD, influencing synaptic enrichment, turnover and diffusion kinetics.

Last, **Chapter 8** concludes with a general discussion about the presented study and its relevance in the context of existing literature. In addition, current challenges and future opportunities are discussed.

## REFERENCES

- Abudayyeh, O.O., Gootenberg, J.S., Konermann, S., Joung, J., Slaymaker, I.M., Cox, D.B., Shmakov, S., Makarova, K.S., Semenova, E., Minakhin, L., et al. (2016). C2c2 is a single-component programmable RNA-guided RNA-targeting CRISPR effector. *Science* 353, aaf5573.
- Barrangou, R., Fremaux, C., Deveau, H., Richards, M., Boyaval, P., Moineau, S., Romero, D.A., and Horvath, P. (2007). CRISPR provides acquired resistance against viruses in prokaryotes. *Science* 315, 1709-1712.
- Betermier, M., Bertrand, P., and Lopez, B.S. (2014). Is non-homologous end-joining really an inherently error-prone process? *PLoS Genet* 10, e1004086.
- Betzig, E. (2015). Single Molecules, Cells, and Super-Resolution Optics (Nobel Lecture). *Angew Chem Int Ed Engl* 54, 8034-8053.
- Bissen, D., Foss, F., and Acker-Palmer, A. (2019). AMPA receptors and their minions: auxiliary proteins in AMPA receptor trafficking. *Cell Mol Life Sci* 76, 2133-2169.
- Boch, J., Scholze, H., Schornack, S., Landgraf, A., Hahn, S., Kay, S., Lahaye, T., Nickstadt, A., and Bonas, U. (2009). Breaking the code of DNA binding specificity of TAL-type III effectors. *Science* 326, 1509-1512.
- Bolotin, A., Quinquis, B., Sorokin, A., and Ehrlich, S.D. (2005). Clustered regularly interspaced short palindrome repeats (CRISPRs) have spacers of extrachromosomal origin. *Microbiology (Reading)* 151, 2551-2561.
- Borgdorff, A.J., and Choquet, D. (2002). Regulation of AMPA receptor lateral movements. *Nature* 417, 649-653.
- Brizzard, B. (2008). Epitope tagging. *Biotechniques* 44, 693-695.
- Brouns, S.J., Jore, M.M., Lundgren, M., Westra, E.R., Slijkhuis, R.J., Snijders, A.P., Dickman, M.J., Makarova, K.S., Koonin, E.V., and van der Oost, J. (2008). Small CRISPR RNAs guide antiviral defense in prokaryotes. *Science* 321, 960-964.
- Brunger, A.T., Choi, U.B., Lai, Y., Leitz, J., White, K.I., and Zhou, Q. (2019). The pre-synaptic fusion machinery. *Curr Opin Struct Biol* 54, 179-188.
- Cajal, S.R. (1888). Estructura de los centros nerviosos de las aves. Con dos laminas litográfica. *Rev Trimes Histol Normal Patol* 1, 1-10.
- Capecchi, M.R. (2005). Gene targeting in mice: functional analysis of the mammalian genome for the twenty-first century. *Nat Rev Genet* 6, 507-512.
- Carroll, D. (2011). Genome engineering with zinc-finger nucleases. *Genetics* 188, 773-782.
- Catsburg, L.A.E., and MacGillavry, H.D. (2020). AMPA receptor trafficking in the developing and mature glutamatergic synapse. In *Synapse Development and Maturation*, J.L.R. Rubenstein, ed. (Elsevier), pp. 507-525.
- Chamma, I., and Thoumine, O. (2018). Dynamics, nanoscale organization, and function of synaptic adhesion molecules. *Mol Cell Neurosci* 91, 95-107.
- Chen, H., Tang, A.H., and Blanpied, T.A. (2018). Subsynaptic spatial organization as a regulator of synaptic strength and plasticity. *Curr Opin Neurobiol* 51, 147-153.
- Cong, L., Ran, F.A., Cox, D., Lin, S., Barretto, R., Habib, N., Hsu, P.D., Wu, X., Jiang, W., Marraffini, L.A., and Zhang, F. (2013). Multiplex genome engineering using CRISPR/Cas systems. *Science* 339, 819-823.
- Coombs, I.D., and Cull-Candy, S.G. (2021). Single-channel mechanisms underlying the function, diversity and plasticity of AMPA receptors. *Neuropharmacology*, 108781.
- Couteaux, R., and Pecot-Dechavassine, M. (1970). [Synaptic vesicles and pouches at the level of "active zones" of the neuromuscular junction]. *C R Acad Hebd Seances Acad Sci D* 271, 2346-2349.
- Crupi, R., Impellizzeri, D., and Cuzzocrea, S. (2019). Role of Metabotropic Glutamate Receptors in Neurological Disorders. *Front Mol Neurosci* 12, 20.
- Dale, H.H., and Gaddum, J.H. (1930). Reactions of denervated voluntary muscle, and their bearing on the mode of action of parasympathetic and related nerves. *J Physiol* 70, 109-144.
- de Wit, J., and Ghosh, A. (2016). Specification of synaptic connectivity by cell surface interactions. *Nat Rev Neurosci* 17, 22-35.
- Deiters, O. (1865). Untersuchungen über Gehirn und Rückenmark des Menschen und der Säugethiere. (Vieweg und Sohn).
- Deltcheva, E., Chylinski, K., Sharma, C.M., Gonzales, K., Chao, Y., Pirezada, Z.A., Eckert, M.R., Vogel, J., and Charpentier, E. (2011). CRISPR RNA maturation by trans-encoded small RNA and host factor RNase III. *Nature* 471, 602-607.
- Descartes, R. (1664). *L'Homme et un traité de la formation du fœtus. Avec les remarques de Louis de la Forge.* (Paris: Jacques le Gras).
- Deveau, H., Barrangou, R., Garneau, J.E., Labonte, J., Fremaux, C., Boyaval, P., Romero, D.A., Horvath, P., and Moineau, S. (2008). Phage response to CRISPR-encoded resistance in *Streptococcus thermophilus*. *J Bacteriol* 190, 1390-1400.
- Diaz-Alonso, J., and Nicoll, R.A. (2021). AMPA receptor trafficking and LTP: Carboxy-termini, amino-termini and TARPs. *Neuropharmacology* 197, 108710.
- Doetschman, T., Gregg, R.G., Maeda, N., Hooper, M.L., Melton, D.W., Thompson, S., and Smithies, O. (1987). Targetted correction of a mutant HPRT gene in mouse embryonic stem cells. *Nature* 330, 576-578.
- Du Bois-Reymond, E.H. (1848). Untersuchungen über thierische elektricität (Berlin: G. Reimer).
- Emperador-Melero, J., and Kaeser, P.S. (2020). Assembly of the presynaptic active zone. *Curr Opin Neurobiol* 63, 95-103.
- Fernandes, D., and Carvalho, A.L. (2016). Mechanisms of homeostatic plasticity in the excitatory synapse. *J Neurochem* 139, 973-996.
- Fossati, M., and Charrier, C. (2021). Trans-synaptic interactions of ionotropic glutamate receptors. *Curr Opin Neurobiol* 66, 85-92.
- Franks, K.M., Stevens, C.F., and Sejnowski, T.J. (2003). Independent sources of quantal variability at single glutamatergic synapses. *J Neurosci* 23, 3186-3195.
- Frerking, M., and Wilson, M. (1996). Saturation of postsynaptic receptors at central synapses? *Curr Opin*

Neurobiol 6, 395-403.

- Fukata, Y., Hirano, Y., Miyazaki, Y., Yokoi, N., and Fukata, M. (2021). Trans-synaptic LGI1-ADAM22-MAGUK in AMPA and NMDA receptor regulation. *Neuropharmacology* 194, 108628.
- Galvani, L. (1792). De viribus electricitatis in motu musculari commentarius. De Bononiensi Scientiarum et Artium Instituto atque Academia commentarii 7, 363–418.
- Garneau, J.E., Dupuis, M.E., Villion, M., Romero, D.A., Barrangou, R., Boyaval, P., Fremaux, C., Horvath, P., Magadan, A.H., and Moineau, S. (2010). The CRISPR/Cas bacterial immune system cleaves bacteriophage and plasmid DNA. *Nature* 468, 67-71.
- Geurts, A.M., Cost, G.J., Freyvert, Y., Zeitler, B., Miller, J.C., Choi, V.M., Jenkins, S.S., Wood, A., Cui, X., Meng, X., et al. (2009). Knockout rats via embryo microinjection of zinc-finger nucleases. *Science* 325, 433.
- Gilbert, L.A., Larson, M.H., Morsut, L., Liu, Z., Brar, G.A., Torres, S.E., Stern-Ginossar, N., Brandman, O., Whitehead, E.H., Doudna, J.A., et al. (2013). CRISPR-mediated modular RNA-guided regulation of transcription in eukaryotes. *Cell* 154, 442-451.
- Golgi, C. (1885). Sulla fina anatomia degli organi centrali del sistema nervoso (Reggio Emilia: S. Calderini e Figlio).
- Gotzke, H., Kilisch, M., Martinez-Carranza, M., Sograte-Idrissi, S., Rajavel, A., Schlichthaerle, T., Engels, N., Jungmann, R., Stenmark, P., Opazo, F., and Frey, S. (2019). The ALFA-tag is a highly versatile tool for nanobody-based bioscience applications. *Nat Commun* 10, 4403.
- Gray, E.G. (1959). Axo-somatic and axo-dendritic synapses of the cerebral cortex: an electron microscope study. *J Anat* 93, 420-433.
- Gray, E.G. (1963). Electron microscopy of presynaptic organelles of the spinal cord. *J Anat* 97, 101-106.
- Groc, L., and Choquet, D. (2020). Linking glutamate receptor movements and synapse function. *Science* 368.
- Haas, K.T., Compans, B., Letellier, M., Bartol, T.M., Grillo-Bosch, D., Sejnowski, T.J., Sainlos, M., Choquet, D., Thoumine, O., and Hossy, E. (2018). Pre-post synaptic alignment through neuroligin-1 tunes synaptic transmission efficiency. *Elife* 7.
- Harris, K.M. (2020). Structural LTP: from synaptogenesis to regulated synapse enlargement and clustering. *Curr Opin Neurobiol* 63, 189-197.
- Hayashi, Y., Ford, L.K., Fioriti, L., McGurk, L., and Zhang, M. (2021). Liquid-Liquid Phase Separation in Physiology and Pathophysiology of the Nervous System. *J Neurosci* 41, 834-844.
- Heintzmann, R., and Huser, T. (2017). Super-Resolution Structured Illumination Microscopy. *Chem Rev* 117, 13890-13908.
- Hell, S.W. (2007). Far-field optical nanoscopy. *Science* 316, 1153-1158.
- Hell, S.W., and Wichmann, J. (1994). Breaking the diffraction resolution limit by stimulated emission: stimulated-emission-depletion fluorescence microscopy. *Opt Lett* 19, 780-782.
- Helm, M.S., Dankovich, T.M., Mandad, S., Rammner, B., Jahne, S., Salimi, V., Koerbs, C., Leibbrandt, R., Urlaub, H., Schikorski, T., and Rizzoli, S.O. (2021). A large-scale nanoscopy and biochemistry analysis of postsynaptic dendritic spines. *Nat Neurosci* 24, 1151-1162.
- Herring, B.E., and Nicoll, R.A. (2016). Long-Term Potentiation: From CaMKII to AMPA Receptor Trafficking. *Annu Rev Physiol* 78, 351-365.
- Herstel, L.J., and Wierenga, C.J. (2021). Network control through coordinated inhibition. *Curr Opin Neurobiol* 67, 34-41.
- Holler, S., Kostinger, G., Martin, K.A.C., Schuhknecht, G.F.P., and Stratford, K.J. (2021). Structure and function of a neocortical synapse. *Nature* 591, 111-116.
- Hosokawa, T., Liu, P.W., Cai, Q., Ferreira, J.S., Levett, F., Butler, C., Sibarita, J.B., Choquet, D., Groc, L., Hossy, E., et al. (2021). CaMKII activation persistently segregates postsynaptic proteins via liquid phase separation. *Nat Neurosci* 24, 777-785.
- Huang, C.Y., and Rasband, M.N. (2018). Axon initial segments: structure, function, and disease. *Ann N Y Acad Sci* 1420, 46-61.
- Ishino, Y., Shinagawa, H., Makino, K., Amemura, M., and Nakata, A. (1987). Nucleotide sequence of the iap gene, responsible for alkaline phosphatase isozyme conversion in *Escherichia coli*, and identification of the gene product. *J Bacteriol* 169, 5429-5433.
- Jacobi, E., and von Engelhardt, J. (2021). Modulation of information processing by AMPA receptor auxiliary subunits. *J Physiol* 599, 471-483.
- Jang, S., Lee, H., and Kim, E. (2017). Synaptic adhesion molecules and excitatory synaptic transmission. *Curr Opin Neurobiol* 45, 45-50.
- Jansen, R., Embden, J.D., Gaastra, W., and Schouls, L.M. (2002). Identification of genes that are associated with DNA repeats in prokaryotes. *Mol Microbiol* 43, 1565-1575.
- Jimenez, A., Friedl, K., and Leterrier, C. (2020). About samples, giving examples: Optimized Single Molecule Localization Microscopy. *Methods* 174, 100-114.
- Jinek, M., Chylinski, K., Fonfara, I., Hauer, M., Doudna, J.A., and Charpentier, E. (2012). A programmable dual-RNA-guided DNA endonuclease in adaptive bacterial immunity. *Science* 337, 816-821.
- Kamalova, A., and Nakagawa, T. (2021). AMPA receptor structure and auxiliary subunits. *J Physiol* 599, 453-469.
- Katz, B. (1969). The Release of Neural Transmitter Substances (Liverpool: University Press).
- Keppler, A., Gendrezig, S., Gronemeyer, T., Pick, H., Vogel, H., and Johnsson, K. (2003). A general method for the covalent labeling of fusion proteins with small molecules in vivo. *Nat Biotechnol* 21, 86-89.
- Khater, I.M., Nabi, I.R., and Hamarneh, G. (2020). A Review of Super-Resolution Single-Molecule Localization Microscopy Cluster Analysis and Quantification Methods. *Patterns (N Y)* 1, 100038.
- Kim, K., Saneyoshi, T., Hosokawa, T., Okamoto, K., and Hayashi, Y. (2016). Interplay of enzymatic and structural functions of CaMKII in long-term potentiation. *J Neurochem* 139, 959-972.
- Klar, T.A., Jakobs, S., Dyba, M., Egner, A., and Hell, S.W. (2000). Fluorescence microscopy with diffraction resolution barrier broken by stimulated emission. *Proc Natl Acad Sci U S A* 97, 8206-8210.
- Knott, G.J., and Doudna, J.A. (2018). CRISPR-Cas guides the future of genetic engineering. *Science* 361, 866-869.

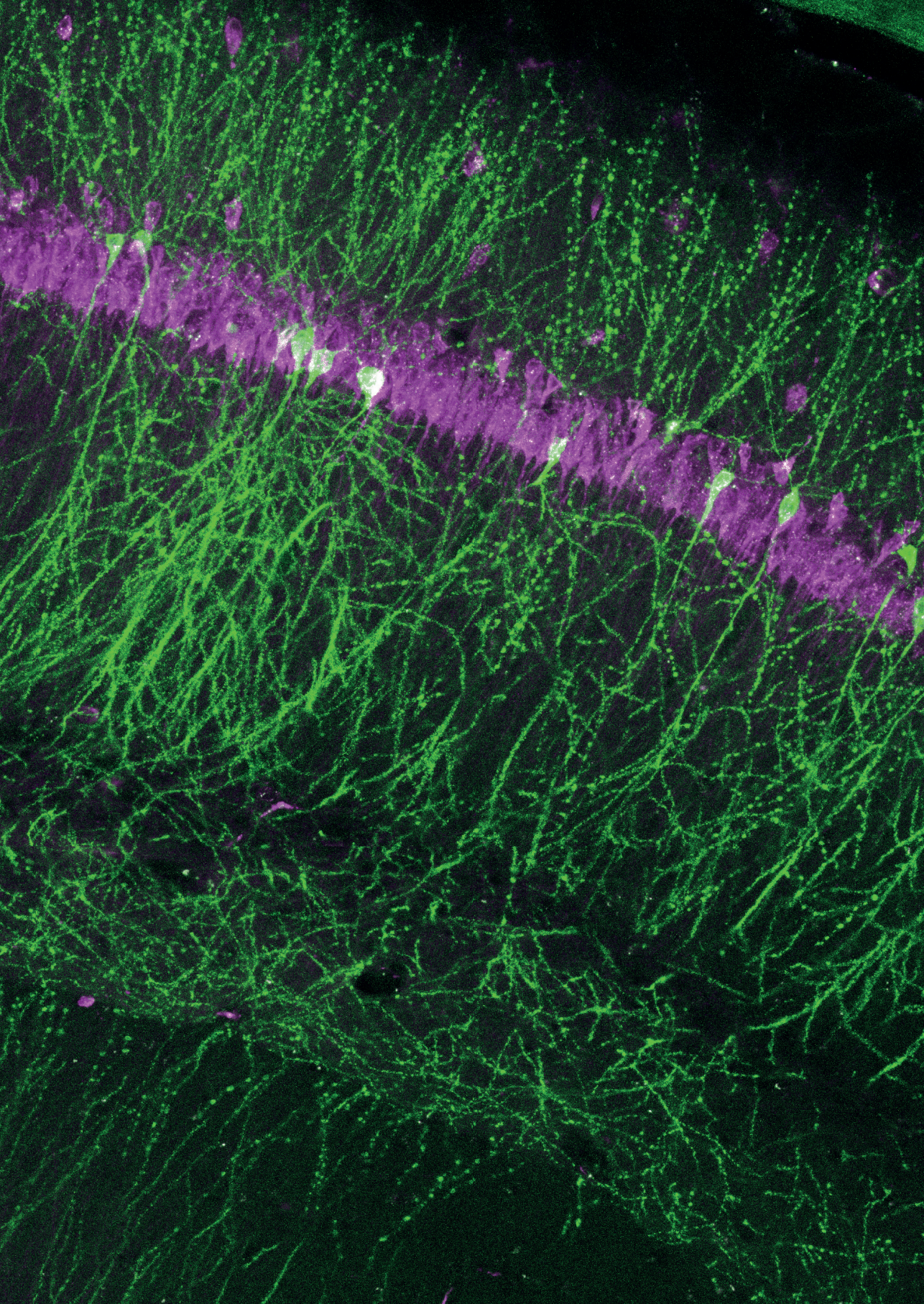
- Komor, A.C., Kim, Y.B., Packer, M.S., Zuris, J.A., and Liu, D.R. (2016). Programmable editing of a target base in genomic DNA without double-stranded DNA cleavage. *Nature* 533, 420-424.
- Lelek, M., Gyparakis, M.T., Beliu, G., Schueder, F., Griffié, J., Manley, S., Jungmann, R., Sauer, M., Lakadamyalim, M., and Zimmer, C. (2021). Single-molecule localization microscopy. *Nature Reviews Methods Primers* 1.
- Lepeta, K., Lourenco, M.V., Schweitzer, B.C., Martino Adami, P.V., Banerjee, P., Catuara-Solarz, S., de La Fuente Revenga, M., Guillem, A.M., Haidar, M., Ijomone, O.M., et al. (2016). Synaptopathies: synaptic dysfunction in neurological disorders - A review from students to students. *J Neurochem* 138, 785-805.
- Leterrier, C. (2018). The Axon Initial Segment: An Updated Viewpoint. *J Neurosci* 38, 2135-2145.
- Lisman, J., and Raghavachari, S. (2006). A unified model of the presynaptic and postsynaptic changes during LTP at CA1 synapses. *Sci STKE* 2006, re11.
- Lisman, J.E., Raghavachari, S., and Tsien, R.W. (2007). The sequence of events that underlie quantal transmission at central glutamatergic synapses. *Nat Rev Neurosci* 8, 597-609.
- Liu, G., Choi, S., and Tsien, R.W. (1999). Variability of neurotransmitter concentration and nonsaturation of postsynaptic AMPA receptors at synapses in hippocampal cultures and slices. *Neuron* 22, 395-409.
- Liu, Y.T., Tao, C.L., Lau, P.M., Zhou, Z.H., and Bi, G.Q. (2019). Postsynaptic protein organization revealed by electron microscopy. *Curr Opin Struct Biol* 54, 152-160.
- Loewi, O. (1922). Über humorale Übertragbarkeit der Herznervenwirkung. *Pflügers Arch Gesamte Physiol Menschen Tiere* 193, 201-213.
- Lopatina, O.L., Malinovskaya, N.A., Komleva, Y.K., Gorina, Y.V., Shuvaev, A.N., Olovyanikova, R.Y., Belozor, O.S., Belova, O.A., Higashida, H., and Salmina, A.B. (2019). Excitation/inhibition imbalance and impaired neurogenesis in neurodevelopmental and neurodegenerative disorders. *Rev Neurosci* 30, 807-820.
- Los, G.V., Encell, L.P., McDougall, M.G., Hartzell, D.D., Karassina, N., Zimprich, C., Wood, M.G., Learish, R., Ohana, R.F., Urh, M., et al. (2008). HaloTag: a novel protein labeling technology for cell imaging and protein analysis. *ACS Chem Biol* 3, 373-382.
- Lowenthal, M.S., Markey, S.P., and Dosemeci, A. (2015). Quantitative mass spectrometry measurements reveal stoichiometry of principal postsynaptic density proteins. *J Proteome Res* 14, 2528-2538.
- MacGillivray, H.D., Kerr, J.M., and Blanpied, T.A. (2011). Lateral organization of the postsynaptic density. *Mol Cell Neurosci* 48, 321-331.
- MacGillivray, H.D., Song, Y., Raghavachari, S., and Blanpied, T.A. (2013). Nanoscale scaffolding domains within the postsynaptic density concentrate synaptic AMPA receptors. *Neuron* 78, 615-622.
- Makarova, K.S., Aravind, L., Grishin, N.V., Rogozin, I.B., and Koonin, E.V. (2002). A DNA repair system specific for thermophilic Archaea and bacteria predicted by genomic context analysis. *Nucleic Acids Res* 30, 482-496.
- Makarova, K.S., Wolf, Y.I., Alkhnbashi, O.S., Costa, F., Shah, S.A., Saunders, S.J., Barrangou, R., Brouns, S.J., Charpentier, E., Haft, D.H., et al. (2015). An updated evolutionary classification of CRISPR-Cas systems. *Nat Rev Microbiol* 13, 722-736.
- Malagon, G., Miki, T., Llano, I., Neher, E., and Marty, A. (2016). Counting Vesicular Release Events Reveals Binomial Release Statistics at Single Glutamatergic Synapses. *J Neurosci* 36, 4010-4025.
- Mali, P., Yang, L., Esvelt, K.M., Aach, J., Guell, M., DiCarlo, J.E., Norville, J.E., and Church, G.M. (2013). RNA-guided human genome engineering via Cas9. *Science* 339, 823-826.
- Martinez-Sanchez, A., Laugks, U., Kochovski, Z., Papantoniou, C., Zinzula, L., Baumeister, W., and Lucic, V. (2021). Trans-synaptic assemblies link synaptic vesicles and neuroreceptors. *Sci Adv* 7.
- Matthews, P.M., Pinggera, A., Kampjut, D., and Greger, I.H. (2021). Biology of AMPA receptor interacting proteins - From biogenesis to synaptic plasticity. *Neuropharmacology* 197, 108709.
- McAllister, A.K., and Stevens, C.F. (2000). Nonsaturation of AMPA and NMDA receptors at hippocampal synapses. *Proc Natl Acad Sci U S A* 97, 6173-6178.
- McDonald, N.A., Fetter, R.D., and Shen, K. (2020). Assembly of synaptic active zones requires phase separation of scaffold molecules. *Nature* 588, 454-458.
- Mikuni, T., Nishiyama, J., Sun, Y., Kamasawa, N., and Yasuda, R. (2016). High-Throughput, High-Resolution Mapping of Protein Localization in Mammalian Brain by In Vivo Genome Editing. *Cell* 165, 1803-1817.
- Miller, J.C., Tan, S., Qiao, G., Barlow, K.A., Wang, J., Xia, D.F., Meng, X., Paschon, D.E., Leung, E., Hinkley, S.J., et al. (2011). A TALE nuclease architecture for efficient genome editing. *Nat Biotechnol* 29, 143-148.
- Mojica, F.J., Diez-Villasenor, C., Garcia-Martinez, J., and Soria, E. (2005). Intervening sequences of regularly spaced prokaryotic repeats derive from foreign genetic elements. *J Mol Evol* 60, 174-182.
- Mojica, F.J., Juez, G., and Rodriguez-Valera, F. (1993). Transcription at different salinities of *Haloflex mediterranei* sequences adjacent to partially modified PstI sites. *Mol Microbiol* 9, 613-621.
- Mojica, F.J.M., Diez-Villasenor, C., Garcia-Martinez, J., and Almendros, C. (2009). Short motif sequences determine the targets of the prokaryotic CRISPR defence system. *Microbiology (Reading)* 155, 733-740.
- Moretto, E., and Passafaro, M. (2018). Recent Findings on AMPA Receptor Recycling. *Front Cell Neurosci* 12, 286.
- Moscou, M.J., and Bogdanove, A.J. (2009). A simple cipher governs DNA recognition by TAL effectors. *Science* 326, 1501.
- Nair, D., Hosy, E., Petersen, J.D., Constals, A., Giannone, G., Choquet, D., and Sibarita, J.B. (2013). Super-resolution imaging reveals that AMPA receptors inside synapses are dynamically organized in nanodomains regulated by PSD95. *J Neurosci* 33, 13204-13224.
- Nishiyama, J., Mikuni, T., and Yasuda, R. (2017). Virus-Mediated Genome Editing via Homology-Directed Repair in Mitotic and Postmitotic Cells in Mammalian Brain. *Neuron* 96, 755-768 e755.
- Nusser, Z., Lujan, R., Laube, G., Roberts, J.D., Molnar, E., and Somogyi, P. (1998). Cell type and pathway dependence of synaptic AMPA receptor number and variability in the hippocampus. *Neuron* 21, 545-559.

- Obashi, K., Taraska, J.W., and Okabe, S. (2021). The role of molecular diffusion within dendritic spines in synaptic function. *J Gen Physiol* 153.
- Palay, S.L. (1958). The morphology of synapses in the central nervous system. *Exp Cell Res* 14, 275-293.
- Pourcel, C., Salvignol, G., and Vergnaud, G. (2005). CRISPR elements in *Yersinia pestis* acquire new repeats by preferential uptake of bacteriophage DNA, and provide additional tools for evolutionary studies. *Microbiology (Reading)* 151, 653-663.
- Qi, L.S., Larson, M.H., Gilbert, L.A., Doudna, J.A., Weissman, J.S., Arkin, A.P., and Lim, W.A. (2013). Repurposing CRISPR as an RNA-guided platform for sequence-specific control of gene expression. *Cell* 152, 1173-1183.
- Raghavachari, S., and Lisman, J.E. (2004). Properties of quantal transmission at CA1 synapses. *J Neurophysiol* 92, 2456-2467.
- Rama, S., Zbili, M., and Debanne, D. (2018). Signal propagation along the axon. *Curr Opin Neurobiol* 51, 37-44.
- Ramsey, A.M., Tang, A.H., LeGates, T.A., Gou, X.Z., Carbone, B.E., Thompson, S.M., Biederer, T., and Blanpied, T.A. (2021). Subsynaptic positioning of AMPARs by LRRTM2 controls synaptic strength. *Sci Adv* 7.
- Rizalar, F.S., Roosen, D.A., and Haucke, V. (2021). A Presynaptic Perspective on Transport and Assembly Mechanisms for Synapse Formation. *Neuron* 109, 27-41.
- Romer, P., Hahn, S., Jordan, T., Strauss, T., Bonas, U., and Lahaye, T. (2007). Plant pathogen recognition mediated by promoter activation of the pepper Bs3 resistance gene. *Science* 318, 645-648.
- Sahl, S.J., Hell, S.W., and Jakobs, S. (2017). Fluorescence nanoscopy in cell biology. *Nat Rev Mol Cell Biol* 18, 685-701.
- Scheefhals, N., and MacGillavry, H.D. (2018). Functional organization of postsynaptic glutamate receptors. *Mol Cell Neurosci* 91, 82-94.
- Schwenk, J., Baehrens, D., Haupt, A., Bildl, W., Boudkkazi, S., Roeper, J., Fakler, B., and Schulte, U. (2014). Regional diversity and developmental dynamics of the AMPA-receptor proteome in the mammalian brain. *Neuron* 84, 41-54.
- Schwenk, J., Boudkkazi, S., Kocylowski, M.K., Brechet, A., Zolles, G., Bus, T., Costa, K., Kollwe, A., Jordan, J., Bank, J., et al. (2019). An ER Assembly Line of AMPA-Receptors Controls Excitatory Neurotransmission and Its Plasticity. *Neuron* 104, 680-692 e689.
- Schwenk, J., Harmel, N., Brechet, A., Zolles, G., Berkefeld, H., Muller, C.S., Bildl, W., Baehrens, D., Huber, B., Kulik, A., et al. (2012). High-resolution proteomics unravel architecture and molecular diversity of native AMPA receptor complexes. *Neuron* 74, 621-633.
- Sheng, M., and Hoogenraad, C.C. (2007). The postsynaptic architecture of excitatory synapses: a more quantitative view. *Annu Rev Biochem* 76, 823-847.
- Sherrington, C., S (1897). The central nervous system. In *A text book of physiology*, M. Foster, ed. (London: Macmillan and Co.), p. 929.
- Sohal, V.S., and Rubenstein, J.L.R. (2019). Excitation-inhibition balance as a framework for investigating mechanisms in neuropsychiatric disorders. *Mol Psychiatry* 24, 1248-1257.
- Sporns, O. (2016). Connectome Networks: From Cells to Systems. In *Micro-, Meso- and Macro-Connectomics of the Brain*, H. Kennedy, D.C. Van Essen, and Y. Christen, eds. (Cham (CH)), pp. 107-127.
- Suarez, L.E., Markello, R.D., Betzel, R.F., and Misic, B. (2020). Linking Structure and Function in Macroscale Brain Networks. *Trends Cogn Sci* 24, 302-315.
- Sudhof, T.C. (2012). The presynaptic active zone. *Neuron* 75, 11-25.
- Sudhof, T.C. (2021). The cell biology of synapse formation. *J Cell Biol* 220.
- Suh, Y.H., Chang, K., and Roche, K.W. (2018). Metabotropic glutamate receptor trafficking. *Mol Cell Neurosci* 91, 10-24.
- Sun, Y., Smirnov, M., Kamasawa, N., and Yasuda, R. (2021). Rapid Ultrastructural Changes in the PSD and Surrounding Membrane after Induction of Structural LTP in Single Dendritic Spines. *J Neurosci* 41, 7003-7014.
- Suzuki, K., Tsunekawa, Y., Hernandez-Benitez, R., Wu, J., Zhu, J., Kim, E.J., Hatanaka, F., Yamamoto, M., Araoka, T., Li, Z., et al. (2016). In vivo genome editing via CRISPR/Cas9 mediated homology-independent targeted integration. *Nature* 540, 144-149.
- Takeuchi, T., Duzkiewicz, A.J., and Morris, R.G. (2014). The synaptic plasticity and memory hypothesis: encoding, storage and persistence. *Philos Trans R Soc Lond B Biol Sci* 369, 20130288.
- Tang, A.H., Chen, H., Li, T.P., Metzbowler, S.R., MacGillavry, H.D., and Blanpied, T.A. (2016). A trans-synaptic nanocolumn aligns neurotransmitter release to receptors. *Nature* 536, 210-214.
- Thomas, K.R., and Capecchi, M.R. (1987). Site-directed mutagenesis by gene targeting in mouse embryonic stem cells. *Cell* 51, 503-512.
- Traynelis, S.F., Wollmuth, L.P., McBain, C.J., Menniti, F.S., Vance, K.M., Ogden, K.K., Hansen, K.B., Yuan, H., Myers, S.J., and Dingledine, R. (2010). Glutamate receptor ion channels: structure, regulation, and function. *Pharmacol Rev* 62, 405-496.
- Uemura, T., Mori, T., Kurihara, T., Kawase, S., Koike, R., Satoga, M., Cao, X., Li, X., Yanagawa, T., Sakurai, T., et al. (2016). Fluorescent protein tagging of endogenous protein in brain neurons using CRISPR/Cas9-mediated knock-in and in utero electroporation techniques. *Sci Rep* 6, 35861.
- van Leeuwenhoek, A. (1695). "Arcana naturae detecta", a collection of his letters Royal Society of London.
- van Vreeswijk, C., and Sompolinsky, H. (1996). Chaos in neuronal networks with balanced excitatory and inhibitory activity. *Science* 274, 1724-1726.
- Vangindertael, J., Camacho, R., Sempels, W., Mizuno, H., Dedecker, P., and Janssen, K.P.F. (2018). An introduction to optical super-resolution microscopy for the adventurous biologist. *Methods Appl Fluoresc* 6, 022003.
- Watson, J.F., Pinggera, A., Ho, H., and Greger, I.H. (2021). AMPA receptor anchoring at CA1 synapses is

- 
- determined by N-terminal domain and TARP gamma8 interactions. *Nat Commun* 12, 5083.
- Wu, X., Cai, Q., Shen, Z., Chen, X., Zeng, M., Du, S., and Zhang, M. (2019). RIM and RIM-BP Form Presynaptic Active-Zone-like Condensates via Phase Separation. *Mol Cell* 73, 971-984 e975.
- Wu, Y.L., Tschanz, A., Krupnik, L., and Ries, J. (2020). Quantitative Data Analysis in Single-Molecule Localization Microscopy. *Trends Cell Biol* 30, 837-851.
- Xie, X., Liaw, J.S., Baudry, M., and Berger, T.W. (1997). Novel expression mechanism for synaptic potentiation: alignment of presynaptic release site and postsynaptic receptor. *Proc Natl Acad Sci U S A* 94, 6983-6988.
- Xu, K., Zhong, G., and Zhuang, X. (2013). Actin, spectrin, and associated proteins form a periodic cytoskeletal structure in axons. *Science* 339, 452-456.
- Zeng, M., Chen, X., Guan, D., Xu, J., Wu, H., Tong, P., and Zhang, M. (2018). Reconstituted Postsynaptic Density as a Molecular Platform for Understanding Synapse Formation and Plasticity. *Cell* 174, 1172-1187 e1116.
- Zeng, M., Shang, Y., Araki, Y., Guo, T., Haganir, R.L., and Zhang, M. (2016). Phase Transition in Postsynaptic Densities Underlies Formation of Synaptic Complexes and Synaptic Plasticity. *Cell* 166, 1163-1175 e1112.
- Zhang, H., Qin, C., An, C., Zheng, X., Wen, S., Chen, W., Liu, X., Lv, Z., Yang, P., Xu, W., et al. (2021). Application of the CRISPR/Cas9-based gene editing technique in basic research, diagnosis, and therapy of cancer. *Mol Cancer* 20, 126.
- Zieger, H.L., and Choquet, D. (2021). Nanoscale synapse organization and dysfunction in neurodevelopmental disorders. *Neurobiol Dis* 158, 105453.
- Ziff, E.B. (1997). Enlightening the postsynaptic density. *Neuron* 19, 1163-1174.







# 2

---

## **ORANGE: A CRISPR/Cas9-based genome editing toolbox for epitope tagging of endogenous proteins in neurons**

Jelmer Willems<sup>1\*</sup>, Arthur P. H. de Jong<sup>1\*</sup>, Nicky Scheefhals<sup>1</sup>, Eline Mertens<sup>1</sup>, Lisa A. E. Catsburg<sup>1</sup>, Rogier B. Poorthuis<sup>2</sup>, Fred de Winter<sup>3</sup>, Joost Verhaagen<sup>3</sup>, Frank J. Meye<sup>2</sup>, Harold D. MacGillavry<sup>1</sup>

PLoS Biology (2020); 18(4): e3000665

---

\* These authors contributed equally to this work.

<sup>1</sup>Cell Biology, Neurobiology and Biophysics, Department of Biology, Faculty of Science, Utrecht University, Utrecht, the Netherlands

<sup>2</sup>Department of Translational Neuroscience, UMC Utrecht Brain Center, Utrecht University, Utrecht, the Netherlands,

<sup>3</sup>Laboratory for Neuroregeneration, Netherlands Institute for Neuroscience, Royal Netherlands Academy of Arts and Sciences, Amsterdam, the Netherlands

---

## ABSTRACT

The correct subcellular distribution of proteins establishes the complex morphology and function of neurons. Fluorescence microscopy techniques are invaluable to investigate subcellular protein distribution, but they suffer from the limited ability to efficiently and reliably label endogenous proteins with fluorescent probes. We developed ORANGE: Open Resource for the Application of Neuronal Genome Editing, which mediates targeted genomic integration of epitope tags in rodent dissociated neuronal culture, in organotypic slices, and in vivo. ORANGE includes a knock-in library for in-depth investigation of endogenous protein distribution, viral vectors and a detailed two-step cloning protocol to develop knock-ins for novel targets. Using ORANGE with (live-cell) superresolution microscopy, we revealed the dynamic nanoscale organization of endogenous neurotransmitter receptors and synaptic scaffolding proteins, as well as previously uncharacterized proteins. Finally, we developed a mechanism to create multiple knock-ins in neurons, mediating multiplex imaging of endogenous proteins. Thus, ORANGE enables quantification of expression, distribution, and dynamics for virtually any protein in neurons at nanoscale resolution.

## INTRODUCTION

Neurons are highly complex cells with numerous functionally and structurally distinct subcellular compartments that are each composed of unique repertoires of molecular components. The correct targeting and localization of protein complexes and their spatial organization within subcellular domains underlies virtually every aspect of neuronal functioning. Thus, investigating the dynamic distribution of proteins in neurons is critical for a mechanistic understanding of brain function. Precise localization of individual protein species using fluorescence microscopy has become an essential technique in many fields of neuroscience and, in particular, for studies on synaptic function, in which protein mislocalization at scales less than 1  $\mu\text{m}$  can already significantly affect synaptic efficacy [1]. Recently developed superresolution imaging methods now routinely achieve spatial resolution as low as tens of nanometers, allowing determination of protein distributions at the molecular scale [2,3]. Consequently, these methods are highly sensitive to experimental alterations that affect protein organization, and efficient labeling techniques that accurately report the localization of endogenous proteins are critical.

Visualization of subcellular protein localization typically relies on antibody-based labeling approaches or overexpression of fluorescently tagged proteins, but both techniques have serious limitations [4]. Immunostaining largely relies on the availability of specific antibodies, which has severely hampered progress for many targets. Immunostaining also precludes labeling and visualization of protein dynamics in live cells, and penetration of antibodies in thick tissue samples is challenging. Additionally, it is often desirable to sparsely label individual cells to measure protein distribution at high contrast, which is difficult to achieve with immunostaining-based techniques. Expression of fluorescently tagged proteins overcomes many of these issues; however, exogenous expression of recombinant proteins can lead to mislocalization and can induce severe morphological and/or physiological artifacts. For instance, overexpression of synaptic proteins such as postsynaptic density protein 95 (PSD95) and SH3 and multiple ankyrin repeat domains protein (Shank) have pronounced effects on synapse number, content, structure, and physiology [5-8]. Exorbitant expression levels can be circumvented by a replacement strategy in which a tagged protein is expressed in a knock-down or knock-out background [9], but this will, at best, only approximate endogenous levels and is uncoupled from endogenous transcriptional or translational

regulatory mechanisms. Recombinant antibody-based approaches have been developed for live-cell imaging of neuronal proteins, but they have so far been restricted to a few targets [10-14]. The generation of fluorescently tagged knock-ins (for instance, in mouse lines) prevents these issues. However, the generation and maintenance of transgenic animals is costly and time consuming, making it an inefficient approach for high-throughput tagging of neuronal proteins. Also, generally, transgenic labeling leads to expression of tagged proteins in all cells, thus limiting the options for imaging in individual cells.

In view of the limitations of current techniques, we sought to develop a protein labeling strategy that meets the following criteria: (1) accurately reports a single protein species at endogenous protein levels and with spatiotemporal expression pattern; (2) can be rapidly developed and expanded to many proteins of interest; (3) does not interfere with protein localization and function; (4) can be applied in dissociated neuronal cultures, organotypic slice culture, and *in vivo*; (5) allows for sparse labeling of neurons; and (6) is compatible with (superresolution) light microscopy of live as well as fixed tissues. We reasoned that labeling of endogenous proteins with fluorescent tags using targeted gene-editing techniques would fulfill all these criteria.

Targeted gene editing using CRISPR/Cas9 facilitates the introduction of donor DNA at specific loci in the genome, effectively tagging endogenous proteins of interest [15,16]. For neuronal cells, several CRISPR/Cas9-based knock-in strategies have been developed, relying on different mechanisms to repair double-stranded breaks (DSBs) introduced by Cas9. One strategy is based on homology-directed repair (HDR) to insert donor DNA into the genomic locus [17,18]. However, HDR preferentially occurs during the S/G2 phases of the cell cycle and is significantly down-regulated in postmitotic cells [19]. This limits the application of HDR in neurons, although successful integration can still be observed with highly elevated donor DNA levels or via a combination of donor cleavage and microhomology arms [20,21]. Additionally, in order to be efficient, HDR requires the addition of long homology arms to the donor DNA, which can be laborious to generate, considerably complicating the development of knock-in constructs.

Alternative strategies are based on nonhomologous end joining (NHEJ) to repair DSBs, which is active throughout the cell cycle, as well as in postmitotic cells, and can be used to insert donor DNA with high efficiency [22-24]. Based on NHEJ, the homology-independent targeted integration (HITI) method for endogenous protein tagging in postmitotic neurons was previously developed and outperformed HDR-based methods [21,24]. We hypothesized that HITI would provide an accessible and scalable approach for the tagging of endogenous proteins in neurons, in dissociated neuronal cultures and organotypic cultures, and *in vivo*. However, applications of this method have so far been limited to a few target proteins [21,24-26]. In addition, designing and cloning of knock-in constructs, the compatibility of DNA delivery methods for various tissue preparations, and validation of NHEJ-based knock-in accuracy and efficiency have until now been quite challenging and have not been addressed systematically.

Here, based on HITI, we developed ORANGE, an Open Resource for the Application of Neuronal Genome Editing, which offers researchers the means to endogenously tag proteins of interest in neurons, allowing for the accurate investigation of protein expression, localization, and dynamics. This toolbox includes (1) a single template vector that contains the complete knock-in cassette, which can be adapted in two straightforward cloning steps to tag virtually any protein of interest, and (2) a library of readily usable knock-in constructs targeting a set of 38 proteins. This library encompasses a wide variety of proteins, including

cytoskeletal components, signaling molecules, endosomal markers, presynaptic and postsynaptic scaffolds, adhesion complexes, and receptors. We show that this tagging strategy facilitates protein labeling in dissociated neuronal culture, in organotypic slice cultures, and in vivo with high accuracy and without overexpression artifacts. Moreover, we demonstrate that this toolbox facilitates live-cell and superresolution imaging of endogenous proteins to resolve their localization and dynamics in neurons at high spatial and temporal resolution. We furthermore show that ORANGE can be combined with the Cre-Lox system driving the conditional expression of genetically encoded reporters. Finally, we developed a Cre-dependent knock-in strategy for multiplex labeling of proteins within single cells. Altogether, we present a robust and easy-to-implement toolbox for the tagging and visualization of endogenous proteins in postmitotic neurons, allowing for in-depth investigation of diverse neuronal cell biological processes.

## RESULTS

### ORANGE knock-in toolbox to fluorescently tag endogenous proteins in neurons

We first aimed to design a simple workflow to facilitate the rapid generation of knock-in constructs using conventional molecular cloning approaches. To this end, we designed a single CRISPR/Cas9 knock-in template vector (pORANGE) based on the original NHEJ-mediated HITI method [24]. Our design allows for the flexible insertion of a unique 20-nucleotide target sequence that guides Cas9 to the genomic locus of interest and a donor sequence containing the knock-in sequence (e.g., green fluorescent protein [GFP]) that will be inserted in the targeted genomic locus (Fig 1A and S1 Fig). The generated knock-in construct contains all elements required for targeted CRISPR/Cas9-based genome editing: (1) a U6-driven expression cassette for the guide RNA (gRNA) targeting the genomic locus of interest, (2) the donor sequence containing the (fluorescent) tag, and (3) a Cas9 expression cassette driven by a universal  $\beta$ -actin promoter (Fig 1A). The donor sequence is generated by standard PCR, with primers introducing a short linker and Cas9 target sequences flanking the donor (Fig 1A). These target sequences are identical to the genomic target sequence. As a result, the gRNA used to create a genomic DSB is also used to remove the donor DNA from the plasmid, allowing for its genomic integration. Importantly, the orientation of the target sequence and protospacer adjacent motif (PAM) sites flanking the donor is inverted compared with the genomic sequence to guarantee that integration occurs in the correct orientation (Fig 1B). For a detailed description of genomic target sequence selection, gRNA sequence, and donor PCR primer design, we refer to the design and cloning protocol in the Materials and methods section (also see S1 Fig). This approach is flexible because the donor sequence can be easily exchanged for different fluorophores, self-labeling enzymes like Halo, small epitope tags like hemagglutinin (HA) and FLAG, or larger donors like GFP-P2A-Cre to meet the specific demands for the experiment (Fig 1C). We found that this cloning strategy is easy to employ and enables the rapid and flexible generation of knock-in constructs.

Using the pORANGE template vector, we designed and generated a library providing knock-in constructs to endogenously label 38 proteins for fluorescence imaging (Fig 2, S2 Fig, and S5 Table). To cover the many areas of neuronal cell biology, we selected proteins representing various molecular processes, including cytoskeletal components, intracellular signaling molecules, trafficking proteins, synaptic scaffolds, and receptor subunits. We were able to directly image the fluorescent GFP signal for many endogenously tagged proteins. However, for less abundant proteins (e.g., calcium channel subunits, presynaptic active zone proteins, and N-methyl-D-aspartate (NMDA) receptor subunits), amplification of the GFP

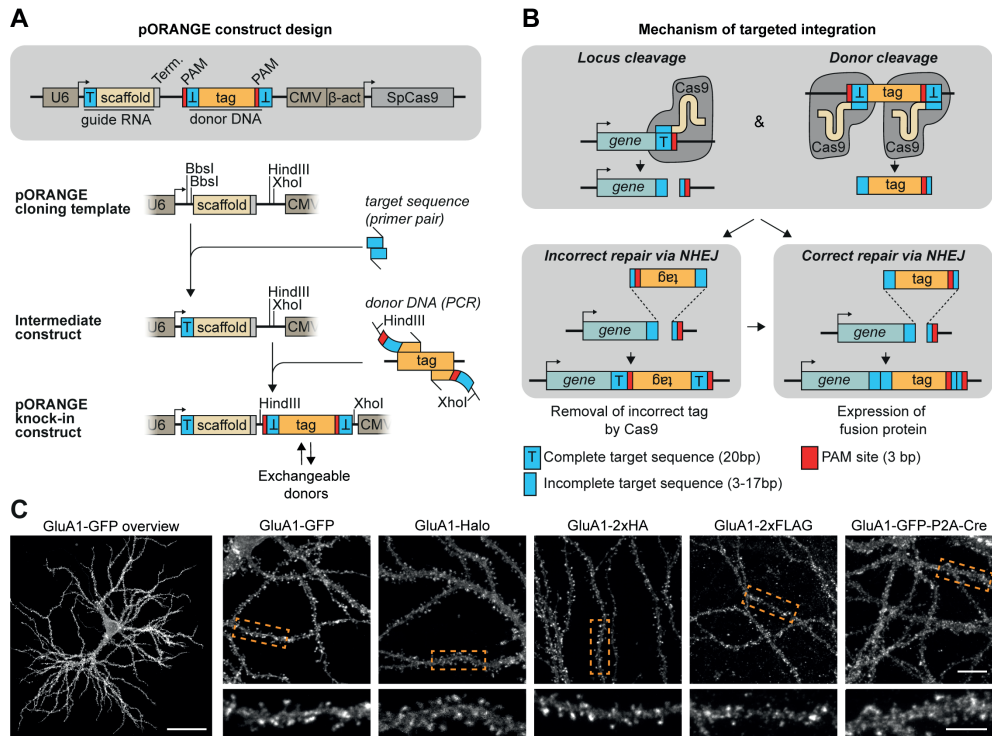


**Fig 1. ORANGE: An easy-to-implement toolbox for endogenous tagging of proteins in neurons**

(A) Overview of the pORANGE knock-in construct. To clone knock-in constructs, first a 20-bp target sequence for the genomic locus of interest is ligated in the guide RNA cassette. Then, the donor sequence containing the tag of interest is generated by PCR and inserted in the donor DNA cassette. (B) Mechanism of ORANGE-mediated gene targeting. (C) Examples of knock-in neurons expressing GluA1 tagged with GFP, HaloTag, small epitope tags (2× HA, 2× FLAG), or GFP-P2A-Cre recombinase. Dashed boxes indicate zooms. Scale bars, 40 μm for the GluA1-GFP overview (far left), 10 μm for individual overviews, and 5 μm for the zooms. GFP, green fluorescent protein; NHEJ, nonhomologous end joining; ORANGE, Open Resource for the Application of Neuronal Genome Editing; T, target sequence; Term, termination sequence. PAM: protospacer adjacent motif; CMV, cytomegalovirus; β-act, β-actin; SpCas9, *Streptococcus pyogenes* Cas9, GluA, Glutamate receptor AMPA 1; HA, hemagglutinin.

tag with anti-GFP antibodies was required to visualize protein distribution (indicated with an asterisk in Fig 2 and S2 Fig). Throughout this study, we refer to knock-in constructs as the name of the protein that is labeled: in N-terminally tagged proteins, the tag is in front of the protein name, and in C-terminally tagged proteins, the tag is after.

For several proteins in our library, no specific antibodies are available. In order to compare their subcellular distribution to what is reported in literature (S1 Table), we costained several knock-ins with pre- or postsynaptic markers and confirmed the expected distribution for all of the constructs we evaluated (S3 Fig). Together, our ORANGE toolbox includes a broad library of knock-in constructs and provides an efficient strategy to adapt or design constructs with relative ease using standardized cloning techniques.

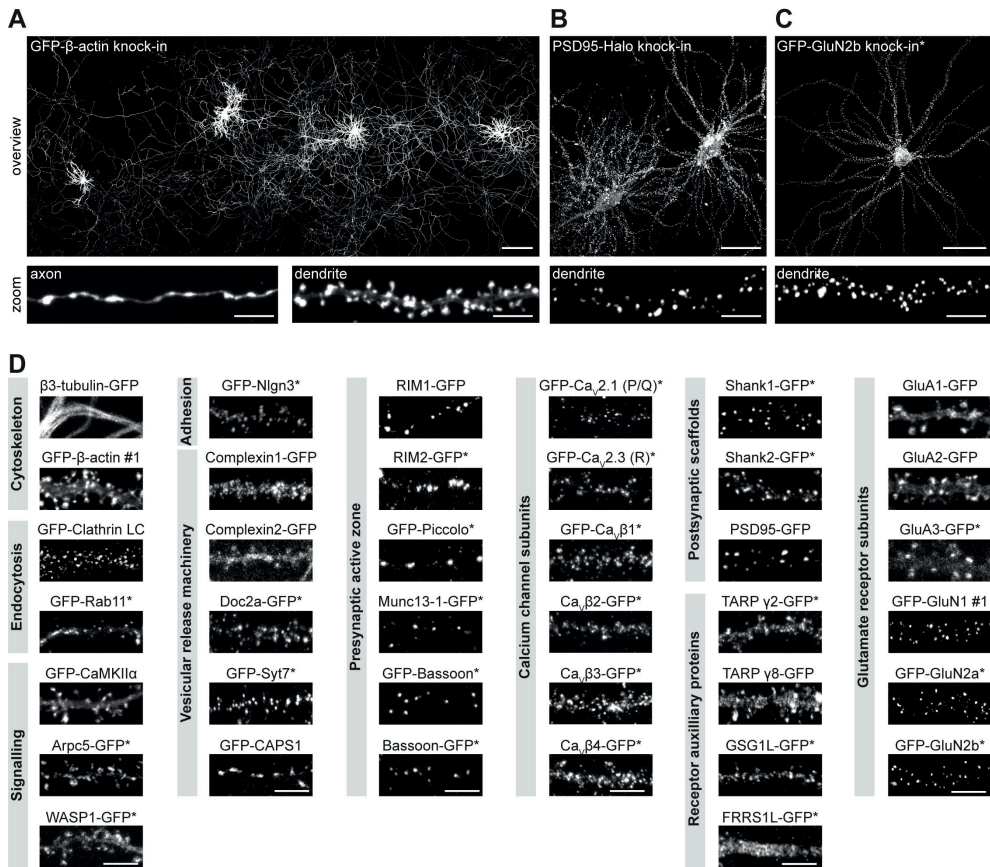


**Fig 2. A versatile ORANGE knock-in library for endogenous tagging of proteins in neurons**

(A) Example at low magnification showing four GFP- $\beta$ -actin knock-in neurons (DIV 21). Zooms show an axon and dendrite, respectively. Scale bars: overview, 200  $\mu$ m; zoom, 5  $\mu$ m. (B) Example of two PSD95-Halo knock-in neurons (DIV 21). Zoom shows a single dendrite. Scale bars: overview, 40  $\mu$ m; zoom, 5  $\mu$ m. (C) Example of GFP-GluN2b knock-in neuron (DIV 21). Scale bars: overview, 40  $\mu$ m; zoom, 5  $\mu$ m. (D) Representative images of ORANGE knock-in neurons, categorized according to protein function or subcellular localization. Neurons were transfected at DIV 3 and imaged at DIV 21. Scale bars, 5  $\mu$ m. Asterisk indicates signal enhancement with anti-GFP staining (Alexa488 or Alexa647). GFP, green fluorescent protein; ORANGE, Open Resource for the Application of Neuronal Genome Editing; DIV, day in vitro; PSD95, postsynaptic protein 95; GluA, glutamate receptor AMPA 1; GluN, Glutamate receptor NMDA 1; LC, light chain; Rab11, ras-related protein 11; CaMKII $\alpha$ , Calcium/calmodulin-dependent protein kinase type II subunit alpha; Arpc5, actin-related protein 2/3 complex subunit 5; WASP1, Wiskott-Aldrich syndrome protein 1; Nlgn3, neuroligin 3; Doc2a, double C2-like domain-containing protein a; Syt7, Synaptotagmin 7; CAPS1, Calcium-dependent activator protein for secretion 1, RIM: Rab3-interacting molecule; Munc13, mammalian uncoordinated 13, CAV, voltage-dependent Ca<sup>2+</sup>-channel, Shank, SH3 and multiple ankyrin repeat domains protein; TARP, Transmembrane AMPAR regulatory protein; GSG1L, Germ cell-specific gene 1-like protein; FRRS1L, Ferric-chelate reductase 1-like protein.

### Viral delivery of ORANGE to label endogenous proteins in dissociated neuronal cultures and organotypic slice cultures and in vivo

Adeno-associated virus (AAV)-based DNA delivery has become a valuable method of administration, especially for in vivo applications. To test whether this approach is compatible

with ORANGE, we generated HaloTag knock-in constructs for PSD95 and Glutamate receptor AMPA 1 (GluA1) and subcloned these into AAV vectors. AAVs were injected in the cornu Ammonis region 1 (CA1) of the hippocampus in Cas9-P2A-GFP transgenic mice [27] (Fig 3A). After 4 weeks, acute slices were prepared and live-stained with Halo-JF646. This resulted in fast labeling deep into the tissue. For both PSD95 and GluA1, efficient knock-in labeling was observed in CA1, as well as in CA3 and subiculum, with additional labeling in the dentate gyrus (Fig 3C and 3D). At higher magnifications, we only observed neurons with punctate, synaptic expression of PSD95-Halo. Similarly, although to a lesser extent, GluA1-Halo was also highly enriched in dendritic spines, as expected (Fig 3E and G). Finally, we used superresolution gated stimulated-emission depletion (gSTED) imaging to resolve individual synapses at high resolution (Fig 3F and H).

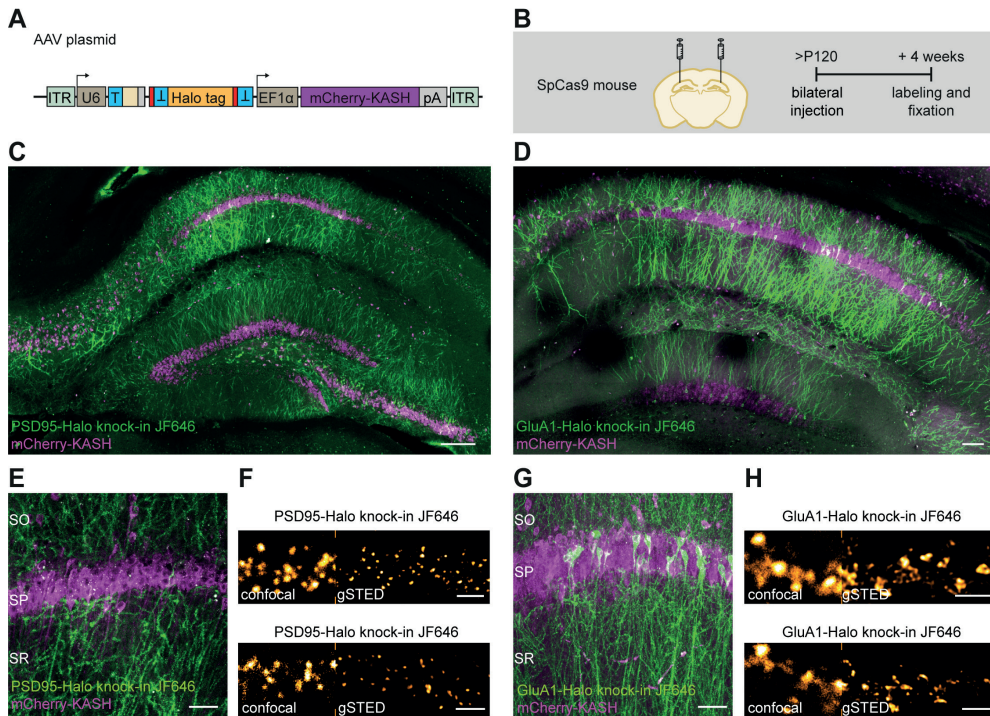


**Fig 3. ORANGE mediates in vivo genome editing**

(A) Overview of ORANGE AAV plasmid. (B) Workflow and time line for in vivo genome editing. (C and D) Confocal images of acute slices from SpCas9 mouse hippocampus injected with PSD95-Halo knock-in (C) and GluA1-Halo knock-in (D) AAV vectors visualized with Halo-JF646 ligand (green). Infected cells are positive for mCherry-KASH (magenta). Scale bar, 100  $\mu$ m. (E and G) Zooms for acute slices as shown in (C) and (D), respectively. Scale bar, 40  $\mu$ m. (F and H) Representative images of confocal and gSTED microscopy in acute slices. Shown are dendrites positive for PSD95-Halo (F) and GluA1-Halo knock-in (H). Scale bar, 2  $\mu$ m. AAV, adeno-associated virus; gSTED, gated stimulated-emission depletion; ORANGE, Open Resource for the Application of Neuronal Genome Editing; SO, stratum oriens; SP, stratum pyramidale; SR, stratum radiatum. SpCas9, Streptococcus pyogenes Cas9; PSD95, postsynaptic protein 95, GluA, Glutamate receptor AMPA, JF646 Janelia Fluor 646; KASH, Klarsicht, ANC-1, Synce Homology; ITR, inverted terminal repeat; T, target sequence; EF1 $\alpha$ , elongation factor 1 $\alpha$ ; pA, polyadenylation.

Next, we tested whether ORANGE knock-ins could also be delivered using lentiviral (LV) vectors. We divided the ORANGE knock-in cassette over two LV constructs (S4A Fig) because the full cassette exceeds the packaging limit of LV particles. Also, premature coexpression



---

of Cas9 and the gRNA during the production of viral particles in packaging cells would lead to removal of the donor DNA. Both in dissociated hippocampal cultures and in organotypic slice cultures, we observed knock-ins, showing that LVs can be used to successfully express ORANGE knock-ins (S4 Fig). Together, these results show that ORANGE is compatible with various modes of DNA delivery suitable for labeling in dissociated neuronal cultures, in organotypic slice cultures and in vivo, broadening the potential applications of this CRISPR/Cas9 genome editing toolbox.

### **ORANGE enables fast and accurate donor integration**

To test the rate of donor integration and subsequent expression of tagged proteins with lipofection-based DNA delivery, we cotransfected dissociated hippocampal neurons at day in vitro (DIV) 3 with a  $\beta$ 3-tubulin-GFP knock-in construct and a construct for soluble mCherry expression (S5 Fig). Because of the high protein turnover rate of  $\beta$ 3-tubulin, integration of the donor should be rapidly observable by expression of the tagged protein. Successful labeling of  $\beta$ 3-tubulin was observed within 24 hours after transfection, albeit at relatively low efficiency ( $1.1\% \pm 0.2\%$   $\beta$ 3-tubulin GFP+/mCherry+ double positive cells). Labeling efficiency increased 10-fold over time and reached a plateau around 96 hours after transfection ( $10.9\% \pm 0.1\%$   $\beta$ 3-tubulinGFP+/mCherry+; S5 Fig), indicating that donor integration preferentially takes place within the first days after transfection.

Next, we determined the accuracy of genomic integration for our knock-in library using confocal microscopy. Expression patterns were in line with available literature (S1 Table), and we did not observe aberrant or diffuse expression of the integrated tag for any of the knock-in constructs in our library. This indicates that off-target integration, or unintended GFP expression directly from the knock-in plasmid, did not occur or is extremely rare (see Discussion).

To get a detailed overview of the precision of donor integration into the targeted genomic locus, we analyzed the genomic sequence after integration for 28 GFP knock-in constructs using next-generation sequencing (S6 Fig). We detected a high frequency of in-frame integration of the GFP tag in the targeted locus for almost all knock-ins (S6B and C Fig). Besides correct integration, we found various insertions and deletions leading to frameshift mutations (S6B and D Fig). We noted that the frequency of indels was variable between different knock-ins, which is likely due to the difference in target sequences, which has been reported to highly determine the accuracy of Cas9-mediated cleavage and NHEJ-mediated repair [28,29]. Notably, the accuracy of donor integration did not correlate with the Doench on-target score [30] (Pearson  $r$ :  $-0.15$ ,  $R^2$ :  $0.02$ ,  $P < 0.05$ ) or Bae out-of-frame score [31] (Pearson  $r$ :  $0.25$ ,  $R^2$ :  $0.06$ ,  $P > 0.05$ ) (S6E and F Fig). In conclusion, although out-of-frame integration occurs at varying frequencies as shown by next-generation sequencing, imaging of our knock-in library suggests that this does not result in a fluorescent signal or aberrant protein expression.

We noted that several of the knock-in constructs with lower in-frame integration, such as GFP- $\beta$ -actin and GFP-Glutamate receptor NMDA 1 (GluN1), also had a low efficiency of knock-in expression in cultured neurons. To test whether this is gene specific or guide sequence specific, and in an attempt to generate more efficient knock-in constructs for these genes, we designed extra knock-in constructs for  $\beta$ -actin (GFP- $\beta$ -actin #2) and GluN1 (GFP-GluN1 #2 and #3) by making use of alternative PAM sites (S7 Fig). All alternative PAM site variants resulted in successful GFP knock-ins in cultured neurons, with expected GFP expression patterns. Again, we did not observe neurons with aberrant distribution of GFP

signal. For both genes, we found that various PAM sites along the same genomic region varied widely in their knock-in efficiency relative to the number of transfected neurons (GFP- $\beta$ -actin knock-in #1:  $0.42\% \pm 0.09\%$ , #2:  $7.4\% \pm 1.1\%$ , Student t test,  $P < 0.05$ ; GFP-GluN1 knock-in #1:  $0.43\% \pm 0.04\%$ , #2:  $3.0\% \pm 0.7\%$ , #3:  $5.6\% \pm 0.4\%$ , ANOVA,  $P < 0.05$ ). These results show that knock-in efficiency is highly dependent on the target site used for integration.

### **ORANGE reliably labels proteins without overexpression artifacts**

To further determine whether the integrated fluorescent tag reliably labels the endogenous target protein, we compared the localization of several knock-ins with specific antibody staining in confocal microscopy. First, we tested the knock-in construct for PSD95, a core postsynaptic scaffold molecule [32] (Fig 4). We transfected dissociated hippocampal cultures with the PSD95-GFP knock-in construct well before synaptogenesis (DIV 3) and fixed the neurons at a mature stage (DIV 21) (Fig 4A-G). In all neurons with a detectable GFP signal, the GFP signal was found in a punctate pattern enriched in dendritic spines, characteristic for endogenous PSD95 expression. The GFP signal closely colocalized with immunolabeled PSD95 and showed a strong correlation with intensity of PSD95 immunostaining in PSD95-GFP knock-in neurons (Pearson  $r$ : 0.72,  $R^2$ : 0.51,  $P < 0.001$ ,  $n = 550$  synapses from 11 neurons; Fig 4B). To test whether the knock-in affects total PSD95 levels, we used the PSD95 antibody staining to compare protein levels between PSD95-GFP knock-in and control neurons that were transfected with soluble GFP (GFP control). Although we observed that, in a subpopulation of PSD95 knock-in neurons, protein levels were modestly lower, PSD95 levels in PSD95-GFP knock-in neurons (relative fluorescence intensity:  $0.84 \pm 0.04$ ,  $n = 17$  neurons) were on average comparable to GFP control neurons ( $0.98 \pm 0.02$ ,  $n = 15$  neurons, ANOVA,  $P > 0.05$ ) (Fig 4C; inset). In contrast, overexpression of PSD95-GFP significantly increased synaptic PSD95 protein levels (relative fluorescence intensity:  $4.2 \pm 0.4$ ,  $n = 17$  neurons,  $P < 0.001$ ). Moreover, synapse size was significantly increased in neurons overexpressing PSD95 ( $0.18 \pm 0.01 \mu\text{m}^2$ ) compared with GFP control neurons ( $0.13 \pm 0.01 \mu\text{m}^2$ , ANOVA,  $P < 0.001$ ) but was unaffected in PSD95-GFP knock-in neurons ( $0.14 \pm 0.001 \mu\text{m}^2$ ,  $P > 0.05$ ; Fig 4D). Lastly, we found that PSD95 was significantly more enriched at synapses in PSD95 knock-in cells (ratio synapse/shaft intensity:  $17.6 \pm 1.4$ ) compared with PSD95-overexpressing neurons ( $11.8 \pm 1.0$ , Student t test,  $P < 0.01$ ; Fig 3E), indicating that a large fraction of overexpressed PSD95 mislocalized to the dendritic shaft.

Transfection of knock-in constructs did not always result in successful knock-in of GFP (S5-7 Fig). To determine whether in transfected but GFP knock-in-negative neurons integration of the GFP tag was simply not successful or integration introduced indels affecting protein expression, we cotransfected neurons with the PSD95-GFP knock-in construct with a Homer1c-mCherry overexpression construct to label synapses. We measured PSD95 levels in Homer1c-mCherry-positive neurons that did not show detectable PSD95-GFP signal (Fig 4F and G). In most of these GFP-negative neurons, PSD95 protein levels were significantly down-regulated (relative fluorescence intensity:  $0.41 \pm 0.06$ ,  $n = 20$  neurons) compared with neurons cotransfected with the empty pORANGE template vector and Homer1c-mCherry ( $0.99 \pm 0.02$ ,  $n = 20$  neurons, Student t test,  $P < 0.001$ ), suggesting partial or complete knock-out of the target protein in transfected but knock-in-negative neurons.

In addition to PSD95, we measured protein levels for several other proteins, including Shank2, Calcium/calmodulin-dependent protein kinase type II subunit alpha (CaMKII $\alpha$ ),  $\beta$ -actin (S8 Fig), and the presynaptic active zone protein Bassoon (Fig 4H

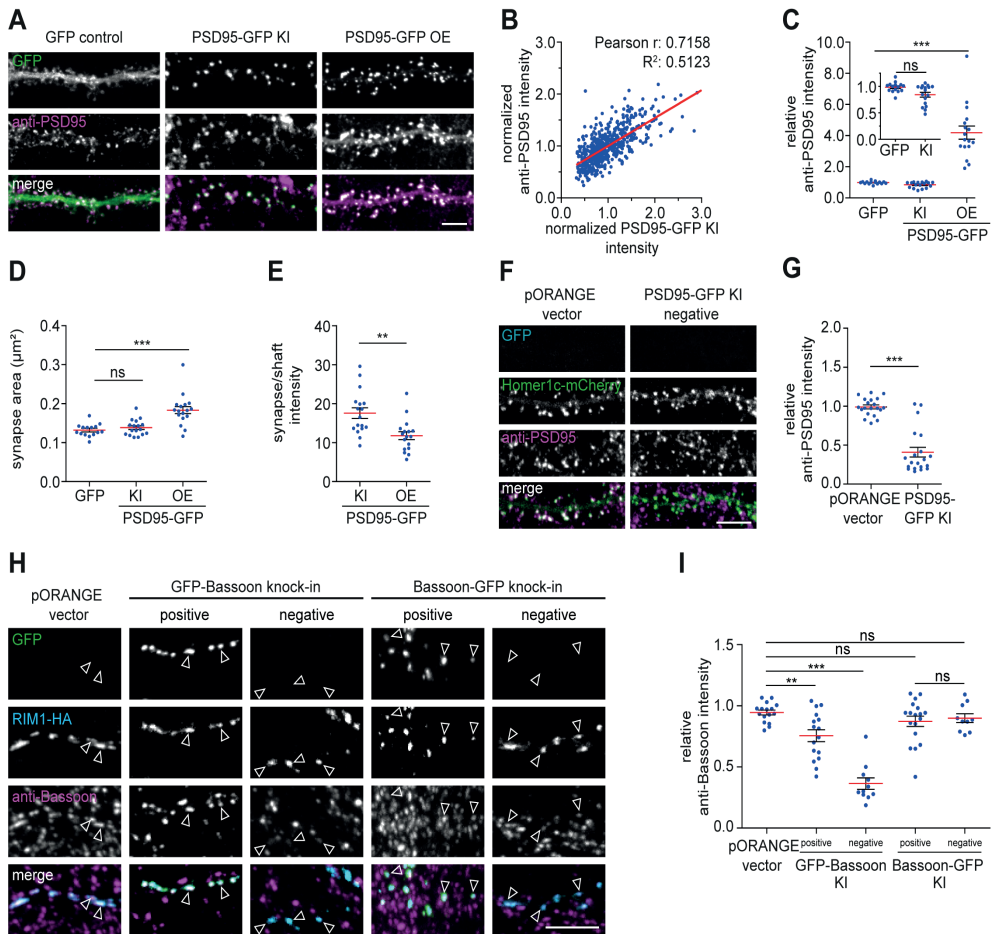


**Fig 4. Validation of ORANGE labeling efficiency**

(A) Representative images of dendrites transfected with soluble GFP, PSD95-GFP knock-in (KI) construct, or a PSD95-GFP overexpression construct (green) stained with anti-PSD95 (magenta, Alexa568). DIV 21. Scale bar, 5  $\mu\text{m}$ . (B) Correlation between PSD95-GFP KI and anti-PSD95 staining intensity. (C) Quantification of synaptic PSD95 levels, (D) synapse area, and (E) PSD95 synapse/shaft intensity. (F) Representative images of dendrites coexpressing Homer1c-mCherry (green) and either the empty pORANGE template vector or PSD95-GFP KI construct (blue) stained with anti-PSD95 (magenta, Alexa647). DIV 21. Scale bar, 5  $\mu\text{m}$ . (G) Quantification of PSD95 levels in transfected but KI-negative neurons. Data are represented as means  $\pm$  SEM. \*  $P < 0.05$ , \*\*  $P < 0.01$ , \*\*\*  $P < 0.001$ , ANOVA or Student t test. Underlying data can be found in S1 Data. GFP, green fluorescent protein; KI, knock-in; ns, not significant; ORANGE, Open Resource for the Application of Neuronal Genome Editing; PSD95, postsynaptic protein 95; DIV, day in vitro; OE, overexpression; RIM1, Rab3-interacting molecule 1; HA, hemagglutinin.

and I) in successful knock-in neurons as well as in knock-in-negative neurons. Additionally, taking advantage of the fact that Bassoon tolerates both N-terminal and C-terminal tagging (S1 Table) [33], we designed GFP-Bassoon and Bassoon-GFP knock-in constructs to compare the effect of tagging the same protein at different positions in the gene. Both N-terminal and C-terminal Bassoon knock-ins showed an identical, punctate expression pattern and colocalized with coexpressed Rab3-interacting molecule 1 (RIM1)-HA, a presynaptic marker (Fig 4H). This indicates that, for Bassoon, endogenous tagging either at the N-terminus or

C-terminus does not interfere with protein localization. Using a specific Bassoon antibody, we found that, like PSD95, most knock-in neurons express Bassoon at endogenous levels. However, the N-terminal-tagged knock-in neurons showed a slightly larger fraction of neurons with reduced levels of Bassoon (relative fluorescence intensity:  $0.75 \pm 0.05$ ,  $n = 16$  neurons,  $P < 0.01$ ) compared with C-terminal-tagged ( $0.87 \pm 0.04$ ,  $n = 18$  neurons,  $P > 0.05$ ) and control cells ( $0.94 \pm 0.01$ ,  $n = 16$  neurons). Notably, neurons transfected with (but negative for) the GFP-Bassoon knock-in showed significantly reduced levels of Bassoon ( $0.36 \pm 0.04$ ,  $n = 11$  neurons,  $P < 0.001$ ), whereas transfection of the Bassoon-GFP knock-in did not affect protein levels in knock-in-negative neurons ( $0.90 \pm 0.04$ ,  $n = 10$  neurons, ANOVA,  $P < 0.05$ ). Furthermore, we found that the GFP signal of the Shank2, CaMKII $\alpha$ , and  $\beta$ -actin knock-ins approximated endogenous levels but that the protein levels in knock-in-negative cells varied between constructs (S8 Fig). Thus, although a successful knock-in results in accurate detection of endogenously tagged proteins, erroneous integration may lead to partial knock-out of the targeted gene in knock-in-negative neurons depending on the protein and position of integration. Altogether, these data demonstrate that ORANGE enables successful integration of fluorescent tags at the targeted genomic locus, resulting in expression of fusion proteins, which reliably reports the localization of proteins of interest, without overexpression artifacts.

### Live-cell imaging of endogenous protein dynamics

In addition to imaging fixed cells, the introduction of fluorescent tags allows for imaging of endogenous protein dynamics in living cells. To demonstrate this directly, we performed live-cell imaging on GFP- $\beta$ -actin knock-in neurons. First, we confirmed that N-terminal tagging of endogenous  $\beta$ -actin with GFP did not alter the actin network based on phalloidin staining of fixed neurons (S8 Fig). Second, we acquired time-lapse images of GFP- $\beta$ -actin knock-in neurons showing the characteristic dynamic behavior of actin in dendritic spines [34,35] (Fig 5A). Jasplakinolide (Jasp), which stabilizes actin filaments and promotes actin polymerization, rapidly reduced dendritic spine dynamics (as measured by an increase in frame-to-frame correlation,  $0.89 \pm 0.01$ ,  $n = 7$  neurons) compared with DMSO control ( $0.84 \pm 0.01$ ,  $n = 7$  neurons, Student t test,  $P < 0.01$ ) (Fig 5B and C). We noted that the diffuse actin signal was depleted from the dendritic shafts after Jasp application, indicating that the enhanced actin polymerization incorporated free actin monomers from the dendritic shaft. We further evaluated this with a fluorescence recovery after photobleaching (FRAP) assay (Fig 5D). In control neurons,  $\beta$ -actin turnover was fast, with a large mobile pool (mobile fraction:  $0.87 \pm 0.01$ ,  $n = 13$  neurons, Fig 5E and F), consistent with measures based on overexpressed  $\beta$ -actin [36]. As expected, addition of Jasp largely abolished turnover of spine  $\beta$ -actin (mobile fraction:  $0.02 \pm 0.01$ ,  $n = 13$  neurons, Student t test,  $P < 0.001$ ), indicating that Jasp induced integration of most GFP- $\beta$ -actin in stable actin filaments. These experiments show that ORANGE knock-ins are compatible with live-cell imaging of endogenous protein dynamics in neurons.

Single-molecule imaging is a powerful tool to investigate the dynamics of individual molecules within living cells. We designed knock-in constructs targeting CaMKII $\alpha$ , an abundant neuronal Ca<sup>2+</sup>-activated signaling protein essential for learning and memory [37]. Confocal microscopy showed that the GFP-CaMKII $\alpha$  knock-in was primarily cytoplasmic with moderate enrichment in spines (Fig 2 and S2 Fig), consistent with previous studies [18,38]. We next replaced GFP for monomeric Eos 3.2 (mEos3.2), a photoconvertible protein compatible with single-molecule tracking based on photoactivated localization

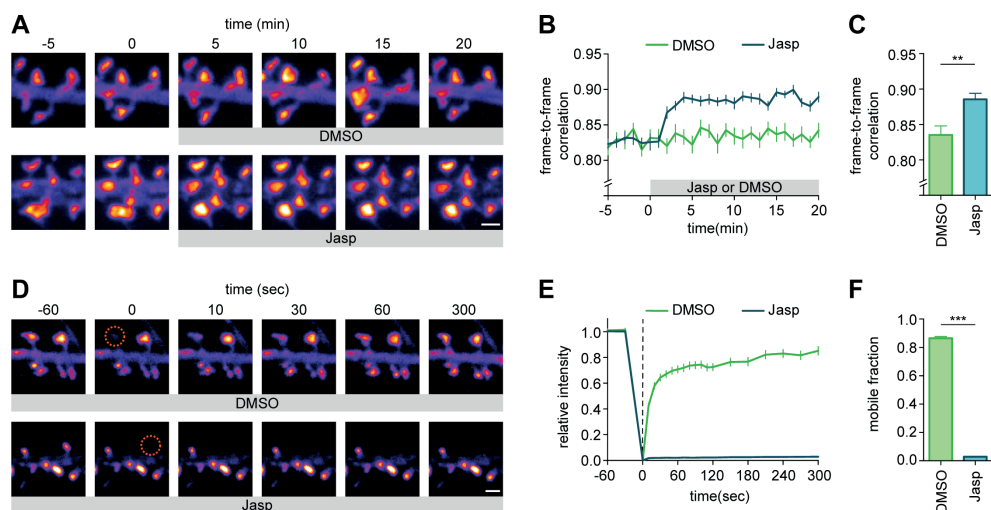


**Fig 5. Live-cell imaging of intracellular endogenous protein dynamics**

(A) Representative images of dendrites transfected with GFP- $\beta$ -actin knock-in imaged over time. DMSO or Jasp was added at time point 0. DIV 21. Scale bar, 1  $\mu$ m. (B) Frame-to-frame correlation of pixel intensity over time for DMSO (green) or Jasp (blue) addition. (C) Quantification of mean frame-to-frame correlation averaged over the last five time points. (D) Representative images of FRAP experiment on dendrites transfected with GFP- $\beta$ -actin knock-in vector. ROIs were bleached at time point 0 (orange circle). Recovery was followed over time. DIV 21. Scale bar, 1  $\mu$ m. (E) FRAP analysis of GFP- $\beta$ -actin knock-in neurons treated with DMSO (control) or Jasp. ROIs were bleached at time point 0 (dotted line). (F) Quantification of mobile fraction calculated from the last five time points of each bleached ROI averaged per neuron. Data are represented as means  $\pm$  SEM. \*\* $P < 0.01$ , \*\*\* $P < 0.001$ , Student t test. Underlying data can be found in S1 Data. FRAP, fluorescence recovery after photobleaching; GFP, green fluorescent protein; Jasp, jasplakinolide; ORANGE, Open Resource for the Application of Neuronal Genome Editing; ROI, region of interest; DIV day in vitro.

microscopy (PALM) [39,40] (S9A Fig). Individual mEos3.2-CaMKII $\alpha$  molecules were imaged to reconstruct a superresolved image of CaMKII $\alpha$  distribution (S9B Fig) and to map single-molecule trajectories in spines and dendrites over time (S9C and D Fig). From the trajectories, we calculated the mean-squared displacements (MSDs) to derive the diffusion coefficient for individual trajectories (S9E and F Fig), revealing two distinct dynamic CaMKII $\alpha$  populations: a mobile population (mean diffusion coefficient  $0.145 \pm 0.049 \mu\text{m}^2/\text{s}$ ) and less-mobile population ( $0.0140 \pm 0.0011 \mu\text{m}^2/\text{s}$ ,  $n = 11$  neurons). Thus, genetic tagging with photoconvertible molecules such as mEos3.2 can be used for live-cell single-molecule tracking PALM experiments to resolve the distribution and dynamics of endogenous, intracellular proteins.

### Superresolution imaging of endogenously expressed proteins in neurons

We envisioned that tagging endogenous proteins particularly presents advantages for superresolution imaging by facilitating labeling of proteins in a subset of neurons and overcoming many artifacts associated with antibody specificity or overexpression of recombinant proteins. Also, this combination would be interesting for studying recently identified proteins with unknown subcellular distribution.

First, we employed our GFP- $\beta$ -actin and  $\beta$ 3-tubulin-GFP knock-in constructs to resolve and correlate their well-known subcellular organization in individual neurons using gSTED

microscopy. Recent superresolution studies have demonstrated that the actin cytoskeleton forms ring-like structures that are periodically organized along axons as well as dendrites [41-43]. We tested whether we could resolve this particular organization of the actin cytoskeleton in individual  $\beta$ -actin knock-in neurons within dense, mature, dissociated hippocampal cultures. Using gSTED imaging, we observed distinct periodic actin structures in both the axon and dendrites (Fig 6A-E). In addition to resolving the actin network, we performed two-color gSTED imaging of  $\beta$ 3-tubulin-GFP knock-in neurons immunolabeled with anti- $\alpha$ -tubulin to resolve the neuronal microtubule network (S10A-C Fig). Thus, ORANGE combined with superresolution imaging is an easily accessible approach to resolve the subcellular distribution of endogenous proteins with high resolution.

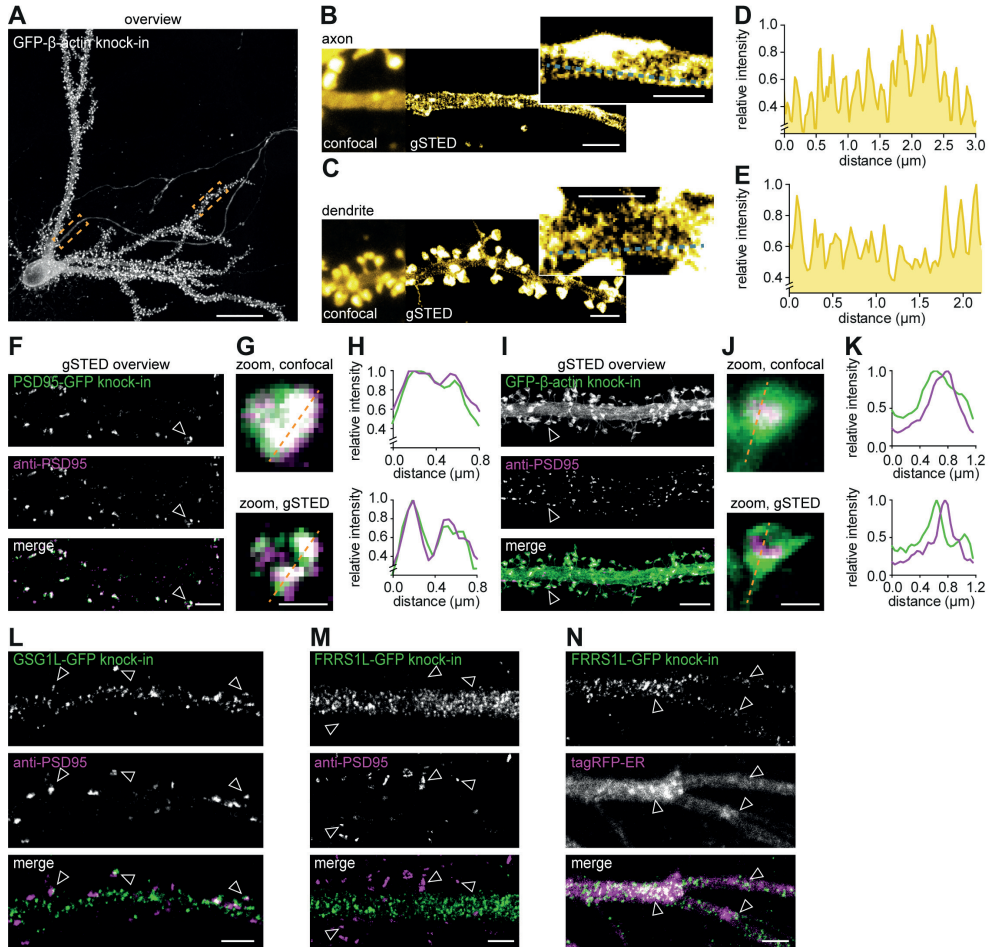


**Fig 6. STED microscopy to resolve the subcellular distribution of endogenous proteins in individual neurons** (A) Representative gSTED image of a GFP- $\beta$ -actin knock-in neuron (DIV 21) enhanced with anti-GFP (ATTO647N). Scale bar, 20  $\mu$ m. (B and C) Zooms of axon (B) and dendrite (C) as indicated with boxes in (A) comparing confocal and gSTED imaging. Scale bar, 2  $\mu$ m; insert scale is 1  $\mu$ m. (D and E) Line scans from zooms in (B) and (C), respectively. (F) Representative gSTED images of dendrites positive for PSD95-GFP knock-in stained with anti-GFP (green, ATTO647N) and anti-PSD95 staining (magenta, Alexa594). DIV 21. Scale bar, 2  $\mu$ m. (G) Zooms from (F) of individual synapses resolved with confocal and gSTED. Scale bar, 500 nm. (H) Line scans of confocal and gSTED images shown in (G). (I) Representative gSTED images of dendrites positive for GFP- $\beta$ -actin knock-in stained

with anti-GFP (green, ATTO647N) and anti-PSD95 (magenta, Alexa594). DIV 21. Scale bar, 2  $\mu\text{m}$ . (J) Zooms from (I) of individual spines resolved with confocal and gSTED. Scale bar, 500 nm. (K) Line scans of confocal and gSTED images shown in (J). (L and M) Representative gSTED images of dendrites positive for GSG1L-GFP (L) or FRRS1L-GFP knock-in (M) stained with anti-GFP (green, Alexa488) and anti-PSD95 (magenta, ATTO647N). DIV 21. Scale bar, 5  $\mu\text{m}$ . (N) Representative images of dendrites positive for FRRS1L-GFP knock-in enhanced with anti-GFP (gSTED, green) and coexpressed with tagRFP-ER (confocal, magenta). DIV 21. Scale bar, 2  $\mu\text{m}$ . GFP, green fluorescent protein; gSTED, gated STED; STED, stimulated-emission depletion; DIV, day in vitro; PSD95, postsynaptic protein 95; GSG1L, Germ cell-specific gene 1-like protein; FRRS1L, Ferric-chelate reductase 1-like protein; RFP, red fluorescent protein; ER, endoplasmic reticulum.

Second, we took advantage of ORANGE to perform two-color gSTED imaging on synaptic proteins. To assess the performance of ORANGE knock-ins compared with conventional antibody staining in resolving subsynaptic protein organization using STED microscopy, we compared the localization of the PSD95-GFP knock-in signal with that of immunolabeled PSD95. Both confocal and gSTED images of individual synapses revealed a high degree of colocalization between the PSD95-GFP knock-in and anti-PSD95 staining (Fig 6F). Additionally, gSTED revealed that even at the subsynaptic level, the PSD95-GFP knock-in and anti-PSD95 staining colocalized (Fig 6G and H). In contrast, two-color gSTED of GFP- $\beta$ -actin knock-in and anti-PSD95 staining revealed that  $\beta$ -actin is enriched in dendritic spines but is largely excluded from the synapse (Fig 6I-K). The differential distribution of the PSD95-GFP and GFP- $\beta$ -actin knock-ins was confirmed by quantifying the degree of colocalization with immunolabeled anti-PSD95 using two independent metrics: the Pearson's correlation coefficient (PCC) and Manders' overlap correlation (MOC) [44,45], highlighting the need for superresolution techniques, such as STED (S10D and F Fig). Additionally, we found that CaMKII $\alpha$  is enriched in dendritic spines and only partially overlapped with PSD95 (S10G-J Fig).

Lastly, we studied the subcellular expression of proteins that have only recently been discovered. High-throughput proteomics studies have identified a number of novel components of the  $\alpha$ -amino-3-hydroxy-5-methyl-4-isoxazolepropionic acid (AMPA) receptor complex that have different topologies and functions [46,47]. Information on the subcellular distribution of these components is sparse and largely based on overexpression, which is known to alter the trafficking and function of AMPA receptors at synapses. Here, we developed knock-in constructs for two AMPA receptor interactors: Germ cell-specific gene 1-like protein (GSG1L) and Ferric-chelate reductase 1-like protein (FRRS1L)/C9orf4. GSG1L has been recently shown to modulate AMPA receptor function [48,49]. Using gSTED imaging, we found that GSG1L localizes throughout the dendritic shaft and in dendritic spines, where it closely associates with synaptic PSD95 (Fig 6L). In contrast, FRRS1L was found to be excluded from synapses (Fig 6M) but showed a punctate distribution in the dendritic shaft, closely associated with the endoplasmic reticulum (ER) (Fig 6N). This is in line with a recent study showing that FRRS1L regulates AMPA receptor trafficking from the ER to control AMPA receptor surface expression [50-53]. Altogether, these results demonstrate the potential of ORANGE to uncover the nanoscale organization of endogenous proteins, in particular those with unknown distribution due to lack of specific antibodies, in individually labeled neurons.

### **Dissection of endogenous NMDA receptor distribution and dynamics within individual synapses**

Based on overexpression and antibody-labeling studies, the spatial organization of NMDA receptors at excitatory synapses has been proposed to be heterogenous, with

receptors accumulating in distinct subsynaptic nanodomains [54-56]. However, because overexpression of individual receptor subunits could affect subunit stoichiometry and function of endogenous receptors [57], we combined ORANGE with superresolution techniques to dissect the distribution and dynamics of NMDA receptors. To visualize the total pool of NMDA receptors, we developed a knock-in construct to endogenously tag the obligatory GluN1 subunit with GFP (Fig 7A). Several studies have consistently estimated that the number of NMDA receptors at individual synapses is relatively low, ranging from 10 to 20 receptor complexes per synapse [32,58]. Despite these low copy numbers, we could detect concentrated dendritic clusters of GFP-GluN1, most of which colocalized with immunolabeled PSD95 (Fig 7A). Interestingly, we found that GFP-GluN1 intensity did not correlate with anti-PSD95 immunolabeling intensity (Fig 7B) (Pearson  $r$ : 0.19,  $R^2$ : 0.038,  $n$  = 450 GluN1 clusters from nine neurons), consistent with earlier studies showing that the total number of NMDA receptors is largely invariable and does not scale with synapse size [59-61]. Using gSTED imaging, we found that although most GFP-GluN1 clusters localized to synapses, some smaller extrasynaptic clusters could be detected (Fig 7C-E). Next, we measured the total GFP-GluN1 cluster area in individual synapses and found a slight correlation with synapse size (Pearson  $r$ : 0.64,  $R^2$ : 0.4087,  $n$  = 266 synapses from three neurons; Fig 7F). Thus, our data suggest that the subsynaptic area covered by NMDA receptors, but not the total number of receptors, scales with synapse size. gSTED imaging of individual synapses also indicated that the subsynaptic distribution of GFP-GluN1 is heterogeneous (Fig 7B, G), with individual synapses containing one or more smaller GFP-GluN1 substructures (Fig 7H) ( $n$  = 266 synapses from three neurons).

To further investigate the subsynaptic distribution of NMDA receptors, we turned to single-molecule localization microscopy (SMLM). The GFP-GluN1 knock-in was immunolabeled with anti-GFP and Alexa647-coupled secondary antibodies for direct stochastic optical reconstruction microscopy (dSTORM) to reconstruct the spatial organization of NMDA receptors at individual synapses with nanometer precision (Fig 7I and J). Clusters of GFP-GluN1 receptors were identified using density-based spatial clustering of applications with noise (DBSCAN) [62]. Next, all localizations within individual clusters were plotted and color-coded for the local density. These local density maps revealed that, within individual clusters, NMDA receptors form distinct nanodomains (Fig 7K), consistent with our gSTED data (Fig 7D). We found that the majority of GFP-GluN1 clusters contained one to three nanodomains with a median size of approximately 62 nm (IQR: 53–71 nm) ( $n$  = 859 GFP-GluN1 clusters from three neurons) (Fig 7L and M). Thus, these SMLM data indicate that endogenous NMDA receptors form distinct subsynaptic nanodomains.

To gain insight in the subsynaptic mobility of endogenously expressed NMDA receptors, we probed the diffusion kinetics of individual receptors using universal point accumulation in nanoscale topography (uPAINT) [63]. Stochastic labeling of individual GFP-tagged receptors with a GFP nanobody coupled to ATTO647N provided a map of individual receptor mobility along stretches of dendrites (Fig 7N and O). Most receptor trajectories mapped within the boundaries of the synapse. Strikingly, we found that these synaptic NMDA receptors were largely immobilized (median diffusion coefficient synaptic tracks: 0.0096  $\mu\text{m}^2/\text{s}$ , IQR: 0.0079–0.0122,  $n$  = 462 tracks from 6 neurons), whereas on average, extrasynaptic receptors diffuse at higher rates (0.0224  $\mu\text{m}^2/\text{s}$ , IQR: 0.0123–0.0419,  $n$  = 307 tracks from 6 neurons) (Fig 7P). Altogether, by combining the ORANGE toolbox with superresolution microscopy, we show that NMDA receptors are enriched in the PSD, where they are highly immobilized and cluster in subsynaptic nanodomains.



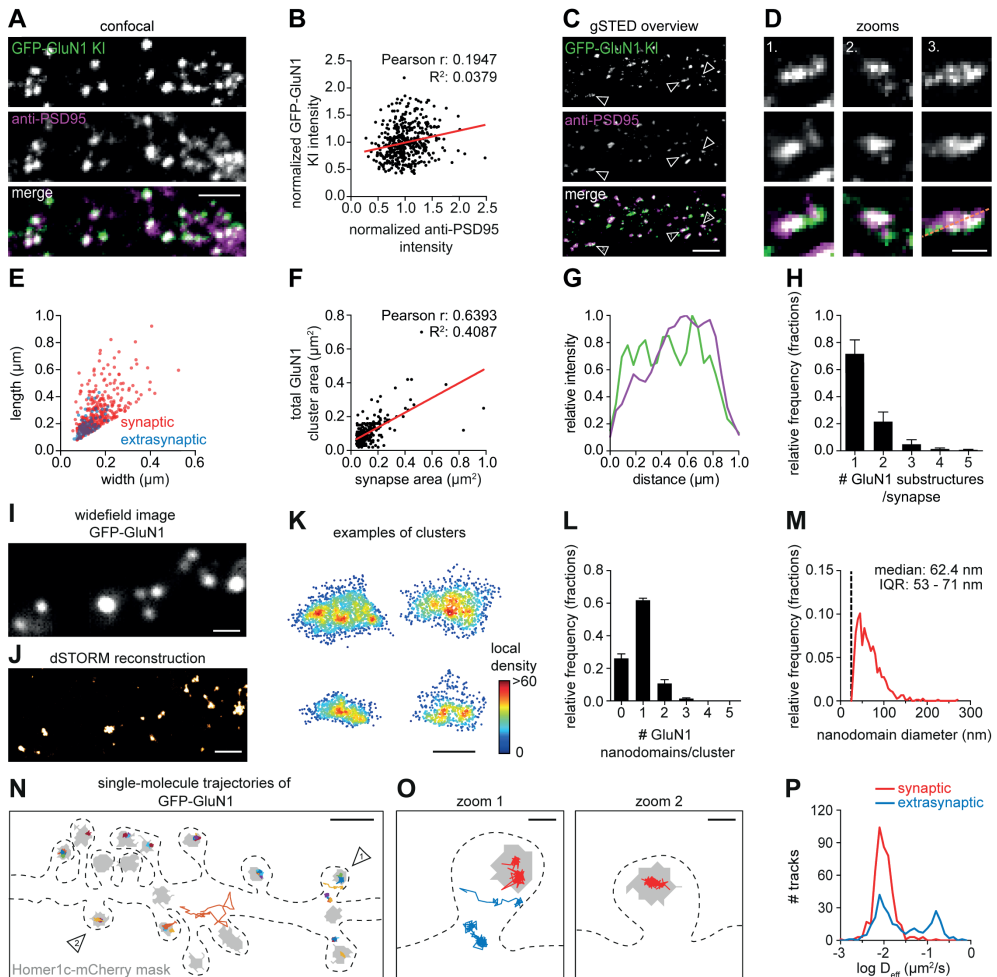


**Fig 7. NMDA receptors concentrate in subsynaptic nanodomains and are highly immobilized in synapses**

(A) Representative images of a dendrite positive for GFP-GluN1 KI (green) stained for PSD95 (magenta, Alexa647). Scale bar, 2  $\mu\text{m}$ . (B) Correlation between GFP-GluN1 KI and anti-PSD95 staining intensity within individual GFP-GluN1 puncta. (C) Representative gSTED images of dendrites positive for GFP-GluN1 KI enhanced with anti-GFP (green, ATTO647N) and anti-PSD95 (magenta, Alexa594). DIV 21. Scale bar, 2  $\mu\text{m}$ . (D) Zooms of individual synapses indicated in (C). Scale bar, 500 nm. (E) FWHM analysis of GFP-GluN1 structures comparing width and length of individual synaptic (red) and extrasynaptic (blue) GluN1 clusters. (F) Correlation between GFP-GluN1 cluster area and synapse area (based on anti-PSD95 staining) for individual synapses. (G) Line scan of synapse zoom 3 in (D). (H) Quantification of the number of GFP-GluN1 substructures per synapse. (I) Representative image of dendrite positive for GFP-GluN1 KI stained with anti-GFP (Alexa647). DIV 21. Scale bar, 1  $\mu\text{m}$ . (J) Single-molecule dSTORM reconstruction of example shown in (I). Scale bar, 1  $\mu\text{m}$ . (K) Examples of individual GFP-GluN1 clusters with single localizations plotted and color-coded based on the local density. Scale bar, 200 nm. (L) Quantification of number of GFP-GluN1 nanodomains per cluster. (M) Frequency distribution of GFP-GluN1 nanodomain size. Dotted line indicates nanodomain size cutoff. Bin size: 5 nm. (N) Representative example of GFP-GluN1 (anti-GFP nanobody conjugated to ATTO647N) single-molecule trajectories in a dendrite plotted with a random color and on top of a synapse mask (gray) based on Homer1c-mCherry widefield image. Dotted line indicates cell outline. DIV 21. Scale bar, 1  $\mu\text{m}$ . (O) Zooms of individual spines indicated in (N) with example trajectories of synaptic (red) or extrasynaptic (blue) receptors. Scale bar, 200 nm. (P) Frequency distribution showing the diffusion coefficient of synaptic and extrasynaptic tracks. Data in bar plots are presented as means  $\pm$  SEM. Underlying data can be found

**Fig. 7 (continued)** in S1 Data. dSTORM, direct stochastic optical reconstruction microscopy; FWHM, Full Width at Half Maximum; GFP, green fluorescent protein; gSTED, gated stimulated-emission depletion; KI, knock-in; NMDA, N-methyl-D-aspartate; GluN, glutamate receptor NMDA; PSD95, postsynaptic protein 95; DIV, day in vitro.

### Cre-dependent coexpression for multiplex labeling of two proteins in single neurons

We have shown that ORANGE mediates the integration of small epitope tags and fluorescent proteins in single genes (Fig 1). Tagging two proteins simultaneously in one neuron for dual-color imaging, however, is challenging using this approach. NHEJ-mediated integration of the donor sequence is homology independent, and therefore, the integration of independent donor sequences cannot be targeted to specific genes but occurs at random [23]. Recently, NHEJ-based, targeted integration of Cre recombinase was used to disrupt the target gene and drive the expression of a second protein used as a reporter of a successful knock-out [25]. Based on this, we reasoned that genomic integration of a fluorescent protein together with Cre recombinase could be used to trigger the expression of a second gRNA from an additional knock-in plasmid. This approach would facilitate the sequential integration of two donor sequences targeted to two genomic loci in a single neuron. To test this, we first developed

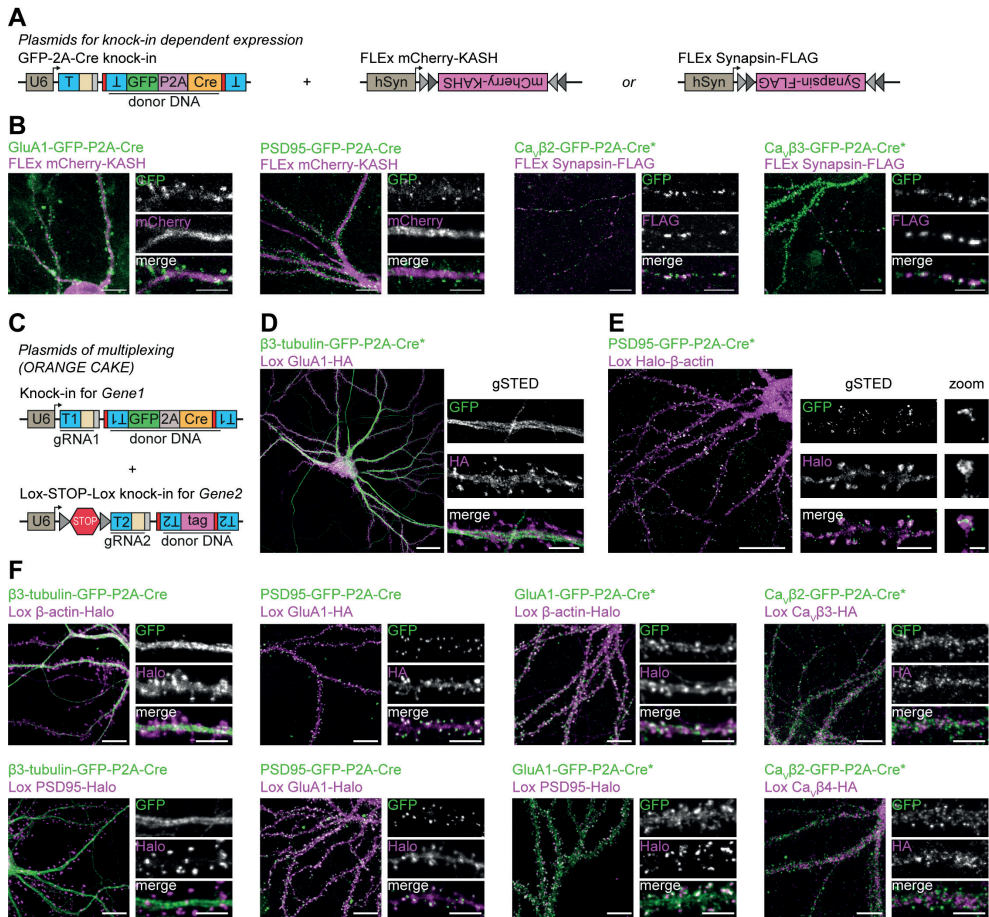


**Fig 8. Cre-dependent coexpression and labeling of two proteins in single neurons**

**Fig. 8 (continued)** (A) Overview of plasmids used for Cre-dependent expression mCherry-KASH or Synapsin-FLAG in knock-in neurons. (B) Examples of GFP-P2A knock-in–driven expression of mCherry-KASH or Synapsin-FLAG (Alexa568) (magenta) for various knock-ins. DIV 21. Scale bars, 10  $\mu\text{m}$  and 5  $\mu\text{m}$  for the overviews and zooms, respectively. (C) Overview of plasmids used for multiplex knock-in of two proteins in single neurons (ORANGE-CAKE). (D and E) Examples of  $\beta$ 3-tubulin-GFP-P2A-Cre (green), Lox GluA1-HA (magenta, Alexa594) double knock-in, (D) and PSD95-GFP-P2A-Cre (green), Lox Halo- $\beta$ -actin (magenta, JF549) double knock-in (E). Shown are overviews (confocal) and zooms (gSTED). DIV 21. Scale bars, 20  $\mu\text{m}$  for the overviews and 5  $\mu\text{m}$  (dendrites) and 500 nm (spine) for the zooms. (F) Examples of various combinations of GFP-P2A-Cre (green) and Lox (magenta) double knock-ins. HA was visualized by anti-HA staining (Alexa594), and Halo with Halo-JF549 ligand. DIV21. Scale bars, 10  $\mu\text{m}$  and 5  $\mu\text{m}$  for the overviews and zooms, respectively. Asterisk indicates enhancement with anti-GFP antibody (Alexa488). CAKE, conditional activation of knock-in expression; FLEEx, flip-excision; GFP, green fluorescent protein; gRNA, guide RNA; gSTED, gated stimulated-emission depletion; ORANGE, Open Resource for the Application of Neuronal Genome Editing. KASH, Klarsicht, ANC-1, Syne Homology; DIV, day in vitro; HA, hemagglutinin; GluA, glutamate receptor AMPA; PSD95, postsynaptic protein 95; JF549, Janelia Fluor 549; T, target sequence; hSyn, human Synapsin; CaV, voltage-dependent  $\text{Ca}^{2+}$ -channel.

knock-in constructs integrating a C-terminal GFP tag fused to a P2A-Cre sequence (GFP-P2A-Cre), leading to bicistronic expression of a GFP-fusion protein and Cre recombinase (Fig 8A). This yielded robust recombination and expression of flip-excision (FLEEx) mCherry and Synapsin-FLAG (Fig 8B). We did, however, observe some cells that only expressed the FLEEx construct without visible GFP signal, suggesting that either Cre expression is somewhat leaky or that very low levels of Cre are already sufficient to recombine FLEEx switches.

Building on GFP-P2A-Cre knock-ins, we developed a pORANGE vector containing a Cre-dependent Lox-STOP-Lox sequence in the U6 promoter [64], which blocks expression of the gRNA until Cre is expressed (Fig 8C). When combined with a GFP-P2A-Cre knock-in, this would mediate reliable dual-color knock-ins with NHEJ because the Lox-STOP-Lox gRNA is only expressed after GFP-P2A-Cre integration is completed and a functional protein has been produced from this allele (S11A Fig). Thus, this mechanism should prevent mix-up of donor sequences in the targeted loci. We dubbed this method conditional activation of knock-in expression (CAKE). Using ORANGE-CAKE, we developed multiplex knock-ins for a range of combinations and used these for dual-color confocal and gSTED microscopy of endogenous proteins (Fig 8D and F). As was observed for FLEEx switches, we also observed occasional expression of Lox-STOP-Lox knock-ins without observable GFP signal (see Discussion). Additionally, for  $\beta$ 3-Tubulin-GFP-P2A-Cre and GluA1-GFP-P2A-Cre, we occasionally observed erroneous integration of donor DNA in the nontargeted locus (e.g., HaloTag labeling from the gene targeted with GFP-P2A-Cre) (S11B and C Fig, see Discussion). Importantly, we never observed expression of Lox-STOP-Lox knock-ins in cultures without expression of Cre recombinase. Together, these data show the feasibility of multiplex labeling in single cells using ORANGE-CAKE to study spatiotemporal protein expression of multiple proteins simultaneously in individual neurons.

## DISCUSSION

Mapping the subcellular distribution of proteins at high spatial resolution is fundamental to understand cell biological processes. Ongoing developments in superresolution imaging technologies have dramatically improved the spatial resolution, allowing the dissection of molecular organization of subcellular structures at nanometer precision. However, a major obstacle remains the availability of a flexible strategy to efficiently and specifically label endogenous proteins, especially in neurons. Here, we developed ORANGE, a simple and scalable toolbox for epitope tagging of endogenous proteins using CRISPR/Cas9, and we

provide a readily usable knock-in library that enables in-depth interrogation of protein distribution and dynamics in postmitotic neurons at high spatial resolution. Although CRISPR/Cas9-based tagging approaches have been developed for neurons, until now, large-scale applications of these methods have been limited. ORANGE offers a single template vector that only requires standard cloning methods. Moreover, we demonstrated that this approach is compatible with various generally used DNA delivery methods, including lipofection, electroporation, LVs, and AAVs, and thus can be used in dissociated neuronal cultures and organotypic slice cultures and *in vivo*. Instead of relying on antibodies that target individual proteins with varying levels of specificity and efficiency, the ORANGE toolbox utilizes fluorescent proteins that directly report protein localization, self-labeling enzymes, or epitope tags for which universal antibodies are available. Moreover, integration of Cre recombinase allowed for tagging of two endogenous proteins in single cells.

We demonstrated the level of accuracy of targeted genomic integration using ORANGE in several ways. First, we analyzed whether insertion of GFP was correct at the genomic level using next-generation sequencing. We detected high frequency of correct integration for many of the knock-ins, although the occurrence of indels is highly variable between individual targets. However, indels should not form a limitation for many purposes, including fluorescent imaging, because only neurons with detectable fluorescent signal are selected, and proteins with out-of-frame integration remain undetectable. At the network level, we expect that the effect of frameshift mutations is limited, especially when using lipofection, because more than 90% of cultured cells are not transfected and remain unedited. Importantly, we noted that the frequency of correct integration did not correlate with Doench on-target score [30] and Bae out-of-frame score [31], scores often used to select a target sequence with a high efficiency. Also, when testing knock-in constructs targeting different target sequences in the same gene, we found significant differences in knock-in efficiency, independent of the Doench and Bae scores. These scores are primarily developed based on knock-out outcomes, which might explain why these scores are not correlated with the accuracy or efficiency of donor integration.

Second, for all our targets, we found that the distribution of the GFP signal was consistent with previous reports of protein localization inferred from immunolabeling or biochemical fractionation experiments. Our results indicate that, when expressed, the tag accurately reports protein localization and does not affect protein levels in most knock-in-positive neurons. These results show that well-designed knock-ins do not affect localization of the targeted protein and that off-target expression of the donor tag is extremely rare. Multiple mechanisms within the design of knock-in construct prevent off-target expression. We selected target sequences with a high MIT score, meaning that the sequence is unique within the genome and that potential off-targets are intergenic or in introns. If off-target integration in protein-coding sequences does occur, the donor orientation will be random (i.e., 50% is in the inverted orientation). Additionally, in 66% of off-target integrations, the donor would be out of frame, and donor integration in a random location within a protein is likely to severely affect folding, leading to degradation of the targeted protein.

Third, with immunocytochemistry, we found that knock-ins were most often expressed at endogenous levels. However, in a few cases, we did observe that the tagged protein was expressed at slightly lower levels compared with the untagged protein in untransfected neurons. This might indicate that, in these neurons, one of the two alleles contains indels after genome editing and/or failed to integrate the donor DNA, consistent with estimates with the HITI method that 30%–50% of knock-in-positive cells show biallelic integration [24]. We

---

also showed that, for C-terminal tagging of PSD95, Shank2, and N-terminal Bassoon (but not C-terminal Bassoon knock-ins), knock-in-negative neurons are likely partial or complete knock-outs. This difference in protein levels, especially for C-terminal-tagged proteins, might be the result of different sensitivity to, for example, nonsense-mediated decay [65]. Ongoing advancements in CRISPR/Cas9 technology are likely to lead to new developments that increase the on-target integration efficiency and precision of this approach. For instance, Cas9 variants with higher specificity could decrease indel frequency [66,67], and the knock-in efficiency and repair accuracy may be predicted based on the target sequence [28,29]. Also, alternative delivery methods such as ribonucleoproteins (RNPs) [68] might increase the efficiency of DNA delivery.

An important advantage of our method is that targeted integration of common epitope tags circumvents the need for developing new specific antibodies. In particular, for proteins that are highly homologous in their amino acid sequence and for which generating specific antibodies is challenging, it is now possible to develop specific knock-in constructs that will report subcellular localization at unmatched specificity. As an example, we demonstrated successful knock-ins for RIM1 and RIM2, two highly homologous active zone proteins for which isoform-specific antibodies are not available. The knock-in constructs presented in our library are designed using the rat genome as a template. However, because of high gene homology, multiple of the knock-in constructs are compatible with the mouse genome (see S2 Table). For example, we have shown that our GluA1 knock-in works both in dissociated rat hippocampal cultures as well as in mouse organotypic hippocampal slice cultures and *in vivo* in mouse brain.

ORANGE is easily employed on targets yet to be characterized. Next-generation sequencing efforts and high-resolution proteomics studies continue to discover the implication of novel proteins in biological processes, but for many of these proteins, specific and efficient antibodies are lacking. For instance, we developed knock-in constructs for two AMPA receptor complex constituents, FRRS1L/C9orf4 and GSG1L, that have only recently been discovered in a high-resolution proteomics study [47]. For both proteins, functional characterization is available [48-50,52,53], but high-resolution information on subcellular distribution was lacking because of the unavailability of specific antibodies. Thus, ORANGE allowed us to visualize and image these proteins at high resolution, showing that, whereas GSG1L is localized on the dendritic shaft and in dendritic spines, FRRS1L is preferentially targeted to the soma and dendritic shaft, seemingly associated with the ER.

The ability to tag endogenous proteins in sparse subsets of cells is particularly advantageous for superresolution approaches. Also, sparse labeling of cells increases contrast and provides internal negative controls because neighboring, nontargeted cells are unlabeled. The resolution of these approaches will detect any distortion in molecular organization due to, for instance, overexpression artifacts, and therefore, these methods are highly sensitive to nonspecific labeling. We exploited the advantages of ORANGE to dissect the subcellular distribution of a number of neuronal proteins using different superresolution imaging approaches. We mapped the distribution of endogenous cytoskeletal elements, signaling proteins, and synaptic receptors. Our experiments demonstrate that endogenous CaMKII $\alpha$  has two distinct kinetic populations. Focusing on glutamate receptors, we found that endogenous NMDA receptors are highly immobilized at synaptic sites and enriched in distinct subsynaptic nanodomains. This particular distribution is likely to shape the efficiency of receptor activation by glutamate [1], and therefore, dissection of the underlying molecular mechanisms is essential for our understanding of synapse physiology. Thus, ORANGE

enables superresolution imaging and live-cell single-molecule tracking of neuronal proteins and thus provides a scalable approach to efficiently and reliably map the dynamic distribution of endogenous proteins at nanometer resolution.

Finally, we show that ORANGE can be used for multiplex labeling and dual-color imaging of endogenous proteins. Multiplex gene editing has remained a challenge in neuronal cells, and existing methods have relatively low efficacy [18] or are limited to specific combinations with small epitope tags [23]. Our CAKE method of sequential genome editing using a GFP-P2A-Cre knock-in and a second Cre-dependent knock-in mediates flexible, multiplex editing for a wide range of combinations, without restrictions on donor DNA sequence. We did observe, however, that some GFP-P2A-Cre knock-ins had reduced GFP fluorescence compared with regular GFP knock-ins. Although it is currently unclear what the cause of this is, it is likely that the substantial increase in mRNA length reduces protein levels [69]. Therefore, the expression level of each knock-in should be carefully assessed for each target. For some GFP-P2A-Cre knock-ins, including  $\beta$ 3-tubulin and GluA1, we did observe occasional erroneous integration of the second, Cre-dependent knock-in. This is likely induced by rapid expression of Cre recombinase from these knock-ins after integration in the first allele, leading to activation of the Cre-dependent knock-in before the second allele has been edited. Indeed, we did already observe GFP expression from  $\beta$ 3-tubulin knock-ins after 24 hours, and it is not unlikely that this time span is insufficient to edit both alleles. Despite these current limitations, we feel that CAKE is a valuable tool to study the localization of multiple endogenous proteins in individual cells.

We believe that ORANGE is a simple and efficient genome editing toolbox that will rapidly advance many fields in biology through the in-depth investigation of protein distribution in cultured cell lines, primary cells, organotypic slice cultures, and animal models, but in particular, ORANGE presents one of the few possibilities to tag proteins in neurons. Further development of tools for cell type-specific targeting of epitope tags would allow interrogation of protein distribution in specialized neuron types in the brain. Apart from epitope tagging, our toolbox can, for example, be used for insertion of enzymes for proximity biotinylation [70], labeling of organelles for electron microscopy [71], or light-sensitive dimerization sequences for optical control over protein or organelle positioning [72,73]. The unprecedented number of applications of ORANGE will undoubtedly deepen our molecular understanding of how the spatial distribution of endogenous proteins contributes to cell biological processes.

## MATERIALS AND METHODS

### Ethics statement

All experiments were approved by the Dutch Animal Experiments Committee (Dier Experimenten Commissie [DEC] AVD1080020173404, AVD1080020173847, and AVD115002016797), performed in line with institutional guidelines of Utrecht University, and conducted in agreement with Dutch law (Wet op de Dierproeven, 1996) and European regulations (Directive 2010/63/EU). Timed pregnant Wistar rats were obtained from Janvier Labs. Wild-type male and female mice were used. Rosa26-Cas9 knock-in mice are originally from [27].

### Antibodies and reagents

Primary antibodies used in this study are the following: rabbit anti-GFP (MBL Sanbio, 598, RRID AB\_591819), rat anti-HA ([3F10], Sigma, 11867423001, RRID AB\_390919), mouse anti-FLAG ([M2], Sigma, F3165, RRID AB\_259529), mouse anti-PSD95 ([K28/43],

---

2

Neuromab, 75-028, RRID AB\_2307331), mouse anti-alpha-tubulin ([B-5-1-2], Sigma, T5168, RRID AB\_477582), mouse anti-Bassoon ([SAP7F407], Enzo, ADI-VAM-PS003-F, RRID AB\_10618753), mouse anti-Shank2 ([N23B/6], Neuromab, 75-088, RRID AB\_2254586), mouse anti-CaMKII $\alpha$  ([6G9], Sigma, C265, RRID AB\_2314080), and ATTO647N-conjugated anti-GFP nanobodies (GFPBooster-ATTO647N, Chromotek). Alexa488-, Alexa568-, Alexa594-, and Alexa647-conjugated secondary antibodies were from Life Technologies. ATTO647N-conjugated secondary antibodies were from Sigma. Alexa594- and Alexa647-conjugated phalloidin was from Life Technologies. Halo-ligands conjugated to Janelia fluorophore 549 (Halo-JF549) and 646 (Halo-JF646) were from Promega.

### **Dissociated neuronal cultures**

Dissociated hippocampal cultures were prepared from embryonic day 18 (E18) rat brains of both genders, as described in [74]. Dissociated neurons were plated on Ø18-mm coverslips coated with poly-L-lysine (37.5  $\mu$ g/ml, Sigma-Aldrich) and laminin (1.25  $\mu$ g/ml, Roche Diagnostics) at a density of 100,000 neurons per well. Neurons were grown in Neurobasal medium (NB) supplemented with 1% penicillin and streptomycin (pen/strep), 2% B27, and 0.5 mM L-glutamine (all from Gibco) (NB-complete medium) at 37 °C in 5% CO<sub>2</sub>. From DIV 1 onward, medium was refreshed weekly by replacing half of the medium with Brainphys neuronal medium supplemented with 2% NeuroCult SM1 neuronal supplement (STEMCELL Technologies) and 1% pen/strep (BP-complete medium).

### **Organotypic hippocampal slice cultures**

Organotypic hippocampal slice cultures were prepared from wild-type mice at postnatal day 6–8. After decapitation, the brain was quickly removed and placed in ice-cold Gey's Balanced Salt Solution (GBSS) containing (mM) 137 NaCl, 5 KCl, 1.5 CaCl<sub>2</sub>, 1 MgCl<sub>2</sub>, 0.3 MgSO<sub>4</sub>, 0.2 KH<sub>2</sub>PO<sub>4</sub>, and 0.85 Na<sub>2</sub>HPO<sub>4</sub> and supplemented with 12.5 mM HEPES, 25 mM glucose, and 1 mM kynurenic acid (pH set at 7.2, osmolarity set at 320 mOsm, sterile filtered). The frontal part of the brain and the cerebellum were removed along the transverse plane, and the hemispheres were then separated along the midline. Hippocampi were dissected and sliced perpendicularly to the long axis of the hippocampus with a thickness of 400  $\mu$ m using a McIlwain Tissue Chopper. Slices were washed in culturing medium (consisting of 48% MEM, 25% HBSS, 25% horse serum, 30 mM glucose, and 12.5 mM HEPES, with pH set at 7.3–7.4 and osmolarity set at 325 mOsm) before being placed on Millicell cell culture inserts (Millipore) in 6-well plates containing culturing medium. Slices were kept at 37 °C with 5% CO<sub>2</sub> until use, and culturing medium was completely replaced twice per week.

### **Design and generation of ORANGE knock-in plasmids**

Cloning of CRISPR/Cas9 knock-in vector pORANGE. To facilitate the generation of knock-in constructs, we developed a simple template vector (pORANGE). For this, we used pSpCas9(BB)-2A-Puro (PX459) V2.0 (Addgene 62988) and replaced SpCas9puro by SpCas9 from pAAV-nEFCas9 (Addgene 87115) flanked by the bipartite SV40 nuclear localization signal (NLS) sequences using the AgeI and EcoRI restriction sites, generating pSpCas9. To facilitate cloning of donor sequences, a multiple cloning site was inserted by annealing two complementary DNA oligos and ligation into the XbaI site of pSpCas9 generating pORANGE.

*Design and cloning of ORANGE knock-in constructs.*

To select regions within a protein of interest suitable for introducing a tag, we carefully examined known protein functions, domains, presence of signal peptides, binding ligands, and (if known) protein structure to minimize potential effects of the inserted tag sequence on protein function. For an overview of literature and design rationality given for each knock-in construct, see S1 Table. For most proteins, this resulted in tagging close to the start or stop codon or just behind the signal peptide. In some cases (including CaMKII $\alpha$ , Rab11, and  $\beta$ -actin knock-in #2), the genes were tagged just before the start codon. PAM sites in these identified regions were located in genomic sequences downloaded from the RGSC5.0/rn5 genome assembly through the UCSC genome browser gateway (<https://genome-euro.ucsc.edu/>). Target sequences were chosen, taking into consideration the MIT guide specificity score [75]. For some of the knock-ins, an extra G nucleotide was incorporated at the start of the target sequence to enhance transcription from the U6 promoter. We have no indication that this altered knock-in efficiency (for all protein target sites, target sequences, and gRNA scores, see S2 Table).

Next, oligos containing the 20-bp target sequences were annealed and ligated into the BbsI sites of pORANGE (Fig 1, S1). Donor sequences were designed to contain the fluorescent tag sequence (GFP or mEos3.2) flanked by two Cas9 target sites identical to the genomic target site. Importantly, to facilitate genomic integration of the donor sequence in the correct orientation, these target sites including PAM sequences were inserted as the reverse complement of the genomic target sequence (Fig 1A, S1). Additional linker sequences of at least three amino acids and additional base pairs to make the donor in frame after integration in the genome were introduced between the target sites and the tag sequence. Also, a start codon and new Kozak sequence or stop codon was introduced in the linker when proteins were tagged before the genomic start or stop codon, respectively. For the CaMKII $\alpha$  knock-in construct, the reverse integration of the incomplete target sequence introduces an additional start codon. Extra base pairs were introduced in the linker to make this extra start codon in frame with the donor. To facilitate exchange of donor tags, in-frame BmtI and AfeI restriction sites were introduced in the linker for some, but not all, knock-in constructs. Primer oligos with overhangs containing all these features were designed to generate the complete donor sequence by PCR. (See S1 Fig for two example designs.) The donor sequences were PCR amplified from a GFP-containing plasmid as template and ligated into the multiple cloning site of the pORANGE vector containing the inserted target sequence to generate the complete knock-in construct. For all primers used to generate the knock-in donor inserts, see S3 Table. To replace GFP in the donor DNA, pORANGE plasmids were digested with BmtI and AfeI, and replacements were generated by primer ligation (in case of 2 $\times$  HA or 2 $\times$  FLAG) or PCR for larger donors.

For LV applications, the ORANGE system was split into two plasmids. To generate pFUGW-Cas9, SpCas9 (from pAAV-nEFCas9) was ligated into the AgeI and EcoRI sites of pFUGW (Addgene 14883). To generate the gRNA and donor containing LV plasmid, first, mCherry-KASH amplified from pAAV-mTubb3 (Addgene 87116) was ligated into the BshTI and EcoRI sites of pFUGW-Cas9 replacing Cas9, yielding pFUGW-mCherry-KASH. Then, the U6 promoter, gRNA, and the donor sequence were amplified by PCR from the pORANGE construct and inserted into the PacI site of pFUGW-mCherry-KASH using Gibson assembly (NEBuilder HiFi DNA assembly cloning kit).

For AAV vectors, we developed a pAAV backbone (pAAV-MCS-mCherry-KASH) containing a multiple cloning site, EF-1 $\alpha$  promoter, and mCherry-KASH using Gibson



---

assembly. Knock-in cassettes containing the U6 promoter, gRNA, and donor DNA were subcloned by digesting pORANGE with PscI/MluI, which was ligated in the NcoI and SgsI sites of pAAV MCS mCherry-KASH.

To create Cre-dependent knock-ins for CAKE, we obtained an mU6 promoter containing a STOP sequence flanked by LoxP551 sites from Addgene (#113160) [64] with PCR. pORANGE backbone was digested with PscI and BbsI to remove the original promoter, and Gibson assembly was used to ligate the PCR product to obtain pORANGE Lox. Knock-ins in pORANGE Lox are cloned with identical methods as regular knock-ins in pORANGE (discussed above).

For the expression of FLEEx switches, the pFSW backbone with synapsin-1 promoter (a gift from Dr. Pascal Kaeser, Harvard Medical School) was digested with KpnI and PacI. Inverted mCherry-KASH and a FLEEx switch based on Addgene #50955 [76] were generated by PCR and ligated with Gibson assembly to obtain pFSW-FLEEx-mCherry-KASH. To replace mCherry-KASH with Synapsin-FLAG, Synapsin-1 with FLAG tag was generated by PCR from pCMV(pr)Synapsin-1Cherry-N1lenti H81 (a gift from A. Jeromin, Allen Brain Institute, Seattle, United States), and ligated in the BmtI/BshTI restriction sites. pCaMK Homer1c-mCherry was cloned via amplification of Homer1c-mCherry from pCMV Homer1c-mCherry [55] using PCR and ligation into the XhoI and MfeI sites of pCaMK mCherry-GluA1-CIBN (Addgene #89444) [72]. All constructs were verified by sequencing.

### **Transfection of dissociated hippocampal cultures**

Neurons were transfected at DIV 3 (for knock-in) or DIV 14–18 (for overexpression) using Lipofectamine 2000 reagent (Invitrogen). Briefly, for one Ø18-mm coverslip covered with 100,000 neurons, 1–2 µg DNA was mixed with 3.3 µl Lipofectamine in 200 µl NB medium and incubated for 30 minutes at room temperature (RT). Next, 500 µl conditioned medium was transferred to a new culture plate and replaced by 300 µl NB supplemented with 0.5 mM L-glutamine. The DNA mix was added to the neurons and incubated at 37 °C and 5% CO<sub>2</sub>. After 90–120 minutes, neurons were transferred to the new culture plate with conditioned medium and 500 µl new NB medium supplemented with L-glutamine, B27, and pen/strep and kept at 37 °C and 5% CO<sub>2</sub> for at least 3 days (for overexpression) and between 1–20 days for knock-in, depending on the experiment.

### **Electroporation of dissociated hippocampal neurons**

For electroporation, hippocampal neurons were collected directly after dissection and dissociation in a 15-ml tube and centrifuged for 5 minutes at 200g. Neurons were resuspended in AMAXA transfection solution (Lonza) (3 × 10<sup>5</sup> neurons per sample), mixed with 8 µg DNA, transferred to a gene pulser cuvette (Biorad), and electroporated using a Lonza Nucleofector 2b. Immediately after electroporation, fresh 37 °C NB medium supplemented with B27, L-glutamine, and pen/strep was added to the cuvette, after which the neurons were plated on a coated Ø18-mm coverslip using a Pasteur pipette. Neurons were incubated at 37 °C and 5% CO<sub>2</sub> for 3 hours, after which all medium was replaced with fresh NB medium supplemented with B27, L-glutamine, and pen/strep.

### **HaloTag labeling of dissociated hippocampal cultures**

HaloTag labeling was performed with cell-permeable Halo-JF549 or Halo-JF646 ligands. Prior to use, ligands were dissolved in DMSO to 200 µM and stored in single-use aliquots at –20 °C. HaloTag ligands were added to culture medium at a final concentration of 200 nM,

and cells were placed back in the incubator for 15 minutes. After rinsing the cells with culture medium, cells were fixed using 4% (w/v) paraformaldehyde (PFA) and 4% (w/v) sucrose in phosphate-buffered saline (PBS) (PFA/Suc).

### **Immunocytochemistry of dissociated hippocampal cultures**

Immunocytochemistry was performed as described below, unless indicated otherwise. Hippocampal neurons were fixed using PFA/Suc for 10 minutes at RT and washed three times in PBS containing 0.1 M glycine (PBS/Gly). Neurons were blocked and permeabilized in blocking buffer (10% [v/v] normal goat serum [NGS] (Abcam) in PBS/Gly with 0.1% [v/v] Triton X100) for 1 hour at 37 °C. Next, coverslips were incubated with primary antibodies diluted in incubation buffer (5% [v/v] NGS in PBS/Gly with 0.1% [v/v] Triton X100) overnight at 4 °C. Coverslips were washed three times for 5 minutes with PBS/Gly and incubated with secondary antibodies diluted 1:400 in incubation buffer for 1 hour at RT. Coverslips were washed three times for 5 minutes in PBS/Gly, dipped in milliQ water (MQ), and mounted in Mowiol mounting medium (Sigma).

### **AAV production**

AAV vectors serotype 5 encoding for GluA1-Halo or PSD95-Halo knock-ins were produced as described in detail in [77] using helper plasmids obtained from [78]. In brief, HEK293T cells were plated 1 day before transfection in Dulbecco's Modified Earl's Medium (DMEM) supplemented with 10% fetal calf serum (FCS) and 1% pen/strep. At 2 hours before transfection, medium was exchanged with Iscove's Modified Dulbecco's Medium (IMDM) containing 10% FCS, 1% pen/strep, and 1% glutamine. Transfection was performed with polyethylenimine (PEI). At 1 day after transfection, medium was exchanged with fresh IMDM with supplements. At 3 days after transfection, medium was aspirated, and cells were harvested using a cell scraper. After three freeze/thaw cycles and treatment with DNaseI, AAV vectors were purified using an iodixanol density gradient and ultracentrifugation (70 minutes, 69,000 rpm at 16 °C using rotor 70Ti [Beckman Coulter]). The fraction containing AAV particles was concentrated with centrifugation (3,220g, 15 minutes at RT) using an Amicon Ultra 15 column (Merck Millipore). Columns were washed 3 times using D-PBS containing 5% sucrose. AAV vectors were stored at -80 °C until use. Titters were measured using qPCR.

### **Stereotactic injection and staining of acute brain slices**

AAV vectors were injected in 4- to 7-month-old Rosa26-Cas9 knock-in mice of either sex [27]. Mice were anaesthetized with an intraperitoneal injection of ketamine (75 mg/kg, Narketan; Vetoquinol BV) and dexmedetomidine (1 mg/kg, Dexdomitor; Orion Pharma). Analgesia was provided before the start of surgery (carprofen, 5 mg/kg, subcutaneous, Carporal; AST Farma BV). Mice were given eye cream (CAF; CEVA Sante Animale BW) and placed in a stereotactic frame (Kopf Instruments). Local anesthesia was applied by spraying lidocaine (100 mg/mL; Xylocaine, AstraZeneca BV), and two holes were drilled for entrance of the injection needles. AAV vectors, 500 nl, with a titer of  $6.2 \times 10^{11}$  gc/ml were injected bilaterally (-2.46 mm posterior to bregma, +/- 2.2 mm lateral from bregma, and -1.3 mm ventral from the skull, under a 10° angle) at 100 nl per minute with a syringe pump (Harvard Apparatus) connected to stainless steel needles (31G, Coopers Needleworks) targeted to the CA1 region of the hippocampus. Needles were left in place for 10 minutes following the injection. After surgery, mice were given atipamezole (2.5 mg/kg, intraperitoneal, SedaStop;

---

AST Farma BV) and saline for rehydration. During the following 7 days, mice continuously received carprofen through their drinking water (0.027 mg/ml).

After 4 weeks, acute brain slices were obtained. Mice were first anaesthetized with isoflurane and decapitated. Brains were rapidly isolated, and 250- $\mu$ m-thick coronal slices were made on a vibratome (Leica VT1200 S) in ice-cold artificial cerebrospinal fluid (ACSF) containing (in mM) 124 NaCl, 26 NaHCO<sub>3</sub>, 11 D-glucose, 2.5 KCl, 1 NaH<sub>2</sub>PO<sub>4</sub>, HEPES 5, 7 MgSO<sub>4</sub>, and 0.5 CaCl<sub>2</sub>. Subsequently, slices were transferred to an immersion-style holding chamber containing 124 NaCl, 26 NaHCO<sub>3</sub>, 11 D-glucose, 2.5 KCl, 1 NaH<sub>2</sub>PO<sub>4</sub>, HEPES 5, 1 MgSO<sub>4</sub>, and 2 CaCl<sub>2</sub>, in which they recovered for at least 1 hour at RT. ACSF solutions were continuously bubbled with carbogen gas (95% O<sub>2</sub>, 5% CO<sub>2</sub>) and had an osmolarity of approximately 300 mOsm. After recovery, slices were stained for 1 hour with 250 nM Halo-JF646 ligand diluted in ACSF. Following rinsing with ACSF, slices were fixed overnight with 4% PFA, washed in PBS, and mounted with VectaShield (VectorLabs).

### **Lentivirus production and infection**

For lentivirus production, HEK293T cells were maintained at a high growth rate in DMEM supplemented with 10% FCS and 1% pen/strep. At 1 day after plating, cells were transfected using PEI (Polysciences) with second-generation LV packaging plasmids (psPAX2 and 2MD2.G) and a pFUGW construct containing the desired insert at a 1:1:1 molar ratio. At 6 hours after transfection, cells were washed once with PBS, and medium was replaced with DMEM containing 1% pen/strep. At 48 hours after transfection, the supernatant was harvested and briefly centrifuged at 700g to remove cell debris. The supernatant was concentrated using Amicon Ultra 15 100K MWCO columns (Milipore), and Cas9 and knock-in viruses were mixed at 1:1 and used immediately for infection. For cultured hippocampal neurons at DIV 2–4, 2–4  $\mu$ l virus was added per well, and neurons were fixed at DIV 21–23 with 4% PFA/Suc for 10 minutes. For organotypic hippocampal slice cultures, virus was injected into the CA1 region at DIV 1 using an Eppendorf Femtojet injector. Slices were fixed at DIV 10 with 4% PFA in PBS for 30 minutes, washed 3 times for 10 minutes with PBS, and mounted with VectaShield (Vector Laboratories).

### **Next-generation sequencing of genomic sites of integration**

Genomic DNA was isolated from electroporated neurons at DIV 4. Neurons were lysed in lysis buffer (100 mM Tris, 50 mM EDTA, 40 mM NaCl, 0.2% SDS [pH 8.5]) and incubated with 100  $\mu$ g/ml Proteinase K (Roche) at 55 °C for 2 hours, followed by 1 hour at 85 °C to inactivate Proteinase K. Genomic DNA was isolated by ethanol precipitation and dissolved in elution buffer (10 mM Tris [pH 8.0]) (Qiagen). Genomic PCR was performed to amplify the 5' and 3' junctions of the integrated donor (for PCR primers used, see S4 Table) using a touchdown PCR and Phusion HF polymerase (Thermo Fisher Scientific). Genomic primers were designed using NCBI Primer-Blast. Knock-ins analyzed were primarily selected based on flanking genomic sequence, and we failed to amplify multiple alleles because of sequence complexity (e.g., sequence repeats, high GC content, or potential secondary structure). Amplicons were only included if they resulted in a well-resolved band on agarose gel. PCR products were separated using agarose gel electrophoresis and subsequently purified using a gel extraction kit (Qiagen). Purified PCR products were pooled with, on average, 10 ng per amplicon and sent for Illumina Miseq 2  $\times$  300 bp next-generation sequencing (Utrecht Sequencing Facility [USEQ], Utrecht, the Netherlands).

Sequencing results were analyzed using CRIS.py [79]. Indel frequencies were plotted

in a heatmap as the average percentage from the forward and reverse reads. The number of forward and reverse reads was averaged per junction for each knock-in and plotted. Indel and in-frame frequencies were also plotted compared with the Doench on-target score [30] and Bae out-of-frame score [31], respectively, obtained for each guideRNA sequence from UCSC genome browser gateway.

### Confocal imaging

Confocal images were acquired with a Zeiss LSM 700. For dissociated hippocampal cultures, neurons were imaged with a 63× NA 1.40 oil objective. A Z-stack containing 7–12 planes at a 0.56- $\mu\text{m}$  interval was acquired with 0.1- $\mu\text{m}$  pixel size, and maximum intensity projections were made for analysis and display. Organotypic and acute slices were imaged with a 20× NA 0.8 objective. Z-stacks were acquired with varying intervals. Image analysis was primarily performed using FIJI software [80]. Quantifications were performed in Excel 2016.

### gSTED superresolution imaging

Imaging was performed with a Leica TCS SP8 STED 3× microscope using an HC PL APO 100×/NA 1.4 oil immersion STED WHITE objective. The 488-nm wavelength of pulsed white laser (80 MHz) was used to excite Alexa488, the 561-nm to excite Alexa568, the 590-nm to excite Alexa594, and the 647-nm to excite Alexa647-, JF646-, and ATTO647N-labeled proteins. Alexa594, Alexa647, JF646, and ATTO647N were depleted with the 775-nm pulsed depletion laser, and we used an internal Leica HyD hybrid detector (set at 100% gain) with a time gate of  $0.3 \leq t_g \leq 6$  ns. Images were acquired as Z-stack using the 100× objective. Maximum intensity projections were obtained for image display and analysis.

In vivo STED images were additionally subjected to deconvolution using Huygens deconvolution software. Deconvolution was performed using the CMLE deconvolution algorithm, with a maximum of 40 iterations and the signal-to-noise ratio (SNR) set at 7.

### Quantification of knock-in efficiency

For quantification of knock-in efficiency over time, hippocampal neurons were transfected at DIV 3 with a 1:1 ratio mixture of pORANGE- $\beta$ 3-tubulin-GFP knock-in and pSM155-mCherry. Coverslips were fixed 24, 48, 72, 96, 120, and 144 hours after transfection using 4% PFA/Suc for 10 minutes at RT, washed three times with PBS/Gly, and mounted in Mowiol mounting medium.

For testing GFP- $\beta$ -actin and GFP-GluN1 knock-in efficiencies, hippocampal neurons were transfected at DIV 3 with a 1:1 ratio mixture of pCaMK-Homer1c-mCherry overexpression construct together with pORANGE-GFP- $\beta$ -actin #1 or #2 or pORANGE-GFP-GluN1 #1, #2, or #3 knock-in constructs. Neurons were fixed at DIV 21 using 4% PFA/Suc for 10 minutes at RT, washed three times with PBS/Gly, and mounted in Mowiol mounting medium.

Neurons were imaged with confocal microscopy as described above. For both experiments, mCherry- or Homer1c-mCherry-positive (i.e., transfected) neurons were manually counted and scored as being knock-in positive or negative. At least 1,000 transfected neurons from two independent neuronal cultures were scored for each time point or experimental condition.

### Quantification of synaptic PSD95 levels and enrichment and synapse size

Hippocampal neurons were transfected at DIV 3 with the pORANGE-PSD95-GFP knock-in construct or at DIV 15 with pSM155-PSD95-GFP overexpression plasmid [55] or pSM155-GFP [55]. At DIV 21, neurons were fixed and stained with mouse anti-PSD95 antibody 1:200

and Alexa594-conjugated secondary antibodies as described above. Neurons were imaged with confocal microscopy as described above. For each neuron, 50 circular regions of interest (ROI) of 1  $\mu\text{m}$  in diameter were drawn around PSD95-GFP-positive synapses. For each ROI, the mean intensity of the GFP signal and anti-PSD95 staining was measured, background was subtracted, and values were normalized to the mean intensity value of all ROIs for both individual channels. Normalized intensity values for the PSD95-GFP knock-in signal and anti-PSD95 signal of individual synapses were plotted. In total, 550 synapses from 11 neurons divided over two independent neuronal cultures were used in the quantification.

To determine relative synaptic PSD95 content, PSD95 staining intensity in 22 circular ROIs of 1  $\mu\text{m}$  in diameter around synapses per transfected (knock-in, overexpression, or GFP control) neuron was measured. Similarly, an equal number of ROIs were drawn around PSD95 puncta of nearby nontransfected neurons within the same image. Intensities of the anti-PSD95 channel were measured, and background was subtracted. Relative PSD95 content was quantified as the average anti-PSD95 intensity in synapses of a transfected neuron divided by those of the nontransfected neurons. To measure synapse size, a threshold was applied to the GFP signal (for PSD95-GFP knock-in and overexpression neurons) or anti-PSD95 signal (for GFP control), and individual synapses were detected using FIJI “Analyze Particles” with a detection size of 0.04-Infinity ( $\mu\text{m}^2$ ) with a detection circularity of 0–1. Measured values were plotted as averages per analyzed neuron. To analyze synaptic enrichment of PSD95, circular ROIs were drawn within synapses and on the dendritic shaft. Mean GFP intensity was measured, background was subtracted, and values were averaged per neuron. Plotted ratio is the average intensity of synaptic GFP signal divided by that of the dendritic shaft. For each condition, at least 15 neurons from two independent neuronal cultures were analyzed.

To compare PSD95 levels in transfected but knock-in-negative neurons, neurons were transfected with a 1:1 ratio of pHomer1c-mCherry and the pORANGE empty vector or pHomer1c-mCherry and pPSD95-GFP knock-in construct at DIV 3. At DIV 21, neurons were fixed and stained for endogenous PSD95 as described above. Homer1c-mCherry-positive neurons were used to locate transfected neurons and to draw ROIs around synapses. For both conditions, 20 neurons from two independent neuronal cultures were analyzed.

### **Quantification of Bassoon, Shank2, CaMKII $\alpha$ , and F-actin levels**

For Bassoon, neurons were transfected at DIV 3 with a 1:1 ratio of RIM1-HA under a synapsin promoter (overexpression construct) [81] and pORANGE template vector (control), pORANGE-GFP-Bassoon knock-in, or pORANGE-Bassoon-GFP knock-in. For Shank2, CaMKII $\alpha$ , and  $\beta$ -actin, neurons were transfected with a 1:1 ratio of pHomer1c-mCherry (overexpression) and pORANGE template vector (control) or pORANGE-Shank2-GFP knock-in, pORANGE-GFP-CaMKII $\alpha$  knock-in, pORANGE-GFP- $\beta$ -actin knock-in #1, or pORANGE-GFP- $\beta$ -actin knock-in #2. Neurons were stained as described above. For  $\beta$ -actin, the neurons were stained with Phalloidin-Alexa594 (Invitrogen) diluted 1:200 in blocking buffer for 1 hour at RT. Coverslips were washed three times for 5 minutes in PBS/Gly and mounted in Mowiol mounting medium. For Bassoon, neurons were stained with anti-GFP (1:2,000) and anti-Bassoon (1:1,000) and anti-HA (1:200) antibodies as described above. For Shank2 and CaMKII $\alpha$ , neurons were stained with anti-Shank2 (1:200) or anti-CaMKII $\alpha$  (1:200) antibodies, respectively. Neurons were imaged with confocal microscopy as described above. Per transfected neuron, both knock-in positive and negative, 20 circular ROIs of 1  $\mu\text{m}$  in diameter were manually drawn around synapses based on Homer1c or RIM signal. Similarly, an equal number of ROIs were drawn around puncta of nearby nontransfected

neurons within the same image based on the antibody staining. To measure relative protein levels, antibody or phalloidin labeling intensities of individual ROI measurements were background subtracted and averaged for each neuron. The average intensity in the transfected neuron relative to the nontransfected neuron from the same image is plotted. For each condition, between 10 and 18 neurons from at least two independent neuronal cultures were analyzed.

### Live-cell imaging of $\beta$ -actin dynamics

Imaging was performed on a spinning disk confocal system (CSU-X1-A1; Yokogawa) mounted on a Nikon Eclipse Ti microscope (Nikon) with Plan Apo VC 100 $\times$  1.40 NA oil objective (Nikon) with excitation from Cobolt Calypso (491 nm) and emission filters (Chroma). The microscope was equipped with a motorized XYZ stage (ASI; MS-2000), Perfect Focus System (Nikon), and Prime BSI sCMOS camera (Photometrics) and was controlled by MetaMorph software (Molecular Devices). Neurons were maintained in a closed incubation chamber (Tokai hit: INUBG2E-ZILCS) at 37 °C in 5% CO<sub>2</sub> in 200  $\mu$ l of conditioned medium.

For studying actin dynamics upon Jasp treatment, neurons were transfected with pORANGE-GFP- $\beta$ -actin knock-in #2 construct at DIV 3 and imaged at DIV 21–23 on a spinning disk confocal system (described above). Every 1 minute, a Z-stack was obtained in a range of 5.5  $\mu$ m (12 planes with 0.5- $\mu$ m intervals). After 5 minutes baseline imaging (6 frames), 100  $\mu$ l/30  $\mu$ M of Jasp (10  $\mu$ M final concentration) or DMSO diluted in conditioned medium was added to the incubation chamber. Imaging was continued for another 20 minutes (21 frames) after addition. For analysis, maximum intensity projections were obtained, and drift was corrected. Background was subtracted in FIJI software using a rolling ball radius of 3.15  $\mu$ m. For each neuron, four ROIs of variable sizes containing at least one spine each were drawn. Integrated densities (InDen) were measured for each frame. Frame-to-frame differences were obtained by subtracting each frame (tx) from the previous (tx–1) using a macro developed by Jacob Pruess. Frame-to-frame differences of the selected ROIs were measured and subtracted from the InDen at tx and normalized to the InDen tx to obtain the frame-to-frame correlation for each ROI at each time point, such that correlation = (InDen tx – [InDen tx – InDen tx–1])/InDen tx. Frame-to-frame correlation was plotted over time. For statistical analysis, the frame-to-frame correlation of the last five time points for each ROI was averaged per cell. For each condition, measurements from 28 ROIs from seven neurons divided over two independent neuronal cultures were used in the analysis.

For FRAP experiments, neurons were transfected with the GFP- $\beta$ -actin knock-in #2 construct at DIV 3 and imaged at DIV 21–23 on a spinning disk confocal system (described above). FRAP experiments were performed using the iLas2 system (Roper Scientific). Experiments were performed in the presence of 10  $\mu$ M Jasp or DMSO added to the imaging chamber 5 minutes before the start of the acquisition. After 2 minutes baseline imaging (single Z-plane, five frames with 30-second intervals), six ROIs with a fixed diameter of 1.26  $\mu$ m containing dendritic spines were bleached using a targeted laser. Imaging during fluorescence recovery was continued for 5 minutes (13 frames with 10-second intervals followed by six frames with 30-second intervals). For analysis, acquisitions were corrected for drift. For each ROI, mean intensities were measured for every time point and corrected for background using the averaged intensity of two background ROIs. For each ROI, intensities were normalized to the averaged intensities of the frames before bleaching and normalized to zero based on the intensity from the first frame after bleaching. Normalized intensities were

---

plotted over time. The mobile fraction of protein was calculated by averaging the normalized intensity of the last five frames for each neuron. For each condition, five neurons divided over two independent neuronal cultures were used in the analysis.

### **Preparation of dissociated hippocampal cultures for gSTED**

Hippocampal neurons were transfected with indicated knock-in constructs at DIV 3 and fixed at DIV 21. Dual-color gSTED imaging (as described above) was performed on PSD95-GFP, GFP- $\beta$ -actin #1, GFP-GluN1 #1, GFP-CaMKII $\alpha$ , GSG1L-GFP, and FRRS1L-GFP knock-in neurons stained with anti-GFP and anti-PSD95. pORANGE FRRS1L-GFP was cotransfected with pSyn tagRFP-ER [82]. (Dual-color) gSTED imaging was additionally performed on extracted cytoskeleton of the GFP- $\beta$ -actin and  $\beta$ 3-tubulin-GFP knock-in neurons. At DIV 7 ( $\beta$ 3-tubulin-GFP knock-in) and DIV 21 (GFP- $\beta$ -actin knock-in), the neuronal cytoskeleton was extracted using extraction buffer (PEM80-buffer [80 mM PIPES, 1 mM EGTA, 2 mM MgCl<sub>2</sub> (pH 6.9)], 0.3% Triton-X, 0.1% glutaraldehyde) for 1 minute at RT. Next, neurons were fixed with PFA/Suc for 10 minutes at RT, washed three times for 5 minutes with PBS/Gly, and subsequently incubated with 1 mg/ml sodium borohydride in PBS for 7 minutes at RT. Coverslips were washed 3 times for 5 minutes with PBS/Gly. The GFP signal was enhanced with anti-GFP staining. The  $\beta$ 3-tubulin-GFP knock-in was additionally stained for  $\alpha$ -tubulin diluted 1:1,000. Anti-GFP primary antibodies were stained with Alexa488- or ATTO647N-conjugated secondary antibodies, and anti-PSD95 and anti- $\alpha$ -tubulin were stained with the Alexa594- or ATTO647N-conjugated secondary antibody (all as described above). To label surface receptors, GFP-GluN1 knock-in neurons were stained with anti-GFP prior to permeabilization and subsequent anti-PSD95 staining.

### **Quantification of colocalization gSTED**

Using ImageJ software, a line scan of interest was drawn to obtain pixel intensity data to assess the degree of colocalization between two structures along that line. To quantify the degree of colocalization between two structures, entire images showing parts of the dendritic tree of a knock-in neuron were used for analysis. First, all dendritic spines (positive for both proteins: PSD95-GFP knock-in and anti-PSD95 staining or GFP- $\beta$ -actin knock-in and anti-PSD95 staining) were selected by drawing ROIs in ImageJ. Next, the ROIs were combined to clear the outside of the ROIs to remove all background from surrounding neurons or dendritic shafts. Then, the ImageJ plug-in “JaCoP” (Just Another Colocalization Plug-in) was used to calculate the PCC and MOC. For the MOC, the thresholding was done manually. These analyses were performed on both the confocal and STED maximum projections of the exact same regions (of a neuron). In total, 10 PSD95-GFP knock-in and seven GFP- $\beta$ -actin knock-in neurons were analyzed from two independent experiments.

### **Confocal and STED quantifications of NMDA receptors**

Neurons were transfected at DIV 3 with the pORANGE-GFP-GluN1 knock-in #1 construct. Neurons were fixed at DIV 21 and stained with anti-PSD95 as described above. Neurons were imaged with confocal microscopy as described above. For each neuron, 50 circular ROIs of 1  $\mu$ m in diameter were drawn around GFP-GluN1-positive synapses. For each ROI, the mean intensity of the GFP signal and anti-PSD95 staining was measured, background was subtracted, and values were normalized to the mean intensity value of all ROIs for both individual channels. Normalized intensity values for the GFP-GluN1 knock-in signal and anti-PSD95 signal of individual synapses were plotted. In total, 450 synapses from nine

neurons divided over two independent neuronal cultures were used in the analysis.

The FIJI plug-in Full Width at Half Maximum (FWHM) macro developed by John Lim was used to measure the FWHM from intensity profiles using Gaussian fitting. Line scans were drawn along the width and length of identified GluN1 substructures (by setting an appropriate brightness/contrast) to obtain the FWHM of the length and width of these substructures. Subsequently, these substructures were categorized as synaptic or extrasynaptic based on the colocalization with PSD95. For image display, the length was plotted against the width for each cluster. In all, 479 GFP-GluN1 clusters (387 synaptic, 92 extrasynaptic) from three neurons were analyzed.

For the quantification of total GluN1 cluster area per synapse, and correlation with synapse area, the same images were used as for the quantification of the FWHM of the GluN1 substructures. Specifically, the STED resolved images were used for the quantification of GluN1 cluster area, whereas the confocal images were used to quantify the area of the PSD, using PSD95 as a marker. First, an ROI was drawn around the knock-in neuron of interest to clear the outside of the ROI, removing all background. Subsequently, the image was subjected to thresholding to isolate the objects of interest from the background and watershedding to separate overlapping objects. Then, all objects (GluN1 clusters and PSDs) were detected using “Analyze Particles” with a detection size of 0.02-Infinity ( $\mu\text{m}^2$ ) for GluN1 substructures and 0.04-Infinity ( $\mu\text{m}^2$ ) for PSDs, and all with a detection circularity of 0–1.

### SMLM and detection

dSTORM imaging was performed on a Nikon Ti microscope equipped with a Nikon 100 $\times$  NA 1.49 Apo total internal reflection fluorescence (TIRF) oil objective, a Perfect Focus System. Effective pixel size is 65 nm. Oblique laser illumination was achieved using a custom illumination pathway with a 60-mW, 405-nm-diode laser (Omicron); a 200-mW, 491-nm-diode laser (Omicron); and a 140-mW, 641-nm-diode laser (Omicron). Emission light was separated from excitation light with a quad-band polychroic mirror (ZT405/488/561/640rpc, Chroma) and additional band-pass emission filters (ET 525/595/700, Chroma). Fluorescence emission was acquired using an ORCA-Flash 4.0v2 CMOS camera (Hamamatsu). Lasers were controlled using Omicron software, whereas all other components were controlled by  $\mu$ Manager software [83].

Live-cell SMLM imaging experiments were performed on a Nikon Ti microscope equipped with a 100 $\times$  NA 1.49 Apo TIRF oil objective, a Perfect Focus System, and an additional 2.5 $\times$  Optovar to achieve an effective pixel size of 64 nm. Oblique laser illumination was achieved using a custom illumination pathway with an AA acousto-optic tunable filter (AA optoelectronics); a 15-mW, 405-nm-diode laser (Power Technology); a 100-mW, 561-nm-DPSS laser (Cobolt Jive); and a 40-mW, 640-nm-diode laser (Power Technology). Emission light was separated from excitation light with a quad-band polychroic mirror (ZT405/488/561/640rpc, Chroma) and additional band-pass emission filters (ET 525/595/700, Chroma). Fluorescence emission was acquired using a DU-897D EMCCD camera (Andor). All components were controlled by  $\mu$ Manager software [83].

Acquired image stacks were analyzed using the ImageJ plug-in Detection of Molecules (DoM) v1.1.5 [84]. Briefly, each image was convoluted with a 2D Mexican hat-type kernel that matches the microscope’s point spread function. Spots were detected by thresholding the images and localized by fitting a 2D Gaussian function using unweighted nonlinear least-squares fitting with the Levenberg–Marquardt algorithm. Drift correction was applied



---

by calculating the spatial cross-correlation function between intermediate superresolved reconstructions.

### Single-molecule tracking PALM and analysis

Neurons were transfected with the mEos3.2-CaMKII $\alpha$  knock-in construct at DIV 3 and imaged at DIV 21–23. Neurons were imaged in extracellular imaging buffer (10 mM HEPES, 120 mM NaCl, 3 mM KCl, 2 mM CaCl<sub>2</sub>, 2 mM MgCl<sub>2</sub>, 10 mM glucose [pH 7.35]) at RT. mEos3.2 molecules were photoconverted from green to red fluorescence using simultaneous 405-nm and 561-nm illumination using TIRF. Stacks of 5,000–7,000 frames were acquired at 50 Hz. PALM reconstruction was made in DoM, plotting localizations based on their localization precision, rendered with a pixel size of 10 × 10 nm. Molecules localized with precision <25 nm were used for further analysis. Tracking was accomplished using custom tracking algorithms in MATLAB (MathWorks) using a tracking radius of 512 nm. For tracks consisting of  $\geq 4$  frames, the instantaneous diffusion coefficient was estimated as described [40]. The first three points of the MSD versus elapsed time (t) plot were used to fit the slope using linear fitting adding a value of 0 at MSD(0). Tracks with a negative slope (<8%) were ignored. The diffusion coefficient  $D_{\text{eff}}$  was then calculated using  $\text{MSD} = 4D_{\text{eff}} t$ . Individual tracks were plotted using MATLAB, and each was given a random color. All single-molecule trajectories from all acquisitions were used to visualize a frequency distribution. On this, we fitted two Gaussian distributions to identify the two kinetic populations. Mean values for the two fits were calculated per analyzed neuron and plotted. In total, 11 neurons from two independent experiments were included in the analysis.

### dSTORM imaging and analysis

Hippocampal neurons were transfected at DIV 3 with the GFP-GluN1 knock-in construct #1 and fixed on DIV 21. Neurons were surface stained with anti-GFP 1:2,000 and Alexa647-conjugated secondaries as described above. Neurons were postfixed in 4% PFA/Suc for 5 minutes, additionally washed 3 times with PBS/Gly, and kept in PBS at 4 °C until imaging. dSTORM imaging was performed in PBS containing 10–50 mM MEA, 5% w/v glucose, 700  $\mu\text{g/ml}$  glucose oxidase, and 40  $\mu\text{g/ml}$  catalase. GFP-GluN1 knock-in-positive neurons were located on GFP signal. For dSTORM, the sample was illuminated (in TIRF) with continuous 647-nm laser light and gradually increasing intensity of 405-nm laser light. Stacks of 10,000–15,000 frames were acquired at 50 Hz. dSTORM reconstruction was made in DoM, plotting localizations based on their localization precision, rendered with a pixel size of 10 × 10 nm. Molecules with a localization precision <15 nm were selected for further analysis. Next, blinking events longer than one frame were filtered out by tracking (tracking radius of 130 nm). GluN1 clusters were identified using the DBSCAN algorithm [62] implemented in MATLAB. Subsequently, the alpha shape was used as the cluster border. Clusters with a density of >5,000 molecules per micrometer were used for further analysis. For each individual cluster, molecules were plotted and color-coded according to the local density [55], defined as the number of molecules within a radius of 5 times the mean nearest neighbor distance of all molecules within the cluster. Molecules with a local density value >40 were considered to be enriched in a nanodomain. Nanodomains were isolated using MATLAB functions `linkage()` and `cluster()`. The polygon circumventing molecules belonging to individual nanodomains was used to calculate the diameter of the nanodomain. Nanodomains containing <5 localizations and diameter <30 nm were rejected. In total, 859 clusters from three neurons from two independent experiments were analyzed.

**uPAINT and analysis**

Neurons transfected with the GFP-GluN1 knock-in construct #1 and pCamk Homer1c-mCherry at DIV 3 were imaged at DIV 21–23 in extracellular imaging buffer supplemented with 0.8% BSA. GFP-GluN1-positive neurons were identified by GFP signal, and ATTO647N-conjugated anti-GFP nanobodies (GFPBooster-ATTO647N, Chromotek) were bath applied to a final dilution of 1:50,000. Imaging was conducted at a 50-Hz frame rate with 640-nm excitation laser illumination (in TIRF). Molecules fitted with a precision  $<50$  were tracked with tracking radius of 512 nm and diffusion coefficient determined for tracks  $>30$  frames. A cell mask was drawn manually to filter out localizations outside neurons due to nonspecifically bound nanobody. Tracking and estimation of the instantaneous diffusion was performed as described for the PALM imaging. Synapses were identified based on widefield Homer1c-mCherry signal as described [85]. Synaptic tracks were defined as tracks in which 80% of the localizations were located within the border of the synapse. All others were considered extrasynaptic. In total, 6 neurons from three independent experiments were analyzed.

**Statistics**

Statistical significance was tested with a Student t test when comparing two groups. A P value below 0.05 was considered significant. If multiple groups were compared, statistical significance was tested with a one-way ANOVA followed by a Bonferroni's multiple comparison. In all figures, \* was used to indicate a P value  $< 0.05$ , \*\* for P  $< 0.01$ , and \*\*\* for P  $< 0.001$ . Reported n is number of neurons, and each experiment was replicated in neuronal cultures from at least two independent preparations. Statistical analysis and graphs were prepared in GraphPad Prism, and figures were generated in Adobe Illustrator CC.

**ADDITIONAL RESOURCES**

Plasmids from this study will be made available through Addgene (see S5 Table).

**ACKNOWLEDGMENTS**

We want to thank all members of the MacGillavry lab for discussions. We want to thank Corette J. Wierenga for providing organotypic hippocampal slice cultures and Onur Basak for helpful discussions. We want to thank Anna Akhmanova, Lukas C. Kapitein, and Corette J. Wierenga for critical reading of the manuscript.

## REFERENCES

1. Biederer T, Kaeser PS, Blanpied TA. Transcellular nanoalignment of synaptic function. *Neuron*. 2017;96(3):680-96. doi: 10.1016/j.neuron.2017.10.006. PubMed PMID: 29096080.
2. Sigal YM, Zhou R, Zhuang X. Visualizing and discovering cellular structures with super-resolution microscopy. *Science*. 2018;361(6405):880-7. Epub 2018/09/01. doi: 10.1126/science.aau1044. PubMed PMID: 30166485.
3. Sahl SJ, Hell SW, Jakobs S. Fluorescence nanoscopy in cell biology. *Nat Rev Mol Cell Biol*. 2017;18(11):685-701. Epub 2017/09/07. doi: 10.1038/nrm.2017.71. PubMed PMID: 28875992.
4. Schnell U, Dijk F, Sjollem KA, Giepmans BN. Immunolabeling artifacts and the need for live-cell imaging. *Nat Methods*. 2012;9(2):152-8. Epub 2012/02/01. doi: 10.1038/nmeth.1855
5. El-Husseini A, Schnell E, Chetkovich D, Nicoll R, Brecht D. PSD-95 involvement in maturation of excitatory synapses. *Science*. 2000;290:1364-8.
6. Roussignol G, Ango F, Romorini S, Tu JC, Sala C, Worley PF, et al. Shank expression is sufficient to induce functional dendritic spine synapses in aspiny neurons. *J Neurosci*. 2005;25(14):3560-70. Epub 2005/04/09. doi: 10.1523/JNEUROSCI.4354-04.2005. PubMed PMID: 15814786.
7. Futai K, Kim MJ, Hashikawa T, Scheiffele P, Sheng M, Hayashi Y. Retrograde modulation of presynaptic release probability through signaling mediated by PSD-95-neurotrophin. *Nat Neurosci*. 2007;10(2):186-95. Epub 2007/01/24. doi: 10.1038/nn1837. PubMed PMID: 17237775.
8. Sala C, Piech V, Wilson NR, Passafium M, Liu G, Sheng M. Regulation of dendritic spine morphology and synaptic function by Shank and Homer. *Neuron*. 2001;31(1):115-30. Epub 2001/08/11. PubMed PMID: 11498055.
9. Schluter OM, Xu W, Malenka RC. Alternative N-terminal domains of PSD-95 and SAP97 govern activity-dependent regulation of synaptic AMPA receptor function. *Neuron*. 2006;51(1):99-111. Epub 2006/07/04. doi: 10.1016/j.neuron.2006.05.016. PubMed PMID: 16815335.
10. Fukata Y, Dimitrov A, Boncompain G, Vielemeyer O, Perez F, Fukata M. Local palmitoylation cycles define activity-regulated postsynaptic subdomains. *J Cell Biol*. 2013;202(1):145-61. Epub 2013/07/10. doi: 10.1083/jcb.201302071. jcb.201302071 [pii]. PubMed PMID: 23836932.
11. Gross GG, Junge JA, Mora RJ, Kwon HB, Olson CA, Takahashi TT, et al. Recombinant probes for visualizing endogenous synaptic proteins in living neurons. *Neuron*. 2013;78(6):971-85. doi: 10.1016/j.neuron.2013.04.017. PubMed PMID: 23791193; PubMed Central PMCID: PMC3779638.
12. Mora RJ, Roberts RW, Arnold DB. Recombinant probes reveal dynamic localization of CaMKIIalpha within somata of cortical neurons. *J Neurosci*. 2013;33(36):14579-90. Epub 2013/09/06. doi: 10.1523/JNEUROSCI.2108-13.2013. PubMed PMID: 24005308; PubMed Central PMCID: PMC3761057.
13. Nizak C, Monier S, del Nery E, Moutel S, Goud B, Perez F. Recombinant antibodies to the small GTPase Rab6 as conformation sensors. *Science*. 2003;300(5621):984-7. Epub 2003/05/10. doi: 10.1126/science.1083911. PubMed PMID: 12738866.
14. Dong JX, Lee Y, Kirmiz M, Palacio S, Dumitras C, Moreno CM, et al. A toolbox of nanobodies developed and validated for use as intrabodies and nanoscale immunolabels in mammalian brain neurons. *Elife*. 2019;8. Epub 2019/10/01. doi: 10.7554/eLife.48750. PubMed PMID: 31566565; PubMed Central PMCID: PMC6785268.
15. Knott GJ, Doudna JA. CRISPR-Cas guides the future of genetic engineering. *Science*. 2018;361(6405):866-9. Epub 2018/09/01. doi: 10.1126/science.aat5011. PubMed PMID: 30166482.
16. Lee SH, Kim S, Hur JK. CRISPR and Target-Specific DNA Endonucleases for Efficient DNA Knock-in in Eukaryotic Genomes. *Mol Cells*. 2018;41(11):943-52. Epub 2018/11/30. doi: 10.14348/molcells.2018.0408. PubMed PMID: 30486613; PubMed Central PMCID: PMC6277560.
17. Uemura T, Mori T, Kurihara T, Kawase S, Koike R, Satoga M, et al. Fluorescent protein tagging of endogenous protein in brain neurons using CRISPR/Cas9-mediated knock-in and in utero electroporation techniques. *Sci Rep*. 2016;6:35861. Epub 2016/10/27. doi: 10.1038/srep35861. PubMed PMID: 27782168; PubMed Central PMCID: PMC5080626.
18. Mikuni T, Nishiyama J, Sun Y, Kamasawa N, Yasuda R. High-Throughput, High-Resolution Mapping of Protein Localization in Mammalian Brain by In Vivo Genome Editing. *Cell*. 2016;165(7):1803-17. Epub 2016/05/18. doi: 10.1016/j.cell.2016.04.044. PubMed PMID: 27180908; PubMed Central PMCID: PMC4912470.
19. Orthwein A, Noordermeer SM, Wilson MD, Landry S, Enchev RI, Sherker A, et al. A mechanism for the suppression of homologous recombination in G1 cells. *Nature*. 2015;528(7582):422-6. Epub 2015/12/10. doi: 10.1038/nature16142. PubMed PMID: 26649820; PubMed Central PMCID: PMC4880051.
20. Nishiyama J, Mikuni T, Yasuda R. Virus-Mediated Genome Editing via Homology-Directed Repair in Mitotic and Postmitotic Cells in Mammalian Brain. *Neuron*. 2017;96(4):755-68 e5. Epub 2017/10/24. doi: 10.1016/j.neuron.2017.10.004. PubMed PMID: 29056297; PubMed Central PMCID: PMC5691606.
21. Yao X, Wang X, Hu X, Liu Z, Liu J, Zhou H, et al. Homology-mediated end joining-based targeted integration using CRISPR/Cas9. *Cell Res*. 2017;27(6):801-14. Epub 2017/05/20. doi: 10.1038/cr.2017.76. PubMed PMID: 28524166; PubMed Central PMCID: PMC5518881.
22. Betermier M, Bertrand P, Lopez BS. Is non-homologous end-joining really an inherently error-prone process? *PLoS Genet*. 2014;10(1):e1004086. Epub 2014/01/24. doi: 10.1371/journal.pgen.1004086. PubMed PMID: 24453986; PubMed Central PMCID: PMC3894167.
23. Gao Y, Hisey E, Bradshaw TWA, Erata E, Brown WE, Courtland JL, et al. Plug-and-Play Protein Modification Using Homology-Independent Universal Genome Engineering. *Neuron*. 2019. Epub 2019/07/06. doi: 10.1016/j.neuron.2019.05.047. PubMed PMID: 31272828.
24. Suzuki K, Tsunekawa Y, Hernandez-Benitez R, Wu J, Zhu J, Kim EJ, et al. In vivo genome editing via CRISPR/Cas9 mediated homology-independent targeted integration. *Nature*. 2016;540(7631):

- 144-9. doi: 10.1038/nature20565. PubMed PMID: 27851729; PubMed Central PMCID: PMC63531785.
25. Spence EF, Dube S, Uezu A, Locke M, Soderblom EJ, Soderling SH. In vivo proximity proteomics of nascent synapses reveals a novel regulator of cytoskeleton-mediated synaptic maturation. *Nat Commun.* 2019;10(1):386. Epub 2019/01/25. doi: 10.1038/s41467-019-08288-w. PubMed PMID: 30674877; PubMed Central PMCID: PMC6344529.
  26. Matsuda T, Oinuma I. Imaging endogenous synaptic proteins in primary neurons at single-cell resolution using CRISPR/Cas9. *Mol Biol Cell.* 2019;30(22):2838-55. Epub 2019/09/12. doi: 10.1091/mbc.E19-04-0223. PubMed PMID: 31509485; PubMed Central PMCID: PMC6789158.
  27. Platt RJ, Chen S, Zhou Y, Yim MJ, Swiech L, Kempton HR, et al. CRISPR-Cas9 knockin mice for genome editing and cancer modeling. *Cell.* 2014;159(2):440-55. Epub 2014/09/30. doi: 10.1016/j.cell.2014.09.014. PubMed PMID: 25263330; PubMed Central PMCID: PMC4265475.
  28. Shen MW, Arbab M, Hsu JY, Worstell D, Culbertson SJ, Krabbe O, et al. Predictable and precise template-free CRISPR editing of pathogenic variants. *Nature.* 2018;563(7733):646-51. Epub 2018/11/09. doi: 10.1038/s41586-018-0686-x. PubMed PMID: 30405244.
  29. van Overbeek M, Capurso D, Carter MM, Thompson MS, Frias E, Russ C, et al. DNA Repair Profiling Reveals Nonrandom Outcomes at Cas9-Mediated Breaks. *Mol Cell.* 2016;63(4):633-46. Epub 2016/08/09. doi: 10.1016/j.molcel.2016.06.037. PubMed PMID: 27499295.
  30. Doench JG, Fusi N, Sullender M, Hegde M, Vaimberg EW, Donovan KF, et al. Optimized sgRNA design to maximize activity and minimize off-target effects of CRISPR-Cas9. *Nat Biotechnol.* 2016;34(2):184-91. Epub 2016/01/19. doi: 10.1038/nbt.3437. PubMed PMID: 26780180; PubMed Central PMCID: PMC4744125.
  31. Bae S, Kweon J, Kim HS, Kim JS. Microhomology-based choice of Cas9 nuclease target sites. *Nat Methods.* 2014;11(7):705-6. Epub 2014/06/28. doi: 10.1038/nmeth.3015. PubMed PMID: 24972169.
  32. Sheng M, Hoogenraad C. The postsynaptic architecture of excitatory synapses: a more quantitative view. *Annu Rev Biochem.* 2007;76:823-47.
  33. Dresbach T, Hempelmann A, Spilker C, tom Dieck S, Altmann WD, Zuschratter W, et al. Functional regions of the presynaptic cytomatrix protein bassoon: significance for synaptic targeting and cytomatrix anchoring. *Mol Cell Neurosci.* 2003;23(2):279-91. Epub 2003/06/19. PubMed PMID: 12812759.
  34. Hotulainen P, Llano O, Smirnov S, Tanhuanpaa K, Faix J, Rivera C, et al. Defining mechanisms of actin polymerization and depolymerization during dendritic spine morphogenesis. *J Cell Biol.* 2009;185(2):323-39. Epub 2009/04/22. doi: 10.1083/jcb.200809046. PubMed PMID: 19380880; PubMed Central PMCID: PMC2700375.
  35. Korobova F, Svitkina T. Molecular architecture of synaptic actin cytoskeleton in hippocampal neurons reveals a mechanism of dendritic spine morphogenesis. *Mol Biol Cell.* 2010;21(1):165-76. Epub 2009/11/06. doi: 10.1091/mbc.E09-07-0596. PubMed PMID: 19889835; PubMed Central PMCID: PMC2801710.
  36. Zheng CY, Petralia RS, Wang YX, Kachar B, Wenthold RJ. SAP102 is a highly mobile MAGUK in spines. *J Neurosci.* 2010;30(13):4757-66. Epub 2010/04/02. doi: 10.1523/JNEUROSCI.6108-09.2010. PubMed PMID: 20357126; PubMed Central PMCID: PMC2874826.
  37. Lisman J, Yasuda R, Raghavachari S. Mechanisms of CaMKII action in long-term potentiation. *Nat Rev Neurosci.* 2012;13(3):169-82. Epub 2012/02/16. doi: 10.1038/nrn3192. PubMed PMID: 22334212; PubMed Central PMCID: PMC4050655.
  38. Shen K, Meyer T. Dynamic control of CaMKII translocation and localization in hippocampal neurons by NMDA receptor stimulation. *Science.* 1999;284(5411):162-6. Epub 1999/04/02. PubMed PMID: 10102820.
  39. Frost NA, Shroff H, Kong H, Betzig E, Blanpied TA. Single-molecule discrimination of discrete perisynaptic and distributed sites of actin filament assembly within dendritic spines. *Neuron.* 2010;67(1):86-99. Epub 2010/07/14. doi: 10.1016/j.neuron.2010.05.026. PubMed PMID: 20624594; PubMed Central PMCID: PMC2904347.
  40. Lu HE, MacGillavry HD, Frost NA, Blanpied TA. Multiple spatial and kinetic subpopulations of CaMKII in spines and dendrites as resolved by single-molecule tracking PALM. *J Neurosci.* 2014;34(22):7600-10. doi: 10.1523/JNEUROSCI.4364-13.2014. PubMed PMID: 24872564; PubMed Central PMCID: PMC4035521.
  41. Xu K, Zhong G, Zhuang X. Actin, spectrin, and associated proteins form a periodic cytoskeletal structure in axons. *Science.* 2013;339(6118):452-6. Epub 2012/12/15. doi: 10.1126/science.1232251. PubMed PMID: 23239625; PubMed Central PMCID: PMC3815867.
  42. D'Este E, Kamin D, Gottfert F, El-Hady A, Hell SW. STED nanoscopy reveals the ubiquity of subcortical cytoskeleton periodicity in living neurons. *Cell Rep.* 2015;10(8):1246-51. Epub 2015/03/04. doi: 10.1016/j.celrep.2015.02.007. PubMed PMID: 25732815.
  43. Han B, Zhou R, Xia C, Zhuang X. Structural organization of the actin-spectrin-based membrane skeleton in dendrites and soma of neurons. *Proc Natl Acad Sci U S A.* 2017;114(32):E6678-E85. Epub 2017/07/26. doi: 10.1073/pnas.1705043114. PubMed PMID: 28739933; PubMed Central PMCID: PMC5559029.
  44. Dunn KW, Kamocka MM, McDonald JH. A practical guide to evaluating colocalization in biological microscopy. *Am J Physiol Cell Physiol.* 2011;300(4):C723-42. Epub 2011/01/07. doi: 10.1152/ajpcell.00462.2010. PubMed PMID: 21209361; PubMed Central PMCID: PMC3074624.
  45. Manders EM, Stap J, Brakenhoff GJ, van Driel R, Aten JA. Dynamics of three-dimensional replication patterns during the S-phase, analysed by double labelling of DNA and confocal microscopy. *J Cell Sci.* 1992; 103 ( Pt 3):857-62. Epub 1992/11/01. PubMed PMID: 1478975.
  46. Bissen D, Foss F, Acker-Palmer A. AMPA receptors and their minions: auxiliary proteins in AMPA receptor trafficking. *Cell Mol Life Sci.* 2019;76(11):2133-69. Epub 2019/04/03. doi: 10.1007/s00018-019-03068-7. PubMed PMID: 30937469; PubMed Central PMCID: PMC6502786.
  47. Schwenk J, Harmel N, Brechet A, Zolles G, Berkefeld H, Muller CS, et al. High-resolution

---

proteomics unravel architecture and molecular diversity of native AMPA receptor complexes.

Neuron. 2012;74(4):621-33. doi: 10.1016/j.neuron.2012.03.034. PubMed PMID: 22632720.

48. Gu X, Mao X, Lussier MP, Hutchison MA, Zhou L, Hamra FK, et al. GSG1L suppresses AMPA receptor-mediated synaptic transmission and uniquely modulates AMPA receptor kinetics in hippocampal neurons. *Nat Commun*. 2016;7:10873. Epub 2016/03/05. doi: 10.1038/ncomms10873. PubMed PMID: 26932439; PubMed Central PMCID: PMC4778064.
49. Shanks NF, Savas JN, Maruo T, Cais O, Hirao A, Oe S, et al. Differences in AMPA and kainate receptor interactomes facilitate identification of AMPA receptor auxiliary subunit GSG1L. *Cell Rep*. 2012;1(6):590-8. Epub 2012/07/21. doi: 10.1016/j.celrep.2012.05.004. PubMed PMID: 22813734; PubMed Central PMCID: PMC3401968.
50. Schwenk J, Boudkkazi S, Kocylowski MK, Brechet A, Zolles G, Bus T, et al. An ER Assembly Line of AMPA-Receptors Controls Excitatory Neurotransmission and Its Plasticity. *Neuron*. 2019;104(4):680-92 e9. Epub 2019/10/13. doi: 10.1016/j.neuron.2019.08.033. PubMed PMID: 31604597.
51. Brechet A, Buchert R, Schwenk J, Boudkkazi S, Zolles G, Siquier-Pernet K, et al. AMPA-receptor specific biogenesis complexes control synaptic transmission and intellectual ability. *Nat Commun*. 2017;8:15910. Epub 2017/07/05. doi: 10.1038/ncomms15910. PubMed PMID: 28675162; PubMed Central PMCID: PMC5500892.
52. Han W, Wang H, Li J, Zhang S, Lu W. Ferric Chelate Reductase 1 Like Protein (FRRS1L) Associates with Dynein Vesicles and Regulates Glutamatergic Synaptic Transmission. *Front Mol Neurosci*. 2017;10:402. Epub 2017/12/26. doi: 10.3389/fnmol.2017.00402. PubMed PMID: 29276473; PubMed Central PMCID: PMC5727121.
53. Stewart M, Lau P, Banks G, Bains RS, Castroflorio E, Oliver PL, et al. Loss of Frrs1l disrupts synaptic AMPA receptor function, and results in neurodevelopmental, motor, cognitive and electrographical abnormalities. *Dis Model Mech*. 2019. Epub 2019/01/30. doi: 10.1242/dmm.036806. PubMed PMID: 30692144.
54. Keller Mayer B, Ferreira JS, Dupuis J, Levett F, Grillo-Bosch D, Bard L, et al. Differential nanoscale topography and functional role of GluN2-NMDA receptor subtypes at glutamatergic synapses. *Neuron*. 2018;100(1):106-19 e7. Epub 2018/10/03. doi: 10.1016/j.neuron.2018.09.012. PubMed PMID: 30269991.
55. MacGillavry HD, Song Y, Raghavachari S, Blanpied TA. Nanoscale scaffolding domains within the postsynaptic density concentrate synaptic AMPA receptors. *Neuron*. 2013;78(4):615-22. Epub 2013/05/31. doi: 10.1016/j.neuron.2013.03.009. PubMed PMID: 23719161.
56. Jezequel J, Johansson EM, Dupuis JP, Rogemond V, Grea H, Keller Mayer B, et al. Dynamic disorganization of synaptic NMDA receptors triggered by autoantibodies from psychotic patients. *Nat Commun*. 2017;8(1):1791. Epub 2017/11/28. doi: 10.1038/s41467-017-01700-3. PubMed PMID: 29176681; PubMed Central PMCID: PMC5702610.
57. Shi S, Hayashi Y, Esteban JA, Malinow R. Subunit-specific rules governing AMPA receptor trafficking to synapses in hippocampal pyramidal neurons. *Cell*. 2001;105(3):331-43. Epub 2001/05/12. doi: S0092-8674(01)00321-X. PubMed PMID: 11348590.
58. Peng J, Kim MJ, Cheng D, Duong DM, Gygi SP, Sheng M. Semiquantitative proteomic analysis of rat forebrain postsynaptic density fractions by mass spectrometry. *J Biol Chem*. 2004;279(20):21003-11. Epub 2004/03/17. doi: 10.1074/jbc.M400103200. PubMed PMID: 15020595.
59. Racca C, Stephenson FA, Streit P, Roberts JD, Somogyi P. NMDA receptor content of synapses in stratum radiatum of the hippocampal CA1 area. *J Neurosci*. 2000;20(7):2512-22. Epub 2000/03/24. PubMed PMID: 10729331.
60. Nimchinsky EA, Yasuda R, Oertner TG, Svoboda K. The number of glutamate receptors opened by synaptic stimulation in single hippocampal spines. *J Neurosci*. 2004;24(8):2054-64. Epub 2004/02/27. doi: 10.1523/JNEUROSCI.5066-03.2004. PubMed PMID: 14985448.
61. Metzbower SR, Joo Y, Benavides DR, Blanpied TA. Properties of Individual Hippocampal Synapses Influencing NMDA-Receptor Activation by Spontaneous Neurotransmission. *eNeuro*. 2019;6(3). Epub 2019/05/22. doi: 10.1523/ENEURO.0419-18.2019. PubMed PMID: 31110134; PubMed Central PMCID: PMC6541874.
62. Ester M, Kriegl H-P, Sander J, Xu X. A density-based algorithm for discovering clusters a density-based algorithm for discovering clusters in large spatial databases with noise. Proceedings of the Second International Conference on Knowledge Discovery and Data Mining; Portland, Oregon. 3001507. AAAI Press; 1996. p. 226-31.
63. Giannone G, Hossy E, Levett F, Constals A, Schulze K, Sobolevsky A, et al. Dynamic super-resolution imaging of endogenous proteins on living cells at ultra high density. *Biophys J*. 2010;99(4):1303-10.
64. Back S, Necarsulmer J, Whitaker LR, Coke LM, Koivula P, Heathward EJ, et al. Neuron-Specific Genome Modification in the Adult Rat Brain Using CRISPR-Cas9 Transgenic Rats. *Neuron*. 2019;102(1):105-19 e8. Epub 2019/02/23. doi: 10.1016/j.neuron.2019.01.035. PubMed PMID: 30792150.
65. Lindeboom RG, Supek F, Lehner B. The rules and impact of nonsense-mediated mRNA decay in human cancers. *Nat Genet*. 2016;48(10):1112-8. Epub 2016/09/13. doi: 10.1038/ng.3664. PubMed PMID: 27618451; PubMed Central PMCID: PMC45045715.
66. Kleinstiver BP, Pattanayak V, Prew MS, Tsai SQ, Nguyen NT, Zheng Z, et al. High-fidelity CRISPR-Cas9 nucleases with no detectable genome-wide off-target effects. *Nature*. 2016;529(7587):490-5. Epub 2016/01/07. doi: 10.1038/nature16526. PubMed PMID: 26735016; PubMed Central PMCID: PMC4851738.
67. Slaymaker IM, Gao L, Zetsche B, Scott DA, Yan WX, Zhang F. Rationally engineered Cas9 nucleases with improved specificity. *Science*. 2016;351(6268):84-8. Epub 2015/12/03. doi: 10.1126/science.aad5227. PubMed PMID: 26628643; PubMed Central PMCID: PMC4714946.
68. Dewari PS, Southgate B, McCarten K, Monogarov G, O'Duibhir E, Quinn N, et al. An efficient and scalable

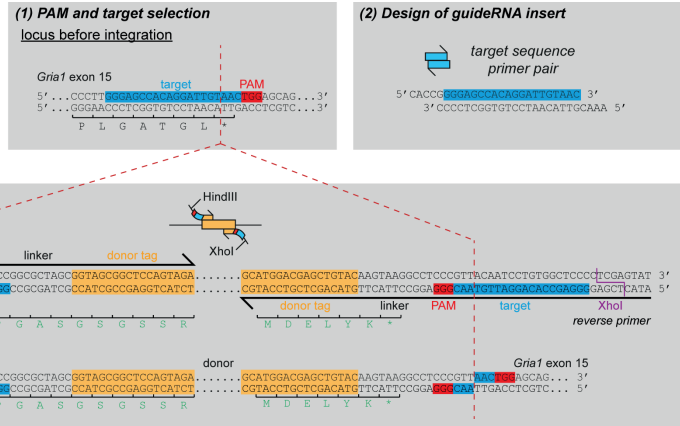
- pipeline for epitope tagging in mammalian stem cells using Cas9 ribonucleoprotein. *Elife*. 2018;7. Epub 2018/04/12. doi: 10.7554/eLife.35069. PubMed PMID: 29638216; PubMed Central PMCID: PMCPCMC5947990.
69. Vogel C, Abreu Rde S, Ko D, Le SY, Shapiro BA, Burns SC, et al. Sequence signatures and mRNA concentration can explain two-thirds of protein abundance variation in a human cell line. *Mol Syst Biol*. 2010;6:400. Epub 2010/08/27. doi: 10.1038/msb.2010.59. PubMed PMID: 20739923; PubMed Central PMCID: PMCPCMC2947365.
  70. Roux KJ, Kim DI, Raida M, Burke B. A promiscuous biotin ligase fusion protein identifies proximal and interacting proteins in mammalian cells. *J Cell Biol*. 2012;196(6):801-10. Epub 2012/03/14. doi: 10.1083/jcb.201112098. PubMed PMID: 22412018; PubMed Central PMCID: PMCPCMC3308701.
  71. Lam SS, Martell JD, Kamer KJ, Deerinck TJ, Ellisman MH, Mootha VK, et al. Directed evolution of APEX2 for electron microscopy and proximity labeling. *Nat Methods*. 2015;12(1):51-4. Epub 2014/11/25. doi: 10.1038/nmeth.3179. PubMed PMID: 25419960; PubMed Central PMCID: PMCPCMC4296904.
  72. Sinnen BL, Bowen AB, Forte JS, Hiester BG, Crosby KC, Gibson ES, et al. Optogenetic Control of Synaptic Composition and Function. *Neuron*. 2017;93(3):646-60 e5. Epub 2017/01/31. doi: 10.1016/j.neuron.2016.12.037. PubMed PMID: 28132827; PubMed Central PMCID: PMCPCMC5300939.
  73. van Bergeijk P, Adrian M, Hoogenraad CC, Kapitein LC. Optogenetic control of organelle transport and positioning. *Nature*. 2015;518(7537):111-4. Epub 2015/01/07. doi: 10.1038/nature14128. PubMed PMID: 25561173; PubMed Central PMCID: PMCPCMC5063096.
  74. Cunha-Ferreira I, Chazeau A, Buijs RR, Stucchi R, Will L, Pan X, et al. The HAUS Complex Is a Key Regulator of Non-centrosomal Microtubule Organization during Neuronal Development. *Cell Rep*. 2018;24(4):791-800. Epub 2018/07/26. doi: 10.1016/j.celrep.2018.06.093. PubMed PMID: 30044976; PubMed Central PMCID: PMCPCMC6083040.
  75. Hsu PD, Scott DA, Weinstein JA, Ran FA, Konermann S, Agarwala V, et al. DNA targeting specificity of RNA-guided Cas9 nucleases. *Nat Biotechnol*. 2013;31(9):827-32. Epub 2013/07/23. doi: 10.1038/nbt.2647. PubMed PMID: 23873081; PubMed Central PMCID: PMCPCMC3969858.
  76. Lin JY, Knutsen PM, Muller A, Kleinfeld D, Tsien RY. ReaChR: a red-shifted variant of channelrhodopsin enables deep transcranial optogenetic excitation. *Nat Neurosci*. 2013;16(10):1499-508. Epub 2013/09/03. doi: 10.1038/nn.3502. PubMed PMID: 23995068; PubMed Central PMCID: PMCPCMC3793847.
  77. Verhaagen J, Hobo B, Ehlert EME, Eggers R, Korecka JA, Hoyng SA, et al. Small Scale Production of Recombinant Adeno-Associated Viral Vectors for Gene Delivery to the Nervous System. *Methods Mol Biol*. 2018;1715:3-17. Epub 2017/12/01. doi: 10.1007/978-1-4939-7522-8\_1. PubMed PMID: 29188502.
  78. Grimm D, Kay MA, Kleinschmidt JA. Helper virus-free, optically controllable, and two-plasmid-based production of adeno-associated virus vectors of serotypes 1 to 6. *Mol Ther*. 2003;7(6):839-50. Epub 2003/06/06. doi: 10.1016/s1525-0016(03)00095-9. PubMed PMID: 12788658.
  79. Connelly JP, Pruetz-Miller SM. CRIS.py: A Versatile and High-throughput Analysis Program for CRISPR-based Genome Editing. *Sci Rep*. 2019;9(1):4194. Epub 2019/03/14. doi: 10.1038/s41598-019-40896-w. PubMed PMID: 30862905; PubMed Central PMCID: PMCPCMC6414496.
  80. Schindelin J, Arganda-Carreras I, Frise E, Kaynig V, Longair M, Pietzsch T, et al. Fiji: an open-source platform for biological-image analysis. *Nat Methods*. 2012;9(7):676-82. Epub 2012/06/30. doi: 10.1038/nmeth.2019. PubMed PMID: 22743772; PubMed Central PMCID: PMCPCMC3855844.
  81. de Jong APH, Roggero CM, Ho MR, Wong MY, Brautigam CA, Rizo J, et al. RIM C2B Domains Target Presynaptic Active Zone Functions to PIP2-Containing Membranes. *Neuron*. 2018;98(2):335-49 e7. Epub 2018/04/03. doi: 10.1016/j.neuron.2018.03.011. PubMed PMID: 29606581; PubMed Central PMCID: PMCPCMC5910229.
  82. Lindhout FW, Cao Y, Kevenaar JT, Bodzeta A, Stucchi R, Boumpoutsari MM, et al. VAP-SCRN1 interaction regulates dynamic endoplasmic reticulum remodeling and presynaptic function. *EMBO J*. 2019;38(20):e101345. Epub 2019/08/24. doi: 10.15252/embj.2018101345. PubMed PMID: 31441084; PubMed Central PMCID: PMCPCMC6792018.
  83. Edelstein A, Amodaj N, Hoover K, Vale R, Stuurman N. Computer control of microscopes using microManager. *Curr Protoc Mol Biol*. 2010;Chapter 14:Unit14.20. Epub 2010/10/05. doi: 10.1002/0471142727.mb1420s92. PubMed PMID: 20890901; PubMed Central PMCID: PMCPCMC3065365.
  84. Yau KW, van Beuningen SF, Cunha-Ferreira I, Cloin BM, van Battum EY, Will L, et al. Microtubule minus-end binding protein CAMSAP2 controls axon specification and dendrite development. *Neuron*. 2014;82(5):1058-73. Epub 2014/06/09. doi: 10.1016/j.neuron.2014.04.019. PubMed PMID: 24908486.
  85. Li TP, Blanpied TA. Control of Transmembrane Protein Diffusion within the Postsynaptic Density Assessed by Simultaneous Single-Molecule Tracking and Localization Microscopy. *Front Synaptic Neurosci*. 2016;8:19. Epub 2016/08/09. doi: 10.3389/fnsyn.2016.00019. PubMed PMID: 27499742; PubMed Central PMCID: PMCPCMC4956670.

## SUPPORTING INFORMATION

### A

#### Example design 1

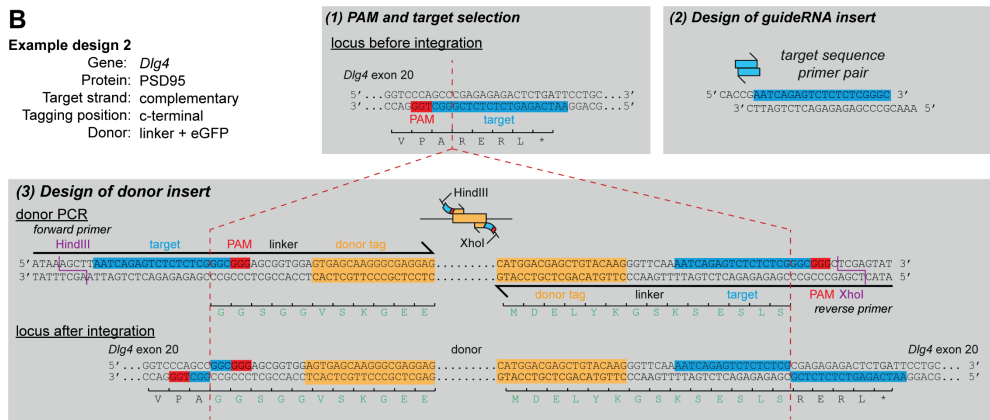
Gene: *Gria1*  
 Protein: GluA1  
 Target strand: coding  
 Tagging position: c-terminal  
 Donor: linker + eGFP



### B

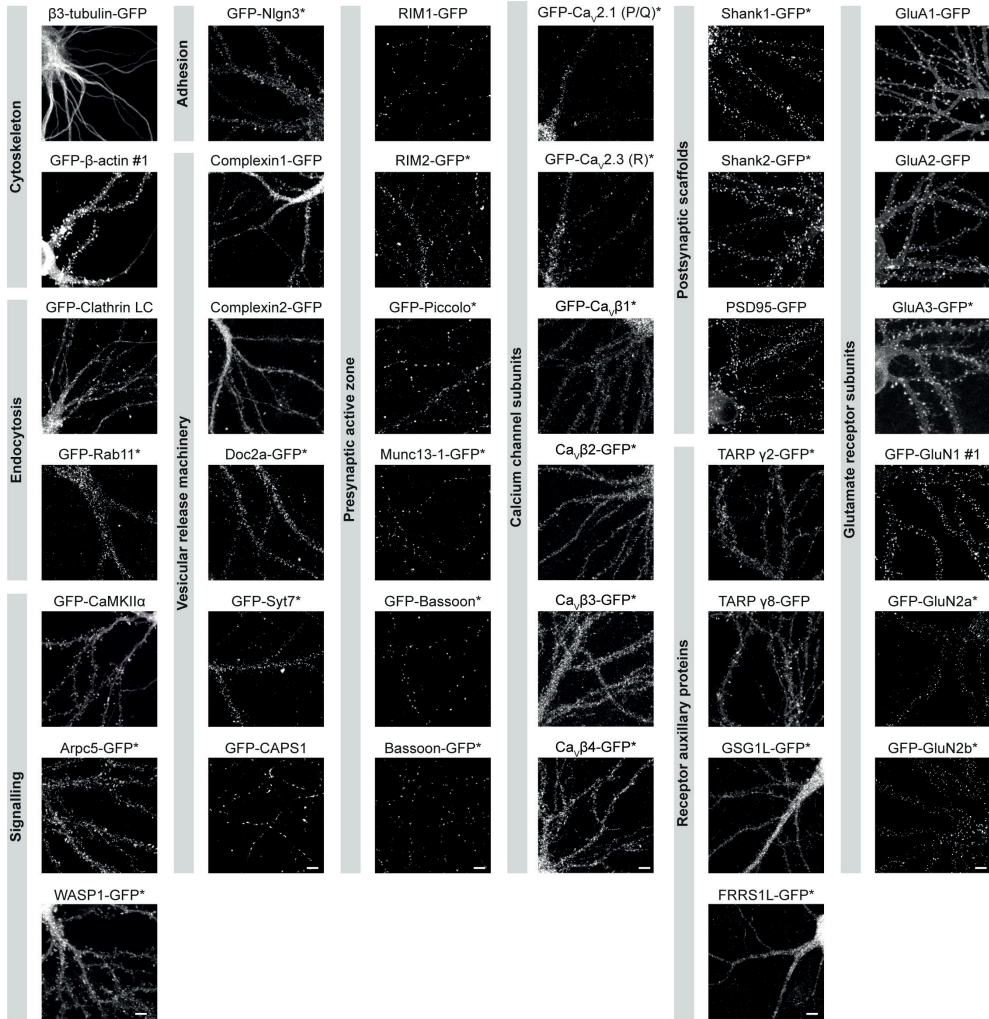
#### Example design 2

Gene: *Dlg4*  
 Protein: PSD95  
 Target strand: complementary  
 Tagging position: c-terminal  
 Donor: linker + eGFP



### S1 Fig. Schematic of knock-in construct design (related to Fig 1)

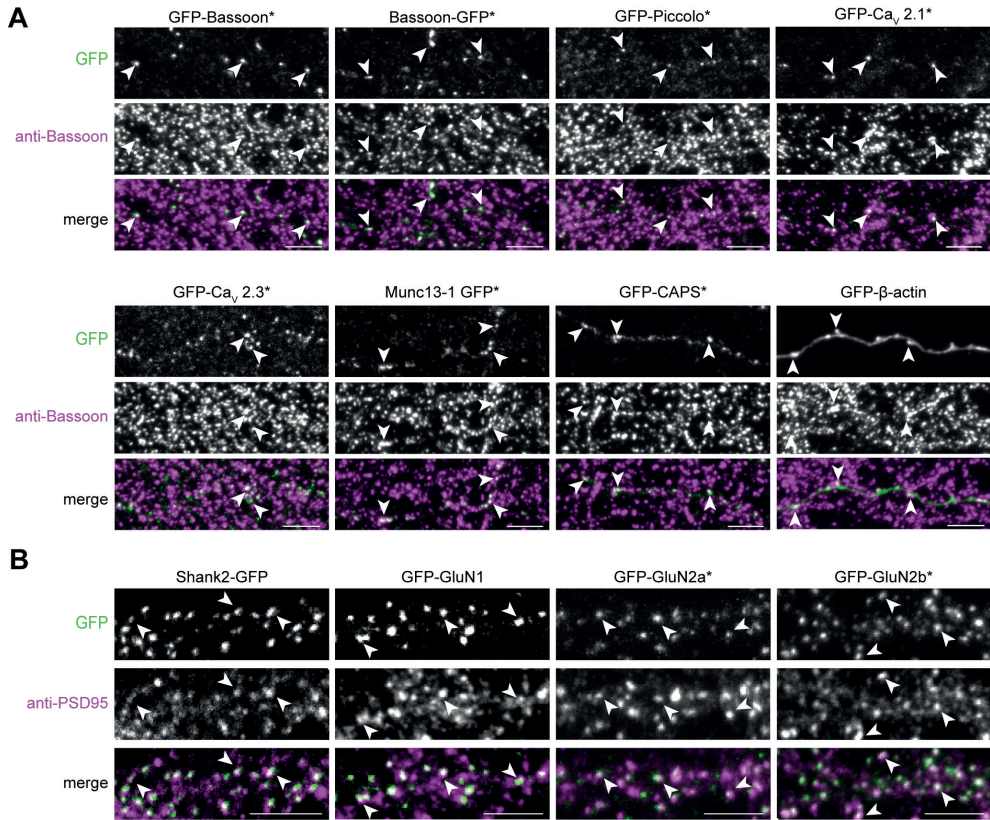
(A and B) Examples of knock-in construct design for *Gria1* (A) and *Dlg4* (B), which contain target sequences in opposite genomic strands. The target sequence is indicated in blue, the PAM sequence is in red, and the part of the primer used for PCR amplification of the donor DNA is shown in yellow. Amino acid sequence is shown under the sequences. Asterisk indicates stop codon. Red dotted lines indicate position of Cas9 cleavage and sites of integration. Purple line indicates restriction enzyme sites used for cloning into pORANGE. ORANGE, Open Resource for the Application of Neuronal Genome Editing; *Gria1*, glutamate ionotropic receptor AMPA type subunit 1; *Dlg4*, Discs Large MAGUK Scaffold Protein 4; PAM, protospacer adjacent motif.



**S2 Fig. ORANGE CRISPR/Cas9 knock-in library (related to Fig 2)**

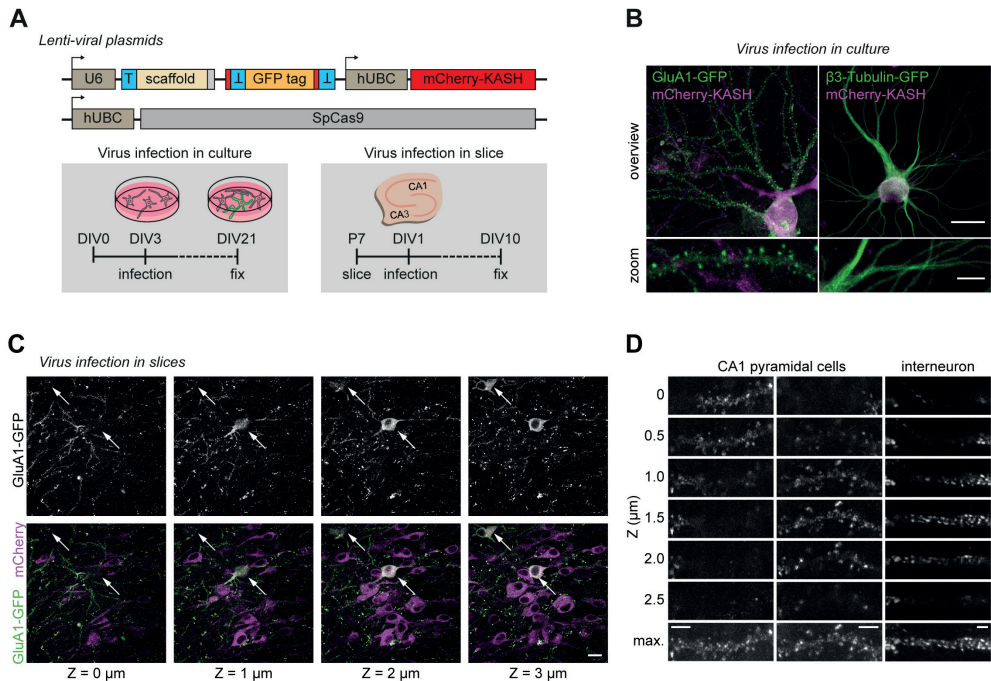
Representative images of cultured hippocampal knock-in neurons. Examples shown are used for zooms shown in Fig 2D. DIV 21. Asterisk indicates signal enhanced using anti-GFP antibodies (Alexa488 or Alexa647). Scale bar, 5  $\mu$ m. GFP, green fluorescent protein; ORANGE, Open Resource for the Application of Neuronal Genome Editing.





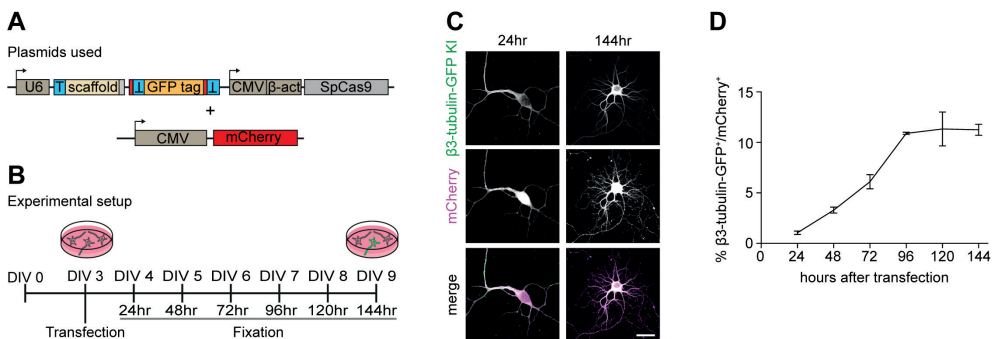
**S3 Fig. Localization of ORANGE knock-ins relative to synaptic makers (related to Fig 2)**

(A) Examples of GFP knock-in (green) relative to anti-Bassoon staining (magenta, Alexa647) as presynaptic marker or (B) anti-PSD95 staining (magenta, Alexa647) as postsynaptic marker in cultured hippocampal neurons. Asterisk indicates signal enhancement using anti-GFP antibodies (Alexa488). Scale bars, 5 μm. Arrows indicate examples of GFP-positive objects. GFP, green fluorescent protein; ORANGE, Open Resource for the Application of Neuronal Genome Editing.



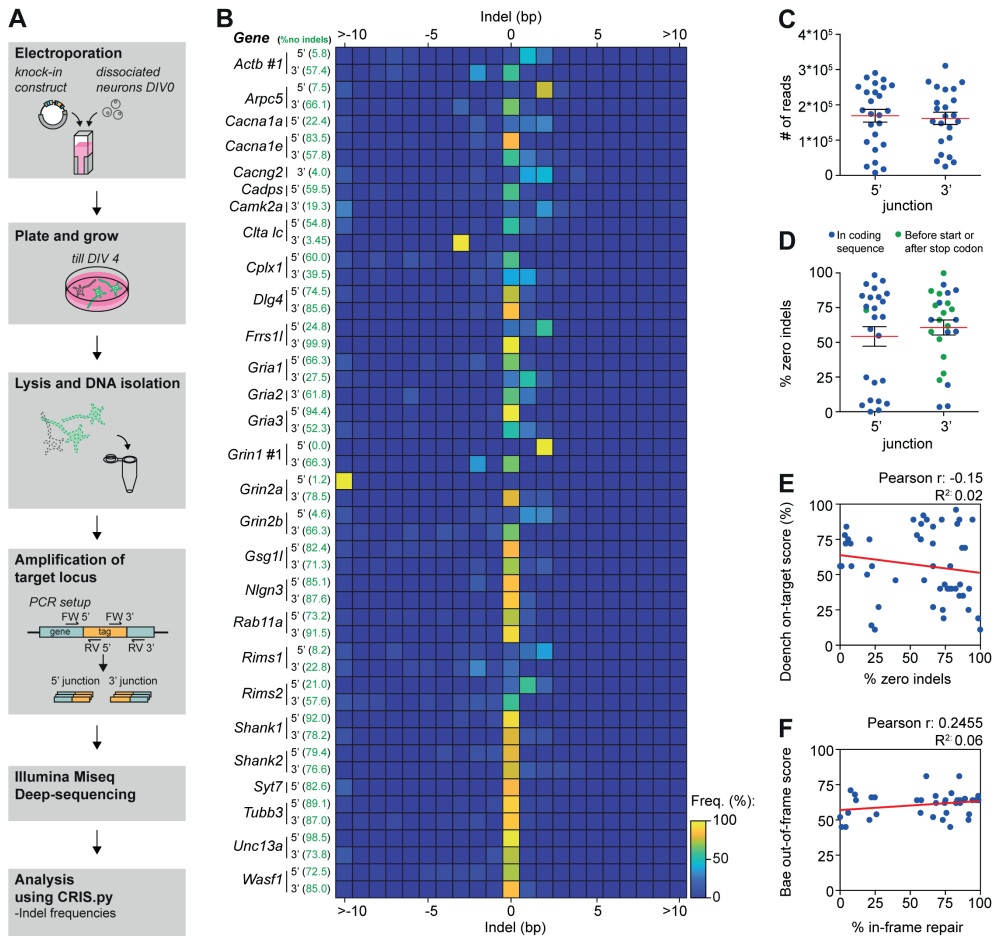
**S4 Fig. ORANGE knock-ins in dissociated neuronal culture and organotypic slices using a dual-lentiviral approach (related to Fig 3)**

(A) Overview of lentiviral constructs and timeline showing age of infection and fixation. (B) Representative images of infected (magenta) primary rat hippocampal neurons positive for GluA1-GFP knock-in or  $\beta$ 3-tubulin-GFP knock-in (green). Scale bars, 20  $\mu$ m and 5  $\mu$ m for the overview and zooms, respectively. (C) Representative images of GluA1-GFP knock-in in organotypic hippocampal slices from mice. Shown are a series of individual 1- $\mu$ m planes from a Z-stack. Arrows indicate GFP-positive cells. Scale bar, 20  $\mu$ m. (D) Representative zooms of GluA1-GFP knock-in dendrites from a CA1 pyramidal cell and an aspiny interneuron. Shown are individual 0.5- $\mu$ m planes from a Z-stack and the maximum projection (max). Scale bar, 2  $\mu$ m. GFP, green fluorescent protein; ORANGE, Open Resource for the Application of Neuronal Genome Editing; GluA1, Glutamate receptor AMPA 1; CA1, Cornu Ammonis region 1.



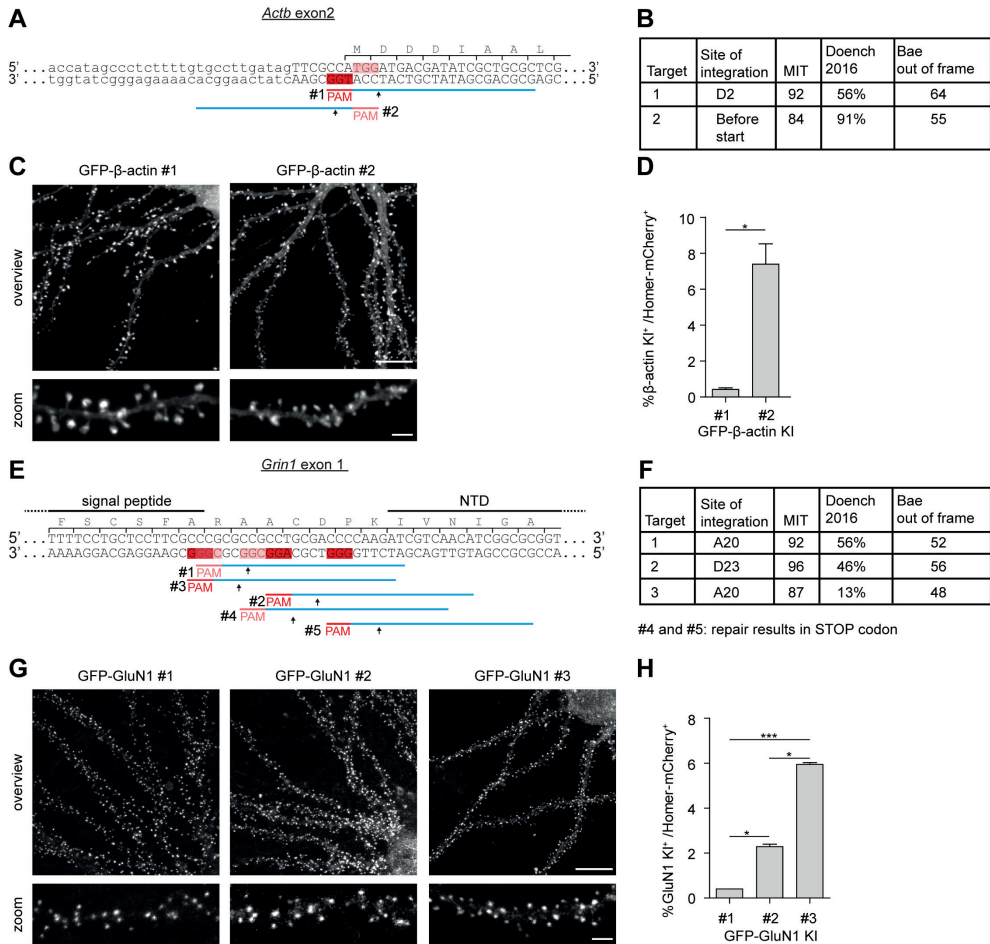
**S5 Fig. Efficiency of ORANGE knock-in over time in cultured neurons (related to Fig 4)**

(A) Schematic overview of knock-in and mCherry reporter plasmids and (B) experimental setup. (C) Representative images of  $\beta$ 3-tubulin-GFP knock-in (green) cotransfected with an mCherry fill (magenta) fixed 24 hours (DIV 4) and 144 hours (DIV 9) after transfection. Scale bar, 20  $\mu$ m. (D) Quantification of  $\beta$ 3-tubulin-GFP knock-in efficiency over time as percentage of transfected (mCherry-positive) neurons. Data are represented as means  $\pm$  SEM. Underlying data can be found in S1 Data. GFP, green fluorescent protein; ORANGE, Open Resource for the Application of Neuronal Genome Editing; DIV, day in vitro.



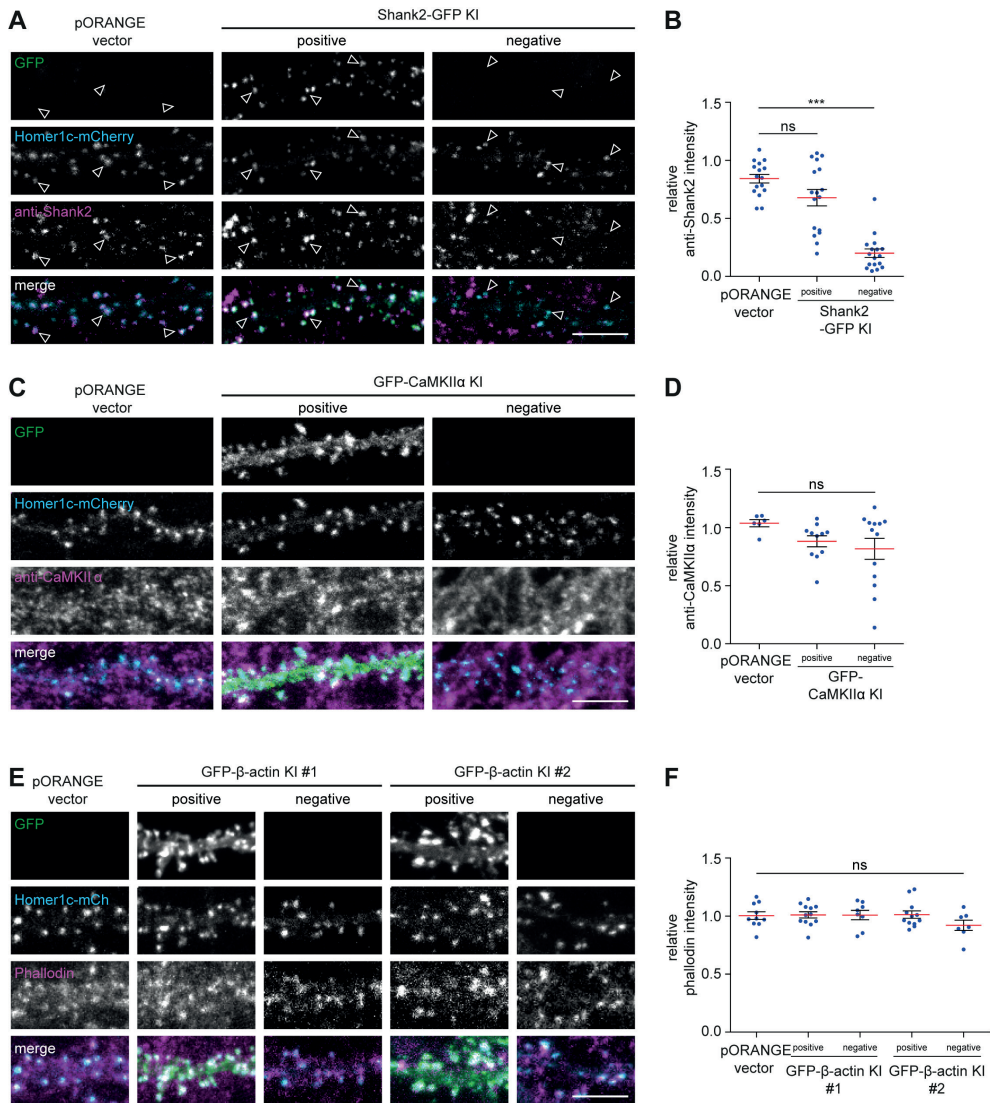
**S6 Fig. Next-generation sequencing of donor integration at targeted locus (related to Fig 4)**

(A) Schematic overview of experimental setup. Neurons were electroporated immediately after dissociation and cultured until DIV 4. Genomic DNA was isolated, and the 5' and 3' junctions of integration were amplified with PCR, pooled, and subjected to next-generation sequencing. (B) Heatmap summarizing the sequencing results for 5' and 3' junction amplicons of the frequency of indel size, as analyzed using CRIS.py. For a few genes, we were only able to amplify one of the two junctions with PCR. (C) Average number of reads obtained with deep sequencing for all successfully analyzed knock-ins (mean 5':  $1.69 \times 10^5$  reads  $\pm 0.18 \times 10^5$ , 3':  $1.57 \times 10^5 \pm 0.16 \times 10^5$ ). (D) Accuracy of knock-in plotted for each junction. Plotted points indicate percentage of zero indels from all knock-ins in (B) (mean 5':  $54.2\% \pm 7.0\%$ , 3':  $60.7\% \pm 5.4\%$ ). Green points indicate minor mutations that do not influence the reading frame for this particular integration (e.g., frame shift after stop codon). (E) Correlation graph between zero indel frequency per amplicon and Doench on-target score of the gRNA target sequence. (F) Correlation graph between correct reading frame integration frequency and Bae out-of-frame score of the gRNA target sequence. Data are presented as means  $\pm$  SEM. Underlying data can be found in S1 Data. gRNA, guide RNA; DIV, day in vitro.



**S7 Fig. Comparison of integration efficiency at different PAM sites in the same gene (related to Fig 4)**

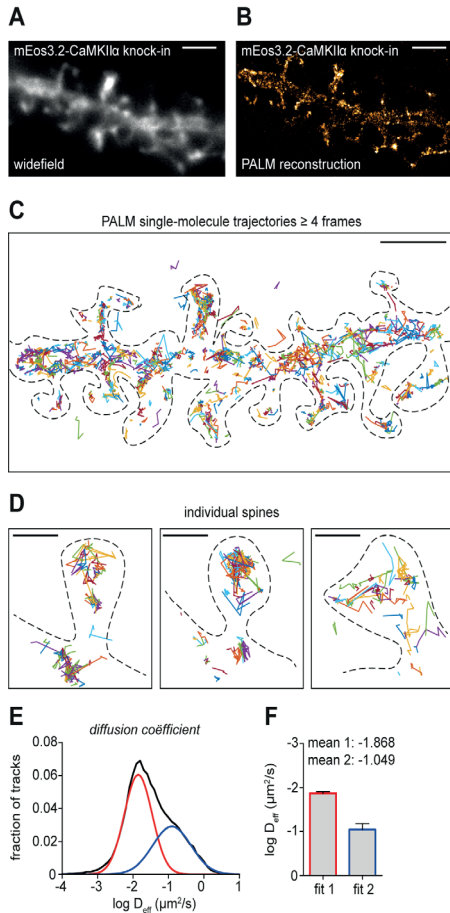
(A and E) Genomic regions of the *Actb* and *Grin1* genes around the targeted integration site are shown. The PAM (red line and red shaded boxes) and target sequences (blue) are shown below for each of the tested knock-ins. Intron sequences are in lowercase, and exon sequences are in uppercase. Additional protein information is shown above the sequence. (B and F) Tables containing information about the site of integration at the protein level and MIT, Doench, and Bae scores of the individual guide RNA sequences (determined based on rat genomic sequence from the UCSC RGSC5.0/rn5 genome assembly). (C and G) Representative images of neurons transfected with the various  $\beta$ -actin (C) or GluN1 (G) knock-in constructs targeting the PAM sites shown in (A) and (E), respectively. Scale bars, 10  $\mu$ m and 2  $\mu$ m for the overviews and zooms, respectively. (D and H) Knock-in efficiency determined as the percentage of GFP- $\beta$ -actin (D) or GFP-GluN1 (H)-positive neurons coexpressing Homer1c-mCherry. Data are presented as means  $\pm$  SEM. \*  $P < 0.05$ , \*\*\*  $P < 0.001$ , ANOVA or Student t test. Underlying data can be found in S1 Data. GFP, green fluorescent protein; PAM, protospacer adjacent motif; *Actb*, Actin Beta; *Grin1*, glutamate ionotropic receptor NMDA type subunit 1; UCSC, University of California Santa Cruz; GluN1, Glutamate receptor NMDA 1.



**S8 Fig. Quantification of Bassoon, Shank2, CaMKII $\alpha$ , and F-actin levels in knock-in neurons (related to Fig 4).**

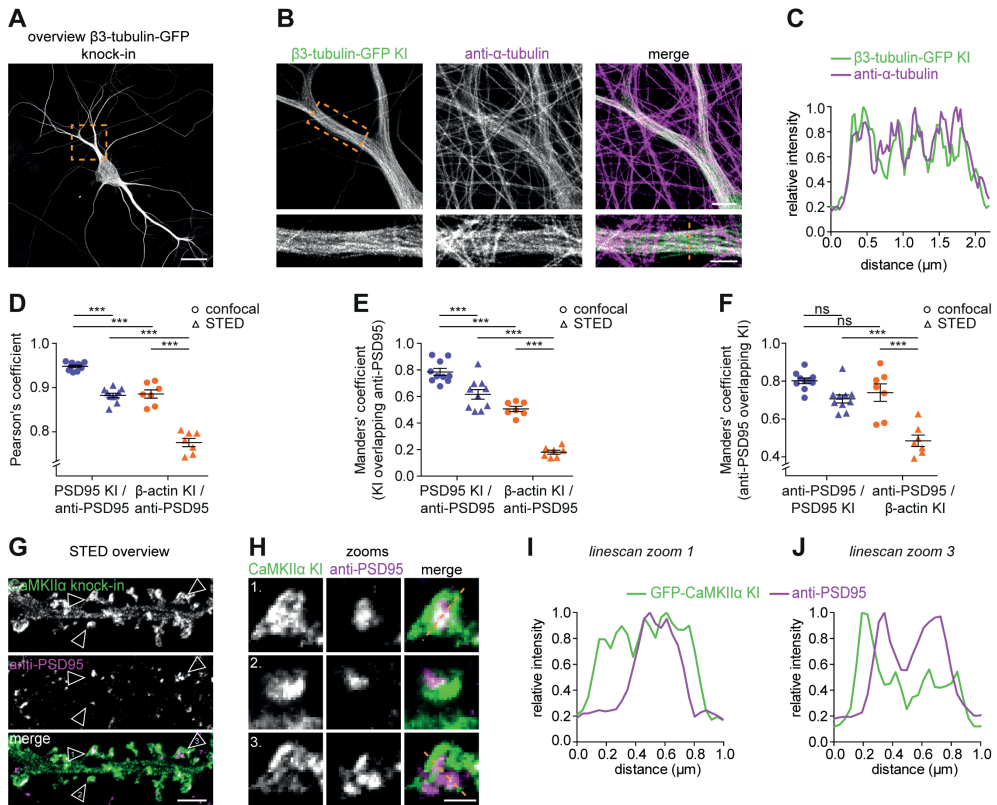
(A) Representative images of neurons transfected with Homer1c-mCherry (cyan) together with pORANGE empty vector as control or Shank2-GFP knock-in (green). Neurons were stained with anti-Shank2 (magenta, Alexa647). (C) Images of neurons transfected with Homer1c-mCherry (cyan) together with pORANGE empty vector as control GFP-CaMKII $\alpha$  knock-in (green). Neurons were stained with anti-CaMKII $\alpha$  (magenta, Alexa647). (E) Neurons transfected with Homer1c-mCherry together with pORANGE empty vector as control, GFP- $\beta$ -actin knock-in #1 or GFP- $\beta$ -actin knock-in #2 (green). Neurons were stained for F-actin using phalloidin (magenta, Alexa647). Scale bar, 5  $\mu$ m. (B, D, and F) Quantification of protein levels relative to transfected neurons. (B) Relative fluorescence intensity: control:  $0.84 \pm 0.04$ ,  $n = 16$  neurons, Shank2-GFP knock-in:  $0.67 \pm 0.07$ ,  $n = 17$  neurons,  $P > 0.05$ , knock-in negative:  $0.20 \pm 0.04$ ,  $n = 17$  neurons,  $P < 0.01$ , ANOVA. (D) Control:  $1.04 \pm 0.03$ ,  $n = 6$  neurons, GFP-CaMKII $\alpha$  knock-in:  $0.88 \pm 0.05$ ,  $n = 11$  neurons,  $P > 0.05$ , knock-in negative:  $0.82 \pm 0.09$ ,  $n = 13$  neurons,  $P > 0.05$ , ANOVA. (F) Control:  $1.00 \pm 0.03$ ,  $n = 10$  neurons, GFP- $\beta$ -actin knock-in #1:  $1.01 \pm 0.03$ ,  $n = 12$  neurons,  $P > 0.05$ , knock-in #1 negative:  $1.01 \pm 0.04$ ,  $n = 8$  neurons,  $P > 0.05$ , GFP- $\beta$ -actin knock-in #2:  $1.01 \pm 0.03$ ,  $n = 12$  neurons,  $P > 0.05$ , knock-in #2 negative:  $0.92 \pm 0.04$ ,  $n = 7$  neurons,  $P > 0.05$ , ANOVA. Data are presented as means  $\pm$  SEM. \*\*\* $P$

**S8 Fig. (continued)**,  $< 0.001$ , ANOVA. Underlying data can be found in S1 Data. GFP, green fluorescent protein; ns, not significant; ORANGE, Open Resource for the Application of Neuronal Genome Editing; SHANK2, SH3 and multiple ankyrin repeat domains protein 2; CaMKII $\alpha$ , Calcium/calmodulin-dependent protein kinase type II subunit alpha.



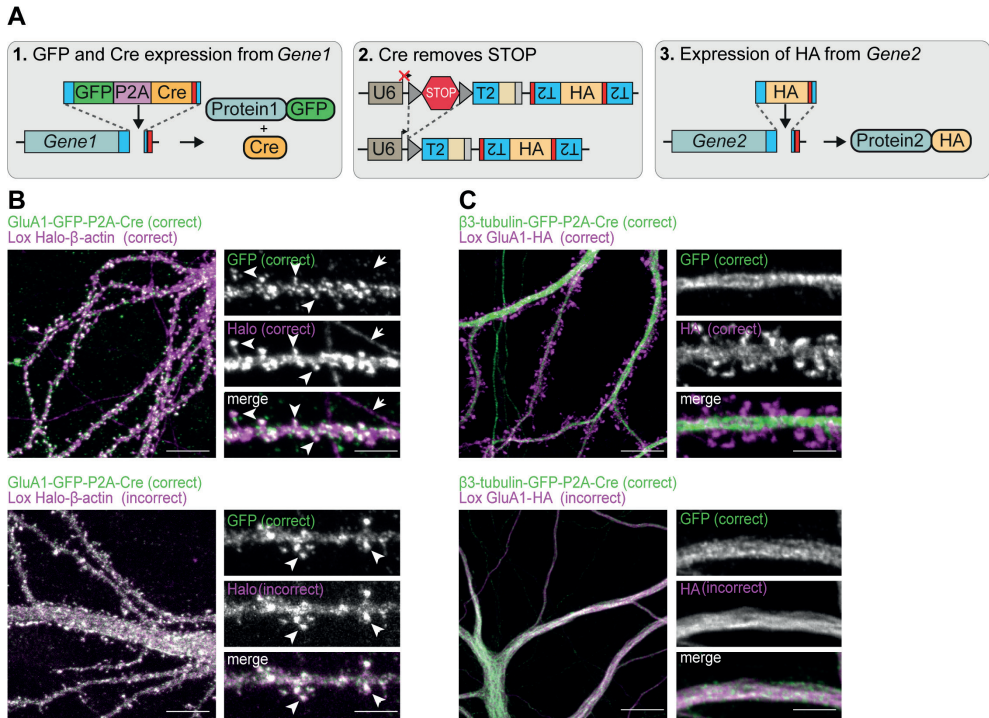
**S9 Fig. Live-cell superresolution PALM imaging of endogenous CaMKII $\alpha$  dynamics (related to Fig 5)**

(A) Example of a dendrite expressing mEos3.2-CaMKII $\alpha$  knock-in. Scale bar, 2  $\mu\text{m}$ . (B) Single-molecule PALM reconstruction of dendrite shown in (A). Scale bar, 2  $\mu\text{m}$ . (C) Individual single-molecule trajectories. Scale bar, 2  $\mu\text{m}$ . Dotted line indicates cell outline. (D) Representative zooms of single-molecule trajectories in individual spines. Scale bar, 200 nm. (E) Frequency distribution of diffusion coefficients derived from single-molecule trajectories (black line). Mixed Gaussian fits (red and blue) indicate two kinetic populations. (F) Quantification of mean diffusion coefficient for each of the two kinetic populations. Data are presented as means  $\pm$  SEM. Underlying data can be found in S1 Data. PALM, photoactivated localization microscopy; CaMKII $\alpha$ , Calcium/calmodulin-dependent protein kinase type II subunit alpha; mEos3.2, monomeric Eos 3.2.



### S10 Fig. gSTED imaging and colocalization analysis (related to Figure 6)

(A) Representative gSTED overview image and zooms (B) of  $\beta$ 3-tubulin-GFP knock-in neurons (DIV 7) extracted and stained with anti-GFP (green, ATTO647N) and anti- $\alpha$ -tubulin (magenta, Alexa594). Scale bars, 20  $\mu$ m, 4  $\mu$ m, and 2  $\mu$ m for the overview and zooms, respectively. (C) Intensity profile along the line indicated in (B). (D) PCC quantifying colocalization between PSD95-GFP or GFP- $\beta$ -actin knock-in signal with anti-PSD95 staining intensity. Related to Fig 6F–K. (E and F) Manders' correlation of PSD95-GFP or GFP- $\beta$ -actin knock-in overlapping with PSD95 staining (M1) (E) or anti-PSD95 staining overlapping with PSD95-GFP or GFP- $\beta$ -actin knock-in (M2) (F) related to Fig 6F–K. Average values: (PSD95, confocal: median PCC = 0.95, M1 = 0.78, M2 = 0.80, STED: PCC = 0.88, ANOVA,  $P < 0.001$ , M1 = 0.62,  $P < 0.001$ , M2 = 0.71,  $P > 0.05$ ,  $n = 10$  neurons) ( $\beta$ -actin, confocal: median PCC = 0.88,  $P < 0.001$ , M1 = 0.50,  $P < 0.001$ , M2 = 0.74,  $P > 0.05$ , STED: median PCC = 0.78, ANOVA,  $P < 0.001$ , M1 = 0.18,  $P < 0.001$ , M2 = 0.48,  $P < 0.001$ ,  $n = 7$  neurons). (G and H) gSTED of dendrites and zooms positive for GFP-CaMKII $\alpha$  knock-in stained with anti-GFP (green, ATTO647N) and anti-PSD95 (magenta, Alexa594). Scale bars, 2  $\mu$ m and 500 nm for (G) and (H), respectively. (I and J) Line scans of individual spines indicated in (H). Data are represented as means  $\pm$  SEM. \*\*\* $P < 0.001$ . ANOVA. Underlying data can be found in S1 Data. GFP, green fluorescent protein; gSTED, gated stimulated-emission depletion; ns, not significant; PCC, Pearson's correlation coefficient; DIV, day in vitro; PSD95, postsynaptic density protein 95; CaMKII $\alpha$ , Calcium/calmodulin-dependent protein kinase type II subunit alpha.



**S11 Fig. Multiplex labeling using CAKE (related to Fig 8)**

(A) Mechanism of sequential knock-in activation using CAKE. (B) Example of correct dual-color labeling (top) and incorrect dual-color labeling (bottom) with GluA1-GFP-P2A-Cre and Lox Halo β-actin. Arrowheads indicate dendritic spines, and arrow indicates the axon. (C) Example of correct dual-color labeling (top) and incorrect dual-color labeling (bottom) with β3-tubulin-GFP-P2A-Cre and Lox GluA1-HA. Scale bar is 10 μm for overview and 5 μm for zooms. CAKE, conditional activation of knock-in expression; GFP, green fluorescent protein; GluA1, Glutamate receptor AMPA 1; HA, hemagglutinin.



**S1 Table.** Design rationale for each ORANGE knock-in. ORANGE, Open Resource for the Application of Neuronal Genome Editing.

Gene	Protein	Endogenous localization	Tag location	Design rationale
<i>Actb</i>	$\beta$ -actin	Cytoskeleton throughout cell, enriched in spines [1]	N-terminal	N-terminal tag is most commonly used, does not interfere with actin localization in neurons, F-actin polymerization or neuronal morphology. See for instance [2], [3], and [4]
<i>Arpc5</i>	Arp2/3 complex subunit 5	Throughout cell, enriched in spines [5]	N-terminal	N-terminal tag does not interfere with Arpc5 localization [3]
<i>Bsn</i>	Bassoon	Presynaptic active zone [6, 7]	N-terminal	N-terminal GFP tag does not affect localization in neurons [6]
			C-terminal	C-terminal GFP tag does not affect localization in neurons [6]
<i>Doc2a</i>	Doc2a	Potentially enriched at synapses [8]	C-terminal	C-terminal GFP tag does not affect function in neurons [9]
<i>Cacna1a</i>	Ca <sub>v</sub> 2.1, P/Q type	Presynaptic terminals, dendritic spines [10]	N-terminal	N-terminal tag does not affect protein localization or function [11], C-terminus contains multiple important localization sequences [12] and [13]
<i>Cacna1e</i>	Ca <sub>v</sub> 2.3, R type	Around presynaptic terminals, inside dendritic spines and shaft [14]	N-terminal	See <i>CACNA1A</i> based on homology.
<i>Cacnb1</i>	Ca <sub>v</sub> $\beta$ 1	Punctate pattern in axons and dendrites, including localization to presynaptic terminals and dendritic spines [15, 16]	N-terminal	Last exon is not included in all splice variants [17] and has few good PAM sites. N-terminal tag does not affect localization or function in homologous proteins [18]
<i>Cacnb2</i>	Ca <sub>v</sub> $\beta$ 2	Punctate pattern in axons and dendrites, including localization to presynaptic terminals and dendritic spines [16]	C-terminal	c-terminal tag does not interfere with localization [16]
<i>Cacnb3</i>	Ca <sub>v</sub> $\beta$ 3	Punctate pattern in axons and dendrites, including localization to presynaptic terminals and dendritic spines [15, 16]	C-terminal	c-terminal tag does not interfere with localization [16]
<i>Cacnb4</i>	Ca <sub>v</sub> $\beta$ 4	Punctate pattern in axons and dendrites, including localization to presynaptic terminals and dendritic spines [15, 16]	C-terminal	c-terminal tag does not interfere with localization [16]
<i>Cacng2</i>	TARP gamma-2 / Stargazin	Punctate pattern in dendrites, enriched in postsynaptic density [19]	Internal, in C-terminal tail	Internal tag in C-tail does not interfere with localization [20]
<i>Cacng8</i>	TARP gamma-8	Punctate pattern in dendrites, enriched in post-synaptic density [19]	Internal, in C-terminal tail	See <i>Cacng2</i> , based on homology
<i>Capdc</i>	CAPS1	Axonal, punctate [21]	N-terminal	Many splice variants lack C-terminus [22]
<i>Camk2a</i>	CaMKII $\alpha$	Soluble throughout cell, moderate enrichment in spines [23]	N-terminal	N-terminal tag does not interfere with localization [24]
<i>Cltc</i>	Clathrin light chain A	Punctate throughout cell [25]	N-terminal	N-terminal tag does not interfere with localization and function [26]
<i>Cplx1</i>	Complexin1	Soluble throughout cell [27]	C-terminal	C-terminal GFP overexpression has similar pattern as endogenous [27, 28]
<i>Cplx2</i>	Complexin2	Soluble throughout cell [27]	C-terminal	See <i>Cplx1</i> , based on homology

S1 Table (continued)

<i>Dlg4</i>	PSD95	Core component of the postsynaptic density [29]	C-terminal	N-terminal residues important for interaction with membranes. C-terminal tagging is commonly used, see for instance [30], [31], [32], and [33]
<i>Frrs11</i>	FRRS1L / C9orf4	Plasma membrane and ER [34]	C-terminal	N-terminal contains potentially important poly-glycine region. C-terminal tagging did not interfere with localization and co-immunoprecipitation experiments in heterologous cells [34]
<i>Gria1</i>	GluA1	Enriched at the postsynaptic density [35]	C-terminal	Both N and C-terminal tags do not interfere with localization, see for instance [36] and [37] C-terminal tagging was chosen based on availability of PAM sites
<i>Gria2</i>	GluA2	Enriched at the postsynaptic density [35]	C-terminal	See <i>Gria1</i> , based on homology
<i>Gria3</i>	GluA3	Enriched at the postsynaptic density [35]	C-terminal	See <i>Gria1</i> , based on homology
<i>Grin1</i>	GluN1	Enriched at the postsynaptic density [38]	N-terminal, after signal peptide	C-terminal residues mediate intracellular interactions [39] and some splice variants leak parts of the C-terminal [40]
<i>Grin2a</i>	GluN2a	Enriched at the postsynaptic density [38]	N-terminal, after signal peptide	C-terminal residues mediate intracellular interactions [39]
<i>Grin2b</i>	GluN2b	Enriched at the postsynaptic density [38]	N-terminal, after signal peptide	C-terminal residues mediate intracellular interactions [39]
<i>Gsg11</i>	GSG1-1	Punctate pattern in dendrites, enriched at the postsynaptic density [41]	N-terminal	C-terminal tag does not interfere with localization and function [42]
<i>Nlgn3</i>	Neuroigin-3	Concentrated in excitatory and inhibitory synapses [43]	N-terminal, after signal peptide	C-terminus mediates intracellular interactions [44]
<i>Pcla</i>	Piccolo	Enriched at presynaptic active zone [45]	N-terminal	N-terminal domains linked to GFP localize to presynaptic terminals [46]. N-terminus was chosen because PAM sites were predicted to be more specific, based on MIT score
<i>Rab11a</i>	Rab11	Punctate labeling of recycling endosomes throughout cell [47, 48]	N-terminal	N-terminal fusion does not affect protein function or localization. See for instance [47, 49]
<i>Rims1</i>	RIM1	Enriched at presynaptic active zone [50, 51]	C-terminal	Deletion of C-terminal domains does not interfere with localization [50]. N-terminus contains important interaction sequences [52]
<i>Rims2</i>	RIM2	Presynaptic active zone [50, 51]	C-terminal	See <i>Rims1</i> , based on homology
<i>Shank1</i>	Shank1	Core component of the postsynaptic density [29]	C-terminal	Shanks are commonly tagged at the N-terminus (see e.g. [53], but also [54]), but C-terminal tagging was chosen here due to unavailability of N-terminal PAM sites. We found C-terminal tagging does not interfere with synaptic localization of Shank1 and Shank2
<i>Shank2</i>	Shank2	Core component of the postsynaptic density [29]	C-terminal	See <i>Shank1</i> .
<i>Syt7</i>	Synaptotagmin-7	Presynaptic terminal [55], potentially also postsynaptic [56]	N-terminal	Based on homology with <i>Syt1</i> : N-terminal tag does not interfere with function, while a C-terminal GFP does interfere with its function in vesicle fusion [57, 58]
<i>Tubb3</i>	$\beta$ 3-tubulin	Soluble and somatodendritic microtubules [59]	C-terminal	Previously shown to correctly tag <i>Tubb3</i> and to be incorporated in the microtubule network. See [60] and [61]
<i>Unc13a</i>	Munc13-1	Presynaptic active zone [62]	C-terminal	c-terminal tag does not interfere with localization or function [63]
<i>Wasf1</i>	WASP1/Wave1	Cytoplasmic, enriched in spines [64]	C-terminal	C-terminal tag does not interfere with localization [3]

S2 Table. Target sequences for ORANGE knock-ins.

Gene	Protein	Target sequence (PAM is underlined)	Site of integration (in or before amino acid)	MIT score (in rat)	Conservation of target sequence in mouse
<i>Actb</i>	$\beta$ -actin #1	CGCAGCGATATCGTCATCCA <u>TGG</u>	D2	96	yes
<i>Actb</i>	$\beta$ -actin #2	TGTGCCTTGATAGTTCGCCA <u>TGG</u>	1 bp before ATG	84	1 mismatch
<i>Arpc5</i>	Arp2/3 complex subunit 5	CCAGTCCAGCTGGACTACAC <u>CGG</u>	STOP	32	yes
<i>Bsn</i>	Bassoon (N-terminal)	GGGCAACGAGGCCAGCCTGG <u>AGG</u>	L7	55	yes
<i>Bsn</i>	Bassoon (C-terminal)	TGGACACAATCACCAGAATG <u>AGG</u>	F3938	61	yes
<i>Cacna1a</i>	Ca <sub>v</sub> 2.1, P/Q	CCGCCTGCGCCGTAGCGGCC <u>CGG</u>	G10	93	yes
<i>Cacna1e</i>	Ca <sub>v</sub> 2.3 R	CAGGATGGCTCGCTTCGGGG <u>AGG</u>	G5	88	yes
<i>Cacnb1</i>	Ca <sub>v</sub> $\beta$ 1	CAGAAGAGCGGCATGTCCC <u>GGG</u>	S8	87	yes
<i>Cacnb2</i>	Ca <sub>v</sub> $\beta$ 2	GAGACACGCACGGTCAATTGG <u>CGG</u>	Q655	85	2 mismatches
<i>Cacnb3</i>	Ca <sub>v</sub> $\beta$ 3	CAGTAGCTGTCTTAGGCCA <u>AGG</u>	W479	73	1 mismatch
<i>Cacnb4</i>	Ca <sub>v</sub> $\beta$ 4	GGCAGCCTCAAAGCCTATGT <u>CGG</u>	H417	73	yes
<i>Cacng2</i>	TARP $\gamma$ 2	CTTCAACACCCTGCCGTCCAC <u>CGG</u>	S265	86	yes
<i>Cacng8</i>	TARP $\gamma$ 8 #1	GGTGACCGTGACCGTGACG <u>CGG</u>	V376	86	no
<i>Cacng8</i>	TARP $\gamma$ 8 #2	CGTGTGGTGTGGACGCGG <u>CGG</u>	A408	87	no
<i>Capdc</i>	CAPS1	AGTCTCGATCCATAGAGGA <u>AGG</u>	S39	75	1 mismatch
<i>Camk2a</i>	CaMKII $\alpha$	CTGCCTGCCAGTGCCAGGAT <u>TGG</u>	2 bp before ATG	29	yes
<i>Clt</i>	Clathrin light chain $\alpha$	GGATCCAACCTCAGCCATGAC <u>CGG</u>	M1	73	no
<i>Cplx1</i>	Complexin1	GTACCTGCCTGGGCCACTGC <u>AGG</u>	L128	59	yes
<i>Cplx2</i>	Complexin2	ATATCTGCCGGGCCACTGC <u>AGG</u>	L128	81	2 mismatches
<i>Dlg4</i>	PSD95	AATCAGAGTCTCTCTCGG <u>GCTGG</u>	R721	80	yes
<i>Doc2a</i>	Doc2a	CTGCAGTCTGTTCAAGCCA <u>CGG</u>	L402	70	no
<i>Frrs11</i>	FRRS1L	TGGCTTGCAGCGGAGGTTA <u>AGG</u>	Stop	70	2 mismatches
<i>Gria1</i>	GluA1	GGGAGCCACAGGATTGTA <u>ACTGG</u>	Stop	72	yes
<i>Gria2</i>	GluA2	TCGAGAGTGTTAAAATTTAG <u>GGG</u>	Stop	64	yes
<i>Gria3</i>	GluA3	CAGAAAGTGTTAAGATCTAG <u>GGG</u>	Stop	71	yes
<i>Grin1</i>	GluN1 #1	TCTTGGGGTCGCAGCGGCG <u>CGG</u>	A20	92	1 mismatch
<i>Grin1</i>	GluN1 #2	GTTGACGATCTTGGGGTCGC <u>AGG</u>	D23	96	1 mismatch
<i>Grin1</i>	GluN1 #3	CTTGGGGTCGCAGCGGCG <u>CGG</u>	A20	87	1 mismatch

S3 Table. Donor PCR primers.

Knock-in		Primer (5' → 3')
GFP-β-actin #1	FW	ATAAAGCTTCGCAGCGATATCGTCATCCAGGGCTAGCGTGAGCAAGGGCGAGGAG
	RV	ATACTCGAGCCCTGGATGACGATATCGCTGCGCTGCCTGACTTGTACAGCTCGTCCATGC
GFP-β-actin #2	FW	TCGAAGACCCCTAGACCCTGGCGAAGTATCAAGGCACATTGCGCATGGCTAGCGGAGTGAGCAAGGGC
	RV	GAGAAGACCCCGAGTGTGCCTTGATAGTTCGCCAGGGAGCGCTTCCACTCTTGTACAGCTCG
Arpc5-GFP	FW	ATAAAGCTTCCAGTTCAGCTGGACTACAGGGAG GGTAGCGGCTCCAGTAGA
	RV	ATACTCGAGCCCTGTAGTCCAGCTGGAAGTGGTACTTGTACAGCTCGTCCATG
GFP-Bassoon	FW	TCGAAGACCCCTAGACCACAGGCTGGCCTCGTTGCCCGTAGCGGAGTGAGCAAGGGCG
	RV	GAGAAGACCCCGAGGGCAACGAGGCCAGCCTGGAGGCAGCGCTCTTGTACAGCTCGTCC
Bassoon-GFP	FW	TCGAAGACCCCTAGATGGACACAATCACCAGAATGCGGAGGTAGCGGAGTGAGCAAGGG
	RV	GAGAAGACCCCGAGGCCCATCTCTGGTATTGTGTCCATTAAGCGCTCTTGTACAGCTCG
GFP-Ca <sub>v</sub> 2.1, P/Q	FW	ATAAAGCTTCCGCTGCGCCGTAGCGGCCGGGTGAGCAAGGGCGAGGAG
	RV	ATACTCGAGCCCGCCGCTACGGCGCAGGGCCCTGAACCCCTGTACAGCTCGTCC
GFP-Ca <sub>v</sub> 2.3 R	FW	ATAAAGCTTCCCCCGAAGCGAGCCATCCTGGTGAGCAAGGGCGAGGAG
	RV	ATACTCGAGCAGGATGGCTCGCTTCGGGGGGAAACTGAACCCCTGTACAGCTCGTCC
GFP-Ca <sub>v</sub> B1	FW	ATAAAGCTTCCCCGGACATGCCGCTCTTCTGGAGTAGCGGAGTGAGCAAGGGCGAGG
	RV	ATACTCGAGCAGAAGAGCGCATGTCCCGGCCAGCGCTGCCCTTGTACAGCTCGTCC
Ca <sub>v</sub> B2-GFP	FW	ATAAAGCTTGAGACACGCACGGTCAITGGGGGAGCTAGCGGAGTGAGCAAGGGCGAGGAG
	RV	ATACTCGAGCCCAATGACCCGTGCGTGTCTCTCAAGCGCTCTTGTACAGCTCGTCCATG
Ca <sub>v</sub> B3-GFP	FW	ATAAAGCTTCAGTAGCTGTCTTAGGCCAGGGAGTGCTAGCGGAGTGAGCAAGGGCGAGG
	RV	ATACTCGAGCCCTGGCCTAAGGACAGCTACTGTCAAGCGCTCTTGTACAGCTCGTCCATG
Ca <sub>v</sub> B4-GFP	FW	ATAAAGCTTGGCAGCCTCAAAGCCTATGTGGGAGGTGCTAGCGGAGTGAGCAAGGGCGAG
	RV	ATACTCGAGCCACATAGGCTTTGAGGCTGCCTCAAGCGCTCTTGTACAGCTCGTCCATG
TARPy2-GFP	FW	ATAAAGCTTCCCTGGACGGCAGGGTGTGAAGGTGAGCAAGGGCGAGGAG
	RV	ATACTCGAGCTTCAACACCCCTGCCGTCCAGGGTCTTGTACAGCTCGTCCATG
TARPy8-GFP #1	FW	ATAAAGCTTGGTGACCGTGACCGTGACCGGGCTAGCGCAGGTAGCGGCTCCAGTAGA
	RV	ATACTCGAGTCCCGGTCACGGTCACGGTACCGCAGCGCTGCCAGCCCTGCACCCGC
TARPy8-GFP #2	FW	ATAAAGCTTGGTGTGGTGTGGACGCGGGCTAGCGCAGGTAGCGGCTCCAGTAGA
	RV	ATACTCGAGTCCCGGTCACGGTCAACACCAACACCGCCAGCGCTGCCAGCCCTGCACCCGC
GFP-CAPS1	FW	ATAAAGCTTCCCTCGCTGGTGGGCTTGAGAGTAGCGGTGGAGTGAGCAAGGGCGAGG
	RV	ATACTCGAGTCTCCAAGCCGACCCAGCGAGGGCTGAACCCCTGTACAGCTCGTCCATG
GFP-CaMKIIα	FW	ATAAAGCTTCCCTCCTGGCACTGGGCAGGCAGAGGATGGTGAGCAAGGGCGAGG
	RV	ATACTCGAGCTGCCTGCCAGTGCCAGGAGGGCTGATCCCTTGTACAGCTCGTCCATGC
mEos3.2-CaMKIIα	FW	ATATCTAGACCCCTCCTGGCACTGGGCAGGCAGGCTAGCACCATGAGTGGATTAAGCCA
	RV	ATAGGATCCCTGCCTGCCAGTGCCAGGAGGGCTCGAGCTCGTCTGGCATTGTCAGGC
GFP-Clathrin LC	FW	ATAAAGCTTGGATCCAACCTCAGCCATGAGGGCAGGTAGCGGAGTGAGCAAGGGCGAGGA
	RV	ATACTCGAGCCCTATGGCTGAGTTGGATCCTCCGCTACCCCTGTACAGCTCGTCCATGC
Complexin1-GFP	FW	ATAAAGCTTCCCGCAGTGGCCAGGCAGGTACAGCGGTGGAGTGAGCAAGGGCGAGG
	RV	ATACTCGAGGTACTGCTGGGCCACTGCGGGTCCACCCTCACTTGTACAGCTCGTCC
Complexin2-GFP	FW	ATAAAGCTTCCCGCAGTGGCCCGGCAGATATGGCTCAGGAGTGAGCAAGGGCGAGG
	RV	ATACTCGAGATATCTCCCGGGCCACTGCGGGTCCGCCATTACTTGTACAGCTCGTCC
PSD95-GFP	FW	ATAAAGCTTAATCAGAGTCTCTCTCGGGCGGGAGCGGTGGAGTGAGCAAGGGCGAGGAG
	RV	ATACTCGAGCCCGCCGAGAGAGACTCTGATTTGAAACCCCTGTACAGCTCGTCCATG

S3 Table (continued)

Doc2a-GFP	FW	ATAAAGCTTCTGCAGTCTGTTCCAGGCCAAGGGTCTGCTAGCGGAGTGAGCAAGGGCGAGG
	RV	ATACTCGAGCCCTTGGCCGTAACAGACTGCAGTCAAGCGCTTTGTACAGCTCGTCC
FRRS1L-GFP	FW	ATAAAGCTTTGGCTTGCAGCGGAGGTTAAGGGAGGTAGCGGCTCCAGTAGA
	RV	ATACTCGAGCCCTAACCTCCGCTGCAAGCCATTACTTGTACAGCTCGTCCATG
GluA1-GFP	FW	ATAAAGCTTACCCTGTTACAATCCTGTGGCTCCCGCGCTAGCGGTAGCGGCTCCAGTAGA
	RV	ATACTCGAGGGGAGCCACAGGATTGTAACGGGAGGCCCTACTTGTACAGCTCGTCCATGC
GluA2-GFP	FW	ATAAAGCTTCCCTAAATTTAACACTCTCGACTCTGCTAGCGGTAGCGGCTCCAGTAGA
	RV	ATACTCGAGTCGAGAGTGTTAAAATTTAGGGGAGGCCCTACTTGTACAGCTCGTCCATGCC
GluA3-GFP	FW	ATAAAGCTTCCCTAGATCTTAACACTTTCTGCTCTGCTAGCGGTAGCGGCTCCAGTAGA
	RV	ATACTCGAGCAGAAAGTGTTAAGATCTAGGGGAGGCCCTACTTGTACAGCTCGTCCATGCC
GFP-GluN1 #1	FW	ATAAAGCTTCTTGGGGTTCGACGGCGCGGGGAGGCAGCGCGTGAGCAAGGGCGAGGAG
	RV	ATACTCGAGCCCCCGCCCTGCGACCCCAAGATCCACTGCCCTTGTACAGCTCGTCCATG
GFP-GluN1 #2	FW	ATAAAGCTTGTGACGATCTTGGGGTTCGACGGCAGCTAGCGGGTGAGCAAGGGCGA
	RV	ATACTCGAGCCTGCGACCCCAAGATCGTCAACGAAGCGCTTCCCTAGAGTACAGCTCGT
GFP-GluN1 #3	FW	ATAAAGCTTCTTGGGGTTCGACGGCGCGCTGGCAGCTAGCGGGTGAGCAAGGGCGAG
	RV	ATACTCGAGCCAGCGCCGCTGCGACCCCAAGGAAGCGCTTCCCTAGAGTACAGCTCGT
GFP-GluN2a	FW	ATAAAGCTTACCACCCGTTCTGCGCCGATCGCGCGTACGCGGTAGCGGCTCCAGTAGA
	RV	ATACTCGAGCGATCCGGCGCAGAACCGGAGGAAGGCCCTACTGCCAGCCCCGACCCCGC
GFP-GluN2b	FW	ATAAAGCTTGACAGCGATGCCGATGCTGGGAGGTCAGCTAGCGGTAGCGGCTCCAGTAGA
	RV	ATACTCGAGCCTCCAGCATCGGCATCGCTGTCAGGCCCTACTAGCCCCGACCCCGCTCC
GSG1-L-GFP	FW	ATAAAGCTTCCCATCACACCCAGTCCCCAGAAGGTAGCGGCTCCAGTAGA
	RV	ATACTCGAGCTGGGGCACTGGGTGTGATGGGGTACTTGTACAGCTCGTCCATG
Nlgn3-GFP	FW	ATAAAGCTTCCCGGGTACTGGCCCTCAGCACCATGGTGAGCAAGGGCGAGGAG
	RV	ATACTCGAGGGTCTGAGGGCCAGTACCCGGGCTTGTACAGCTCGTCCATG
Piccolo-GFP	FW	TCGAAGACCCTAGACAAGCTCGCCTCGTTGCCACGGAGGCTAGCGGAGTGAGCAAGGGC
	RV	GAGAAGACCCGAGCCCTGGGCAACGAGGCGAGCTTCCAGCGCTTGTACAGCTCGTC
GFP-Rab11	FW	ATAAAGCTTCCATGCGCGCGCGGAGGAGCTGAATGGTGAGCAAGGGCGAGGAG
	RV	ATACTCGAGCAGCTCCTCGCGCGCCATGGGTTCTTGTACAGCTCGTCCATG
RIM1-GFP	FW	ATAAAGCTTGATAGGAGTTACTATGACGGGATCTGCTAGCGGTAGCGGCTCCAGTAGA
	RV	ATACTCGAGCCGTCATAGTAACTCCTATCCTAGGCCCTACTTGTACAGCTCGTCCATGC
RIM2-GFP	FW	ATAAAGCTTGTATGAACGAGAGTAAGAGGGTCTGCTAGCGGAGTGAGCAAGGGCGAGG
	RV	ATACTCGAGCCCTTACTCTCGTTCATAGCATCAAGCGCTTGTACAGCTCGTCCATG
Shank1-GFP	FW	ATAAAGCTTCCCTCACCTCCTCCAGGAAAAATTAGTGAGCAAGGGCGAGGAG
	RV	ATACTCGAGAATTTTCTGGAGAGGTGAGGGTACTTGTACAGCTCGTCCATG
Shank2-GFP	FW	ATAAAGCTTCCCTTATCTGTCCAGCAGCTGTAGTGAGCAAGGGCGAGGAG
	RV	ATACTCGAGAACAGCTGCTGGACAGATAAGGGTACTTGTACAGCTCGTCCATG
GFP-Syt7	FW	ATAAAGCTTCCCCGGGTCGGGTACATGGTCGCTAGCGGAGTGAGCAAGGGCGAGGAGC
	RV	ATACTCGAGGACCATGACCGGGACCCGGCGGAAGCGCTTGTACAGCTCGTCCATGCC
β3-tubulin-GFP	FW	ATAAAGCTTGTGCGAGCAACTTCACTTGGGGGATCAGCGGTGAGCAAGGGCGAGGAG
	RV	ATACTCGAGCCAAAGTGAAGTTGCTCGCAGCATTACTTGTACAGCTCGTCCATGC
Munc13-1-GFP	FW	ATAAAGCTTCAAAAACCGCGCTAGGGCGCGGGAGCGGTGAGTGAGCAAGGGCGAGGAG
	RV	ATACTCGAGCCCGCCCTAGCGCGGTTTTGTTACTTGTACAGCTCGTCCATG
WASP1-GFP	FW	ATAAAGCTTCCCTCTCACTCCAGCCAGTCTACAAGGTAGCGGCTCCAGTAGA
	RV	ATACTCGAGGTAGACTGGCTGGAGTGAGAGGGTACTTGTACAGCTCGTCCATG

S4 Table. Genomic PCR primers.

Gene	Knock-in	Junction	Forward (5' → 3')	Reverse (5' → 3')	Size product (bp)
<i>Actb</i>	GFP-β-actin #1	5'	TTCTTTGTGCCCTGAGCTT	CTGAACTTGTGGCCGTTTAC	237
		3'	CATGGTCCTGCTGGAGTTCGTG	ATACCCACCATCACACCCCTG	312
<i>Arpc3</i>	Arpc5-GFP	5'	TGCCTGGGGCATAATAGGTG	CTGAACTTGTGGCCGTTTAC	283
		3'	CATGGTCCTGCTGGAGTTCGTG	GCTGAGAGAAACAGATGCTACC	192
<i>Cacna1a</i>	GFP-Cav2.1	5'	TCTTGCAGAATGGCCCCG	CTGAACTTGTGGCCGTTTAC	129
<i>Cacna1e</i>	GFP-Cav2.3	5'	TGTGTGGATAAAGGCTCCGA	CTGAACTTGTGGCCGTTTAC	217
		3'	CATGGTCCTGCTGGAGTTCGTG	TTTACTGCTTGTAGGCCGGC	198
<i>Cacng2</i>	TARPy2-GFP	3'	CATGGTCCTGCTGGAGTTCGTG	AGCTGTTATCCCTGTCCGAGT	164
<i>Cadps</i>	GFP-CAPS1	5'	CATCTTTTGCACCCCAAGCC	CTGAACTTGTGGCCGTTTAC	283
<i>Camk2a</i>	GFP-CaMKIIα	3'	CATGGTCCTGCTGGAGTTCGTG	CAAGAGGCTGATCCCCATGC	190
<i>Cplx1</i>	Complexin1-GFP	5'	CGACCAAGAAGGCTATCCC	CTGAACTTGTGGCCGTTTAC	206
		3'	CATGGTCCTGCTGGAGTTCGTG	GTCAGTGATGGCAGTACGGG	302
<i>Dlg4</i>	PSD95-GFP	5'	TGACTTGCAGCCATCGTAGA	CTGAACTTGTGGCCGTTTAC	200
		3'	CATGGTCCTGCTGGAGTTCGTG	TGGGCTATTAGTCCACACCA	175
<i>Frrs1l</i>	FRRS1L-GFP	5'	TCAGAGCGCGTTGTCAGTAT	CTGAACTTGTGGCCGTTTAC	248
		3'	CATGGTCCTGCTGGAGTTCGTG	TGCTTGACAACCCTGTCTGA	264
<i>Gria1</i>	GluA1-GFP	5'	CAAGTCCATGCAATCCATCCC	CTGAACTTGTGGCCGTTTAC	201
		3'	CATGGTCCTGCTGGAGTTCGTG	TGCTCCCATATGGTCGTGGT	204
<i>Gria2</i>	GluA2-GFP	3'	CATGGTCCTGCTGGAGTTCGTG	AGGACGCGACAAGAAAAGCTAA	144
<i>Gria3</i>	GluA3-GFP	5'	CCACCAACACTCAGAATTACGC	CTGAACCTTGTGGCCGTTTAC	205
		3'	CATGGTCCTGCTGGAGTTCGTG	CCTGACAAAGAGACACGGTC	241
<i>Grin1</i>	GFP-GluN1 #1	5'	CCCGGGCTCCTAGAGAA	CTGAACTTGTGGCCGTTTAC	276
		3'	CATGGTCCTGCTGGAGTTCGTG	CCAAGAGCCGTGTCGTTAT	199
<i>Grin2a</i>	GFP-GluN2a	5'	TGGGGTCGGGTTTCATACTTG	CTGAACTTGTGGCCGTTTAC	335
		3'	CATGGTCCTGCTGGAGTTCGTG	AGTTCGCGTCTGTACAGTC	195
<i>Grin2b</i>	GFP-GluN2b	5'	AGGATGTGTCCACAACGTG	CTGAACTTGTGGCCGTTTAC	297
		3'	CATGGTCCTGCTGGAGTTCGTG	CACCCGGGAACTACTGAGA	229
<i>Gsg1l</i>	GSG1-L-GFP	5'	AAGCAGCAGAGCTAAACCGT	CTGAACTTGTGGCCGTTTAC	175
		3'	CATGGTCCTGCTGGAGTTCGTG	GAGCTGAGTCCACAGCACAG	165
<i>Nlgn3</i>	Neuroigin-3-GFP	5'	CCTATTGGGCTGATGCTGTGA	CTGAACCTTGTGGCCGTTTAC	274
		3'	CATGGTCCTGCTGGAGTTCGTG	TACCCCAAGGATTGGTCCAC	178
<i>Rab11a</i>	GFP-Rab11	5'	AAGCTCTTCGCTCGGGTTAC	CTGAACCTTGTGGCCGTTTAC	196
		3'	CATGGTCCTGCTGGAGTTCGTG	CCCCAAATGGGCTATCGGTG	147
<i>Rims1</i>	RIM1-GFP	5'	GGGTGTGGCTCAAATCTTGT	CTGAACCTTGTGGCCGTTTAC	291
		3'	CATGGTCCTGCTGGAGTTCGTG	GTGGCTCTACTAGCATGTCC	316
<i>Rims2</i>	RIM2-GFP	5'	GGCCGCATGGATCACAAATC	CTGAACCTTGTGGCCGTTTAC	284
		3'	CATGGTCCTGCTGGAGTTCGTG	TTATCCCTAGACGTGGGCTCC	227
<i>Shank1</i>	Shank1-GFP	5'	ACCACGAGATTGATGGCTCC	CTGAACCTTGTGGCCGTTTAC	223
		3'	CATGGTCCTGCTGGAGTTCGTG	GGGGCAGACACAGTTTTAGC	209
<i>Shank2</i>	Shank2-GFP	5'	ACAATGAGATTACGGCAGC	CTGAACCTTGTGGCCGTTTAC	223
		3'	CATGGTCCTGCTGGAGTTCGTG	TGCTTGCCACCACACATTT	156
<i>Syt7</i>	GFP-Syt7	5'	AGCGGCGGCAGAGAAG	CTGAACCTTGTGGCCGTTTAC	194
<i>Tubb3</i>	β3-tubulin-GFP	5'	CCGAGAGCAACATGAACGAC	CTGAACCTTGTGGCCGTTTAC	217
		3'	CATGGTCCTGCTGGAGTTCGTG	AAAGGTGGCTAAAACGGGGAG	312
<i>Unc13a</i>	Munc13-1-GFP	5'	TCAAGCTCAAGTCCGACACG	CTGAACCTTGTGGCCGTTTAC	151
		3'	CATGGTCCTGCTGGAGTTCGTG	ATCCCGCCTGTATTTGACAG	321
<i>Wasf1</i>	WASP1-GFP	5'	AGCGGATTGAAAACGACGTG	CTGAACCTTGTGGCCGTTTAC	232
		3'	CATGGTCCTGCTGGAGTTCGTG	AACATTTTCAAAGTCAAGCGCCA	203

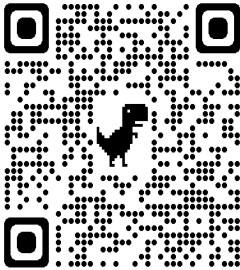
S5 Table. Overview ORANGE constructs with Addgene IDs. ORANGE, Open Resource for the Application of Neuronal Genome Editing.

Gene	Protein	Plasmid name	Addgene ID
<i>Actb</i>	$\beta$ -actin (KI #1)	pORANGE GFP-Actb KI	131479
	$\beta$ -actin (KI #2)	pORANGE GFP-Actb KI #2	139666
<i>Arpc5</i>	Arp2/3 complex subunit 5	pORANGE GFP-Arpc5 KI	131503
<i>Bsn</i>	Bassoon (N-terminal)	pORANGE GFP-Bsn KI	139664
	Bassoon (C-terminal)	pORANGE Bsn-GFP KI	139665
<i>FRRS1L</i>	Frrs11 (C9orf4)	pORANGE C9orf4-GFP KI	131472
<i>Cacna1a</i>	Ca <sub>v</sub> 2.1, (P/Q type)	pORANGE GFP-CACNA1A KI	131480
<i>Cacna1e</i>	Ca <sub>v</sub> 2.3 (R type)	pORANGE GFP-CACNA1E KI	131481
<i>Cacnb1</i>	Ca <sub>v</sub> $\beta$ 1	pORANGE GFP-Cacnb1 KI	139660
<i>Cacnb2</i>	Ca <sub>v</sub> $\beta$ 2	pORANGE Cacnb2-GFP KI	139661
<i>Cacnb3</i>	Ca <sub>v</sub> $\beta$ 3	pORANGE Cacnb3-GFP KI	139662
<i>Cacnb4</i>	Ca <sub>v</sub> $\beta$ 4	pORANGE Cacnb4-GFP KI	139663
<i>Cacng2</i>	TARP $\gamma$ 2	pORANGE CACNG2-GFP KI	131504
<i>Cacng8</i>	TARP $\gamma$ 8 (KI #1)	pORANGE CACNG8-GFP KI #1	131473
	TARP $\gamma$ 8 (KI #2)	pORANGE CACNG8-GFP KI #2	131474
<i>Cadps</i>	CAPS1	pORANGE GFP-CADPS KI	131482
<i>Camk2a</i>	CaMKII $\alpha$	pORANGE GFP-Camk2a KI	131484
		pORANGE mEos3.2-Camk2a KI	131493
<i>Ctla</i>	Clathrin light chain $\alpha$	pORANGE GFP-Ctla KI	131483
<i>Cplx1</i>	Complexin1	pORANGE Cplx1-GFP KI	131475
<i>Cplx2</i>	Complexin2	pORANGE Cplx2-GFP KI	131476
<i>Dlg4</i>	PSD95	pORANGE Dlg4-GFP KI	131477
<i>Doc2a</i>	Doc2a	pORANGE Doc2A-GFP KI	131478
<i>Gria1</i>	GluA1	pORANGE Gria1-GFP KI	131489
<i>Gria2</i>	GluA2	pORANGE Gria2-GFP KI	131490
<i>Gria3</i>	GluA3	pORANGE Gria3-GFP KI	131491
<i>Grim1</i>	GluN1 #1	pORANGE GFP-Grim1 KI	131485
	GluN1 #2	pORANGE GFP-Grim1 KI #2	139658
	GluN1 #3	pORANGE GFP-Grim1 KI #3	139659
<i>Grim2a</i>	GluN2a	pORANGE GFP-Grim2a KI	131486
<i>Grim2b</i>	GluN2b	pORANGE GFP-Grin2b KI	131487
<i>GSG1-1</i>	GSG1-1	pORANGE GSG11-GFP KI	131492
<i>Nlgn3</i>	Neuroigin-3	pORANGE GFP-Nlgn3 KI	131501
<i>Pclo</i>	Piccolo	pORANGE GFP-Pclo KI	139657
<i>Rab11a</i>	Rab11	pORANGE GFP-RAB11a KI	131499
<i>Rims1</i>	RIM1	pORANGE Rims1-GFP KI	131494

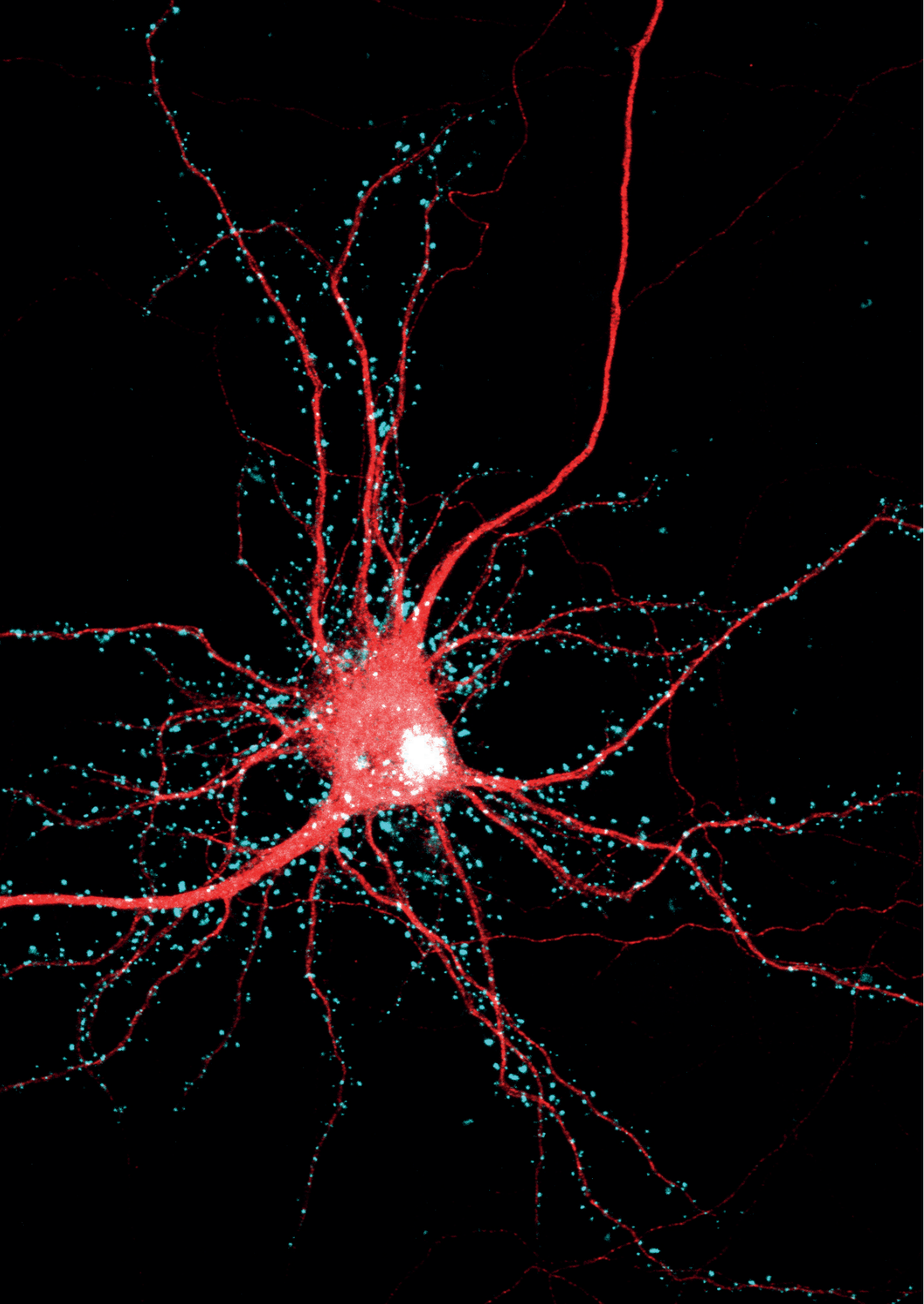
S5 Table (continued)

<i>Rims2</i>	RIM2	pORANGE Rims2-GFP KI	131495
<i>Shank1</i>	Shank1	pORANGE Shank1-GFP KI	131500
<i>Shank2</i>	Shank2	pORANGE Shank2-GFP KI	131496
<i>Syt7</i>	Synaptotagmin-7	pORANGE GFP-Syt7 KI	131488
<i>Tubb3</i>	$\beta$ 3-tubulin	pORANGE Tubb3-GFP KI	131497
<i>Unc13a</i>	Munc13-1	pORANGE unc13a-GFP KI	131498
<i>WASF</i>	WASP1/Wave1	pORANGE WASF1-GFP KI	131502
<i>Lentiviral constructs</i>		pFUGW-mCherry-KASH	131505
		pFUGW SpCas9	131506
		pFUGW ORANGE Gria1-GFP KI _mCherry-KASH	131507
		pFUGW ORANGE Tubb3-GFP KI _mCherry-KASH	131508
		pFSW FLEx mCherry-KASH	139652
<i>AAV constructs</i>		pFSW FLEx Synapsin-FLAG	139653
		pAAV MCS mCherry KASH	139654
		pAAV ORANGE Gria1a HaloTag KI	139655
<i>Cloning template vector</i>		pAAV ORANGE Dlg4 HaloTag KI	139656
		pORANGE Cloning template vector	131471
		pORANGE LOX Cloning template vector	139651

S1 Data. Raw data. Available at:







# 3

---

## **Duplex labeling and manipulation of neuronal proteins using sequential CRISPR/Cas9 gene editing**

Wouter J. Droogers, Jelmer Willems, Harold D. MacGillavry\*,  
Arthur P.H. de Jong\*

eNeuro (2022); ENEURO.0056-22.2022

---

\* These authors contributed equally to this work.  
Cell Biology, Neurobiology and Biophysics, Department of Biology, Faculty of Science, Utrecht University, Utrecht, the Netherlands

---

## ABSTRACT

CRISPR/Cas9-mediated knock-in methods enable the labeling of individual endogenous proteins to faithfully determine their spatiotemporal distribution in cells. However, reliable multiplexing of knock-in events in neurons remains challenging because of cross talk between editing events. To overcome this, we developed conditional activation of knock-in expression (CAKE), allowing efficient, flexible, and accurate multiplex genome editing. To diminish cross talk, CAKE is based on sequential, recombinase-driven guide RNA (gRNA) expression to control the timing of genomic integration of each donor sequence. We show that CAKE is broadly applicable in rat neurons to co-label various endogenous proteins, including cytoskeletal proteins, synaptic scaffolds, ion channels and neurotransmitter receptor subunits. To take full advantage of CAKE, we resolved the nanoscale co-distribution of endogenous synaptic proteins using super-resolution microscopy, demonstrating that their co-organization correlates with synapse size. Finally, we introduced inducible dimerization modules, providing acute control over synaptic receptor dynamics in living neurons. These experiments highlight the potential of CAKE to reveal new biological insight. Altogether, CAKE is a versatile method for multiplex protein labeling that enables the detection, localization, and manipulation of endogenous proteins in neurons.

## SIGNIFICANCE STATEMENT

Accurate localization and manipulation of endogenous proteins is essential to unravel neuronal function. While labeling of individual proteins is achievable with existing gene editing techniques, methods to label multiple proteins in neurons are limiting. We introduce a new CRISPR/Cas9 strategy, CAKE, achieving faithful duplex protein labeling using sequential editing of genes. We use CAKE to visualize the co-localization of essential neuronal proteins, including cytoskeleton components, ion channels and synaptic scaffolds. Using super-resolution microscopy, we demonstrate that the co-organization of synaptic scaffolds and neurotransmitter receptors scales with synapse size. Finally, we acutely modulate the dynamics of synaptic receptors using labeling with inducible dimerization domains. Thus, CAKE mediates accurate duplex endogenous protein labeling and manipulation to address biological questions in neurons.

## INTRODUCTION

The spatiotemporal distribution of proteins dictates virtually all functions of cells, and the accurate detection of endogenous proteins is an essential strategy in cell biological research (Choquet et al, 2021). Because protein overexpression and antibody labeling have significant limitations in accuracy and specificity, there is a pressing need to develop novel techniques that detect endogenous proteins in biological preparations. Recent CRISPR/Cas9-based genome editing methods have addressed this need by inserting (fluorescent) tags in specific genes, creating knock-ins, and now make it possible to reliably detect endogenous protein distribution with fluorescence microscopy in a wide variety of biological preparations (Schmid-Burgk et al, 2016; Auer et al, 2014; Nakade et al, 2014; Suzuki et al, 2016; Artegiani et al, 2020; Mikuni et al, 2016). However, simultaneous labeling of multiple protein species in individual cells remains challenging with commonly used genome editing methods, particularly in post-mitotic cells such as neurons. We reasoned that such genetic tools are mandatory to study the co-distribution of proteins, and would present an elegant approach to manipulate the distribution and dynamics of endogenous proteins.

The fact that neurons are postmitotic cells severely complicates both simple and

multiplex genome editing strategies: it prevents the isolation and expansion of desired clones to create isogenic cell lines and precludes multiple independent rounds of gene modification. Furthermore, insertion of the donor DNA using the highly accurate homology-directed repair (HDR) pathway predominantly occurs in the S/G2 phases of mitosis (Orthwein et al, 2015), and is strongly disfavored in nondividing cells. While successful genomic insertion of epitope tags using HDR in neurons has been reported (Nishiyama et al, 2017; Matsuda & Oinuma, 2019), most neuronal knock-in methods instead utilize the more efficient, but error-prone non-homologous end joining (NHEJ) mechanism which remains active in postmitotic cells. Most NHEJ-based methods target the coding sequence of genes (Willems et al, 2020; Suzuki et al, 2016; Gao et al, 2019; Schmid-Burgk et al, 2016), but more recent strategies replace endogenous exons (Fang et al, 2021; Danner et al, 2021) or introduce novel exons in intronic sequences (Zhong et al, 2021) to mitigate the effects of indel mutations. Indels can also be reduced in neurons using microhomology-mediated end joining (MMEJ, Yao et al, 2017).

Although these methods faithfully label individual proteins in neurons, multiplex epitope tagging using CRISPR/Cas9 has remained challenging. While achievable with HDR, its efficacy is generally too low for routine use (Mikuni et al, 2016; Matsuda & Oinuma, 2019). NHEJ in turn, operates without homology between donor DNA and target locus, and therefore the donor DNA can indiscriminately integrate in any double-stranded break (DSB), leading to a high degree of donor integration in the incorrect locus (i.e. crosstalk, Fig. 1A). Gao et al., 2019 circumvented this problem by creating donor DNAs that prevent protein labeling when inserted in the incorrect gene. This strategy successfully generated double knock-ins, but has restrictions on the location of the protein tag, and indels or integration of the incorrect donor may generate null mutations (Gao et al, 2019).

We reasoned that crosstalk between donor DNAs could be diminished by separating genome editing events in time (Fig. 1B, also see Chylinski et al., 2019). Using our NHEJ-based Open Resource for the Application of Neuronal Genome Editing (ORANGE) toolbox we previously achieved this for a small number of genes with a mechanism we dubbed Conditional Activation of Knock-in Expression (CAKE) (Willems et al, 2020). In this approach, a GFP-2A-Cre donor sequence was fused to the first gene, which after successful knock-in switched on the expression of the second knock-in vector (Fig. 1-1A). However, we did observe crosstalk between the loci for some knock-in combinations, suggesting insufficient control over the delay between the two genome editing events (Willems et al, 2020).

To overcome this, we implemented major improvements of our CAKE strategy that result in reproducible multiplex genome editing in neuronal preparations. We demonstrate that, with Cre-dependent knock-in vectors and precise timing of Cre-recombinase activation, a high rate of correct double knock-in cells can be attained, while strongly diminishing crosstalk. Furthermore, we applied CAKE to study and manipulate the positioning of multiple endogenous proteins simultaneously in individual cells, illustrating that CAKE is a versatile method to resolve complex biological questions.

## RESULTS

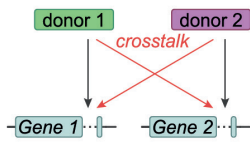
### CAKE creates double knock-ins in neurons

We reasoned that accurate multiplex knock-ins in neurons could be achieved by separating genome editing events in time using a Cre-dependent conditional activation mechanism (Fig. 1A-B). In a previous study we achieved this by fusing GFP-2A-Cre to the first gene to activate a second knock-in construct with a Cre-dependent single guide RNA (gRNA; Willems et al.,

2020; Fig. 1-1A). This mechanism successfully yielded double knock-in cells for a variety of gene combinations, illustrating the potential of sequential gene editing (Willems et al, 2020). However, appreciable crosstalk between the knock-ins still occurred, suggesting we had insufficient control over the delay between genome editing events (Fig. 1-1C).

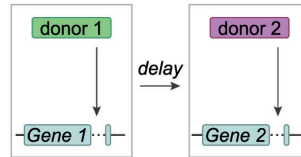
### A Problem

*Simultaneously active knock-ins*



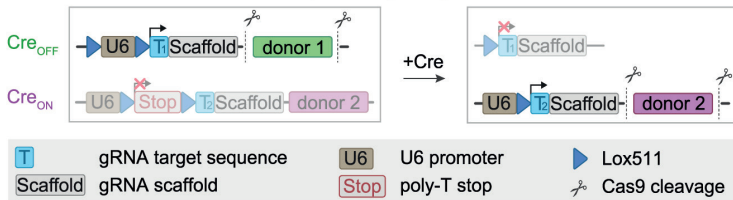
### B Solution

*Sequentially active knock-ins*



### C Strategy

*Conditional Activation of Knock-in Expression (CAKE)*



### D

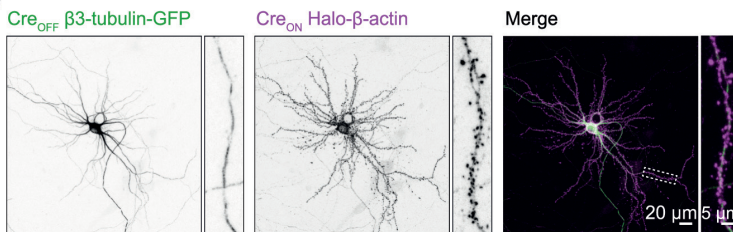


**Figure 1. Multiplex labeling of endogenous proteins using CAKE**

(A) Illustration of the problem of multiplex knock-in strategies based on NHEJ. With simultaneous editing of multiple genes, donor DNAs can be integrated in either allele, leading to crosstalk. (B) Proposed solution for multiplex knock-ins. By introducing a delay between two genome editing events, crosstalk can be avoided. CAKE is designed to control the delay between the two events, using Cre- or FLP-recombinase. (C) CAKE strategy. The CreOFF vector is active in the absence of Cre, leading to editing of the first target gene, and removal of the Cre-OFF donor for subsequent genomic integration. Upon addition of Cre, gRNA expression from CreOFF is deactivated, and gRNA expression from CreON vector is enabled for editing the second target gene. See Figure 4 for example methods to deliver active Cre. All donors contain a fluorophore or epitope tag flanked by a PAM- and target sequence (not shown, see Fig. 1-3B and Willems et al., 2020). (D) Example confocal image of a CreOFF  $\beta$ 3-tubulin-GFP and CreON Halo- $\beta$ -actin knock-in. 20  $\mu$ L lenti-Cre was added at DIV 7, and cells were fixed at DIV 14.

Here, we introduce two major improvements of this CAKE strategy (Fig. 1C). First, to obtain full control over the switch from the first to the second gRNA, we separately introduced Cre expression. We either used lentiviral infection of a Cre-expressing vector or lipofection of a 4OH-tamoxifen-inducible Cre-expressing construct. Second, to reduce crosstalk, we redesigned the first knock-in vector such that gRNA expression of the first vector is switched off by Cre, effectively limiting further editing of the first targeted locus (also see Chylinski et al., 2019). We refer to the first knock-in vector as CreOFF (gRNA expression is switched off by Cre), and the second knock-in vector as CreON (gRNA expression switched on by Cre, see Fig. 1B). This sequential knock-in strategy yielded a mosaic of fluorescent cells, with

cells positive for the CreOFF or CreON knock-ins (Fig. 1-2) and a fraction of double knock-in cells that are positive for both the CreON and CreOFF knock-ins (Fig. 1D).

We first compared the updated CAKE strategy with our previous GFP-2A-Cre based method (Willems et al., 2020), using knock-in constructs for  $\beta$ 3-tubulin and  $\beta$ -actin, delivered to cultured rat hippocampal neurons with lipofectamine (Fig. 1-1). Since the distribution patterns of  $\beta$ 3-tubulin and  $\beta$ -actin in neurons are well-known to be segregated in different subcellular compartments, this allowed us to easily quantify knock-in efficacy and accuracy. We systematically counted all fluorescent cells per coverslip, scoring them as a correct knock-in cell for  $\beta$ 3-tubulin-GFP or Halo- $\beta$ -actin; a double knock-in cell, or, if donor crosstalk had occurred, as an incorrect knock-in cell. Strikingly, while both methods lead to a similar number of single and double knock-in cells, the updated strategy nearly completely abolished crosstalk between knock-ins (Fig. 1-1D). Furthermore, we noted that for some genes GFP-2A-Cre fusion resulted in reduced expression levels, probably due to the increase in mRNA length (Willems et al, 2020). Importantly, no such effect was found for the improved CAKE method (Fig. 1-1E). Thus, CAKE faithfully created double knock-ins in cultured hippocampal neurons.

### **CAKE can be applied to multiple gene combinations**

To test if we could generalize the application of CAKE to other gene pairs, we generated a set of CreOFF and CreON knock-in vectors targeting a diversity of neuronal proteins. These knock-ins include synaptic scaffolding proteins (PSD95, Homer1 and MPP2) and neurotransmitter receptor subunits (GluA1, GluN1). We also added voltage- and Ca<sup>2+</sup>-gated ion channels (CaV2.3, SK2, BK), where the limited availability of antibodies has hampered (co-)localization analysis in neurons. Similar to  $\beta$ 3-tubulin and  $\beta$ -actin knock-in vectors, these CAKE combinations yielded mosaic fluorescent labeling in cultured neurons. Importantly, we identified multiple double knock-in cells for many gene combinations (Fig. 2A). This illustrates the potential for CAKE to study the spatiotemporal co-expression of a wide range of proteins.

### **CAKE is compatible with multiple CRISPR-Cas9 knock-in strategies**

Because CAKE is based on sequential gRNA expression, we reasoned that our method should be compatible with other recently developed CRISPR/Cas9 knock-in strategies (e.g. Fang et al., 2021; Gao et al., 2019; Schmid-Burgk et al., 2016; Zhong et al., 2021). To assess the flexibility of CAKE, we implemented the CRISPR-mediated insertion of exon (CRISPIE) approach, which introduces designer exons in intronic sequences to mitigate the effect of indel mutations (Zhong et al, 2021). We inserted an exon containing Halo into the first intron of Homer1 by flanking the donor DNA with splicing acceptor and donor sites (Fig. 2-1). The resulting CreOFF vector was successfully combined with a CreON ORANGE vector to attain double knock-in cells (Fig. 2B). Thus, various NHEJ-based CRISPR-Cas9 methods can be adopted and combined with CAKE to create multiplex knock-ins.

### **Controlling CAKE with Flp-recombinase**

To extend the utility of CAKE, we created CAKE vectors that are controlled by Flp-recombinase (FlpOFF and FlpON, Fig. 1-3 and Fig. 2B). The Frt and stop codon sequence were contained within the gRNA, which was reported to have a higher efficacy compared to integration in the U6 promoter (Chylinski et al, 2019). The switch between FlpOFF and FlpON gRNA expression was controlled using a lentivirus expressing FlpO (lenti-Flp).

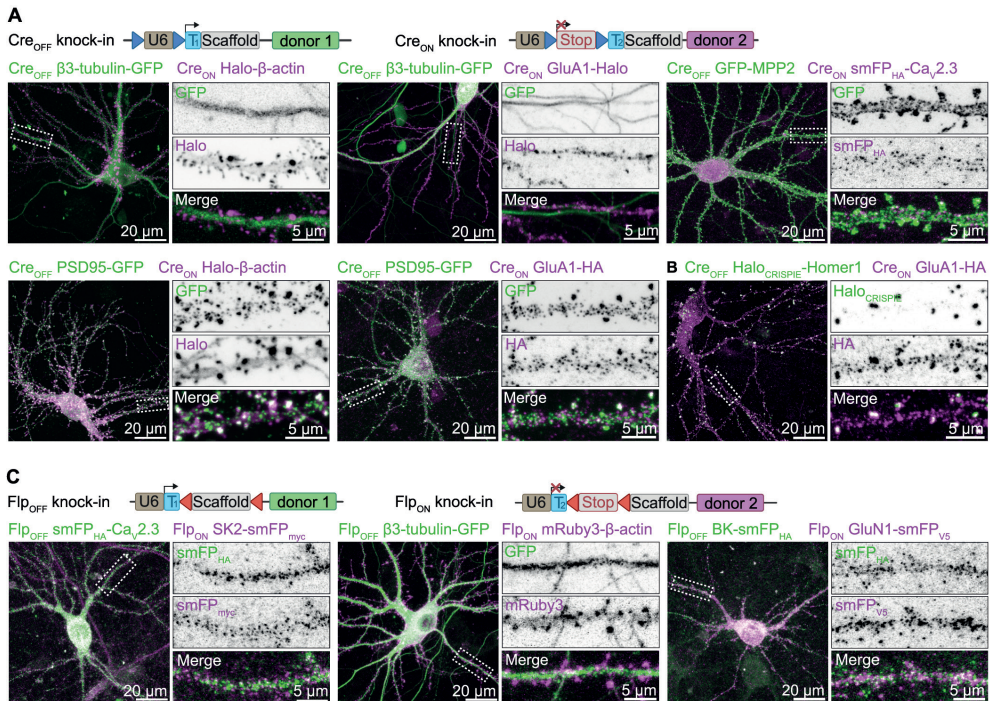


**Figure 2. CAKE generates double knock-ins for a variety of genes**

(A) Top: Overview of CreOFF and CreON knock-in constructs. Bottom: example confocal microscopy images of CAKE knock-in cells controlled by Cre-recombinase. For CreOFF β3-tubulin-GFP / CreON GluA1-Halo, lenti GFP-Cre was used, which labels infected nuclei. The remaining examples were obtained with lenti-Cre without GFP, or with ERT2-Cre-ERT2. Lentivirus or 100 nM 4OH-tamoxifen was added at DIV 7. Cells were fixed at DIV 14. (B) Example confocal image of CreOFF HaloCRISPIE-Homer1 and CreON GluA1-HA double knock-in cells. CRISPIEHalo donor DNA is inserted into intron 1 of Homer1 as a novel exon (see Fig. 2-1 and Zhong et al., 2021). Double knock-in was obtained using ERT2-Cre-ERT2 and 100 nM 4OH-tamoxifen was added at DIV 7. Cells were fixed at DIV 14. (C) Top: Overview of FlpOFF and FlpON knock-in constructs. Bottom: example confocal microscopy images of CAKE knock-ins controlled by lenti-FlpO-recombinase, added on DIV 7. Cells were fixed at DIV 14.

Flp-controlled CAKE performed comparable to Cre-controlled CAKE, and resulted in single and double knock-in cells for a variety of gene combinations (Fig. 2C). Finally, we developed a Cre<sup>ON</sup>-Flp<sup>OFF</sup> knock-in vector, enabling intersectional activation of gRNA expression (Fig. 1-3A). Thus, CAKE can be performed with both Cre and Flp-recombinase.

### Knock-in efficacy is modulated by donor DNA levels

Initially, the number of double knock-in cells per coverslip was too low for many applications (Fig. 1-1D). Therefore, we next set out a series of experiments to increase the number of double knock-in cells per sample, using CreOFF β3-tubulin-GFP and CreON Halo-β-actin knock-in vectors. In early experiments we noticed that vector amounts used in transfection affected knock-in efficacy. To thoroughly test this, we systematically varied the amount of the CreOFF knock-in vector in our transfection mixture between 20 and 197 fmol (which equals to 50 to 500 ng DNA) per coverslip, while keeping CreON fixed at 178 fmol, and scored all fluorescent cells per coverslip at day in vitro (DIV) 14. Strikingly, we found a strong inverse relationship between CreOFF β3-tubulin-GFP vector amount and the number of β3-tubulin-

GFP positive cells (Fig. 3A,  $p = 0.006$ , 2-way ANOVA). Furthermore, lower CreOFF amounts also increased the number of Halo- $\beta$ -actin positive cells, even though we kept the amount of CreON vector constant in all conditions (Fig. 3A,  $p = 0.04$ , 2-way ANOVA). This interplay suggests competition between the two knock-ins, which continues after the Cre-dependent switch has occurred. Together with an increase in single knock-in cells, we observed a strong increase in double knock-in cells to between 5 and 8 cells per coverslip at the lowest CreOFF  $\beta$ 3-tubulin-GFP amount (Fig. 3A,  $p = 0.001$ , 2-way ANOVA). In that condition, 82% of knock-in cells was  $\beta$ 3-tubulin-GFP positive, 14% was Halo- $\beta$ -actin positive, and 3.4% was double positive. Crucially, the number of incorrect knock-in neurons (i.e. donor crosstalk for one of the targeted genes) remained low (1-2 cells per coverslip, <1% of all knock-in cells), although the absolute number slightly increased with lower DNA amount ( $p = 0.02$ , 2-way ANOVA). In the same experiment, we tested if the timing of Cre infection (infection at DIV 3, 7 or 9) affects the number of knock-in neurons. In contrast to the strong effect of vector amount, the timing of Cre expression did not influence the number of single or double knock-in neurons (Fig. 3A, CreOFF  $p = 0.90$ , CreON  $p = 0.88$ , double knock-in  $p = 0.49$ , incorrect knock-in  $p = 0.50$ , 2-way ANOVA), suggesting that either knock-in efficacy for this gene combination is insensitive to Cre timing, or that the onset of lentiviral-mediated Cre expression is too slow to observe an effect. Similar results were obtained for CreOFF GluA1-GFP and CreON PSD95-Halo, though the sensitivity for DNA amount appeared to differ between individual knock-in constructs (Fig. 3-1A). We then tested if further reduction of vector amount enhanced knock-in efficacy, and varied the amount of both the CreOFF and CreON vectors. Here, we found that the optimum for CreOFF  $\beta$ 3-tubulin-GFP is around 3.9 fmol DNA per coverslip. CreON Halo- $\beta$ -actin performed best around 36 fmol per coverslip, and efficacy dropped steeply below 3.6 fmol (Fig. 3B). This is in line with our previous observation that increased amounts of CreOFF knock-in vector negatively affect the CreON knock-in efficacy (Fig. 3A).

We hypothesized that the inverse relationship between DNA amount and knock-in efficacy is due to competition between donor DNAs. To test if increasing donor DNA copies per cell decreases knock-in efficacy, we generated ORANGE  $\beta$ 3-tubulin knock-in vectors with 1, 2, 3 or 4 independent copies of the donor DNA (Fig. 3C-E). Using these vectors, we found a clear negative correlation between the number of donor DNA copies and the number of  $\beta$ 3-tubulin-GFP positive cells per coverslip (Fig. 3E,  $p = 0.023$ ,  $R^2 = 0.42$ ).

Finally, to separate effects of gRNA and donor DNA levels, we replaced the CreOFF  $\beta$ 3-tubulin-GFP vector with a CreOFF gRNA vector and a minicircle GFP donor (Fig. 3-1B). Previous studies found that minicircle donors often outperform large donor plasmids, likely because Cas9-mediated cleavage of the donor plasmid can lead to integration of the vector backbone (Danner et al, 2021; Schmid-Burgk et al, 2016; Suzuki et al, 2016). We found that, at high donor levels, minicircle donor DNA performed similar to ORANGE donor plasmids, but knock-in efficacy was reduced at lower minicircle levels (Fig. 3-1C). The reason for this reduction is unclear, but we cannot exclude that at low amounts of minicircle DNA the transfection efficacy is reduced. Similar to knock-in vector-delivered donor, the high amounts of the (CreOFF-activated) minicircle donor also decreased the efficacy of the CreON Halo- $\beta$ -actin knock-in (Fig. 3-1C). Importantly, increasing CreOFF gRNA expression level had no effect on knock-in efficacy for both the CreOFF and CreON knock-in. Thus, under our experimental conditions, a single vector containing both the gRNA and donor DNA leads to the highest knock-in efficacy. Taken together, we conclude that donor DNA levels modulate knock-in efficacy.



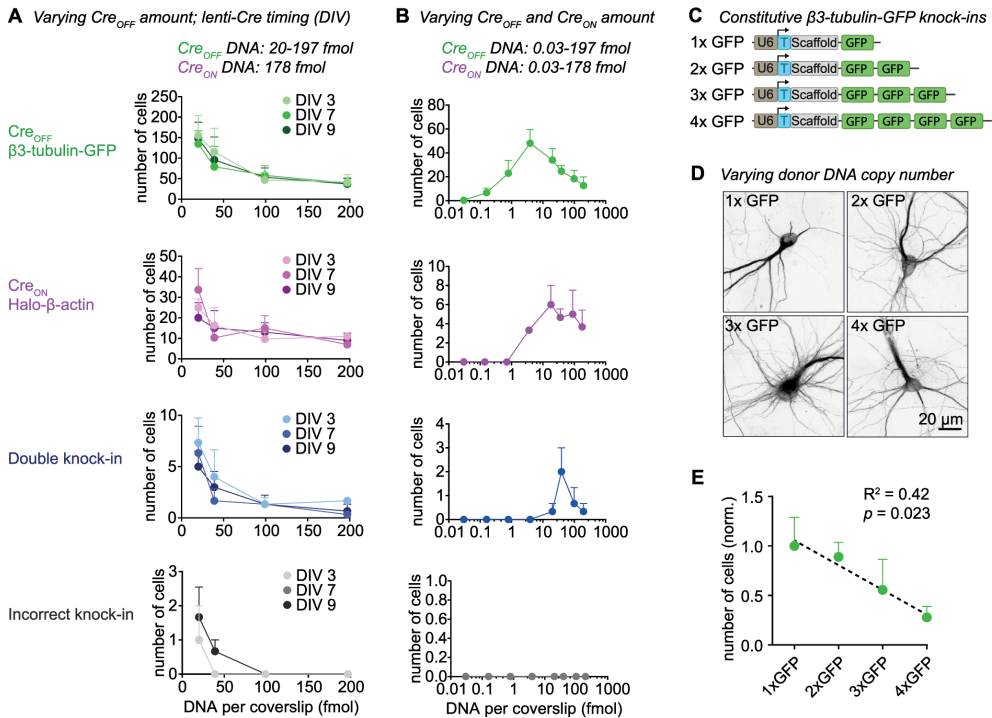


**Figure 3. Donor DNA amount controls knock-in efficacy**

(A) Number of fluorescent cells per coverslip for each knock-in, as a function of CreOFF β3-Tubulin-GFP vector amount. 20 μL lenti-Cre was added at DIV 3, 7 or 9.  $n = 3$  coverslips,  $N = 3$  independent cultures. (B) Number of fluorescent cells per coverslip for each knock-in. Both the amount of CreOFF and CreON vector were varied; 20 μL lenti-Cre was added at DIV 7.  $n = 3$  coverslips,  $N = 3$  independent cultures. (C) pORANGE β3-tubulin knock-in constructs used to titrate the amount of donor DNA. Each GFP donor has its own PAM and target sequence (not shown), and thus every GFP donor can be cleaved independently from the vector. (D) Example confocal images of β3-tubulin-GFP knock-in cells using 1 to 4 GFP donors per vector. (E) Number of fluorescent cells as a function of number of GFP donors. Data was normalized to average number of knock-ins in the 1xGFP condition.  $R^2 = 0.42$ ,  $p = 0.023$ , model linear regression (dotted black line).  $n = 3$  coverslips,  $N = 3$  independent cultures.

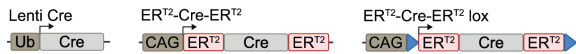
### Tamoxifen-inducible Cre controls CreON knock-in efficacy

In the experiments described above, we consistently observed a lower efficacy of CreON compared to the CreOFF knock-ins. To improve the efficacy of CreON knock-ins, we switched to 4OH-tamoxifen inducible Cre (ERT2-Cre-ERT2), which ensures rapid onset of Cre activation (Matsuda & Cepko, 2007) and superior control over timing, compared to lentiviral-mediated Cre expression. As found by others (e.g. Forni et al., 2006; Higashi et al., 2009), we observed that strong, sustained activation of ERT2-Cre-ERT2 appears toxic to neurons, which resulted in fewer single and double knock-in cells (Fig. 4-1B). To prevent toxicity, we reduced the vector encoding for ERT2-Cre-ERT2 to 2 fmol per coverslip, and we developed a self-inactivating Cre, by flanking ERT2-Cre-ERT2 with LoxP sites (ERT2-Cre-ERT2 lox, adapted from Pfeifer et al., 2001; Silver and Livingston, 2001). Under these conditions, 4OH-tamoxifen induced a dose-dependent increase in CreON and double knock-ins (CreON  $p = 0.0001$ ; double knock-in  $p = 0.0001$ , 2-way ANOVA), without affecting the number of CreOFF knock-in cells (Fig. 4B,  $p = 0.70$ , 2-way ANOVA). A ten-fold increase in ERT2-Cre-ERT2 lox vector (to 20 fmol) increased the number of CreON at low 4OH-

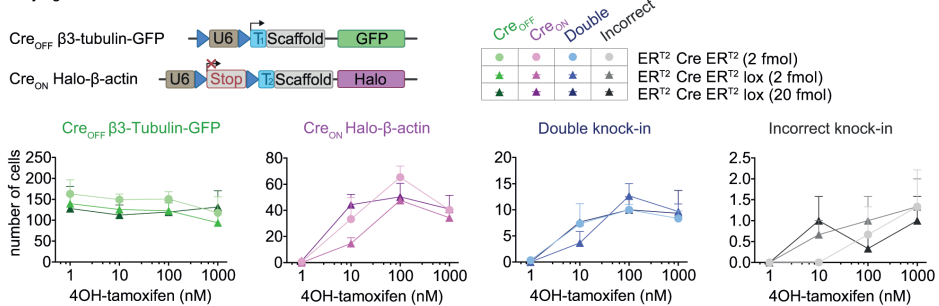
tamoxifen concentrations (Fig. 4B,  $p = 0.025$ , 2-way ANOVA post-hoc comparison), but did not further increase efficacy at 100 or 1000 nM 4-OH-tamoxifen. Overall, no statistical difference was observed between ERT2-Cre-ERT2 and ERT2-Cre-ERT2 lox conditions (CreOFF knock-ins  $p = 0.44$ , CreON knock-ins  $p = 0.10$ , double knock-ins  $p = 0.98$ , 2-way ANOVA). The number of incorrect knock-ins remained low (about 1 per coverslip at 1000 nM 4OH-tamoxifen), and was also similar between the Cre conditions (Fig. 4B,  $p = 0.80$ , 2-way ANOVA). Thus, at low vector concentrations ERT2-Cre-ERT2 accurately controls gRNA expression, while minimizing cytotoxicity.

Finally, we directly compared lenti-Cre and ERT2-Cre-ERT2, and found that ERT2-Cre-ERT2 did not boost the number of double knock-in neurons significantly (Fig. 4C). Taken together, multiple methods for Cre delivery and activation can be used to control CAKE, without obvious differences in the number of knock-in neurons. All subsequent experiments are based on ERT2-Cre-ERT2, activated on DIV 7 with 100 nM 4OH-tamoxifen.

### A Cre recombinase constructs



### B Varying Cre and 4OH-tamoxifen concentrations



### C Direct comparison between Lenti-Cre and ERT2-Cre-ERT2

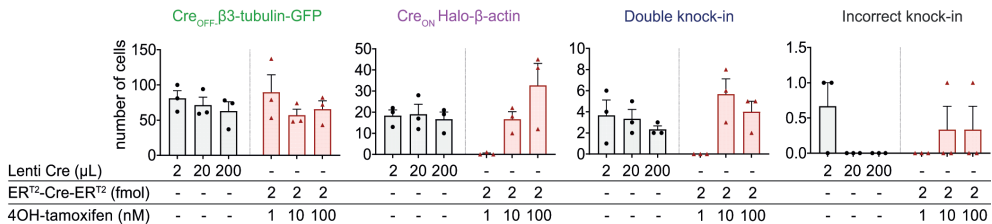


### Figure 4. Comparison of methods to deliver and activate Cre-recombinase

(A) Overview of Cre-recombinase constructs. (B) Number of fluorescent knock-in cells per coverslip using ERT2-Cre-ERT2 constructs. 4OH-tamoxifen was added at the indicated concentration at DIV 7.  $n = 3$  coverslips,  $N = 3$  independent cultures. 71% of knock-in cells was  $\beta_3$ -tubulin-GFP positive, 24% was Halo- $\beta$ -actin positive, and 5.0% was double positive. (C) Comparison of Lenti-Cre and ERT2-Cre-ERT2. Lenti-Cre and 4OH-tamoxifen were added at DIV 7.  $n = 3$  coverslips,  $N = 3$  independent cultures.

### Crosstalk between knock-ins is dependent on timing of Cre activation

While testing several CAKE combinations, we noticed that one particular combination, using CreOFF GluA1-Halo and CreON FIpOFF smFPV5-CaV2.3, showed an unusually high rate of donor crosstalk (Fig. 5A-C). Specifically,  $\sim 90\%$  of these incorrect knock-ins

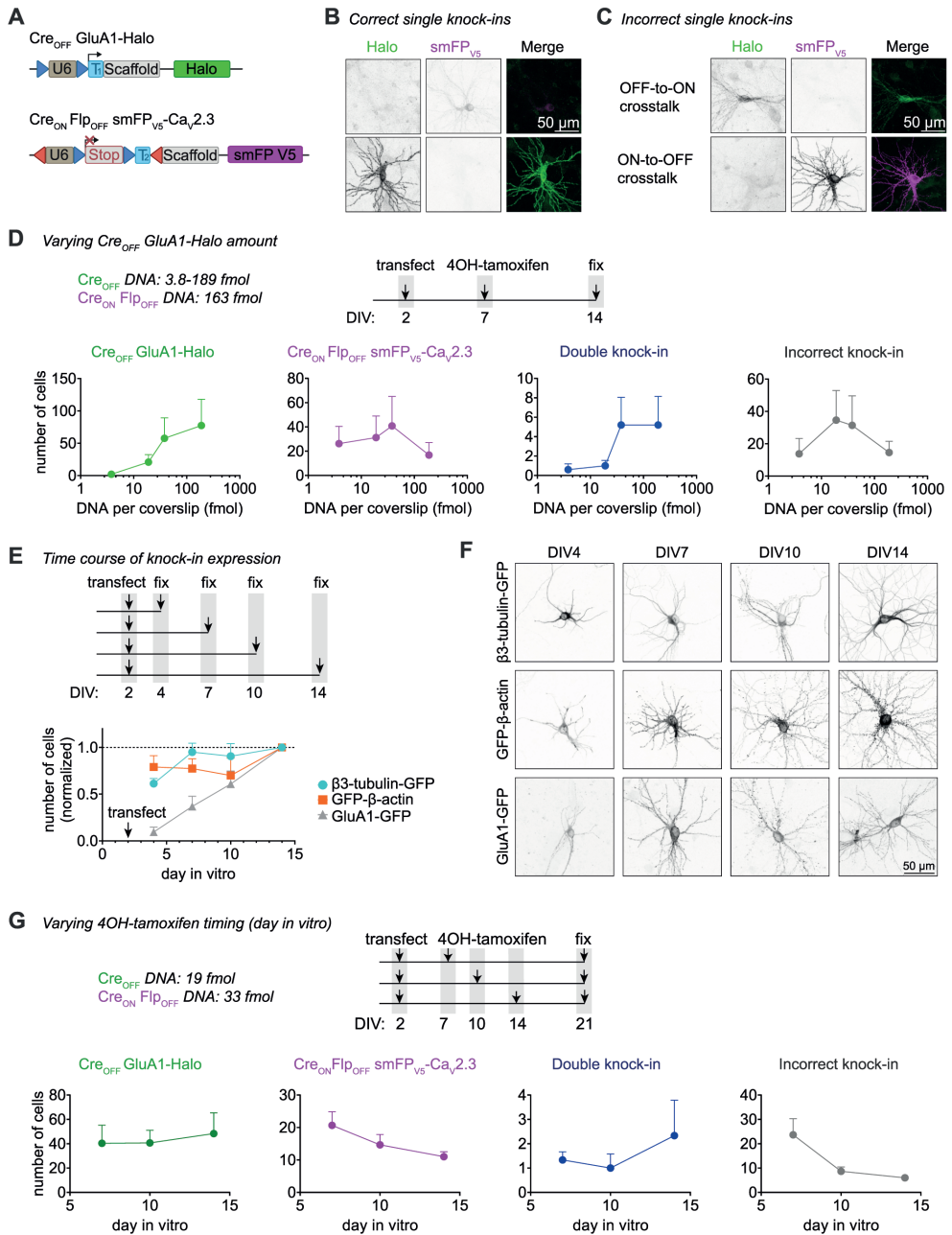


**Figure 5. Delaying Cre activation reduces knock-in crosstalk**

(A) Overview of used DNA constructs. (B-C) Example images of correct (B) and incorrect (C) knock-in neurons. Cells were incubated with 100 nM 4OH-tamoxifen at DIV 7, and fixed at DIV 14. Images in B and C were taken with same acquisition settings to illustrate differences in expression level between CaV2.3 (top) and GluA1 (bottom). (D) Top: experimental design. Bottom: Number of fluorescent cells per coverslip for each knock-in, as a function of CreOFF GluA1-Halo vector amount. 100 nM 4OH-tamoxifen was added at DIV 7. Cells were fixed at DIV 14.  $n = 5$  coverslips,  $N = 5$  independent cultures. (E) Top: experimental design. Experiment was performed without Cre or

**Figure 5 (continued)** 4OH-tamoxifen. Bottom: Number of fluorescent cells per coverslip at different timepoints, normalized to the number of cells at DIV 14.  $n = 4$  coverslips,  $N = 4$  independent cultures. (F) Example confocal microscopy images of cells fixed at different DIVs from E. Image acquisition settings were kept identical per knock-in. (G) Top: experimental design. Bottom: Number of fluorescent cells per coverslip for each knock-in, as a function of the DIV at which 100 nM 4OH-tamoxifen was added.  $n = 3$  coverslips,  $N = 3$  independent cultures.

were smFPV5-positive in a staining pattern expected for GluA1 (ON-to-OFF crosstalk). To understand why the CAKE mechanism failed to prevent crosstalk in this experiment, we decided to investigate this further.

Several features of these two knock-in constructs favor the detection of ON-to-OFF crosstalk. Firstly, both gRNAs target the same position in the reading frame of their respective target genes (frame +1). Secondly, CreOFF GluA1-Halo targets the GluA1 C-terminus with a stop codon in the Halo donor, while Cre-ON FlpOFF smFPV5-CaV2.3 targets the CaV2.3 N-terminus. Thus, ON-to-OFF crosstalk would lead to an in-frame addition of smFPV5 in *Gria1*, while OFF-to-ON crosstalk would introduce an early stop codon in *Cacna1e*, likely preventing protein expression from the allele.

To test if crosstalk could be prevented, we first titrated the amount of Cre-*OFF* GluA1-Halo vector. Unexpectedly, we found that higher Cre-*OFF* GluA1-Halo load increased the number of GluA1-Halo knock-in cells (even though the effect was not obvious in statistical analysis due to high variability between cultures (Fig. 5D,  $p = 0.21$ , 1-way ANOVA), the opposite of what we previously found for CreOFF  $\beta$ 3-tubulin (Fig. 3A). Higher Cre-*OFF* GluA1-Halo load also appeared to increase the number of double knock-in cells and incorrect knock-ins (CreON FlpOFF smFPV5-CaV2.3  $p = 0.80$ , double knock-ins  $p = 0.26$ , incorrect knock-ins  $p = 0.63$ ). At 38 fmol CreOFF vector, about 25% of all fluorescent cells were incorrect (predominantly ON-to-OFF crosstalk).

We hypothesized that this crosstalk is due to a low editing rate of *Gria1* compared to genes with lower rates of crosstalk (e.g. *Tubb3* and *Actb*, Fig. 3), which continues after Cre activation at DIV 7. Indeed, several studies demonstrated that both the appearance of DSBs, as well as (DNA-repair dependent) indels are highly dependent on the sequence of the target locus, and that repair of DSBs may continue for multiple days (Park et al, 2021; Liu et al, 2020; Rose et al, 2017). To compare editing rates over time, we transfected CreOFF GFP knock-ins for  $\beta$ 3-tubulin,  $\beta$ -actin and GluA1 at DIV 2, and fixed and counted the number of GFP positive cells at DIV 4, 7, 10 and 14 (Fig. 5E). For all knock-ins, we found that the number of GFP-positive cells increased over time ( $p = 1.0 \times 10^{-5}$ , 2-way ANOVA), and this effect differed between knock-in constructs ( $p = 5.0 \times 10^{-5}$ , interaction  $p = 0.012$ , 2-way ANOVA). Importantly, while the number of  $\beta$ 3-tubulin and  $\beta$ -actin knock-in neurons increased at a similar rate ( $p = 0.81$ , 2-way ANOVA post-hoc comparison), the number of GluA1 knock-in neurons increased much slower ( $\beta$ 3-tubulin vs. GluA1  $p = 0.0006$ ,  $\beta$ -actin vs GluA1  $p = 3.5 \times 10^{-3}$ , 2-way ANOVA post-hoc comparison) and continued to increase after DIV 10.

Finally, we tested if delaying Cre activation, by delaying the addition of 4OH-tamoxifen, would reduce ON-to-OFF crosstalk (Fig. 5G). We found that delaying 4OH-tamoxifen addition had no effect on the number of single or double knock-in neurons (Cre-*OFF* GluA1-Halo  $p = 0.91$ , CreON FlpOFF smFPV5-CaV2.3  $p = 0.17$ , double knock-ins  $p = 0.59$ , 1-way ANOVA), but clearly diminished the number of incorrect knock-in cells ( $p = 0.041$ , 1-way ANOVA). Thus, while editing of *Gria1* is much slower compared to other genes, crosstalk can be largely reduced by delayed activation of Cre.

---

## CAKE enables dual-color single-molecule localization microscopy of endogenous synaptic proteins

Mapping the localization of endogenous synaptic proteins is crucial for our understanding of the brain (Choquet et al, 2021). In particular, deciphering which proteins regulate AMPA receptor nanoscale clustering in glutamatergic synapses will be pivotal in understanding synaptic transmission. Interestingly, AMPA receptors have been shown to be concentrated in subsynaptic PSD95 nanodomains (Nair et al, 2013; MacGillavry et al, 2013). Here, we used CAKE to uncover the nanoscale co-organization of endogenously tagged PSD95 and the AMPA receptor subunit GluA1 at glutamatergic synapses with dual-color single-molecule localization microscopy (SMLM).

Mapping the localization of endogenous synaptic proteins is crucial for our understanding of the brain (Choquet et al, 2021). In particular, deciphering which proteins regulate AMPA receptor nanoscale clustering in glutamatergic synapses will be pivotal in understanding synaptic transmission. Interestingly, AMPA receptors have been shown to be concentrated in subsynaptic PSD95 nanodomains (Nair et al, 2013; MacGillavry et al, 2013). Here, we used CAKE to uncover the nanoscale co-organization of endogenously tagged PSD95 and the AMPA receptor subunit GluA1 at glutamatergic synapses with dual-color single-molecule localization microscopy (SMLM).

As expected, endogenously tagged PSD95 and GluA1 co-localized at synapses (Fig. 6A). Using custom local density-based cluster analysis (based on Chen et al., 2020 and MacGillavry et al., 2013), we identified nanodomains of both GluA1 and PSD95 within individual synapses (Fig. 6B). Synapses contained on average more PSD95 nanodomains, but larger GluA1 nanodomains (Fig. 6-1A-B, nanodomain number  $p = 2.0 \times 10^{-4}$ , nanodomain diameter  $p = 6.4 \times 10^{-8}$ , unpaired t-test). These GluA1 nanodomains occurred on average only 14 nm closer to the center of the postsynaptic density (PSD) (Fig. 6C,  $p = 5.2 \times 10^{-8}$ , unpaired t-test), and the distance between PSD95 and GluA1 nanodomains only slightly increased with larger PSDs (Fig. 6D,  $p = 0.0002$ ,  $R^2 = 0.021$ , model linear regression). This suggests that PSD95 and GluA1 have similar synaptic topologies across synapse sizes. To further assess the co-organization of PSD95 and GluA1, we used a local density-based colocalization index (Fig. 6E and Fig. 6-17C; see Materials and Methods for details). Individual synapses had highly variable degrees of co-localization of PSD95 and GluA1 (Fig. 6-1C). In addition, the co-localization of PSD95 and GluA1 was correlated with PSD size (Fig. 6F,  $p = 1.0 \times 10^{-15}$ ,  $R^2 = 0.19$ ), suggesting that stronger synapses have a tighter association between GluA1 and PSD95. Lastly, we observed that co-localization between GluA1 and PSD95 was higher inside nanodomains compared to the rest of the PSD (Fig. 6G, PSD95  $p = 6.1 \times 10^{-6}$ , GluA1  $p = 1.6 \times 10^{-7}$ , one-sample t-test), confirming previous observations (Nair et al, 2013; MacGillavry et al, 2013). In summary, CAKE allowed us to reveal the tight nanoscale co-organization of endogenous PSD95 and AMPA receptors, which correlated with synapse size.

## Acute immobilization of endogenous synaptic AMPA receptors using inducible heterodimerization

Labeling of two endogenous proteins simultaneously in single neurons is a powerful means to measure and modulate their (functional) co-localization, but experiments are often hampered by overexpression artifacts. For example, the amount of PSD95 as well as AMPA receptors determine synaptic strength, and overexpression of these synaptic components can result in altered synaptic function (Schnell et al, 2002; El-Husseini et al, 2000). Interestingly, precise control of lateral diffusion and synaptic exchange of AMPA receptors is important for both basal transmission and synaptic plasticity (Groc & Choquet, 2020). Thus, studying the

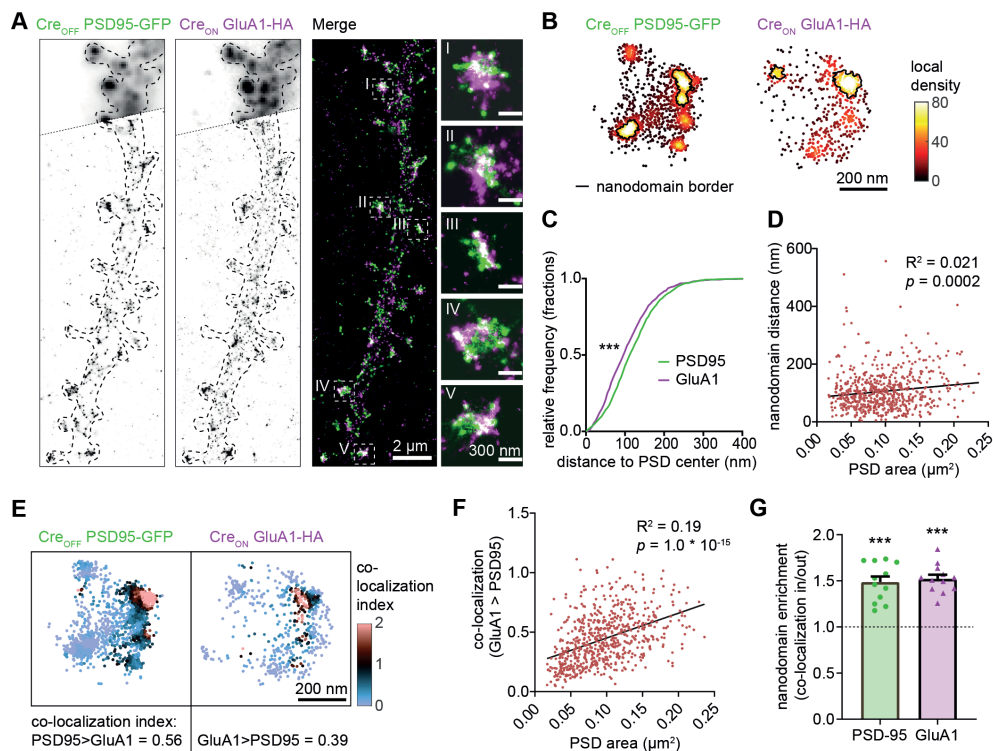


**Figure 6. Dual-color SMLM reveals nanoscale co-organization of endogenous PSD95 and GluA1**

(A) SMLM reconstruction of PSD95-GFP and GluA1-HA. Top part of the two channels shows widefield image of the same dendrite. Pixel size of reconstruction:  $12 \times 12$  nm. (B) Example synapse showing the local density values of PSD95 and GluA1 localizations. Nanodomains are outlined with a black line. (C) Nanodomain topology of PSD95 and GluA1 nanodomains. Cumulative distributions of the distance between nanodomain and PSD center for both PSD95 (green) and GluA1 (magenta). GluA1 nanodomains reside on average 14 nm closer to the PSD center. \*\*\*  $p = 5.2 \times 10^{-8}$ , Mann-Whitney test. 1285 nanodomains were analyzed for PSD95 and 774 nanodomains were analyzed for GluA1.  $n = 12$  neurons,  $N = 4$  independent cultures. (D) Distance between PSD95 and GluA1 nanodomains correlates weakly with PSD size. PSD size is based on the cluster of PSD95 localizations inside the synapse (see Materials & Methods).  $R^2 = 0.021$ ,  $p = 0.0002$ , model linear regression (black line). 656 synapses were analyzed.  $n = 12$  neurons,  $N = 4$  independent cultures. (E) Example synapse showing the co-localization index of PSD95 and GluA1 localizations. The average co-localization index of this synapse is indicated below the graph. (F) The co-localization of GluA1 with PSD95 localizations correlates with PSD size.  $R^2 = 0.192$ ,  $p = 1.0 \times 10^{-15}$ , model linear regression (black line). 656 synapses were analyzed.  $n = 12$  neurons,  $N = 5$  independent cultures. (G) PSD95 and GluA1 are both enriched in nanodomains of the other channel. Relative co-localization of PSD95 and GluA1 inside versus outside nanodomains is plotted. Dotted line represents null hypothesis (no nanodomain enrichment). PSD95 \*\*\*  $p = 6.1 \times 10^{-6}$ , GluA1 \*\*\*  $p = 1.6 \times 10^{-7}$ , one sample t-test.

trafficking and anchoring of AMPA receptors requires methods that accurately modulate the localization of endogenous proteins in living neurons. Here, we used CAKE to label AMPA receptors and PSD95 with inducible dimerization modules to acutely manipulate AMPA receptor anchoring at the synapse. More specifically, we generated C-terminal CAKE knock-in constructs to label GluA1 and PSD95 with the rapalog-inducible dimerization domains FRB and FKBP respectively (Fig. 7A; Kapitein et al., 2010). Addition of rapalog would then anchor AMPA receptors to PSD95 proteins at the synapse, thus reducing receptor exchange between the PSD and the extrasynaptic membrane (Fig. 7B).

We performed live-cell spinning disk imaging experiments to measure the fluorescence recovery after photobleaching (FRAP) at synapses to quantify GluA1 turnover under basal conditions and after the addition of rapalog (Fig. 7C-D). Under basal conditions, the fluorescence recovery of GluA1 receptors was  $0.31 \pm 0.04$  (Fig. 7E-F), which is consistent with previous studies (Chen et al., 2021; Fang et al., 2021). We incubated neurons with rapalog for 20 minutes, and measured FRAP dynamics on a different dendrite of the same neuron. Rapalog induced a strong decrease in fluorescence recovery ( $0.20 \pm 0.04$ ) of GluA1, indicating successful anchoring of AMPA receptors to PSD95 (Fig. 7E-F,  $p = 0.018$ , paired t-test). Importantly, we did not observe a decrease of GluA1 turnover in neurons that were not treated with rapalog (Fig. 7-1,  $p = 0.86$ , paired t-test). We found no significant change in the enrichment of GluA1 at the synapse after rapalog (Fig. 7G,  $p = 0.21$ , paired t-test). Together, these results show that CAKE allows for labeling and rapidly inducible dimerization of endogenous proteins in living neurons.

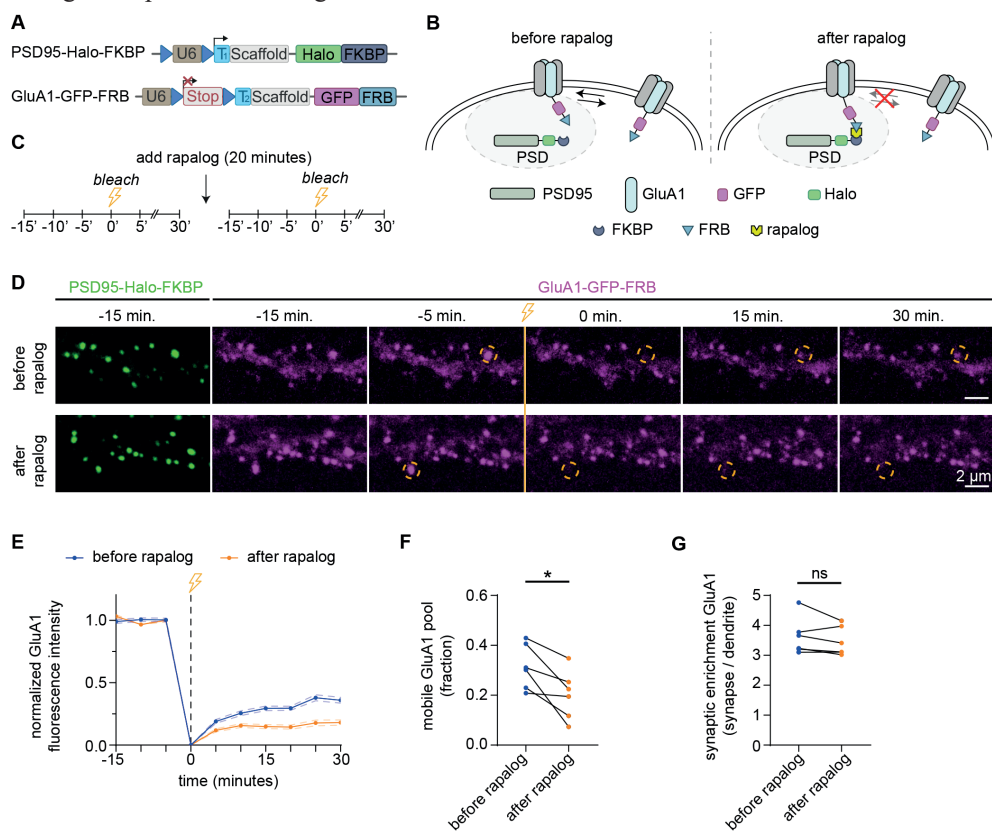


**Figure 7. Live-cell modulation of endogenous AMPA receptor anchoring using CAKE**

(A) Overview of DNA constructs used. (B) Graphical overview of synaptic anchoring of AMPA receptors using rapalog. FRB (fused to GluA1), binds to FKBP (fused to PSD95), preventing exchange of synaptic receptors. (C) Imaging protocol. Neurons are imaged every 5 minutes using spinning disk confocal microscopy. FRAP is performed twice, before and after the incubation with rapalog for 20 minutes. (D) Example FRAP acquisition before and after incubation with rapalog. GluA1-GFP-FRB in magenta and PSD95-Halo-FKBP in green. Spines indicated with orange circle are bleached just before timepoint 0 minutes. (E) FRAP curves of spines bleached before and after incubation with rapalog. Data is normalized to the average intensity before bleaching. 63 spines before rapalog and 66 spines after rapalog were bleached.  $n = 6$  cells,  $N = 5$  independent cultures. (F) Average recovery of fluorescence

**Figure 7 (Continued)** per neuron, averaged over the last 4 frames, reflecting the mobile pool of receptors. After rapalog, the mobile pool of receptors is less than before rapalog. \*  $p = 0.018$ , paired t-test.  $n = 6$  cells,  $N = 5$  independent cultures. (G) Synaptic enrichment of GluA1-GFP-FRB at synapses before and after rapalog incubation are similar. Synaptic enrichment is the relative fluorescence intensity at the synapse compared to the dendrite.  $p = 0.21$ , paired t-test.  $n = 6$  cells,  $N = 5$  independent cultures.

## DISCUSSION

Accurate detection and manipulation of endogenous proteins is essential to understand cell biological processes, which motivated laboratories across cell biology to develop highly efficient CRISPR genome editing methods for endogenous epitope tagging (Schmid-Burgk et al, 2016; Nakade et al, 2014; Suzuki et al, 2016; Nishiyama et al, 2017; Auer et al, 2014; Artegiani et al, 2020; Danner et al, 2021; Lackner et al, 2015). Multiplex editing using NHEJ-based CRISPR/Cas9 methods remains limited due to the high degree of crosstalk that occurs between two knock-in loci (Gao et al, 2019; Willems et al, 2020). In the current study we present CAKE, a mechanism to diminish crosstalk between NHEJ-based CRISPR/Cas9 knock-ins using sequential activation of gRNA expression. We demonstrate that this mechanism strongly reduces crosstalk between knock-in loci, and results in dual knock-ins for a wide variety of genes. Finally, we showed that CAKE can be directly applied to reveal new biological insights. CAKE allowed us to perform two-color super-resolution microscopy and acute manipulation of the dynamics of endogenous proteins in neurons, together revealing new insights in the nanoscale organization of synaptic proteins.

### Factors that influence knock-in efficacy

The CAKE mechanism presented here creates a mosaic of CreON and CreOFF knock-ins, and the number of double knock-in cells depends on the efficacy of each knock-in vector. Therefore, to obtain a high number of double knock-in cells, the efficacy of both the CreON and CreOFF knock-in vector must be optimized. We identified three parameters that regulate the efficacy for single- and double knock-ins in neurons. Firstly, the efficacy of gRNAs varies widely, and even gRNAs that target sequences a few base pairs apart in the same locus can have dramatically different knock-in rates (Willems et al, 2020; Fang et al, 2021; Zhong et al, 2021; Danner et al, 2021). Thus, the efficacy of each individual gRNA must be optimized in order to increase the chance of successful multiplex labeling in neurons. gRNA performance is dependent on many factors, including the rate of DNA cleavage and repair (Liu et al, 2020; Rose et al, 2017; Park et al, 2021) and the propensity of the target locus for indel mutations (Liu et al, 2020; Rose et al, 2017; Shen et al, 2018). While some of these parameters can be predicted computationally (Park et al, 2021; Shen et al, 2018; Doench et al, 2014), the efficacy of each individual gRNA should be verified experimentally. We performed most experiments with gRNAs that we and others previously found to yield a high number of single knock-ins (Suzuki et al, 2016; Willems et al, 2020).

Secondly, we found knock-in efficacy to be highly sensitive to knock-in vector amount. For multiple knock-ins, we found that reducing the amount of knock-in vector increased the number of knock-in positive cells, with the optimum for  $\beta 3$ -tubulin as little as 3.9 fmol vector DNA per coverslip. We propose that this inverse relationship is due to competition between donor DNA molecules for integration. In line with these observations, knock-in vectors with multiple donors reduced the number of  $\beta 3$ -tubulin-GFP positive cells. Donor competition could also explain why we consistently needed more knock-in vector for the CreON knock-in, as remaining donor from the CreOFF vector could compete for integration in the target locus after Cre activation. Importantly, for reasons incompletely understood, the optimum



---

vector amount differs considerably between knock-in constructs. A striking example in this respect is GluA1, which requires a 10-to-50-fold high vector load to reach the maximum number of knock-in cells. We also observed that onset of GluA1 knock-in expression is much slower compared to other genes, and thus there may be a relationship between the editing rate of the targeted locus, and the amount of donor DNA required for successful integration.

Thirdly, the timing of Cre expression and activation may influence the number of incorrect knock-in cells. For CreOFF GluA1 / CreON CaV2.3 we found that delaying the activation of ERT2-Cre-ERT2 by 7 days diminished crosstalk between the knock-ins. This is in line with our observation that GluA1 knock-ins are completed at a much slower rate than other genes tested here. We did not observe an effect of infection day for lenti-Cre with CreOFF  $\beta$ -tubulin and Cre-ON  $\beta$ -actin. However, the slow onset of expression from lentiviral vectors (in the order of days; Hioki et al., 2007) makes lentivirus a weak method to observe an effect Cre timing, in particular compared to the rapid activation of ERT2-Cre-ERT2 (Matsuda & Cepko, 2007). Additionally, donor integration in *Tubb3* appears to be relatively fast, which limits the window for crosstalk to occur.

### **Comparison of CAKE with other CRISPR/Cas9 strategies**

Previous studies for NHEJ-based multiplex knock-ins had restrictions on donor DNA design and the target loci that could be combined (e.g. N-terminal or C-terminal knock-ins), and these methods could inadvertently reduce protein expression from the targeted allele (Gao et al., 2019; Willems et al., 2020). The CAKE knock-in strategy presented here lifts these limitations, and can be used with any locus and donor DNA design. Importantly, because CAKE only relies on sequential gRNA expression, it is expected to be compatible with any combination of NHEJ-based knock-in modalities.

Multiple CRISPR/Cas9 modalities have been developed to generate knock-ins in neuronal preparations, predominantly based on NHEJ. The first generation of tools, including HITI (Suzuki et al., 2016), ORANGE (Willems et al., 2020) and HiUGE (Gao et al., 2019) directly edit the coding sequence of genes to insert a fluorophore or epitope tag. This simplifies design and limits the number of cloning steps required, at the expense of potential indel mutations that disrupt the reading frame (Suzuki et al., 2016; Willems et al., 2020). HiUGE further simplifies design by using a universal donor DNA, but requires the expression of an extra gRNA to make the donor available for integration (Gao et al., 2019). All three methods leave a small scar of a few base pairs after knock-in completion. MMEJ-based techniques yield seamless knock-ins by using homology between the donor and target gene (Yao et al., 2017). This homology, however, is unlikely to have a major effect in preventing double knock-in crosstalk: because an MMEJ-donor is blunt ended, it can integrate in any DSB. Second generation NHEJ-based techniques are scarless and are relatively insensitive to indels, by replacing exons (TKIT, Fang et al., 2021) or introducing novel exons (CRISPIE, Zhong et al., 2021). While the cloning of CRISPIE knock-ins is more straightforward compared to TKIT, it may be challenging to find a suitable location for integrating a novel exon, without disrupting protein folding or function. Finally, the recently proposed PASTE strategy obtains single and multiplex knock-ins without creating DSBs, and might be applicable in neurons as well (Ioannidi et al., 2021).

### **Application of CAKE for labeling and manipulation of endogenous proteins**

CAKE opens possibilities to study localization, mobility and function of endogenous proteins at multiple levels. For instance, the nanoscale organization of synaptic proteins profoundly

influences information transfer at synapses (Rebola et al, 2019; Tang et al, 2016; MacGillavry et al, 2013; Nair et al, 2013), and CAKE may present an invaluable tool to decipher synapse organization using endogenous protein labeling under stringent conditions required for super resolution microscopy. Indeed, we were able to accurately determine the subsynaptic colocalization of GluA1 and PSD95, which scaled linearly with PSD size. This suggests that AMPAR confinement at PSD95 clusters is associated with synapse strength, since PSD size is correlated with synaptic weight (Holler et al, 2021). To study protein-protein interactions CAKE could also be applied in combination with Förster resonance energy transfer reporters, bimolecular fluorescence complementation (Tebo & Gautier, 2019), or proximity biotinylation assays (De Munter et al, 2017).

Our results also illustrate the potential of CAKE to manipulate the localization, mobility and functionality of endogenous proteins, for instance by recruiting or anchoring proteins and organelles in living cells using optogenetic or chemical dimerization modules. Trafficking and sub-cellular positioning of proteins is crucial for all cellular processes, and this unique combination of techniques allows manipulation of endogenous protein dynamics in cells. For example, directed positioning of receptors (Sinnen et al, 2017) or even entire organelles (Van Bergeijk et al, 2015) have previously been shown to influence synaptic strength and neuronal development respectively.

The method of Cre expression or activation can be tailored to experimental needs, and besides viral Cre delivery or ERT2-Cre-ERT2, users can consider for instance doxycycline-dependent Cre, TAT-Cre or a mouse line that expresses Cre. Regardless of the method, the timing of Cre activity should be carefully characterized, to prevent crosstalk between CreOFF and CreON knock-ins. The conditional activation of CRISPR/Cas9 knock-ins also opens new avenues for detailed analysis of endogenous proteins in individual cell types. By restricting Cre or Flp expression using cell-type specific promoters (Taniguchi et al, 2011; He et al, 2016), combined with CreON or FlpON, one could map out the spatiotemporal expression of proteins in a wide variety of cells at unprecedented precision.

Taken together, we created and validated a series of CRISPR tools for sequential genome editing to create multiplex knock-ins with NHEJ, and demonstrate the value of these tools for determining and manipulating protein distribution in neurons.

## MATERIALS AND METHODS

### Ethics statement

All experiments were approved by the Dutch Animal Experiments Committee (Dier Experimenten Commissie (DEC; AVD1080020173404), performed in line with institutional guidelines of Utrecht University, and conducted in agreement with Dutch law (Wet op de Dierproeven, 1996) and European regulations (Directive 2010/63/EU). Timed pregnant Wistar rats were obtained from Janvier Labs.

### Molecular cloning

Constructs were made using standard laboratory techniques. All CAKE knock-in backbones are numbered as pORANGE CAKE (pOCx); see Fig. 1-3A and Table 1 for a complete overview. For most pOCx vectors, variants with and without CAG SpCas9 were created. Design rationales of all new knock-ins are found in Table 3. All primer sequences are found in Table 4.

The CreON knock-in vector (pOC1, Addgene #183420) is based on pORANGE LOX from (Willems et al., 2020, Addgene #139651), where CAG HA-SpCas9 was removed with

---

XmaI and NotI and replaced with primers AJ19164 and AJ19165 using primer ligation.

To clone the CreOFF knock-in vector (pOC2, Addgene #183421), lox-U6-lox was created by PCR from pOC1 with primers AJ19169 and AJ20047, digested with PscI and Bsp1407I, and ligated into pOC1 that was digested with PscI and Bsp1407I as well.

The CreON FlpOFF knock-in vector (pOC3, Addgene #183423) was based on pOC1, where one Frt site was cloned into the gRNA scaffold (Chylinski et al, 2019) and one before the U6 promoter. PCR fragments were obtained with primers AJ20124 – AJ20126, AJ20127 – AJ20125 and AJ20120 - AJ20121 using pOC1 as template. pOC1 was digested with NheI and PscI, and all fragments were ligated using HiFi assembly (New England Biolabs, Ipswich, United Kingdom).

The FlpON knock-in vector (pOC4, Addgene #183424) was designed analogous to Chylinski et al., 2019. PCR fragments were created using primers AJ20120 - AJ20121 with pOC1 as template, and primers AJ20122 – AJ20116 and AJ20117 – AJ20121 with pORANGE empty (Addgene #131471, Willems et al., 2020) as template. pORANGE was digested with PscI and NheI, and all fragments were ligated with HiFi assembly.

The FlpOFF knock-in vector (pOC5, Addgene #183424) was designed similar as in Chylinski et al., 2019. PCR fragments were obtained with primers AJ21030 - AJ21031 with pOC3 as template, and AJ20122 and AJ21032 with pOC4 as template. pOC3 was digested with PscI and HindIII and fragments were ligated with HiFi assembly.

To obtain pORANGE  $\beta$ 3-tubulin-2xGFP (Addgene #183443), the donor DNA from pORANGE  $\beta$ 3-tubulin-GFP (Willems et al, 2020) was isolated using XmaI and XbaI, and ligated in the XbaI site of pORANGE  $\beta$ 3-tubulin-GFP. Subsequently, to create pORANGE  $\beta$ 3-tubulin with 3xGFP (Addgene #183444) or 4x-GFP (Addgene #183445), the pORANGE  $\beta$ 3-tubulin-2xGFP double donor DNA was isolated with XmaI and XbaI, and ligated in the XbaI site of pORANGE  $\beta$ 3-tubulin-GFP or pORANGE  $\beta$ 3-tubulin-2xGFP, respectively. Due to the repeated sequences, the orientation of the inserts could not be confirmed, but this should not affect performance of the knock-in.

pFUGW-NLS-Cre (Addgene #183425) was created using a PCR reaction for NLS-Cre with primers AJ20128 - AJ20129 using pFUGW-GFP-NLS-Cre (a gift from Pascal Kaeser, Harvard Medical School Boston MA; Kaeser et al., 2011) as template. The PCR product was digested with NheI and XbaI, and ligated in NheI and XbaI sites of pFUGW.

pFUGW-NLS-FlpO (Addgene #183448) was created using a PCR reaction for NLS-FlpO with primers AJ20130 - AJ20131 using pAAV hSynapsin FlpO (Addgene #60663), a gift from Massimo Scanzianis (Xue et al, 2014), as template. The PCR product was digested with NheI and XbaI, and ligated in NheI and XbaI sites of pFUGW.

pCAG ERT2-Cre-ERT2 (Addgene #183447) lox was created by digesting pCAG ERT2-Cre-ERT2 (Matsuda & Cepko, 2007) with EcoRI and NotI. Both resulting DNA fragments were mixed with primers AJ21053 and AJ21054, and ligated with HiFi assembly.

All knock-ins were based on ORANGE (Suzuki et al, 2016; Willems et al, 2020) and cloned in pOCx backbones as described in Figure 1-3B. For a complete description of knock-in design and cloning, see Extended Data 1-4. gRNA target sequences can be found in Table 2. Fluorophores and epitope tags in the donor DNAs were exchanged using universal BmtI and AfeI restriction sites that are present in linker sequences surrounding the fluorophore. smFPs were obtained from Addgene #59759 (HA) and #59758 (V5), a gift from Loren Looger (Viswanathan et al, 2015).

For Rapalog-inducible assays, FKBP (primer JW381 ad JW382) and FRB (primer JW375 and JW376) were amplified using PCR (both a gift from Lukas Kapitein; Kapitein, Schlager,

et al., 2010). These fragments were cloned into the AfeI site of pOC2 Dlg4-Halo (Addgene #183449) and pOC1 Gria1-GFP (Addgene #183430), respectively, using HiFi assembly.

The design of pOC2 CRISPIE Halo-Homer1 (Addgene #183446) was adapted from the strategy of Zhong et al., 2021 and described in Figure S4. The donor DNA was ordered as a gBlock from Addgene and PCR amplified using WD0116 and WD0117. Donor consists of Halo flanked by the splicing acceptor and donor of exon 8 of Septin 3 (Fig. 2-1). Splicing acceptor and donor include 100 bp intronic and 10 bp exonic sequences. Target sequences were selected using CRISPOR and the BROAD institute sgRNA designer (Concordet & Hacussler, 2018; Doench et al, 2016).

### Antibodies and reagents

The following primary antibodies were used in this study: mouse anti-GFP 1:2000 dilution (Thermo Fisher, RRID: AB\_221568), rabbit anti-GFP 1:2000 (MBL, RRID: AB\_591819) rabbit anti-Halo 1:1000 (Promega, RRID: AB\_713650), rat anti-HA 1:500 (Sigma-Aldrich, RRID: AB\_390919) mouse anti V5 1:1000 (Invitrogen, RRID: AB\_2556564). Alexa488-, Alexa568-, and Alexa647-conjugated secondary antibodies were used at 1:500 dilution, obtained from Life Technologies. CF568-conjugated secondary antibodies were used at 1:600 dilution, obtained from Sigma-Aldrich. Molecular biology reagents were obtained from Thermo Fisher. GFP minicircle for  $\beta$ 3-tubulin were custom made at System Biosciences (Palo Alto, CA, USA), produced from pTubb3 MC (Addgene #87112, Suzuki et al., 2016). 4OH-tamoxifen was acquired from Sigma-Aldrich (cat. no H7904), and kept at 20 mM in ethanol in single use aliquots at -20°C. For Halo labeling, Halo Ligands JF549 (Promega, GA1110) and JF646 (Promega, GA1121) were used (Grimm et al, 2015). Both dyes were dissolved using DMSO to 0.2 mM upon arrival. Working concentration was 0.2  $\mu$ M (1:1000). For FKBP-FRB dimerization, we used Rapalog (TaKaRa, Shiga, Japan, #635057).

### Dissociated neuronal cultures

Dissociated hippocampal cultures were prepared from embryonic day 18 (E18) rat brains of both genders (Kapitein et al, 2010b). Dissociated neurons were plated on  $\emptyset$ 18mm coverslips coated with poly-L-lysine (37.5  $\mu$ g/ml, Sigma-Aldrich) and laminin (1.25  $\mu$ g/ml, Roche Diagnostics, Rotkreuz, Switzerland) at a density of 100,000 neurons per well, in Neurobasal medium (NB), supplemented with 1% penicillin and streptomycin (pen/strep), 2% B27, and 0.5 mM L-glutamine (all from Gibco; (NB-complete medium) at 37°C in 5% CO<sub>2</sub>. From DIV 1 onwards, medium was refreshed every 7 days by replacing half of the medium with Brainphys neuronal medium supplemented with 2% NeuroCult SM1 neuronal supplement (Stem cell technologies, Köln, Germany) and 1% pen/strep (BP-complete medium).

### Transfection of dissociated hippocampal neurons

Neurons were transfected at DIV 1-3 using Lipofectamine 2000 (Invitrogen). For one  $\emptyset$ 18-mm coverslip seeded with 100,000 neurons, up to 2  $\mu$ g DNA was used, which typically results in a few hundred to one thousand transfected cells per coverslip. DNA concentrations were determined using Nanodrop. For CAKE double knock-ins, the mixture contained 3.9 – 197 fmol (10-500 ng) CreOFF knock-in, 3.6 – 178 fmol (10-500 ng) CreON knock-in, and 171 (500 ng) pCAG FLAG-SpCas9 expression. Experiments with inducible Cre used 2-20 fmol (10-100 ng) pCAG ERT2-Cre-ERT2 (Addgene #3777, Matsuda and Cepko, 2007) per coverslip. DNA was mixed with 3.3  $\mu$ L Lipofectamine in 200  $\mu$ L NB medium and incubated for 30 minutes at room temperature (RT). Next, 500  $\mu$ L conditioned medium was transferred

---

to a new culture plate and replaced by 300  $\mu$ L NB supplemented with 0.5 mM L-glutamine. The DNA/Lipofectamine mix was added to the culture and incubated at 37°C and 5% CO<sub>2</sub>. After 90–120 minutes, coverslips were transferred to the new culture plate with conditioned medium and 500  $\mu$ L new BP-complete and kept at 37°C and 5% CO<sub>2</sub> for between 1–20 days, depending on the experiment.

### **Immunocytochemistry**

Hippocampal neurons were fixed at DIV 14–23 in 80 mM PIPES, 1 mM EGTA, 2 mM MgCl pH 6.8 and 4% paraformaldehyde (Electron Microscopy Sciences, Hatfield, PA, USA), for 5–10 minutes at 37°C and washed three times in PBS containing 0.1 M glycine (PBS/Gly). Neurons were blocked and permeabilized in blocking buffer (10% [v/v] normal goat serum [NGS] (Abcam, Cambridge, United Kingdom) in PBS/Gly with 0.1% [v/v] Triton X100) for 1 hour at 37°C. Next, coverslips were incubated with primary antibodies diluted in incubation buffer (5% [v/v] NGS in PBS/Gly with 0.1% [v/v] Triton X100) for 2 hrs at RT or overnight at 4°C, depending on the antibodies used. Coverslips were washed three times with PBS/Gly and incubated with secondary antibodies diluted 1:500 in incubation buffer for 1 hour at RT. Coverslips were washed three times in PBS/Gly, dipped in milliQ water (MQ), and mounted in Mowiol mounting medium (Sigma-Aldrich).

### **Lentivirus production**

For lentivirus production, HEK293T cells were maintained at a high growth rate in DMEM (Lonza, Basel, Switzerland) supplemented with 10% fetal calf serum (Corning) and 1% pen/strep. 1 day after plating on 10 cm dishes, cells at ~70% confluency were transfected using Polyethylenimine (PEI, Polysciences, Warrington, PA, USA) with second-generation lentiviral packaging vectors (psPAX2 and 2MD2.G) and pFUGW-NLS-FlpO, pFUGW-NLS-Cre or pFUGW-GFP-NLS-Cre at a 1:1:1 molar ratio. At 6 hours after transfection, cells were washed once with PBS, and medium was replaced with 10 mL DMEM containing 1% pen/strep. At 48 hours after transfection, the supernatant was harvested, centrifuged 5 min at 700g to remove cell debris, and stored in aliquots at -80°C until use. Cultured hippocampal neurons were infected at DIV 3–9 with 20  $\mu$ L virus added per well, unless indicated otherwise.

### **Quantification of knock-in efficacy**

To determine the efficacy of knock-ins, samples were fixed at DIV 14, and stained with primary and secondary antibodies as described above. Coverslips were examined with epifluorescence on a Nikon Eclipse 80i upright microscope Plan Fluor 20x air (N.A. 0.75) or Plan Fluor 40x oil (N.A. 1.30) objective, CoolLED pE-300white illumination and Chroma ET-GFP/mCherry (59022) filter set. Coverslips were scanned top to bottom and fluorescent cells were scored manually based on staining pattern in one of four categories. For instance, for CreOFF  $\beta$ 3-tubulin GFP / CreON Halo- $\beta$ -actin, the categories were 1) GFP correct (GFP staining pattern corresponds with  $\beta$ 3-tubulin expression); 2) Halo correct (Halo staining pattern corresponds with  $\beta$ -actin pattern); 3) double correct (Both GFP and Halo have the correct staining pattern in the same cell); 4) incorrect (GFP staining pattern corresponds with  $\beta$ -actin and/or Halo corresponds with  $\beta$ 3-tubulin). Results were obtained from 3 independent cultures with 1 coverslip per culture, unless stated otherwise.

### **Confocal microscopy**

Confocal images were acquired with a Zeiss LSM 700, using a EC Plan-Neofluar 40x oil

(N.A.1.30) or Plan-Apochromat 63x oil (N.A. 1.40) objective and 488 nm, 555 nm and 633 nm laser excitation lines. Images were acquired as z-stacks containing planes at 0.5  $\mu\text{m}$  interval, with 0.1  $\mu\text{m}$  pixel size and 2x pixel averaging. All images are displayed as maximum intensity projections. Images in Figure S2A-B were acquired as tile scans, and stitched using Zeiss Zen Black 2.3 SP1 software.

### Spinning disc microscopy with FRAP

Neurons were transfected at DIV 2 as described above with pOC2 Dlg4-Halo-FKBP (33 fmol), pOC1 Gria1-GFP-FRB (33 fmol), pCAG ERT2-Cre-ERT2 (2 fmol) and pCAG FLAG-Cas9 (90 fmol). At DIV 7, 4OH-tamoxifen (100 nM) was added to the neurons. At DIV 21, just before imaging, neurons were live-labeled with Halo-ligand JF549 (diluted 1:1000 in conditioned medium) for 15 minutes and washed in conditioned medium for 10 minutes before mounting.

Imaging was performed on a spinning disk confocal system (CSU-X1-A1; Yokogawa, Musashino, Japan) mounted on a Nikon Eclipse Ti microscope (Nikon, Tokyo, Japan) with Plan Apo VC 100x 1.40 NA oil objective (Nikon) with excitation from Cobolt Calypso (491 nm) and Cobolt Jive (561 nm), and emission filters (Chroma, Bellows Falls, VT, USA). The microscope was equipped with a motorized XYZ stage (ASI; MS-2000), Perfect Focus System (Nikon), Prime BSI sCMOS camera (Photometrics, Tucson, AZ, USA), and was controlled by MetaMorph software (Molecular Devices, San Jose, CA, USA). Neurons were mounted in a Ludin-chamber (Life Imaging Services) with 450  $\mu\text{L}$  extracellular buffer (in mM: 140 NaCl, 3 KCl, 10 HEPES, 2.7 CaCl<sub>2</sub>, 2 MgCl<sub>2</sub>, and 10 D-glucose. pH 7.35) and maintained in a closed incubation chamber (Tokai hit: INUBG2E-ZILCS) at 37 °C.

Double knock-in neurons were imaged for 15 minutes, acquiring a Z-stack of 3 planes (0.5  $\mu\text{m}$  interval) every 5 minutes. Hereafter, pre-selected ROIs (1.3  $\mu\text{m}$  in diameter) on spines were bleached using the ILas2 system (Roper Scientific, Sarasota, FL, USA). After bleaching, the neurons were imaged every 5 minutes for a total of 30 minutes. Following the first acquisition, cells were incubated in 1  $\mu\text{M}$  rapalog for 20 minutes. Next, a different part of the same neuron was selected for a second (after rapalog) round of FRAP imaging. As a control, CreON GluA1-GFP-FRB positive neurons were imaged following the same protocol, but without the addition of rapalog.

Acquisitions were corrected for drift and a maximum projection of the Z-stack was used for analysis. For each ROI and timepoint, mean intensities were measured and corrected for background and bleaching. Mean intensities were normalized to 1 using the averaged intensities of the frames before bleaching, and normalized to 0 based on the intensity from the first frame after bleaching. The mobile fraction of GluA1-GFP-FRB was calculated by averaging the normalized intensity of the last 4 frames for each ROI. Analysis was performed using FIJI and Excel.

Synapse enrichment before and after rapalog was calculated as the ratio between synapse and dendritic shaft intensity using 10 ROIs (250 nm diameter) each. For this analysis, we used the images from timepoint -15 minutes.

### Dual-color SMLM

Neuron were transfected at DIV 1 as described above with pOC2 PSD95-GFP (7.9 fmol), pOC1 GluA1-HA (44 fmol), pCAG ERT2-Cre-ERT2 (2 fmol) and pCAG FLAG-Cas9 (90 fmol). 100 nM 4OH-tamoxifen was added at DIV 7. At DIV 23, cultures were fixed and stained with primary and secondary antibodies as described above. PSD95-GFP and GluA1-

HA were labeled with Alexa647 and CF568-conjugated secondary antibodies, respectively. SMLM was performed on the Nanoimager S from ONI (Oxford Nanoimaging Ltd., Oxford, United Kingdom), fitted with a 100x 1.4NA oil-immersion objective, four laser lines (405 nm, 561 nm and 640 nm), an XYZ closed-loop piezo stage and a sCMOS camera (ORCA Flash 4, Hamamatsu). Integrated filters are used to split far-red emission onto the right side of the camera and blue-green-red emission spectra on the left side, enabling simultaneous dual-color imaging. The imaging chamber was temperature-controlled at 30°C to prevent fluctuations in temperature during the time course of an experiment that might affect the alignment of the channels. Channel alignment was performed before each imaging session using 100-nm TetraSpeck beads (T-7279, Invitrogen) and the ONI software aiming for an alignment error of SD < 7 nm as measured from 2000 points total across a maximum of 20 fields of view. Imaging was performed in near-TIRF using a motorized mirror. During acquisition, neurons were kept in a STORM buffer (pH 8.0) containing 50 mM Tris, 10 mM NaCl, 10% w/v D-glucose, 5 mM MEA, 700 µg/ml glucose oxidase, and 40 µg/ml catalase. For each double knock-in neuron, 20,000 frames were acquired at 50 Hz. NimOS software from ONI was used for detection of single molecule localization events. Resulting localization tables were drift-corrected using Detection of Molecules (DoM) plugin v.1.2.1 for ImageJ ([https://github.com/ekatrukha/DoM\\_Utrecht](https://github.com/ekatrukha/DoM_Utrecht)). dSTORM reconstruction was made using DoM with pixel size of 12 x 12 nm (Fig. 6A). Analysis was continued in MATLAB (2021a).

Localizations were filtered out if localization precision was > 30 nm for GluA1 and > 25 nm for PSD95, or photon count was < 300 or > 30,000 photons. Consecutive localizations in a radius of 60 nm were removed. If consecutive localizations persisted for more than 10 frames, the initial localization was also removed. ROIs outlining the synapse were defined based on the full width half maximum (FWHM) using a widefield image of PSD95-GFP taken before dSTORM acquisition. Synapses were only analyzed further if they contained > 800 localizations for PSD95 and > 400 localizations for GluA1, or if they were > 0.02 µm<sup>2</sup> or < 0.3 µm<sup>2</sup> in size. For each localization in a given synapse, the local density was calculated as the number of localizations within a radius of 5 \* the mean nearest neighbor distance (MacGillavry et al, 2013). Localizations were deemed part of a nanodomain if its local density was > 40. Nanodomains were isolated using the MATLAB functions *linkage()* and *cluster()*. Subsequently, nanodomains were subclustered if they contained multiple local density peaks that were > 80% of the maximum local density, further than 80 nm apart and separated by a local minimum of < 30% of the maximum local density. The nanodomain boundary was constructed using the Voronoi diagrams circumventing the localizations. Nanodomains with < 5% of the localizations in a synapse or a diameter of < 30 nm were excluded. The center of the PSD was calculated using the function *centroid()* and based on the PSD95 cluster inside the synapse, identified using DBSCAN (Ester et al, 1996). Nanodomain distance between PSD95 and GluA1 was calculated for each nanodomain as the distance to its closest nanodomain in the other channel. Co-localization analysis of PSD95 and GluA1 was performed as described in (Willems and MacGillavry, 2022) As a first step in determining the co-localization between two clusters, the local density is determined for each localization in both channels. The mean nearest neighbor distance (MNND) is determined within the PSD using the MATLAB function *knnsearch*. Next, for each localization, the local density (*LD*) is defined as the number of localizations within a radius defined by the effective resolution making use of the MATLAB function *rangesearch*. For each channel, the *LD* values are averaged together to obtain  $LD_A$  and  $LD_B$ . Effective resolution was calculated as (Gould et al, 2009):

$$effective\ resolution = \sqrt{MNND^2 + \varepsilon^2}$$

where  $\varepsilon$  is the localization error.

The co-localization index is determined as the number of localizations of channel B ( $N$ ) within a radius ( $d$ ) around each localization in channel A ( $A_i$ ) normalized to the mean LD of the localizations in channel B ( $(LD)_B$ ), with  $d$  being the effective resolution of the localizations in channel B:

$$CI_i^A(d) = \frac{N_{A_i}^B(d)}{LD_B}$$

Thus, for channel B, the co-localization index values are calculated as:

$$CI_i^B(d) = \frac{N_{B_i}^A(d)}{LD_A}$$

The co-localization indices calculated for each localization individually are used to plot a co-localization map and averaged to obtain a mean co-localization index per synapse for both channels (Fig. 6E).

### Data representation and statistics

All experiment were performed in at least 3 independent cultures. Data is shown as average values, error bars represent standard error of the mean (SEM). When comparing two experimental groups, an unpaired t-test was used, except for the FRAP analysis, which was analyzed with a paired t-test. If groups were not normally distributed, the non-parametric Mann-Whitney test was used. Cell counting experiments were analyzed with a 1-way or 2-way ANOVA, and for results with  $p < 0.05$ , a post hoc test with Tukey-Kramer correction was performed to test for differences between individual groups. Table 5 provides an overview of all statistical tests used per Figure.

### ACKNOWLEDGEMENTS

This work was supported by the European Research Council (ERC-StG 716011 to HDM), NWO (OCENW.KLEIN.163 to HDM) and a NARSAD Young Investigator Grant from the Brain & Behavior Research Foundation (grant number 29452) to AdJ. We thank Manon Westra for contribution to single molecule localization scripts, and Martin Harterink for critically reading the manuscript.

### AUTHOR CONTRIBUTIONS

Conceptualization: AdJ, Methodology: AdJ, Software: WD, JW, Formal analysis: WD, JW, AdJ, Investigation: WD, JW, AdJ, Writing – original draft preparation: AdJ, Writing – Review & editing: WD, JW, HDM, Visualization: WD, JW, AdJ, Supervision: AdJ, HDM, Funding Acquisition: AdJ, HDM

### COMPETING INTERESTS

The authors declare no competing interests.

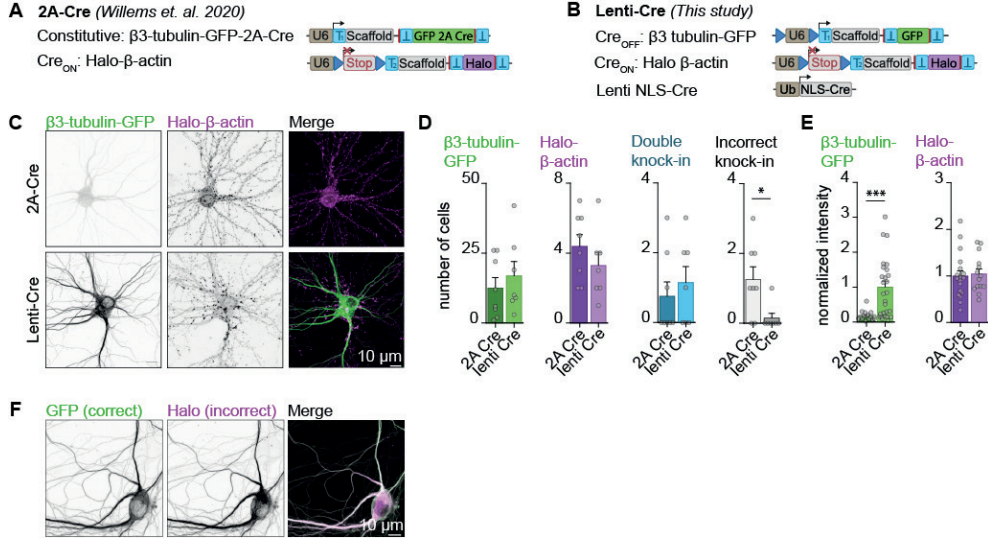


## REFERENCES

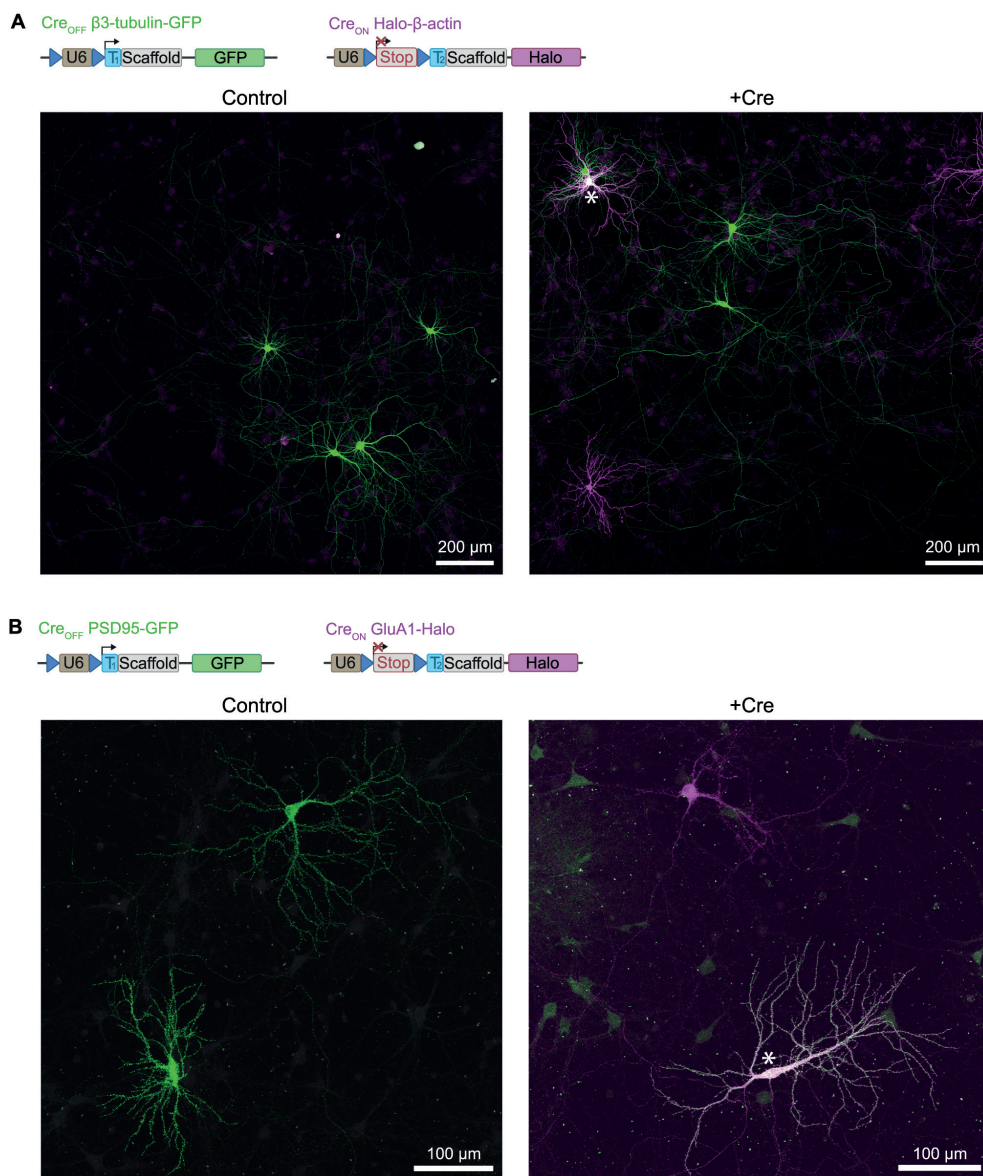
- Artegiani B, Hendriks D, Beumer J, Kok R, Zheng X, Joore I, Chuva de Sousa Lopes S, van Zon J, Tans S, Clevers H (2020) Fast and efficient generation of knock-in human organoids using homology-independent CRISPR-Cas9 precision genome editing. *Nat Cell Biol* 22:321–331.
- Auer TO, Duroure K, De Cian A, Concordet JP, Del Bene F (2014) Highly efficient CRISPR/Cas9-mediated knock-in in zebrafish by homology-independent DNA repair. *Genome Res* 24:142–153.
- Ballesteros-Merino C, Lin M, Wu WW, Ferrandiz-Huertas C, Cabañero MJ, Watanabe M, Fukazawa Y, Shigemoto R, Maylie J, Adelman JP, Luján R (2012) Developmental profile of SK2 channel expression and function in CA1 neurons. *Hippocampus* 22:1467–1480.
- Baumgartner M, Weiss A, Fritzius T, Heinrich J, Moelling K (2009) The PDZ protein MPP2 interacts with c-Src in epithelial cells. *Exp Cell Res* 315:2888–2898.
- Chen H, Roth RH, Lopez-Ortega E, Tan HL, Huganir RL (2021) AMPA Receptors Exist in Tunable Mobile and Immobile Synaptic Fractions In Vivo. *eNeuro* 8:1–8.
- Chen J-H, Blanpied TA, Tang A-H (2020) Quantification of Trans-synaptic Protein Alignment: A Data Analysis Case for Single-molecule Localization Microscopy. *Methods* 174:72.
- Choquet D, Sainlos M, Sibarita JB (2021) Advanced imaging and labelling methods to decipher brain cell organization and function. *Nat Rev Neurosci* 22:237–255.
- Chylinski K, Hubmann M, Hanna RE, Yanchus C, Michlits G, Uijttewaal ECH, Doench J, Schramek D, Elling U (2019) CRISPR-Switch regulates sgRNA activity by Cre recombination for sequential editing of two loci. *Nat Commun* 10:5454.
- Concordet J-P, Haeussler M (2018) CRISPOR: intuitive guide selection for CRISPR/Cas9 genome editing experiments and screens. *Nucleic Acids Res* 46:W242–W245.
- Danner E, Lebedin M, de la Rosa K, Kühn R (2021) A homology independent sequence replacement strategy in human cells using a CRISPR nuclease. *Open Biol* 11:200283.
- De Munter S, Görmemann J, Derua R, Lesage B, Qian J, Heroes E, Waelkens E, Van Eynde A, Beullens M, Bollen M (2017) Split-BioID: a proximity biotinylation assay for dimerization-dependent protein interactions. *FEBS Lett* 591:415–424.
- Doench JG, Fusi N, Sullender M, Hegde M, Vaimberg EW, Donovan KF, Smith I, Tothova Z, Wilen C, Orchard R, Virgin HW, Listgarten J, Root DE (2016) Optimized sgRNA design to maximize activity and minimize off-target effects of CRISPR-Cas9. *Nat Biotechnol* 34:184–191.
- Doench JG, Hartenian E, Graham DB, Tothova Z, Hegde M, Smith I, Sullender M, Ebert BL, Xavier RJ, Root DE (2014) Rational design of highly active sgRNAs for CRISPR-Cas9-mediated gene inactivation. *Nat Biotechnol* 32:1262–7.
- El-Husseini AE, Schnell E, Chetkovich DM, Nicoll RA, Bredt DS (2000) PSD-95 involvement in maturation of excitatory synapses. *Science* (80-) 290:1364–8.
- Ester M, Kriegl H, Sander J, Kdd XX (1996) A density-based algorithm for discovering clusters in large spatial databases with noise. *AAAI Press* 226–31.
- Fang H, Bygrave AM, Roth RH, Johnson RC, Huganir RL (2021) An optimized CRISPR/Cas9 approach for precise genome editing in neurons. *Elife* 10:1–25.
- Forni PE, Scuoppo C, Imayoshi I, Taulli R, Dastrù W, Sala V, Betz UAK, Muzzi P, Martinuzzi D, Vercelli AE, Kageyama R, Ponzetto C (2006) High levels of Cre expression in neuronal progenitors cause defects in brain development leading to microencephaly and hydrocephaly. *J Neurosci* 26:9593–9602.
- Gao Y, Hisey E, Bradshaw TWA, Erata E, Brown WE, Courtland JL, Uezu A, Xiang Y, Diao Y, Soderling SH (2019) Plug-and-Play Protein Modification Using Homology-Independent Universal Genome Engineering. *Neuron* 103:583–597.
- Giraldez T, Hughes TE, Sigworth FJ (2005) Generation of functional fluorescent BK channels by random insertion of GFP variants. *J Gen Physiol* 126:429–438.
- Gould TJ, Verkhusha V V, Hess ST (2009) Imaging biological structures with fluorescence photoactivation localization microscopy. *Nat Protoc* 4:291–308.
- Grimm JB, English BP, Chen J, Slaughter JP, Zhang Z, Revyakin A, Patel R, Macklin JJ, Normanno D, Singer RH, Lionnet T, Lavis LD (2015) A general method to improve fluorophores for live-cell and single-molecule microscopy. *Nat Methods* 12:244–250.
- Groc L, Choquet D (2020) Linking glutamate receptor movements and synapse function. *Science* (80-) 368.
- He M, Tucciarone J, Lee SH, Nigro MJ, Kim Y, Levine JM, Kelly SM, Krugikov I, Wu P, Chen Y, Gong L, Hou Y, Osten P, Rudy B, Huang ZJ (2016) Strategies and Tools for Combinatorial Targeting of GABAergic Neurons in Mouse Cerebral Cortex. *Neuron* 91:1228–1243.
- Higashi AY, Ikawa T, Muramatsu M, Economides AN, Niwa A, Okuda T, Murphy AJ, Rojas J, Heike T, Nakahata T, Kawamoto H, Kita T, Yanagita M (2009) Direct Hematological Toxicity and Illegitimate Chromosomal Recombination Caused by the Systemic Activation of CreER T2. *J Immunol* 182:5633–5640.
- Hioki H, Kameda H, Nakamura H, Okunomiya T, Ohira K, Nakamura K, Kuroda M, Furuta T, Kaneko T (2007) Efficient gene transduction of neurons by lentivirus with enhanced neuron-specific promoters. *Gene Ther* 14:872–882.
- Holler S, Köstinger G, Martin KAC, Schuhknecht GFP, Stratford KJ (2021) Structure and function of a neocortical synapse. *Nature* 1–6.
- Ioannidi EI, Yarnall MTN, Schmitt-Ulms C, Krajewski RN, Lim J, Villiger L, Zhou W, Jiang K, Roberts N, Zhang L, Vakulskas CA, Walker JA, Kadina AP, Zepeda AE, Holden K, Gootenberg JS, Abudayyeh OO (2021) Drag-and-drop genome insertion without DNA cleavage with CRISPR-directed integrases. *bioRxiv* 2021.11.01.466786.
- Kaesler PS, Deng L, Wang Y, Dulubova I, Liu X, Rizo J, Südhof TC (2011) RIM proteins tether Ca<sup>2+</sup> channels to presynaptic active zones via a direct PDZ-domain interaction. *Cell* 144:282–295.

- Kapitein LC, Schlager MA, Van Der Zwan WA, Wulf PS, Keijzer N, Hoogenraad CC (2010a) Probing intracellular motor protein activity using an inducible cargo trafficking assay. *Biophys J* 99:2143–2152.
- Kapitein LC, Yau KW, Hoogenraad CC (2010b) Microtubule Dynamics in Dendritic Spines. *Methods Cell Biol* 97:111–132.
- Kim G, Luján R, Schwenk J, Kelley MH, Aguado C, Watanabe M, Fakler B, Maylie J, Adelman JP (2016) Membrane palmitoylated protein 2 is a synaptic scaffold protein required for synaptic SK2-containing channel function. *Elife* 5:1–18.
- Lackner DH, Carré A, Guzzardo PM, Banning C, Mangena R, Henley T, Oberndorfer S, Gapp B V., Nijman SMB, Brummelkamp TR, Bürckstümmer T (2015) A generic strategy for CRISPR-Cas9-mediated gene tagging. *Nat Commun* 2015 6:1–7.
- Liu Y, Zou RS, He S, Nihongaki Y, Li X, Razavi S, Wu B, Ha T (2020) Very fast CRISPR on demand. *Science* (80-) 368:1265–1269.
- MacGillavry HD, Song Y, Raghavachari S, Blanpied TA (2013) Nanoscale Scaffolding Domains within the Postsynaptic Density Concentrate Synaptic AMPA Receptors. *Neuron* 78:615–622.
- Matsuda T, Cepko CL (2007) Controlled expression of transgenes introduced by in vivo electroporation. *Proc Natl Acad Sci U S A* 104:1027–1032.
- Matsuda T, Oinuma I (2019) Imaging endogenous synaptic proteins in primary neurons at single-cell resolution using CRISPR/Cas9. *Mol Biol Cell* 30:2838–2855.
- Mikuni T, Nishiyama J, Sun Y, Kamasawa N, Yasuda R (2016) High-Throughput, High-Resolution Mapping of Protein Localization in Mammalian Brain by In Vivo Genome Editing. *Cell* 165:1803–1817.
- Nair D, Hossy E, Petersen JD, Constals A, Giannone G, Choquet D, Sibarita J-B (2013) Super-resolution imaging reveals that AMPA receptors inside synapses are dynamically organized in nanodomains regulated by PSD95. *J Neurosci* 33:13204–24.
- Nakade S, Tsubota T, Sakane Y, Kume S, Sakamoto N, Obara M, Daimon T, Sezutsu H, Yamamoto T, Sakuma T, Suzuki KIT (2014) Microhomology-mediated end-joining-dependent integration of donor DNA in cells and animals using TALENs and CRISPR/Cas9. *Nat Commun* 5:1–3.
- Nishiyama J, Mikuni T, Yasuda R (2017) Virus-Mediated Genome Editing via Homology-Directed Repair in Mitotic and Postmitotic Cells in Mammalian Brain. *Neuron* 96:755–768.
- Orthwein A, Noordermeer SM, Wilson MD, Landry S, Enchev RI, Sherker A, Munro M, Pinder J, Salsman J, Dellaire G, Xia B, Peter M, Durocher D (2015) A mechanism for the suppression of homologous recombination in G1 cells. *Nature* 528:422–426.
- Park Jihye, Lim JM, Jung I, Heo SJ, Park Jinman, Chang Y, Kim HK, Jung D, Yu JH, Min S, Yoon S, Cho SR, Park T, Kim HH (2021) Recording of elapsed time and temporal information about biological events using Cas9. *Cell* 184:1047–1063.
- Pfeifer A, Brandon EP, Kootstra N, Gage FH, Verma IM (2001) Delivery of the Cre recombinase by a self-deleting lentiviral vector: Efficient gene targeting in vivo. *Proc Natl Acad Sci U S A* 98:11450–11455.
- Rademacher N, Schmerl B, Lardong JA, Wahl MC, Shoichet SA (2016) MPP2 is a postsynaptic MAGUK scaffold protein that links SynCAM1 cell adhesion molecules to core components of the postsynaptic density. *Sci Rep* 6:1–10.
- Rebola N, Reva M, Kirizs T, Szoboszlaj M, Lőrincz A, Moneron G, Nusser Z, DiGregorio DA (2019) Distinct Nanoscale Calcium Channel and Synaptic Vesicle Topographies Contribute to the Diversity of Synaptic Function. *Neuron* 104:693–710.
- Rose JC, Stephany JJ, Valente WJ, Trevillian BM, Dang H V., Bielas JH, Maly DJ, Fowler DM (2017) Rapidly inducible Cas9 and DSB-ddPCR to probe editing kinetics. *Nat Methods* 14:891–896.
- Sailer CA, Kaufmann WA, Kogler M, Chen L, Sausbier U, Ottersen OP, Ruth P, Shipston MJ, Knaus HG (2006) Immunolocalization of BK channels in hippocampal pyramidal neurons. *Eur J Neurosci* 24:442–454.
- Sala C, Piëch V, Wilson NR, Passafaro M, Liu G, Sheng M (2001) Regulation of Dendritic Spine Morphology and Synaptic Function by Shank and Homer. *Neuron* 31:115–130.
- Schmid-Burgk JL, Höning K, Ebert TS, Hornung V (2016) CRISPaint allows modular base-specific gene tagging using a ligase-4-dependent mechanism. *Nat Commun* 7.
- Schnell E, Sizemore M, Karimzadegan S, Chen L, Bredt DS, Nicoll RA (2002) Direct interactions between PSD-95 and stargazin control synaptic AMPA receptor number. *Proc Natl Acad Sci U S A* 99:13902–13907.
- Shen MW, Arbab M, Hsu JY, Worstell D, Culbertson SJ, Krabbe O, Cassa CA, Liu DR, Gifford DK, Sherwood RI (2018) Predictable and precise template-free CRISPR editing of pathogenic variants. *Nature* 563:646–651.
- Sinnen BL, Bowen AB, Forte JS, Hiester BG, Crosby KC, Gibson ES, Dell’Acqua ML, Kennedy MJ (2017) Optogenetic Control of Synaptic Composition and Function. *Neuron* 93:646–660.
- Sun J, Zhu G, Liu Y, Standley S, Ji A, Tunuguntla R, Wang Y, Claus C, Luo Y, Baudry M, Bi X (2015) UBE3A Regulates Synaptic Plasticity and Learning and Memory by Controlling SK2 Channel Endocytosis. *Cell Rep*.
- Suzuki K et al. (2016) In vivo genome editing via CRISPR/Cas9 mediated homology-independent targeted integration. *Nature* 540:144–149.
- Tang A-H, Chen H, Li TP, Metzbowser SR, MacGillavry HD, Blanpied TA (2016) A trans-synaptic nanocolumn aligns neurotransmitter release to receptors. *Nature* 536:210–4.
- Taniguchi H, He M, Wu P, Kim S, Paik R, Sugino K, Kvitsani D, Fu Y, Lu J, Lin Y, Miyoshi G, Shima Y, Fishell G, Nelson SB, Huang ZJ (2011) A Resource of Cre Driver Lines for Genetic Targeting of GABAergic Neurons in Cerebral Cortex. *Neuron* 71:995–1013.
- Tebo AG, Gautier A (2019) A split fluorescent reporter with rapid and reversible complementation. *Nat Commun* 10:1–8.
- Van Bergeijk P, Adrian M, Hoogenraad CC, Kapitein LC (2015) Optogenetic control of organelle transport and positioning. *Nature* 518:111–114.
- Viswanathan S et al. (2015) High-performance probes for light and electron microscopy. *Nat Methods* 12:568–576.
- Willems J, de Jong APH, Scheefhals N, Mertens E, Catsburg LAE, Poorthuis RB, de Winter F, Verhaagen J, Meye

- 
- FJ, MacGillavry HD (2020) ORANGE: A CRISPR/Cas9-based genome editing toolbox for epitope tagging of endogenous proteins in neurons. *PLoS Biol* 18:e3000665.
- Willems J, MacGillavry HD (2022) A coordinate-based co-localization index to quantify and visualize spatial associations in single-molecule localization microscopy. *Sci Rep* 12:1–12.
- Xue M, Atallah B V., Scanziani M (2014) Equalizing excitation–inhibition ratios across visual cortical neurons. *Nat* 2014 5117511 511:596–600.
- Yang MY, Camara AKS, Aldakkak M, Kwok WM, Stowe DF (2017) Identity and function of a cardiac mitochondrial small conductance Ca<sup>2+</sup>-activated K<sup>+</sup> channel splice variant. *Biochim Biophys Acta - Bioenerg* 1858:442–458.
- Yao X et al. (2017) Homology-mediated end joining-based targeted integration using CRISPR/Cas9. *Cell Res* 27:801–814.
- Zhong H, Ceballos CC, Massengill CI, Muniak MA, Ma L, Qin M, Petrie SK, Mao T (2021) High-fidelity, efficient, and reversible labeling of endogenous proteins using CRISPR-based designer exon insertion. *Elife* 10:99–117.

**SUPPLEMENTAL INFORMATION**

**Figure 1-1. Improved CAKE mechanism reduces crosstalk between knock-ins**

(A) Overview of original CAKE knock-in mechanism introduced in (Willems et al, 2020), referred to as 2A-Cre throughout this Figure. The constitutively active knock-in labels  $\beta$ 3-tubulin with GFP-2A-Cre. Cre expression from this allele then activates gRNA expression for the Cre-ON Halo- $\beta$ -actin knock-in. (B) Overview of improved CAKE constructs introduced in this study (see main text) which will be referred to as Lenti-Cre throughout this Figure. Lentivirus encoding for Cre is added at DIV 7, which switches off gRNA expression for CreOFF, and switches on gRNA expression for CreON. (C) Example confocal images of CAKE double knock-ins using the 2A-Cre or Lenti-Cre mechanism. (D) Average number of single and double knock-in cells per coverslip for 2A-Cre and Lenti-Cre CAKE. 2A-Cre n = 8 coverslips, lenti-Cre n = 7 coverslips, N = 4 independent cultures.  $\beta$ 3-tubulin-GFP p = 0.50, Halo- $\beta$ -actin p = 0.29, double knock-in p = 0.53, incorrect knock-in \* p = 0.019, unpaired t-test. (E) Average fluorescence intensity in proximal dendrites of single knock-ins, normalized per culture. For  $\beta$ 3-tubulin-GFP: 2A-Cre n = 21 cells, lenti-Cre n = 25 cells, N = 3 independent cultures. For Halo- $\beta$ -actin: 2A-Cre n = 18 cells, lenti-Cre n = 14 cells, N = 3 independent cultures.  $\beta$ 3-tubulin-GFP \* p = 0.001, Halo- $\beta$ -actin p = 0.29, unpaired t-test. (F) Example confocal image of an incorrect double knock-in. Fluorescence signal of both GFP and Halo are consistent with  $\beta$ 3-tubulin distribution, suggesting that the Halo donor was inserted in Tubb3.

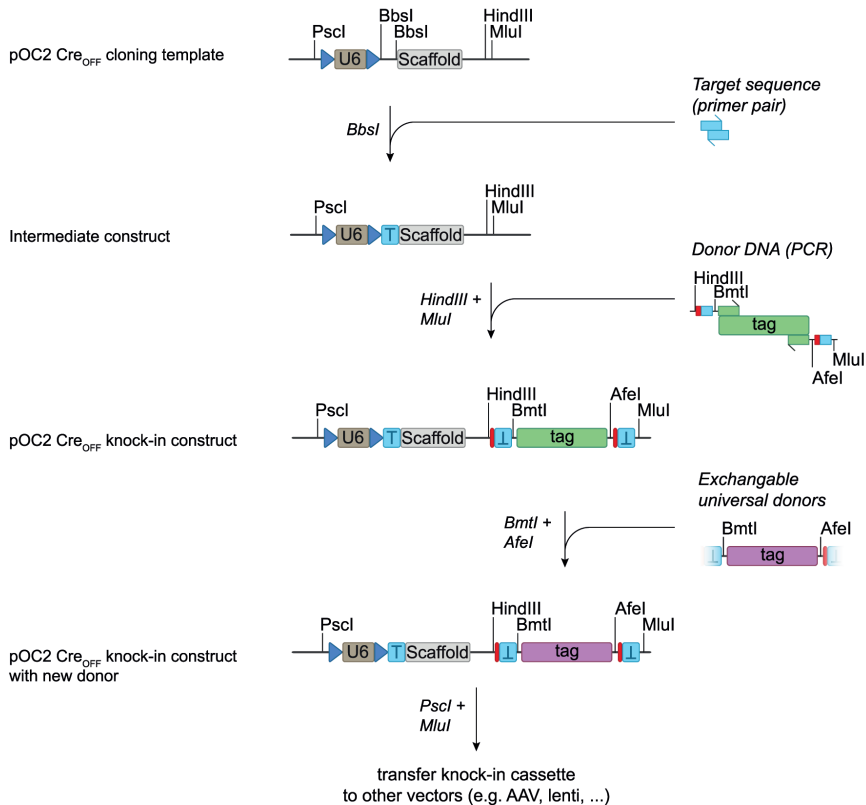


**Figure 1-2. Low magnification images of CAKE knock-in cultures.**

(A) Low magnification images of DIV 14 culture transfected with Cre<sub>OFF</sub> β3-tubulin-GFP and Cre<sub>ON</sub> Halo-β-actin knock-in vectors. Control is unstimulated, +Cre condition was infected with 20 μL lenti-Cre at DIV 7. Notice that CAKE leads to a mosaic of single and double knock-ins (indicated with \*). Fluorescent neurons are surrounded by untransfected cells. (B) As in A, for Cre<sub>OFF</sub> PSD95-GFP and Cre<sub>ON</sub> GluA1-Halo.

**A Overview of pORANGE and pOCx vectors**

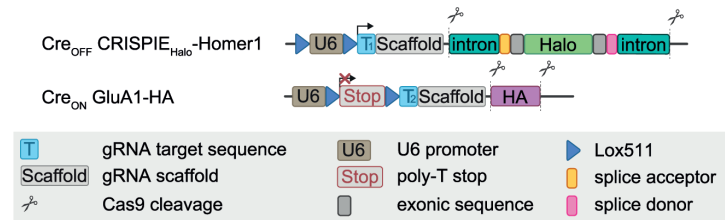
Plasmid	Recombination Cre Flp	gRNA expression cassette	U6	U6 promoter
pORANGE	none none	-U6 T Scaffold-	T	gRNA target sequence
pOC1 Cre <sub>ON</sub>	on none	-U6 Stop T Scaffold-	Scaffold	gRNA scaffold
pOC2 Cre <sub>OFF</sub>	off none	→U6 T Scaffold-	PAM	
pOC3 Cre <sub>ON</sub> /Flp <sub>OFF</sub>	on off	←U6 Stop T Scaffold-	Stop	poly-T stop
pOC4 Flp <sub>ON</sub>	none on	-U6 T Stop Scaffold-	tag	protein tag (GFP, Halo, smFP...)
pOC5 Flp <sub>OFF</sub>	none off	-U6 T Scaffold←	Lox511	
			Fr	
			Transcription active	
			Transcription inhibited	

**B Cloning guide for making CAKE knock-ins**

**Figure 1-3. Overview and cloning guide for CAKE template vector library**

(A) Overview of pORANGE (Willems et al, 2020) and the CAKE template vectors introduced in this study. All vectors contain a multiple cloning site for addition of the donor DNA. (B) Cloning guide to create CAKE knock-in constructs. The example shows a step-by-step protocol for pOC2 CreOFF knock-in vectors, but identical cloning steps apply to all pOC vectors shown in A. #1 shows the empty pOC2 template vector. After digestion with BbsI, a primer pair encoding for the gRNA target sequence is added to obtain the intermediate construct (#2). The donor DNA, which always contains a protospacer adjacent motif (PAM) and target sequence (Suzuki et al, 2016) is obtained with standard PCR techniques. Figure S1 of Willems et al., (2020) contains a detailed description on design of the donor DNA. The donor is cloned using HindIII and MluI restriction sites to obtain the final pOC2 knock-in construct (#3). Most of the knock-in constructs used in this study contain BmtI and AfeI restriction sites around the fluorophore, for universal exchange of donors between knock-in vectors, without the need of PCR (shown in #4,

**Figure 1-3 (continued)** optional). The entire knock-in cassette, containing U6-driven gRNA expression, Lox511 and/or Frt sites and the donor DNA, can be removed from pOC vectors using PscI and MluI restriction sites. A complete description of Cas9 target sequence selection, knock-in design and cloning can be found in Extended Data 1-4.

**A** Constructs used for CRISPIE double knock-in



**B** CRISPIE strategy

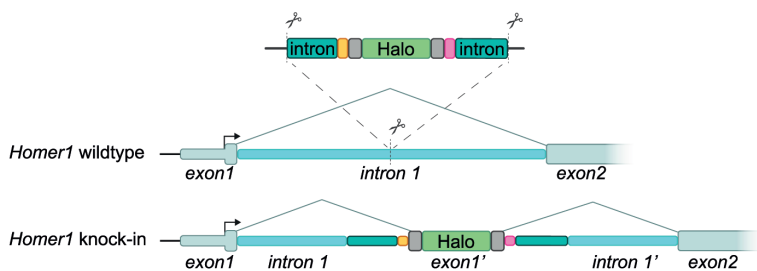
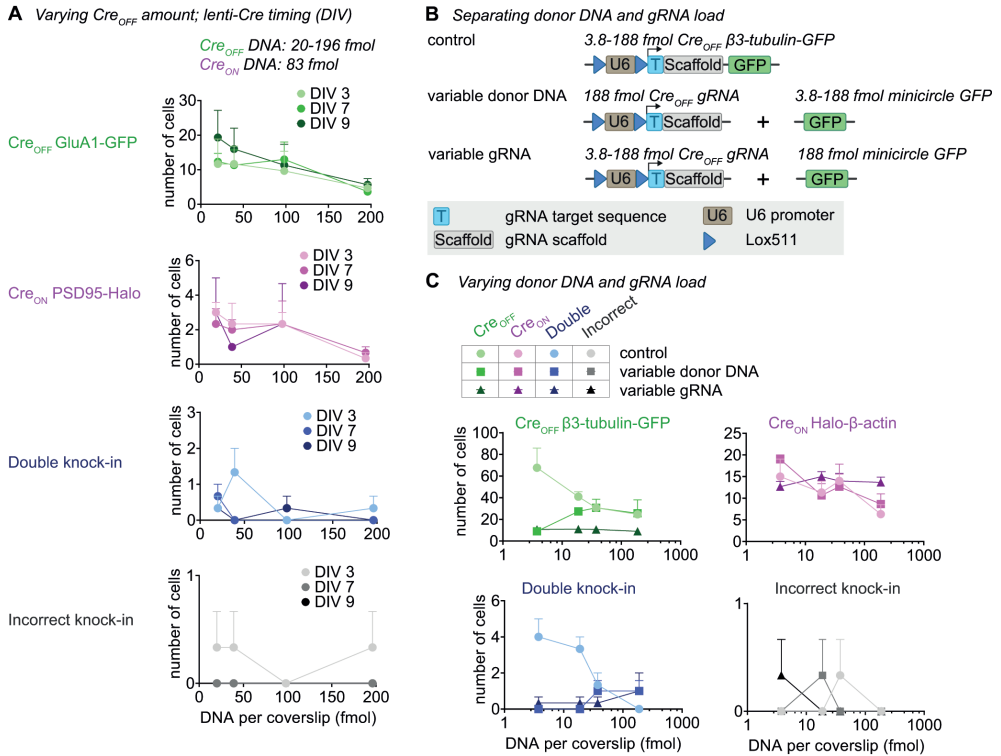


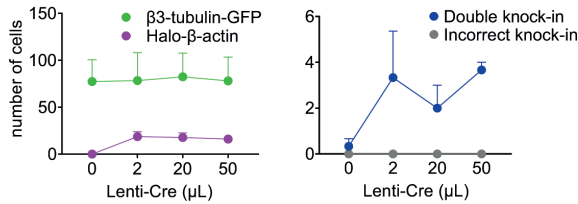
**Figure 2-1. Overview of CRISPIE strategy.**

(A) Overview of DNA constructs used for the CRISPIE double knock-in. (B) Visual representation of the CRISPIE modality. Halo, flanked by the splicing acceptor and donor sites of exon 8 of Septin3, is inserted into the first intron of Homer1 following Cas9 cleavage. Halo then functions as exon1' and will be integrated in the mRNA.





### A Lentivirus-mediated Cre expression



### B Varying Cre and 4OH-tamoxifen concentrations

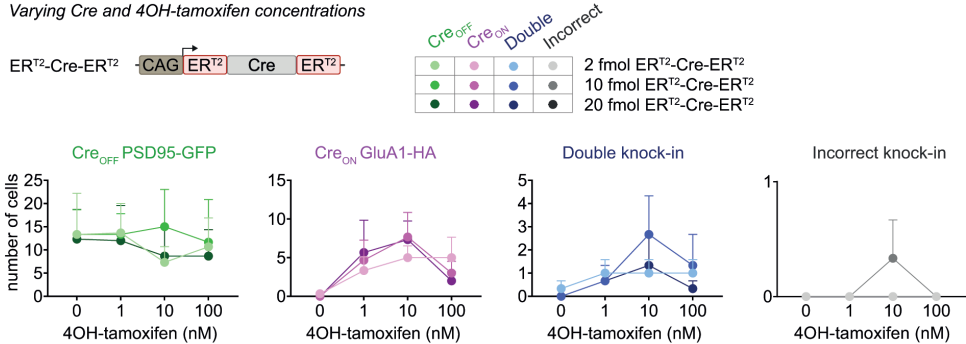


### Figure 4-1. Optimization of lenti-Cre and ERT2-Cre-ERT2

(A) Number of fluorescent cells per coverslip as a function of the amount of lenti-Cre used for infection. Experiments were performed with Cre<sub>OFF</sub> β3-tubulin-GFP and Cre<sub>ON</sub> Halo-β-actin. Lenti-Cre was added at DIV 7.  $n = 2$  coverslips  $N = 2$  independent cultures. 70% of knock-in cells was PSD95-GFP positive, 30% was GluA1-HA positive, and 6.9% was double positive. (B) Number of fluorescent cells per coverslip as a function of 4OH-tamoxifen concentration and amount of pCAG ERT2-Cre-ERT2 vector at transfection. At 2 fmol (10 ng) pCAG ERT2-Cre-ERT2, 4OH-tamoxifen results in a dose dependent increase in the number of Cre<sub>ON</sub> knock-ins. Higher vector load (10-20 fmol) does not lead to more knock-in cells, but increases ERT2-Cre-ERT2 cytotoxicity at 100 nM 4OH-tamoxifen.  $n = 3$  coverslips,  $N = 3$  independent cultures,

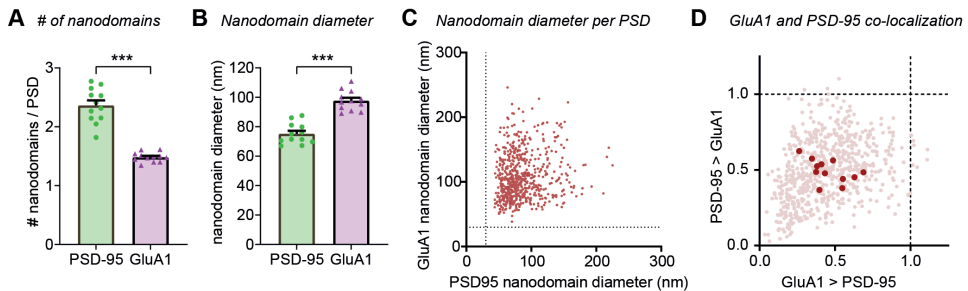


### Figure 6-1. PSD95 and GluA1 have distinct nanoscale organizations

(A) Number of nanodomains of PSD95 and GluA1 per PSD. \*\*\*  $p = 0.0002$ , unpaired t-test. (B) Nanodomain diameter for PSD95 and GluA1. \*\*\*  $p = 6.4 \times 10^{-8}$ , unpaired t-test. (C) Nanodomain diameter for PSD95 and GluA1 per PSD. Dotted line represents minimal threshold of nanodomain diameter. (D) Co-localization index for both PSD95 and GluA1, plotted per synapse (transparent red dots) and neuron (red dots).

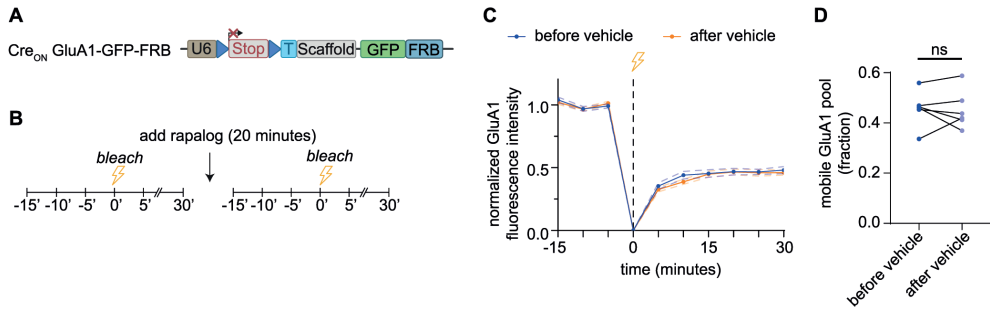


**Figure 7-1. Live-cell anchoring of AMPA receptors control**

(A) Overview of DNA construct used. (B) Imaging protocol. Neurons are live-cell imaged using spinning disk microscopy every 5 minutes. FRAP is performed twice, before and after vehicle incubation for 20 minutes. (C) FRAP curves of spines bleached before and after vehicle incubation. Data is normalized to the average intensity before bleaching. 34 spines before vehicle and 42 spines after vehicle were bleached.  $n = 6$  cells,  $N = 5$  independent cultures. (D) Average recovery of fluorescence per neuron, averaged over the last 4 frames, reflecting the mobile pool of receptors. No difference was observed before and after vehicle.  $p = 0.86$ , paired t-test.  $N = 6$  cells,  $N = 5$  independent cultures

**Table 1. Vectors**

All vectors that were used in this study are listed with their name, purpose, source and Addgene ID.

Vector	Purpose	Source	Addgene ID
pOC1 cloning template vector	Cre <sub>ON</sub> knock-in vector	This study	183420
pOC2 cloning template vector	Cre <sub>OFF</sub> knock-in vector	This study	183421
pOC3 cloning template vector	Cre <sub>ON</sub> Flp <sub>OFF</sub> knock-in vector	This study	183422
pOC4 cloning template vector	Flp <sub>ON</sub> knock-in vector with FLAG-SpCas9 expression	This study	183423
pOC5 cloning template vector	Flp <sub>OFF</sub> knock-in vector	This study	183424
pFUGW NLS-Cre	Lentiviral Cre vector	This study	183425
pFUGW GFP-NLS-Cre	Lentiviral GFP-Cre vector	(Kaeser <i>et al.</i> , 2011)	n/a
pFUGW NLS-FlpO	Lentiviral FlpO vector	This study	183448
pCAG ERT2 Cre ERT2	Tamoxifen-inducible Cre	(Matsuda & Cepko, 2007)	13777
pCAG ERT2 Cre ERT2 lox	Cre <sub>OFF</sub> tamoxifen-inducible Cre	This study	183447
pOC1 Halo-Actb	Cre <sub>ON</sub> knock-in for Halo-β-actin	This study	183426
pOC1 Grial-HA	Cre <sub>ON</sub> knock-in for GluA1-HA	This study	183427
pOC1 Grial-GFP-FRB	Cre <sub>OFF</sub> knock-in for GluA1-GFP-FRB	This study	183428
pOC2 GFP-Actb	Cre <sub>OFF</sub> knock-in for GFP-β-actin	This study	183429
pOC2 Grial-GFP	Cre <sub>OFF</sub> knock-in for GluA1-GFP	This study	183430
pOC2 Tubb3 no donor	Cre <sub>OFF</sub> gRNA expression for β3-tubulin	This study	183431
pOC2 Tubb3-GFP	Cre <sub>OFF</sub> knock-in for β3-tubulin-GFP	This study	183432
pOC2 Grial-Halo	Cre <sub>OFF</sub> knock-in for GluA1-Halo	This study	183433
pOC2 GFP-Mpp2	Cre <sub>OFF</sub> knock-in for GFP-MPP2	This study	183434
pOC2 Dlg4-Halo-FKBP	Cre <sub>OFF</sub> knock-in for PSD95-Halo-FKBP	This study	183435
pOC3 smFP-HA-Cacna1e	Cre <sub>ON</sub> Flp <sub>OFF</sub> knock-in for smFP-HA-CaV2.3	This study	183436
pOC4 mRuby3-Actb	Flp <sub>ON</sub> knock-in for mRuby3-β-actin	This study	183437
pOC4 smFP-myc-Kenn2	Flp <sub>ON</sub> knock-in for smFP-myc-SK2	This study	183438
pOC4 Grin1-smFP-V5	Flp <sub>ON</sub> knock-in for GluN1-smFP-V5	This study	183439
pOC5 Tubb3-GFP	Flp <sub>OFF</sub> knock-in for β3-tubulin-GFP	This study	183440
pOC5 smFP-HA-Cacna1e	Flp <sub>OFF</sub> knock-in for smFP-HA-CaV2.3	This study	183441
pOC5 Kennal-smFP-HA	Flp <sub>OFF</sub> knock-in for BK-smFP-HA	This study	183442
pORANGE Tubb3-GFP	GFP knock-in for β3-tubulin-GFP (1x donor)	(Willems <i>et al.</i> , 2020)	131497
pORANGE Tubb3-2xGFP	GFP knock-in for β3-tubulin-GFP (2x donor)	This study	183443
pORANGE Tubb3-3xGFP	GFP knock-in for β3-tubulin-GFP (3x donor)	This study	183444
pORANGE Tubb3-4xGFP	GFP knock-in for β3-tubulin-GFP (4x donor)	This study	183445
pORANGE Tubb3-GFP-2A-Cre	GFP-2A-Cre knock-in for β3-tubulin-GFP	(Willems <i>et al.</i> , 2020)	n/a
pTubb3 MC	Minicircle GFP donor for β3-tubulin	(Suzuki <i>et al.</i> , 2016)	87112
pOC2 CRISPIE-Halo-Homer1	Cre <sub>ON</sub> knock-in for CRISPIE-Halo-Homer1	This study	183446
pOC2 Dlg4-Halo	Cre <sub>OFF</sub> knock-in for PSD95-Halo	This study	183449

**Table 2. CRISPR knock-ins**

All knock-ins that were used in this study are listed with their gene and protein name, target sequence and target properties.

Gene	Protein	Target sequence (PAM is underlined)	Site of integration (in or before amino acid)	MIT score (in rat)	Conservation of target sequence in mouse	Source
<i>Actb</i>	$\beta$ -actin	TGTGCCCTGATAGTTCGCCA <u>TGG</u>	1 bp before ATG	84	1 mismatch	(Willems <i>et al.</i> , 2020)
<i>Cacna1e</i>	Ca <sub>v</sub> 2.3 (R-type)	CAGGATGGCTCGCTTCGGGG <u>AGG</u>	G5	88	Yes	(Willems <i>et al.</i> , 2020)
<i>Dlg4</i>	PSD95	AATCAGAGTCTCTCTCGGGC <u>TGG</u>	R721	80	Yes	(Willems <i>et al.</i> , 2020)
<i>Gria1</i>	GluA1	GGGAGCCACAGGATTGTAAC <u>TGG</u>	STOP codon	72	Yes	(Willems <i>et al.</i> , 2020)
<i>Homer1</i>	Homer1	TATATGCCTCCGGTGCCCA <u>AGG</u>	G2	49	Yes	This study
<i>Kcnma1</i>	BK	GAACGTA <u>CTCTCTGTTGTCGGGC</u>	D1201	86	Yes	This study
<i>Kcnm2</i>	SK2	TAGCTACTCTCAGATGAAGT <u>TGG</u>	T571	68	1 mismatch	This study
<i>Mpp2</i>	MPP2	TCAGAGTTCGTGGCAGCAAC <u>CGG</u>	A4	74	1 mismatch	This study
<i>Tubb3</i>	$\beta$ 3-tubulin	GCTGCGAGCAACTTCACTT <u>GGG</u>	STOP codon	59	Yes	(Willems <i>et al.</i> , 2020)
<i>Grin1</i>	GluN1	CTTGGGGTCCGAGCGCGC <u>TGG</u>	A20	85	Yes	(Willems <i>et al.</i> , 2020)

**Table 3. Design rationale for new knock-ins**

For each knock-in made in this study, the gene and protein name, endogenous location, tag location and design rationale are listed.

Gene	Protein	Endogenous location	Tag location	Design rationale
<i>Homer1</i>	Homer1	Enriched in dendritic spines and PSD (Sala <i>et al.</i> , 2001)	N-terminus	The tag is inserted at the second amino acid of Homer1, thereby minimizing effects on functional domains.
<i>Kcnma1</i>	BK	Punctate distribution in axons, dendrite and soma (Sailer <i>et al.</i> , 2006)	C-terminus	C-terminal addition of fluorophore does not affect localization or function of BK (Giraldez <i>et al.</i> , 2005)
<i>Kcnm2</i>	SK2	Punctate distribution in axons and dendrites (Ballesteros-Merino <i>et al.</i> , 2012; Sun <i>et al.</i> , 2015)	C-terminus	C-terminal tagging does not appear to affect SK-channel function (Yang <i>et al.</i> , 2017)
<i>Mpp2</i>	MPP2	Punctate signal in dendrites; enriched in dendritic spines but absent from PSD (Kim <i>et al.</i> , 2016; Rademacher <i>et al.</i> , 2016)	N-terminus	N-terminal, but not C-terminal sequences are present in all splice variants; N-terminal tagging does not disrupt protein expression (Baumgartner <i>et al.</i> , 2009)

**Table 4. Primers**

All primers used to make the vectors that were constructed in this study.

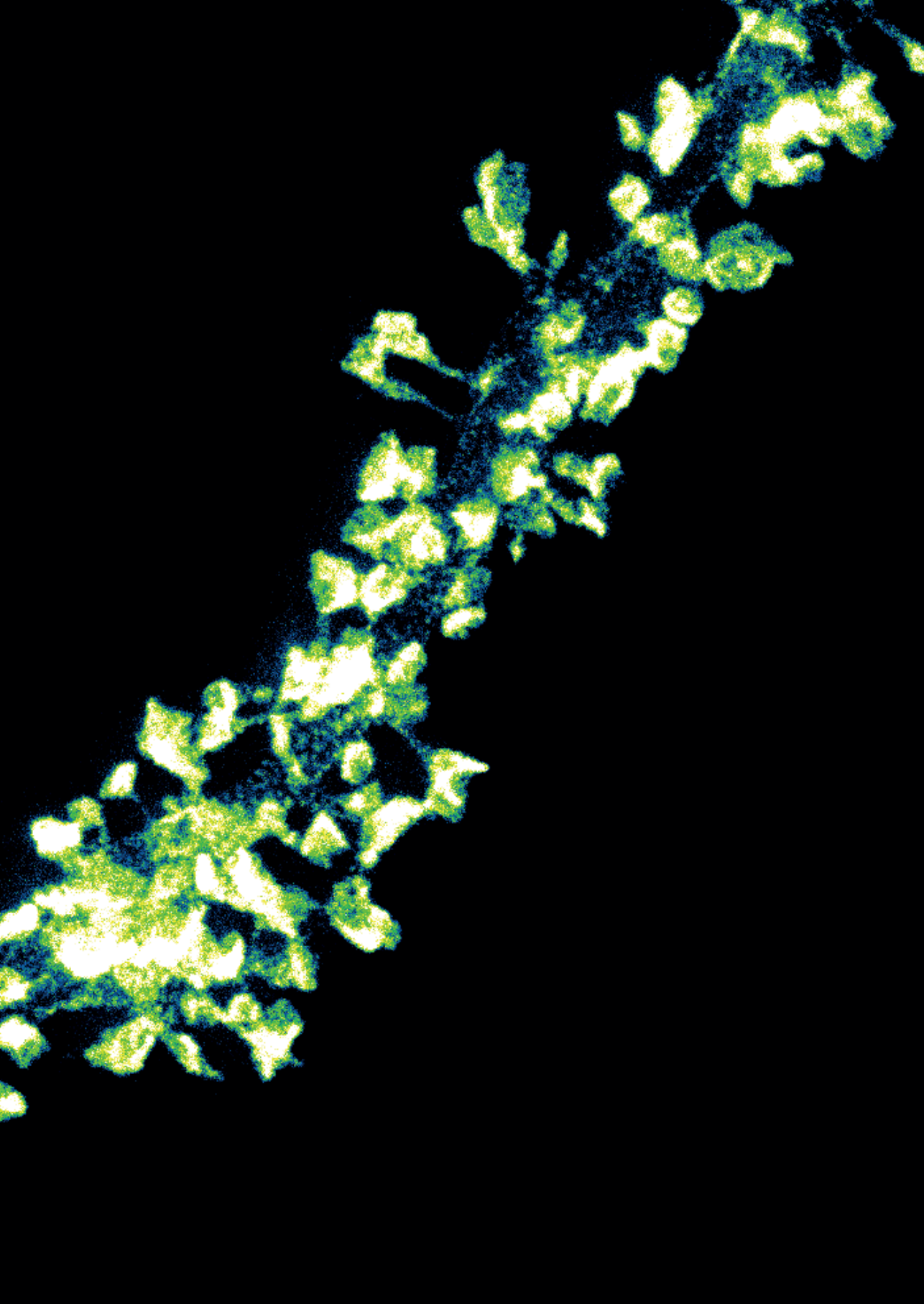
Name	Sequence	Purpose
AJ19164	CTAGGACGCGTTAACTTACGGTAAATGGCCCGGC	Removal of Ca <sub>9</sub> from pORANGE LOX
AJ19165	GGCCGCGGGCCATTACCCTAAGTTAACCGCTC	Removal of Ca <sub>9</sub> from pORANGE LOX
AJ19069	TTGCTCACATGTATAACTTCGTATAGTATAAATTA TACGAAGTTATGATCCGACGCCGCC	Clone pOC2 Cre <sub>OFF</sub>
AJ20047	TATCTTCTGTACACGAAGACAAACAGGCTTATAAC TTCGTATAATTTATACTATACGAAGTTATACTAACTTTACAGT	Clone pOC2 Cre <sub>OFF</sub>
AJ20116	GGCGGCCGCAAAAAAAAAAAGAAAGTTCTATACTTT CTAGAGAATAGGAACTTCCAGCATAGCTCTTAAACAGGCTTCTCG	Clone pOC4 Flp <sub>ON</sub>
AJ20117	CAGAATTCGGCTCGAGGGAAGTTCTATTCTCTAG AAAGTATAGGAACCTCCAGCATAGCAAGTTTAAATAAGGCTAGTCCGTTATC	Clone pOC4 Flp <sub>ON</sub>
AJ20120	AAAGTATAGGAACCTCCAGCATAGCAAGTTAAAA TAAGGCTAGTCCGTTATC	Clone pOC3 Cre <sub>ON</sub> Flp <sub>OFF</sub> ; pOC4 Flp <sub>ON</sub>
AJ20121	CCTCGAGTCGACAATTGCTAGCAAGC	Clone pOC3 Cre <sub>ON</sub> Flp <sub>OFF</sub> ; pOC4 Flp <sub>ON</sub>
AJ20122	CGGCCTTTTACGGTTCTCTGG	Clone pOC3 Cre <sub>ON</sub> Flp <sub>OFF</sub> ; pOC4 Flp <sub>ON</sub>
AJ20124	TGCTGGCCTTTTGTCTACATGTGAAGTTCCTATTCT CTAGAAAGTATAGGAACTTCGATCCGACGCCGCCATC	Clone pOC3 Cre <sub>ON</sub> Flp <sub>OFF</sub>
AJ20125	GCTGGAAGTTCCTATACTTTCTAGAGAATAGGAACTT CCAGCATAGCTCTAAACAGGCTTCTTIG	Clone pOC3 Cre <sub>ON</sub> Flp <sub>OFF</sub>
AJ20126	GGTGCTTGTGAGTTCCTCTGAGG	Clone pOC3 Cre <sub>ON</sub> Flp <sub>OFF</sub>
AJ20127	CGATTTTGAATTCGTTCTCAGAGGAAC	Clone pOC3 Cre <sub>ON</sub> Flp <sub>OFF</sub>
AJ20128	ATACTATCTAGAACAAACATGGGCAAGAA GAAGAGGAAGGTGTCCAATTAC	Clone pFUGW-NLS-Cre
AJ20129	ATTGTTAACGGATCCGCTAGCC	Clone pFUGW-NLS-Cre
AJ20130	ATACTTTCTAGAGCCGCCACCATGGCTCC	Clone pFUGW-NLS-Flp <sup>0</sup>
AJ20131	ATACAAGCTAGCTCAGATCCGCTGTTGATG	Clone pFUGW-NLS-Flp <sup>0</sup>
AJ21030	TGGAAAGGACGAAACACCCGGGTCTTCGAGAAGACCT GTTTTAGACTATGCTGG	Clone pOC5 Flp <sub>OFF</sub>
AJ21031	TTGTAGCAAGCTTCTAGAAAAAAAAAAAAAGAGTT CCTATACTTTCTAGAGAATAGGAACTTCGAATTGGCGCACGCG	Clone pOC5 Flp <sub>OFF</sub>
AJ21032	CGAAGACCCGGTGTTCCTGTC	Clone pOC5 Flp <sub>OFF</sub>
AJ21053	GTCATCATTTTGGCAAAGGCTAGCATAAATTCGTATAGCATA CATTATACGAAGTTATGAATTCGCCGGTGAGCCGCCA	Clone pCAG ER <sup>T2</sup> -Cre-ER <sup>T2</sup> lox
AJ21054	TTCCCTGCCACAGCTTGATAGCGGCCGCATAAATTCGTATAGC ATACATTATACGAAGTTATGGCCGCACTCCTCAGGTGCAGGC	Clone pCAG ER <sup>T2</sup> -Cre-ER <sup>T2</sup> lox
WD0116	ATAAAGCTTTATATGCTCCCGGTGCCAGGGGAGCCAGGGAATAAGACG	Clone pOC2 CRISPIE-Halo-Homer1
WD0117	ATAACGCGTCCCTGGGCACCGGAGGCATATAGAATAATATCATAGCATCC	Clone pOC2 CRISPIE-Halo-Homer1
JW381	CACGCTCGAGATTTCCGGCAGCGGAGGCAGCGCTGGAGTGCAGGTGGAAACCAT	Clone pOC2 PSD95-Halo-FKBP
JW382	GAGACTCTGATTTAGCGTCTGACTCCTCCAGTTTTAGAAAGCTCCACATCGAA	Clone pOC2 PSD95-Halo-FKBP
JW375	GAGCTGTACAGCGCTTCTGGTGGTGGTAGCTACGT	Clone pOC1 GluA1-GFP-FRB
JW376	CAGGATTGTAACGGGAGCAGTCTGACTCACTTTGAGATTCTCGGAACACAT	Clone pOC1 GluA1-GFP-FRB

3

**Table 5. Statistical table**

Overview of all statistical tests that were performed, including figure number, description, data structure, the type of test and the power (statistic).

Fig.	Description	Data Structure	Type of test	Power (statistic)
3A	$\beta$ 3-tubulin (Cre <sub>OFF</sub> DNA)	Normal distribution	2-way ANOVA	F(3, 24) = 5.3
3A	$\beta$ -actin (Cre <sub>OFF</sub> DNA)	Normal distribution	2-way ANOVA	F(3, 24) = 4.6
3A	Double (Cre <sub>OFF</sub> DNA)	Normal distribution	2-way ANOVA	F(3, 24) = 7.6
3A	Incorrect (Cre <sub>OFF</sub> DNA)	Normal distribution	2-way ANOVA	F(3, 24) = 4.2
3B	$\beta$ 3-tubulin (DNA)	Normal distribution	ANOVA	F(7, 16) = 3.9
3B	$\beta$ -actin (DNA)	Normal distribution	ANOVA	F(7, 16) = 3.4
3B	Double (DNA)	Normal distribution	ANOVA	F(7, 16) = 2.3
3B	Incorrect (DNA)	Normal distribution	ANOVA	F(7, 16) = 0
3E	Donor copy number	Normal distribution	Linear regression	F(1, 10) = 7.2
4B	$\beta$ 3-tubulin (4OH-tamoxifen)	Normal distribution	2-way ANOVA	F(3, 24) = 0.49
4B	$\beta$ -actin (4OH-tamoxifen)	Normal distribution	2-way ANOVA	F(3, 24) = 27.6
4B	Double (4OH-tamoxifen)	Normal distribution	2-way ANOVA	F(3, 24) = 14.4
4B	Incorrect (4OH-tamoxifen)	Normal distribution	2-way ANOVA	F(3, 24) = 3.1
4C	Double (lenti vs. tamoxifen)	Normal distribution	Unpaired <i>t</i> -test	t(13) = 1.8
5D	GluA1 (DNA)	Normal distribution	Kruskal-Wallis	statistic = 9.2
5D	Ca <sub>v</sub> 2.3 (DNA)	Normal distribution	Kruskal-Wallis	statistic = 1.6
5D	Double (DNA)	Normal distribution	Kruskal-Wallis	statistic = 5.7
5D	Incorrect (DNA)	Normal distribution	Kruskal-Wallis	statistic = 3.0
5E	Time (DIV)	Normal distribution	2-way ANOVA	F(3, 35) = 12.5
5E	Knock-in	Normal distribution	2-way ANOVA	F(2, 35) = 13.3
5E	Interaction	Normal distribution	2-way ANOVA	F(6, 35) = 3.2
5G	GluA1	Normal distribution	ANOVA	F(2, 6) = 0.099
5G	Ca <sub>v</sub> 2.3	Normal distribution	ANOVA	F(2, 6) = 2.4
5G	Double	Normal distribution	ANOVA	F(2, 6) = 0.56
5G	Incorrect	Normal distribution	ANOVA	F(2, 6) = 5.7
6C	Nanodomain-PSD distance	Non-uniform	Mann-Whitney	statistic = 426143
6D	PSD size vs. ND distance	Non-uniform	Linear regression	F(1, 642) = 13.8
6F	PSD size vs. co-localization	Non-uniform	Linear regression	F(1, 654) = 155.7
6G	PSD95 (ND enrichment)	Normal distribution	one-sample <i>t</i> -test	t(11) = 8.1
6G	GluA1 (ND enrichment)	Normal distribution	one-sample <i>t</i> -test	t(11) = 11.6
7F	Mobile GluA1 before/after	Normal distribution	Paired <i>t</i> -test	t(5) = 3.4
7G	GluA1 synaptic enrichment	Normal distribution	Paired <i>t</i> -test	t(5) = 1.4
1-1D	$\beta$ 3-tubulin (2A vs. lenti)	Normal distribution	Unpaired <i>t</i> -test	t(13) = 0.69
1-1D	$\beta$ -actin (2A vs. lenti)	Normal distribution	Unpaired <i>t</i> -test	t(13) = 1.1
1-1D	Double (2A vs. lenti)	Normal distribution	Unpaired <i>t</i> -test	t(13) = 0.64
1-1D	Incorrect (2A vs. lenti)	Normal distribution	Unpaired <i>t</i> -test	t(13) = 2.7
1-1E	$\beta$ 3-tubulin (2A vs. lenti)	Normal distribution	Unpaired <i>t</i> -test	t(44) = 4.5
1-1E	$\beta$ -actin (2A vs. lenti)	Normal distribution	Unpaired <i>t</i> -test	t(30) = 0.29
3-1A	GluA1 (Cre <sub>OFF</sub> DNA)	Normal distribution	2-way ANOVA	F(3, 24) = 2.2
3-1A	PSD95 (Cre <sub>OFF</sub> DNA)	Normal distribution	2-way ANOVA	F(3, 24) = 2.5
3-1A	Double (Cre <sub>OFF</sub> DNA)	Normal distribution	2-way ANOVA	F(3, 24) = 1.3
3-1A	Incorrect (Cre <sub>OFF</sub> DNA)	Normal distribution	2-way ANOVA	F(3, 24) = 0.33
3-1C	$\beta$ 3-tubulin (Plasmid)	Normal distribution	2-way ANOVA	F(2, 24) = 18.6
3-1C	$\beta$ -actin (Plasmid)	Normal distribution	2-way ANOVA	F(2, 24) = 0.72
3-1C	Double (Plasmid)	Normal distribution	2-way ANOVA	F(2, 24) = 11.4
3-1C	Incorrect (Plasmid)	Normal distribution	2-way ANOVA	F(2, 24) = 0
4-1B	PSD95 (4OH-tamoxifen)	Normal distribution	2-way ANOVA	F(3, 24) = 0.16
4-1B	GluA1 (4OH-tamoxifen)	Normal distribution	2-way ANOVA	F(3, 24) = 4.8
4-1B	Double (4OH-tamoxifen)	Normal distribution	2-way ANOVA	F(3, 24) = 1.7
4-1B	Incorrect (4OH-tamoxifen)	Normal distribution	2-way ANOVA	F(3, 24) = 1
6-1A	# of nanodomains	Normal distribution	Unpaired <i>t</i> -test	t(22) = 10.0
6-1B	Nanodomain diameter	Normal distribution	Unpaired <i>t</i> -test	t(22) = 7.9
7-1D	Mobile GluA1 (no rapalog)	Normal distribution	Paired <i>t</i> -test	t(5) = 0.18



# 4

---

## **Single-molecule localization microscopy of subcellular protein distribution in neurons**

Jelmer Willems\*, Manon Westra\*, Harold D. MacGillavry

Methods in Molecular Biology (2022); 2440, 271-288

---

\* These authors contributed equally to this work.  
Cell Biology, Neurobiology and Biophysics, Department of Biology, Faculty of Science, Utrecht University, Utrecht, the Netherlands



---

## ABSTRACT

Over the past years several forms of super-resolution fluorescence microscopy have been developed that offer the possibility to study cellular structures and protein distribution at a resolution well below the diffraction limit of conventional fluorescence microscopy (<200 nm). A particularly powerful super-resolution technique is single-molecule localization microscopy (SMLM). SMLM enables the quantitative investigation of subcellular protein distribution at a spatial resolution up to tenfold higher than conventional imaging, even in live cells. Not surprisingly, SMLM has therefore been used in many applications in biology, including neuroscience. This chapter provides a step-by-step SMLM protocol to visualize the nanoscale organization of endogenous proteins in dissociated neurons but can be extended to image other adherent cultured cells. We outline a number of methods to visualize endogenous proteins in neurons for live-cell and fixed application, including immunostaining, the use of intrabodies for live-cell SMLM, and endogenous tagging using CRISPR/Cas9.

## KEY WORDS

super-resolution microscopy, single-molecule localization microscopy, stochastic optical reconstruction microscopy, photoactivated localization microscopy, neuron, synapse

## 1. INTRODUCTION

Fluorescence microscopy is instrumental for the investigation of subcellular protein organization which is critical to understand cellular function in health and disease. The development of super-resolution microscopy techniques such as single-molecule localization microscopy (SMLM) has tremendously increased the ability to resolve protein distribution achieving resolution below 30 nm. SMLM relies on the sequential acquisition of sparse, single emitting fluorophores that label a structure of interest. The spatial isolation of individual fluorescent events allows the accurate localization of the center point of each emission event with nanometer precision. Together, the spatial coordinates of individual localizations accumulated over thousands of frames are used to reconstruct a super-resolved image [1] (Figure 1A). Importantly, in SMLM the resolution of the image is no longer determined by the diffraction limit but relies on the localization precision of fluorophores and the density of localized molecules that label the structure of interest. The localization precision ( $s$ ) is determined by a number of factors such as background noise and pixel size [2], but is mostly dependent on the number of photons ( $N$ ) emitted by the fluorophore as:

$$\sigma = 1/\sqrt{N}$$

The localization density equally contributes to the resolving power: too few localizations will result in a poor reconstruction of the structure of interest. This can be formalized based on the Nyquist-Shannon sampling criterium such that to achieve a certain resolution, fluorophores have to be sampled at a density at least twice as high as the desired spatial frequency [3]. It is therefore important to optimize labeling strategies to achieve a high labeling density.

In the recent years, a multitude of SMLM approaches have been developed, including techniques such as photoactivated localization microscopy (PALM) [4,5], (direct) stochastic optical reconstruction microscopy (d)STORM [6,7], point accumulation for imaging in nanoscale topography (PAINT) [8] and MINFLUX [9]. Here, we will describe the use of PALM and (d)STORM (Figure 1B). In PALM, a low-power activation laser is used to

stochastically photoactivate or photoconvert subsets of fluorescent proteins in the active state. The most commonly used fluorescent protein is mEos3.2, which switches from green to red fluorescence upon illumination by 405-nm light and yields relatively high photon counts [10]. In (d)STORM reversible blinking of organic dyes is induced by high-intensity laser power under reducing buffer conditions resulting in the reversible transition of the fluorophores into a long-lived dark state [11,12]. Organic dyes can be coupled to a protein of interest via dye-conjugated antibodies or using self-labeling enzymes like Halo- [13] SNAP- [14] and CLIP-tags [15]. Dyes suitable for dSTORM include but are not limited to Alexa647 and JF646 (*see* Note 1).

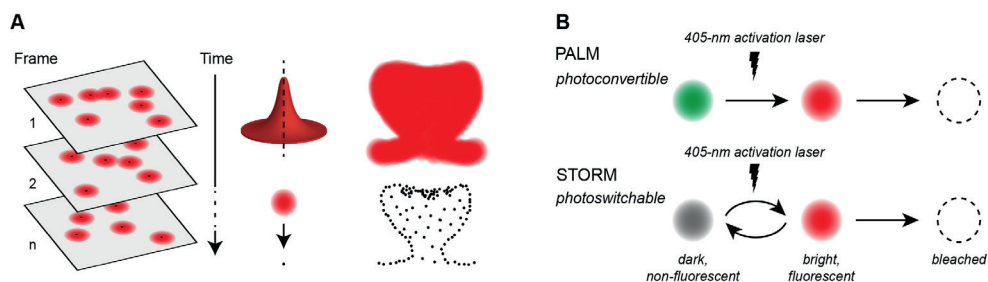


**Figure 1. Principle of single-molecule localization microscopy.**

(A) Single emitters are recorded over a large number of frames. Each identified event is fitted to localize the centroid position of the fluorophore. Together, these localizations form the reconstructed image, which is no longer diffraction limited. (B) PALM: fluorophores change their emission spectrum upon activation with 405-nm laser. STORM: fluorophores can reversibly switch between dark, non-emissive and bright, emissive states in a stochastic manner.

The different SMLM approaches each have their own advantages and disadvantages and the choice for the optimal technique ultimately depends on the goal of the experiment and which type of results would allow for testing the hypothesis [16-18]. This is especially true for SMLM experiments, which often involve extensive post-imaging analysis [19]. For example, STORM imaging usually yields more localization events than PALM due to signal amplification by immunostaining. Also, the organic dyes used for STORM imaging yield a higher photon count, and thus generally result in a higher localization precision [10,12]. On the other hand, PALM imaging is compatible with live-cell imaging, and does not require fixation and additional labeling steps, and thus effectively preserves ultrastructure.

For every fluorescence imaging technique, but particularly for SMLM, the method used to label a protein of interest is critical, as the quality of the final image depends on the properties of the fluorophore, coupling distance of the fluorophore to the protein of interest and labeling density but is also highly sensitive to experimental alterations that affect protein organization [20,21]. Ideally, the labeling strategy should thus allow the visualization of endogenously expressed proteins using a small tag or label that yields a high signal to noise ratio, and that preserves the cellular ultrastructure (*also see* Note 2). We recently developed a CRISPR/Cas9-based genome editing toolbox that enables the accurate tagging of endogenous proteins in neurons, allowing the investigation of native protein complexes [22]. Importantly, this approach omits the need for specific antibodies and does not rely on overexpression of proteins that could have adverse effects.

Here we describe a SMLM protocol with three parallel workflows, each using a different labeling strategy (i) live-cell PALM using expression of mEos3.2-fused intrabodies recognizing the synaptic scaffold protein PSD-95 [23], and dSTORM making use of either

(ii) endogenous tagging with HaloTag [13,22], or (iii) conventional labeling using antibodies (Figure 2A). This protocol aims to provide a starting point for setting up SMLM experiments and thus elaborates on several important experimental steps in the notes section. Additionally, we describe several considerations for data processing and visualization steps. As examples, the approaches are used to super-resolve the distribution of endogenous synaptic receptor proteins and their scaffolds in dissociated hippocampal rat neurons, but the described methodologies are in principle applicable to other adherent cell types.

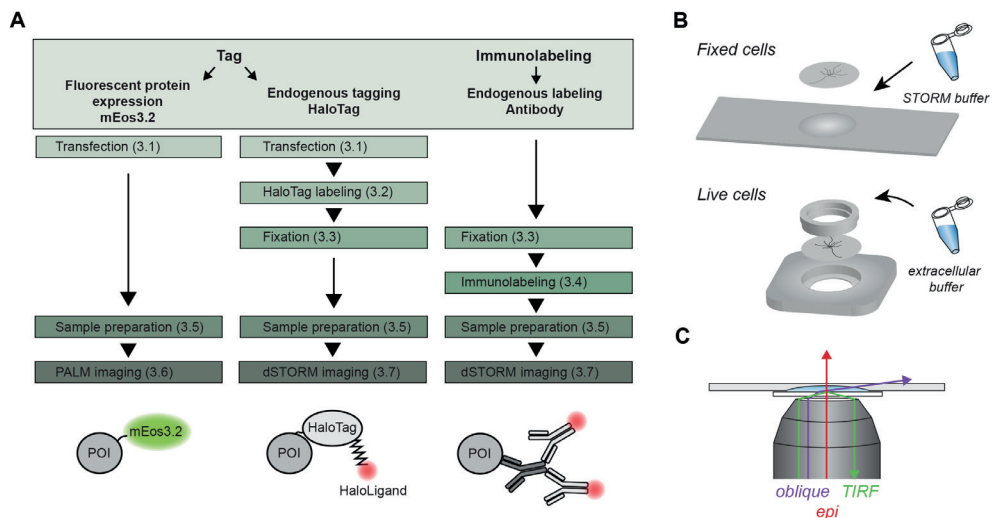


**Figure 2. SMLM experimental workflow.**

(A) Experimental workflow for 1. PALM imaging of mEos3.2, 2. dSTORM imaging of HaloTag on endogenously tagged proteins, and 3. dSTORM imaging of endogenously labeled proteins. (B) Top: mounting of the coverslip upside down on a concave slide filled with STORM buffer. Bottom: mounting of the coverslip with live cells in a Ludin chamber with extracellular buffer on top. (C) Visualizing the different angles of the laser through the sample for epifluorescence, oblique illumination and TIRF imaging. POI, protein of interest.

## 2. MATERIALS

### 2.1 Cell-culture and transfection

1. Dissociated rat hippocampal cultures on 18-mm coverslips in 1 mL neuronal culture medium.
2. BrainPhys neuronal medium.
3. BP full medium: BrainPhys neuronal medium, 2% (v/v) NeuroCult SM1 neuronal supplement and 1% penicillin-streptomycin.
4. BP incubation medium: Brainphys neuronal medium, 0.5 mM L-glutamine.
5. Lipofectamine 2000.
6. Water bath 37 °C.
7. Cell culture incubator (37 °C, 5% CO<sub>2</sub>).
8. DNA plasmids: pORANGE GluA1-HaloTag knock-in [22] and PSD95.FingR-mEos3.2 [23].

### 2.2 HaloTag labeling

1. HaloLigand-JF646 stock: 140 µg/ml in DMSO. Store as 1 µL single-use aliquots at -20

°C. Protect from direct light.

- Humidified incubation chamber (plastic tray, wrapped in aluminum foil and with some moist tissues).

### 2.3 Fixation and Immunolabeling

- PEM buffer: 80 mM PIPES, 2 mM MgCl<sub>2</sub>, 5 mM EGTA, pH 6.8. Filter before use (<0.3 μm filter). Store at 4 °C for a maximum of two weeks.
- PFA (EM grade 32% glass ampoule). After opening, store at 4 °C in a closed tube. Warning: PFA is toxic, and quite volatile. Take proper safety precautions.
- Fixative PEM-PFA: Dilute PFA 1:8 in PEM buffer to obtain a 4% PFA solution. Prepare fresh.
- Phosphate buffered saline (PBS).
- PBS-Gly: 0.1 M glycine in PBS.
- Blocking buffer (prepare fresh): 10% (v/v) normal goat serum (NGS), 0.1% (v/v) Triton X-100 in PBS-Gly.
- Antibody buffer (prepare fresh): 5% (v/v) normal goat serum (NGS), 0.1% (v/v) Triton X-100 in PBS-Gly.
- Humidified incubation chamber (plastic tray, wrapped in aluminum foil and with some moist tissues).
- Primary antibody: mouse anti-Bassoon (Enzo, RRID AB\_10618753).
- Secondary antibody: goat anti-mouse-Alexa647.

### 2.4 Imaging buffers and mounting

- GLOX: 70 mg/mL glucose oxidase, 4 mg/ml catalase in PBS. Snap-freeze ~10 μL aliquots and store at -80 °C for up to a year. Keep thawed aliquots for maximum 1 week at 4 °C.
- MEA stock: 1 M cysteamine in 150 mM HCl. Store as ~10 μL single-use aliquots at -80 °C for maximum 1 year. MEA is sensitive to oxygen. Prevent exposure of the powder or dissolved solution to air as much as possible.
- Tris-glucose buffer: 50 mM Tris, 10 mM NaCl, 10% (w/v) glucose, pH 8.0. Filter through 0.2 μm filter. Store at 4 °C for up to two weeks, but check before use as the glucose in this buffer makes it prone to contamination.
- STORM-buffer (prepare fresh for each coverslip, just before mounting): Add 1 μL GLOX and 0.5 - 2 μL MEA to 100 μL Tris-glucose buffer. Preferably, prewarm the Tris-glucose buffer.
- Extracellular buffer: 10 mM HEPES, 120 mM NaCl, 3 mM KCl, 2 mM CaCl<sub>2</sub>, 2 mM MgCl<sub>2</sub>, 10 mM glucose, pH 7.35. Store at 4 °C for up to two weeks, but check before use as the glucose in this buffer makes it prone to contamination.
- Concave mounting slide (for dSTORM) (Figure 2B).
- Vacuum pump.
- Ludin chamber / imaging ring (for PALM) (Figure 2B).

### 2.5 Microscope setup

The imaging system described here is the setup used in our laboratory but can serve as an example to lay out the principal requirements for a suitable microscope setup. We use the commercially available Nanoimager microscope (Oxford Nanoimaging; ONI), equipped with a 100x oil-immersion objective (Olympus Plan Apo, NA 1.4) and a XYZ closed-loop piezo stage. Imaging lasers: 561-nm and 640-nm (>200 mW). Activation laser: 405 nm (>50

---

mW). An adjustable mirror for adjusting the angle of illumination. Camera for fluorescence detection: sCMOS (ORCA Flash 4, Hamamatsu), with an effective pixel size of 117 nm (*see* Note 3). Integrated filters are used to split far-red emission onto the right side of the camera and blue-green-red emission spectra on the left side. The imaging chamber can be temperature controlled. Continuous feedback control over the focus position is critical. This is built into some microscope models (as is the case for the NanoImager), or can be added with separate accessories.

## 2.6 Software

Integrated ONI software is used for detection and fitting of single-molecule blinking events. Alternatively, freely available options can be used: 3D-Daostorm [24], Picasso [25], Thunderstorm [26], DoM [27], ZOLA-3D [28], Fit3Dspline (integrated into SMAP) [29], SMAP [30] and Decode [31]. For additional processing steps, we use MATLAB.

## 3. METHODS

All steps are performed at room temperature, unless mentioned otherwise. See Figure 2A for a flowchart indicating which steps to follow for each individual method.

For immunostaining, go to 3.4.

### 3.1 Transfection of dissociated hippocampal rat neurons

Perform all steps in a sterile flow hood. DNA plasmids for the generation of a Halo knock-in are transfected on day in vitro (DIV) 3, and those expressing an intrabody at DIV 14 (*see* Note 4).

1. Prepare fresh 300  $\mu$ L BP incubation medium and 500  $\mu$ L BP full medium for each coverslip to be transfected. Warm to 37  $^{\circ}$ C.
2. Prepare the lipofectamine mix by diluting 3.3  $\mu$ L Lipofectamine 2000 in 100  $\mu$ L BrainPhys neuronal medium (without supplements) per coverslip to be transfected. Incubate for 5 minutes at room temperature.
3. For each coverslip, prepare a 1.5 mL microtube with 1  $\mu$ g of DNA and add 100  $\mu$ L BrainPhys neuronal medium (without supplements).
4. Add the lipofectamine mix to the DNA mix, gently mix using a pipette and incubate 30 minutes. DNA-Lipofectamine complex is stable for several hours at room temperature.
5. Transfer 50% (500  $\mu$ L) of the conditioned medium from each well to a new 12-wells plate. Add 500  $\mu$ L fresh BP full medium to each well of this new plate. Place this 'new plate' in the incubator.
6. Add 300  $\mu$ L BP incubation medium to each coverslip with neurons.
7. Using a pipette, gently drop the DNA-Lipofectamine mix onto the cells and place the plate in the incubator for 1-2 hours.
8. Transfer the coverslips to the 'new plate'.
9. Grow the neurons until DIV 21. Refresh half the medium with new BP full medium once a week.

For HaloTag labeling, go to step 3.2. For PALM imaging, go to step 3.5.

### 3.2 Live-cell HaloTag labeling

*See* Note 5 for more information about self-labeling enzymes.

During the labeling procedure, prevent exposure to direct light as much as possible.

1. Prepare an incubation chamber with a piece of parafilm.
2. Dilute the HaloLigand (JF646) 1:1000 in conditioned medium (1 mL medium is enough for 12 coverslips). Mix well by pipetting up and down.
3. Place drops of ~80  $\mu\text{L}$  on the parafilm and gently place the coverslips upside down on these drops. Place the incubation chamber in the incubator (37 °C, 5% CO<sub>2</sub>) for 15 minutes.
4. Transfer the coverslips back to the conditioned medium and continue with fixation (step 3.3) (*see Note 5*).

### 3.3 Fixation

*See Note 6* for more information about the importance of fixation and other methods.

1. Freshly prepare and prewarm PEM-PFA mixture at 37 °C.
2. Remove medium from cells using a vacuum pump and add 500  $\mu\text{L}$  fixative to the coverslip. Perform this step according to the PFA MSDS and handling protocols.
3. Incubate for 5-10 minutes with PEM-PFA.
4. Wash 3 times 5 minutes with PBS-Gly (1 mL). Samples can be stored and kept stable for several days at 4 °C in PBS.

In case of no antibody staining, go to step 3.5.

### 3.4 Immunolabeling

1. Incubate coverslips with ~250  $\mu\text{L}$  blocking buffer and incubate for 1 hour at 37 °C (*see Note 7*).
2. Prepare primary antibody dilutions in antibody buffer (50  $\mu\text{L}$  per coverslip).
3. Prepare an incubation chamber with parafilm. Place drops (~50  $\mu\text{L}$ ) with the antibody mixture on the parafilm and gently place the coverslips upside down on the drops.
4. Incubate for 2 hours at room temperature or overnight at 4 °C (*see Note 7*).
5. Wash three times 5 minutes with PBS-Gly.
6. Dilute secondary Alexa647-conjugated antibodies 1:400 in antibody buffer (50  $\mu\text{L}$  per coverslip).
7. Incubate the coverslips as in step 3 for 1 hour (at room temperature).
8. Wash three times 5 minutes with PBS-Gly.
9. Post fixation (optional): Wash once with PBS (no glycine) and perform another fixation with PEM-PFA for 5 minutes, and wash three times with PBS-Gly (*see Note 8*).
10. Store the coverslips in PBS until mounting. Samples remain stable for several days if kept at 4 °C and protected from light.

### 3.5 Sample preparation and mounting

#### 3.5.1 Live-cell PALM:

1. Preheat the microscope chamber to 37 °C.
2. Preheat extracellular buffer to 37 °C and filter (< 0.3  $\mu\text{m}$  filter).
3. Mount the coverslip in an imaging ring or Ludin chamber (Figure 2B). Gently wash the coverslip once with extracellular buffer before adding up to 500  $\mu\text{L}$  of extracellular buffer as final volume. Handle cells with care, try to avoid cells from drying and pipette slowly.
4. Continue at step 3.6.

#### 3.5.2 dSTORM:

1. Preheat the microscope chamber to 30 °C (*see Note 9*).

2. Prepare fresh STORM buffer (prepare just before mounting to prevent too much exposure to air).
3. Put 100  $\mu$ L STORM buffer on the concave slide and place the coverslip upside down, with the cells facing the buffer (Figure 2B).
4. Use tweezers or a pipette tip to stabilize the coverslip. Using a vacuum pump, remove excess buffer surrounding the coverslip. Next, gently apply some pressure on top of the coverslip and remove excess buffer. Relieve the pressure slowly. Try to prevent air bubbles from entering the buffer. The coverslip should now be stably fixed to the microscope slide.
5. Continue at step 3.7.

### 3.6 PALM imaging

1. Locate the transfected mEos3.2-positive cell using low laser powers or light source (488 nm wavelength). Avoid long exposures, as mEos3.2 is prone to photobleaching and will be converted by 488-nm light.
2. Set acquisition parameters: The number of frames depends largely on the number of blinking events that can be detected over time. Usually, this is somewhere between 5,000-20,000 frames. The exposure time and frame rate are of major importance for the quality of the acquisitions. For PALM imaging, we usually take a 50-ms (20 Hz) frame rate (*see* Note 10).
3. Set the angle of the laser to obtain oblique illumination (Figure 2C) (*see* Note 11).
4. Optional: Make a snapshot of the mEos3.2 using the 488-nm laser (at low laser power). We do not recommend this for low-expressing proteins for the same reason as mentioned at point 3.6.1. Alternatively, use a co-transfected marker in the far-red channel. Obtaining a diffraction-limited image can be useful for comparison with the super-resolution image later on.
5. Turn on green laser (561-nm). At first, single-molecule switching events will occur without usage of the 405-nm activation laser. Suitable 561-nm laser intensity should be balanced based on the sample, with the goal being the observation of clear single-molecule events. When this is the case, start the acquisition.
6. Gradually increase 405-nm laser intensity to enhance the conversion of green to red fluorescence, but make sure the blinking events do not become too dense and start to overlap.
7. Export the acquisition as a multi-layer TIF file.

### 3.7 dSTORM imaging (on Alexa647 or HaloLigand JF646)

1. Locate cells using low laser power light source.
2. Set acquisition parameters: The number of frames depends largely on the number of blinking events that can be detected over time. Usually, this is somewhere between 5,000-20,000 frames. The exposure time and frame rate are of major importance for the quality of the acquisitions. For STORM, we usually take a 50-ms (20 Hz) frame rate (*see* Note 10).
3. Set the angle of the laser to obtain oblique illumination (Figure 2C) (*see* Note 11).
4. Optional: Make a snapshot using the 642-nm laser (at low laser power). Alternatively, use a co-transfected marker in the green or red channel. Obtaining a diffraction-limited image can be useful for comparison with the super-resolution image later on.
5. Turn on red laser (642 nm). With high laser power, try to get most fluorophores to the

dark state. Initially, and especially for samples with high labeling density, this might require slightly higher laser powers than required for imaging (*see* Note 12).

6. Start the acquisition as soon as blinking events can be clearly identified as individual emission events.
7. Gradually increase 405-nm laser intensity to increase the number of blinking events per frame, but make sure the blinking events do not become too dense and start to overlap.
8. When finished, export the acquisition as multi-layer TIF file.

### 3.8 Data processing

1. Detection and fitting of single-molecules can be performed using a broad range of freely available software packages. We use ONI software integrated as part of the Nanoimager system. The software detects single emission events and uses fitting routines to estimate the coordinates of the molecules (Figure 1A). The output is usually a results table, containing the coordinates of each fitted localization, together with parameters like the frame number, photon count and localization precision. Alternative and freely available software options are provided in the material section (2.5).
2. Drift correction: As SMLM acquisitions take minutes to acquire, lateral drift can occur. Drift correction is a feature integrated in most processing software tools.
3. Filtering recurrent localizations (optional but strongly advised): Although many single-molecule emission events are short-lived, they can still be in the 'on state' for consecutive frames. To correct for this, these localizations can be filtered out, or merged. This feature is integrated in most processing software. If this step results in a significant reduction in the number of localizations, consider imaging with longer exposure time and higher laser power (*see* Note 10).
4. Filtering on localization precision: Considered one of the most important filtering steps, filtering on localization precision allows for the removal of localization events that are either the result of noise or overlapping localizations. Alternatively, or in addition to, filtering on the shape of the Gaussian can be performed. The latter being helpful in removing overlapping emission events. We usually filter out all localizations with a localization precision of  $> 15$  nm for STORM and  $> 25$  nm for PALM imaging. This difference has to do with the fact that organic dyes provide more photons per emission event compared to fluorescent proteins, and thus a better average localization precision.
5. Filtering on photon count: Additional filtering on photon count might help to reduce the amount of noise in the dataset due to localizations derived from non-emission events. Note that localizations with a low photon count often have a low localization precision as well and most are probably filtered out when filtering just on the localization precision.

### 3.9 Visualization and data analysis

1. Rendering/Binning: The most common method of visualizing SMLM datasets is by binning the localizations into pixels. The localizations are converted to pixels and plotted as a Gaussian distribution with the standard deviation adjusted by the localization precision. Figure 3 shows examples of rendered super-resolution plots with their diffraction-limited images, for both PALM imaging of mEos3.2-tagged intrabodies targeting PSD95 and dSTORM imaging of HaloTag-GluA1 and antibody-tagged Bassoon. Commonly used pixel sizes for rendering are in the range of 10-50 nm or half the average localization precision. Combining a rendered image with a diffraction-limited snapshot of the same region, allows for visualization of the improvement in resolution



and judgement of image quality as much can be learned by "just looking at the thing" [32].

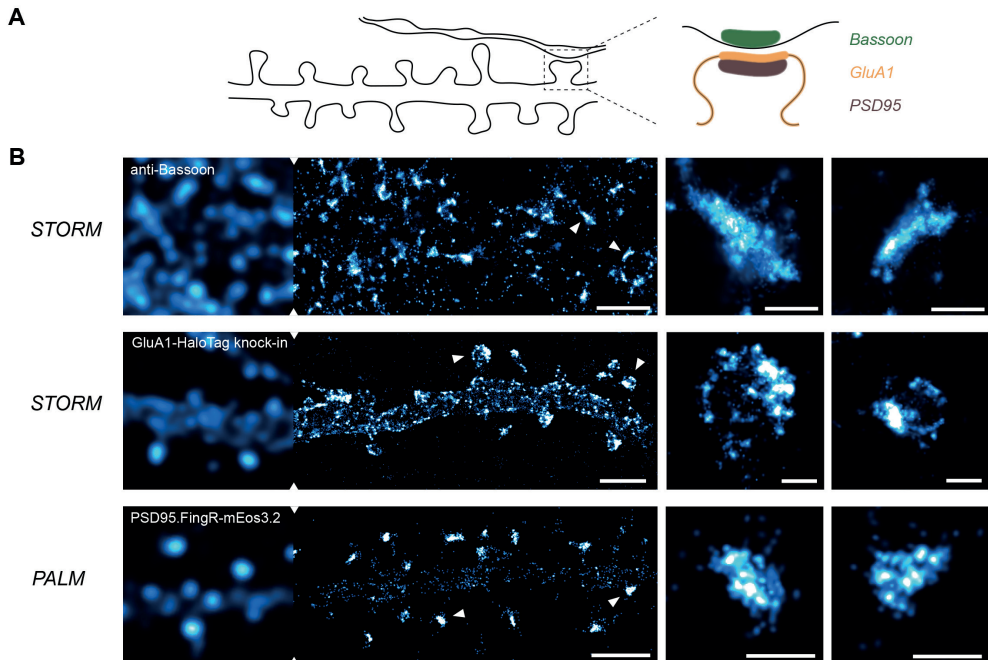


**Figure 3. SMLM of synaptic proteins.**

(A) Illustration of the expected localization of different synaptic proteins in the dendrite or axon. Scaffolding protein Bassoon localizes in the active zone of the presynaptic bouton, glutamate receptor GluA1 is localized on the dendritic membrane with an enrichment on the postsynaptic membrane, and PSD95 is a postsynaptic scaffolding protein. (B) Examples of dSTORM acquisitions of Bassoon using immunolabeling, endogenously tagged GluA1 with HaloTag, and live-cell PALM of PSD95 using expression of mEos3.2-fused intrabodies. Comparing the diffraction-limited image on the left part with the SMLM acquisition. Scalebars: 2  $\mu\text{m}$ , zooms: 300 nm.

2. Analyzing SMLM datasets: Extracting information about protein distribution in SMLM datasets can be challenging, and highly depends on your research question. A good way to start is exploring the heterogeneity in protein density using the molecular coordinates of the localizations instead of rendered images (Figure 4). Density can thus not only be determined from pixel intensity but can be calculated directly from the molecular coordinates. Examples of these are the so-called local density values and Voronoi diagrams. See Figure 4B for a comparison of these different plotting methods.
3. The local density value is calculated as the number of localizations in a given radius (in this case 5 times the mean nearest neighbor distance (MNND)) [33]. To calculate the local density, we use the MATLAB functions `knnsearch` (for determining the NND) and `rangeseach` (for the local density). The outcome can be used as color-code for plotting, as well as being used for further analysis. We use 5 times the MNND as this normalizes for differences in overall localization density across the field of view and between datasets.
4. Voronoi diagrams are aimed to segment localizations into areas, reflecting the density based on the distance of each localization to its neighbors. Thus, the area of each so-called Voronoi cell, reflects its density relative to the overall density of the acquisition. Voronoi

diagrams can be generated using the MATLAB function `voronoi`. The area of individual Voronoi cells can be calculated from the output vertices.

5. Statistical analysis: Both the local density and Voronoi diagrams can yield important information about protein density. Further image analysis including cluster detection is often very specific to distinct biological questions. Therefore, we would like to refer to other sources for more information regarding SMLM post-imaging analysis options including cluster detection, segmentation, protein counting and co-localization [34,19,35].

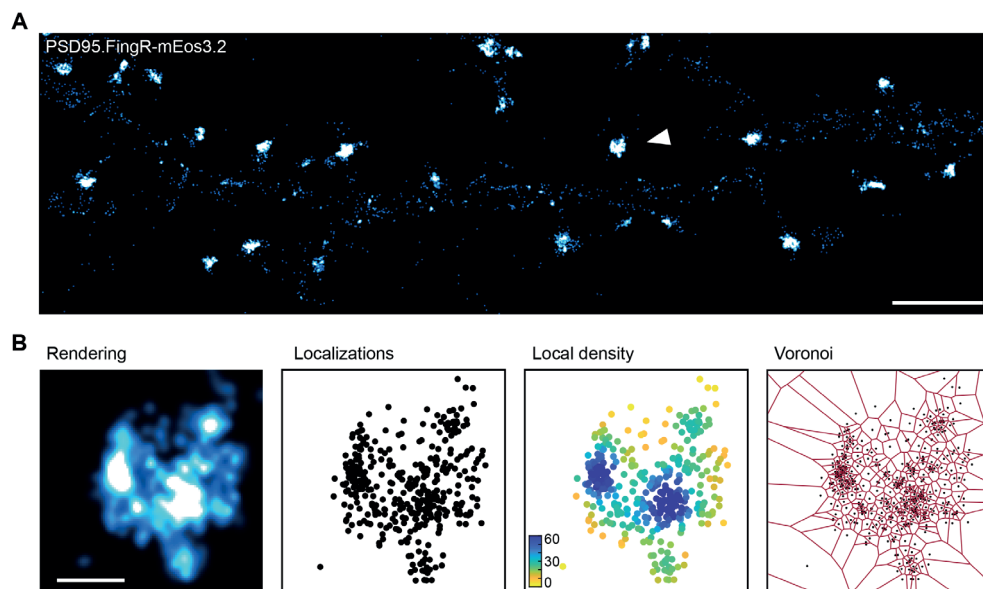


**Figure 4. Data visualization and evaluation.**

(A) Rendered image from a SMLM acquisition of PSD95.FingR-mEos3.2. (B) Examples of different visualization and evaluation options. Rendering: localizations are converted to pixels by plotting them as Gaussians with integrated density 1 and the localization error as SD. Localizations: Plotting the centroids of the fluorophores. Local density: Each localization is color-coded for the number of localizations within a given radius. Voronoi: Boundaries can be drawn that assign each localization to their own area that includes all points closer to that localization than any other localization. This area reflects its density relative to the overall density. Scalebar: 2  $\mu\text{m}$ , zoom: 200 nm.

#### 4. NOTES

**1:** Dye selection for dSTORM. Alexa647 is considered as the best dye for dSTORM, but other dyes work as well and new dyes suitable for dSTORM are constantly being developed, mostly in the far-red emission spectrum. Besides Alexa647 and JF646, another dye that works well in our hands is CF568. CF568 is a bit more difficult to get into the dark state (also see Note 12), and thus not advised for very dense protein structures or proteins with high expression levels. Note that imaging CF568 requires a different laser for excitation than described in the protocol (where Alexa647 and JF646 are used).

**2:** Choice of labeling method. In our experience, protein abundance and the availability of specific antibodies are the main challenges that impact the quality of labeling, and thus the choice of method. For example, PALM on endogenous proteins is only feasible for medium to highly expressed proteins. For STORM, endogenous tagging of a protein with HaloTag

---

can be used, but with the note that the dye to protein ratio is much lower than labeling with antibodies. Alternatively, and not described here, proteins can be tagged with other fluorescent proteins like GFP or small epitope tags like HA, FLAG and ALFA-tag, which can be subsequently labeled with organic dyes using antibodies or nanobodies, significantly amplifying the signal and making it possible to perform dSTORM.

**3:** Pixel size. The optimal pixel size for a given experiment depends on the number of expected photons and background. Usually, a pixel size in the range of 100-160 nm is used, based on the point spread function [2].

**4:** Optimal DIV for transfection of hippocampal rat neurons. For genomic tagging of a gene (coding for a protein of interest) we advise to transfect at a relatively young age (DIV2-5). As neurons mature, the transfection efficiency drops quite significantly. Also, and especially for proteins with a low turnover, a longer window between transfection and imaging allows for more of the protein pool to be replaced with the tagged version [22]. For exogenous expression of a fusion protein or intrabody, the optimal window between transfection and imaging day has to be optimized for individual constructs, but we usually use 3-7 days between transfection and imaging. If exogenous expression of a recombinant fusion protein is used, it is critical make sure the level of overexpression does not alter the localization of the protein.

**5:** HaloTag Ligand labeling. HaloTag is a haloalkane dehalogenase enzyme which is designed to covalently bind to synthetic ligands (HaloLigand) [13] (Figure 2A). The HaloTag can be coupled to the protein of interest, for example via genomic tagging (as used in this protocol), or through exogenous expression of HaloTag fusion proteins. The HaloLigand is commercially available conjugated to organic dyes. As the HaloTag – HaloLigand binding is enzymatic, live-cell labeling is preferred over labeling of already fixed samples. In addition to the protocol described here, always check the protocol of the supplier and adjust if needed. The HaloTag Ligand-JF646 used in this protocol is membrane permeable. Thus, both intracellular and extracellular HaloTag-fused proteins are labeled. The optimal length of labeling has to be determined experimentally. Extensive washing of the HaloLigand before fixation is not needed. Besides the potential harmful effects of washing on living cells, most fixatives do not react with the HaloLigand as it is not a protein. The washing steps after fixation will remove any unbound HaloLigand.

**6:** Type and length of fixation. A good fixation protocol is considered one of the most important steps of any super-resolution imaging technique as it is key to the preservation of the cell's ultrastructure. Sometimes, glutaraldehyde is used as a fixative in addition to or to replace PFA. When used, additional quenching steps (to reduce autofluorescence) using fresh NaBH<sub>4</sub> are advised. Alternatively, fixation using ice-cold methanol is sometimes used, but this is not compatible with all antibodies and might negatively influence the ultrastructure, particularly membrane-associated complexes, more than PFA. Therefore, we do not recommend this for SMLM. Although 10 minutes of PEM-PFA fixation is the standard, staining quality can benefit from optimizing the duration of fixation.

**7:** Blocking and immunolabeling. The protocol described here is a general protocol for immunolabeling that is used in our lab. Other blocking reagents like bovine serum albumin

(BSA) can be used instead of NGS. Also, the duration and temperature of the antibody incubation step, as well as antibody concentration has to be optimized experimentally for each protein labeling.

**8:** Post-fixation. Although not a must, post-fixation allows for better preservation of the staining if imaging is not performed directly after labeling. Post-fixed cells can be stored for several days in PBS at 4 °C.

**9:** Temperature control of microscope. Preheating and controlling the temperature of the microscope system is also advised for fixed samples. During an acquisition, heat is produced which might cause some drift, which in our hands is reduced if the temperature is already stable at around 30 °C. Therefore, we also advise to keep the STORM buffer and glass slides at least at room temperature.

**10:** Exposure time, frame rate and laser power. Longer exposure time/lower frame rate allows for more photons to be collected from single emission events, which positively influences the localization precision. However, a long exposure time can also increase the chance of overlapping single-molecules, and when performing PALM in live cells, the movement of molecules within the exposure time of a single frame reduces the localization precision due to motion blurring. Depending on the camera, imaging smaller ROIs can allow for a higher frame rate. Alternatively, higher laser power can be used, but this reduces the lifetime of an emission event.

**11:** Illumination angle. SMLM experiments are generally performed with near TIRF illumination or so-called oblique illumination. Oblique illumination can be achieved by changing the angle of illumination towards full TIRF. Adjust the angle so that in-focus fluorescence events are mostly retained, but that out-of-focus events are not excited.

**12:** Induction of dark state. In the presence of the reducing STORM buffer, high laser power will turn molecules into the dark state. The most common issue faced, is the inability of reducing the number of blinks per frame causing individual emission events to overlap. Using a higher concentration of MEA in the STORM buffer can help. Alternatively, 2-beta-mercapto-ethanol (BME) is sometimes used instead of MEA, depending on the organic dye used for imaging. In our hands, using a few short pulses of the 488-nm or 561-nm laser can help to bring more far-red emitting dyes to the dark state, but with the risk of irreversible photo-bleaching.

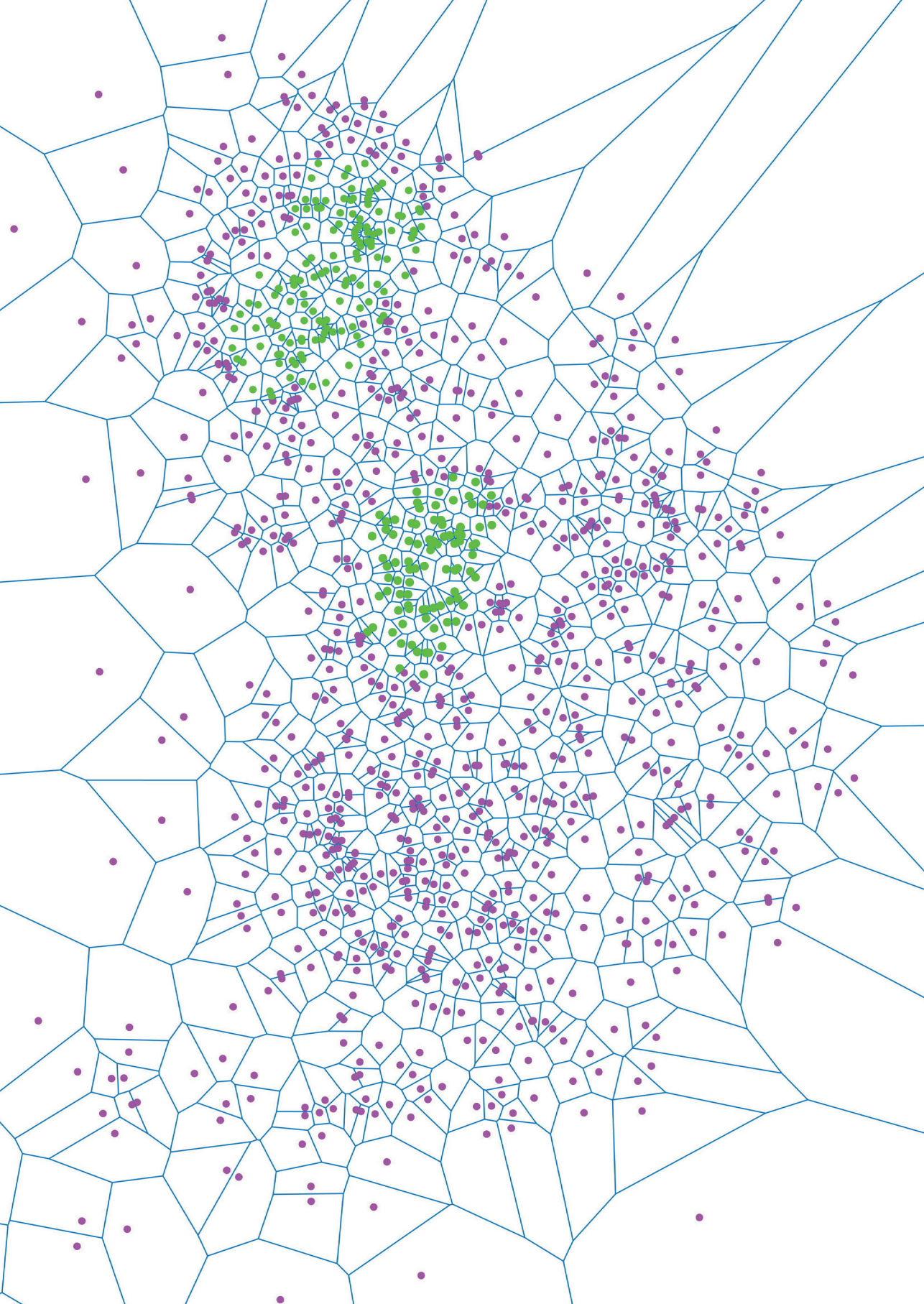
## ACKNOWLEDGEMENTS

This work was supported by the Netherlands Organization for Scientific Research (ALW-VIDI 171.029 to HDM) and the European Research Council (ERC-StG 716011 to HDM).

## REFERENCES

1. Vangindertael J, Camacho R, Sempels W, Mizuno H, Dedecker P, Janssen KPF (2018) An introduction to optical super-resolution microscopy for the adventurous biologist. *Methods Appl Fluoresc* 6 (2):022003. doi:10.1088/2050-6120/aaae0c
2. Thompson RE, Larson DR, Webb WW (2002) Precise nanometer localization analysis for individual fluorescent probes. *Biophys J* 82 (5):2775-2783. doi:10.1016/S0006-3495(02)75618-X
3. Gould TJ, Verkhusa VV, Hess ST (2009) Imaging biological structures with fluorescence photoactivation localization microscopy. *Nat Protoc* 4 (3):291-308. doi:10.1038/nprot.2008.246
4. Betzig E, Patterson GH, Sougrat R, Lindwasser OW, Olenych S, Bonifacino JS, Davidson MW, Lippincott-Schwartz J, Hess HF (2006) Imaging intracellular fluorescent proteins at nanometer resolution. *Science* 313 (5793):1642-1645. doi:10.1126/science.1127344
5. Hess ST, Girirajan TP, Mason MD (2006) Ultra-high resolution imaging by fluorescence photoactivation localization microscopy. *Biophys J* 91 (11):4258-4272. doi:10.1529/biophysj.106.091116
6. Rust MJ, Bates M, Zhuang X (2006) Sub-diffraction-limit imaging by stochastic optical reconstruction microscopy (STORM). *Nat Methods* 3 (10):793-795. doi:10.1038/nmeth929
7. Heilemann M, van de Linde S, Schüttelz M, Kasper R, Seefeldt B, Mukherjee A, Tinnefeld P, Sauer M (2008) Subdiffraction-resolution fluorescence imaging with conventional fluorescent probes. *Angew Chem Int Ed Engl* 47 (33):6172-6176. doi:10.1002/anie.200802376
8. Jungmann R, Avendano MS, Woehrstein JB, Dai M, Shih WM, Yin P (2014) Multiplexed 3D cellular super-resolution imaging with DNA-PAINT and Exchange-PAINT. *Nat Methods* 11 (3):313-318. doi:10.1038/nmeth.2835
9. Balzarotti F, Eilers Y, Gwosch KC, Gynna AH, Westphal V, Stefani FD, Elf J, Hell SW (2017) Nanometer resolution imaging and tracking of fluorescent molecules with minimal photon fluxes. *Science* 355 (6325):606-612. doi:10.1126/science.aak9913
10. Li H, Vaughan JC (2018) Switchable Fluorophores for Single-Molecule Localization Microscopy. *Chem Rev* 118 (18):9412-9454. doi:10.1021/acs.chemrev.7b00767
11. Dempsey GT, Vaughan JC, Chen KH, Bates M, Zhuang X (2011) Evaluation of fluorophores for optimal performance in localization-based super-resolution imaging. *Nat Methods* 8 (12):1027-1036. doi:10.1038/nmeth.1768
12. Samanta S, Gong W, Li W, Sharma A, Shim I, Zhang W, Das P, Pan W, Liu L, Yang Z, Qu J, Kim JS (2019) Organic fluorescent probes for stochastic optical reconstruction microscopy (STORM): Recent highlights and future possibilities. *Coordination Chemistry Reviews* 380:17-34 Contents. doi:10.1016/j.ccr.2018.08.006
13. Los GV, Encell LP, McDougall MG, Hartzell DD, Karassina N, Zimprich C, Wood MG, Learish R, Ohana RF, Urh M, Simpson D, Mendez J, Zimmerman K, Otto P, Vidugiris G, Zhu J, Darzins A, Klaubert DH, Bulleit RF, Wood KV (2008) HaloTag: a novel protein labeling technology for cell imaging and protein analysis. *ACS Chem Biol* 3 (6):373-382. doi:10.1021/cb800025k
14. Keppler A, Gendreizig S, Gronemeyer T, Pick H, Vogel H, Johnsson K (2003) A general method for the covalent labeling of fusion proteins with small molecules in vivo. *Nat Biotechnol* 21 (1):86-89. doi:10.1038/nbt765
15. Gautier A, Juillerat A, Heinis C, Correa IR, Jr., Kindermann M, Beauflis F, Johnsson K (2008) An engineered protein tag for multiprotein labeling in living cells. *Chem Biol* 15 (2):128-136. doi:10.1016/j.chembiol.2008.01.007
16. Jacquemet G, Carisey AF, Hamidi H, Henriques R, Letierrier C (2020) The cell biologist's guide to super-resolution microscopy. *J Cell Sci* 133 (11). doi:10.1242/jcs.240713
17. Schermelleh L, Ferrand A, Huser T, Eggeling C, Sauer M, Biehlermaier O, Drummen GPC (2019) Super-resolution microscopy demystified. *Nat Cell Biol* 21 (1):72-84. doi:10.1038/s41556-018-0251-8
18. Wait EC, Reiche MA, Chew TL (2020) Hypothesis-driven quantitative fluorescence microscopy - the importance of reverse-thinking in experimental design. *J Cell Sci* 133 (21). doi:10.1242/jcs.250027
19. Wu YL, Tschanz A, Krupnik L, Ries J (2020) Quantitative Data Analysis in Single-Molecule Localization Microscopy. *Trends Cell Biol* 30 (11):837-851. doi:10.1016/j.tcb.2020.07.005
20. Jimenez A, Friedl K, Letierrier C (2020) About samples, giving examples: Optimized Single Molecule Localization Microscopy. *Methods* 174:100-114. doi:10.1016/j.ymeth.2019.05.008
21. Yang X, Specht CG (2020) Practical Guidelines for Two-Color SMLM of Synaptic Proteins in Cultured Neurons. In: Yamamoto N, Okada Y (eds) *Single Molecule Microscopy in Neurobiology*. *Neuromethods*. Humana, New York, NY. doi:10.1007/978-1-0716-0532-5\_9
22. Willems J, de Jong APH, Scheefhals N, Mertens E, Catsburg LAE, Poorthuis RB, de Winter F, Verhaagen J, Meye FJ, MacGillavry HD (2020) ORANGE: A CRISPR/Cas9-based genome editing toolbox for epitope tagging of endogenous proteins in neurons. *PLoS Biol* 18 (4):e3000665. doi:10.1371/journal.pbio.3000665
23. Gross GG, Junge JA, Mora RJ, Kwon HB, Olson CA, Takahashi TT, Liman ER, Ellis-Davies GC, McGee AW, Sabatini BL, Roberts RW, Arnold DB (2013) Recombinant probes for visualizing endogenous synaptic proteins in living neurons. *Neuron* 78 (6):971-985. doi:10.1016/j.neuron.2013.04.017
24. Babcock H, Sigal YM, Zhuang X (2012) A high-density 3D localization algorithm for stochastic optical reconstruction microscopy. *Opt Nanoscopy* 1 (6). doi:10.1186/2192-2853-1-6
25. Schnitzbauer J, Strauss MT, Schlichthaerle T, Schueder F, Jungmann R (2017) Super-resolution microscopy with DNA-PAINT. *Nat Protoc* 12 (6):1198-1228. doi:10.1038/nprot.2017.024
26. Ovesny M, Krizek P, Borkovec J, Svindrych Z, Hagen GM (2014) ThunderSTORM: a comprehensive ImageJ plug-in for PALM and STORM data analysis and super-resolution imaging. *Bioinformatics* 30 (16):2389-2390. doi:10.1093/bioinformatics/btu202
27. Chazeau A, Katrukha EA, Hoogenraad CC, Kapitein LC (2016) Studying neuronal microtubule organization and microtubule-associated proteins using single molecule localization microscopy. *Methods Cell Biol* 131:127-149. doi:10.1016/bs.mcb.2015.06.017

28. Aristov A, Lelandais B, Rensen E, Zimmer C (2018) ZOLA-3D allows flexible 3D localization microscopy over an adjustable axial range. *Nat Commun* 9 (1):2409. doi:10.1038/s41467-018-04709-4
29. Li Y, Mund M, Hoess P, Deschamps J, Matti U, Nijmeijer B, Sabinina VJ, Ellenberg J, Schoen I, Ries J (2018) Real-time 3D single-molecule localization using experimental point spread functions. *Nat Methods* 15 (5):367-369. doi:10.1038/nmeth.4661
30. Ries J (2020) SMAP: a modular super-resolution microscopy analysis platform for SMLM data. *Nat Methods* 17 (9):870-872. doi:10.1038/s41592-020-0938-1
31. Speiser A, Muller L-R, Matti U, Obara CJ, Legant WR, Kreshuk A, Macke JH, Ries J, Turaga SC (2020) Deep learning enables fast and dense single-molecule localization with high accuracy. *BioRxiv*. doi:10.1101/2020.10.26.355164
32. Mund M, Ries J (2020) How good are my data? Reference standards in superresolution microscopy. *Mol Biol Cell* 31 (19):2093-2096. doi:10.1091/mbc.E19-04-0189
33. MacGillavry HD, Song Y, Raghavachari S, Blanpied TA (2013) Nanoscale scaffolding domains within the postsynaptic density concentrate synaptic AMPA receptors. *Neuron* 78 (4):615-622. doi:10.1016/j.neuron.2013.03.009
34. Khater IM, Nabi IR, Hamarneh G (2020) A Review of Super-Resolution Single-Molecule Localization Microscopy Cluster Analysis and Quantification Methods. *Patterns (N Y)* 1 (3):100038. doi:10.1016/j.patter.2020.100038
35. Baddeley D, Bewersdorf J (2018) Biological Insight from Super-Resolution Microscopy: What We Can Learn from Localization-Based Images. *Annu Rev Biochem* 87:965-989. doi:10.1146/annurev-biochem-060815-014801



# 5

---

## **A coordinate-based co-localization index to quantify and visualize spatial associations in single-molecule localization microscopy**

Jelmer Willems and Harold D. MacGillavry

Scientific Reports (2022); 12(1): 4676

---

Cell Biology, Neurobiology and Biophysics, Department of Biology, Faculty of Science, Utrecht University, Utrecht, the Netherlands



---

## ABSTRACT

Visualizing the subcellular distribution of proteins and determining whether specific proteins co-localize is one of the main strategies in determining the organization and potential interactions of protein complexes in biological samples. The development of super-resolution microscopy techniques such as single-molecule localization microscopy (SMLM) has tremendously increased the ability to resolve protein distribution at nanometer resolution. As super-resolution imaging techniques are becoming instrumental in revealing novel biological insights, new quantitative approaches that exploit the unique nature of SMLM datasets are required. Here, we present a new, local density-based algorithm to quantify co-localization in dual-color SMLM datasets. We show that this method is broadly applicable and only requires molecular coordinates and their localization precision as inputs. Using simulated point patterns, we show that this method robustly measures the co-localization in dual-color SMLM datasets, independent of localization density, but with high sensitivity towards local enrichments. We further validated our method using SMLM imaging of the microtubule network in epithelial cells and used it to study the spatial association between proteins at neuronal synapses. Together, we present a simple and easy-to-use, but powerful method to analyze the spatial association of molecules in dual-color SMLM datasets.

## INTRODUCTION

The precise spatial organization of protein complexes within subcellular domains underlies fundamental cellular processes such as migration, cell division and intercellular communication. A central goal in cell biology is therefore to define the mechanisms that control protein distribution and their assembly into functional multi-protein complexes. Fluorescence microscopy evolved to be a powerful and popular strategy to investigate whether specific proteins co-localize and assemble in macromolecular complexes in cells. The development of super-resolution microscopy techniques has tremendously increased the ability to resolve protein distribution at unprecedented resolution<sup>1,2</sup>. In particular, single-molecule localization microscopy (SMLM) techniques such as photoactivated localization microscopy (PALM)<sup>3,4</sup>, (direct) stochastic optical reconstruction microscopy ((d)STORM)<sup>5,6</sup>, point accumulation for imaging in nanoscale topography (PAINT)<sup>7</sup> and MINIFLUX<sup>8</sup> achieve a spatial resolution down to only a few tens of nanometers. At this scale, protein organization within subcellular compartments and organelles can be effectively investigated and SMLM has been instrumental in numerous recent discoveries in cell biology<sup>9</sup>.

In SMLM, individual fluorophores are stochastically activated so that during image acquisition, sequential frames contain only a small subset of isolated emission events<sup>10,11</sup>. These events are collected over many thousands over frames and can then be localized using computational fitting routines that determine the position of single molecules with nanometer precision. These localizations are then used to reconstruct a super-resolved image with a ~10X improved spatial resolution (<30 nm) compared to conventional, diffraction-limited images. Thus, SMLM images are principally built from a list of molecular coordinates, providing unique opportunities to quantitatively analyze the spatial distribution of molecules in cells and extract new meaningful biological insights<sup>12,13</sup>. As super-resolution imaging techniques continue to undergo significant technical improvements at a rapid pace, there is an increasing demand for quantitative approaches that exploit the unique nature of SMLM datasets.

One approach to analyze SMLM datasets is to use image analysis methods developed for conventional fluorescence images. The coordinate-based data is then first converted to intensity-based, pixelated images by means of binning. As a result, however, considerable

information is lost as the gain in resolution by using super-resolution imaging is then partially undone. Also, the conversion to pixelated images relies on additional processing steps that are often parameter-driven, influencing the resulting image. Therefore, a multitude of approaches have been developed that quantify coordinate-based images directly<sup>13,14</sup>. Specifically, statistical spatial analysis methods such as Ripley's K function and derivatives thereof<sup>15,16</sup>, or cross-correlation analysis<sup>17-19</sup> are often used to determine if observed point patterns are homogeneous, dispersed, or clustered. Furthermore, various dedicated cluster analyses have been developed to detect and segment clusters in point patterns that use hierarchical, density-based clustering algorithms<sup>20,21</sup>, Voronoi tessellation<sup>22,23</sup>, or Bayesian methods<sup>24</sup>.

To explore if proteins interact or assemble in functional complexes in cells, dual-color fluorescence microscopy is often used to detect co-localization of two labeled molecules. Co-localization can then be quantified as the degree of overlap using Manders' overlap coefficient<sup>25</sup>, or correlation, e.g. Pearson's  $r$ <sup>26</sup> of pixel intensities across the entire image or region of interest (ROI). In SMLM datasets the concept of co-localization however is less trivial to quantify, as two molecules are highly unlikely to be in the exact same position. In SMLM, co-localization is therefore often defined as a measure of intermolecular distance, or spatial association. Several co-localization methods have been developed that directly analyze point patterns by extending spatial analysis methods<sup>27,28</sup>, Voronoi tessellation<sup>29</sup>, or combine cluster detection with co-localization analysis<sup>30-32</sup>. While all these methods have their strengths, they are often embedded in other software pipelines, need user-defined parameters, are focused on detecting co-localization in datasets that contain clusters.

Here, we combined and adapted some of these existing approaches and propose a local density-based co-localization analysis for dual-color SMLM data. We show that it is broadly applicable, does not rely on user-defined setting of parameters and only requires molecular coordinates and their localization precision as inputs. Using computational simulations of SMLM datasets, we show that this method robustly detects spatial association between two channels, independent of localization density. We present this method as a stand-alone MATLAB routine that can be used in combination with virtually all post-imaging processing tools that are used to extract and filter localizations from SMLM images. We further validated our method using SMLM of the microtubule network in U2OS cells and finally applied it to study protein distribution at neuronal synapses. Together, we present a simple and easy-to-use, yet powerful method to measure co-localization in dual-color SMLM datasets.

## RESULTS

### A local density-based co-localization index to quantify spatial association of molecules in dual-color SMLM

In dual-color SMLM experiments, the density of localizations can vary significantly across the field of view and between the two channels. This depends on the local abundance of the labeled proteins, labeling strategy, and data processing and filtering steps. To normalize for these variations, in the first step we calculate the local density ( $LD$ ) value for each localization in a given dataset by counting the number of localizations within a distance  $d$ . The distance  $d$  thus determines the sensitivity of the  $LD$ -value and could be linked to the mean nearest neighbor distance (MNND)<sup>31,33</sup>. However, while theoretically a smaller  $d$  would be beneficial for the detection of sub-micron differences in localization density, the effective resolution obtained with SMLM data is limited by a combination of both the MNND and the localization error ( $\epsilon$ )<sup>34,35</sup>. Therefore, the localization error and MNND are determined by taking the average value over all localizations. Together, we use the effective resolution as a

---

single value calculated for the complete dataset as  $d$ .

$$d = \sqrt{MNND^2 + \varepsilon^2}$$

In this way, the LD-value assigned to each localization represents the density around this localization in a manner that normalizes across variations in density within the full dataset, thus representing the effective resolution.

Then, to determine the coordinate-based co-localization between two channels, we took a similar strategy as for calculating the LD-value. To calculate the co-localization index  $CI$ , for each localization in channel A the number of localizations in channel B are counted within the distance set by the effective resolution in channel B (Fig. 1a). This number is then divided by the mean LD-value of the localizations in channel B. Thus, the co-localization index  $CI$  for the  $i$ th localization in channel A is computed as:

$$CI_i^A = \frac{N_{Ai}^B(d_B)}{(LD_B)}$$

where  $N_{Ai}^B$  is the number of localizations in channel B within the distance  $d$  around the  $i$ th localization in channel A. Conversely, for each localization in channel B the  $CI$  is calculated as:

$$CI_i^B = \frac{N_{Bi}^A(d_A)}{(LD_A)}$$

Thus, the co-localization index of any given localization is a measure of the local density of nearby molecules in the other channel (Fig. 1a). If the local density of  $Ai$  in channel B is the same as the average local density in channel B,  $CI_i^A$  will be equal to 1.

To demonstrate this approach, we used simulated dual-color SMLM datasets of randomly distributed localizations with varying degrees of overlap between the channels (ranging from 0 to 100% overlap; Fig. 1b). Since the co-localization index is determined for each localization individually, co-localization can be visualized as a scatter plot color-coded for the co-localization index. These ‘co-localization maps’ visualize the spatial distribution of co-localization between the channels (Fig. 1c). Averaging the co-localization index of these localizations for 100 simulated ROIs showed that, the local density-based co-localization index scales linearly between 0 and 1 for homogeneously distributed point patterns, where 0 indicates no co-localization and 1 indicates complete co-localization (co-localization index channel A, 0% overlap:  $0.0067 \pm 0.0002$ , 25% overlap:  $0.25 \pm 0.001$ , 50% overlap:  $0.51 \pm 0.002$ , 75% overlap:  $0.76 \pm 0.002$ , 100% overlap:  $1.00 \pm 0.001$ ,  $P < 0.001$ , ANOVA,  $n = 100$  point patterns/condition; Fig. 1c). In addition, we performed similar simulations, using sets of multiple overlapping and non-overlapping clusters (Fig. S1a-c) and challenged the method with simulations in which the localizations in channel A are surrounding, but not overlapping localizations in channel B, in a relative confined area (Fig. S2).

Next, we aimed to investigate the effect of variations that usually occur in an experimental setting. First, to investigate the effect of variations in the effective resolution on the observed co-localization, we considered the 50% overlap condition in (Fig. 1b) and varied the localization densities (which influences the MNND) (Fig. 1d) or localization error (Fig. 1e). Importantly, the co-localization index remained close to the ground truth across a wide range of localization densities and localization errors (Fig. 1d, e). The co-localization was only slightly overestimated when the localization error was too high ( $>50$  nm) or the localization

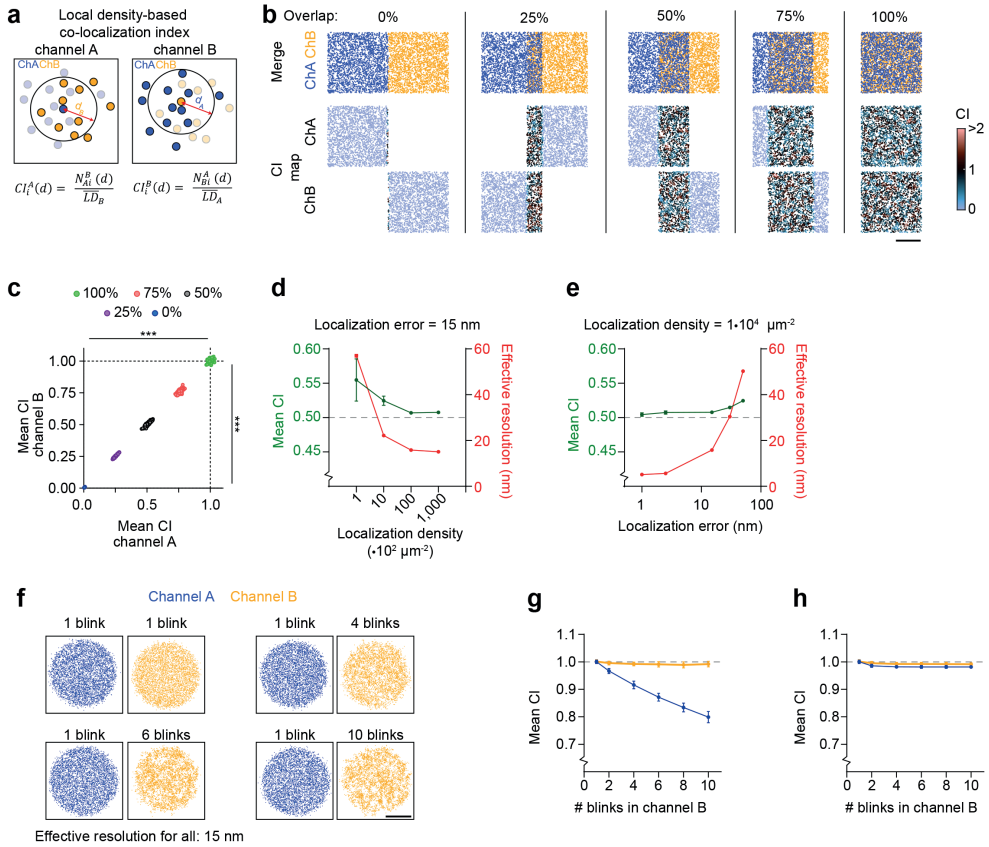


**Figure 1. Local density-based co-localization index**

(a) Concept of coordinate-based co-localization. (b) Simulations of point distributions with 1,000 localizations with an average localization error of 15 nm (effective resolution  $\sim 16$  nm) and different amount of overlap between the two channels. Shown are a merge and the co-localization maps. The color code indicates the degree of co-localization. Scale bar, 100 nm. (c) Graph of mean co-localization index of 100 simulated point patterns for each of the conditions shown in (b). (d) Effect of changing localization density on the effective resolution and co-localization outcome (in case of 50% overlapping structures as in A). (e) Effect of changing localization precision on the effective resolution and co-localization outcome (in case of 50% overlapping structures as in a). (f) Simulations of point distributions with increased blinking in channel B (yellow) versus channel A (blue), without changing the total number of localizations. Scale bar, 200 nm. (g) Analysis of co-localization for channel A (blue) and B (yellow). Number of blinks in channel A remained at 1. (h) Analysis of co-localization with increased blinking in channel B, thereby also increasing the total number of localizations relative to channel A. Data are represented as means  $\pm$  SEM. \*\*\*  $P < 0.001$ , ANOVA. CI, co-localization index; LD, local density; ns, not significant.

density was too low ( $< 1000 \mu\text{m}^{-2}$ ), i.e., conditions that are generally considered to be insufficient to reconstruct valuable SMLM images. To illustrate this further, we additionally used simulated sets of multiple clusters containing of which half of them have overlap with the second channel and decreased the density of localizations in the second channel (Fig. S1d-f). As expected, co-localization is robustly measured over a large range of densities.

Second, we tested the influence of differences in localization blinking kinetics as organic dyes can undergo multiple on-off switching cycles. To test this, we simulated a spatial pattern without blinking (channel A) and measured overlap with a channel with increasing blinking

---

(channel B) but keeping the total number of localizations between the channels the same (Fig. 1f). With increased blinking, small artificial clusters occurred in channel B, lowering the measured co-localization between the channels, as the spatial distribution of the localizations starts to differ (Fig. 1g). This effect is limited in cases where the labeling density, and thus the number of dyes in the sample, is the same between the channels. As such, more blinking results in more localizations, thereby only marginally affecting the spatial distribution, and thus not influencing the co-localization between the channels (Fig 1h).

Lastly, we tested the effect of background localizations on the outcome of the co-localization. As all localizations were included in the analysis, increasing the background influenced co-localization outcome (Fig. S1g-i). Thus, depending on the biological question, background should be taken into account during pre-processing steps prior to co-localization analysis.

In summary, our approach provides a robust method to determine the spatial co-localization between localizations in dual-color SMLM experiments. It provides a measure for the similarity in spatial distribution, independent from density and reflecting the effective resolution. The algorithm is available as a MATLAB function that requires the x-y coordinates of the localizations in the two channels and their localization error as the only inputs (MATLAB Code S1, Method section, and Supplementary test data sets).

### **Detection of spatial association within highly crowded regions**

In biological samples, proteins are usually not homogeneously distributed, but are often concentrated in spatially organized subcellular compartments that contain local variations in enrichments, or nanoscale subdomains<sup>36-38</sup>. Within SMLM datasets, this results in substantial variations in local densities across the analyzed image. We reasoned that our approach would be resistant to this and could reveal local, spatially defined regions of co-localization between two channels even within highly crowded molecular structures. Using simulated point distributions, we tested the influence of differences in local density between channels and the effect of local enrichments on the outcome of the co-localization index in three ways.

First, we simulated circular clusters with randomly distributed localizations in two channels and varied the local enrichment of localizations in channel A with increasing local density towards the center of the cluster (Fig. 2a). Since the overall distribution in channel B remained similar, the measured co-localization index for channel A remained constant at values around 1 (Fig. 2a, b). In contrast, the co-localization index values of channel B decreased with increasing local densities in channel A (Fig. 2b), as an increasing fraction of localizations in channel B is associated with a relatively lower local density in channel A. Note that the co-localization maps also directly visualize the spatial distribution of co-localization, with lower co-localization index values for channel B at the edges of the cluster where molecules in channel A are less concentrated.

Second, we simulated a scenario where two proteins co-cluster within a structure. To do so, we simulated ROIs in which the localizations in channel B are now also increasingly concentrated, overlapping with the area of high local density in channel A (Fig. 2c). As expected, in this situation the co-localization index values of channel A decrease, as a decreasing fraction of localizations overlap with the localizations in channel B (Fig. 2c, d). For channel B however, the average co-localization index reached values above 1 because these localizations associated with significantly higher (~2x) local densities in channel A compared to the mean local density of channel A (Fig. 2d). Thus, co-localization values >1 indicate that the localizations of channel B are enriched towards a local enrichment in

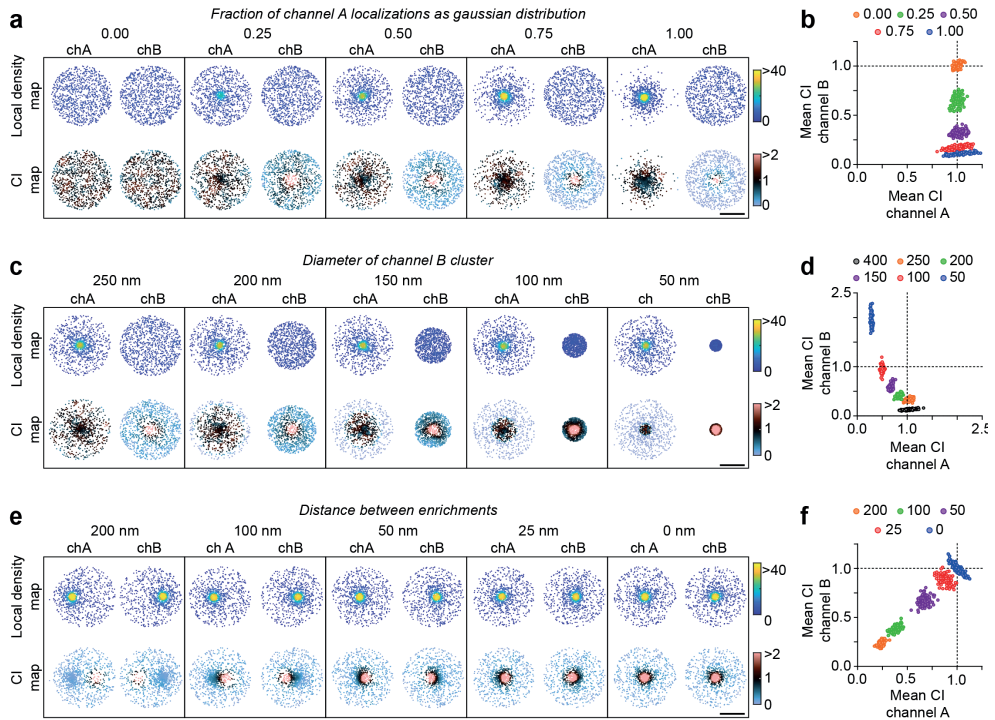


**Figure 2. Detection of spatial association within highly confined regions**

(a) Examples of simulated clusters in which points in channel A are increasingly concentrated towards the center of the cluster whereas channel B remains homogenous in each condition. (c) Examples of simulated point patterns with the cluster in channel B varying in size. (e) Examples of simulated point patterns in which both channels have a local enrichment with varying distances between the two enrichments. For each of the tests in (a, c, e) a map is shown color-coded for the local density (top) or the co-localization index (CI; bottom). For all clusters, the effective resolution used as search radius was  $\sim 16$  nm. (b, d, f) Graphs showing mean co-localization index for 100 simulated point patterns per condition for the experiments show in (a, c, e) respectively. Scale bar for a, c, e, 100 nm. CI, co-localization index; Ch, channel.

channel A. This shows that the co-localization index reliably reports and visualizes co-clustering of localizations that are spatially confined in small structures or domains.

Third, we evaluated the behavior of the co-localization index in simulations of two overlapping clusters, but with non-overlapping local enrichments (Fig. 2e). As expected, the closer these local enrichments were positioned towards each other, the closer the average co-localization index approached a value of 1 (Fig. 2f). Note that the average co-localization index is close to 1 when two random distributions overlap (Fig. 2a, first example), but also when local enrichments within clusters completely overlap (Fig. 2e, last example) as in both cases the localizations in the two channels have the same distribution. Thus, co-localization as measured here reports the similarity in spatial distribution. Nevertheless, the spatial distribution of the co-localization values of the individual localizations visualized in the co-localization maps revealed clear differences in the extent and position of co-localization between the two conditions. As mentioned earlier, the degree by which co-localization can be detected between two objects (or two objects can be considered non-overlapping), is dependent on the effective resolution of the data<sup>34,35</sup>. To test this further, we repeated

---

the simulations of Figure 2e, varying the localization error (Fig. S3). As expected, higher effective resolution, i.e., lower localization error, allows for higher sensitivity towards detecting partially overlapping structures.

Together, these simulations demonstrate that our method provides a robust analysis of spatial co-localization between two sets of localizations that is intuitive to interpret and provides a visual output of local co-localization. Our method thus measures co-localization, as a measure of similarity in spatial distributions, independent of density and even revealing co-clustering of proteins within densely crowded structures.

### Detecting co-localization in biological samples

Next, we wished to validate the co-localization index on experimental data from well-characterized cellular structures. We therefore labeled the microtubule network in U2OS cells using immunostaining for alpha-tubulin and acquired SMLM images using dSTORM (Fig. 3a). Localizations with a localization precision  $< 25$  nm (Fig. 3b) were selected for rendering a super-resolution image. Then, to approach perfect co-localization, we randomly divided all localizations into two channels (1:1) and determined the co-localization across multiple ROIs. As expected, the individual channels revealed close co-localization between the two channels (Fig. 3c), resulting in average co-localization values very close to 1 (co-localization index:  $1.00 \pm 0.003$  for channel A and  $1.00 \pm 0.004$  for channel B,  $n = 18$  ROIs from 3 cells; Fig. 3c, d). To test the sensitivity of the co-localization index, we tested conditions in which the localizations of channel B were laterally shifted or rotated relative to channel A. The introduction of small amounts of lateral shift significantly lowered the co-localization within ROIs (25 nm:  $0.61 \pm 0.02$ , 50 nm:  $0.36 \pm 0.02$ , 75 nm:  $0.26 \pm 0.02$ , 100 nm:  $0.22 \pm 0.02$ , 200 nm:  $0.15 \pm 0.01$ ,  $P < 0.001$ , ANOVA; Fig. 3c, d). Similarly, rotating channel B relative to channel A significantly reduced the co-localization (2 degrees:  $0.42 \pm 0.02$ , 10 degrees:  $0.17 \pm 0.01$ , 45 degrees:  $0.10 \pm 0.009$ , 90 degrees:  $0.12 \pm 0.009$ ,  $P < 0.001$ , ANOVA; Fig. 3e, f). Note that the residual co-localization is mostly the result of remaining microtubule cross-points (Fig. 3e), indicating the sensitivity of this approach and the usefulness of visualizing the co-localization maps.

Next, we randomly split the same dataset with varying relative molecular densities (1:9 and 1:99) between the channels. As expected from the simulations in Figure 1 and S1, changing the localization density did not significantly alter the outcome of the co-localization analysis (density ratio 1:9,  $1.00 \pm 0.004$  for channel A and  $0.99 \pm 0.005$  for channel B, density ratio 1:99,  $0.99 \pm 0.01$  for channel A and  $1.03 \pm 0.01$  for channel B,  $P > 0.05$ , ANOVA; Fig. 3g, h).

We next used these datasets to compare our method to two existing co-localization methods (Fig. S4). First, we compared our method with ClusDoC32. ClusDoc uses an optimized cutoff of 0.4 on the -1 (anti-correlated) to +1 (perfectly correlated distributions) scale developed earlier by Malkusch et al<sup>28</sup>, to obtain a value for the percentage of co-localizing localizations. Our approach (Fig. S4a) outperformed ClusDoC, as the latter showed a higher sensitivity to differences in density between the two channels (Fig. S4b). Second, we tested Coloc-Tesseler, which uses Voronoi diagrams with Manders' and Spearman correlations as readouts<sup>29</sup>. Similar to our approach, the Manders' correlation readout of Coloc-Tesseler correctly measured the co-localization in two overlapping channels with similar distribution and densities, although slightly underestimating co-localization when the density in one of the channels becomes lower (Fig S4c). In contrast, we found the Spearman correlation to consistently underestimate co-localization, similar as shown earlier<sup>29</sup>, and more sensitive to

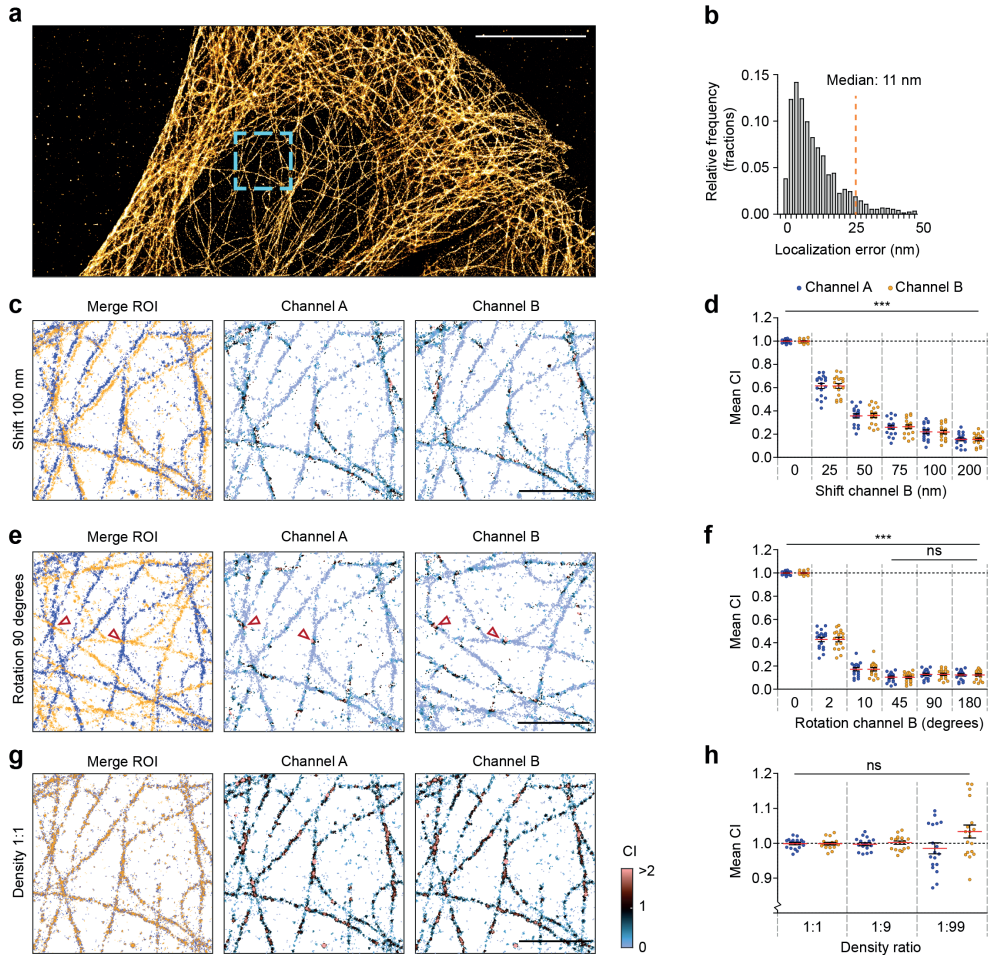


**Figure 3. Application and validation of co-localization index on a biological sample**

(a) dSTORM imaging was performed on U2OS cells labeled with anti-alpha-tubulin antibodies. Shown is a rendered reconstruction of all localizations. Scale bar, 10  $\mu$ m. (b) Frequency distribution of the localization precision across all localizations. Localizations with localization precision > 25 nm (orange line) were removed from the dataset. Bin size, 2 nm. (c) Example ROI in which channel B is shifted 100 nm to the right relative to channel A. (d) Graph showing mean co-localization with varying amounts of shift. (e) Example in which channel B is rotated 90 degrees relative to channel A. Two microtubule cross-points are indicated with red arrows. Scalebar in (c, e, g), 2  $\mu$ m. (f) Graph showing mean co-localization for individual ROIs with varying degree of rotation of channel B. (g) The localization dataset was randomly split into two channels (A, blue; B, yellow), with varying density ratios. Shown is an example ROI, indicated with a blue box in (a) with a 1:1 ratio. Also shown are the maps color-coded for the co-localization index. (h) Graph showing mean co-localization index for individual ROIs with varying density ratios. N = 18 ROIs from 3 cells. Data are represented as means  $\pm$  SEM. Ns, not significant, \*\*\* P < 0.001, ANOVA. ROI, region of interest; CI, co-localization index.

changes in density between the channels (Fig S4d).

Together, these results demonstrate that the local density-based co-localization index presented here is a simple, yet very powerful tool in detecting and visualizing the degree of spatial co-localization in biological samples.



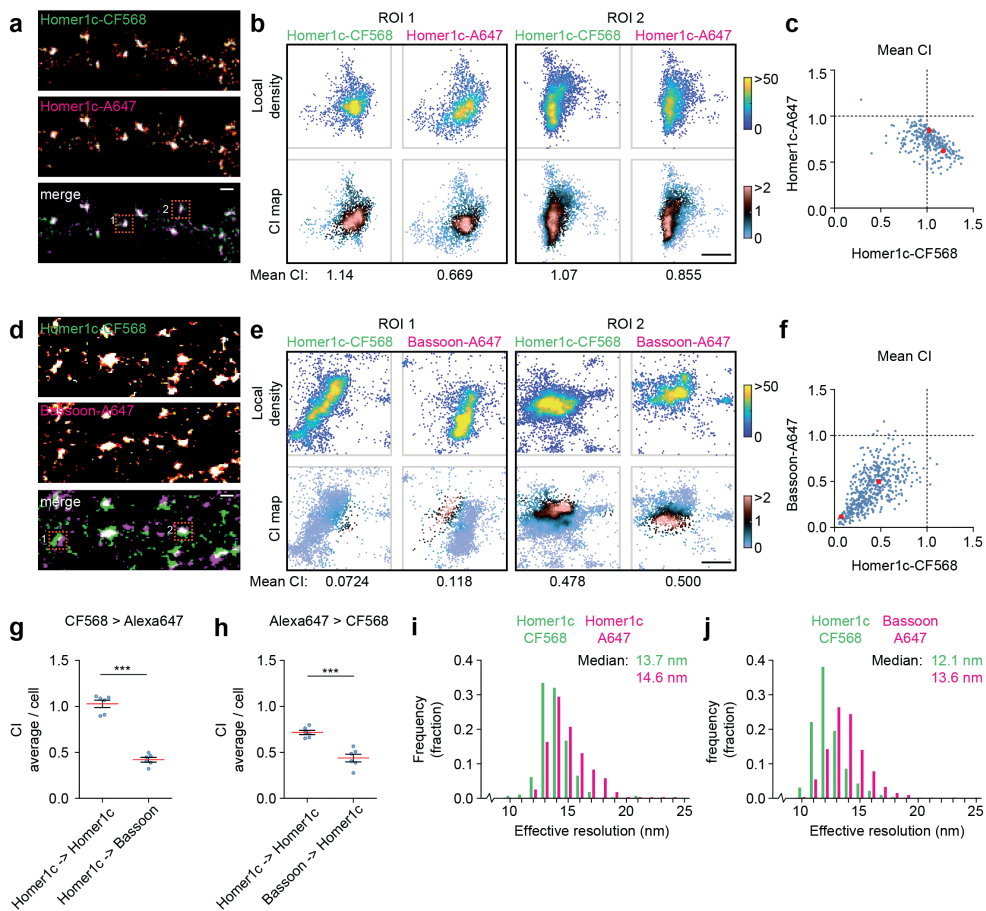


**Figure 4. Measuring co-localization at neuronal synapses**

(a) Rendered image of dual-color dSTORM on Homer1c in the dendrite of a hippocampal neuron. Homer1c was labeled with both CF568 (green) and Alexa647 (magenta). Scale bar, 500 nm. (b) Plots of two example ROIs (indicated with orange boxes in A). Shown are plots color-coded for the local density as well as the co-localization index. Scale bar, 200 nm. (c) Graph of mean co-localization index for 282 synapses from 6 neurons. Example synapses shown in B are plotted in red. (d) Rendered image of dual-color dSTORM on Homer1c labeled with CF568 (green) and Bassoon labeled with Alexa647 (magenta). (e) Example plots of ROIs indicated with orange boxes in (d). Scale bar, 200 nm. (f) Graph of mean co-localization index for 304 synapses from 6 neurons. Example synapses shown in E are plotted in red. (g, h) Graphs showing mean co-localization index averaged per neuron for the CF568 channel (g) and Alexa647 channel (h), comparing the co-localization of Homer1c and Bassoon. (i, j) Frequency distribution plots showing the calculated effective resolution and search radius  $d$ . Bin size, 1 nm. Data are represented as means  $\pm$  SEM. \*\*\*  $P < 0.001$ , Student  $t$  test. ROI, region of interest; CI, co-localization index.

### Detecting co-localization in dual-color SMLM images of neuronal synapses

As a final test case of our method, we turned to neuronal synapses. At synapses, a plethora of protein species are closely packed, both at the presynaptic active zone that is closely aligned with postsynaptic proteins, with only several nanometers between them. The subsynaptic clustering and relative positioning of synaptic proteins is critically important for synaptic transmission<sup>31,33,39,40</sup>.

We reasoned that our co-localization index might be very well-suited for measuring the degree of spatial association between proteins in these dense structures. To this end, we performed dual-color dSTORM on cultured hippocampal neurons co-labeled for the postsynaptic protein Homer1c and the presynaptic protein Bassoon. We first labeled the postsynaptic protein Homer1c with both CF568- and Alexa647- (A647) coupled secondary antibodies (Fig. 4a). As expected, the labeling in the two channels overlapped almost completely and we found a high degree of co-localization between the two channels, also apparent from the co-localization maps of individual synapses (Fig. 4b, c). Next, we analyzed the co-localization index between Homer1c and Bassoon localizations (Fig. 4d, e). As expected, the co-localization between these proteins was significantly lower, and varied largely between individual ROIs, indicative for only partial overlap (co-localization index CF568 > Alexa647:  $1.03 \pm 0.04$  for Homer1c > Homer1c and  $0.42 \pm 0.03$  for Homer1c > Bassoon,  $n = 6$  neurons,  $P < 0.001$ , Student t test; Fig. 4g), (co-localization index Alexa647 > CF568:  $0.72 \pm 0.023$  for Homer1c > Homer1c and  $0.44 \pm 0.04$  for Homer1c > Bassoon,  $n = 6$  neurons,  $P < 0.001$ , Student t test; Fig. 4h). Importantly, the average co-localization values corresponded well with the observed overlap: synapses with non-overlapping Homer1c-Bassoon clusters had a low average co-localization index while synapses with partially overlapping clusters resulted in a higher average co-localization index (example synapses, Fig. 4e). Note that variations in co-localization index most likely result from the relative orientations of presynaptic and postsynaptic structures with respect to the focal plane (Fig. 4f). Despite differences in the biophysical properties of these dyes which are partially reflected by small differences in the observed effective resolution (Fig. 4i, j), our approach robustly reports co-localization at sub-diffraction resolution. Together, these results show that the co-localization index as described here, can be used as a reliable method to quantify the spatial association of molecules in dual-color SMLM data.

## DISCUSSION

The development of SMLM approaches has revolutionized cell biology permitting the precise investigation of the nanoscale organization of protein within cells. SMLM images are essentially coordinate-based datasets, providing unique opportunities to quantify the spatial distribution of molecules. Here, we present a method to quantify the spatial association of molecules in dual-color SMLM data. We first benchmarked the method *in silico* with various simulated point patterns that mimic commonly found distributions in biological samples. We found that our method is resistant to variations in overall localization density and adequately detects spatial co-localization in fields with randomly distributed points, as well as within highly crowded clusters. Importantly, our method takes the localization density and localization error into account, such that the reported co-localization is on the scale relative to the effective resolution<sup>34,35</sup> of the dataset. We noted from simulated as well as experimental data, that the accuracy of the localization index is more sensitive to the localization density than the localization precision. Ideally, the effective resolution is thus limited by the localization precision and not the molecular density. In addition, we tested the effect of blinking kinetics and background localizations on the outcome of co-localization. We furthermore showed that our co-localization method is versatile and can be applied to various types of biological samples, including the microtubule network in epithelial cells, a sample with distinct differences in localization density across the field of view, and neuronal synapses, structures with a highly dense accumulation of heterogeneously distributed proteins.

---

We also compared our co-localization index with previously described methods, Coloc-Tesseler<sup>23</sup> and ClusDoC<sup>32</sup>. While Coloc-Tesseler performed well when using the Manders' correlation as an output, ClusDoC underestimated co-localization in datasets with varying densities. Of note, the definition of co-localization in ClusDoC (which integrates a co-localization method developed by Malkusch et al.<sup>28</sup>), is different from the method presented here, as ClusDoC measures co-clustering. Co-localization as measured in our method, provides a measure for the similarity in spatial distributions between the channels, and is thus independent of localization density, and does not rely on (co-)clustering of molecules.

In conclusion, the method presented here provides a versatile approach to quantify co-localization in dual-color SMLM experiments. The algorithm is available as a MATLAB function, which can be easily incorporated into existing analysis pipelines and could potentially be extended to 3D datasets and triple- or more -channel experiments. Thus, we believe that the co-localization method described here, will serve as a fast and easy-to-use approach to measure spatial associations between molecules in multi-color SMLM-datasets and will be instrumental in unveiling the molecular organization in subcellular compartments.

## METHODS

### Antibodies

Primary antibodies used in this study are the following: Mouse anti-alpha-tubulin ([B-5-1-2], Sigma, T5168, RRID AB\_477582), Rabbit Anti-GFP (MBL Sanbio, 598, RRID AB\_591819) and mouse anti-Bassoon ([SAP7F407], Enzo, ADI-VAM-PS003-F, RRID AB\_10618753). Alexa647-conjugated secondary antibodies were from Life Technologies (A21236 and A21245). CF568 conjugated secondary antibodies were from Sigma (SAB4600085).

### Ethics statement

All experiments were approved by the Dutch Animal Experiments Committee (Dier Experimenten Commissie [DEC], work protocol project number: AVD1080020173404), performed in line with institutional guidelines of Utrecht University, and conducted in agreement with Dutch law (Wet op de Dierproeven, 1996) and European regulations (Directive 2010/63/EU). Timed pregnant Wistar rats were obtained from Janvier Labs. The study was carried out in compliance with the ARRIVE guidelines.

### DNA-plasmids

pCMV-Homer1c-GFP<sup>41</sup>

### Calculation of local density and co-localization index

The local density is determined for each localization in both channels. First, for each localization, the NND is determined within a given ROI using the MATLAB function *knnsearch*, with input  $(x,y,'k',2)$ , and output  $[IDX,D]$ , to obtain the distance ( $D$ ) for the first nearest neighbor that is not itself. The NND for each localization was averaged to obtain the MNND. Next, for each localization, the local density ( $LD$ ) is defined as the number of localizations within a radius defined by the effective resolution making use of the MATLAB function *rangesearch*. For each channel, the  $LD$  values are averaged together to obtain  $LD_A$  and  $LD_B$ . Effective resolution was calculated as<sup>34</sup>,

$$effective\ resolution = \sqrt{MNND^2 + \varepsilon^2}$$

where  $\varepsilon$  is the localization error, determined as the average of the complete dataset.

The co-localization index ( $CI$ ) is determined as the number of localizations of channel B ( $N$ ) within a radius ( $d$ ) around each localization in channel A ( $A_i$ ) normalized to the mean local density of the localizations in channel B ( $LD_B$ ), with  $d$  being the effective resolution of the localizations in channel B.

$$CI_i^A = \frac{N_{Ai}^B(d_B)}{(LD_B)}$$

Thus, for the second channel, the  $CI$  values are calculated as:

$$CI_i^B = \frac{N_{Bi}^A(d_A)}{(LD_A)}$$

The  $CI$  values calculated for each localization individually can be used to plot a co-localization map and averaged to obtain a single mean- $CI$  value of the full ROI for both channels.

We integrated these calculations in a MATLAB function (Code S1) with the input being the x and y coordinates of channel A and B and their localization errors. The function will return a MATLAB structure, with fields containing the average co-localization index for each channel, the calculated effective resolution ( $d$ ) as well as the  $CI$  values for the individual localizations (See Code S1).

## Simulations

To generate random localization clusters in squares, for each x and y coordinate, a value  $\rho$  (between 0 and 1) was generated using the MATLAB function *rand*. x and y were calculated as  $\rho$  multiplied by the cluster dimensions (250 x 250 nm). This was repeated for the second channel. Differences in overlap were generated by increasing the x coordinate of the second channel (+62.5 nm for every 25% decrease in overlap). For each condition, we simulated 100 clusters.

For circular clusters, randomly distributed x and y coordinates were calculated as  $x = \sqrt{(\rho)} * \cos(\theta) * d$  and  $y = \sqrt{(\rho)} * \sin(\theta) * d$ , where  $\theta$  is a random angle (between 0 and  $2\pi$ ) and  $d$  is the diameter of the full cluster. Background localizations were simulated by generating randomly placed coordinates in a square as described above at a density based on the signal/background ratio of the clusters. Background localizations were then removed from the clusters themselves. Clusters with a local enrichment were generated by combining a set randomly distributed localizations with a set localizations distributed as gaussian distribution. For gaussian distributions, values  $\rho$  were generated using the MATLAB function *randn*. x and y were calculated as  $x = \sigma * \rho * \cos(\theta) * d + dc$  and  $y = \sigma * \rho * \sin(\theta) * d$ , with  $\sigma$  being the standard deviation (0.33 for the examples in Fig. 2a, c and 0.25 in Fig. 2e and Fig. S1),  $\theta$  and  $d$  as described above, and  $dc$  being the distance from the center of the cluster (in nm). For the simulations shown in Fig. 2a we combined randomly distributed localizations with localizations in a gaussian distribution in varying ratios (1:0, 3:1, 1:1, 1:3, 0:1). For simulations in Fig. 2e, we used a ratio of 1:1, but changed  $dc$  to position the local-enrichment relative to the center of the cluster. For all conditions, we simulated 100 independent point patterns.

Localization error was simulated by offsetting the x and y coordinates with random distance, derived from a gaussian distribution (MATLAB function *randn*), with the sigma being the intended localization error. A localization error of 15 nm was used if not indicated differently. Blinking was simulated by adding additional localizations around existing ones, with offset derived from a Gaussian distribution (MATLAB function *randn*), with the sigma varied as the localization error.

---

### **U2OS cell culture**

U2OS cells (ATCC HTB-96) were grown in DMEM (Lonza) supplemented with 10% fetal calf serum (Sigma), 2 mM glutamine and 1% penicillin and streptomycin (pen/strep) (Gibco). One day before fixation and immunostaining, cells were plated on 18-mm coverslips and grown to ~50% confluency.

### **Immunolabeling of microtubules in U2OS cells**

U2OS cells were incubated in pre-warmed (37°C) cytoskeleton extraction buffer (PEM80 buffer [80 mM PIPES, 1 mM EGTA, 2 mM MgCl<sub>2</sub> (pH 6.9)], 0.3% [v/v] Triton-X100, 0.1% [v/v] glutaraldehyde) for 1 minute at room temperature (RT). Next, the cells were further fixed using 4% (w/v) paraformaldehyde (PFA) and 4% (w/v) sucrose in phosphate-buffered saline (PBS) (PFA/Suc) for 10 minutes at RT, washed three times for 5 minutes with PBS containing 0.1 M glycine (PBS/Gly), and subsequently incubated with 1 mg/ml sodium borohydride in PBS for 7 minutes at RT. Coverslips were washed 3 times for 5 minutes with PBS/Gly. Next, the coverslips were incubated in 2% bovine serum albumin (BSA) and 0.1% Triton-X100 in PBS/Gly for 1 hour at 37°C. Next, microtubules were labeled using anti- $\alpha$ -tubulin primary antibody, diluted 1:1000 in 1% BSA [w/v], 0.1% [v/v] Triton-X100 in PBS/Gly, overnight at 4°C. Cells were washed three times 5 minutes with PBS and incubated with goat anti-mouse secondary antibodies conjugated to Alexa647 diluted 1:400 in 1% [w/v] BSA, 0.1% [v/v] Triton-X100 in PBS/Gly. After one hour, cells were washed three times 5 minutes with PBS and subsequently post-fixed with PFA/Suc for 5 minutes. Cells were washed three times with PBS/Gly after which cells were kept in PBS till imaging.

### **Dissociated neuron cultures**

Dissociated hippocampal cultures were prepared from embryonic day 18 (E18) rat brains of both genders, as described in 42 and in accordance to the approved DEC work-protocol as mentioned in the ethics statements above. Mother rats were sacrificed by gradual fill CO<sub>2</sub>/O<sub>2</sub>. Subsequently the uterus containing the pups is taken out and is stored in a sterile ice cold environment. After the pups were sedated by the cold, they were removed from the uterus and decapitated. Dissociated neurons were plated on Ø18-mm coverslips coated with poly-L-lysine (37.5 µg/ml, Sigma-Aldrich) and laminin (1.25 µg/ml, Roche Diagnostics) at a density of 100,000 neurons per well. Neurons were grown in Neurobasal medium (NB) supplemented with 1% pen/strep, 2% [v/v] B27, and 0.5 mM L-glutamine (all from Gibco) (NB-complete medium) at 37°C in 5% CO<sub>2</sub>. From days in vitro (DIV) 1 onward, medium was refreshed weekly by replacing half of the medium with Brainphys neuronal medium (BP) supplemented with 2% [v/v] NeuroCult SM1 neuronal supplement (STEMCELL Technologies) and 1% pen/strep (BP-complete medium).

### **Transfection of hippocampal neurons**

Neurons were transfected at DIV 15 using Lipofectamine 2000 reagent (Invitrogen). Briefly, for one coverslip, 1–2 µg DNA was mixed with 3.3 µl Lipofectamine in 200 µl BP medium and incubated for 30 minutes at RT. Next, 500 µl conditioned medium was transferred to a new culture plate and replaced by 300 µl BP supplemented with 0.5 mM L-glutamine. The DNA mix was added to the neurons and incubated at 37°C and 5% CO<sub>2</sub>. After 90–120 minutes, neurons were transferred to the new culture plate with conditioned medium and 500 µl fresh BP-complete medium and kept at 37°C and 5% CO<sub>2</sub> till fixation at DIV 21.

### Immunolabeling of neuronal cultures

Neurons were fixed at DIV 21 in PFA/Suc for 10 minutes at RT after which they were washed 3 times 5 minutes in PBS/Gly. Next, the coverslips were incubated in blocking buffer (10% [v/v] normal goat serum [NGS] (Abcam), in PBS/Gly with 0.1% [v/v] Triton X100) for 1 hour at 37°C. Next, coverslips were incubated with primary antibodies diluted in incubation buffer (5% [v/v] NGS in PBS/Gly with 0.1% [v/v] Triton X100) overnight at 4°C. Coverslips were next washed 3 times 5 minutes with PSD/Gly and incubated with secondary antibodies diluted 1:400 in incubation buffer for 1 hour at RT. Next, coverslips were washed 3 times 5 minutes in PBS, post fixed in 4% PFA/Suc for 5 minutes, additionally washed 3 times with PBS/Gly, and kept in PBS at 4°C until imaging.

### SMLM and filtering of raw localization data

SMLM experiments were performed using the Nanoimager microscope (Oxford Nanoimaging; ONI) equipped with a 100x oil-immersion objective (Olympus Plan Apo, NA 1.4) and an XYZ closed-loop piezo stage. Imaging was performed using 473-nm, 561-nm and 640-nm lasers for GFP, CF568 and Alexa647 excitation respectively. Fluorescence was detected using a sCMOS camera (ORCA Flash 4, Hamamatsu). Integrated filters were used to split far-red emission onto the right side of the camera and blue-green-red emission spectra on the left side, enabling simultaneous dual-color imaging.

The imaging chamber was temperature-controlled at 30°C to prevent fluctuations in temperature during the time course of an experiment that might affect the alignment of the channels. Channel alignment was performed before each imaging session using 100-nm TetraSpeck beads (T-7279, Invitrogen) and the ONI software aiming for an alignment error of  $SD < 8$  nm as measured from 2000 points total across a maximum of 20 fields of view. Imaging was performed in near-TIRF (angle: 53.5°) using a motorized mirror and all images were acquired at 50 Hz.

Coverslips with neurons labeled as described above were mounted on concave slides in dSTORM-buffer (50 mM Tris, 10 mM NaCl, pH 8.0, supplemented with 5–20 mM MEA, 10% [w/v] glucose, 700 µg/ml glucose oxidase, and 40 µg/ml catalase). Transfected neurons were localized using low laser powers. At low laser powers, a snapshot was obtained of all channels, used later for selection of ROIs.

Dual-color dSTORM was performed simultaneously for CF568 and Alexa647. First, a pulse of high laser power of both the 561-nm and 640-nm lasers was used to bring the dyes into the dark state. Next, laser powers were lowered to around 100-200 mW. The acquisition was started when clear individual (non-overlapping) blinking was observed. 405-nm laser power was increased on demand based the number of blinking events. Imaging was continued for 20.000 frames or till no blinking events could be observed.

Localization coordinates were obtained and corrected for XY-drift using the ONI-software (version 1.12, software integrated with ONI microscope). From here onwards, analyses was continued in MATLAB (version 2019b). Localizations with a x-y-precision of  $>50$  nm were filtered out. Next, tracking with a tracking radius of 60 nm was performed to find localizations that were detected in multiple consecutive imaging frames. For each track, we selected the localization with the smallest localization error and filtered those further using a  $< 25$  nm cutoff, being the final filtered dataset. Rendered reconstructions were made in Detection of Molecules (DoM), downloaded from: [https://github.com/ekatruxha/DoM\\_Utrecht](https://github.com/ekatruxha/DoM_Utrecht). Localization plots were made in MATLAB

---

### **Analysis of co-localization in microtubule dataset**

Single-color dSTORM datasets were filtered on localization precision and tracking as described above. Next, the datasets were split by generating  $n$  unique random numbers between 1 and  $n$  using the MATLAB function `randperm`, where  $n$  is the number of localizations in the dataset. These numbers were used to assign localizations between two channels in ratios 1:1, 1:9 and 1:99. Translation was introduced by adding various distances to the  $x$  and  $y$  localizations of channel B. For rotations, the localizations of channel B were rotated around the center of the selected ROI by varying angles between 2 and 180 degrees. For the comparison with ClusDoC, we made use of the MATLAB function `ClusDoC`<sup>32</sup>, downloaded from: <https://github.com/PRNicovich/ClusDoC>. We used the default settings, i.e., 0.4 as co-localization cutoff. Data was plotted as the fraction of co-localizing localizations. For Coloc-Tesseler, we made use of the stand-alone software downloaded from: <https://github.com/flevet/Coloc-Tesseler>. For both comparisons, we used the data shown in (Fig. 3g, h), to make the comparison.

### **Analysis of co-localization in neuronal synapses**

For synaptic structures, we selected ROIs of 702x702 nm (6x6 pixels at a pixel size of 117 nm) which we subsequently analyzed for co-localization analysis as described above.

### **Statistics**

Statistical significance was tested with a Student's  $t$ -test when comparing two groups. A  $P$  value below 0.05 was considered significant. If multiple groups were compared, statistical significance was tested with a one-way ANOVA followed by a Bonferroni's multiple comparison test. In all figures, \* was used to indicate a  $P$  value  $< 0.05$ , \*\* for  $P < 0.01$ , and \*\*\* for  $P < 0.001$ . Reported  $n$  is number of cells or ROIs as indicated in the text or figure legend, and all biological experiments were replicated in cultures from at least two independent preparations. Statistical analysis and graphs were prepared in GraphPad Prism, and figures were generated in Adobe Illustrator CC.

### **ACKNOWLEDGEMENTS**

We want to thank all members of the MacGillavry lab for helpful discussions. This work was supported by the European Research Council (ERC-StG 716011 to HDM).

### **AUTHOR CONTRIBUTIONS STATEMENT**

JW and HMG conceived the study; JW performed the experiments and analyzed data; JW wrote analysis code; JW and HMG wrote the manuscript.

### **DATA AVAILABILITY**

All data generated or analyzed during this study are included in this published article (and its Supplementary Information files). A test dataset (based on Fig 3e, f) and scripts, together with a brief user guide are included as Supplementary information.

### **ADDITIONAL INFORMATION**

The authors declare no competing interests.

## REFERENCES

- 1 Sigal, Y. M., Zhou, R. & Zhuang, X. Visualizing and discovering cellular structures with super-resolution microscopy. *Science* 361, 880-887, doi:10.1126/science.aau1044 (2018).
- 2 Schermelleh, L. et al. Super-resolution microscopy demystified. *Nat Cell Biol* 21, 72-84, doi:10.1038/s41556-018-0251-8 (2019).
- 3 Betzig, E. et al. Imaging intracellular fluorescent proteins at nanometer resolution. *Science* 313, 1642-1645 (2006).
- 4 Hess, S., Girirajan, T. & Mason, M. Ultra-high resolution imaging by fluorescence photoactivation localization microscopy. *Biophys J* 91, 4258-4272 (2006).
- 5 Rust, M. J., Bates, M. & Zhuang, X. Sub-diffraction-limit imaging by stochastic optical reconstruction microscopy (STORM). *Nat Methods* 3, 793-795, doi:nmeth929 [pii] 10.1038/nmeth929 (2006).
- 6 Heilemann, M. et al. Subdiffraction-resolution fluorescence imaging with conventional fluorescent probes. *Angew Chem Int Ed Engl* 47, 6172-6176, doi:10.1002/anie.200802376 (2008).
- 7 Jungmann, R. et al. Multiplexed 3D cellular super-resolution imaging with DNA-PAINT and Exchange-PAINT. *Nat Methods* 11, 313-318, doi:10.1038/nmeth.2835 (2014).
- 8 Balzarotti, F. et al. Nanometer resolution imaging and tracking of fluorescent molecules with minimal photon fluxes. *Science* 355, 606-612, doi:10.1126/science.aak9913 (2017).
- 9 Sahl, S. J., Hell, S. W. & Jakobs, S. Fluorescence nanoscopy in cell biology. *Nat Rev Mol Cell Biol* 18, 685-701, doi:10.1038/nrm.2017.71 (2017).
- 10 Dempsey, G. T., Vaughan, J. C., Chen, K. H., Bates, M. & Zhuang, X. Evaluation of fluorophores for optimal performance in localization-based super-resolution imaging. *Nat Methods* 8, 1027-1036, doi:10.1038/nmeth.1768 (2011).
- 11 Samanta, S. et al. Organic fluorescent probes for stochastic optical reconstruction microscopy (STORM): Recent highlights and future possibilities. *Coordination Chemistry Reviews* 380, 17-34 Contents, doi:https://doi.org/10.1016/j.ccr.2018.08.006 (2019).
- 12 Baddeley, D. & Bewersdorf, J. Biological Insight from Super-Resolution Microscopy: What We Can Learn from Localization-Based Images. *Annu Rev Biochem* 87, 965-989, doi:10.1146/annurev-biochem-060815-014801 (2018).
- 13 Wu, Y. L., Tschanz, A., Krupnik, L. & Ries, J. Quantitative Data Analysis in Single-Molecule Localization Microscopy. *Trends Cell Biol* 30, 837-851, doi:10.1016/j.tcb.2020.07.005 (2020).
- 14 Khater, I. M., Nabi, I. R. & Hamarneh, G. A Review of Super-Resolution Single- Molecule Localization Microscopy Cluster Analysis and Quantification Methods. *Patterns* 1, doi:10.1016/j.patter.2020.100038 (2020).
- 15 Ripley, B. D. Modelling Spatial Patterns. *Journal of the Royal Statistical Society* 39, 172-212 (1977).
- 16 Owen, D. M. et al. PALM imaging and cluster analysis of protein heterogeneity at the cell surface. *J Biophotonics* 3, 446-454, doi:10.1002/jbio.200900089 (2010).
- 17 Sengupta, P. et al. Probing protein heterogeneity in the plasma membrane using PALM and pair correlation analysis. *Nat Methods* 8, 969-975, doi:10.1038/nmeth.1704 [pii] (2011).
- 18 Veatch, S. L. et al. Correlation functions quantify super-resolution images and estimate apparent clustering due to over-counting. *PLoS One* 7, e31457, doi:10.1371/journal.pone.0031457 PONE-D-11-10542 [pii] (2012).
- 19 Sherman, E. et al. Functional nanoscale organization of signaling molecules downstream of the T cell antigen receptor. *Immunity* 35, 705-720, doi:10.1016/j.immuni.2011.10.004 (2011).
- 20 Ester, M., Kriegel, H. P., Jörg, S. & Xu, X. A. in *Proc. 2nd International Conference on Knowledge Discovery and Data Mining* 226-231 (IAAI, Portland, 1996).
- 21 Ankerst, M., Breunig, M. M., Kriegel, H. P. & Sander, J. OPTICS: Ordering points to identify the clustering structure. *SIGMOD Rec. (ACM Spec. Interes. Gr. Manag. Data)*, doi:10.1145/304181.304187 (1999).
- 22 Andronov, L., Orlov, I., Lutz, Y., Vonesch, J. L. & Klaholz, B. P. ClusterViSu, a method for clustering of protein complexes by Voronoi tessellation in super-resolution microscopy. *Sci Rep* 6, 24084, doi:10.1038/srep24084 (2016).
- 23 Levet, F. et al. SR-Tesseler: a method to segment and quantify localization-based super-resolution microscopy data. *Nat Methods* 12, 1065-1071, doi:10.1038/nmeth.3579 (2015).
- 24 Rubin-Delanchy, P. et al. Bayesian cluster identification in single-molecule localization microscopy data. *Nat Methods* 12, 1072-1076, doi:10.1038/nmeth.3612 (2015).
- 25 Manders, E. M. M., Verbeek, F. J. & Aten, J. A. Measurement of co-localization of objects in dual-colour confocal images. *Journal of Microscopy* 169, 375-382, doi:10.1111/j.1365-2818.1993.tb03313.x (1993).
- 26 Pearson, K. VII. Mathematical contributions to the theory of evolution.—III. Regression, heredity, and panmixia. *Philosophical Transactions of the Royal Society of London. Series A, Containing Papers of a Mathematical or Physical Character* 187, 253-318, doi:10.1098/rsta.1896.0007 (1896).
- 27 Rossy, J., Cohen, E., Gaus, K. & Owen, D. M. Method for co-cluster analysis in multichannel single-molecule localisation data. *Histochem Cell Biol* 141, 605-612, doi:10.1007/s00418-014-1208-z (2014).
- 28 Malkusch, S. et al. Coordinate-based colocalization analysis of single-molecule localization microscopy data. *Histochem Cell Biol* 137, 1-10, doi:10.1007/s00418-011-0880-5 (2012).
- 29 Levet, F. et al. A tessellation-based colocalization analysis approach for single-molecule localization microscopy. *Nat Commun* 10, 2379, doi:10.1038/s41467-019-10007-4 (2019).
- 30 Chen, J. H., Blanpied, T. A. & Tang, A. H. Quantification of trans-synaptic protein alignment: A data analysis case for single-molecule localization microscopy. *Methods* 174, 72-80, doi:10.1016/j.ymeth.2019.07.016 (2020).
- 31 Tang, A. H. et al. A trans-synaptic nanocolumn aligns neurotransmitter release to receptors. *Nature* 536, 210-214, doi:10.1038/nature19058 (2016).
- 32 Pageon, S. V., Nicovich, P. R., Mollazade, M., Tabarin, T. & Gaus, K. Clus-DoC: a combined cluster detection and colocalization analysis for single-molecule localization microscopy data. *Mol Biol Cell* 27, 3627-3636,



- 
- doi:10.1091/mbc.E16-07-0478 (2016).
- 33 MacGillavry, H. D., Song, Y., Raghavachari, S. & Blanpied, T. A. Nanoscale scaffolding domains within the postsynaptic density concentrate synaptic AMPA receptors. *Neuron* 78, 615-622, doi:10.1016/j.neuron.2013.03.009 (2013).
  - 34 Gould, T. J., Verkhusha, V. V. & Hess, S. T. Imaging biological structures with fluorescence photoactivation localization microscopy. *Nat Protoc* 4, 291-308, doi:10.1038/nprot.2008.246 (2009).
  - 35 Shroff, H., Galbraith, C. G., Galbraith, J. A. & Betzig, E. Live-cell photoactivated localization microscopy of nanoscale adhesion dynamics. *Nat Methods* 5, 417-423, doi:10.1038/nmeth.1202 (2008).
  - 36 Garcia-Parajo, M. F., Cambi, A., Torreno-Pina, J. A., Thompson, N. & Jacobson, K. Nanoclustering as a dominant feature of plasma membrane organization. *J Cell Sci* 127, 4995-5005, doi:10.1242/jcs.146340 (2014).
  - 37 Goyette, J. & Gaus, K. Mechanisms of protein nanoscale clustering. *Curr Opin Cell Biol* 44, 86-92, doi:10.1016/j.ceb.2016.09.004 (2017).
  - 38 Scheefhals, N. & MacGillavry, H. D. Functional organization of postsynaptic glutamate receptors. *Mol Cell Neurosci* 91, 82-94, doi:10.1016/j.mcn.2018.05.002 (2018).
  - 39 Chen, H., Tang, A. H. & Blanpied, T. A. Subsynaptic spatial organization as a regulator of synaptic strength and plasticity. *Curr Opin Neurobiol* 51, 147-153, doi:10.1016/j.conb.2018.05.004 (2018).
  - 40 Nair, D. et al. Super-resolution imaging reveals that AMPA receptors inside synapses are dynamically organized in nanodomains regulated by PSD95. *J Neurosci* 33, 13204-13224, doi:10.1523/JNEUROSCI.2381-12.2013 (2013).
  - 41 Scheefhals, N. et al. Shank Proteins Couple the Endocytic Zone to the Postsynaptic Density to Control Trafficking and Signaling of Metabotropic Glutamate Receptor 5. *Cell Rep* 29, 258-269 e258, doi:10.1016/j.celrep.2019.08.102 (2019).
  - 42 Kapitein, L. C., Yau, K. W. & Hoogenraad, C. C. Microtubule dynamics in dendritic spines. *Methods Cell Biol* 97, 111-132, doi:10.1016/S0091-679X(10)97007-6 (2010).

## SUPPLEMENTAL INFORMATION

## MATLAB Code S1

```

function CIX = CI_index(x1, y1, x2, y2, LP1, LP2)
% ; NAME:
% ;     CI_index
% ; PURPOSE:
% ;     Calculates the co-localization index between two channels in SMLM datasets
% ;
% ; CALLING SEQUENCE:
% ;     CIX = CI_index(x1, y1, x2, y2, LP1, LP2)
% ;
% ; INPUTS:
% ;     x1 and y1 being the coordinates of the first channel
% ;     x2 and y2 being the coordinates of the second channel
% ;     LP1 and LP2 being the average localization precision of x and y (in the same units as x and y)
% ;
% ; OUTPUTS:
% ;     CIX: struct with a row for each channel containing the fields:
% ;     .NND_each_loc      : containing the nearest neighbor of each localization
% ;     .MNND             : mean nearest neighbor distance
% ;     .effective_resolution : effective resolution used as search radius
% ;     .LD_each_loc      : local-density value of all localizations
% ;     .MLD              : local-density value averaged over all localizations
% ;     .opposing_LD_each_loc : local-density each localization experiences in the other channel
% ;     .CI_each_loc      : Co-localization index of each localization
% ;     .mean_CI          : Co-localization index averaged over all localizations
% ;
% ;
% ; Jelmer Willems, 2021
% ;
% ;
% LOCAL-DENSITY
channel=1;
while channel < 3
    if channel == 1
        x = x1;
        y = y1;
        LP = LP1;
    else
        x = x2;
        y = y2;
        LP = LP2;
    end

    % find NND distance
    [IDX,D]=knnsearch([x,y],[x,y],'k',2);
    MNND=mean(D(:,2));

    % save NND and MNND in output struct
    CIX(channel).NND_each_loc=D(:,2);
    CIX(channel).MNND=MNND;

    % determine effective resolution as search radius
    effective_resolution=sqrt((MNND^2)+(LP^2));
    CIX(channel).effective_resolution=effective_resolution;

    % find all localizations in search radius
    IDR=rangesearch([x,y],[x,y],effective_resolution);

    % determine local density for each localization and the mean of all loc
    local_density = zeros(1,length(IDR));
    for alllocs = 1:length(IDR)
        local_density(alllocs,1) = length(IDR {alllocs,1});
    end
    mean_local_density = mean(local_density);

```

---

```

% save local density in output struct
CIX(channel).LD_each_loc = local_density;
CIX(channel).MLD = mean_local_density;

channel=channel+1;
end

% CO-LOCALIZATION INDEX
active_channel = 1;
while active_channel <3

% selection of required data for active channel
if active_channel == 1
localizations_assayX = x1;
localizations_assayY = y1;
localizations_otherX = x2;
localizations_otherY = y2;
other_channel = 2;
else
localizations_assayX = x2;
localizations_assayY = y2;
localizations_otherX = x1;
localizations_otherY = y1;
other_channel = 1;
end
mean_local_density_other = CIX(other_channel).MLD;
effective_resolution = CIX(other_channel).effective_resolution;

% find all neighbors in the opposing channel within the search radius
IDQ=rangesearch([localizations_otherX,localizations_otherY],[localizations_assayX,localizations_
assayY],effective_resolution);

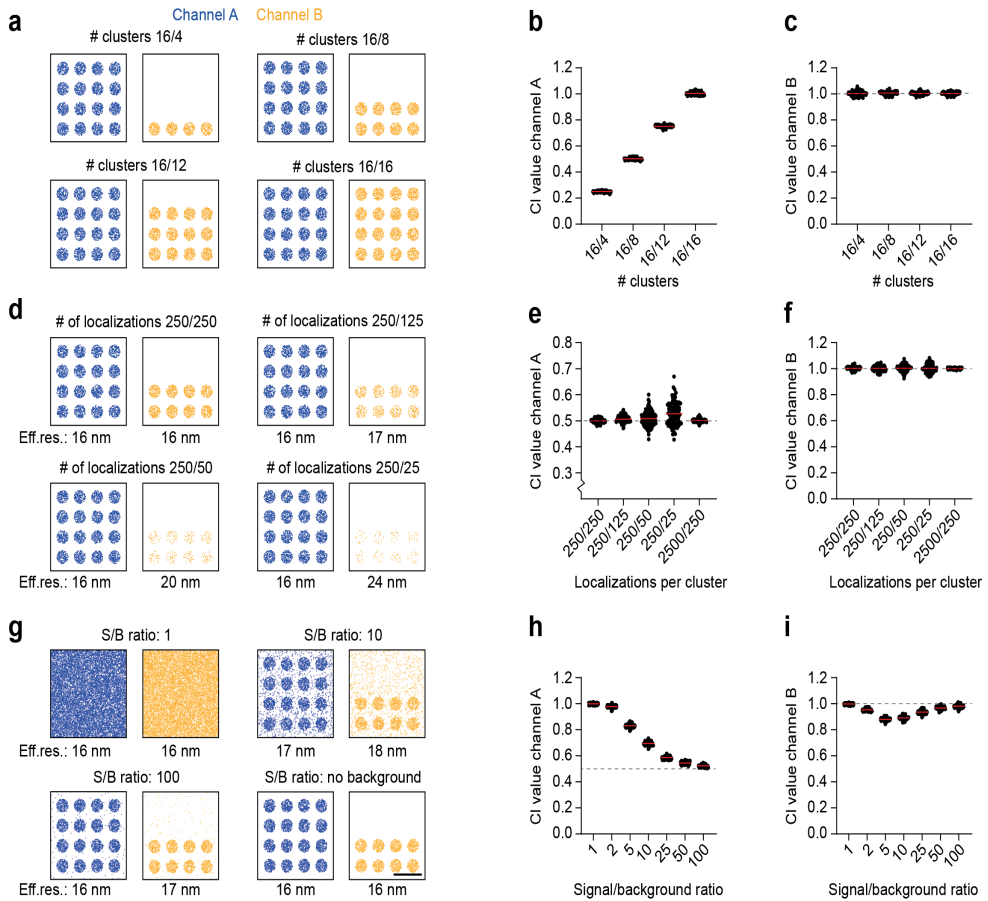
% determine local density of all localizations in opposing channel
opposing_local_density = zeros(1,length(IDQ));
for alllocs=1:length(IDQ)
opposing_local_density(alllocs,1)=length(IDQ{alllocs,1});
end

% normalize to mean local density to obtain co-localization index
CI_index_all_localization=opposing_local_density/(mean_local_density_other-1);
Mean_CI_ROI=mean(CI_index_all_localization);

% save in output struct
CIX(active_channel).opposing_LD_each_loc=opposing_local_density;
CIX(active_channel).CI_each_loc=CI_index_all_localization;
CIX(active_channel).Mean_CI=Mean_CI_ROI;

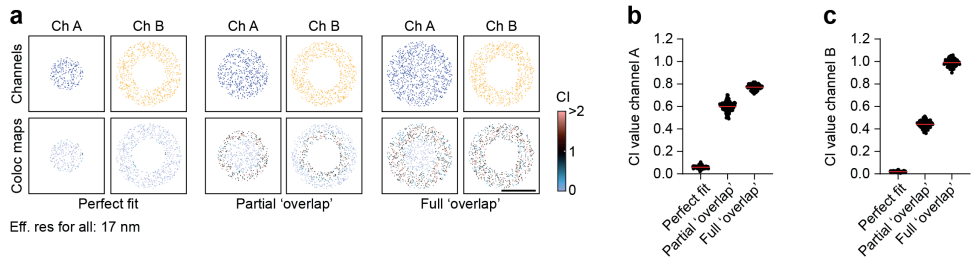
active_channel=active_channel+1;
end
end

```



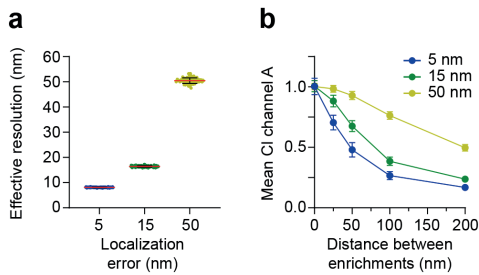
**Supplementary Figure S1, related to figure 1: Co-localization measurements on multiple clusters with varying densities and background**

(a) Simulations of multiple clusters in a channel, varying the number of clusters plotted in the second channel. (d) Simulations showing 16 clusters in channel A and 8 clusters in channel B, titrating the density of the clusters in channel B. (g) Simulations similar to (a,d) but with changing signal/background density ratios. Scale bar, 500 nm. (b,e,h) Co-localization in channel A as measured for the various conditions of which some are shown in (a,d,g). (c,f,i) Co-localization values for channel B. In all graphs, the dotted line indicates the theoretical overlap between the clusters and without background. Average effective resolution is shown below the conditions. CI, co-localization index; Eff. Res, effective resolution; S/B, Signal/background.



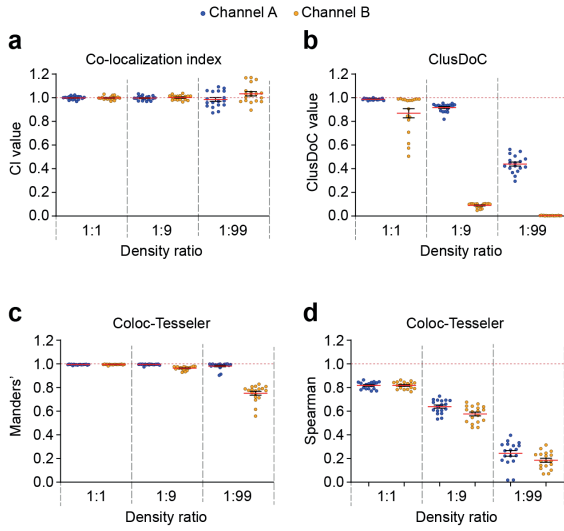
**Supplementary Figure S2, related to figure 1: Co-localization of surrounding spatial distribution**

(a) Simulated clusters in which channel B (yellow) is surrounding channel A (blue), with no overlap (perfect fit), partial overall and full overlap (albeit no overlap in the center). Co-localization maps show that co-localization is only measured in those areas where co-localization occurs. Scale bar, 250 nm. (b,c) Graphs showing co-localization values measured for channel A and B respectively across the conditions shown in (a). CI, co-localization index; Eff. Res, effective resolution; Ch, channel.



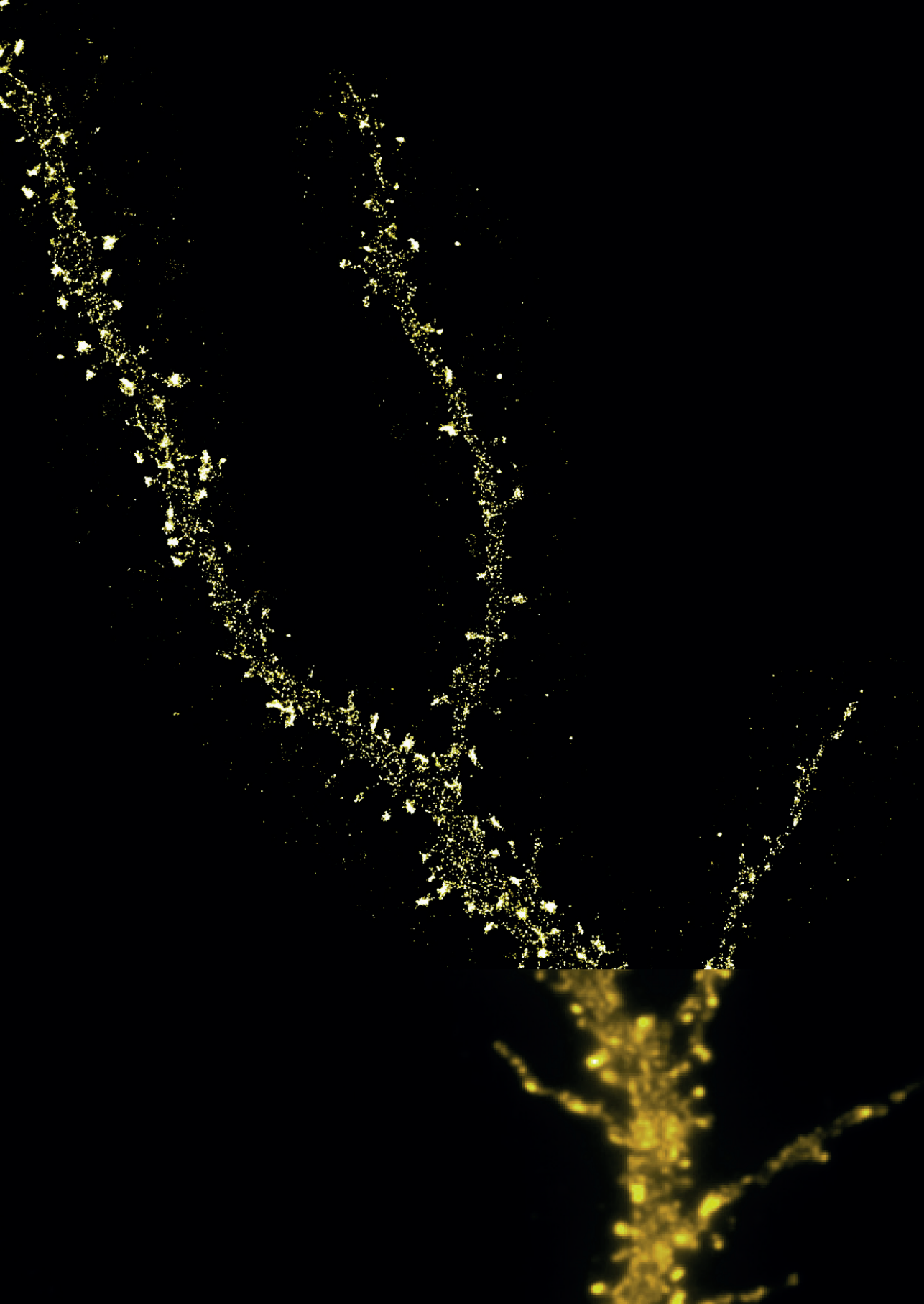
**Supplementary Figure S3, related to figure 2E: Effects of changing effective resolution on measuring co-localization**

(a) Effective resolution over the varying localization errors but constant localization densities. (b) Graphs showing mean co-localization index measured at clusters decreasing overlap at three different localization errors (5 nm, 15 nm and 50 nm). Data are represented as means  $\pm$  SEM. ROI, region of interest.



**Supplementary Figure S4, related to figure 3a,d: Comparison of co-localization index with ClusDoC and Coloc-Tesseler**

(a) Replicate of graph show as figure 3h in the mean text (for comparison), showing the co-localization index as measured across ROIs with different relative localization densities. (b) Co-localization as measured with ClusDoC. Values show percentage of co-localizing localizations (as fraction) across the density ratios. (c,d) Coloc-Tesseler analysis of co-localization, with both Manders' (c) and Spearman correlation (d) output measurements across the measured density ratios. Orange dotted line indicates the theoretical co-localization between the channels.



# 6

---

## **Mapping and manipulating the synaptic distribution of endogenous AMPAR - auxiliary protein complexes**

Jelmer Willems, Naomi C.T. Rijk and Harold D. MacGillavry

---

Cell Biology, Neurobiology and Biophysics, Department of Biology, Faculty of Science, Utrecht University, Utrecht, the Netherlands



---

## ABSTRACT

At excitatory synapses, a multitude of scaffolding molecules form the postsynaptic density that holds and precisely positions glutamate receptor complexes, which is thought to critically determine the efficiency of synaptic transmission. Moreover, proteomic studies have identified a large group of so-called auxiliary proteins that regulate glutamate receptor trafficking, modulate gating properties and are crucial for synaptic plasticity. Yet, many questions remain related to how these proteins contribute to receptor organization at synapses. This is partially due to a lack of tools that allow precise mapping of endogenous receptor complexes at synapses. Here, we developed a library of CRISPR/Cas9 knock-in constructs to label endogenous AMPA receptors (AMPARs) and their auxiliary proteins with fluorophores to study the spatiotemporal expression of native AMPAR complexes in hippocampal neurons. We found that the synaptic expression of the auxiliary proteins TARP $\gamma$ 8 and Shisa6 is closely coupled to that of the core AMPAR complex. In addition, we show that although the PDZ ligand of these proteins contributes to AMPAR positioning, removal of these domains in endogenous proteins only modestly affected protein stability and synaptic receptor levels. This suggests that other interaction motifs are important too, or that there is a high degree of redundancy among the different auxiliary proteins. Together, our results support a mechanism where a large variety of auxiliary protein families have unique but partially redundant contributions to the trafficking and positioning of synaptic AMPARs.

## INTRODUCTION

Synaptic communication through activation of  $\alpha$ -amino-3-hydroxy-5-methyl-4-isoxazolepropionic acid receptors (AMPA) is fundamental for basal transmission (Traynelis et al., 2010). The number of AMPA receptors in the synapse determines synaptic strength. Thus, synaptic strength can be modulated by mechanisms that control receptor trafficking to and anchoring in the synapse such as during synaptic plasticity (Baranovic, 2021; Diaz-Alonso and Nicoll, 2021). In addition, recent advantages in super-resolution microscopy revealed that synaptic scaffolding molecules as well as receptors cluster into nanodomains closely aligned with presynaptic release sites, thereby increasing the efficacy of transmission (Biederer et al., 2017). Thus, studying the mechanisms that control receptor trafficking to and positioning within synapses is critical.

The core AMPAR complex is a heterodimer consisting of four different subunits, GluA1-4 (Greger and Mayer, 2019; Zhao et al., 2019). The relative expression of the subunits changes throughout brain development and widely differs between brain regions (Schwenk et al., 2014). In the hippocampus, AMPARs are mainly GluA1/2 and GluA2/3 heterodimers with a smaller proportion of GluA1 homomers. In contrast, GluA4 expression is highest in early brain development while in the mature brain GluA4 is mostly restricted to the cerebellum. This subunit diversity plays a critical role in AMPAR functioning such that they influence receptor gating, activation kinetics, and trafficking (Chatterjee et al., 2019; Diaz-Alonso and Nicoll, 2021; Diering and Huganir, 2018).

In recently years, multiple families of so-called AMPAR auxiliary proteins have been identified (Chen et al., 2014; Schwenk et al., 2019; Schwenk et al., 2012). These auxiliary proteins have been shown to play critical roles in practically all lifetime stages of the receptor including AMPAR biogenesis, intracellular trafficking, membrane diffusion, synaptic positioning, gating kinetics and play an active role during synaptic plasticity (Bissen et al., 2019; Jacobi and von Engelhardt, 2021; Matthews et al., 2021). Together, the diversity in AMPA core subunits and auxiliary proteins, make the AMPAR complex an extremely flexible

and versatile platform for tuning the strength of a given synapse.

The synaptic positioning of AMPARs at synapses is largely regulated via the transmembrane AMPAR regulatory proteins (TARP) (Chen et al., 2000; Tomita et al., 2003). Like the core GluA subunits, there is regional diversity among these TARP proteins throughout the brain, with TARP $\gamma$ 8 being by far highest expressed member in the hippocampus (Schwenk et al., 2014), while TARP $\gamma$ 2 (also known as stargazin), is by far the most studied. Several other TARPs including  $\gamma$ 3,  $\gamma$ 4,  $\gamma$ 5 and  $\gamma$ 7 have also been associated with AMPAR functioning. TARP proteins bind the AMPAR core complex in the transmembrane region and interact directly with the synaptic scaffold PSD95 through a four amino acid PDZ ligand on the end of their long C-terminal tail (Hafner et al., 2015; Schnell et al., 2002; Sumioka et al., 2010). TARP $\gamma$ 2 or TARP $\gamma$ 8 are important for the membrane localization of AMPAR as individual knockouts of both TARP $\gamma$ 2 or TARP $\gamma$ 8 lead to a strong reduction in AMPAR expression at the membrane (Rouach et al., 2005; Schnell et al., 2002). Moreover, assembly of TARPs into the AMPAR complex is crucial for endoplasmic reticulum (ER) exit suggesting it to be a permanent member of the receptor (Schwenk et al., 2019). However, other studies have suggested that TARPs interact more freely with the core receptor complex (Constals et al., 2015; Tomita et al., 2004).

Another family of auxiliary proteins associated with AMPAR positioning are the Shisa protein family (also known as cystine-knot AMPAR modulating proteins (CKAMP)). Like the TARP family, only a few members (Shisa6-9), exhibit functions related the AMPAR, all with their own brain region specific expression patterns (Farrow et al., 2015; Pei and Grishin, 2012; von Engelhardt et al., 2010). Shisas are thought to bind the AMPAR through an arginine rich region just downstream of their transmembrane domain, while requiring its N-terminal cysteine rich region for their function on the AMPAR (Khodosevich et al., 2014). Like the TARP family, Shisas exhibit a C-terminal PDZ ligand that has been shown to directly interact with PSD95 (Karataeva et al., 2014; Khodosevich et al., 2014; Klaassen et al., 2016). The importance of this PDZ interaction for AMPAR anchoring relative to the TARPs is unknown but removal of the PDZ ligand does negatively influence AMPAR functioning. In addition, Shisa9 has been shown to occur in same complex together with TARP $\gamma$ 8 and together regulate AMPAR surface expression and functional kinetics (Khodosevich et al., 2014). Regarding Shisa7, there is a bit of controversy as one study has shown Shisa7 to influence AMPAR functioning, yet another study showed it to locate exclusively to inhibitory synapses, being an auxiliary protein of the Gamma-aminobutyric acid (GABA) receptor (Han et al., 2019; Schmitz et al., 2017).

Besides the TARP and Shisa families, there is a big pool of other auxiliary proteins. These include GSG1L, which has a similar structure compared to the TARPs, but shows to have more opposite effects on AMPAR gating compared to the TARPs, by part because of the lack of a critical PDZ ligand (Gu et al., 2016; Mao et al., 2017). We and others showed that this protein localizes to synapses, but at low levels in the hippocampus (Schwenk et al., 2012; Willems et al., 2020). The cornichon (CNIH) family of auxiliary proteins are another group of abundant auxiliary proteins. Although lacking a PDZ binding ligand, they have been shown to modulate both the surface trafficking and functioning of AMPARs and can compete with TARP proteins for binding spots in the AMPAR complex (Herring et al., 2013; Kato et al., 2010; Mauric et al., 2013; Nakagawa, 2019; Schwenk et al., 2009; Shi et al., 2010). The Dispanin family includes proline-rich transmembrane protein (PRRT) 1 (aka Dispanin1 or Syndig4), PRRT2 (aka Dispanin3) and Syndig1 (aka Dispanin2). Fairly understudied, they are able to bind AMPAR and modulate their function, increasing synaptic strength via

---

stabilization of AMPAR at the synapse driven by synaptic activity (Kalashnikova et al., 2010; Kaur et al., 2016; Kirk et al., 2016; Matt et al., 2018). Lastly, a vast group of auxiliary proteins, including FRRS1L and PORCN, have been associated with the ER trafficking of the AMPAR, aiding in the assembly of the heterodimeric complex controlling that only mature AMPAR complexes are transported to the membrane (Schwenk et al., 2019).

In recent years, the functional roles and structural interactions between AMPARs and their auxiliary proteins have been studied and reviewed extensively (Abdollahi Nejat et al., 2021; Bissen et al., 2019; Jacobi and von Engelhardt, 2021; Kamalova and Nakagawa, 2021). Yet, progress in understanding the mechanisms that establish receptor organization at synapses and the role of these auxiliary proteins is hindered due to the lack of tools that allow precise mapping of endogenous receptor complexes at synapses. Here, we applied CRISPR/Cas9 knock-ins to label endogenous AMPARs and their auxiliary proteins with fluorophores to study the spatiotemporal expression of native AMPAR complexes in hippocampal neurons. We questioned if the expression of the AMPAR core-subunits is linked to the synaptic expression of these auxiliary proteins, and investigate the role of the C-terminal PDZ ligand of TARP $\gamma$ 2, TARP $\gamma$ 8 and Shisa6 on auxiliary protein trafficking and anchoring at the synapse.

## RESULTS

### Mapping the localization of AMPAR auxiliary proteins in hippocampal neurons

In order to tag and visualize endogenous AMPAR auxiliary proteins, we generated CRISPR/Cas9 GFP knock-in plasmids based on ORANGE (Willems et al., 2020), for proteins that were described to be expressed in the hippocampus (Schwenk et al., 2014; Schwenk et al., 2012). Previously, we have already generated knock-ins for the GluA1-3 subunits and TARP $\gamma$ 2, TARP $\gamma$ 8, GSG1L and FRRS1L, resolving their subcellular localization (Willems et al., 2020). For an overview of the knock-in plasmids generated see Supplemental Table S1. We expressed GFP knock-in plasmids in dissociated hippocampal rat cultures at days in vitro 3 (DIV3) and visualized them on DIV21. Since many of these proteins have a low abundance, we amplified the signal with an anti-GFP antibody on permeabilized cells to visualize both surface and intracellular protein pools. We successfully obtained knock-ins for a broad range of auxiliary proteins, with TARP $\gamma$ 2/ $\gamma$ 8, Shisa6/9 and Dispanin family members PRRT1 and Syndig1 showing clear localization to the synapse (labeled by Homer1c), similar to the core AMPAR core subunits GluA1-3 (Figure 1A). PRRT2 showed a broader distribution throughout dendrites as well as the axon (also see Figure S1A), which fits well with its described function in presynaptic neurotransmitter release (Valente et al., 2016). We were unsuccessful in creating reliable knock-ins for proteins of the CNIH family. These proteins were expected to be highly expressed in the hippocampus, but we only observed low expressing puncta distributed throughout the dendrites, with minimal overlap of CNIH1 and 2 with synapses (Figure S1B). We cannot exclude that this is due to labeling artifacts or site of labeling in the protein as we were unsuccessful in tagging the corresponding gene at a different location.

For Shisa7, we set out to investigate the localization relative to excitatory and inhibitory synapses more closely. Co-staining with PSD95 or Gephyrin did not show Shisa7 to be exclusively enriched at one or both of the synapse types, although puncta were clearly visible at PSD95 positive synapses, and less at Gephyrin positive synapses (Figure S2). PORCN, like previously shown for FRRS1L is localized to the dendritic shaft, most likely in the ER, where it is known to be involved in AMPAR biogenesis (Schwenk et al., 2014). Lastly, we also generated a knock-in of Noelin1 (aka Olfactomedin-1), which is known to be secreted

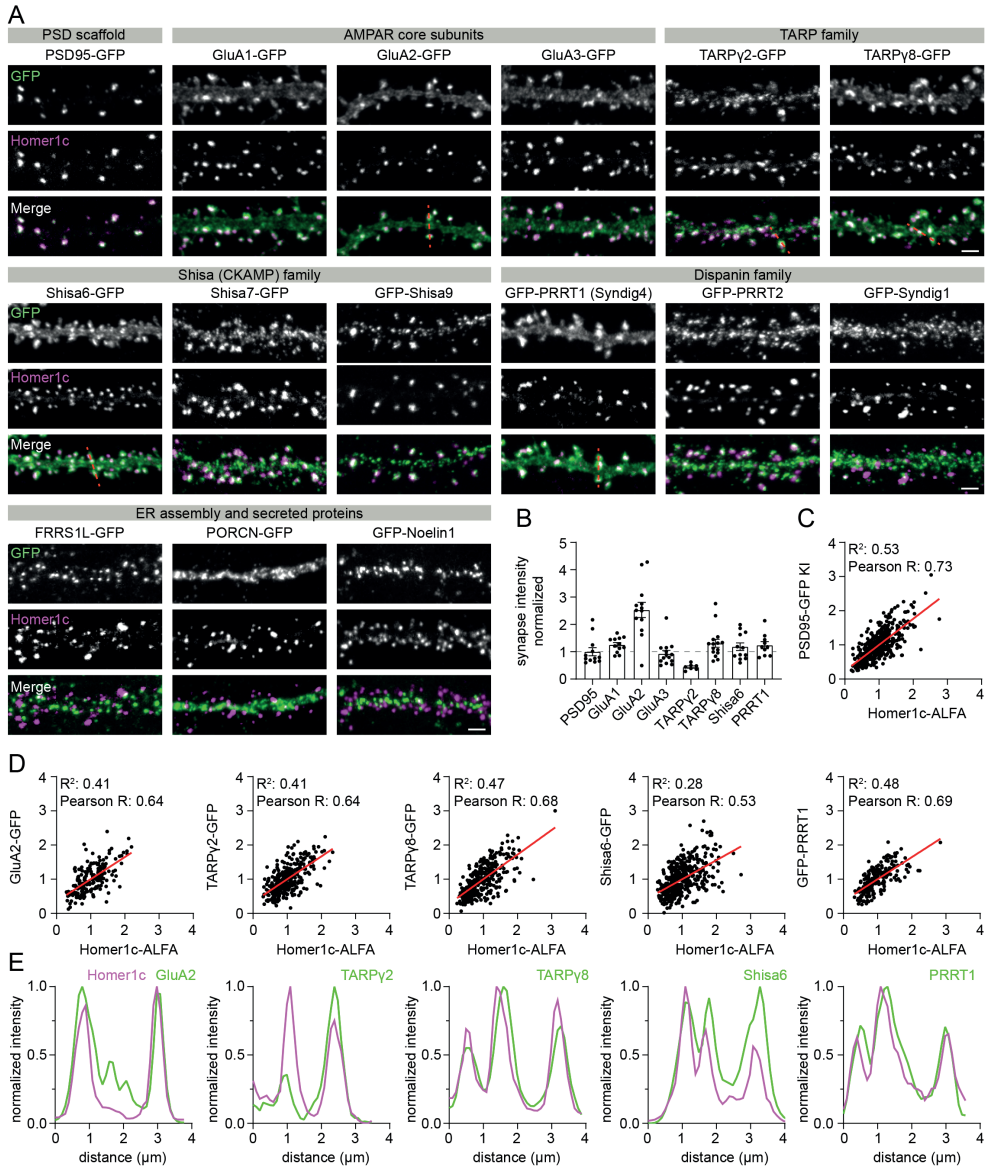


**Figure 1. Mapping the subcellular localization of AMPARs and their auxiliary proteins.**

(A) GFP-knock-ins, co-transfected with Homer1c-ALFA (DIV3) and stained with GFP antibodies at DIV21. GFP is in front of the protein name in case of a N-terminal knock-in, and behind if the tag is either internal or C-terminal. Scale bar is 2  $\mu$ m. (B) Synapse intensity of a selection of the knock-ins, labeled with anti-GFP nanobodies and normalized against PSD95-GFP knock-in intensity (grey dotted line). (C) Correlation between Homer1c-ALFA and PSD95-GFP knock-in expression normalized to the mean intensity of each protein. (D) Similar to (C), but for other selected knock-ins. Each data point corresponds to a synapse. Red line indicates linear fit. (E) Intensity line plots of orange dotted lines in (A), normalized against the max intensity. The knock-in is plotted in green, Homer1c in magenta.

---

and bound to the extracellular domains of AMPAR influencing its lateral mobility (Pandya et al., 2018). We found expression to localize to large puncta in the dendritic shaft, likely to be intracellular vesicles, although this must be confirmed.

Next, we measured the relative intensity of the auxiliary proteins in relation to the core GluA1-3 subunits and normalized to PSD95 knock-in levels for comparison (Figure 1B). For this, we selected proteins with sufficient expression levels and that showed a similar distribution as the GluA subunits and thus are likely to interact with synaptic AMPAR complexes. As expected, we found GluA2 (normalized intensity:  $2.53 \pm 0.28$ ) to be the most dominant AMPAR subunit followed by GluA1 ( $1.26 \pm 0.079$ ) and GluA3 ( $0.93 \pm 0.12$ ), suggesting that in our dissociated hippocampal cultures, most AMPAR are GluA1/2 or 2/3 heterodimers. Next we found that TARP $\gamma$ 8 ( $1.31 \pm 0.15$ ), Shisa6 ( $1.18 \pm 0.14$ ) and PRRT1 ( $1.24 \pm 0.13$ ) all have similar synaptic intensities, approximately half that of GluA2, with much lower levels of TARP $\gamma$ 2 ( $0.44 \pm 0.042$ ). Based on literature, we would expect a GluA2-TARP of 1:1 based on two TARP proteins per AMPAR complex. Interestingly, and comparing the synaptic intensities with a knock-in for PSD95, suggests there is one TARP $\gamma$ 8, Shisa6, PRRT1 and PSD95 present for each AMPAR (two GluA2 with either two GluA1 or GluA3 subunits).

Lastly, we measured the correlation between synaptic intensity of the knock-ins and expression of expressed Homer1c (Figure 1C). We found a clear correlation in intensity between Homer1c and the auxiliary proteins ( $P < 0.001$ , Pearson correlation coefficient). However, as visible from an increased spread and by observing individual synapses in the images, we did observe clear synapse to synapse differences, which seemed more predominant for TARP $\gamma$ 2 and Shisa6 compared to TARP $\gamma$ 8, PRRT1 and the AMPAR core subunit GluA2 (Figure 1D), suggesting that auxiliary protein expression contributes to synapse diversification, even within individual neurons.

### **Synaptic expression of TARP $\gamma$ 8 and Shisa6 is linked to presence of AMPAR core subunits**

Previous studies have shown that the expression of AMPARs is largely dependent on that of the TARP proteins, with the stargazer mouse (TARP $\gamma$ 2 deficient) and TARP $\gamma$ 8 knockout mouse, showing a large reduction in AMPAR surface expression levels (Fukaya et al., 2006; Rouach et al., 2005; Vandenberghe et al., 2005). Thus, we hypothesized the synaptic expression of TARP $\gamma$ 8 and Shisa6 requires these proteins to be in a complex with the AMPAR core subunits. Thus, in the absence of core-subunits, these auxiliary protein would not be able to trafficked properly.

To address this, we generated a CRISPR/Cas9 double knockout plasmid for GluA1 and GluA2, coded by the genes *Gria1* and *Gria2* respectively (Figure 2A), of which the GluA2 knockout target sequence being described previously (Incontro et al., 2014). Transfection of this knockout plasmid at DIV3 successfully results in near complete loss of both GluA1 and GluA2 in all targeted neurons at DIV21 (normalized intensity GluA1 KO:  $0.074 \pm 0.0096$ , GluA2 KO:  $0.20 \pm 0.039$ ,  $P < 0.001$  ANOVA); Figure 2B, C). By depleting both GluA1 and 2, we expect to also deplete GluA3, as in contrast to GluA1, GluA3 cannot form functional homomeric complexes (Coleman et al., 2016). In addition to validation of the double knockout, we confirmed the efficacy of single knockouts (Figure S3). Next, we tested if we could combine these knockouts with our ORANGE knock-ins. Both GluA1 and GluA2 knockout work at high efficacy while still allowing for the correct knock-in of GFP into the PSD95 coding gene (*Dlg4*), and without affecting its synaptic localization (Figure S4).

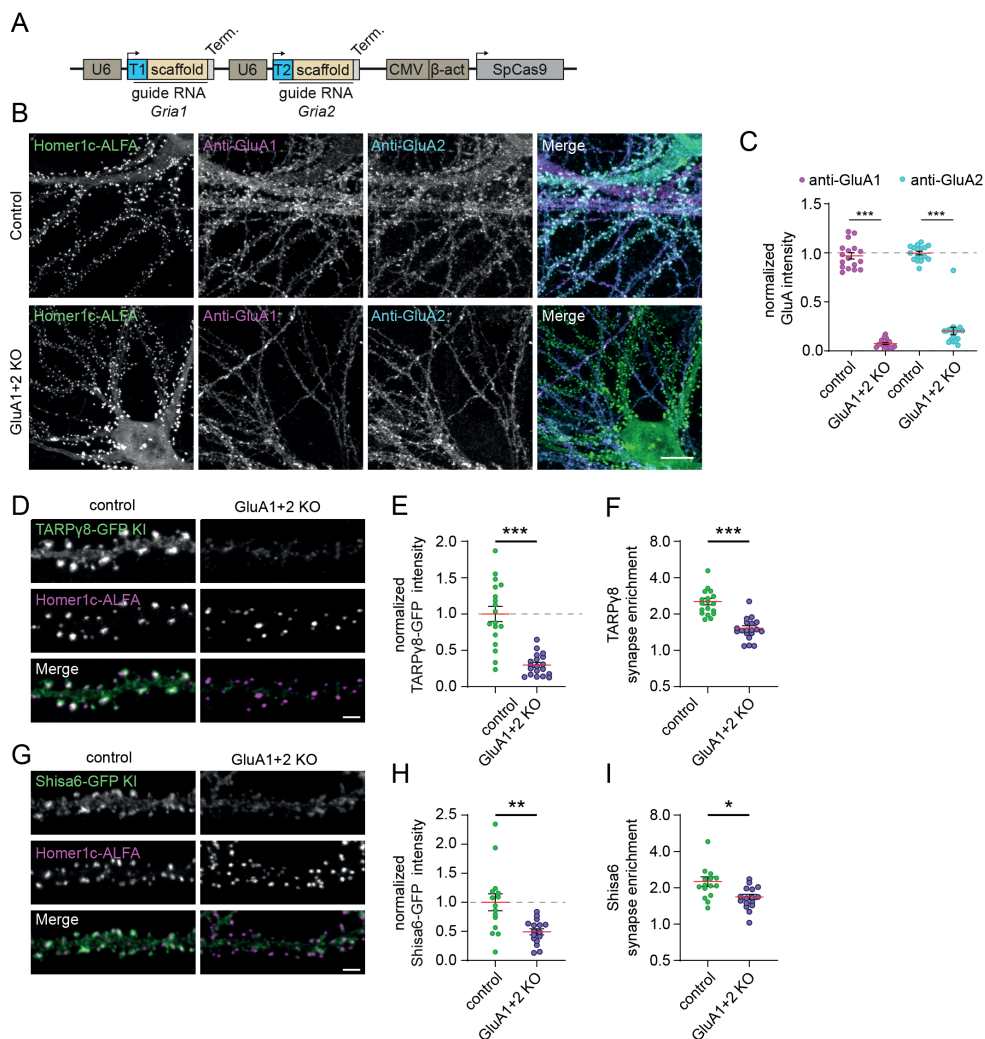


**Figure 2. GluA1 and GluA2 double-knockout and its effects on the synaptic expression of TARPy8 and Shisa6.** (A) Overview of double-knockout plasmid, containing two target sequences (T1 and T2) targeting the genes coding for GluA1 and GluA2 (*Gria1* and *Gria2*) respectively. (B) Representative images of neurons expressing a control plasmid (no target sequences), or the double-knockout plasmid, co-transfected with Homer1c-ALFA (green) and stained with anti-GluA1 (magenta) and anti-GluA2 (cyan). Scale bar is 10  $\mu$ m. (C) Quantification of knockout efficiency. Anti-GluA intensities from transfected neurons were normalized against those of surrounding non-transfected neurons. (D, G) Representative images of TARPy8-GFP (D) or Shisa6-GFP (G) knock-ins (green) co-transfected with Homer1c-ALFA (magenta) and either a control plasmid or double GluA1+2 knockout plasmid. Scale bar is 2  $\mu$ m. (E, H) Quantification of TARPy8-GFP (E) or Shisa6-GFP (H) synaptic intensity, normalized to the average of the control (grey dotted line). (F, I) Synaptic enrichment of TARPy8-GFP (F) or Shisa6-GFP (I). Data are represented as means  $\pm$  SEM. \*  $P < 0.05$ , \*\*  $P < 0.01$ , \*\*\*  $P < 0.001$ , Student t test. KO, knockout.

Having established that we can combine knockouts with knock-ins, we compared the expression of TARPy8 and Shisa6 knock-ins, in the background of a GluA1+2 double knockout. We found that for both TARPy8 (normalized synaptic intensity:  $0.29 \pm 0.034$ ,  $P < 0.001$  Student t test) and Shisa6 ( $0.49 \pm 0.052$ ,  $P < 0.01$ , student t test), fluorescence intensity

at synapses is reduced (Figure 2D, E, G, H). In addition, remaining TARP $\gamma$ 8 and Shisa6 protein is also less well enriched in the synapse (synaptic enrichment TARP $\gamma$ 8 control:  $2.54 \pm 0.16$ , GluA1+2 KO:  $1.52 \pm 0.077$ ,  $P < 0.001$ , Shisa6 control:  $2.26 \pm 0.21$ , GluA1+2 KO:  $1.68 \pm 0.087$ ,  $P < 0.05$ , student t test; Figure 2F,I ), and did not accumulate in the soma of the neurons (not quantified). To test whether this loss in expression could be linked to a specific GluA subunit, we repeated the experiment with single knockouts for GluA1 or GluA2 (Figure 3). Both GluA1 and GluA2 single knockouts resulted in a large reduction of TARP $\gamma$ 8 expression at the synapse (normalized synaptic intensity TARP $\gamma$ 8: GluA1 KO:  $0.41 \pm 0.053$ ,  $P < 0.001$ , GluA2 KO:  $0.41 \pm 0.051$ ,  $P < 0.001$ ; Figure 3A-C). In contrast, synaptic intensity of Shisa6 is only reduced in the GluA2 knockout (GluA1 KO:  $0.77 \pm 0.052$ ,  $P > 0.05$ , GluA2 KO:  $0.76 \pm 0.049$ ,  $P < 0.05$  Student t test); Figure 3D-F). Moreover, we found that the reduction in synaptic enrichment of TARP $\gamma$ 8 and Shisa6 is stronger for the GluA2 knockout (synapse/shaft intensity ratio TARP $\gamma$ 8, GluA2 control:  $2.83 \pm 0.13$ , GluA2 KO:  $1.64 \pm 0.092$ ,  $P < 0.001$ ; Shisa6, GluA2 control:  $2.63 \pm 0.10$ , GluA2 KO:  $2.01 \pm 0.095$ ,  $P < 0.001$ ) compared to the GluA1 knockout (TARP $\gamma$ 8, GluA1 control:  $3.04 \pm 0.15$ , GluA1 KO:  $2.49 \pm 0.18$ ,  $P < 0.05$ ; Shisa6, GluA1 control:  $2.84 \pm 0.11$ , GluA1 KO:  $2.70 \pm 0.12$ ,  $P >$

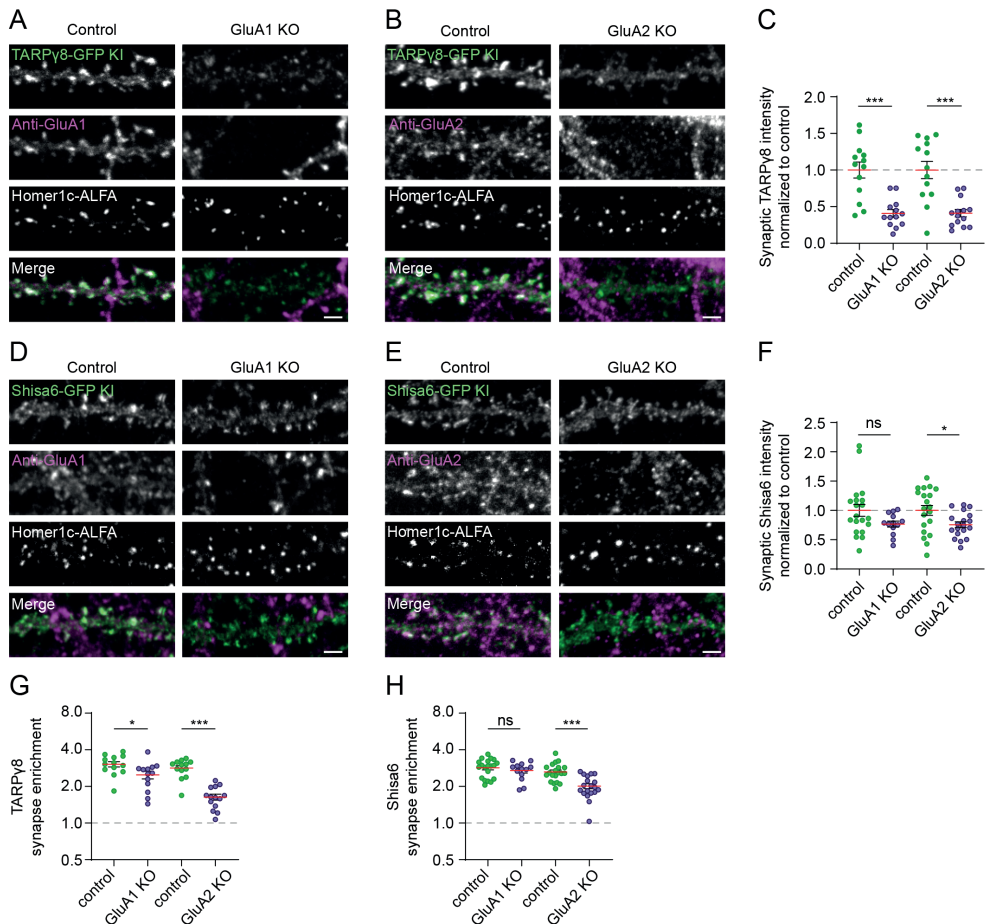


Figure 3. Effects of single GluA1 or GluA2 knockout on synaptic expression of TARP $\gamma$ 8 and Shisa6.

**Figure 3 (continued)** (A,B ) Representative images of TARP $\gamma$ 8-GFP knockin (green), co-transfected with Homer1c-ALFA (not in the merge) and a control plasmid, or knockout plasmid for GluA1 (A) or GluA2 (B) and also stained with anti-GluA1 or anti-GluA2 respectively (magenta). Scale bar is 2  $\mu$ m. (D, E) Representative images of Shisa6-GFP (green), co-transfected with Homer1c-ALFA (not in the merge) and a control plasmid, or knockout plasmid for GluA1 (D) or GluA2 (E) and also stained with anti-GluA1 or anti-GluA2 respectively (magenta). Scale bar is 2  $\mu$ m. (C, F) Quantification of TARP $\gamma$ 8-GFP (C) and Shisa6-GFP (F) synaptic intensities normalized to the mean of the control conditions. (G, H) Quantification of the effects of single GluA knockout on synapse enrichment of TARP $\gamma$ 8-GFP (G) and Shisa6-GFP (H). Data are represented as means  $\pm$  SEM. ns not significant, \*  $P < 0.05$ , \*\*\*,  $P < 0.001$ , Student t test. KO, knockout.

0.05, student t test; Figure 3G, H). Thus, these results indicate that the synaptic expression of TARP $\gamma$ 8 and Shisa6 is directly linked to the expression of the AMPAR core subunits, and is required for their expression at the synapse.

### Generation of $\Delta$ PDZ ligand mutants using a novel knock-in replacement strategy

Next, we investigated the synaptic anchoring properties of the TARP proteins and Shisa6. the PDZ ligand of the TARP and Shisa proteins can bind directly to PSD95. Previously, a TARP $\gamma$ 8 knock-in mouse line lacking the PDZ ligand ( $\Delta$ PDZ), showed impaired basal transmission (Sumioka et al., 2011), but with normal LTP, suggesting that AMPAR-TARP $\gamma$ 8- $\Delta$ PDZ complexes can still traffic to the synapse. In contrast, overexpression of an AMPAR fused to WT TARP $\gamma$ 8 in AMPAR knockout background could rescue of basal transmission, but a TARP $\gamma$ 8- $\Delta$ PDZ fusion could not (Sheng et al., 2018; Watson et al., 2021). Moreover, it is important to consider that there is level of redundancy between TARP (and potentially Shisa) proteins and other auxiliary proteins, contributing to AMPAR trafficking to and anchoring in the synapse. Therefore, we questioned whether endogenously tagged TARP and Shisa6 proteins without ( $\Delta$ PDZ) PDZ ligand are still able to traffic to and anchor at the synapse, thus measuring the relative importance of this PDZ ligand as part of a native AMPAR.

Previously, we tagged TARP $\gamma$ 2 and TARP $\gamma$ 8 with a GFP tag, inserted in the c-tail (glycine rich region) of the proteins, thereby (if in frame) leaving the PDZ ligand unharmed (Willems et al., 2020). Here, we generated C-terminal knock-ins, aiming to tag the TARP $\gamma$ 2, TARP $\gamma$ 8, Shisa6 and Shisa7 with a GFP tag, but replacing the c-terminus including critical PDZ ligand (Figure 4A). Thus, in the donor, in addition to a GFP tag, we also added the last  $\sim$ 12 amino acids including PDZ ligand and new stop codon. This way, we could also make a donor in which we left out the PDZ ligand creating a GFP-tagged  $\Delta$ PDZ mutant knock-in. Note that we used the WT variants created here also in Figure 1 and 2. The C-terminal Shisa7 knock-in (Figure 1 and S2) was also created using this approach.

We validated the correct integration of these donors using Sanger sequencing (Figure S5). First, we isolated genomic DNA from neurons electroporated with the knock-in constructs. Next, we amplified the 5' and 3' junctions surrounding the integrated donor. Although successfully for most targets, we were unable to amplify the 5' junction of the TARP $\gamma$ 8 knock-in. This was probably caused due to secondary structure in the genomic DNA as we were also unable to amplify the unedited TARP $\gamma$ 8 locus. Ligated into pJET vectors, we analyzed individual clones using Sanger sequencing, and found that integration was highly accurate for the majority of clones (Figure S5). Some indels did occur, but these were mostly after the stop codon and likely because of some homology between the donor and genomic sequence. Importantly, we could confirm the integration of the GFP tag together with the C-terminal replacement for both the WT and  $\Delta$ PDZ knock-ins. Additionally, the expression pattern of the WT TARP $\gamma$ 8 knock-in generated here, shows a similar expression pattern as the GFP knock-in we created previously (Willems et al., 2020) (Figure S6A). In addition, we



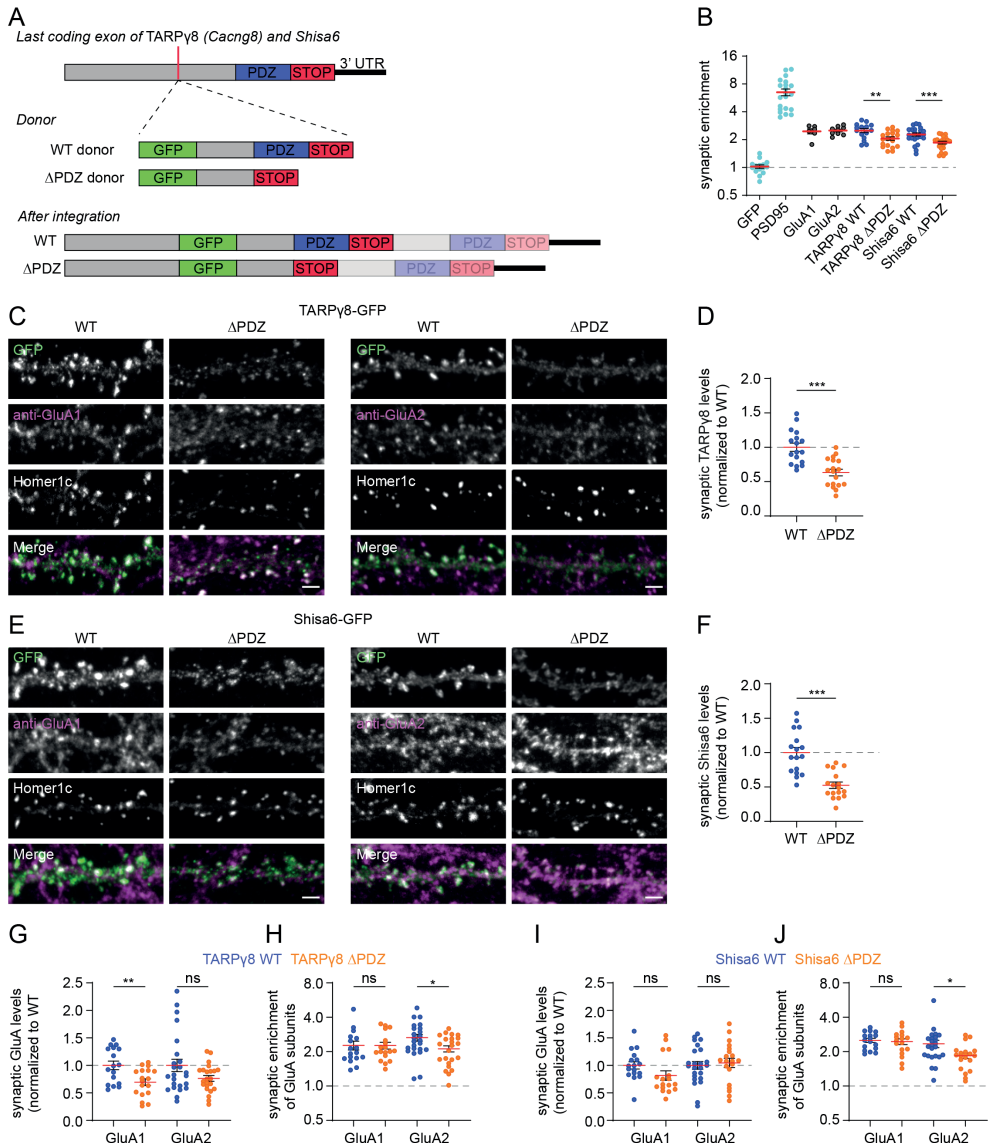


**Figure 4. Generation of C-terminal  $\Delta$ PDZ mutant knock-ins for TARP proteins and Shisa6, and their effects on synaptic localization.**

(A) Overview of knock-in strategy. A double stranded break is induced ~36 base pairs upstream of the stop codon. A donor DNA is integrated that contains a GFP tag, the remaining C-terminal base pairs including (WT) or excluding ( $\Delta$ PDZ) the PDZ ligand and a new stop codon. After integration in the genome, the former c-tail will remain untranslated with the protein thus containing an internal GFP tag and either a replica of the WT c-tail or a c-tail without PDZ ligand. (B) Synapse enrichment of GFP expression comparing WT and  $\Delta$ PDZ knock-ins compared to enrichment of GFP fill, PSD95-GFP, GluA1-GFP and GluA2-GFP knock-ins. (C, D) Representative images of TARP $\gamma$ 8-GFP (C) and Shisa6-GFP (D), comparing WT with  $\Delta$ PDZ (green), co-transfected with Homer1c-ALFA (not in merge), and stained for anti-GluA1 or anti-GluA2 respectively (magenta). Scale bar is 2  $\mu$ m. (E, F) Synaptic intensity of TARP $\gamma$ 8-GFP (E) and Shisa6-GFP (F), comparing WT with  $\Delta$ PDZ, normalized to the mean of the WT. (G, I) Synaptic intensities of anti-GluA1 and anti-GluA2 in TARP $\gamma$ 8-GFP (G) and Shisa6-GFP (I), comparing WT

**Figure 4 (continued)** and  $\Delta$ PDZ. Intensities normalized to WT condition. (H, J) Synaptic enrichment of anti-GluA1 and anti-GluA2 in TARP $\gamma$ 8-GFP (H) and Shisa6-GFP (J), comparing WT and  $\Delta$ PDZ. Intensities normalized to WT condition. Data are represented as means  $\pm$  SEM. ns not significant, \*  $P < 0.05$ , \*\*  $P < 0.01$ , \*\*\*,  $P < 0.001$ , Student t test.

also generated a N-terminal knock-in for Shisa6, showing an identical expression pattern to the C-terminal tagged version (Figure S6B). Together, this approach thus allows us to successfully generate WT and  $\Delta$ PDZ knock-ins for the TARP and Shisa proteins.

### Localization of $\Delta$ PDZ TARP $\gamma$ 8 and Shisa6 mutants and its effect on localization of GluA1 and 2.

To test the effects of PDZ removal on TARP $\gamma$ 8 and Shisa6 localization, we expressed these knock-ins in neurons and compared their localization towards the synapse in comparison to a GFP fill, postsynaptic density (PSD) scaffold PSD95 and the core subunits GluA1-3 (Figure 4B, C, E). The WT TARP $\gamma$ 8 and Shisa6 showed a similar synaptic enrichment compared to the core subunits (synapse/shaft intensity ratio GluA1:  $2.46 \pm 0.16$ , GluA2:  $2.51 \pm 0.087$ , TARP $\gamma$ 8 WT:  $2.50 \pm 0.12$ , Shisa6 WT:  $2.27 \pm 0.089$ ,  $P > 0.05$  ANOVA; Figure 4B). Note that we measure both surface and internal protein pools. Removal of the PDZ ligand of TARP $\gamma$ 8 and Shisa6 significantly reduced synaptic enrichment, albeit not completely (TARP $\gamma$ 8  $\Delta$ PDZ:  $2.06 \pm 0.089$ ,  $P < 0.01$ , Shisa6  $\Delta$ PDZ:  $1.86 \pm 0.065$ ,  $P < 0.001$ , student t test). We found similar results for TARP $\gamma$ 2 (Figure S7). Measuring the intensity of TARP $\gamma$ 8 and Shisa6 at the synapse, we found that removal of the PDZ ligand also reduced overall expression at the synapse (normalized synaptic intensity TARP $\gamma$ 8 WT:  $1.00 \pm 0.059$ , TARP $\gamma$ 8  $\Delta$ PDZ:  $0.63 \pm 0.049$ ,  $P < 0.001$ ; Shisa6 WT:  $1.00 \pm 0.075$ , Shisa6  $\Delta$ PDZ:  $0.52 \pm 0.047$ ,  $P < 0.001$ , student t test; Figure 4D, F). This indicates that the PDZ ligands of both proteins contribute to their synaptic anchoring, but that there are additional mechanisms in place to recruit TARP $\gamma$ 8 and Shisa6 to the synapse.

In addition to effects on the synaptic expression of the TARP $\gamma$ 8 and Shisa6 themselves, we questioned if there are any effects of TARP $\gamma$ 8- and Shisa6- PDZ removal on the synaptic localization of the core AMPAR complex. To test this, we co-labeled the WT and  $\Delta$ PDZ knock-ins for TARP $\gamma$ 8 and Shisa6 with antibodies against GluA1 or GluA2 (Figure 4C, E). Next, we measured GluA intensity and enrichment in synapses of knock-in positive neurons. We found, likely influenced by a large amount of variation in the dataset, a small (but significant) reduction in GluA1 intensity (normalized GluA1 intensity in TARP $\gamma$ 8 WT:  $1.00 \pm 0.077$ , TARP $\gamma$ 8  $\Delta$ PDZ:  $0.70 \pm 0.060$ ,  $P < 0.01$ ) and a trend for GluA2 (normalized GluA2 intensity in TARP $\gamma$ 8 WT:  $1.00 \pm 0.011$ , TARP $\gamma$ 8  $\Delta$ PDZ:  $0.76 \pm 0.052$ ,  $P < 0.05$ , student t test) in the TARP $\gamma$ 8- $\Delta$ PDZ mutant (Figure 4G), with GluA2 also displaying slightly reduced synaptic enrichment (synapse/shaft ratio of GluA2, TARP $\gamma$ 8 WT:  $2.65 \pm 0.18$ , TARP $\gamma$ 8  $\Delta$ PDZ:  $2.12 \pm 0.13$ ,  $P < 0.05$ , student t test; Figure 4H). For Shisa6, we also observed a slight (non-significant) reduction in GluA1 levels (Shisa6 WT:  $1.00 \pm 0.066$ , Shisa6  $\Delta$ PDZ:  $0.82 \pm 0.086$ ,  $P > 0.05$ ) but not GluA2 (Shisa6 WT:  $1.00 \pm 0.070$ , Shisa6  $\Delta$ PDZ:  $1.05 \pm 0.085$ ,  $P > 0.05$ , student t test; Figure 4I). Similar to TARP $\gamma$ 8, removal of the PDZ ligand from Shisa6 resulted in reduced synaptic enrichment of GluA2 (synapse/shaft ratio of GluA2, Shisa6 WT:  $2.34 \pm 0.18$ , Shisa6  $\Delta$ PDZ:  $1.84 \pm 0.10$ ,  $P < 0.05$ ), but not GluA1 (Shisa6 WT:  $2.51 \pm 0.11$ , Shisa6  $\Delta$ PDZ:  $2.45 \pm 0.14$ ,  $P > 0.05$ , student t test; Figure 4J). Together, these results indicate that the PDZ ligands of TARP $\gamma$ 8 and Shisa6 only partially contribute to the positioning of AMPAR complexes at synapses.

## The PDZ ligand of TARP $\gamma$ 8 but not Shisa6 regulates synaptic turnover

We reasoned that a loss of PDZ ligands would disturb the anchoring of TARP $\gamma$ 8 and Shisa6 at the synapse and thus its ability to be retained there. Since we only found a slight reduction in synaptic enrichment of these proteins, we hypothesized that there might be more predominant role for the PDZ ligand in the synaptic turnover.

To measure this, we performed live-cell imaging combined with fluorescence recovery after photobleaching (FRAP) to measure the turnover of proteins and compare this in relation to the turnover of GluA1 and GluA2 (Figure 5A, B). Interestingly, we found that the kinetics of endogenous GluA1 turnover is slightly faster than that of GluA2 (Tau GluA1 (min.):  $1.19 \pm 0.096$ , GluA2:  $1.86 \pm 0.27$ ,  $P < 0.05$ ; Figure 5G), but with a similar mobile fraction (mobile fraction GluA1:  $0.78 \pm 0.025$ , GluA2:  $0.71 \pm 0.029$ ,  $P > 0.05$ ; Figure 5H). Next, we

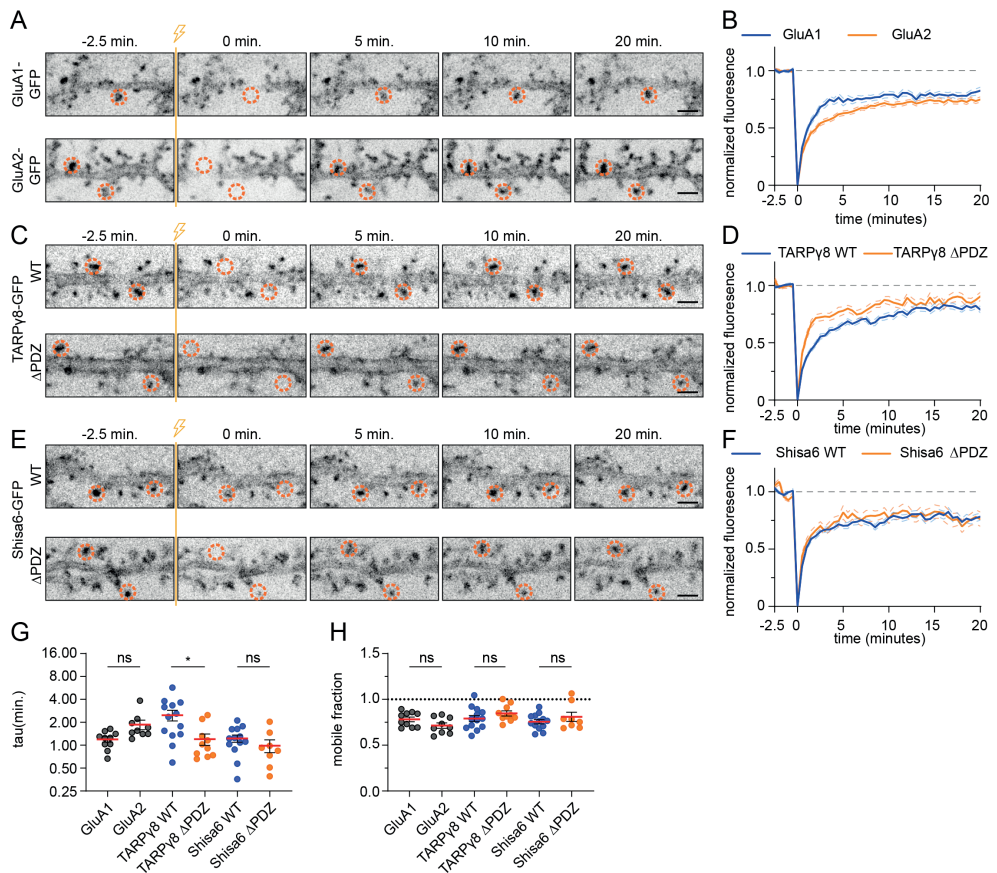


**Figure 5. Fluorescence recovery after photobleaching measuring synaptic turnover of WT and  $\Delta$ PDZ TARP $\gamma$ 8 and Shisa6.**

(A, C, E) Representative images of FRAP imaging on GluA1-GFP and GluA2-GFP (A), TARP $\gamma$ 8 WT and  $\Delta$ PDZ (C) and Shisa6-GFP WT and  $\Delta$ PDZ (E). Spine heads indicated with orange dotted circles were bleached at timepoint zero, also illustrated with the yellow line. Imaging was performed with 30 second intervals. Scale bar is 2  $\mu$ m. (B, D, F) normalized fluorescence intensity of analyzed spines over time. Data was normalized against the average of the data points before bleaching. (G) Tau values as measured from a one-phase association curve averaged per neuron. (H) Mobile fraction, calculated by averaging the spine intensities of the last five frames averaged per neuron. Data are represented as means  $\pm$  SEM. ns not significant, \*  $P < 0.05$ . Student t test.

measured FRAP dynamics of TARP $\gamma$ 8 WT and  $\Delta$ PDZ (Figure 5C, D). The TARP $\gamma$ 8  $\Delta$ PDZ mutant, shows faster recovery compared the WT (Tau TARP $\gamma$ 8 WT (min.):  $2.48 \pm 0.40$ , TARP $\gamma$ 8  $\Delta$ PDZ:  $1.20 \pm 0.20$ ,  $P < 0.05$ , student t test; Figure 5G). No difference was observed in the mobile fraction (TARP $\gamma$ 8 WT:  $0.79 \pm 0.033$ , TARP $\gamma$ 8  $\Delta$ PDZ:  $0.85 \pm 0.028$ ,  $P > 0.05$ ; Figure

5H). In contrast to TARP $\gamma$ 8, we did not find a difference in FRAP kinetics between the Shisa6 WT and  $\Delta$ PDZ mutant (Tau Shisa6 WT (min.):  $1.23 \pm 0.14$ , Shisa6  $\Delta$ PDZ:  $0.98 \pm 0.19$ ,  $P > 0.05$ ; Figure 5G, mobile fraction Shisa6 WT:  $0.76 \pm 0.024$ , Shisa6  $\Delta$ PDZ:  $0.81 \pm 0.050$ ,  $P > 0.05$ , student t test; Figure 5H). In summary, these results show that the PDZ ligand of TARP $\gamma$ 8, but not Shisa6, influences the dynamics of these proteins at the synapse.

### Subsynaptic clustering of TARP $\gamma$ 8 and Shisa6

So far, our results showed that removal of the PDZ ligand from TARP $\gamma$ 8 and Shisa6 does not completely abolish their localization at the synapse. This could in part, be explained by compensatory mechanisms between the auxiliary proteins, especially if expressed at endogenous levels. In addition, we also have to take into consideration that we observed a partial loss of protein levels at the synapse upon removal of the PDZ ligand (Figure 4). PSD95 has been shown to cluster in subsynaptic nanodomains aligning with presynaptic release sites (MacGillavry et al., 2013; Nair et al., 2013; Tang et al., 2016). As TARP $\gamma$ 8 and Shisa6 PDZ ligands both directly interact with PSD95, we tested whether deleting the PDZ ligand might alter their subsynaptic organization using direct stochastic optical reconstruction microscopy (dSTORM).

For this, we first, created WT and  $\Delta$ PDZ variants of TARP $\gamma$ 8 and Shisa6 harboring a spaghetti monster HA (smFP-HA) tag instead of the GFP tag used so far, as it can be effectively amplified using specific HA antibodies (Viswanathan et al., 2015), crucial for obtaining sufficient signal required for dSTORM. Next, we performed dSTORM imaging reconstructing the nanoscale organization of TARP $\gamma$ 8 and Shisa6 in dendrites (Figure 6A, B, G, H). We investigated the nanoscale organization by measuring the local density within clusters, selected based on the spine head (Figure 6C, I). We found that both TARP $\gamma$ 8 and Shisa6 cluster into nanodomains (number of nanodomains/cluster TARP $\gamma$ 8 WT:  $1.43 \pm 0.053$ , Shisa6 WT:  $1.37 \pm 0.037$ ; Figure 6D, J). This number was not altered in the  $\Delta$ PDZ mutants (TARP $\gamma$ 8  $\Delta$ PDZ:  $1.35 \pm 0.042$ , Shisa6  $\Delta$ PDZ:  $1.34 \pm 0.024$ , both  $P > 0.05$ , student t test). In addition, we did not find differences in nanodomain size between WT and  $\Delta$ PDZ (nanodomain diameter TARP $\gamma$ 8 WT (nm):  $135.7 \pm 6.97$ , TARP $\gamma$ 8  $\Delta$ PDZ:  $135.9 \pm 5.13$ ,  $P > 0.05$ ; Shisa6 WT:  $127.2 \pm 4.86$ , Shisa6  $\Delta$ PDZ:  $135.6 \pm 4.64$ ,  $P > 0.05$ , student t test). Interestingly, the sizes of the auxiliary protein nanodomains are considerably larger than the  $\sim 80$  nm reported for PSD95 (MacGillavry et al., 2013). Last, we measured if the density of the localizations in the nanodomains relative to outside is affected by removal of the PDZ ligand. The density was not affected in the  $\Delta$ PDZ mutants (localization density in/out TARP $\gamma$ 8 WT:  $3.27 \pm 0.083$ , TARP $\gamma$ 8  $\Delta$ PDZ:  $3.10 \pm 0.083$ ,  $P > 0.05$ ; Shisa6 WT:  $3.21 \pm 0.046$ , Shisa6  $\Delta$ PDZ:  $3.23 \pm 0.086$ ,  $P > 0.05$ , student t test; Figure 6F, L). Together, this indicates that synaptically localized TARP $\gamma$ 8 and Shisa6 proteins without the PDZ ligand are not affected in their ability to cluster into subsynaptic nanodomains.

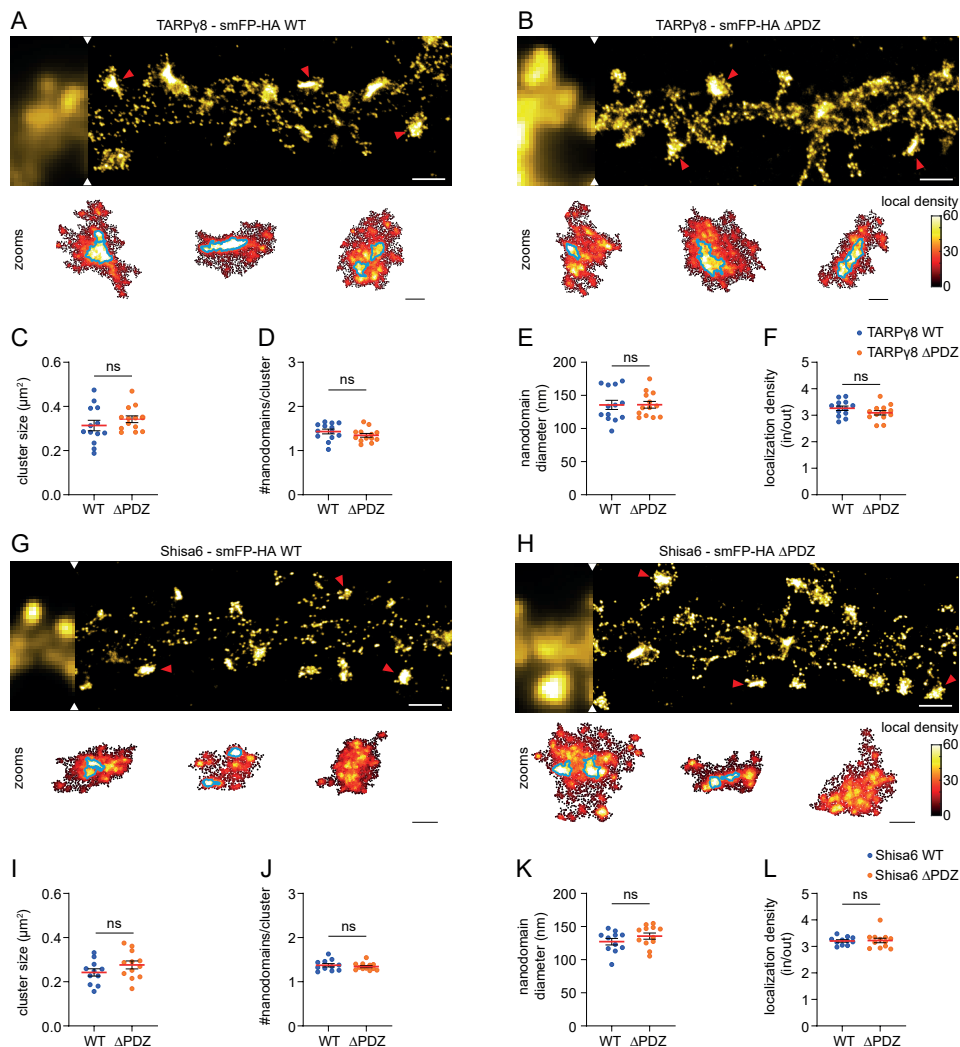


**Figure 6. Subsynaptic clustering of TARP $\gamma$ 8 and Shisa6 in nanodomains.**

(A, B) Representative dSTORM reconstructions (pixel size 10 nm) of TARP $\gamma$ 8 WT (A) and  $\Delta$ PDZ (B), tagged with smFP-HA tags. Overlap with corresponding widefield images is shown. Scale bar is 2  $\mu$ m. Zooms show local density analysis of clusters indicated with red arrows in (A) and (B). Localizations are plotted with color code indicating their local density value. Nanodomains are outlined in blue. Scale bar of zooms is 200 nm. (G, H) Same as (A) and (B) but for Shisa6 WT (G) and  $\Delta$ PDZ (H). (C, I) Cluster size of analyzed structures. (D, J) Average number of nanodomains per cluster. (E, K) Average nanodomains diameter. (F, L) Average localization density of the localization in/out of nanodomains. Each datapoint in the graphs shows the average value per analyzed neuron. Data are represented as means  $\pm$  SEM. ns not significant. Student t test.

## DISCUSSION

### Mapping the localization of AMPAR auxiliary proteins

In this study, we mapped the subsynaptic localization of AMPAR auxiliary proteins. Several of these proteins showed a clear synaptic localization, similar to that of the core AMPAR including the proteins of the TARP and Shisa families but also PRRT1, member of the

Dispanin family. Unexpectedly, we could not detect high levels of the CNIH proteins, even though these proteins, especially CHIN2, are expected to have expression levels close to that of the TARP proteins. Alternatively, it has been found that CNIH2 and 3 show maximum mRNA and protein expression early after birth, which then decline towards adulthood (Mauric et al., 2013). Thus it would be interesting to test the expression of these knock-ins at different stages in neuronal development. We also labeled Noelin1, which is expected to be secreted and bind to surface expressed AMPAR. We found that it mainly localizes to the dendritic shaft, possibly in intracellular vesicles. It would thus be interesting to test whether these puncta show overlap with markers of the exocytotic machinery like Ras-related protein 6 (Rab6).

We found that the relative expression of the core AMPAR subunits GluA1-3 reflects what has been described previously, suggesting most AMPARs to be GluA1/2 and GluA2/3 heterodimers. Interestingly, we found that the intensity of TARP $\gamma$ 8, the main TARP expressed in hippocampal neurons, is around half that of GluA2, suggesting the availability of one TARP per AMPAR complex, different from a 2:1 TARP:AMPA ratio, described in literature (Schwenk et al., 2012). Moreover, we found that there is a large variability in the synaptic content of several auxiliary proteins, relative to the synaptic scaffold Homer1c. Indeed, within brain regions, and even along the length of a single neuron's dendrite, synapses display a remarkable diversity in size, shape, electrical properties and proteomic composition (Cizeron et al., 2020; Grant and Fransen, 2020; Micheva et al., 2010; Zhu et al., 2018), fitting well with the idea that synapse specificity is in part determined by the relative levels of auxiliary proteins.

### **Combining simultaneous CRISPR/Cas9 knock-in and knockout in the same neuron**

We show that we can combine CRISPR/Cas9 knock-ins based on our ORANGE method (Willems et al., 2020), with knockouts. A powerful combination that allows us to endogenously tag a protein of interest, while generating a complete knockout of other proteins. Since the ORANGE method is based on non-homologous end joining, the donor of the knock-in can also be integrated into the double stranded break intended. to make a knockout in the GluA1 and GluA2 genes. Thus, this could theoretically result in labeling of GluA1 or GluA2 with the tag meant to label the knock-in. To prevent this, first we only used donors that contain a stop codon. Since the GluA1 and GluA2 knockout constructs used here make use of target sequence targeting the first exon of the genes, any unintended (in-frame) tagging of GluA1 or GluA2 with the donor DNA, will not result in a functional labeled GluA protein. Second, the knockouts target the exon close to the exon-intron boundary, which possibly influences mRNA splicing if the donor DNA would be integrated at such a location. Because of this, we were unable to generate GluA1 and GluA2 knock-ins using the target sites used for the knockouts (not shown). Together, these measures make sure that we can reliably combine a NHEJ-based knock-in with a knockout allowing for studying endogenous protein localization and dynamics while selectively and efficiency depleting neurons of other protein species.

### **Expression dependency of auxiliary proteins and AMPAR core subunits**

The assembly of the AMPAR complex in the ER is a tightly regulated process. It has been shown that the complex can only leave the ER if bound to a TARP (Schwenk et al., 2019). Complete knockout of TARP $\gamma$ 8 shows reduced AMPAR protein, but not mRNA levels (Fukaya et al., 2006; Rouach et al., 2005). In contrast, knockout of Shisa6 does not influence synaptic content of AMPAR (Klaassen et al., 2016). Here, we show that the knockout of the

---

core AMPAR subunits reduces the synaptic localization of TARP $\gamma$ 8 and Shisa6. Although we did not observe strong accumulation of the proteins in the ER (either dendrites or soma), it would be interesting to test whether this also extended to total protein levels, measured by for example western blotting and perform similar measurements for other auxiliary proteins.

### **Anchoring of AMPARs through the PDZ ligand of TARP $\gamma$ 8 and Shisa6**

We also investigated the role of the PDZ ligand of TARP $\gamma$ 8 and Shisa6 in AMPAR positioning. Strikingly, and partially unexpected, removing the PDZ ligand of the endogenous proteins had only mild effects on the synaptic localization and trafficking of the auxiliary proteins themselves, and the localization of the AMPAR core complex. Although we observed increased synaptic turnover kinetics for TARP $\gamma$ 8  $\Delta$ PDZ and a reduction in synaptic expression of both TARP $\gamma$ 8  $\Delta$ PDZ and Shisa6  $\Delta$ PDZ, a significant pool of protein seemed to localize and anchor correctly, even at a subsynaptic level. This indicates, that even though the PDZ ligand of these individual proteins play a role in AMPAR positioning, there is some form of redundancy in this process. First, redundancy within the TARP and Shisa families could partially explain why localization of the AMPAR complex, including the auxiliary proteins themselves is only mildly affected. Although TARP $\gamma$ 8 is the most abundant TARP, we also found TARP $\gamma$ 2 expression in our neuronal preparations. In addition, several studies have indicated that surface expressed TARP $\gamma$ 2 is more synaptically enriched compared to TARP $\gamma$ 8 (Bessa-Neto et al., 2021; Inamura et al., 2006; Sumioka et al., 2011), which might indicate some differences in their importance for AMPAR anchoring, independent from their relative abundance. Second, the synaptic localization and anchoring of AMPARs is likely to be influenced by other auxiliary protein families, and even the core GluA subunits themselves. For example, the N-terminal domain of the GluA2 subunit has been shown to influence AMPAR positioning at the synapse (Diaz-Alonso et al., 2017; Watson et al., 2017; Watson et al., 2021). Third, it is currently unknown if the interaction between the AMPAR core complex and auxiliary proteins like TARPs and Shisa, is a permanent one, or if they can exchange as suggested (Constals et al., 2015; Tomita et al., 2004). What we do know is that at least the association of TARP proteins with the AMPA core is critical for exit of the complex from the ER (Schwenk and Fakler, 2021). Exchange of TARPs from the core AMPAR complex, could explain why we observe slower FRAP dynamics for TARP $\gamma$ 8 WT in comparison to the GluA1 and GluA2 subunits, and Shisa6. Fourth, motifs other than the PDZ ligands could influence auxiliary protein and AMPAR positioning. For example, the highly charged tail of TARP protein could undergo phase separation with scaffolding molecules such as PSD95 concentrating it in the synapse (Zeng et al., 2019). Together, our results show, that the synaptic trafficking and anchoring of AMPARs is driven through a combination of multiple auxiliary proteins. While overexpression of WT or mutant auxiliary proteins can yield important insight into their function (for example in (Bats et al., 2007; Watson et al., 2021)), this study makes clear that when expressed at endogenous levels, effects of for example PDZ removal are more subtle.

In summary, we developed a set of novel labeling tools to map the subcellular localization of endogenous AMPAR auxiliary proteins. We have extended this with tools that allow for combining knock-ins with knockouts and generating C-terminal mutant knock-ins. These have enabled us to study the anchoring of these proteins at endogenous levels. Taken together, our results suggest that AMPAR trafficking to, and anchoring at the synapse is a process that cannot be explained by a single auxiliary protein, but rather is a well-balanced cooperation between auxiliary protein families, which thus results in a high degree of redundancy. Further

research will have to elude the relative importance of the individual auxiliary protein species on AMPAR trafficking and positioning, and thereby how they influence the functionality of native complexes during synaptic activity and plasticity. In addition, the diversity in AMPAR auxiliary proteins could allow for synapse specification. Thus, it will be of interest to investigate the auxiliary protein composition at individual synapses.

## **MATERIALS AND METHODS**

### **Ethics statement**

All experiments were approved by the Dutch Animal Experiments Committee (Dier Experimenten Commissie [DEC], work protocol project number: AVD1080020173404), performed in line with institutional guidelines of Utrecht University, and conducted in agreement with Dutch law (Wet op de Dierproeven, 1996) and European regulations (Directive 2010/63/EU). Timed pregnant Wistar rats were obtained from Janvier Labs.

### **Antibodies and reagents**

Primary antibodies used in this study are the following: rabbit anti-GFP (MBL Sanbio, 598, RRID AB\_591819), mouse anti-GFP ([3E6], Thermo Fisher Scientific, A-11120, RRID AB\_221568), rat anti-HA ([3F10], Sigma, 11867423001, RRID AB\_390919), mouse anti-PSD95 ([K28/43], Neuromab, 75-028, RRID AB\_2307331), mouse anti-Gyphrin ([mAb7a], Synaptic Systems, 147 011, RRID AB\_887717), anti-GFP nanobody-ATTO488 (Nanotag, N0304-At488-L), anti-PSD95 nanobody-Alexa647 (NanoTag, N3702-AF647-L), anti-ALFA nanobody-Cy3 (NanoTag N1502-SC3-L). Alexa488-, Alexa568-, and Alexa647-conjugated secondary antibodies were from Life Technologies.

### **Dissociated neuronal cultures**

Dissociated hippocampal cultures were prepared from embryonic day 18 (E18) rat brains of both genders, as described in (Kapitein et al., 2010) and in accordance to the approved DEC work-protocol as mentioned in the ethics statements above. Pregnant rats were sacrificed by gradual fill CO<sub>2</sub>/O<sub>2</sub>. Subsequently the uterus containing the pups is taken out and is stored in a sterile ice-cold environment. After the pups were sedated by the cold, they were removed from the uterus and decapitated. Dissociated neurons were plated on Ø18-mm coverslips coated with poly-L-lysine (37.5 µg/ml, Sigma-Aldrich) and laminin (1.25 µg/mL, Roche Diagnostics) at a density of 100,000 neurons per well. Neurons were grown in Neurobasal medium (NB) supplemented with 1% pen/strep, 2% [v/v] B27, and 0.5 mM L-glutamine (all from Gibco) (NB-complete medium) at 37°C in 5% CO<sub>2</sub>. From days in vitro (DIV) 1 onward, medium was refreshed weekly by replacing half of the medium with Brainphys neuronal medium (BP) supplemented with 2% [v/v] NeuroCult SM1 neuronal supplement (STEMCELL Technologies) and 1% pen/strep (BP-complete medium).

### **DNA plasmids**

ORANGE knock-ins for GluA1-GFP (Addgene #131489), GluA2-GFP (Addgene #131490), PSD95-GFP (Addgene #131477), TARP $\gamma$ 2-GFP (Addgene #131504), TARP $\gamma$ 8-GFP (Addgene #131474), FRRS1L-GFP (also known as C9orf4, Addgene #131472) and pCamK-Homer1c-mCherry, pORANGE Cloning template vector (Addgene #131471) were used from (Willems et al., 2020). pSpCas9(BB)-2A-Puro (PX459) V2 (Addgene #62988). pX333 (Addgene #64073) was from (Maddalo et al., 2014). pCAG\_smFP HA (Addgene: #59759) was from (Viswanathan et al., 2015). pCAG\_PSD95.FingR-eGFP-CCR5TC (Addgene



---

#46295) is from (Gross et al., 2013). pCMV-eGFP is from (Du et al., 2006).

### **Cloning of plasmids made in this study**

pCamK-Homer1c-ALFA was cloned by replacing the mCherry tag from pCamK-Homer1c-mCherry using AgeI and NotI sites. The ALFA tag (Gotzke et al., 2019), (SRLEELRRRLTE) was inserted as primer dimer.

GFP knock-in plasmids were made as described previously (Willems et al., 2020), with the only difference being that we replaced the HA tag of SpCas9 in the pORANGE cloning template vector, with a FLAG tag using Gibson assembly. A detailed overview of all knock-in plasmids made in this study, including target sequences Supplement Table S1. Donor inserts were amplified from pCAG\_PSD95.FingR-eGFP-CCR5TC. Donor PCR primers are listed in Supplement Table S2.

CRISPR knockout plasmids were made using pSpCas9(BB)-2A-Puro (PX459) V2. Target sequences for Gria1 (GCCCCTCTCACTCACCTATCTGG) and Gria2 (CTAACAGCATACAGATAGGTAGG), with overhangs that allowed for ligation into the BbsI sites of pSpCas9(BB)-2A-Puro (PX459) V2. An additional G base was inserted before the guideRNA of Gria2. Double knockout plasmids were made by ligation of the guideRNA primer dimers for Gria1 and Gria2 knockout in the BbsI and BsaI sites of pX333 respectively. The guideRNA against Gria2 was described before (Incontro et al., 2014).

Spaghetti monster HA (smFP HA) tag was amplified from pCAG\_smFP HA and ligated into the knock-in plasmids replacing GFP or Halo tags (HaloTag plasmids not used in this study) using BmtI and AfeI sites. All plasmids were verified by sanger sequencing.

### **Transfection of dissociated hippocampal cultures**

Knock-in and knockout plasmids were transfected at DIV3. Briefly, for one Ø18-mm coverslip covered with 100,000 neurons, 1–2 µg DNA was mixed with 3.3 µL Lipofectamine in 200 µL NB medium and incubated for 30 minutes at room temperature (RT). Next, 500 µL conditioned medium was transferred to a new culture plate and replaced by 300 µL NB supplemented with 0.5 mM L-glutamine. The DNA mix was added to the neurons and incubated at 37 °C and 5% CO<sub>2</sub>. After 90–120 minutes, neurons were transferred to the new culture plate with conditioned medium and 500 µL new NB medium supplemented with L-glutamine, B27, and pen/strep and kept at 37 °C and 5% CO<sub>2</sub> till DIV18–22 at which the experiments were performed,

### **Immunocytochemistry of dissociated hippocampal cultures**

Hippocampal neurons were fixed using 4% paraformaldehyde (PFA) in PEM80 buffer (80 mM PIPES, 2 mM MgCl<sub>2</sub>, 5 mM EGTA, pH 6.8) for 10 minutes at 37 °C and washed three times in PBS containing 0.1 M glycine (PBS/Gly). Neurons were blocked and permeabilized in blocking buffer (10% [v/v] normal goat serum [NGS] (Abcam) in PBS/Gly with 0.1% [v/v] Triton X100) for 1 hour at 37 °C. Next, coverslips were incubated with primary antibodies diluted in incubation buffer (5% [v/v] NGS in PBS/Gly with 0.1% [v/v] Triton X100) overnight at 4 °C. Coverslips were washed three times for 5 minutes with PBS/Gly and incubated with secondary antibodies diluted 1:400 in incubation buffer for 1 hour at RT. Labeling with nanobodies was included in the secondary antibody step. For confocal microscopy, coverslips were washed three times for 5 minutes in PBS/Gly, dipped in milliQ water (MQ), and mounted in Mowiol mounting medium (Sigma). For dSTORM, the coverslips were kept in PBS until mounting for imaging.

## Confocal imaging

Confocal images were acquired with a Zeiss LSM 700 and imaging was performed with a 63× NA 1.40 oil objective. A Z-stack containing 7–12 planes at a 0.56- $\mu\text{m}$  interval was acquired with 0.1- $\mu\text{m}$  pixel size, and maximum intensity projections were made for analysis and display. Image analysis was primarily performed using FIJI software (Schindelin et al., 2012). Quantifications were performed in Excel 2016 or GraphPad PRISM 8.

## Confocal analysis of synapse intensity of auxiliary protein knock-ins

Neurons were transfected with knock-in plasmids and pCamK-Homer1c-ALFA at DIV3 and fixed at DIV as described above. Neurons were stained with anti-PSD95 (Alexa647), anti-ALFA (Cy3) and anti-GFP (Atto488) nanobodies (all diluted 1:500) and imaged with confocal microscopy. For the images in Figure 1, neurons were stained using a rabbit anti-GFP antibody (dilution 1:2000) instead of the nanobody as several of the knock-ins are not abundant enough to visualize with a nanobody only. Mean synapse (GFP + anti-GFP nanobody Atto488) intensities were measured using 4x4 pixel (400x400 nm) sized regions of interest (ROI)s. Intensity values were background subtracted and normalized against the mean intensity of the PSD95-GFP knock-in signal. Correlation between Homer1c and the knock-ins was determined by Pearson correlation (GraphPad PRISM8). Line-scans were made in ImageJ, normalized to the max intensity along a  $\pm 4 \mu\text{m}$  line.

## Knockout validation analysis

Knockout plasmids were transfected together with PSD95-GFP knock-in, pCMV-eGFP, or pCamK-Homer1c-ALFA at DIV3. Neurons were fixed on DIV21. GluA1 and GluA2 were stained (dilution of primaries 1:500 and 1:200 respectively) in combination with anti-ALFA nanobodies (dilution 1:500), and imaged with a confocal microscope. KO validation was performed by measuring mean GluA intensity along  $\pm 10 \mu\text{m}$  line-scans with thickness 10 pixels (1  $\mu\text{m}$ ) along transfected or knock-in positive neurons. These mean intensities were corrected for background and normalized against the mean intensity of dendrites (also measured using line-scans) within the same image.

## Analysis of synapse intensity and synapse enrichment of auxiliary proteins and core GluA subunits

Knock-in plasmids for the auxiliary proteins were transfected at DIV3 together with Homer1c-ALFA and fixed at DIV21. Neurons were stained with rabbit-anti-GFP antibodies (dilution 1:2000) and anti-ALFA nanobodies (dilution 1:500). For effects on GluA subunits, neurons were also stained with anti GluA1 or anti-GluA2 (dilution of primaries 1:500 and 1:200 respectively). Imaging was performed by confocal making use of same microscopy settings across conditions. Synapse and dendritic shaft intensity were measured in 10x10 pixel (1x1  $\mu\text{m}$ ) ROIs, placed based on Homer1c-ALFA as synapse marker (20 ROI per neuron). Intensities were background subtracted and normalized to the corresponding control. For synapse enrichments, we divided synaptic intensities with those on the dendritic shaft. Neurons from at least two independent neuronal cultures were included in the analysis.

## Genomic analysis of knock-in accuracy

### *Electroporation of dissociated neurons*

For electroporation, hippocampal neurons were collected directly after dissection and

---

dissociation in a 15-ml tube and centrifuged for 5 minutes at 200g. Neurons were resuspended in AMAXA transfection solution (Lonza) ( $3 \times 10^5$  neurons per sample), mixed with 8  $\mu\text{g}$  DNA, transferred to a gene pulser cuvette (Biorad), and electroporated using a Lonza Nucleofector 2b. Immediately after electroporation, fresh 37 °C NB medium supplemented with B27, L-glutamine, and pen/strep was added to the cuvette, after which the neurons were plated on a coated Ø18-mm coverslip using a Pasteur pipette. Neurons were incubated at 37 °C and 5% CO<sub>2</sub> for 3 hours, after which all medium was replaced with fresh NB medium supplemented with B27, L-glutamine, and pen/strep.

### *Genomic analysis*

Genomic DNA was isolated from electroporated neurons at DIV 4. Neurons were lysed in lysis buffer (100 mM Tris, 50 mM EDTA, 40 mM NaCl, 0.2% SDS [pH 8.5]) and incubated with 100  $\mu\text{g}/\text{ml}$  Proteinase K (Roche) at 55 °C for 2 hours, followed by 1 hour at 85 °C to inactivate Proteinase K. Genomic DNA was isolated by ethanol precipitation and dissolved in elution buffer (10 mM Tris [pH 8.0]) (Qiagen). Genomic PCR was performed to amplify the 5' and 3' junctions of the integrated donor (for PCR primers used, see Table S3) using a touchdown PCR and Phusion HF polymerase (Thermo Fisher Scientific). Genomic primers were designed using NCBI Primer-Blast. Knock-ins analyzed were primarily selected based on flanking genomic sequence. Amplicons were only included if they resulted in a well-resolved band on agarose gel. PCR products were separated using agarose gel electrophoresis and subsequently purified using a gel extraction kit (Qiagen). Purified PCR products were ligated into the pJET vector according to the manufacture protocol (pJET cloning kit, Thermo Fisher Scientific). Individual clones were analyzed by Sanger sequencing (Macrogen) using pJET primers from the pJET cloning kit.

### **Live-cell imaging and FRAP**

Live-cell imaging was performed on a spinning disk confocal system (CSU-X1-A1; Yokogawa) mounted on a Nikon Eclipse Ti microscope (Nikon) with Plan Apo VC 100 $\times$  1.40 NA oil objective (Nikon) with excitation from Cobolt Calypso (491 nm), and emission filters (Chroma). The microscope was equipped with a motorized XYZ stage (ASI; MS-2000), Perfect Focus System (Nikon), and Prime BSI sCMOS camera (Photometrics), and was controlled by MetaMorph software (Molecular Devices). Neurons were maintained in a closed incubation chamber (Tokai hit: INUBG2E-ZILCS) at 37 °C in 5% CO<sub>2</sub> in 400  $\mu\text{L}$  conditioned medium.

FRAP experiments were performed using the ILas2 system (Roper Scientific). After 2 minutes baseline imaging (single Z-plane, five frames with 30-second interval), pre-selected ROIs with a fixed diameter of 1.26  $\mu\text{m}$  containing dendritic spines were bleached using a targeted laser. Imaging during fluorescence recovery was continued for 20 minutes (41 frames with 30-second interval).

### **FRAP analysis**

For analysis, acquisitions were corrected for drift. For each ROI, mean intensities were measured for every time point and corrected for background using the averaged intensity of two background ROIs. For each ROI, intensities were normalized to 1 based on the averaged intensities of the frames before ROI bleaching and normalized to zero based on the intensity from the first frame after bleaching. Data was corrected for general photobleaching by measuring intensity from 4 non-bleached spines. Normalized intensities were plotted over

time. The mobile fraction of protein was determined by averaging the normalized intensity of the last five frames for each neuron. Tau values were calculated from fitting the recovery datapoints with a one-phase association curve (GraphPad PRISM8),  $Y_0 = X_0$ . For each condition, data was collected over three independent neuronal cultures.

### **dSTORM imaging**

SMLM experiments were performed using the Nanoimager microscope (Oxford Nanoimaging; ONI) equipped with a 100x oil-immersion objective (Olympus Plan Apo, NA 1.4) and an XYZ closed-loop piezo stage. Imaging was performed using a 640-nm laser. Fluorescence was detected using a sCMOS camera (ORCA Flash 4, Hamamatsu). Integrated filters were used to split far-red emission onto the right side of the camera and blue-green-red emission spectra on the left side, enabling simultaneous dual-color imaging.

The imaging chamber was temperature-controlled at 30°C to prevent fluctuations in temperature during the time course of an experiment that might affect the alignment of the channels. Channel alignment was performed before each imaging session using 100-nm TetraSpeck beads (T-7279, Invitrogen) and the ONI software aiming for an alignment error where the standard deviation is  $< 8$  nm as measured from 2000 points total across a maximum of 20 fields of view. Imaging was performed in near-TIRF (angle: 53.5°) using a motorized mirror and all images were acquired at 50 Hz.

Knock-in plasmids were transfected at DIV3 and fixed at DIV21. Neurons were stained with anti-HA antibodies (dilution 1:400) and Alexa647 conjugated secondary antibodies. Coverslips were mounted on concave slides in dSTORM-buffer (50 mM Tris, 10 mM NaCl, pH 8.0, supplemented with 40 mM MEA, 10% [w/v] glucose, 700 µg/mL glucose oxidase, and 40 µg/mL catalase). Transfected neurons were localized using low laser powers. At low laser powers, a widefield image was acquired. dSTORM was performed simultaneously for Alexa647. First, a pulse of high laser power of the 640-nm laser was used to bring the dyes into the dark state. Next, laser powers were lowered to around 100-200 mW. The acquisition was started when clear individual (non-overlapping) blinking was observed. 405 nm laser power was increased on demand based the number of blinking events. Imaging was continued for 20,000 frames or till no blinking events could be observed.

### **dSTORM analysis**

NimOS software from ONI was used for detection of single molecule localization events and drift correction. Resulting localization tables were additionally drift-corrected using Detection of Molecules (DoM) plugin v.1.2.1 for ImageJ ([https://github.com/ekatruxha/DoM\\_Utrecht](https://github.com/ekatruxha/DoM_Utrecht)) if required. dSTORM reconstruction were made using DoM with pixel size of 10 nm. Analysis was continued in MATLAB.

Localizations were filtered out if localization precision was  $> 50$  nm, or photon count was  $< 300$  or  $> 30,000$  photons. Consecutive localizations in a radius of 60 nm were removed. If consecutive localizations persisted for more than 10 frames, the initial localization was also removed. Next, datasets were further filtered, removing all localization with a localization precision  $> 25$  nm. ROIs outlining spine heads were defined based the widefield image of the knock-in and drawn by hand. ROIs were only analyzed further if out if they contained  $> 800$  localizations, or if they were  $> 0.02$  µm<sup>2</sup> or  $< 0.5$  µm<sup>2</sup> in size. DBScan analysis within the manual drawn ROI was used to define the final cluster border and reported cluster size. Then, for each localization in a given cluster, the local density was calculated as the number of localizations within a radius of 5 x the mean nearest neighbor distance (MacGillavry

---

et al., 2013). Localizations were deemed part of a nanodomain if its local density was  $> 40$ . Nanodomains were isolated using the MATLAB functions `linkage()` and `cluster()`. Subsequently, nanodomains were subclustered if they contained multiple local density peaks that were  $> 80\%$  of the maximum local density, further than 80 nm apart and separated by a local minimum of  $< 30\%$  of the maximum local density. The nanodomain boundary was constructed using the Voronoi diagrams circumventing the localizations. Nanodomains of which the number of localizations was  $< 5\%$  of that of the total cluster, and nanodomains with a diameter of  $< 30$  nm were excluded.

### Statistics

Statistical significance was tested with a student t test when comparing two groups. A P value below 0.05 was considered significant. If multiple groups were compared, statistical significance was tested with a one-way ANOVA followed by a Bonferroni's multiple comparison. Note that although in several occasions more than two conditions were plotted in the same graph, each condition had its own control, and thus a student t test was performed between conditions (also see figure legends). In all figures, \* was used to indicate a P value  $< 0.05$ , \*\* for  $P < 0.01$ , and \*\*\* for  $P < 0.001$ . Reported n is number of neurons, and each experiment was replicated in neuronal cultures from at least two independent preparations if not indicated differently. Statistical analysis and graphs were prepared in GraphPad PRISM 8, and figures were generated in Adobe Illustrator CC.

### ACKNOWLEDGEMENTS

This work was supported by the European Research Council (ERC-StG 716011) to HDM. We thank Manon Westra and Wouter Droogers for contribution to single molecule localization scripts, and Bert Jan Korte and Naomi Steenbeek for their contribution to validation of CRISPR knockouts. We thank the members of the MacGillavry lab for discussions.

## REFERENCES

- Abdollahi Nejat, M., Klaassen, R.V., Spijker, S., and Smit, A.B. (2021). Auxiliary subunits of the AMPA receptor: The Shisa family of proteins. *Curr Opin Pharmacol* 58, 52-61.
- Baranovic, J. (2021). AMPA receptors in the synapse: Very little space and even less time. *Neuropharmacology* 196, 108711.
- Bats, C., Groc, L., and Choquet, D. (2007). The interaction between Stargazin and PSD-95 regulates AMPA receptor surface trafficking. *Neuron* 53, 719-734.
- Bessa-Neto, D., Beliu, G., Kuhlemann, A., Pecoraro, V., Doose, S., Retailleau, N., Chevrier, N., Perrais, D., Sauer, M., and Choquet, D. (2021). Bioorthogonal labeling of transmembrane proteins with non-canonical amino acids unveils masked epitopes in live neurons. *Nat Commun* 12, 6715.
- Biederer, T., Kaeser, P.S., and Blanpied, T.A. (2017). Transcellular Nanoalignment of Synaptic Function. *Neuron* 96, 680-696.
- Bissen, D., Foss, F., and Acker-Palmer, A. (2019). AMPA receptors and their minions: auxiliary proteins in AMPA receptor trafficking. *Cell Mol Life Sci* 76, 2133-2169.
- Chatterjee, S., Ade, C., Nurik, C.E., Carrejo, N.C., Dutta, C., Jayaraman, V., and Landes, C.F. (2019). Phosphorylation Induces Conformational Rigidity at the C-Terminal Domain of AMPA Receptors. *J Phys Chem B* 123, 130-137.
- Chen, L., Chetkovich, D.M., Petralia, R.S., Sweeney, N.T., Kawasaki, Y., Wenthold, R.J., Bredt, D.S., and Nicoll, R.A. (2000). Stargazin regulates synaptic targeting of AMPA receptors by two distinct mechanisms. *Nature* 408, 936-943.
- Chen, N., Pandya, N.J., Koopmans, F., Castelo-Szekel, V., van der Schors, R.C., Smit, A.B., and Li, K.W. (2014). Interaction proteomics reveals brain region-specific AMPA receptor complexes. *J Proteome Res* 13, 5695-5706.
- Cizeron, M., Qiu, Z., Koniaris, B., Gokhale, R., Komiyama, N.H., Fransen, E., and Grant, S.G.N. (2020). A brainwide atlas of synapses across the mouse life span. *Science* 369, 270-275.
- Coleman, S.K., Hou, Y., Willibald, M., Semenov, A., Moykkynen, T., and Keinanen, K. (2016). Aggregation Limits Surface Expression of Homomeric GluA3 Receptors. *J Biol Chem* 291, 8784-8794.
- Constals, A., Penn, A.C., Compans, B., Toulme, E., Phillipat, A., Marais, S., Retailleau, N., Hafner, A.S., Coussen, F., Hossy, E., and Choquet, D. (2015). Glutamate-induced AMPA receptor desensitization increases their mobility and modulates short-term plasticity through unbinding from Stargazin. *Neuron* 85, 787-803.
- Diaz-Alonso, J., and Nicoll, R.A. (2021). AMPA receptor trafficking and LTP: Carboxy-termini, amino-termini and TARPs. *Neuropharmacology* 197, 108710.
- Diaz-Alonso, J., Sun, Y.J., Granger, A.J., Levy, J.M., Blankenship, S.M., and Nicoll, R.A. (2017). Subunit-specific role for the amino-terminal domain of AMPA receptors in synaptic targeting. *Proc Natl Acad Sci U S A* 114, 7136-7141.
- Diering, G.H., and Hugarin, R.L. (2018). The AMPA Receptor Code of Synaptic Plasticity. *Neuron* 100, 314-329.
- Du, G., Yonekubo, J., Zeng, Y., Osisami, M., and Frohman, M.A. (2006). Design of expression vectors for RNA interference based on miRNAs and RNA splicing. *FEBS J* 273, 5421-5427.
- Farrow, P., Khodosevich, K., Sapir, Y., Schulmann, A., Aslam, M., Stern-Bach, Y., Monyer, H., and von Engelhardt, J. (2015). Auxiliary subunits of the CKAMP family differentially modulate AMPA receptor properties. *Elife* 4, e09693.
- Fukaya, M., Tsujita, M., Yamazaki, M., Kushiya, E., Abe, M., Akashi, K., Natsume, R., Kano, M., Kamiya, H., Watanabe, M., and Sakimura, K. (2006). Abundant distribution of TARP gamma-8 in synaptic and extrasynaptic surface of hippocampal neurons and its major role in AMPA receptor expression on spines and dendrites. *Eur J Neurosci* 24, 2177-2190.
- Gotzke, H., Kilisch, M., Martinez-Carranza, M., Sograte-Idrissi, S., Rajavel, A., Schlichthaerle, T., Engels, N., Jungmann, R., Stenmark, P., Opazo, F., and Frey, S. (2019). The ALFA-tag is a highly versatile tool for nanobody-based bioscience applications. *Nat Commun* 10, 4403.
- Grant, S.G.N., and Fransen, E. (2020). The Synapse Diversity Dilemma: Molecular Heterogeneity Confounds Studies of Synapse Function. *Front Synaptic Neurosci* 12, 590403.
- Greger, I.H., and Mayer, M.L. (2019). Structural biology of glutamate receptor ion channels: towards an understanding of mechanism. *Curr Opin Struct Biol* 57, 185-195.
- Gross, G.G., Junge, J.A., Mora, R.J., Kwon, H.B., Olson, C.A., Takahashi, T.T., Liman, E.R., Ellis-Davies, G.C., McGee, A.W., Sabatini, B.L., et al. (2013). Recombinant probes for visualizing endogenous synaptic proteins in living neurons. *Neuron* 78, 971-985.
- Gu, X., Mao, X., Lussier, M.P., Hutchison, M.A., Zhou, L., Hamra, F.K., Roche, K.W., and Lu, W. (2016). GSG1L suppresses AMPA receptor-mediated synaptic transmission and uniquely modulates AMPA receptor kinetics in hippocampal neurons. *Nat Commun* 7, 10873.
- Hafner, A.S., Penn, A.C., Grillo-Bosch, D., Retailleau, N., Poujol, C., Phillipat, A., Coussen, F., Sainlos, M., Opazo, P., and Choquet, D. (2015). Lengthening of the Stargazin Cytoplasmic Tail Increases Synaptic Transmission by Promoting Interaction to Deeper Domains of PSD-95. *Neuron* 86, 475-489.
- Han, W., Li, J., Pelkey, K.A., Pandey, S., Chen, X., Wang, Y.X., Wu, K., Ge, L., Li, T., Castellano, D., et al. (2019). Shisa7 is a GABAA receptor auxiliary subunit controlling benzodiazepine actions. *Science* 366, 246-250.
- Herring, B.E., Shi, Y., Suh, Y.H., Zheng, C.Y., Blankenship, S.M., Roche, K.W., and Nicoll, R.A. (2013). Cornichon proteins determine the subunit composition of synaptic AMPA receptors. *Neuron* 77, 1083-1096.
- Inamura, M., Itakura, M., Okamoto, H., Hoka, S., Mizoguchi, A., Fukazawa, Y., Shigemoto, R., Yamamori, S., and Takahashi, M. (2006). Differential localization and regulation of stargazin-like protein, gamma-8 and stargazin in the plasma membrane of hippocampal and cortical neurons. *Neurosci Res* 55, 45-53.
- Incontro, S., Asensio, C.S., Edwards, R.H., and Nicoll, R.A. (2014). Efficient, complete deletion of synaptic proteins using CRISPR. *Neuron* 83, 1051-1057.
- Jacobi, E., and von Engelhardt, J. (2021). Modulation of information processing by AMPA receptor auxiliary subunits. *J Physiol* 599, 471-483.

- Kalashnikova, E., Lorca, R.A., Kaur, I., Barisone, G.A., Li, B., Ishimaru, T., Trimmer, J.S., Mohapatra, D.P., and Diaz, E. (2010). SynDIG1: an activity-regulated, AMPA-receptor-interacting transmembrane protein that regulates excitatory synapse development. *Neuron* 65, 80-93.
- Kamalova, A., and Nakagawa, T. (2021). AMPA receptor structure and auxiliary subunits. *J Physiol* 599, 453-469.
- Kapitein, L.C., Yau, K.W., and Hoogenraad, C.C. (2010). Microtubule dynamics in dendritic spines. *Methods Cell Biol* 97, 111-132.
- Karataeva, A.R., Klaassen, R.V., Stroder, J., Ruiperez-Alonso, M., Hjorth, J.J., van Nierop, P., Spijker, S., Mansvelder, H.D., and Smit, A.B. (2014). C-terminal interactors of the AMPA receptor auxiliary subunit Shisa9. *PLoS One* 9, e87360.
- Kato, A.S., Gill, M.B., Ho, M.T., Yu, H., Tu, Y., Siuda, E.R., Wang, H., Qian, Y.W., Nisenbaum, E.S., Tomita, S., and Brecht, D.S. (2010). Hippocampal AMPA receptor gating controlled by both TARP and cornichon proteins. *Neuron* 68, 1082-1096.
- Kaur, I., Yarov-Yarovoy, V., Kirk, L.M., Plambeck, K.E., Barragan, E.V., Ontiveros, E.S., and Diaz, E. (2016). Activity-Dependent Palmitoylation Controls SynDIG1 Stability, Localization, and Function. *J Neurosci* 36, 7562-7568.
- Khodosevich, K., Jacobi, E., Farrow, P., Schulmann, A., Rusu, A., Zhang, L., Sprengel, R., Monyer, H., and Engelhardt, J. (2014). Coexpressed auxiliary subunits exhibit distinct modulatory profiles on AMPA receptor function. *Neuron* 83, 601-615.
- Kirk, L.M., Ti, S.W., Bishop, H.I., Orozco-Llamas, M., Pham, M., Trimmer, J.S., and Diaz, E. (2016). Distribution of the SynDIG4/proline-rich transmembrane protein 1 in rat brain. *J Comp Neurol* 524, 2266-2280.
- Klaassen, R.V., Stroeder, J., Coussen, F., Hafner, A.S., Petersen, J.D., Renancio, C., Schmitz, L.J., Normand, E., Lodder, J.C., Rotaru, D.C., et al. (2016). Shisa6 traps AMPA receptors at postsynaptic sites and prevents their desensitization during synaptic activity. *Nat Commun* 7, 10682.
- MacGillavry, H.D., Song, Y., Raghavachari, S., and Blanpied, T.A. (2013). Nanoscale scaffolding domains within the postsynaptic density concentrate synaptic AMPA receptors. *Neuron* 78, 615-622.
- Maddalo, D., Manchado, E., Concepcion, C.P., Bonetti, C., Vidigal, J.A., Han, Y.C., Ogrudowski, P., Crippa, A., Reikhtman, N., de Stanchina, E., et al. (2014). In vivo engineering of oncogenic chromosomal rearrangements with the CRISPR/Cas9 system. *Nature* 516, 423-427.
- Mao, X., Gu, X., and Lu, W. (2017). GSG1L regulates the strength of AMPA receptor-mediated synaptic transmission but not AMPA receptor kinetics in hippocampal dentate granule neurons. *J Neurophysiol* 117, 28-35.
- Matt, L., Kirk, L.M., Chenuaux, G., Specia, D.J., Puhger, K.R., Pride, M.C., Qneibi, M., Haham, T., Plambeck, K.E., Stern-Bach, Y., et al. (2018). SynDIG4/Prnt1 Is Required for Excitatory Synapse Development and Plasticity Underlying Cognitive Function. *Cell Rep* 22, 2246-2253.
- Matthews, P.M., Pinggera, A., Kampjut, D., and Greger, I.H. (2021). Biology of AMPA receptor interacting proteins - From biogenesis to synaptic plasticity. *Neuropharmacology* 197, 108709.
- Mauric, V., Molders, A., Harmel, N., Heimrich, B., Sergeeva, O.A., and Klocker, N. (2013). Ontogeny repeats the phylogenetic recruitment of the cargo exporter cornichon into AMPA receptor signaling complexes. *Mol Cell Neurosci* 56, 10-17.
- Micheva, K.D., Busse, B., Weiler, N.C., O'Rourke, N., and Smith, S.J. (2010). Single-synapse analysis of a diverse synapse population: proteomic imaging methods and markers. *Neuron* 68, 639-653.
- Nair, D., Hosy, E., Petersen, J.D., Constals, A., Giannone, G., Choquet, D., and Sibarita, J.B. (2013). Super-resolution imaging reveals that AMPA receptors inside synapses are dynamically organized in nanodomains regulated by PSD95. *J Neurosci* 33, 13204-13224.
- Nakagawa, T. (2019). Structures of the AMPA receptor in complex with its auxiliary subunit cornichon. *Science* 366, 1259-1263.
- Pandya, N.J., Seeger, C., Babai, N., Gonzalez-Lozano, M.A., Mack, V., Lodder, J.C., Gouwenberg, Y., Mansvelder, H.D., Danielson, U.H., Li, K.W., et al. (2018). Noelin1 Affects Lateral Mobility of Synaptic AMPA Receptors. *Cell Rep* 24, 1218-1230.
- Pei, J., and Grishin, N.V. (2012). Unexpected diversity in Shisa-like proteins suggests the importance of their roles as transmembrane adaptors. *Cell Signal* 24, 758-769.
- Rouach, N., Byrd, K., Petralia, R.S., Elias, G.M., Adesnik, H., Tomita, S., Karimzadegan, S., Kealey, C., Brecht, D.S., and Nicoll, R.A. (2005). TARP gamma-8 controls hippocampal AMPA receptor number, distribution and synaptic plasticity. *Nat Neurosci* 8, 1525-1533.
- Schindelin, J., Arganda-Carreras, I., Frise, E., Kaynig, V., Longair, M., Pietzsch, T., Preibisch, S., Rueden, C., Saalfeld, S., Schmid, B., et al. (2012). Fiji: an open-source platform for biological-image analysis. *Nat Methods* 9, 676-682.
- Schmitz, L.J.M., Klaassen, R.V., Ruiperez-Alonso, M., Zamri, A.E., Stroeder, J., Rao-Ruiz, P., Lodder, J.C., van der Loo, R.J., Mansvelder, H.D., Smit, A.B., and Spijker, S. (2017). The AMPA receptor-associated protein Shisa7 regulates hippocampal synaptic function and contextual memory. *Elife* 6.
- Schnell, E., Sizemore, M., Karimzadegan, S., Chen, L., Brecht, D.S., and Nicoll, R.A. (2002). Direct interactions between PSD-95 and stargazin control synaptic AMPA receptor number. *Proc Natl Acad Sci U S A* 99, 13902-13907.
- Schwenk, J., Baehrens, D., Haupt, A., Bildl, W., Boudkkazi, S., Roeper, J., Fakler, B., and Schulte, U. (2014). Regional diversity and developmental dynamics of the AMPA-receptor proteome in the mammalian brain. *Neuron* 84, 41-54.
- Schwenk, J., Boudkkazi, S., Kocylowski, M.K., Brechet, A., Zolles, G., Bus, T., Costa, K., Kollwe, A., Jordan, J., Bank, J., et al. (2019). An ER Assembly Line of AMPA-Receptors Controls Excitatory Neurotransmission and Its Plasticity. *Neuron* 104, 680-692 e689.
- Schwenk, J., and Fakler, B. (2021). Building of AMPA-type glutamate receptors in the endoplasmic reticulum and its implication for excitatory neurotransmission. *J Physiol* 599, 2639-2653.
- Schwenk, J., Harmel, N., Brechet, A., Zolles, G., Berkefeld, H., Muller, C.S., Bildl, W., Baehrens, D., Huber, B.,

- Kulik, A., et al. (2012). High-resolution proteomics unravel architecture and molecular diversity of native AMPA receptor complexes. *Neuron* 74, 621-633.
- Schwenk, J., Harmel, N., Zolles, G., Bildl, W., Kulik, A., Heimrich, B., Chisaka, O., Jonas, P., Schulte, U., Fakler, B., and Klocker, N. (2009). Functional proteomics identify cornichon proteins as auxiliary subunits of AMPA receptors. *Science* 323, 1313-1319.
- Sheng, N., Bemben, M.A., Diaz-Alonso, J., Tao, W., Shi, Y.S., and Nicoll, R.A. (2018). LTP requires postsynaptic PDZ-domain interactions with glutamate receptor/auxiliary protein complexes. *Proc Natl Acad Sci U S A* 115, 3948-3953.
- Shi, Y., Suh, Y.H., Milstein, A.D., Isozaki, K., Schmid, S.M., Roche, K.W., and Nicoll, R.A. (2010). Functional comparison of the effects of TARPs and cornichons on AMPA receptor trafficking and gating. *Proc Natl Acad Sci U S A* 107, 16315-16319.
- Sumioka, A., Brown, T.E., Kato, A.S., Bredt, D.S., Kauer, J.A., and Tomita, S. (2011). PDZ binding of TARPgamma-8 controls synaptic transmission but not synaptic plasticity. *Nat Neurosci* 14, 1410-1412.
- Sumioka, A., Yan, D., and Tomita, S. (2010). TARP phosphorylation regulates synaptic AMPA receptors through lipid bilayers. *Neuron* 66, 755-767.
- Tang, A.H., Chen, H., Li, T.P., Metzbowser, S.R., MacGillavry, H.D., and Blanpied, T.A. (2016). A trans-synaptic nanocolumn aligns neurotransmitter release to receptors. *Nature* 536, 210-214.
- Tomita, S., Chen, L., Kawasaki, Y., Petralia, R.S., Wenthold, R.J., Nicoll, R.A., and Bredt, D.S. (2003). Functional studies and distribution define a family of transmembrane AMPA receptor regulatory proteins. *J Cell Biol* 161, 805-816.
- Tomita, S., Fukata, M., Nicoll, R.A., and Bredt, D.S. (2004). Dynamic interaction of stargazin-like TARPs with cycling AMPA receptors at synapses. *Science* 303, 1508-1511.
- Traynelis, S.F., Wollmuth, L.P., McBain, C.J., Menniti, F.S., Vance, K.M., Ogden, K.K., Hansen, K.B., Yuan, H., Myers, S.J., and Dingledine, R. (2010). Glutamate receptor ion channels: structure, regulation, and function. *Pharmacol Rev* 62, 405-496.
- Valente, P., Castroflorio, E., Rossi, P., Fadda, M., Sterlini, B., Cervigni, R.I., Prestigio, C., Giovedi, S., Onofri, F., Mura, E., et al. (2016). PRRT2 Is a Key Component of the Ca<sup>2+</sup>-Dependent Neurotransmitter Release Machinery. *Cell Rep* 15, 117-131.
- Vandenbergh, W., Nicoll, R.A., and Bredt, D.S. (2005). Interaction with the unfolded protein response reveals a role for stargazin in biosynthetic AMPA receptor transport. *J Neurosci* 25, 1095-1102.
- Viswanathan, S., Williams, M.E., Bloss, E.B., Stasevich, T.J., Speer, C.M., Nern, A., Pfeiffer, B.D., Hooks, B.M., Li, W.P., English, B.P., et al. (2015). High-performance probes for light and electron microscopy. *Nat Methods* 12, 568-576.
- von Engelhardt, J., Mack, V., Sprengel, R., Kavenstock, N., Li, K.W., Stern-Bach, Y., Smit, A.B., Seeburg, P.H., and Monyer, H. (2010). CKAMP44: a brain-specific protein attenuating short-term synaptic plasticity in the dentate gyrus. *Science* 327, 1518-1522.
- Watson, J.F., Ho, H., and Greger, I.H. (2017). Synaptic transmission and plasticity require AMPA receptor anchoring via its N-terminal domain. *Elife* 6.
- Watson, J.F., Pinggera, A., Ho, H., and Greger, I.H. (2021). AMPA receptor anchoring at CA1 synapses is determined by N-terminal domain and TARP gamma8 interactions. *Nat Commun* 12, 5083.
- Willems, J., de Jong, A.P.H., Scheefhals, N., Mertens, E., Catsburg, L.A.E., Poorthuis, R.B., de Winter, F., Verhaagen, J., Meye, F.J., and MacGillavry, H.D. (2020). ORANGE: A CRISPR/Cas9-based genome editing toolbox for epitope tagging of endogenous proteins in neurons. *PLoS Biol* 18, e3000665.
- Zeng, M., Diaz-Alonso, J., Ye, F., Chen, X., Xu, J., Ji, Z., Nicoll, R.A., and Zhang, M. (2019). Phase Separation-Mediated TARP/MAGUK Complex Condensation and AMPA Receptor Synaptic Transmission. *Neuron* 104, 529-543 e526.
- Zhao, Y., Chen, S., Swensen, A.C., Qian, W.J., and Gouaux, E. (2019). Architecture and subunit arrangement of native AMPA receptors elucidated by cryo-EM. *Science* 364, 355-362.
- Zhu, F., Cizeron, M., Qiu, Z., Benavides-Piccione, R., Kopanitsa, M.V., Skene, N.G., Koniaris, B., DeFelipe, J., Fransen, E., Komiyama, N.H., and Grant, S.G.N. (2018). Architecture of the Mouse Brain Synaptome. *Neuron* 99, 781-799 e710.



## SUPPELMENTAL INFORMATION

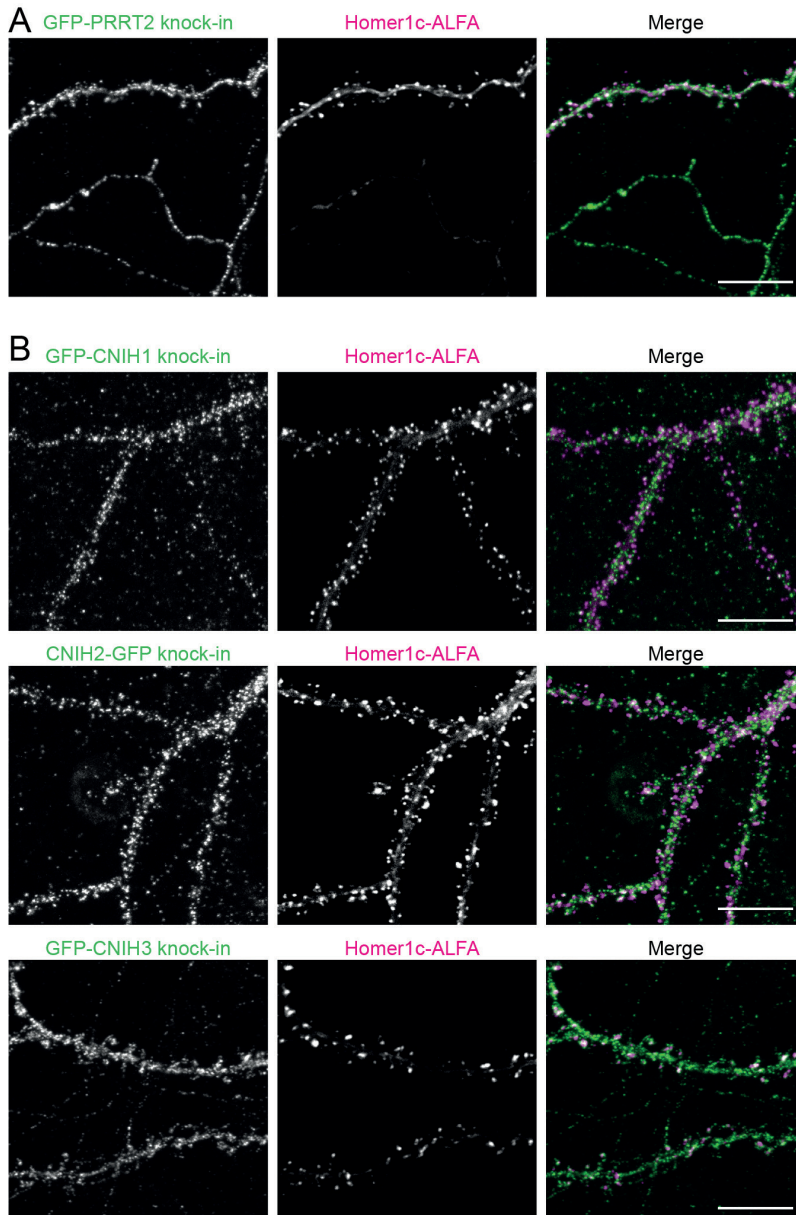


**Figure S1, (related to figure 1). Localization of PRRT2 and cornichon protein family.**

(A) Representative image of GFP-PRRT1 knock-in (green) co-transfected with Homer1c-ALFA (magenta) and stained with anti-GFP antibodies. Scale bar is 10  $\mu\text{m}$ . (B) Representative images of GFP knock-ins for the cornichon family members CNIH1,2 and 3. Scale bar is 10  $\mu\text{m}$ .

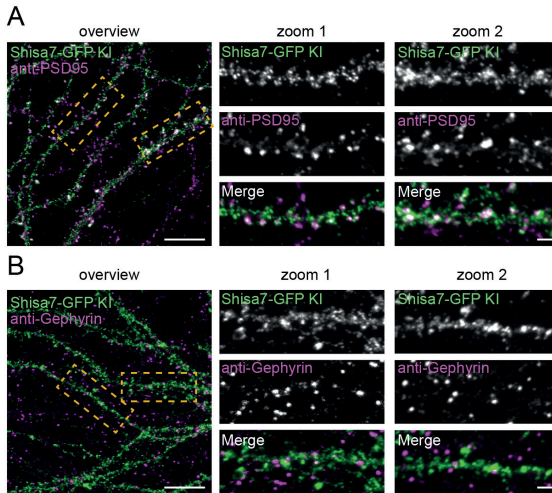


**Figure S2, (related to figure 1). Localization of Shisa7 in respect to PSD95 or Gephyrin.**

(A,B) Representative image of Shisa7-GFP knock-in stained with anti-GFP (green) and anti-PSD95 (A) (magenta) or anti-Gephyrin (B) antibodies. Zooms are indicated with yellow boxes. Scale bar in overviews are 10  $\mu\text{m}$ , and in the zooms are 2  $\mu\text{m}$ .

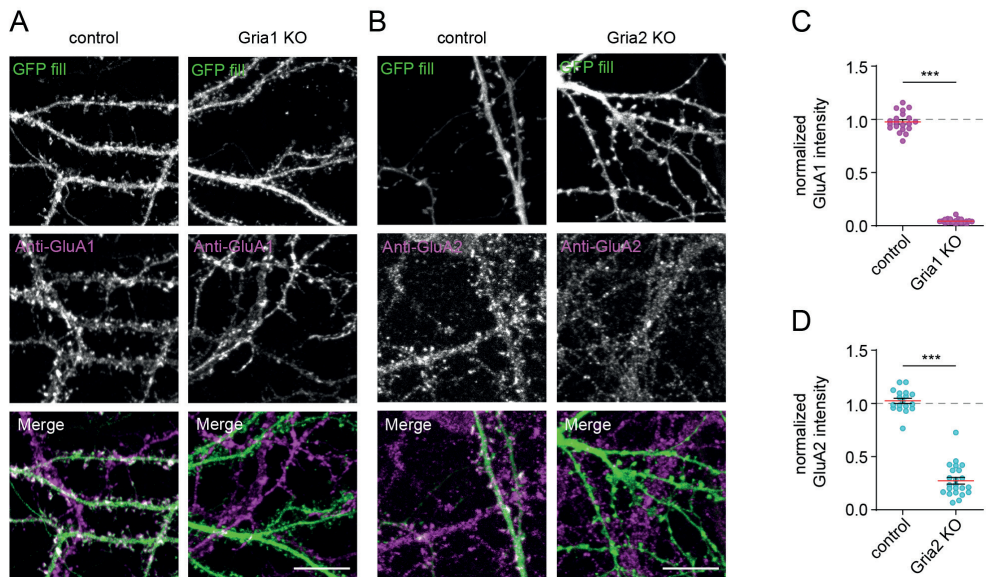


**Figure S3, (related to figure 2). Validation of single GluA1 and GluA2 knockouts.**

(A,B) Representative images of neurons transfected with a GFP fill plasmid (green) and a control plasmid or GluA1 KO (A) or GluA2 KO (B). Neurons were stained with anti-GluA1 (A) or anti-GluA2 (B) antibodies (magenta). Scale bars are 10  $\mu\text{m}$ . (C,D) Quantification of GluA1 (C) or GluA2 (D) levels comparing control and GluA1 or GluA2 knockout respectively. Measured intensities from transfected neurons were normalized against non-transfected neurons in the same images. Data are represented as means  $\pm$  SEM. ns not significant, \*\*\*  $P < 0.001$ . Student t test. KO, knockout.

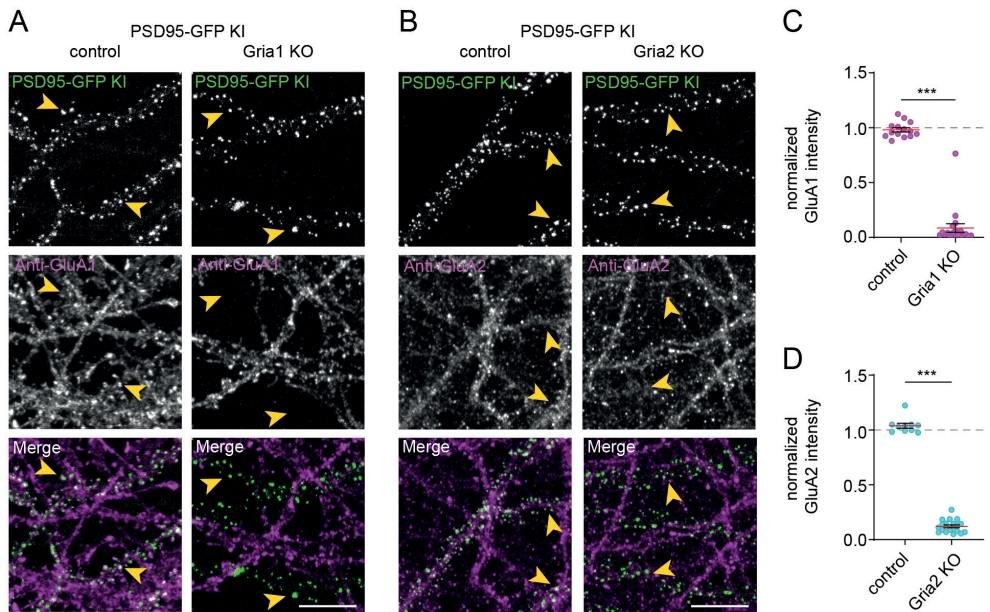


**Figure S4, (related to figure 2). Validation of single GluA1 and GluA2 knockouts in the background of a PSD95-GFP knock-in.**

(A,B) Representative images of neurons transfected with a PSD95-GFP knock-in (green) and a control plasmid or GluA1 KO (A) or GluA2 KO (B). Neurons were stained with anti-GluA1 (A) or anti-GluA2 (B) antibodies (magenta). Scale bars are 10  $\mu$ m. (C,D) Quantification of GluA1 (C) or GluA2 (D) levels comparing control and GluA1 or GluA2 knockout respectively. Measured intensities from transfected neurons were normalized against non-transfected neurons in the same images. Data are represented as means  $\pm$  SEM. ns not significant, \*\*\*  $P < 0.001$ . Student t test. KO, knockout.

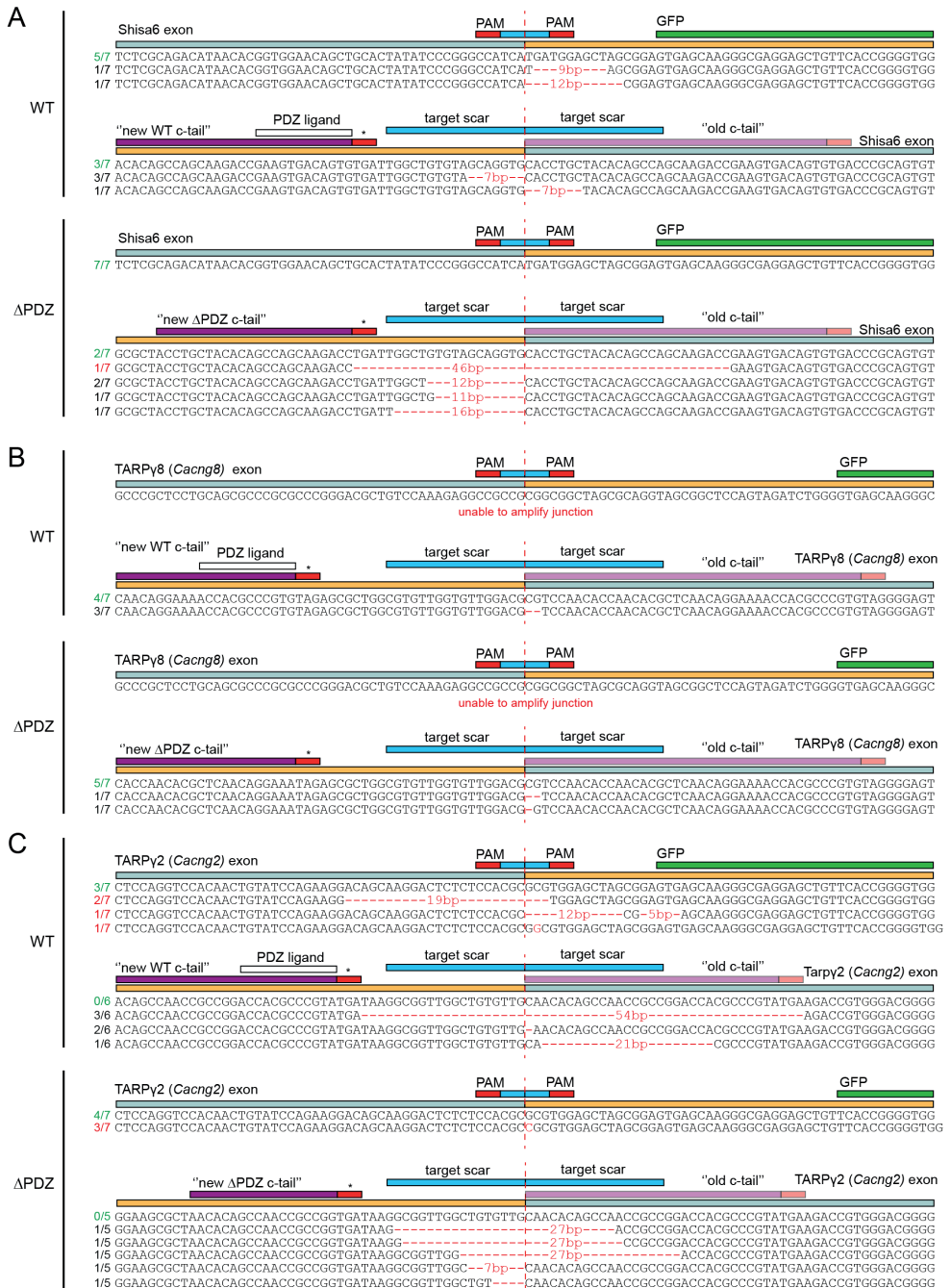


**Figure S5, (related to figure 4). Genomic analysis of indels at integration sites of C-terminal WT and  $\Delta$ PDZ GFP donors in Shisa6, TARPy8 and TARPy2.**

(A,B,C) 5' and 3' junctions of the donor covering the integration sites were amplified from genomic DNA, and analyzed using sanger sequencing. Analysis was performed for Shisa6 (A), TARPy8 (B) and TARPy2 (C). The exon is annotated with a blue bar, the donor with a yellow bar. Other features including the new stop codon (red box with \*), target scars and residual PAM sequences, and site of integration (red dotted line) are shown. Deletion (-) **Figure**

S5 (continued) or insertions are shown in red. The former ('old') c-tail is made transparent. Between five and 7 clones per junction were analyzed (except for the 5' TARP $\gamma$ 8 junction). Scores at the left of the sequences shown in green represent the expected sequence. If red, the mutation results in a mutated or truncated coding sequence.

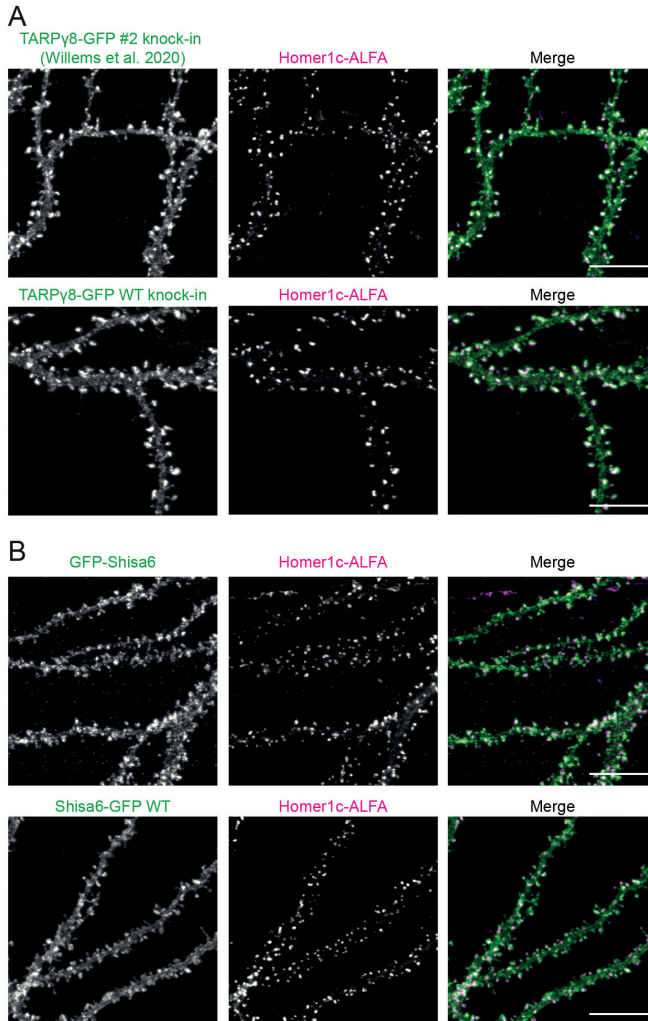


**Figure S6, (related to figure 4). Expression of TARP $\gamma$ 8 and Shisa6 WT replacement knock-ins with other knock-in variants.**

(A) Representative images of TARP $\gamma$ 8-GFP knock-in as published previously and the WT variant created in Figure 4 (green), co-transfected with Homer1c-ALFA (magenta). (B) Representative images of a N-terminal GFP-Shisa6 knock-in and WT C-terminal Shisa6-GFP knock-in co-transfected with Homer1c-ALFA (magenta). Scale bars are 10  $\mu$ m.

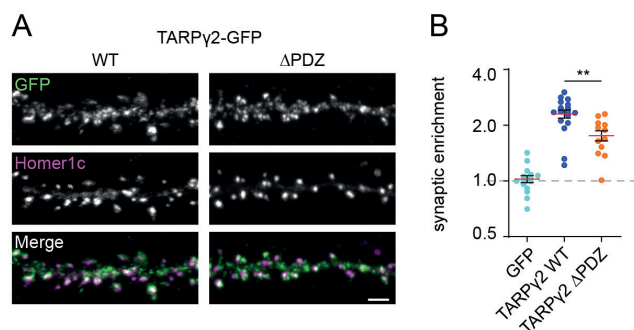


**Figure S7, (related to figure 4). Effects of PDZ ligand removal on TARPy2 localization.**

(A) Representative images of TARPy2 WT or  $\Delta$ PDZ (green), co-transfected with Homer1c-ALFA (magenta). Scale bar is 2 $\mu$ m. (B) Quantification of synaptic enrichment comparing WT and  $\Delta$ PDZ, but also including the GFP-fill from Figure 4. Data are represented as means  $\pm$  SEM. ns not significant, \*\*  $P < 0.01$ . Student t test.

### Supplement Table S1. Overview of knock-ins generated in this study

Knockin	Gene	Target sequence and PAM	Amino acid site of integration	Internal plasmid code
GFP-Shisa6	<i>Shisa6</i>	CCCGGCAGCAGCGCCCGCCGTTGG	A31	JW239
GFP-CNIH1	<i>CNIH1</i>	AGTGAACGCCATGGCCGGGGAGG	Before start	JW225
CNIH2-GFP	<i>CNIH2</i>	ACGTTGGTGAGCTTCTAAGGGGG	STOP	JW231
GFP-CNIH3	<i>CNIH3</i>	GAAAGTGAAGGCCATGGCTGAGG	Before start	JW233
GFP-Shisa9	<i>Shisa9</i>	GCCGGGCAGGAGCGAGCTGGG	R24	JW261
PORCN-GFP	<i>Porcn</i>	ATATGCCTCAGCCTATGAGACGG	L459	JW255
GFP-PRRT1	<i>Prrt1</i>	GAGACATGCTCGCAAGCGCTGG	Before start	JW257
GFP-PRRT2	<i>Prrt2</i>	GAGATGGGAGAGGGCCGGTGGGG	Before start	JW265
GFP-Noelin1	<i>Olfm1</i>	GTATTGAGGCCACCAAGCGAGGG	S28	JW245
Syndig1-GFP	<i>Syndig1</i>	CCAGCCTTTGGAAGCTCACAGG	STOP	JW273
Tarpy8-GFP WT, Tarpy8-GFP $\Delta$ PDZ Tarpy8-smFP-HA WT, Tarpy8-smFP-HA $\Delta$ PDZ	<i>Cacng8</i>	CGTGTGGTGTGGACGCGGCGG	A408	JW276 JW277 JW304 JW305
Tarpy2-GFP WT, Tarpy2-GFP $\Delta$ PDZ	<i>Cacng2</i>	GGCGGTTGGCTGTGTTGGCGTGG	A313	JW288 JW289
Shisa6-GFP WT, Shisa6-GFP $\Delta$ PDZ Shisa6-smFP-HA WT, Shisa6-smFP-HA $\Delta$ PDZ	<i>Shisa6</i>	TGGCTGTGTAGCAGGTGTGATGG	H509	JW279 JW280 JW298 JW299
Shisa7-GFP WT, Shisa7-GFP $\Delta$ PDZ	<i>Shisa7</i>	CGTCTGTGTCAGTGCAGG	R549	JW282 JW283

Supplemental Table S2. Overview of donor primers

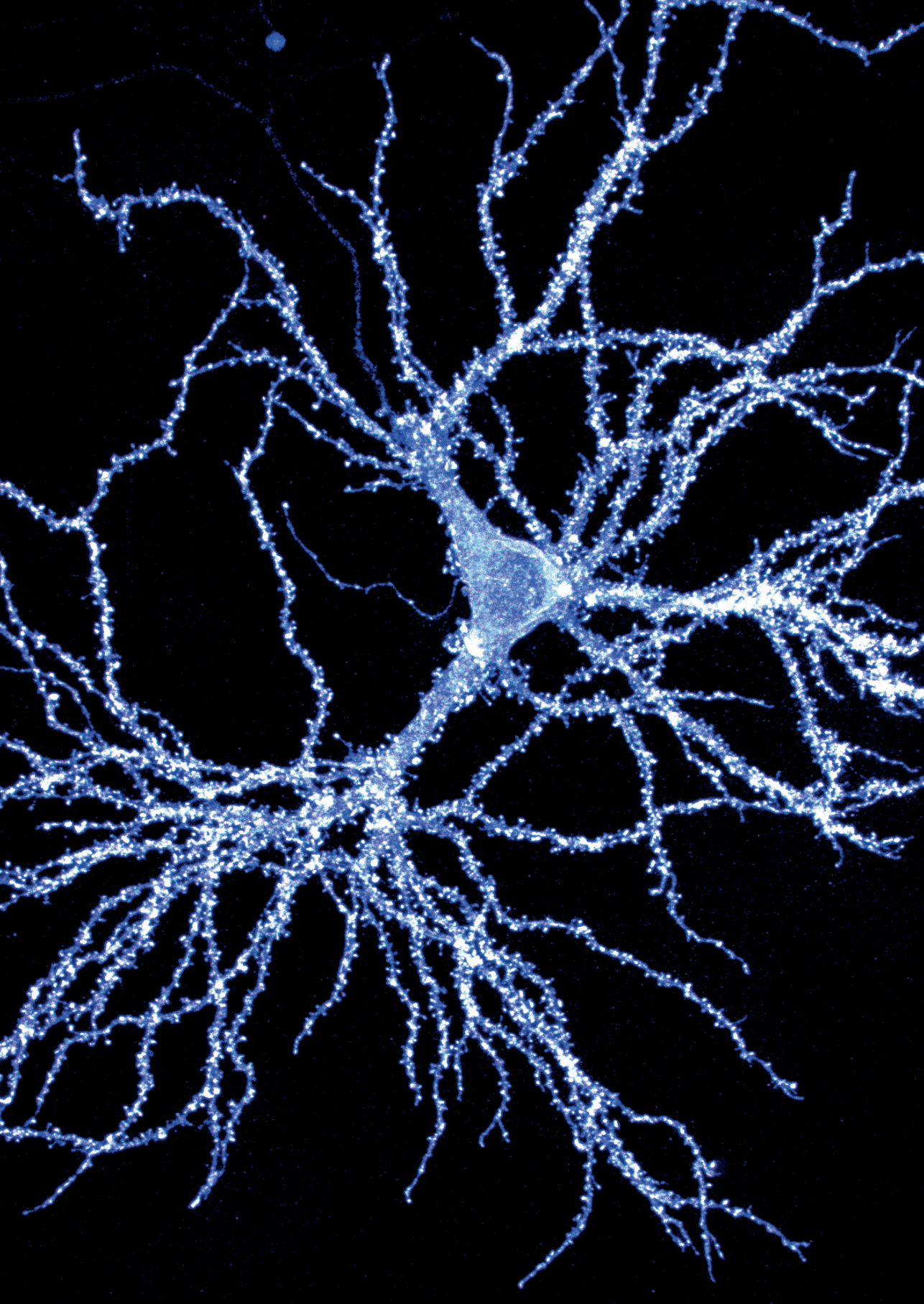
Plasmid		Donor PCR forward primer 5'→3'
GFP-Shisa6	FW	ATAAAGCTTCCACGGGCGGCTGCGCCGGGAGCTAGCGGGGTGAGCAAGGGCG
	RV	TATCTCGAGCCCGGCGCAGACGCCGCCGAGGCTAGCGCTTCCCCTAGAGTACAGCTCGT
GFP-CNIH1	FW	ATAAAGCTTAGTGAACGCCATGGCCGGGAGGCCGGCCATGGCTAGCGGAGTGAGC
	RV	ATACTCGAGCCTCCCGGCCATGGCGTTCCTCCGCCAGCGCTTCCACTCTTGACAG
CNIH2-GFP	FW	ATAAAGCTTCCACCTTAGAAGCTCACCAACGCTCAGTAGCGGGGTGAGCAAGGGC
	RV	ATCTCGAGACGTTGGTGAGCTTCTAAGGTGGTTAAGCGCTAGAGTACAGCTCGTCCATGC
GFP-CNIH3	FW	ATAAAGCTTGAAGTGAAGGCCATGGCTGAGGTACAGCATGGCTAGCGGAGTGAGCAA
	RV	ATACTCGAGCCTCAGCCATGGCCTTCACTTTCCGCCAGCGCTTCCACTCT
GFP-Shisa9	FW	ATAAAGCTTCCGAGCTCGCTCCTGCGCCCGGCTGCTAGCGGGGTGAGCAAGGGCGAGGAG
	RV	TATCTCGAGCCCGGCGCAGGAGCGAGCTCGGCCAGCGCTTCCCCTAGAGTACAGCTCG
PORC N-GFP	FW	ATAAAGCTTATATGCGCTCAGCCTATGAGACGGCGCTAGCGGTAGCGGCTCCAGTAGA
	RV	ATACTCGAGCCGTCTCATAGGCTGAGGCATATTTAAGCGCTCCCTGCACCCGCTCCAGC
GFP-PRRT 1	FW	ATAAAGCTTGACGACATGCTCGCAAGCGCAGGACGGGGCCATGGCTAGCGGAGTGAGCAA
	RV	ATACTCGAGCTCGCGCTTCCGAGCATGTCGTCACAGCGCTTCCACTCTTGACAG
GFP-PRRT 2	FW	ATAAAGCTTGAGATGGGAGAGGGCCGGTGAAGACGGGGCCATGGCTAGCGGAGTGAGCAA
	RV	ATACTCGAGCCTCACCAGCCCTCTCCATCTCTCCAGCGCTTCCACTCTTGACAGCTCG
GFP-Noelin 1	FW	ATAAAGCTTGATTGAGGCCACCAGCGAGGGTCTGCTAGCGGTAGCGGCTCCAGTAGA
	RV	TATCTCGAGCCCTCGCTGGTGGCCCTCAATACCAGCGCTCCAGCCCTGCACCCGCTCC
Syndig 1-GFP	FW	ATAAAGCTTCCAGCCTTTGAAAGCTCACAGGCGCTAGCGGTAGCGGCTCCAGTAGATC
	RV	GAGCCTGTGAGCTTTCCAAAGGCTGGTTAAGCGCTCCCTGCACCCGCTCCAGC
Tarpy8-GFP WT	FW	ATAGCTAGCGCAGGTAGCGGCTCCAGTAGA
	RV	ATAAGCGCTCTACACGGGCGTGGTTTTCTGTTGAGCGTGGTGGTTAGACGCTCCAGCGCCAGCTCC
Tarpy8-GFP ΔPDZ	FW	ATAGCTAGCGCAGGTAGCGGCTCCAGTAGA
	RV	ATAAGCGCTCTATTTCTGTTGAGCGTGGTGGTTAGACGCTCCAGCGCCAGCTCCCCT
Tarpy2-GFP WT	FW	ATAAAGCTTGGCGTTGGCTGTGTTGGCGTGGAGCTAGCGGAGTGAGCAAGGGC
	RV	ATCTCGAGCCACGCCAACACAGCCAACCCTTATCATACGGGCGTGGTCCGGCGGTTGGCTGTGTTAGCGCTTCCACTCTTGATACAG
Tarpy2-GFP ΔPDZ	FW	ATAAAGCTTGGCGTTGGCTGTGTTGGCGTGGAGCTAGCGGAGTGAGCAAGGGC
	RV	ATCTCGAGCCACGCCAACACAGCCAACCCTTATCACCGGCGGTTGGCTGTGTTAGCGCTTCCACTCTTGATACAG
Shisa6-GFP WT	FW	ATAAAGCTTTGGCTGTGTAGCAGGTGTGATGGAGCTAGCGGAGTGAGCAAGGGC
	RV	CTCGAGCCATCACACCTGCTACACAGCCAATCAGTCTTCTGCTGGCTGTGTAGCAGGTAGCGCTTCCACTCTTGATACAG
Shisa6-GFP ΔPDZ	FW	ATAAAGCTTTGGCTGTGTAGCAGGTGTGATGGAGCTAGCGGAGTGAGCAAGGGC
	RV	CTCGAGCCATCACACCTGCTACACAGCCAATCAGTCTTCTGCTGGCTGTGTAGCAGGTAGCGCTTCCACTCTTGATACAG
Shisa7-GFP WT	FW	ATAAAGCTTCGTTCTTCTGCTGGCAGTGCGCAGGAGCTAGCGGAGTGAGCAAGGGC
	RV	ATCTCGAGCCTGCGCACTGCCAGCAAGAAGCTTATCAGACAGTCACTTCTGTTCTTCTGCTGGCAGTAGCGCTTCCACTCTTGATACAG
Shisa7-GFP ΔPDZ	FW	ATAAAGCTTCGTTCTTCTGCTGGCAGTGCGCAGGAGCTAGCGGAGTGAGCAAGGGC
	RV	ATCTCGAGCCTGCGCACTGCCAGCAAGAAGCTTATCAGTCTTCTGCTGGCAGTAGCGCTTCCACTCTTGATACAG

Supplemental Table S3. Genomic DNA primers

Target	Direction	Sequence 5' → 3'
GFP	FW	CATGGTCTGCTGGAGTTCGTG
	RV	CTGAACCTTGTTGGCGTTTAC
TARPy2	FW	TGAAGGGCTTCAACACCCTG
	RV	GCGTATGGAAGGTCTCCCG
TARPy8	RV	GGGCGCACTCCCCTACA
Shisa6	FW	TGACCCGTTACCGCATGA
	RV	CTCACCCCTGCCCTACTCTG







# 7

---

## **Synaptic anchoring of AMPA receptors through their N-terminal domain**

Jelmer Willems, Marc van Amstel, Manon Westra and  
Harold D. MacGillavry

---

Cell Biology, Neurobiology and Biophysics, Department of Biology, Faculty of  
Science, Utrecht University, Utrecht, the Netherlands

---

## ABSTRACT

AMPA receptors (AMPArs) are the main contributors to basal synaptic transmission, and their synaptic recruitment and anchoring is fundamental to activity-driven synaptic plasticity. Mechanisms mediating AMPAR recruitment and anchoring at the synapse involve the intracellular C-terminal domain of the AMPAR and AMPAR-binding auxiliary proteins. However, recent studies have found strong evidence that the extracellular N-terminal domain (NTD) of the AMPAR is also involved in synaptic anchoring. Here, we used live-cell (super-resolution) imaging of NTD-lacking AMPARs to study its influence on synaptic immobilization. We found that the NTD of GluA1-3 are all crucial for their localization and turnover at synapses. Moreover, using single-molecule tracking experiments, we found a subunit-specific role for the NTD on synaptic and extrasynaptic diffusion of individual receptors. Finally, as a proof-of-principle, we developed a strategy to acutely remove the NTD from wild-type AMPAR subunits, opening doors for future research. Together, these findings help understand how AMPAR are immobilized at synapses.

## INTRODUCTION

At glutamatergic synapses, AMPA receptors (AMPArs) are the main contributors to basal synaptic transmission. As AMPARs have a relatively low affinity to glutamate, their correct trafficking to and anchoring at the synaptic membrane is crucial for efficient signal transmission (Anggono and Haganir, 2012; Chen et al., 2018; Makino and Malinow, 2009; Opazo and Choquet, 2011). As such, the process synaptic plasticity can actively increase (synaptic potentiation) or decrease (synaptic depression) the number of receptors at the synapses, modulating synaptic strength (Nicoll, 2017). Thus studying the mechanisms that govern receptor immobilization at synapses, is crucial to understand the molecular underpinnings of synaptic plasticity (Nabavi et al., 2014; Nicoll, 2017; Whitlock et al., 2006).

AMPArs are tetrameric heterodimers, consisting of subunits GluA1-4 which have differential expression patterns throughout the brain (Schwenk et al., 2014). In the hippocampus, most AMPARs are GluA1/2 or GluA2/3 heterodimers, with a smaller fraction of GluA1 homomers (Traynelis et al., 2010). AMPAR exhibit a large extracellular N-terminal domain (NTD), and a ligand binding domain (LBD). Four transmembrane helices (TMD) bridge the membrane and together form the receptor pore. A long intracellular and largely unfolded C-tail (CTD) harbors a multitude of interaction and modification sites, extending deep into the synapse (Kamalova and Nakagawa, 2021). In contrast to the LBD and TMD, the NTD and CTD share a low degree of homology between the GluA subunits allowing for subunit-specific modulation of AMPAR trafficking and functioning (Diaz-Alonso and Nicoll, 2021; Shi et al., 2001).

The trafficking and anchoring of AMPAR at the synapse are, to an important degree, regulated through so-called AMPAR auxiliary proteins, including those of the TARP and Shisa families (Bissen et al., 2019; Harb et al., 2021). Binding to the TMD and LBD of the AMPAR, they form the link between AMPARs and synaptic scaffolding molecules such as PSD95 (Opazo et al., 2012). Mapping the interaction sites between TARP proteins and AMPAR subunit GluA2, suggest a role for the NTD in stabilizing the AMPAR-TARP complex (Cais et al., 2014). In addition, post-translational modifications such as phosphorylation sites in the CTD have been extensively studied, being associated with surface expression, lateral diffusion and receptor endocytosis (Guguste and Jia, 2021; Shi et al., 2001). For example, several GluA2 CTD specific interactions are associated with receptor endocytosis (Lu et al., 2007), while GluA1 CTD specific phosphorylation is regulating fast AMPAR recruitment to the

PSD during LTP (Lee et al., 2003). In contrast to the CTD, the NTD is relatively understudied, even though its size comprises ~40% of the total protein. As the NTD extends considerably into the synaptic cleft, it could act as a binding platform for presynaptic proteins (Garcia-Nafria et al., 2016). Earlier studies have described interactions of the AMPAR-NTD with presynaptic pentraxins and N-cadherin (Saglietti et al., 2007; Sia et al., 2007). More recently, neuroligin-1 and Noelin1 have been found to interact with the NTD, influencing long-term and short-term plasticity respectively (Jiang et al., 2021; Pandya et al., 2018). In addition, several synaptic adhesion molecules including neuroligin, interacting with neuroligin (Haas et al., 2018; Mondin et al., 2011) and LRRTM2 (de Wit et al., 2009; Ramsey et al., 2021), have been associated with AMPAR clustering at synapses, although it remains unknown if they bind AMPARs directly.

At a functional level, the NTD has been shown to modulate synaptic transmission and plasticity in a subunit-dependent manner (Diaz-Alonso et al., 2017; Watson et al., 2017). The NTD of GluA1 was shown to be required for synaptic delivery and the induction of LTP. In contrast, NTD-lacking GluA2 subunits were trafficked to the synapse, but result in impaired basal transmission. Recently, it was established that both the anchoring of AMPAR via TARP protein PDZ ligands and the NTD are required for correct synaptic positioning (Watson et al., 2021). Where TARP proteins likely are responsible for synaptic recruitment, the NTD of GluA2 finetunes the positioning within the synapse.

Here, we aimed to study the role of the AMPAR NTD in receptor anchoring at the synapse, and investigated whether this process is subunit-specific. We used NTD-lacking mutant receptors to map their localization and turnover at synapses. Furthermore, we used single-molecule tracking to investigate the role of the NTD in both synaptic and extrasynaptic diffusion kinetics, and lastly propose a new strategy to study the NTD of WT AMPAR subunits.

## RESULTS

### The NTD of AMPARs is involved in synaptic trafficking

In order to study the role of the AMPAR-NTD on the subcellular localization of AMPARs, we generated Super ecliptic pHluorin (SEP) tagged variant of the GluA1-3 subunits, with (WT) and without NTD ( $\Delta$ NTD) and expressed these in dissociated hippocampal rat neurons. Using live-cell imaging, we measured the synaptic expression of these subunits relative to the extrasynaptic pool on the dendritic shaft (Figure 1). For all three subunits, we observed a strong reduction in synaptic enrichment for  $\Delta$ NTD-GluAs compared to WT (synapse enrichment: WT-GluA1:  $1.38 \pm 0.12$ ,  $\Delta$ NTD-GluA1:  $0.99 \pm 0.063$ ,  $P < 0.05$ ; WT-GluA2:  $1.62 \pm 0.11$ ,  $\Delta$ NTD-GluA2:  $0.92 \pm 0.072$ ,  $P < 0.001$ ; WT-GluA3:  $1.53 \pm 0.072$ ,  $\Delta$ NTD-GluA3:  $0.90 \pm 0.097$ ,  $P < 0.001$ , Student t test; Figure 1B). In addition, while GluA1 and 3 lacking the NTD seemed to be expressed on the surface (not quantified), for  $\Delta$ NTD-GluA2, we often observed non-homogenous structures in the dendritic shaft, which might indicate that this mutant partially affected in its ability to traffic to the plasma membrane, and is retained in the endoplasmic reticulum (ER). These results show that the NTD of all three main AMPAR subunits is required for the proper trafficking to and/or anchoring at the synapse.

### The AMPAR-NTD is required for synaptic anchoring

Next, we questioned the importance of the NTD in synaptic anchoring of the AMPAR. If the NTD is important for synaptic anchoring and thus its immobilization at the synapse, the turnover of AMPAR subunits without NTD would be affected. To test this, we performed

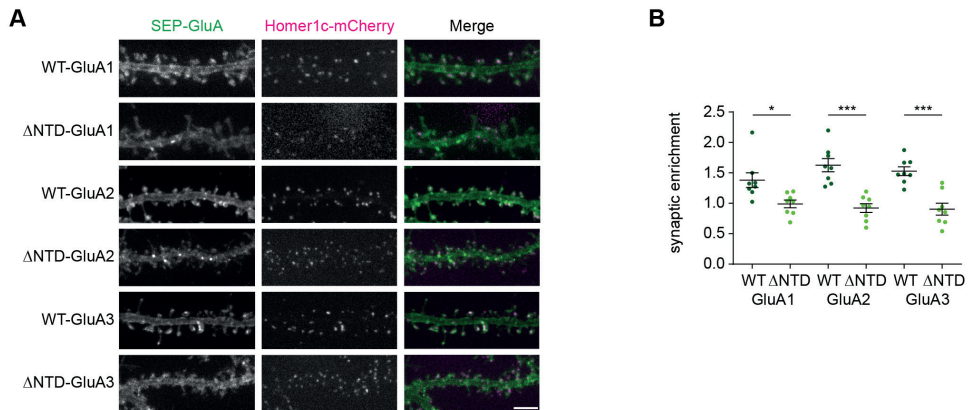


**Figure 1. Subcellular distribution of WT and  $\Delta$ NTD GluAs in hippocampal neurons**

(A) Representative live-cell images of recombinant SEP-tagged GluA1-3 WT and  $\Delta$ NTD (green) co-transfected with Homer1c-mCherry (magenta). Scale bar, 5  $\mu$ m. (B) Synaptic enrichment measurements (synapse, shaft ratio), comparing WT and  $\Delta$ NTD GluAs.  $n = 8$  neurons per condition. Data are represented as means  $\pm$  SEM. Data are represented as means  $\pm$  SEM. \*  $P < 0.05$ , \*\*\*  $P < 0.001$ , Student t test.

fluorescence recovery after photobleaching (FRAP) experiments (Figure 2). Overexpressed WT-GluA2 and 3 subunits show a turnover close to 50-60% over 10 minutes recovery time, with GluA1 overexpressed subunits (which are likely to predominantly form GluA1 homomers), showing a slightly higher turnover (mobile receptor pool: WT-GluA1:  $0.70 \pm 0.035$ , WT-GluA2:  $0.53 \pm 0.022$ , WT-GluA3:  $0.58 \pm 0.029$ ; Figure 2D-G). Removing the NTD, significantly increased the synaptic turnover of all three GluA subunits, reaching levels similar to that of ‘freely diffusing’ AMPARs on the dendritic shaft ( $\Delta$ NTD-GluA1:  $0.84 \pm 0.055$ ,  $P < 0.05$ ,  $\Delta$ NTD-GluA2:  $0.77 \pm 0.032$ ,  $P < 0.001$ ,  $\Delta$ NTD-GluA3:  $0.74 \pm 0.041$ ,  $P < 0.01$ , ANOVA; Figure 2D-G). Together, these results indicate that the NTD of all three subunits are required for the proper anchoring of AMPARs at the synapse.

### Subunit-specific effects of NTD removal on AMPAR surface diffusion

Immobilization of AMPARs at the synapse, but also their diffusion kinetics over the synaptic and extrasynaptic membrane have been studied extensively (Borgdorff and Choquet, 2002; Choquet and Opazo, 2022). While AMPARs can be stably anchored at the synapse, they are still able to diffuse, allowing the rapid exchange of receptors between synaptic and extrasynaptic pools. At the same time, the extrasynaptic receptors can diffuse into the synapse and captured on demand. The NTD could potentially interact with proteins in the extracellular matrix, influencing lateral diffusion. Thus, we reasoned that there might be a role for the NTD in the diffusion kinetics of both synaptic and extrasynaptic receptors. In order to probe these kinetics and to get a better understanding of the diffusion kinetics of single receptors we performed universal point accumulation in nanoscale topography (uPAINT) (Figure 3). SEP-tagged GluA subunits with and without NTD were expressed in neurons and stochastically labeled with anti-GFP nanobodies, coupled to ATTO647N providing a map of individual receptor mobility along dendrites (Figure 3A, D, G). Next, we calculated the diffusion kinetics of WT- and  $\Delta$ NTD-GluAs (Figure 3B, E, H). These trajectories were assigned to either being synaptic or extrasynaptic based on a Homer1c-mCherry derived mask (also see methods). We found that synaptic GluA2 and GluA3, but not GluA1 diffusion coefficients were increased

in the  $\Delta$ NTD compared to the WT-GluAs (median diffusion coefficient synaptic tracks: WT-GluA1:  $0.012 \mu\text{m}^2/\text{s}$ , IQR: 0.011-0.015,  $\Delta$ NTD-GluA1:  $0.011 \mu\text{m}^2/\text{s}$ , IQR: 0.0078-0.017,  $P > 0.05$ , WT-GluA2:  $0.016 \mu\text{m}^2/\text{s}$ , IQR: 0.014-0.018,  $\Delta$ NTD-GluA2:  $0.023 \mu\text{m}^2/\text{s}$ , IQR: 0.021-0.024,  $P < 0.05$ , WT-GluA3:  $0.0083 \mu\text{m}^2/\text{s}$ , IQR: 0.0071-0.011,  $\Delta$ NTD-GluA3:  $0.014 \mu\text{m}^2/\text{s}$ , IQR: 0.012-0.015,  $P < 0.01$ , ANOVA; Figure 3C, F, I). Interestingly, the extrasynaptic pools of GluA2 and GluA3, also showed an increase in their diffusion kinetics (WT-GluA1:  $0.022 \mu\text{m}^2/\text{s}$ , IQR: 0.020-0.025,  $\Delta$ NTD-GluA1:  $0.029 \mu\text{m}^2/\text{s}$ , IQR: 0.021-0.031,  $P > 0.05$ , WT-GluA2:  $0.027 \mu\text{m}^2/\text{s}$ , IQR: 0.021-0.031,  $\Delta$ NTD-GluA2:  $0.036 \mu\text{m}^2/\text{s}$ , IQR: 0.030-0.043,  $P < 0.05$ , WT-GluA3:  $0.019 \mu\text{m}^2/\text{s}$ , IQR: 0.014-0.024,  $\Delta$ NTD-GluA3:  $0.030 \mu\text{m}^2/\text{s}$ , IQR: 0.023-0.040,  $P < 0.01$ , ANOVA). These findings indicate an important role for the NTD in AMPAR surface mobility, in addition to anchoring at the synapse.

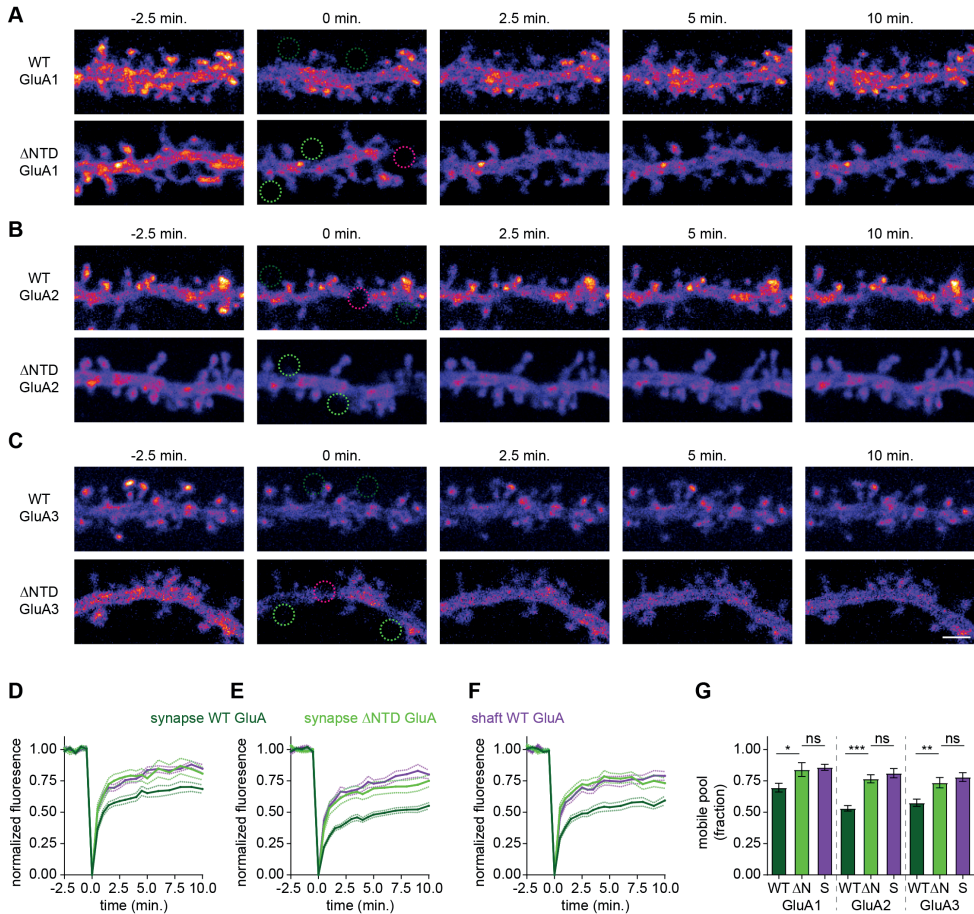
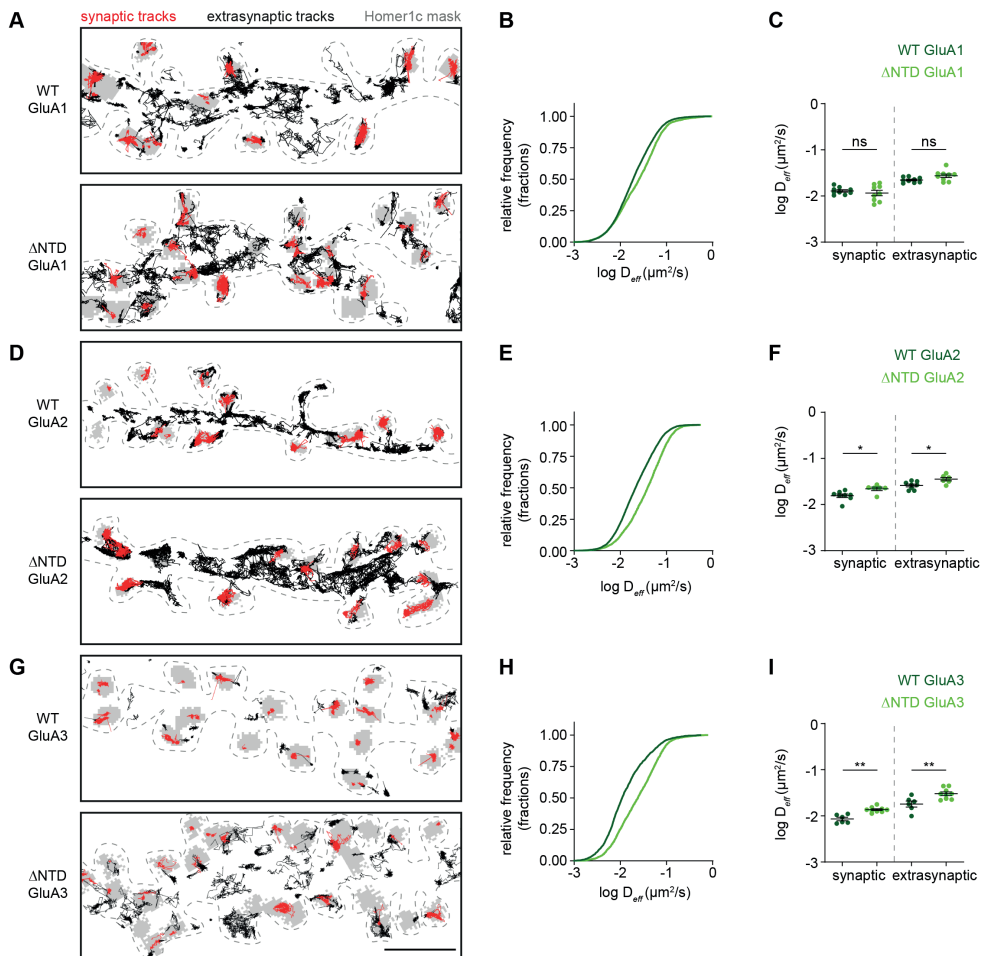


Figure 2. Live-cell imaging of synaptic turnover of WT and  $\Delta$ NTD GluA subunits (A, B, C) Representative live-cell images of recombinant GluA1 (A), GluA2 (B) and GluA3 (C) comparing WT and  $\Delta$ NTD. Bleaching was performed at timepoint 0 min in spines (green ROI) and dendritic shaft (magenta ROI). Scale bar,  $2 \mu\text{m}$ . (D, E, F) Normalized fluorescence intensity curves related to (A,B,C) respectively. Recovery curves of fluorescence intensity are shown for WT synaptic (dark green),  $\Delta$ NTD (light green) and the dendritic shaft (magenta). (G) Quantification of the mobile fraction, of GluA subunits based on the last 3 timepoints of the recovery curves in (D, E, F).  $n = 16-72$  ROIs from 4-9 neurons per condition. Data are represented as means  $\pm$  SEM. Data are represented as means  $\pm$  SEM. ns, not significant, \*  $P < 0.05$ , \*\*  $P < 0.01$ , \*\*\*  $P < 0.001$ , ANOVA.



**Figure 3. Probing the diffusion kinetics of WT and  $\Delta$ NTD GluAs using uPAINT**

(A, D, G) Representative plots of single-molecule trajectories for recombinant GluA1 (A), GluA2 (D) and GluA3 (G). A synapse mask, based on Homer1c-mCherry is shown in grey. Synaptic tracks are shown in red and extrasynaptic tracks in black. Dotted line indicates cell outline. Scale bar, 2  $\mu$ m. (B, E, H) Relative frequency distribution of diffusion coefficients derived from all tracks in (A,D,G) respectively and comparing WT (dark green) and  $\Delta$ NTD (light green) GluA subunits. (C, F, I) Diffusion coefficients for GluA1 (C), GluA2 (F) and GluA3 (I), averaged per cell separately comparing synaptic and extrasynaptic tracks.  $n = 6-9$  neurons per condition. Data are represented as means  $\pm$  SEM. Data are represented as means  $\pm$  SEM. ns, not significant, \*  $P < 0.05$ , \*\*  $P < 0.01$ , ANOVA.

### Developing tools to acutely remove the NTD from AMPARs

During AMPAR assembly, interactions between the NTDs of GluA subunits are important for the formation of heterodimeric complexes (Leuschner and Hoch, 1999; Rossmann et al., 2011). Although NTD lacking AMPARs can still form functional receptors (Herguedas et al., 2013; Pasternack et al., 2002), we cannot exclude that the phenotypes identified so far, could be partially the result of complications in AMPAR assembly and their subsequent trafficking to the membrane. Thus, we sought to develop a strategy to acutely remove the NTD from AMPARs, after their trafficking to the plasma membrane. For this reason, we designed a SEP-tagged version of GluA2, with a Tobacco Etch Virus (TEV) cleavage site and

ALFA-tag incorporated in between the NTD and NTD-LBD linker (Figure 4A). The TEV cleavage site, can be cut by the very specific TEV protease, thus actively cutting the NTD, together with the SEP-tag from the rest of the protein. As a proof-of-principle experiment, we expressed SEP-NTD-TEV-ALFA-GluA2 together with Homer1c-mCherry in neurons, and followed the synaptic intensity of the SEP signal over time, while incubating the neurons with TEV protease. As expected, addition of TEV protease led to a steady decrease of the SEP signal over the period of 60 minutes (Figure 4B, D). In control neurons, in the absence of TEV-protease, the loss of SEP signal was limited, probably reflecting fluorescence bleaching (Figure 4C,D). In some neurons incubated with TEV protease, residual SEP signal remained on the dendritic shaft (Figure 4B, example 2). To investigate this more closely, we live-labeled SEP-NTD-TEV-ALFA-GluA2, with anti-ALFA nanobodies, thus specifically labeling the surface expressed AMPAR pool (Figure 4E). The images and the relative intensity along a line scan (Figure 4F) indeed indicated that part of the SEP signal originates from intracellular compartments. Since SEP-signal is usually quenched in low-pH compartments such as in

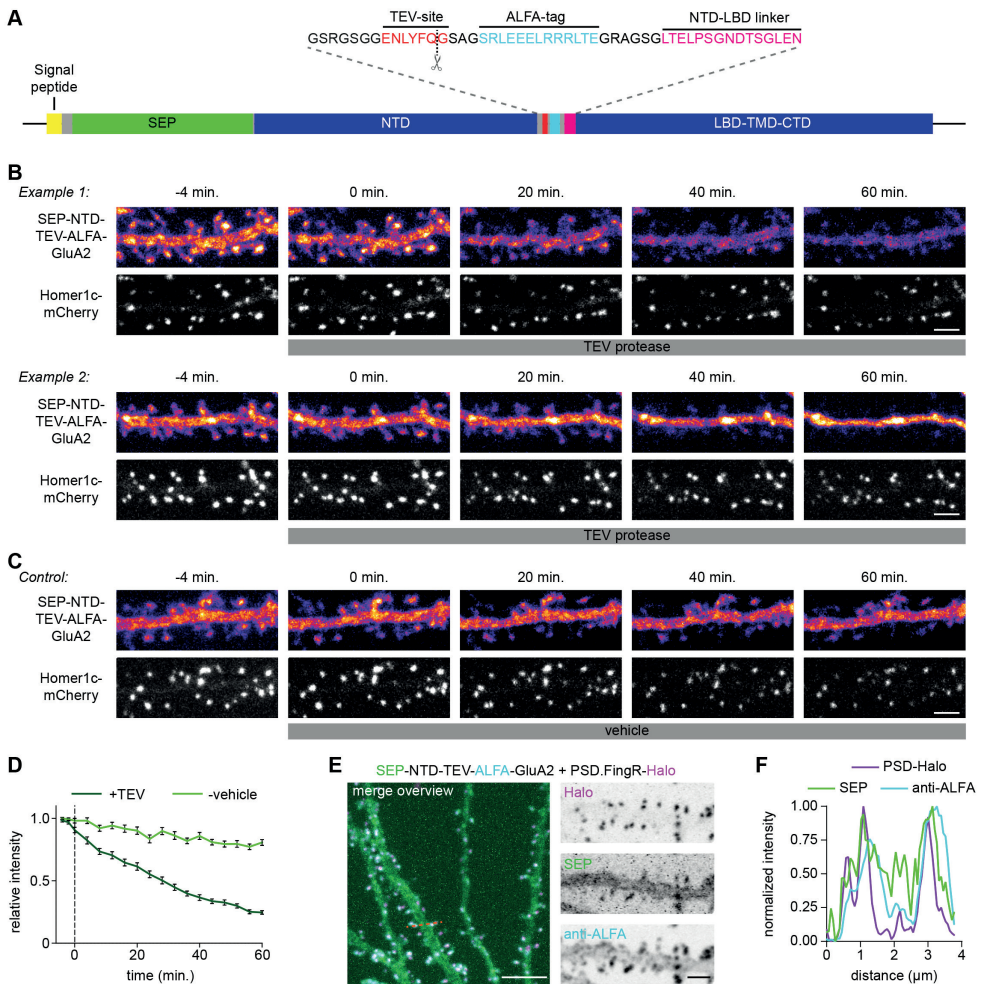


Figure 4. Acute removal of the NTD from GluA subunits



**Figure 4 (continued)** (A) Schematic overview of recombinant SEP-tagged GluA2 subunit with a TEV cleavage site and ALFA-tag incorporated between the NTD and NTD-LBD linker. Dotted line with scissors in the TEV-site indicates the cleavage site by TEV-protease. Linkers are shown in grey. (B) Two examples of live-cell imaging on SEP-NTD-TEV-ALFA-GluA2. TEV protease was added at timepoint 0 min. Scale bar: 2  $\mu$ m (C) Example as in (B) but without addition of TEV-protease. Scale bar: 2  $\mu$ m (D) Relative synaptic intensity of SEP over time as measured from neurons treated with TEV protease or vehicle. Dotted line indicates addition of TEV/vehicle. (E) Example live-cell image of SEP-NTD-TEV-ALFA-GluA2 (green), co-transfected with PSD.FingR-Halo, labeled with HaloLigand-JF549 (magenta) and anti-ALFA nanobodies (cyan). Scale bar overview: 5  $\mu$ m, zoom: 2  $\mu$ m. (F) Normalized intensity as measured from line scan indicated in (E). n = 48 ROIs from 12 neurons (+TEV) and n = 24 ROIs from 6 neurons (vehicle). Data are represented as means  $\pm$  SEM.

endosomes, the signal probably originated from the ER. Together, these results indicate that the NTD can be acutely removed from surface-expressed AMPARs using TEV proteases, providing an exciting new tool to study the role of the NTD in the anchoring and exchange of AMPARs at synapses.

## DISCUSSION

In this study, we mapped and investigated the role of the AMPAR-NTD in synaptic recruitment and anchoring. We found that the NTD of all three GluA subunits is essential for the enrichment of AMPAR at the synapse. In addition, we showed that depletion of the NTD, decreased the immobilization of AMPARs at synapses, resulting in higher synaptic turnover. Finally, we studied the diffusion kinetics of individual receptors, and found a subunit-specific role for the NTD. Importantly, while depleting the NTD of GluA2 and GluA3 increased diffusion of both synaptic and extrasynaptic receptors, the NTD of GluA1 did not.

Together with earlier studies, the NTD is now well established to have an important role in the recruitment of AMPARs to and anchoring at the synapse. The NTD could thus have an important role in finetuning the clustering of receptors at synapses, possibly by clustering into nanodomains, and regulating the alignment with presynaptic release sites. However, while depletion of the NTD does influence the density of AMPARs at the synapse, effects on subsynaptic clustering were found to be limited (Watson et al., 2021). Alternatively, the NTD could be important for the alignment of subsynaptic clusters with presynaptic release sites (Tang et al., 2016) Tang et al., 2016), a hypothesis still to be tested. In this line of thought, the recruitment of AMPARs to the synapse and its subsynaptic clustering is likely to be largely driven by auxiliary proteins such as the TARPs, while other processes such as phase separation could also be involved (Zeng et al., 2019).

The mechanisms by which the NTD regulates synaptic anchoring of AMPARs remain unknown. Interactions with presynaptic proteins as well as transsynaptic adhesion molecules have been described, affecting AMPAR functioning, likely by influencing its synaptic positioning (Bhourri et al., 2018; Dai et al., 2019; Farhy-Tselnicker et al., 2017; Lee et al., 2017; Ramsey et al., 2021; Sia et al., 2007). Interestingly, a cerebellin-1 and neuronal pentraxin-1 based synthetic protein was able to interact with AMPARs, induce their clustering at synapses and thereby restoring synaptic function, in various disease models (Suzuki et al., 2020). It is surprising that proteomics studies on AMPAR subunits have not identified many interactions with presynaptic and transsynaptic proteins (Li et al., 2013; Schwenk et al., 2012; Schwenk et al., 2009; Shanks et al., 2012; von Engelhardt et al., 2010). This could suggest that many of the NTD interactions are relatively weak and thus are lost in the purification process.

We and others have studied the function of the NTD by expression of a mutant GluA protein, lacking the NTD. While NTD-lacking GluAs can still form functional receptors, their role in receptor assembly, and potential role in intracellular trafficking, can be of influence

on the experimental readout of synaptic anchoring and surface trafficking. For this reason, we developed a TEV protease-based method to acutely remove the NTD from GluAs. While successful, the reduction of SEP signal from the neuronal surface was relatively slow as expected from the enzyme kinetics and compared to an earlier study which used TEV-protease to cleave a tag from AMPARs (Nair et al., 2013). Either the cleavage by TEV-protease is inefficient, the sequence is not easily accessible, or the SEP-NTD are have interactions that slows their diffusion out of the synaptic cleft. It would therefore be interesting to compare the kinetics of NTD cleavage to that of a SEP tag alone, which would reveal if the NTD is retained at the synapse by other proteins. In addition, thrombin protease has been shown to rapidly cleave proteins from the cell-surface and could be an alternative for TEV-protease (Ramsey et al., 2021).

In summary, we have shown that the NTD has an essential role in the synaptic recruitment and anchoring of AMPAR. While the exact mechanisms remain to be resolved, our study and others show indications for a clear subunit-specific role for the NTD in these processes.

## MATERIALS AND METHODS

### Ethics statement

All experiments were approved by the Dutch Animal Experiments Committee (Dier Experimenten Commissie [DEC], work protocol project number: AVD1080020173404), performed in line with institutional guidelines of Utrecht University, and conducted in agreement with Dutch law (Wet op de Dierproeven, 1996) and European regulations (Directive 2010/63/EU). Timed pregnant Wistar rats were obtained from Janvier Labs.

### DNA-plasmids

SEP- $\Delta$ NTD-GluA constructs were made using Gibson assembly, removing N23-A391 of GluA1, S26-T398 of GluA2 and N26-P401 of GluA3.

pCAG\_PSD95.FingR-HaloTag was made by replacing the GFP tag from pCAG\_PSD95.FingR-eGFP-CCR5TC (Addgene #46295) (Gross et al., 2013) using Gibson assembly.

SEP-NTD-TEV-ALFA-GluA constructs were made using restriction cloning. First, the NTD of GluA as amplified using PCR, flanking the fragment with MluI and XhoI sites. The TEV-cleavage site and ALFA tag (Gotzke et al., 2019), (SRLEEELRRRLTE), we ordered as a primer dimer, surrounded by overhangs from XhoI and AscI sites. The rest of GluA (from the NTD-LBD linker onwards) was amplified using PCR, flanked by AscI and XbaI sites. All fragments were ligated into SEP-GluA plasmids (cut with MluI and XbaI). pCMV-Homer1c-mCherry was obtained from (Scheefhals et al., 2019).

### Dissociated neuronal cultures

Dissociated hippocampal cultures were prepared from embryonic day 18 (E18) rat brains of both genders, as described in (Kapitein et al., 2010) and in accordance to the approved DEC work-protocol as mentioned in the ethics statements above. Pregnant rats were sacrificed by gradual fill CO<sub>2</sub>/O<sub>2</sub>. Subsequently the uterus containing the pups is taken out and is stored in a sterile ice-cold environment. After the pups were sedated by the cold, they were removed from the uterus and decapitated. Dissociated neurons were plated on Ø18-mm coverslips coated with poly-L-lysine (37.5 µg/ml, Sigma-Aldrich) and laminin (1.25 µg/mL, Roche Diagnostics) at a density of 100,000 neurons per well. Neurons were grown in Neurobasal medium (NB) supplemented with 1% pen/strep, 2% [v/v] B27, and 0.5 mM L-glutamine (all from Gibco) (NB-complete medium) at 37°C in 5% CO<sub>2</sub>. From days in vitro (DIV) 1

---

onward, medium was refreshed weekly by replacing half of the medium with Brainphys neuronal medium (BP) supplemented with 2% [v/v] NeuroCult SM1 neuronal supplement (STEMCELL Technologies) and 1% pen/strep (BP-complete medium).

### **Transfection**

DIV 10 (FRAP, live SEP and PALM). 3.3  $\mu$ l Lipofectamine 2000 reagent (Invitrogen) and 2  $\mu$ g of DNA were mixed together with 100  $\mu$ l BP and 100 $\mu$ l NB per coverslip. This mix was incubated for 30 minutes at room temperature after which 500  $\mu$ l of medium of the neuronal plate was transferred to a new plate. 300  $\mu$ l NB with L-glutamine (0.5 mM) was added to the neuronal plate together with 200  $\mu$ l of the Lipofectamine/DNA/NB/BP mix. This was then incubated at 37°C and 5% CO<sub>2</sub> for 2 hours after which coverslips were transferred towards the new plate with 500 $\mu$ l conditioned medium at which 500 $\mu$ l new supplemented NB (1% (v/v) P/S and 2% (v/v) SM1) was added.

### **Live-cell imaging**

Live-cell imaging was performed on a Nikon Eclipse Ti with Perfect Focus System. The microscope contained a Plan Apo VC 100x N.A. 1.40 oil objective to achieve a 67 nm pixel size. 491 nm (Cobolt Calypso), 561 nm (Cobolt Jive) and 642 nm (Vortran Stradus) lasers were used for excitation. ET-GFP (49002), ET-mCherry (49008) and ET-Cy5 (49006) filters were used to separate emission and excitation wavelengths. Fluorescence emission was captured with an Evolve 512 EMCCD camera (Photometrics). The microscope was equipped with a motorized XYZ stage (ASI; MS-2000), Perfect Focus System (Nikon), and was controlled by MetaMorph software (Molecular Devices). Neurons were maintained in a closed incubation chamber (Tokai hit: INUBG2E-ZILCS) at 37°C in extracellular buffer (10 mM HEPES, 120 mM NaCl, 3 mM KCl, 2 mM CaCl<sub>2</sub>, 2 mM MgCl<sub>2</sub>, 10 mM glucose [pH 7.35]).

### **Quantification of synaptic enrichment of WT and $\Delta$ NTD GluAs**

Hippocampal rat neurons were transfected on DIV 10 with SEP( $\Delta$ NTD)-GluA1-3 and FKBP-Homer1c- mCherry as described above. Imaging was performed on DIV 22-23 as above. A z-stack of 12 slices (0.5  $\mu$ m) was made per cell at a single timepoint.

Maximum intensity projections were made and analyzed using FIJI software. Fluorescence intensity of SEP-GluAs were measured on spines and shaft in 10 regions of interest (ROIs) of 8\*8 pixels (~ 512\*512 nm) and background subtracted. Synapse over shaft ratios were calculated and averaged per neuron. Neurons from at least two independent cultures were included in the analysis.

### **Live-cell surface labeling of GluAs**

SEP-NTD-TEV-ALFA-GluA2 was co-transfected with PSDFingR-Halo at DIV17 and imaged at DIV21 as above. Neurons were incubated with anti-ALFA nanobodies conjugated to Alexa647 (N1502-AF647-L, NanoTag) diluted 1:1000 in extracellular buffer and HaloLigand-JF549 (Promega). A z-stack of 12 slices (0.5  $\mu$ m) was made at a single timepoint. Maximum intensity projection was made and analyzed using FIJI software. A lines ROI (4  $\mu$ m) was drawn to measure and plot the intensity of PSDFingR, SEP and ALFA. Intensities were normalized to the minimal and maximal intensity values.

### **FRAP-imaging and analysis**

FRAP experiments were performed using the ILas2 system (Roper Scientific). After 2.5

minutes baseline imaging (single Z-plane, five frames with 30-second interval), pre-selected ROIs with a fixed diameter of 1.26  $\mu\text{m}$  containing dendritic spines were bleached using a targeted laser. Imaging during fluorescence recovery was continued for 10 minutes (10 frames with 30-second interval and 5 frames with 1-minute interval).

For analysis, acquisitions were corrected for drift. For each ROI, mean intensities were measured for every time point and corrected for background using the averaged intensity of two background ROIs. For each ROI, intensities were normalized to 1 based on the averaged intensities of the frames before ROI bleaching and normalized to zero based on the intensity from the first frame after bleaching. Data was corrected for general photobleaching by measuring intensity from non-bleached spines. Normalized intensities were plotted over time. The mobile fraction of protein was determined by averaging the normalized intensity of the last four frames for each neuron. For each condition, data was collected over three independent neuronal cultures.

### Single-molecule tracking and analysis

Live-cell single-molecule tracking was performed on a Nikon Ti microscope equipped with a 100 $\times$  NA 1.49 Apo TIRF oil objective, a Perfect Focus System, and an additional 2.5 $\times$  Optovar to achieve an effective pixel size of 64 nm. Oblique laser illumination was achieved using a custom illumination pathway with an AA acousto-optic tunable filter (AA opto-electronics); a 15-mW, 405-nm-diode laser (Power Technology); a 100-mW, 561-nm-DPSS laser (Cobolt Jive); and a 40-mW, 640-nm-diode laser (Power Technology). Emission light was separated from excitation light with a quad-band polychroic mirror (ZT405/488/561/640rpc, Chroma) and additional band-pass emission filters (ET 525/595/700, Chroma). Fluorescence emission was acquired using a DU-897D EMCCD camera (Andor). All components were controlled by  $\mu$ Manager software.

Neurons were transfected with SEP tagged WT or  $\Delta$ NTD GluA constructs and Homer1c-mCherry as described above. Imaging was performed in extracellular buffer supplemented with 1.5% bovine serum albumin (Sigma). ATTO647N- conjugated anti-GFP nanobodies (GFPBooster-ATTO647N, Chromotek) were bath applied to a final dilution of 1:50,000. Imaging was conducted at a 50-Hz frame rate with 640-nm excitation laser illumination (in TIRF). Localization were fitted using detection of molecules (DoM), downloaded from: [https://github.com/ekatruxha/DoM\\_Utrecht](https://github.com/ekatruxha/DoM_Utrecht). Molecules fitted with a precision  $< 50$  were tracked with tracking radius of 512 nm and diffusion coefficient determined for tracks  $> 30$  frames. A cell mask was drawn manually to filter out localizations outside neurons due to nonspecifically bound nanobody. Tracking was accomplished using custom tracking algorithms in MATLAB (MathWorks) using a tracking radius of 512 nm. For tracks consisting of  $> 30$  frames, the instantaneous diffusion coefficient was estimated as described (Lu et al., 2014). The first three points of the MSD versus elapsed time (t) plot were used to fit the slope using linear fitting adding a value of 0 at MSD(0). Tracks with a negative slope ( $< 8\%$ ) were ignored. The diffusion coefficient  $D_{\text{eff}}$  was then calculated using  $\text{MSD} = 4D_{\text{eff}}t$ . A synapse mask was made based on the full width half maximum (FWHM) Homer1c-mCherry expression as previously described (Li and Blanpied, 2016). Synaptic tracks were tracks that were localized for at least 80 percent within the borders of a synaptic mask. The remaining tracks were considered as extrasynaptic. Diffusion coefficients of all tracks for WT and  $\Delta$ NTD were plotted in a cumulative frequency distribution. In addition, diffusion coefficient averages of synaptic and extrasynaptic tracks were averaged per neuron and were plotted in bar plots. For each condition, data was collected over at least two independent

---

neuronal cultures.

### **Statistics**

Statistical significance was tested with a student t test when comparing two groups. A P value below 0.05 was considered significant. If multiple groups were compared, statistical significance was tested with a one-way ANOVA followed by a Bonferroni's multiple comparison. Note that although in several occasions more than two conditions were plotted in the same graph, each condition had its own control, and thus a student t test was performed between conditions (also see figure legends). In all figures, \* was used to indicate a P value < 0.05, \*\* for P < 0.01, and \*\*\* for P < 0.001. Reported n is number of neurons, and each experiment was replicated in neuronal cultures from at least two independent preparations if not indicated differently. Statistical analysis and graphs were prepared in GraphPad PRISM 8, and figures were generated in Adobe Illustrator CC.

### **ACKNOWLEDGEMENTS**

This work was supported by the European Research Council (ERC-StG 716011) to HDM. We thank the members of the MacGillavry lab for discussions.

## REFERENCES

- Anggono, V., and Huganir, R.L. (2012). Regulation of AMPA receptor trafficking and synaptic plasticity. *Curr Opin Neurobiol* 22, 461-469.
- Bhouri, M., Morishita, W., Temkin, P., Goswami, D., Kawabe, H., Brose, N., Sudhof, T.C., Craig, A.M., Siddiqui, T.J., and Malenka, R. (2018). Deletion of LRRTM1 and LRRTM2 in adult mice impairs basal AMPA receptor transmission and LTP in hippocampal CA1 pyramidal neurons. *Proc Natl Acad Sci U S A* 115, E5382-E5389.
- Bissen, D., Foss, F., and Acker-Palmer, A. (2019). AMPA receptors and their minions: auxiliary proteins in AMPA receptor trafficking. *Cell Mol Life Sci* 76, 2133-2169.
- Borgdorff, A.J., and Choquet, D. (2002). Regulation of AMPA receptor lateral movements. *Nature* 417, 649-653.
- Cais, O., Herguedas, B., Krol, K., Cull-Candy, S.G., Farrant, M., and Greger, I.H. (2014). Mapping the interaction sites between AMPA receptors and TARPs reveals a role for the receptor N-terminal domain in channel gating. *Cell Rep* 9, 728-740.
- Chen, H., Tang, A.H., and Blanpied, T.A. (2018). Subsynaptic spatial organization as a regulator of synaptic strength and plasticity. *Curr Opin Neurobiol* 51, 147-153.
- Choquet, D., and Opazo, P. (2022). The role of AMPAR lateral diffusion in memory. *Semin Cell Dev Biol* 125, 76-83.
- Dai, J., Aoto, J., and Sudhof, T.C. (2019). Alternative Splicing of Presynaptic Neurexins Differentially Controls Postsynaptic NMDA and AMPA Receptor Responses. *Neuron* 102, 993-1008 e1005.
- de Wit, J., Sylwestrak, E., O'Sullivan, M.L., Otto, S., Tiglio, K., Savas, J.N., Yates, J.R., 3rd, Comoletti, D., Taylor, P., and Ghosh, A. (2009). LRRTM2 interacts with Neurexin1 and regulates excitatory synapse formation. *Neuron* 64, 799-806.
- Diaz-Alonso, J., and Nicoll, R.A. (2021). AMPA receptor trafficking and LTP: Carboxy-termini, amino-termini and TARPs. *Neuropharmacology* 197, 108710.
- Diaz-Alonso, J., Sun, Y.J., Granger, A.J., Levy, J.M., Blankenship, S.M., and Nicoll, R.A. (2017). Subunit-specific role for the amino-terminal domain of AMPA receptors in synaptic targeting. *Proc Natl Acad Sci U S A* 114, 7136-7141.
- Farhy-Tselnicker, I., van Casteren, A.C.M., Lee, A., Chang, V.T., Aricescu, A.R., and Allen, N.J. (2017). Astrocyte-Secreted Glypican 4 Regulates Release of Neuronal Pentraxin 1 from Axons to Induce Functional Synapse Formation. *Neuron* 96, 428-445 e413.
- Garcia-Nafria, J., Herguedas, B., Watson, J.F., and Greger, I.H. (2016). The dynamic AMPA receptor extracellular region: a platform for synaptic protein interactions. *J Physiol* 594, 5449-5458.
- Gotzke, H., Kilisch, M., Martinez-Carranza, M., Sograte-Idrissi, S., Rajavel, A., Schlichthaerle, T., Engels, N., Jungmann, R., Stenmark, P., Opazo, F., and Frey, S. (2019). The ALFA-tag is a highly versatile tool for nanobody-based bioscience applications. *Nat Commun* 10, 4403.
- Gross, G.G., Junge, J.A., Mora, R.J., Kwon, H.B., Olson, C.A., Takahashi, T.T., Liman, E.R., Ellis-Davies, G.C., McGee, A.W., Sabatini, B.L., et al. (2013). Recombinant probes for visualizing endogenous synaptic proteins in living neurons. *Neuron* 78, 971-985.
- Gugustea, R., and Jia, Z. (2021). Genetic manipulations of AMPA glutamate receptors in hippocampal synaptic plasticity. *Neuropharmacology* 194, 108630.
- Haas, K.T., Compans, B., Letellier, M., Bartol, T.M., Grillo-Bosch, D., Sejnowski, T.J., Sainlos, M., Choquet, D., Thoumine, O., and Hossy, E. (2018). Pre-post synaptic alignment through neuroligin-1 tunes synaptic transmission efficiency. *Elife* 7.
- Harb, A., Vogel, N., Shaib, A., Becherer, U., Bruns, D., and Mohrmann, R. (2021). Auxiliary Subunits Regulate the Dendritic Turnover of AMPA Receptors in Mouse Hippocampal Neurons. *Front Mol Neurosci* 14, 728498.
- Herguedas, B., Krieger, J., and Greger, I.H. (2013). Receptor heteromeric assembly-how it works and why it matters: the case of ionotropic glutamate receptors. *Prog Mol Biol Transl Sci* 117, 361-386.
- Jiang, C.H., Wei, M., Zhang, C., and Shi, Y.S. (2021). The amino-terminal domain of GluA1 mediates LTP maintenance via interaction with neuroplastin-65. *Proc Natl Acad Sci U S A* 118.
- Kamalova, A., and Nakagawa, T. (2021). AMPA receptor structure and auxiliary subunits. *J Physiol* 599, 453-469.
- Lee, H.K., Takamiya, K., Han, J.S., Man, H., Kim, C.H., Rumbaugh, G., Yu, S., Ding, L., He, C., Petralia, R.S., et al. (2003). Phosphorylation of the AMPA receptor GluR1 subunit is required for synaptic plasticity and retention of spatial memory. *Cell* 112, 631-643.
- Lee, S.J., Wei, M., Zhang, C., Maxeiner, S., Pak, C., Calado Botelho, S., Trotter, J., Sterky, F.H., and Sudhof, T.C. (2017). Presynaptic Neuronal Pentraxin Receptor Organizes Excitatory and Inhibitory Synapses. *J Neurosci* 37, 1062-1080.
- Leuschner, W.D., and Hoch, W. (1999). Subtype-specific assembly of alpha-amino-3-hydroxy-5-methyl-4-isoxazole propionic acid receptor subunits is mediated by their n-terminal domains. *J Biol Chem* 274, 16907-16916.
- Li, K.W., Chen, N., and Smit, A.B. (2013). Interaction proteomics of the AMPA receptor: towards identification of receptor sub-complexes. *Amino Acids* 44, 1247-1251.
- Li, T.P., and Blanpied, T.A. (2016). Control of Transmembrane Protein Diffusion within the Postsynaptic Density Assessed by Simultaneous Single-Molecule Tracking and Localization Microscopy. *Front Synaptic Neurosci* 8, 19.
- Lu, H.E., MacGillavry, H.D., Frost, N.A., and Blanpied, T.A. (2014). Multiple spatial and kinetic subpopulations of CaMKII in spines and dendrites as resolved by single-molecule tracking PALM. *J Neurosci* 34, 7600-7610.
- Lu, J., Helton, T.D., Blanpied, T.A., Racz, B., Newpher, T.M., Weinberg, R.J., and Ehlers, M.D. (2007). Postsynaptic positioning of endocytic zones and AMPA receptor cycling by physical coupling of dynamin-3 to Homer. *Neuron* 55, 874-889.
- Makino, H., and Malinow, R. (2009). AMPA receptor incorporation into synapses during LTP: the role of lateral movement and exocytosis. *Neuron* 64, 381-390.
- Mondin, M., Labrousse, V., Hossy, E., Heine, M., Tessier, B., Levet, F., Poujol, C., Blanchet, C., Choquet, D., and

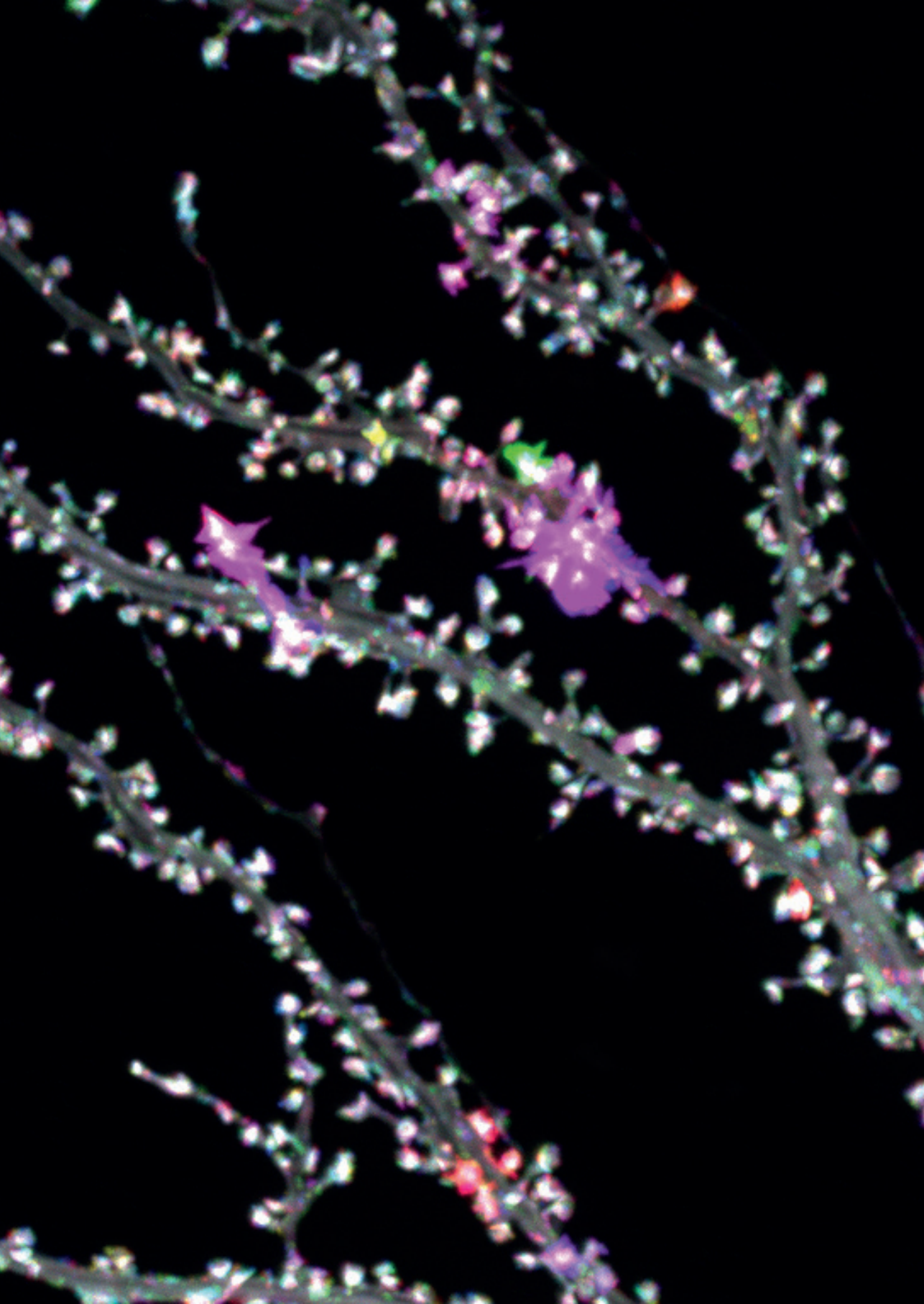
---

Thoumine, O. (2011). Neurexin-neuroligin adhesions capture surface-diffusing AMPA receptors through PSD-95 scaffolds. *J Neurosci* 31, 13500-13515.

- Nabavi, S., Fox, R., Proulx, C.D., Lin, J.Y., Tsien, R.Y., and Malinow, R. (2014). Engineering a memory with LTD and LTP. *Nature* 511, 348-352.
- Nair, D., Hossy, E., Petersen, J.D., Constals, A., Giannone, G., Choquet, D., and Sibarita, J.B. (2013). Super-resolution imaging reveals that AMPA receptors inside synapses are dynamically organized in nanodomains regulated by PSD95. *J Neurosci* 33, 13204-13224.
- Nicoll, R.A. (2017). A Brief History of Long-Term Potentiation. *Neuron* 93, 281-290.
- Opazo, P., and Choquet, D. (2011). A three-step model for the synaptic recruitment of AMPA receptors. *Mol Cell Neurosci* 46, 1-8.
- Opazo, P., Sainlos, M., and Choquet, D. (2012). Regulation of AMPA receptor surface diffusion by PSD-95 slots. *Curr Opin Neurobiol* 22, 453-460.
- Pandya, N.J., Seeger, C., Babai, N., Gonzalez-Lozano, M.A., Mack, V., Lodder, J.C., Gouwenberg, Y., Mansvelder, H.D., Danielson, U.H., Li, K.W., et al. (2018). Noelin1 Affects Lateral Mobility of Synaptic AMPA Receptors. *Cell Rep* 24, 1218-1230.
- Pasternack, A., Coleman, S.K., Joupila, A., Mottershead, D.G., Lindfors, M., Pasternack, M., and Keinänen, K. (2002). Alpha-amino-3-hydroxy-5-methyl-4-isoxazolepropionic acid (AMPA) receptor channels lacking the N-terminal domain. *J Biol Chem* 277, 49662-49667.
- Ramsey, A.M., Tang, A.H., LeGates, T.A., Gou, X.Z., Carbone, B.E., Thompson, S.M., Biederer, T., and Blanpied, T.A. (2021). Subsynaptic positioning of AMPARs by LRRTM2 controls synaptic strength. *Sci Adv* 7.
- Rossmann, M., Sukumaran, M., Penn, A.C., Vepriintsev, D.B., Babu, M.M., and Greger, I.H. (2011). Subunit-selective N-terminal domain associations organize the formation of AMPA receptor heteromers. *EMBO J* 30, 959-971.
- Saglietti, L., Dequidt, C., Kamieniarz, K., Rousset, M.C., Valnegri, P., Thoumine, O., Beretta, F., Fagni, L., Choquet, D., Sala, C., et al. (2007). Extracellular interactions between GluR2 and N-cadherin in spine regulation. *Neuron* 54, 461-477.
- Scheefhals, N., Catsburg, L.A.E., Westerveld, M.L., Blanpied, T.A., Hoogenraad, C.C., and MacGillavry, H.D. (2019). Shank Proteins Couple the Endocytic Zone to the Postsynaptic Density to Control Trafficking and Signaling of Metabotropic Glutamate Receptor 5. *Cell Rep* 29, 258-269 e258.
- Schwenk, J., Baehrens, D., Haupt, A., Bildl, W., Boudkkazi, S., Roeper, J., Fakler, B., and Schulte, U. (2014). Regional diversity and developmental dynamics of the AMPA-receptor proteome in the mammalian brain. *Neuron* 84, 41-54.
- Schwenk, J., Harmel, N., Brechet, A., Zolles, G., Berkefeld, H., Muller, C.S., Bildl, W., Baehrens, D., Huber, B., Kulik, A., et al. (2012). High-resolution proteomics unravel architecture and molecular diversity of native AMPA receptor complexes. *Neuron* 74, 621-633.
- Schwenk, J., Harmel, N., Zolles, G., Bildl, W., Kulik, A., Heimrich, B., Chisaka, O., Jonas, P., Schulte, U., Fakler, B., and Klocker, N. (2009). Functional proteomics identify cornichon proteins as auxiliary subunits of AMPA receptors. *Science* 323, 1313-1319.
- Shanks, N.F., Savas, J.N., Maruo, T., Cais, O., Hirao, A., Oe, S., Ghosh, A., Noda, Y., Greger, I.H., Yates, J.R., 3rd, and Nakagawa, T. (2012). Differences in AMPA and kainate receptor interactomes facilitate identification of AMPA receptor auxiliary subunit GSG1L. *Cell Rep* 1, 590-598.
- Shi, S., Hayashi, Y., Esteban, J.A., and Malinow, R. (2001). Subunit-specific rules governing AMPA receptor trafficking to synapses in hippocampal pyramidal neurons. *Cell* 105, 331-343.
- Sia, G.M., Beique, J.C., Rumbaugh, G., Cho, R., Worley, P.F., and Huganir, R.L. (2007). Interaction of the N-terminal domain of the AMPA receptor GluR4 subunit with the neuronal pentraxin NP1 mediates GluR4 synaptic recruitment. *Neuron* 55, 87-102.
- Suzuki, K., Elegheert, J., Song, I., Sasaki, H., Senkov, O., Matsuda, K., Kakegawa, W., Clayton, A.J., Chang, V.T., Ferrer-Ferrer, M., et al. (2020). A synthetic synaptic organizer protein restores glutamatergic neuronal circuits. *Science* 369.
- Tang, A.H., Chen, H., Li, T.P., Metzbowler, S.R., MacGillavry, H.D., and Blanpied, T.A. (2016). A trans-synaptic nanocolumn aligns neurotransmitter release to receptors. *Nature* 536, 210-214.
- Traynelis, S.F., Wollmuth, L.P., McBain, C.J., Menniti, F.S., Vance, K.M., Ogden, K.K., Hansen, K.B., Yuan, H., Myers, S.J., and Dingledine, R. (2010). Glutamate receptor ion channels: structure, regulation, and function. *Pharmacol Rev* 62, 405-496.
- von Engelhardt, J., Mack, V., Sprengel, R., Kavenstock, N., Li, K.W., Stern-Bach, Y., Smit, A.B., Seeburg, P.H., and Monyer, H. (2010). CKAMP44: a brain-specific protein attenuating short-term synaptic plasticity in the dentate gyrus. *Science* 327, 1518-1522.
- Watson, J.F., Ho, H., and Greger, I.H. (2017). Synaptic transmission and plasticity require AMPA receptor anchoring via its N-terminal domain. *Elife* 6.
- Watson, J.F., Pinggera, A., Ho, H., and Greger, I.H. (2021). AMPA receptor anchoring at CA1 synapses is determined by N-terminal domain and TARPs gamma8 interactions. *Nat Commun* 12, 5083.
- Whitlock, J.R., Heynen, A.J., Shuler, M.G., and Bear, M.F. (2006). Learning induces long-term potentiation in the hippocampus. *Science* 313, 1093-1097.
- Zeng, M., Diaz-Alonso, J., Ye, F., Chen, X., Xu, J., Ji, Z., Nicoll, R.A., and Zhang, M. (2019). Phase Separation-Mediated TARP/MAGUK Complex Condensation and AMPA Receptor Synaptic Transmission. *Neuron* 104, 529-543 e526.







# 8

---

## General Discussion

Jelmer Willems

---

Cell Biology, Neurobiology and Biophysics, Department of Biology, Faculty of Science, Utrecht University, Utrecht, the Netherlands

---

The dynamic protein organization at excitatory synapses is the driving force behind synaptic communication. A well-balanced machinery controlling the dynamic exchange of molecules like glutamatergic receptors allow for synaptic plasticity, fundamental to learning and memory. The general aim of this thesis was to develop novel methods to study the localization and dynamics of endogenous proteins at neuronal synapses.

To summarize, in **chapter 2** we first developed a new CRISPR/Cas9 based strategy to label endogenous proteins in neurons. We further expanded on this technique in **chapter 3**, allowing for duplex labeling and manipulation of multiple endogenous proteins. Second, we described a protocol for single-molecule localization microscopy important for studying protein organization at a sub-micrometer scale (**chapter 4**), and developed a new analytic method to analyze co-localization in dual-color SMLM datasets (**chapter 5**). Third, we used the techniques developed in the preceding chapters to study the synaptic organization of AMPAR – auxiliary proteins (**chapter 6**), and studied the role of the N-terminal domain (NTD) of the AMPAR in synaptic anchoring (**chapter 7**). In this final chapter, I will discuss the key findings, current challenges and provide a perspective for future studies.

## HARNESSING THE POWER OF GENOME EDITING TO LABEL PROTEINS IN NEURONS

Investigating the dynamic distribution of proteins in neurons is critical for a mechanistic understanding of brain function (Choquet et al., 2021). However, labeling and visualizing proteins of interest at high spatial resolution is far from trivial. A lack of specific antibodies, overexpression artifacts, the need for sparse cell labeling and live-cell imaging of low abundant proteins, are just a few challenges researchers face when starting to address biological questions. In view of these challenges, we invested in developing a reliable CRISPR/Cas9 based genome editing approach to label endogenous proteins in neurons. Genetically tagging of genes in dividing cells using CRISPR/Cas9 technology has been around for almost a decade (Banan, 2020; Liu et al., 2022). Generally, this process requires the cleavage of the intended genomic site, and providing a donor DNA flanked with sequences that have homology to the genomic integration site. The DNA repair mechanism of homologous repair, then allows for the integration of the donor (Al-Zain and Symington, 2021; Koch et al., 2018). Even if efficiency is low, cells can be sorted, clone selected and expanded, yielding a cell population with high knock-in efficiency. Expanding this to post-mitotic cell types like neurons has remained limited as repair mechanisms active in these cells are largely driven through NHEJ (Delacote and Lopez, 2008; Iyama and Wilson, 2013; Lieber, 2010). Some studies have shown some success, efficiency remains low (Mikuni et al., 2016; Nishiyama et al., 2017; Uemura et al., 2016) and most of these studies targeted neuronal progenitors in the embryo. The inability to generate knock-ins in neurons using HDR lies in that the conventional donors that rely on homology arms, are not integrated as intended (no recombination) or not integrated at all. In **chapter 2**, we have developed a CRISPR/Cas9 based approaches based on NHEJ to tag endogenous proteins in neurons allowing for efficient knock-in generation in neurons. Using NHEJ, we established an easy to implement strategy to generate knock-ins in neurons, that achieves knock-in efficiencies >10% for many of the tested target proteins. We have also shown that this approach works with various DNA delivery modalities such that it can be applied to neuronal cultures as well as in vivo. Below, I will discuss the current challenges and opportunities in using NHEJ-based knock-in approaches that arose from these and other studies.

*Knock-in accuracy and efficiency*

A major concern that quickly arises when using NHEJ over HDR is the accuracy of DNA editing. While NHEJ is considered error-prone, whether repair results in DNA alterations is highly dependent on the type of DNA damage and cellular conditions (Betermier et al., 2014). In the absence of a donor DNA, a double stranded break can be repaired with high precision by the NHEJ pathway, but can subsequently undergo another round of cleavage, a process which is repeated till errors do occur and the target site gets destroyed, and hence mutations are introduced (Pannunzio et al., 2018). Thus, the error-prone nature of NHEJ can be overcome by the introduction of a donor DNA early in the repair process. In case of HDR, integration is very precise, and although mutations at donor-genome junctions can occur, they are quite rare (Al-Zain and Symington, 2021). Since NHEJ is much more active in cells, we expect that the number of integration events is much lower for HDR than for NHEJ. Thus, higher knock-in efficiencies can be obtained with NHEJ over HDR, because integration events occur more often, albeit with a slightly higher chance of mutations at the genome-donor junctions. Important to note is that accuracy of integration is often analyzed by amplifying genome-donor junctions. Thus, no information is obtained about genomic sites where integration did not occur. Likely, and consistent with our findings, this can result in a large degree of knockouts in cells where the knock-in was unsuccessful. This is especially problematic for in vivo labeling where the goal is to label a few cells, and knock-out cells could have undesired effects on a functional level. Furthermore, for most of the knock-in methods that have been developed for targeting neuronal cells, we do not know whether knock-ins are mostly biallelic or monoallelic. Technically, these concerns are hard to tackle, requiring single-cell sorting and target amplification of knock-in positive cells. The HITI method (on which our ORANGE toolbox is based), showed a 30–50% biallelic integration, varying strongly between cell types, and not analyzed in brain cells (Suzuki et al., 2016). As an alternative approach, we used extensive validation of total protein levels using antibody staining, showing that for most targets, protein levels are comparable to endogenous levels for most successful knock-in cells, suggesting a high degree of biallelic knock-ins. Nevertheless, it is crucial to develop accessible methods to analyze knock-in accuracy in a more detailed and high-throughput manner.

In an attempt to achieve higher knock-in efficiencies by addressing knock-in accuracy, two NHEJ based methods (TKIT and Crispie) have been recently developed that aim to integrate tags in intronic instead of coding regions (Fang et al., 2021, Zhong et al., 2021). Knock-in efficiency should therefore be increased, because small mutations at the integration sites do not affect the reading frame. Targeted Knock-In with Two (TKIT) guides, is based on the complete replacement of an exon with a donor exon, including the exon-intron splicing sites (Fang et al., 2021). This method is especially well-suited for replacing small exons. The Crispie method is based on the introduction of a completely new exon into an intronic region. Requiring only one guide sequence (in contrast to TKIT that requires two), this approach is however limited by the fact that introns have to be located as such that the protein product allow for a protein tag at that position. With multiple NHEJ-based methods being developed (which also includes (Gao et al., 2019)), there are now multiple approaches to tag a neuronal protein of interest, although I believe that our ORANGE method is the most easy and straightforward to implement.

Beside increasing the accuracy of integration, there are multiple other ways in which knock-in efficiency can be optimized. For example, we found that lowering the concentration of donor DNA in cells increased knock-in efficiency (**chapter 3**). This was surprising as we

---

would expect the opposite to happen. Although this seems to differ between integration sites, donors are likely to compete for integration, or in some cases, could integrate as multiple concatenated copies. Other studies have shown that binding of the donor to the Cas9-guide RNA complex, such that the donor is recruited to the site of DNA-cleavage, can increase efficiency (Carlson-Stevermer et al., 2017). This indicates that not the amount of donor per se, but the availability of donor for integration is important. As such, we also need to consider that the donor is provided by cleavage from the knock-in plasmid which could also be an integration limiting step. Together, much can still be gained from optimizing donor availability for integration.

Knock-in efficiency can also be very dependent on the specific guideRNA. In **chapter 2**, we showed that three (overlapping) target sequences could result in over a tenfold difference in efficiency. Tools to predict on-target efficiency of have been described, but we did not find a correlation with knock-in efficiency (Bae et al., 2014; Doench et al., 2016). The main reason is that these prediction tools are based on the efficient generation of knockouts. Although several guideRNA features, such as polyT sequences are known to limit gRNA function (Xu et al., 2015), many others also seem to be cell type specific (Liu et al., 2020). Thus, future studies will have to take on the challenge of developing better prediction models for guideRNA efficiency for knock-in generation.

Aimed to increase knock-in, multiple studies have tried to modulate the cellular repair mechanisms. Most of these studies are focused on reducing NHEJ activity in favor of HDR activity (Nambiar et al., 2022). For example, pharmacological downregulation of components the NHEJ pathway have been used (Pawelczak et al., 2018). In addition, Cas9 fusions with HDR promoting proteins also have been shown to increase efficacy of knock-in via HDR (Jayavaradhan et al., 2019; Tran et al., 2019). It would therefore be interesting to explore whether such approaches could also be used to enhance NHEJ based methods. For example, active recruitment of DNA end-binding proteins to the site of cleavage such as Ku70/80, that protect DNA ends to exonuclease activity, could favor NHEJ (Brandsma and Gent, 2012).

Lastly, several new knock-in methods have been described that aim to achieve high knock-in efficiencies by using different knock-in strategies. For example, the use of single-stranded DNA donors with homology arms were used to generate knock-ins in brain cortex of embryos using in utero electroporation (Meyerink et al., 2022). These donors are probably better suited for directing HDR mechanism compared to double-stranded donors. Another method used a cleavage deficient Cas9 fused to a integrase enzyme, to integrate large donor DNAs into genomic sites without cleavage of the DNA (Ioannidi et al., 2021). Data on whether or not this approach works in post-mitotic cells is so-far limited to primary human hepatocytes. In addition, the size of this Cas9-integrase fusion could be problematic for efficient delivery in vivo.

In summary, NHEJ mediated knock-in approaches can be highly efficient, but it remains challenging to identify the optimal conditions for improving efficacy and accuracy. Future studies should thus focus on better prediction tools for guideRNA selection, strategies to increase donor DNA availability and maybe even modulate NHEJ activity such that accuracy of integration is increased.

### *DNA delivery*

We have shown that our ORANGE method can be used with many different gene delivery systems. Importantly, we have shown efficient genome editing using regular transfection methods such as lipofection, even though transfection efficacy of such methods is only ~1%.

Low efficacy of transfection can also be a benefit, as most neurons surrounding a knock-in cells remain unedited wild-type cells, and therefore, network properties can safely be studied. However, with some knock-ins having low knock-in efficiencies, the biggest increase in obtaining more knock-in cells in a given sample, is therefore likely to be gained by increasing efficacy of DNA delivery. First, we have used electroporation to deliver DNA to neurons with high efficacy, but we found this to severely impact neuronal viability. Optimizing electroporation protocols to increase cell viability while keeping high transduction efficacy has to be explored. Second, we have shown that lentiviruses can be used, but although they target much more cells compared to lipofection, the number of knock-in cells was not notably higher. This is likely because lentiviral infections rely on additional intracellular processing steps such as the conversion of single-stranded RNA to double-stranded DNA and, the effective number of donor copies entering a neuron are likely to be lower than for lipofection. Third, AAV viruses can also be used which are especially well-suited for tissue. We have shown efficient generation of knock-ins in vivo brain of a mature SpCas9 mouse. Unfortunately, the relatively small packaging limit of AAV particles (~5kb) is problematic for making SpCas9 expressing AAVs, that together with a promoter and polyA reach that limit. Although we were able to make measurable AAV titers for SpCas9, using this virus in WT mice brain slices severely reduced knock-in efficiency compared those of the SpCas9 mouse line (data not in this thesis). It would therefore be key to optimize SpCas9 packaging in AAV and its expression when used for infection. In addition, smaller Cas proteins such as *Staphylococcus aureus* Cas9 (SaCas9) could be used, although requiring a different and more limiting PAM sequence (Ran et al., 2015). Alternatively, split SpCas9 approaches have been developed in which two halves of the protein are expressed separately and recombine into a functional protein while expressed (Chew et al., 2016; Wright et al., 2015). This process was even made inducible, allowing for active control over SpCas9 activity (Zetsche et al., 2015).

In recent years, several interesting alternative methods for SpCas9, guideRNA and donor delivery have been developed. Transfection of preloaded SpCas9-gRNA protein complexes showed promising genome editing results even in post-mitotic cells (Stahl et al., 2017). In addition, multiple studies have aimed on constructing virus-like particles (VLPs), carrying DNA and/or Cas proteins (Banskota et al., 2022; Gee et al., 2020; Hamilton et al., 2021; Montagna et al., 2018). These VLPs are constructed using modified viral gag packing proteins, and a recent study have shown the possibility to use mammalian gag homologs for VLP formation (Segel et al., 2021). These VLPs can be engineered, and thus could provide promising, safe, efficient, and non-packaging limit restricted method for gene delivery in cultured cells and in tissue.

### *Multiplexing*

In the context of biological questions, its often required to visualize two (or more) proteins in the same neuron. Since NHEJ based donors do not have homology-arms, the main challenge when targeting multiple genes was to control integration events such that there is no crosstalk between the donors. In **chapter 2**, we have introduced duplex labeling using Cre-recombinase. As proof of principle, we showed that C-terminal knock-in of a donor containing a P2A peptide and Cre, could activate a second knock-in plasmid only at the moment that the first knock-in was successfully established. In **chapter 3**, we further optimized this approach, establishing a more robust approach in which Cre recombinase activation can be induced separately, either via expression from a lentivirus or using tamoxifen based induction of Cre (Matsuda and Cepko, 2007). Knock-in events are hereby separated in time, thus preventing

---

donor mix-up to a large extent and without influencing the donor of the first knock-in with a Cre module. Nevertheless, some crossover of donors was still observed, in a target specific manner. In addition, efficiencies remain low as two knock-ins have to be successful in a single neuron. Thus, and especially for multiplexing, increasing knock-in efficacies (as discussed above) will be key in expanding these toolboxes in the future. Finally, the use of Cre-activatable gRNAs used here for multiplexing, could also be used to drive cell-type specific activation of knock-in expression, for example in existing Cre-driver mouse lines.

#### *Future opportunities for genome editing in neurons*

The development of CRISPR/Cas9 knock-in methodologies for neuronal preparations has opened a door to many new applications, also beyond protein labeling and localization. In **chapter 3** for example, we showed that we can actively modulate protein dynamics in cells by knock-in of dimerization modules in receptor and scaffolding molecules, thereby study receptor turnover at synapses.

Studying disease-related mutation in the context of endogenous protein expression has become possible without the need of generating animal models. Whereas conventional methods included the overexpression of recombinant proteins, we can now introduce mutations without disturbing regular protein transcription and translation machinery. Although overexpression of mutant proteins can yield important information about function, its relative importance can be overinterpreted. This is particularly important in the context of cellular processes in which there is partial redundancy and/or dependencies among proteins. In **chapter 6**, we used ORANGE to generate C-terminal knock-ins replacing the C-terminal tail of several AMPAR – auxiliary proteins, with a mutant C-tail lacking the important PDZ ligand. Our data showed much more subtle changes to receptor anchoring in synapses, compared to other studies such as (Watson et al., 2021). Another study used knock-ins to delete full domains from a protein, by integrating a tag, stop-codon and 3' polyA in the coding sequence (Gao et al., 2019). This way, they could validate that  $\beta$ IV-spectrin requires its ankyrin binding domain for localization at the AIS. It would be interesting to explore these strategies further. The TKIT approach which enables replacement of full exons (Fang et al., 2021), is also interesting in this respect, as mutations can be made much more flexible, without being restricted to C-terminal depletions or replacements.

Since ORANGE and other knock-in methods now allow for tagging of endogenous proteins in sparsely labeled cells, it also becomes possible to quantitatively investigate subcellular compartments such as synapses. Several approaches have been developed that allow for counting protein numbers, for example using step-wise bleaching of fluorescence, or using quantitative super-resolution techniques (Hummert et al., 2021). Together, these could provide a powerful combination allowing investigation of protein copy number.

Local protein synthesis has been described to play an active role in synapse maintenance, with protein translation being driven by processes such as synaptic plasticity (Das et al., 2021; Hafner et al., 2019). Recently, our ORANGE technique was used to visualize the local synthesis of endogenous PSD95,  $\beta$ -actin and CaMKII proteins during synaptic potentiation and depression (Donlin-Asp et al., 2021).

Labeling proteins using CRISPR/Cas9 also could have major implications for the use of proteomics studies (Dolgalev and Poverennaya, 2021). For example, it would be interesting to fuse proteins to biotin ligases such as BirA and APEX (Rhee et al., 2013; Roux et al., 2012). These proteins can biotinylate proteins in their close vicinity, which can be isolated using streptavidin based affinity purification. When combined with the ORANGE knock-in

system, proteomics studies can be performed studying endogenous protein composition at synapses. Similarly, knock-ins of smaller affinity tags such as His-, FLAG- or Strep-Tags can be used to label proteins which can then be affinity purified and analyzed using mass-spectrometry (Dalvai et al., 2015). Moreover, specific synapses can be genetically labeled by targeting the pre- and post- synaptic cells separately with a split GFP approach similar to the GFP reconstitution across synaptic partners (GRASP) approach (Choi et al., 2018; Kim et al., 2011). Only those synapses where these two cell types make contact will show GFP fluorescence, which can then be isolated for proteomics studies into protein composition. Together, these opportunities thus reduce the requirement of antibodies, and could be an alternative to expression of recombinant proteins, thus enabling studies into native protein composition.

## THE POWER AND CHALLENGES FOR SINGLE-MOLECULE IMAGING APPROACHES

The development of super-resolution microscopy approaches has enabled in-depth investigation of protein localization with sub-micron spatial resolution (Jacquemet et al., 2020; Schermelleh et al., 2019). As such, super-resolution methods such as single molecule localization microscopy rely on effective and reliable labeling of proteins. In **chapter 4**, we described a protocol for one color single-molecule localization microscopy of endogenous proteins, with special emphasis on parameters that influence imaging quality. This is important, as the sensitivity of such methods, can severely impact imaging quality and thereby data interpretation (Wu et al., 2020). Related to this, in chapter 5, we developed a new method for analyzing co-localization in single-molecule localization microscopy, parameter-free, and optimized to analyze highly clustered and density diverse datasets. Together, with the ongoing developments in protein labeling strategies, imaging modalities and analysis software, these super-resolution techniques become key instruments in solving biological questions.

### *Signal amplification*

In **chapter 2 and 3**, we developed methods to endogenously label proteins. While this solves many problems with the lack of specific antibodies and overexpression artifacts, it also introduces at least one: insufficient signal amplification for low abundant proteins. In practical terms, this means that additional labeling approaches such as antibody labeling on integrated tags is needed to get sufficient labeling, often even requiring polyclonal antibodies over monoclonal antibodies. This can give problems because of a linkage error, introduced between the target protein and the organic dye. Moreover, at protein dense structures like the neuronal synapse, antibody crowding can induce the formation of artificial clusters, such the target protein density and antibody labeling density are no longer linear (Jimenez et al., 2020; Mund and Ries, 2020). These effects are important considerations, especially if clustering of proteins is analyzed as a biological relevant process. The development of conjugatable ligands such as Halo are great for minimizing the linkage error, but do not provide the amplification that antibody labeling does (Los et al., 2008). Similarly, the introduction of non-natural amino acids which can be labeled with organic dyes by click-chemistry can also be used, but are expected severely impact protein expression levels if used in combination with knock-in approaches (Arsic et al., 2022; Bessa-Neto et al., 2021). The development of nanobodies, either directly conjugated to organic dyes or via secondary nanobody labeling also are increasingly used. In **chapter 6**, we successfully used labeling of spaghetti monster



---

HA tags (Viswanathan et al., 2015), integrated using ORANGE, allowing for significant signal amplification of endogenous proteins with monoclonal antibodies. Beside labeling, optimization of dye properties (Dempsey et al., 2011; Wang et al., 2022) as well as further development of techniques such as DNA-PAINT (Molle et al., 2016; Sharonov and Hochstrasser, 2006; Wang et al., 2017), and optimized systems for multi-color imaging (Siemons et al., 2022), could also be of great promise towards more reliable labeling and imaging standards for endogenous proteins in the future.

### *SMLM data analysis and data interpretation*

With the development of super-resolution techniques such as those based on SMLM, comes the need for methodologies that aim to analyze this data as such, that it can be used for answering biological questions (Wu et al., 2020). This relates to both judgement of data quality and the analysis itself. It is often easy to see things that are not there, overinterpreting poor data. In this context, in chapter 5, we developed a parameter-free method for measuring co-localization in SMLM datasets taking into account the effective resolution of the dataset, thus limiting over- or under-interpretation. In conclusion, super-resolution methodologies such as SMLM have giving a major boost to our understanding of cellular architecture. However, we always should be remain critical towards our data quality, the methods we use to analyze these data and the biological conclusions we derive from them (Wait et al., 2020).

## **RESOLVING THE SUBSYNAPTIC DISTRIBUTION OF GLUTAMATE RECEPTORS**

The trafficking and organization of AMPARs at excitatory synapses is crucial for synaptic communication. In **chapter 6 and 7**, we have studied how AMPAR are anchored at the synapse. We found that the correct targeting of AMPARs is not governed by a single mechanism or interacting protein, but rather depends on multiple mechanism that include the interaction with multiple auxiliary proteins and the AMPAR NTD. This allows for a high degree of finetuning of AMPAR density at the synapses, as well was functionally through modifying gating kinetics.

### *Contribution of auxiliary proteins to receptor anchoring*

In chapter 6, we mapped and studied the role of auxiliary proteins in the anchoring of AMPARs. We found that although seemingly required for synaptic anchoring, removal of the PDZ ligands for TARPy2/8 or Shisa6, did not fully abolish their localization at the synapses. This showed that there has to be a high degree of functional redundancy among the auxiliary protein families. This raises two important questions. What is the relative importance of each of the auxiliary proteins? And are there other features within these auxiliary proteins, that are involved in synaptic anchoring?

The complexity of AMPAR-auxiliary protein constituents is a direct result of evolution. NMDAR and kainate receptor subunits have been shown exist for longer than most auxiliary proteins, with iGluRs present in almost all eukaryotic species, even those lacking a nervous system (Ramos-Vicente et al., 2021). The TARP family of proteins appears around the same time as the AMPARs, while homologs of the mammalian cornichon family existed before AMPARs did. Most auxiliary protein families including the Shisa and Dispanin families as well as the expansion within all the protein families evolved much later, with many of these individual proteins only being conserved among vertebrates (Ramos-Vicente and Bayes, 2020). This implies that the diversity in auxiliary proteins is strongly linked to nervous

system complexity. The GluA subunits that form the receptor core, thus act as a platform that can be modified with auxiliary proteins, finetuning the receptor for a specific cell or even specific synapses. This is also reflected by the diversity in expression patterns across the brain (Schwenk et al., 2014). For example, the members of the TARP family show strong brain region diversity in expression patterns being the most common auxiliary protein in the hippocampus, but almost absent in other brain regions. Differences in for example their intracellular tail length (Hafner et al., 2015) and extracellular domains, could have differential influences on receptor anchoring as well as differentially influence receptor gating (Cais et al., 2014; Herguedas et al., 2022). To learn more, it will be of interest to functionally dissect the channel properties of AMPARs, bound to different auxiliary proteins. Moreover, it would be of interest to study AMPAR composition in different neuron types maybe even at individual synapses, and link this to synaptic functioning. It is not unlikely that alterations in the relative expression of auxiliary proteins that affect receptor functioning at specific synapses, could be involved in neurological disorders.

We and others have shown that the C-terminal PDZ ligand of various auxiliary proteins plays an important role in synaptic anchoring. However, other features in the auxiliary proteins could contribute to this. For example, highly charged regions, such as those in the tail of the TARP proteins, could take part in processes such as phase separation (Zeng et al., 2019). It would be interesting if other auxiliary proteins such as those of the Shisa family, but also the C-terminal tails of the GluA subunits also exhibit some of these features. Taken together, the major challenges ahead are thus to better understand the stoichiometry of the AMPAR complex with its auxiliary proteins and to dissect how this contributes to synapse specificity.

#### *AMPA N-terminal domain as platform for transsynaptic interactions*

In addition to auxiliary proteins, several earlier studies have indicated an important regulatory role for the AMPAR NTD in synaptic anchoring (Diaz-Alonso et al., 2017; Watson et al., 2017). Moreover, the NTD domains has been shown to influence receptor functioning in a subunit dependent manner (Watson et al., 2021). Like the C-terminal tail, the NTDs are less well conserved among the AMPAR subunits compared to the ligand-binding, and transmembrane domains. In **chapter 7**, we showed that (overexpressed) AMPARs lacking a NTD are severely impacted in their ability to traffic to and anchor in the synapse. In addition, NTD lacking receptors showed increased mobility and diffusion kinetics. This suggest that the NTD is somehow important for synapse anchoring. Another study recently showed, that removing the NTD, reduces sub-synaptic clustering of AMPARs (Watson et al., 2021). In contrast, in chapter 6, we found that while AMPAR auxiliary proteins TARPy8 and Shisa6 are involved in the synaptic localization of AMPARs, they seem to contribute little to subsynaptic clustering. The NTD thus is likely to interact with other proteins within the synaptic cleft, and thereby regulate its subsynaptic positioning relative to presynaptic release sites. So far, the evidence for transsynaptic interactions through the NTD is limited. Several interacting proteins have been described, but not confirmed by others (Garcia-Nafria et al., 2016). It might be that most of these interactions are weak, and only do interact because of their close proximity to each other within the synaptic cleft. It would be interesting to study the synaptic anchoring properties of the NTD more closely. For example, expression of the NTD, fused to an artificial transmembrane domain, could reveal whether the NTD alone, is sufficient for synaptic targeting. In addition, combined with proximity crosslinking and affinity purification, this could be used to ‘fish’ for potential NTD-interacting proteins.

---

Moreover, we showed as proof-of-principle the active removal of the NTD from the cell surface. It would be interesting to test whether this acute removal of the NTD, increases membrane diffusion and eventual decoupling from the synapse.

In conclusion, the roles that govern the positioning of AMPARs at the synapse are complex. The TARP proteins, and to a lesser degree the other auxiliary proteins such as the cornichons and Shisa families, target AMPARs to the synapse. At the synapse, NTD of the AMPAR core subunits influences its correct sub-synaptic positioning, and possibly prevents synaptic exit. Finally, the diversity and regional expression patterns of individual auxiliary protein family members, allow cell type and maybe even synapse-specific finetuning of AMPAR functioning as additional layer of regulation.

### **CONCLUDING REMARKS**

Our ability to study the subcellular architecture of cells goes hand in hand with the development of new techniques to do so. By developing a novel toolbox for genome editing in neuronal cells, we took away many technical restraints that limited our ability to study single protein species at high spatial resolution. The techniques described in this thesis will undoubtedly aid in addressing numerous biological questions. Nevertheless, I want to stress that the development of these techniques does not make overexpression of recombinant proteins obsolete but rather provides new tools for the cell biologists' toolbox. Using these techniques, we studied the synaptic anchoring of AMPARs, revealing an important role for the AMPARs N-terminal domain and the AMPAR auxiliary proteins in this process. Taken together, it will be exciting to see how the technological advantages and biological insights as presented in this thesis enable new biological questions to be addressed, at neuronal synapses, in the brain and beyond.

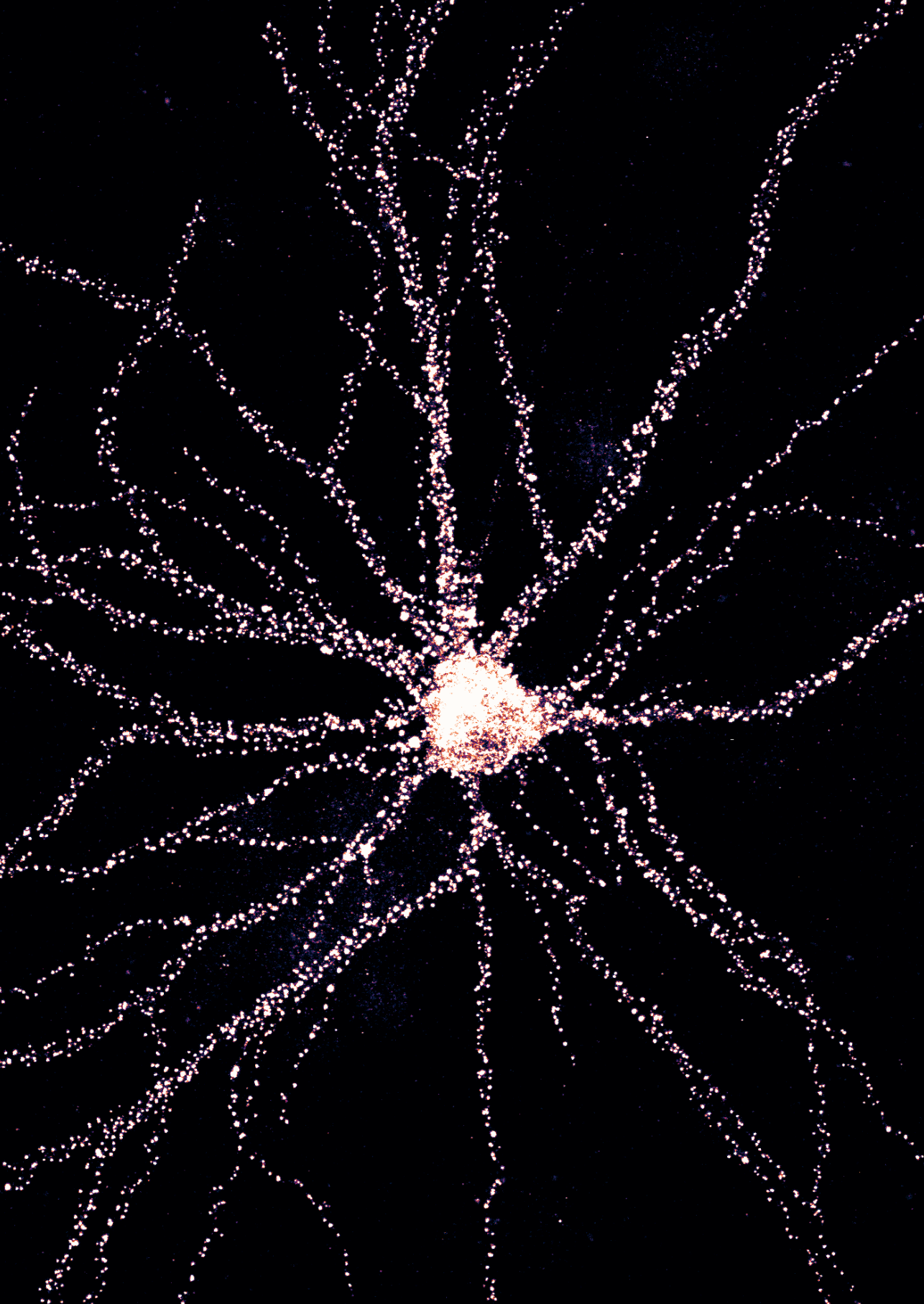
## REFERENCES

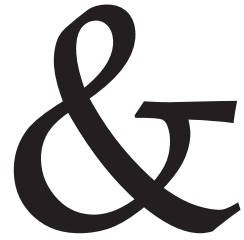
- Al-Zain, A.M., and Symington, L.S. (2021). The dark side of homology-directed repair. *DNA Repair (Amst)* 106, 103181.
- Arsic, A., Hagemann, C., Stajkovic, N., Schubert, T., and Nikic-Spiegel, I. (2022). Minimal genetically encoded tags for fluorescent protein labeling in living neurons. *Nat Commun* 13, 314.
- Bae, S., Kweon, J., Kim, H.S., and Kim, J.S. (2014). Microhomology-based choice of Cas9 nuclease target sites. *Nat Methods* 11, 705-706.
- Banan, M. (2020). Recent advances in CRISPR/Cas9-mediated knock-ins in mammalian cells. *J Biotechnol* 308, 1-9.
- Banskota, S., Raguram, A., Suh, S., Du, S.W., Davis, J.R., Choi, E.H., Wang, X., Nielsen, S.C., Newby, G.A., Randolph, P.B., et al. (2022). Engineered virus-like particles for efficient in vivo delivery of therapeutic proteins. *Cell* 185, 250-265 e216.
- Bessa-Neto, D., Beliu, G., Kuhlemann, A., Pecoraro, V., Doose, S., Retailleau, N., Chevrier, N., Perrais, D., Sauer, M., and Choquet, D. (2021). Bioorthogonal labeling of transmembrane proteins with non-canonical amino acids unveils masked epitopes in live neurons. *Nat Commun* 12, 6715.
- Betermier, M., Bertrand, P., and Lopez, B.S. (2014). Is non-homologous end-joining really an inherently error-prone process? *PLoS Genet* 10, e1004086.
- Brandsma, I., and Gent, D.C. (2012). Pathway choice in DNA double strand break repair: observations of a balancing act. *Genome Integr* 3, 9.
- Cais, O., Herguedas, B., Krol, K., Cull-Candy, S.G., Farrant, M., and Greger, I.H. (2014). Mapping the interaction sites between AMPA receptors and TARPs reveals a role for the receptor N-terminal domain in channel gating. *Cell Rep* 9, 728-740.
- Carlson-Stevermer, J., Abdeen, A.A., Kohlenberg, L., Goedland, M., Molugu, K., Lou, M., and Saha, K. (2017). Assembly of CRISPR ribonucleoproteins with biotinylated oligonucleotides via an RNA aptamer for precise gene editing. *Nat Commun* 8, 1711.
- Chew, W.L., Tabebordbar, M., Cheng, J.K., Mali, P., Wu, E.Y., Ng, A.H., Zhu, K., Wagers, A.J., and Church, G.M. (2016). A multifunctional AAV-CRISPR-Cas9 and its host response. *Nat Methods* 13, 868-874.
- Choi, J.H., Sim, S.E., Kim, J.I., Choi, D.I., Oh, J., Ye, S., Lee, J., Kim, T., Ko, H.G., Lim, C.S., and Kaang, B.K. (2018). Interregional synaptic maps among engram cells underlie memory formation. *Science* 360, 430-435.
- Choquet, D., Sainlos, M., and Sibarita, J.B. (2021). Advanced imaging and labelling methods to decipher brain cell organization and function. *Nat Rev Neurosci* 22, 237-255.
- Dalvai, M., Loehr, J., Jacquet, K., Huard, C.C., Roques, C., Herst, P., Cote, J., and Doyon, Y. (2015). A Scalable Genome-Editing-Based Approach for Mapping Multiprotein Complexes in Human Cells. *Cell Rep* 13, 621-633.
- Das, S., Vera, M., Gandin, V., Singer, R.H., and Tutucci, E. (2021). Intracellular mRNA transport and localized translation. *Nat Rev Mol Cell Biol* 22, 483-504.
- Delacote, F., and Lopez, B.S. (2008). Importance of the cell cycle phase for the choice of the appropriate DSB repair pathway, for genome stability maintenance: the trans-S double-strand break repair model. *Cell Cycle* 7, 33-38.
- Dempsey, G.T., Vaughan, J.C., Chen, K.H., Bates, M., and Zhuang, X. (2011). Evaluation of fluorophores for optimal performance in localization-based super-resolution imaging. *Nat Methods* 8, 1027-1036.
- Diaz-Alonso, J., Sun, Y.J., Granger, A.J., Levy, J.M., Blankenship, S.M., and Nicoll, R.A. (2017). Subunit-specific role for the amino-terminal domain of AMPA receptors in synaptic targeting. *Proc Natl Acad Sci U S A* 114, 7136-7141.
- Doench, J.G., Fusi, N., Sullender, M., Hegde, M., Vaimberg, E.W., Donovan, K.F., Smith, I., Tothova, Z., Wilen, C., Orchard, R., et al. (2016). Optimized sgRNA design to maximize activity and minimize off-target effects of CRISPR-Cas9. *Nat Biotechnol* 34, 184-191.
- Dolgalev, G., and Poverennaya, E. (2021). Applications of CRISPR-Cas Technologies to Proteomics. *Genes (Basel)* 12.
- Donlin-Asp, P.G., Polisseni, C., Klimek, R., Heckel, A., and Schuman, E.M. (2021). Differential regulation of local mRNA dynamics and translation following long-term potentiation and depression. *Proc Natl Acad Sci U S A* 118.
- Fang, H., Bygrave, A.M., Roth, R.H., Johnson, R.C., and Haganir, R.L. (2021). An optimized CRISPR/Cas9 approach for precise genome editing in neurons. *Elife* 10.
- Gao, Y., Hisey, E., Bradshaw, T.W.A., Erata, E., Brown, W.E., Courtland, J.L., Uezu, A., Xiang, Y., Diao, Y., and Soderling, S.H. (2019). Plug-and-Play Protein Modification Using Homology-Independent Universal Genome Engineering. *Neuron* 103, 583-597 e588.
- Garcia-Nafria, J., Herguedas, B., Watson, J.F., and Greger, I.H. (2016). The dynamic AMPA receptor extracellular region: a platform for synaptic protein interactions. *J Physiol* 594, 5449-5458.
- Gee, P., Lung, M.S.Y., Okuzaki, Y., Sasakawa, N., Iguchi, T., Makita, Y., Hozumi, H., Miura, Y., Yang, L.F., Iwasaki, M., et al. (2020). Extracellular nanovesicles for packaging of CRISPR-Cas9 protein and sgRNA to induce therapeutic exon skipping. *Nat Commun* 11, 1334.
- Hafner, A.S., Donlin-Asp, P.G., Leitch, B., Herzog, E., and Schuman, E.M. (2019). Local protein synthesis is a ubiquitous feature of neuronal pre- and postsynaptic compartments. *Science* 364.
- Hafner, A.S., Penn, A.C., Grillo-Bosch, D., Retailleau, N., Poujol, C., Philippat, A., Coussen, F., Sainlos, M., Opazo, P., and Choquet, D. (2015). Lengthening of the Stargazin Cytoplasmic Tail Increases Synaptic Transmission by Promoting Interaction to Deeper Domains of PSD-95. *Neuron* 86, 475-489.
- Hamilton, J.R., Tsuchida, C.A., Nguyen, D.N., Shy, B.R., McGarrigle, E.R., Sandoval Espinoza, C.R., Carr, D., Blaeschke, F., Marson, A., and Doudna, J.A. (2021). Targeted delivery of CRISPR-Cas9 and transgenes enables complex immune cell engineering. *Cell Rep* 35, 109207.
- Herguedas, B., Kohegyi, B.K., Dohrke, J.N., Watson, J.F., Zhang, D., Ho, H., Shaikh, S.A., Lape, R., Krieger, J.M., and Greger, I.H. (2022). Mechanisms underlying TARP modulation of the GluA1/2-gamma8 AMPA receptor.

Nat Commun 13, 734.

- Hummert, J., Tashev, S.A., and Herten, D.P. (2021). An update on molecular counting in fluorescence microscopy. *Int J Biochem Cell Biol* 135, 105978.
- Ioannidi, E.I., Yarnall, M.T.N., Schmitt-Ulms, C., N. Krajcski, R., Lim, J., Villiger, L., Zhou, W., Jiang, K., Roberts, N., Zhang, L., et al. (2021). Drag-and-drop genome insertion without DNA cleavage with CRISPR-directed integrases. *BioRxiv*.
- Iyama, T., and Wilson, D.M., 3rd (2013). DNA repair mechanisms in dividing and non-dividing cells. *DNA Repair (Amst)* 12, 620-636.
- Jacquemet, G., Carissey, A.F., Hamidi, H., Henriques, R., and Leterrier, C. (2020). The cell biologist's guide to super-resolution microscopy. *J Cell Sci* 133.
- Jayavaradhan, R., Pillis, D.M., Goodman, M., Zhang, F., Zhang, Y., Andreassen, P.R., and Malik, P. (2019). CRISPR-Cas9 fusion to dominant-negative 53BP1 enhances HDR and inhibits NHEJ specifically at Cas9 target sites. *Nat Commun* 10, 2866.
- Jimenez, A., Friedl, K., and Leterrier, C. (2020). About samples, giving examples: Optimized Single Molecule Localization Microscopy. *Methods* 174, 100-114.
- Kim, J., Zhao, T., Petralia, R.S., Yu, Y., Peng, H., Myers, E., and Magee, J.C. (2011). mGRASP enables mapping mammalian synaptic connectivity with light microscopy. *Nat Methods* 9, 96-102.
- Koch, B., Nijmeijer, B., Kueblbeck, M., Cai, Y., Walther, N., and Ellenberg, J. (2018). Generation and validation of homozygous fluorescent knock-in cells using CRISPR-Cas9 genome editing. *Nat Protoc* 13, 1465-1487.
- Lieber, M.R. (2010). The mechanism of double-strand DNA break repair by the nonhomologous DNA end-joining pathway. *Annu Rev Biochem* 79, 181-211.
- Liu, G., Lin, Q., Jin, S., and Gao, C. (2022). The CRISPR-Cas toolbox and gene editing technologies. *Mol Cell* 82, 333-347.
- Liu, G., Zhang, Y., and Zhang, T. (2020). Computational approaches for effective CRISPR guide RNA design and evaluation. *Comput Struct Biotechnol J* 18, 35-44.
- Los, G.V., Encell, L.P., McDougall, M.G., Hartzell, D.D., Karassina, N., Zimprich, C., Wood, M.G., Learish, R., Ohana, R.F., Urh, M., et al. (2008). HaloTag: a novel protein labeling technology for cell imaging and protein analysis. *ACS Chem Biol* 3, 373-382.
- Matsuda, T., and Cepko, C.L. (2007). Controlled expression of transgenes introduced by in vivo electroporation. *Proc Natl Acad Sci U S A* 104, 1027-1032.
- Meyerink, B.L., Pratiksha, K., Tiwari, N.K., Kittock, C.M., Klein, A., Evans, C., and Pilaz, L.-J. (2022). Breasi-CRISPR: an efficient genome editing method to interrogate protein localization and protein-protein interactions in the embryonic mouse cortex. *BioRxiv*.
- Mikuni, T., Nishiyama, J., Sun, Y., Kamasawa, N., and Yasuda, R. (2016). High-Throughput, High-Resolution Mapping of Protein Localization in Mammalian Brain by In Vivo Genome Editing. *Cell* 165, 1803-1817.
- Molle, J., Raab, M., Holzmeister, S., Schmitt-Monreal, D., Grohmann, D., He, Z., and Tinnefeld, P. (2016). Superresolution microscopy with transient binding. *Curr Opin Biotechnol* 39, 8-16.
- Montagna, C., Petris, G., Casini, A., Maule, G., Franceschini, G.M., Zanella, I., Conti, L., Arnoldi, F., Burrone, O.R., Zentilin, L., et al. (2018). VSV-G-Enveloped Vesicles for Traceless Delivery of CRISPR-Cas9. *Mol Ther Nucleic Acids* 12, 453-462.
- Mund, M., and Ries, J. (2020). How good are my data? Reference standards in superresolution microscopy. *Mol Biol Cell* 31, 2093-2096.
- Nambiar, T.S., Baudrier, L., Billon, P., and Ciccia, A. (2022). CRISPR-based genome editing through the lens of DNA repair. *Mol Cell* 82, 348-388.
- Nishiyama, J., Mikuni, T., and Yasuda, R. (2017). Virus-Mediated Genome Editing via Homology-Directed Repair in Mitotic and Postmitotic Cells in Mammalian Brain. *Neuron* 96, 755-768 e755.
- Pannunzio, N.R., Watanabe, G., and Lieber, M.R. (2018). Nonhomologous DNA end-joining for repair of DNA double-strand breaks. *J Biol Chem* 293, 10512-10523.
- Pawelczak, K.S., Gavande, N.S., VanderVere-Carozza, P.S., and Turchi, J.J. (2018). Modulating DNA Repair Pathways to Improve Precision Genome Engineering. *ACS Chem Biol* 13, 389-396.
- Ramos-Vicente, D., and Bayes, A. (2020). AMPA receptor auxiliary subunits emerged during early vertebrate evolution by neo/subfunctionalization of unrelated proteins. *Open Biol* 10, 200234.
- Ramos-Vicente, D., Grant, S.G., and Bayes, A. (2021). Metazoan evolution and diversity of glutamate receptors and their auxiliary subunits. *Neuropharmacology* 195, 108640.
- Ran, F.A., Cong, L., Yan, W.X., Scott, D.A., Gootenberg, J.S., Kriz, A.J., Zetsche, B., Shalem, O., Wu, X., Makarova, K.S., et al. (2015). In vivo genome editing using Staphylococcus aureus Cas9. *Nature* 520, 186-191.
- Rhee, H.W., Zou, P., Udeshi, N.D., Martell, J.D., Mootha, V.K., Carr, S.A., and Ting, A.Y. (2013). Proteomic mapping of mitochondria in living cells via spatially restricted enzymatic tagging. *Science* 339, 1328-1331.
- Roux, K.J., Kim, D.I., Raida, M., and Burke, B. (2012). A promiscuous biotin ligase fusion protein identifies proximal and interacting proteins in mammalian cells. *J Cell Biol* 196, 801-810.
- Schermelleh, L., Ferrand, A., Huser, T., Eggeling, C., Sauer, M., Biehlmaier, O., and Drummen, G.P.C. (2019). Super-resolution microscopy demystified. *Nat Cell Biol* 21, 72-84.
- Schwenk, J., Bachrens, D., Haupt, A., Bildl, W., Boudkazi, S., Roeper, J., Fakler, B., and Schulte, U. (2014). Regional diversity and developmental dynamics of the AMPA-receptor proteome in the mammalian brain. *Neuron* 84, 41-54.
- Segel, M., Lash, B., Song, J., Ladha, A., Liu, C.C., Jin, X., Mekhedov, S.L., Macrae, R.K., Koonin, E.V., and Zhang, F. (2021). Mammalian retrovirus-like protein PEG10 packages its own mRNA and can be pseudotyped for mRNA delivery. *Science* 373, 882-889.
- Sharonov, A., and Hochstrasser, R.M. (2006). Wide-field subdiffraction imaging by accumulated binding of diffusing probes. *Proc Natl Acad Sci U S A* 103, 18911-18916.
- Siemons, M.E., Jurriens, D., Smith, C.S., and Kapitein, L.C. (2022). 3D multi-color far-red single-molecule

- localization microscopy with probability-based fluorophore classification. *BioRxiv*.
- StaaHL, B.T., Benekareddy, M., Coulon-Bainier, C., Banfal, A.A., Floor, S.N., Sabo, J.K., Urnes, C., Munares, G.A., Ghosh, A., and Doudna, J.A. (2017). Efficient genome editing in the mouse brain by local delivery of engineered Cas9 ribonucleoprotein complexes. *Nat Biotechnol* 35, 431-434.
- Suzuki, K., Tsunekawa, Y., Hernandez-Benitez, R., Wu, J., Zhu, J., Kim, E.J., Hatanaka, F., Yamamoto, M., Araoka, T., Li, Z., et al. (2016). In vivo genome editing via CRISPR/Cas9 mediated homology-independent targeted integration. *Nature* 540, 144-149.
- Tran, N.T., Bashir, S., Li, X., Rossius, J., Chu, V.T., Rajewsky, K., and Kuhn, R. (2019). Enhancement of Precise Gene Editing by the Association of Cas9 With Homologous Recombination Factors. *Front Genet* 10, 365.
- Uemura, T., Mori, T., Kurihara, T., Kawase, S., Koike, R., Satoga, M., Cao, X., Li, X., Yanagawa, T., Sakurai, T., et al. (2016). Fluorescent protein tagging of endogenous protein in brain neurons using CRISPR/Cas9-mediated knock-in and in utero electroporation techniques. *Sci Rep* 6, 35861.
- Viswanathan, S., Williams, M.E., Bloss, E.B., Stasevich, T.J., Speer, C.M., Nern, A., Pfeiffer, B.D., Hooks, B.M., Li, W.P., English, B.P., et al. (2015). High-performance probes for light and electron microscopy. *Nat Methods* 12, 568-576.
- Wait, E.C., Reiche, M.A., and Chew, T.L. (2020). Hypothesis-driven quantitative fluorescence microscopy - the importance of reverse-thinking in experimental design. *J Cell Sci* 133.
- Wang, B., Xiong, M., Susanto, J., Li, X., Leung, W.Y., and Xu, K. (2022). Transforming Rhodamine Dyes for (d) STORM Super-Resolution Microscopy via 1,3-Disubstituted Imidazolium Substitution. *Angew Chem Int Ed Engl* 61, e202113612.
- Wang, Y., Woehrstein, J.B., Donoghue, N., Dai, M., Avendano, M.S., Schackmann, R.C.J., Zoeller, J.J., Wang, S.S.H., Tillberg, P.W., Park, D., et al. (2017). Rapid Sequential in Situ Multiplexing with DNA Exchange Imaging in Neuronal Cells and Tissues. *Nano Lett* 17, 6131-6139.
- Watson, J.F., Ho, H., and Greger, I.H. (2017). Synaptic transmission and plasticity require AMPA receptor anchoring via its N-terminal domain. *Elife* 6.
- Watson, J.F., Pinggera, A., Ho, H., and Greger, I.H. (2021). AMPA receptor anchoring at CA1 synapses is determined by N-terminal domain and TARP gamma8 interactions. *Nat Commun* 12, 5083.
- Wright, A.V., Sternberg, S.H., Taylor, D.W., StaaHL, B.T., Bardales, J.A., Kornfeld, J.E., and Doudna, J.A. (2015). Rational design of a split-Cas9 enzyme complex. *Proc Natl Acad Sci U S A* 112, 2984-2989.
- Wu, Y.L., Tschanz, A., Krupnik, L., and Ries, J. (2020). Quantitative Data Analysis in Single-Molecule Localization Microscopy. *Trends Cell Biol* 30, 837-851.
- Xu, H., Xiao, T., Chen, C.H., Li, W., Meyer, C.A., Wu, Q., Wu, D., Cong, L., Zhang, F., Liu, J.S., et al. (2015). Sequence determinants of improved CRISPR sgRNA design. *Genome Res* 25, 1147-1157.
- Zeng, M., Diaz-Alonso, J., Ye, F., Chen, X., Xu, J., Ji, Z., Nicoll, R.A., and Zhang, M. (2019). Phase Separation-Mediated TARP/MAGUK Complex Condensation and AMPA Receptor Synaptic Transmission. *Neuron* 104, 529-543 e526.
- Zetsche, B., Volz, S.E., and Zhang, F. (2015). A split-Cas9 architecture for inducible genome editing and transcription modulation. *Nat Biotechnol* 33, 139-142.
- Zhong H, Ceballos CC, Massengill CI, Muniak MA, Ma L, Qin M, Petrie SK & Mao T (2021) High-fidelity, efficient, and reversible labeling of endogenous proteins using CRISPR-based designer exon insertion. *Elife* 10: 99–117.





## **Addendum**

Nederlandse samenvatting

Curriculum vitae

List of publications

Dankwoord

---



---

## NEDERLANDSE SAMENVATTING

Communicatie tussen hersencellen (aka neuronen) is fundamenteel voor het functioneren van ons brein. Neuronen versturen signalen via axonen en ontvangen via dendrieten. Het contact punt tussen twee neuronen heet de synaps. Hier worden chemische signalen (neurotransmitters), vanuit de axon losgelaten. Receptoren in de ontvangende neuron worden hierdoor geactiveerd. De sterkte van het signaal is erg afhankelijk de hoeveelheid receptoren die de neurotransmitters kunnen opvangen. Processen die de hoeveelheid van deze receptoren in de synaps reguleren worden dan ook gelinkt aan het ontwikkelen van herinneringen en leren, en worden beïnvloed door neuronale activiteit. Om te begrijpen hoe neuronale communicatie werkt, moeten we dieper inzoomen op de architectuur van eiwitten in de synaps. Receptoren zoals de AMPA receptor worden in de synapsen verankerd via AMPA receptor hulp-eiwitten. Deze gaan een interactie aan met eiwitten in de post-synaptische-dichtheid, een zeer geconcentreerd netwerk van eiwitten die als een soort van parkeerplaats dient voor receptoren. Voor referentie: een synaps in ongeveer 1 micrometer (0.001 millimeter) in doorsnede.

Voor het bestuderen van de eiwit organisatie in synapsen, hebben we methoden nodig om deze eiwitten te visualiseren. Dit is uitdagend door de kleine schaal van de synaps, maar ook door een gebrek aan technieken om individuen eiwitten goed te labelen. In het huidige proefschrift hebben wij daarom nieuwe methoden ontwikkeld, die ons in staat stellen om individuen eiwitten zichtbaar te maken in hersencellen, zodat we de organisatie van receptoren in de synaps kunnen bestuderen.

In hoofdstuk 2 en 3 gebruiken wij DNA manipulatie om eiwitten te labelen. Door middel van het CRISPR/Cas9 systeem kunnen we het DNA gen coderende voor specifieke eiwitten, open knippen. Vervolgens kan hier een nieuw stuk DNA in worden gezet, coderende voor een fluorescent eiwit of een klein eiwit-label. Dit nieuwe stukje DNA wordt geïntegreerd door middel van het cel-eigen DNA-schade reparatie mechanisme. De eiwitten die vervolgens van deze genen worden gemaakt, zullen dan dus een fluorescerend label dragen, welke zichtbaar kan worden gemaakt met fluorescentie microscopie. In hoofdstuk 2 hebben wij deze techniek zodanig ontwikkeld dat wij deze kunnen toepassen in hersencellen, hersenweefsel, en in een intact brein. Deze techniek noemen wij ORANGE. Wij laten zien dat deze methode niet alleen erg nauwkeurig is, maar ons ook in staat stelt om eiwitten te visualiseren voor welke dat voorheen erg moeilijk, al dan niet onmogelijk was. Hiermee worden ook veel van de nadelen weggenomen die andere methoden zoals antilichaam labelen en over-expressie van eiwitten met zich mee brengen. In hoofdstuk 3 hebben wij deze methode verder ontwikkeld, zodat we twee eiwitten kunnen labelen in dezelfde neuron. Dit is belangrijk, omdat veel biologische inzichten voortkomen vanuit de context tussen twee verschillende eiwitten. Samenvattend stellen de ontwikkeling van deze methoden ons en andere onderzoekers nu in staat om endogene eiwitten zichtbaar te maken in neuronen.

In hoofdstuk 4 en 5 beschrijven wij methoden voor superresolutie microscopie. Dit zijn microscopische methoden die ons in staat stellen om structuren kleiner dan ~200 nanometer te bestuderen. Door de natuurkundige diffractie limiet van het licht, kan dit niet met normale microscopie. Eén van deze super-resolutie microscopie methoden is individuele-molecule lokalisatie microscopie. In plaats van alle moleculen in een object tegelijkertijd te visualiseren, laten we de individuele moleculen ‘blinken’ en hiermee dus individueel zichtbaar maken. In hoofdstuk 4 beschrijven wij een protocol om deze vorm van microscopie toe te passen op endogene eiwitten in neuronen. Deze individuele ‘blinks’ kunnen dan met

grote precisie worden gedetecteerd en hun locatie worden bepaald met een resolutie tot wel 5-10 nanometer. In plaats van een plaatje of foto, bestaat deze data daarom uit coördinaten. In hoofdstuk 5 beschrijven wij om die reden een nieuwe analytische methode om overlap tussen twee eiwitten te kunnen meten aan de hand van deze coördinaten. Door het meten van de lokale dichtheid van moleculen kunnen wij een co-lokalisatie index berekenen. Hiermee kunnen wij nu meten of twee eiwitten lokaal samen clusteren of elkaar juist uitsluiten.

In hoofdstuk 6 en 7 gebruiken wij de technieken ontwikkeld in de voorgaande hoofdstukken om meer te leren over de organisatie van AMPA receptoren in de synaps. Eerst hebben wij met gebruik van ORANGE de hulp-eiwitten zichtbaar gemaakt die vanuit de literatuur gelinkt worden aan de rekrutering en ankeren van AMPA receptoren in de synaps. Met name de eiwitten TARP $\gamma$ 8 en Shisa6 zijn van interesse. Deze eiwitten volgen de distributie van AMPA receptoren in neuronen, en komen hoog tot expressie. Onze resultaten in hoofdstuk 6 laten zien dat de aanwezigheid van deze eiwitten gecorreleerd is aan die van de AMPAR zelf, wat suggereert dat de mechanismes die deze eiwitten naar de synaps lokaliseren aan elkaar gelinkt zijn. Vervolgens hebben wij ook gekeken naar de mechanismen die TARP $\gamma$ 8 en Shisa6 (en dus indirect de AMPA receptor) in de synaps ankeren. Wij vonden dat het C-terminale PDZ ligand van de TARP $\gamma$ 8 en Shisa6 eiwitten hiervoor belangrijk is, maar zeker niet het volledige mechanisme verklaard. Er is naar alle waarschijnlijkheid dan ook geen grote mate van invloed van meerdere eiwitten. Om hier meer inzicht in te krijgen hebben wij in hoofdstuk 7 meer onderzoek gedaan naar hoe de AMPA receptor zelf in de synaps kan ankeren. Met name een groot N-terminaal domein is beschreven als mogelijk interactie platform waarmee het kan binden aan eiwitten in het axonale kant van de synaps. Hoewel hier weinig direct bewijs voor is laten onze experimenten zien dat zonder dit N-terminale domein, de AMPA receptor niet meer goed lokaliseert naar de synaps, de verankering is aangedaan en de diffusie van de receptoren in het membraan van de synaps verhoogt is. Dit laat dus zien dan het N-terminale domein van de AMPA receptor inderdaad betrokken is bij de rekrutering en verankering in de synaps. Dit sluit ook aan bij andere onderzoeken, die al aantoonen dat zonder dit domein, de sterkte van neuronale signaal overdracht sterk verminderd is.

Samenvattend bied dit proefschrift nieuwe manieren om gedetailleerd onderzoek te doen naar de eiwit organisatie in neuronen, specifiek door de ontwikkeling van nieuwe methoden om individuele eiwitten te kunnen labelen. Dit stelde ons in staat om o.a. de verankering van receptoren in de neuronale synaps te besturen. Deze ontwikkelingen hebben zeker invloed de manier waarop dit soort onderzoek gedaan. Het is dan ook interessant om te zien hoe andere onderzoekers de technieken beschreven in dit proefschrift kunnen inzetten voor andere biologische vragen, die ons beter helpen te begrijpen hoe onze hersenen werken.



---

## CURRICULUM VITAE

Jelmer Willems was born on 18th of November 1993 in Holten, the Netherlands. In 2011 he finished his high school education (HAVO) at the Scholengemeenschap de Waerdenborch in Holten. The same year, he started his bachelor Biology and Medical Laboratory research at the Saxion University of Applied Sciences in Deventer. During his studies in 2013, he performed an internship in the lab of dr. Ben Giepmans at the UMCG in Groningen, where he used electron microscopy to study viruses as potential cause of Type 1 Diabetes. In 2015, he performed a second bachelor internship in the lab of prof. Bé Wierenga and dr. Derick G. Wansink at the Radboud Institute for Molecular Life Sciences in Nijmegen, where he used CRISPR/Cas9 technology targeting toxic RNA molecules involved in Myotonic dystrophy. Hereafter, he obtained his bachelor degree. Motivated by an interest in scientific research, in September 2015, he continued with a master degree in Molecular and Cellular Life Sciences at Utrecht University. During his first master internship in the lab of prof. Lukas C. Kapitein, he studied organelle positioning using molecular biology techniques and fluorescence microscopy. Part of this work is published (*ACS synthetic biology*, 2017). Developing a keen interest in molecular cell biology, he then wrote his master thesis under the supervision of dr. Harold D. MacGillavry, diving into the mechanisms underlying neuronal spine formation. In the second year of his masters, he performed a final internship in the lab of Prof. Piet Gros, using protein purification and biochemistry methods to study proteins involved in the regulation of the complement system. In 2017, he obtained his Master's degree and shortly after, started his PhD in the lab of dr. Harold D. MacGillavry at the department of Cell biology, Neurobiology and Biophysics at Utrecht University, of which the results are presented in the current thesis.



---

**LIST OF PUBLICATIONS**

- 2022 **Duplex labeling and manipulation of neuronal proteins using sequential CRISPR/Cas9 gene editing** - Wouter J. Droogers, [Jelmer Willems](#), Harold D. MacGillavry, Arthur P.H. de Jong. eNeuro; ENEURO.0056-22.2022
- 2022 **A coordinate-based co-localization index to quantify and visualize spatial associations in single-molecule localization microscopy** - [Jelmer Willems](#) & Harold D. MacGillavry. Scientific Reports; 12(1): 4676
- 2022 **Single-molecule localization microscopy of subcellular protein distribution in neurons** - [Jelmer Willems](#)\*, Manon Westra\*, Harold D. MacGillavry. Methods in Molecular Biology; 2440, 271-288
- 2020 **ORANGE: A CRISPR/Cas9-based genome editing toolbox for epitope tagging of endogenous proteins in neurons** - [Jelmer Willems](#)\*, Arthur P. H. de Jong\*, Nicky Scheefhals, Eline Mertens, Lisa A. E. Catsburg, Rogier B. Poorthuis, Fred de Winter, Joost Verhaagen, Frank J. Meye, Harold D. MacGillavry, PLoS Biology ;18(4): e3000665
- 2020 **Microtubule Minus-End Binding Protein CAMSAP2 and Kinesin-14 Motor KIFC3 Control Dendritic Microtubule Organization** - Yujie Cao, Joanna Lipka, Riccardo Stucchi, Mithila Burute, Xingxiu Pan, Sybren Portegies, Roderick Tas, [Jelmer Willems](#), Lena Will, Harold D. MacGillavry, Maarten Altelaar, Lukas C. Kapitein, Martin Harterink, Casper C. Hoogenraad. Current Biology 30(5):899-908.e6
- 2017 **A Phytochrome-Derived Photoswitch for Intracellular Transport** - Max Adrian, Wilco Nijenhuis, Rein I. Hoogstraaten, [Jelmer Willems](#), Lukas C. Kapitein. ACS Synthetic Biology 6(7):1248-1256

\*Equal contribution



---

## DANKWOORD

Dit was het dan, het einde van 4 jaar (en nu al weer bijna 5) waarin ik heb mogen leren, ervaren, uitdenken en doen. Dat alles kon natuurlijk niet zonder de mensen die ik in de afgelopen jaren heb mogen leren kennen tijdens mijn tijd in Utrecht, en natuurlijk ook diegenen daar buiten, die zonder altijd te weten wat ik nu precies deed, mij enorm gesteund hebben.

Harold, de eerste keer dat wij elkaar ontmoete, was toen ik als student - en nog geen idee hebbende wat ik wilde - bij jou op gesprek ging voor een masterstage. Phebe had de gesprekken geregeld dus ik wist eigenlijk helemaal niet wie ik voor me had. Ik weet nog goed dat ik je vroeg in welk jaar van je PhD je zat, om er daarna achter te komen dat het je tweede postdoc was....auw... Je had wel een gaaf project over filamin A voorgesteld, maar het kwaad was al geschiet, je koos voor een andere student. Hoe gaat het eigenlijk met dat project ;)? Ander half jaar later kwam het dan toch tot een masterthesis onder jouw supervisie. Ik mocht uitzoeken hoe spines gevormd werden, en kon zo een interesse ontwikkelen voor de neuronale celbiologie. Een uitstapje naar de biochemie als tweede stage was niet voldoende om die interesse weg te nemen en dus informeerde ik maar eens naar de mogelijkheden voor een PhD positie. 1 dag later en een gesprek van nog geen uurtje en het was wel ongeveer rond. Gedurende mijn PhD heb ik de vrijheid gehad om mijzelf te ontwikkelen, eigen ideeën uit te denken, en bovenal veel gave proeven te doen. Van het initiële idee van AMPARs tellen in synapsen kwam uiteindelijk niet al te veel, maar daarvoor in de plaats hebben we veel gave technieken kunnen ontwikkelen. Jouw enthousiasme, positieve houding en oneindige hoeveelheid nieuwe ideeën bleven de projecten altijd vooruit gaan. Zelfs als ik nog te veel uitdagingen zag omdat een proef nog niet helemaal goed werkte kon jij zo lekker enthousiast reageren met iets van de strekking: Het werkt toch?, het is opgelost! Harold, nogmaals bedankt voor alles wat ik de afgelopen jaren van je heb mogen leren. Ik waardeer enorm de vrijheid die jij mij hebt gegeven om veel eigen invulling aan de projecten te geven! Ik heb mogen zien hoe jouw lab is ontstaan en is gegroeid. Het beste toegewenst aan jou en de toekomst van het MacLab!

Beste Lukas, als promotor en met jouw enorme kennis van de microscopie en celbiologie heb jij de afgelopen jaren een aanzienlijke bijdrage geleverd aan mijn ontwikkeling als wetenschapper. Na mijn twee eerdere stages op het HBO was ik een beetje sceptisch over of ik het echte fundamentele onderzoek wel wilde doorzetten, maar het jaar dat ik in jouw groep heb mogen stage-lopen heeft dat helemaal omgedraaid! Ik heb enorm veel mogen leren over onderzoek doen, kritisch literatuur lezen, presenteren en zelfvertrouwen opbouwen. Het was een zwaar maar achteraf voor mij zeer belangrijk jaar. Bedankt voor alles de afgelopen jaren vanaf mij stage tot nu, van input op projecten, nieuwe ideeën, het enthousiasme waarmee jij vaak kon vertellen en natuurlijk ook voor het kritische lezen en feedback geven op deze thesis.

Beste Anna, Ik ken vrijwel geen mensen met zoveel kennis van de wetenschap dan u. Altijd scherp, doorvragend en kritisch. De Spinoza prijs was dan ook meer dan verdiend. U bent een voorbeeld voor veel jonge wetenschappers. Corette, jij liet mensen zoals ik ook nadenken over de functionele aspecten van mijn projecten. Dank voor alles de afgelopen jaren en heel veel succes in Nijmegen! Ginny, thinking of you I somehow have always remember you running two confocal microscopes (and maybe even the spinning-disk) simultaneously when

---

I came into the confocal room for the first time around 8AM. I've seen your lab grow the past few years and wish you all the luck in the future. Agate, Frederik and Florian, good luck with your labs in the department. I'm sure you will do great science and contribute to the future of the department!

Ik wil ook graag alle overige leden van mijn beoordeling- en leescommissie bedanken, Guus Smit, Jeroen Pasterkamp, Mike Boxem, Ronald van Kesteren en Maarten Kole.

Dan mijn paranimfen,

Manon!! De afgelopen jaren heb ik zo veel van je mogen leren en om/met je mogen lachen. Ik waardeer enorm jouw kritische houding en vastberadenheid om fundamentele principes te willen begrijpen. Indrukwekkend is het hoe jij het ogenschijnlijke simpele principe van diffusie zo gedetailleerd kon ontleden dat het toch allemaal iets moeilijker bleek te zijn dan iedereen dacht. Zonder alles wat ik van jou heb geleerd was een groot deel van het wat er in deze thesis staat nooit van de grond gekomen. Manon, master in het debuggen, sneller maken, en leesbaar maken van scripts welke ik ooit eens met variabelen namen als "akdfjng" in elkaar had geflanst. Een kleine MatLab vraag veranderde bij ons al snel in een lange discussie, waarin stapels A4tjes vol werd getekend met lokalisaties, cirkels, pijlen, loops, tracks, confinement regio's, voronoi cellen en ga zo maar door. En niet te vergeten dat er Tonys op tafel kwamen voor de eerste of snelste oplossing voor een uitdaging en de SMLM analysepipeline van een half uur naar enkele minuten ging. Ik ga dit soort (best wel nerdy) momenten enorm missen!

Wouter, het mannetje van alles. Ongelofelijk wat jij in die krappe twee jaar (en startende toen corona toesloeg) allemaal hebt bereikt. Van CRISPR, neuronaal werk, slices, Ephys, superresolutie, expansie, .....Als je zo doorgaat heb jij over twee jaar zelfs met *C.elegans* gewerkt. Jij bracht een flinke portie nieuwe energie in het CRISPR project met als resultaat het eNeuro paper. Dank voor alle gezelligheid, hulp met het nog onoverzichtelijker maken van SMLM scripts en de vele borrels! Heel veel succes de aankomende jaren! Jij bent nu de enige echte expert van alles in het MacLab.

Daarnaast zijn er natuurlijk nog de andere mensen van het enige echte MacLab!

Arthur, wat een wetenschapper ben jij zeg! Rustig, cool, vastberaden, kennis van alles, goede vragensteller, geduldig, soms een beetje gek, liefhebber van goede koffie, maar bovenal een fantastische collega, kantoorgenoot en mentor. Je kwam in het MacLab toen mijn CRISPR side-project(je) net een beetje vorm begon te krijgen. Niet veel later nam nog net niet mijn hele project over haha. Jouw kennis en inzet hebben het ORANGE project tot het project gemaakt dat het uiteindelijk is geworden. En dan bedoel ik niet alleen het acroniem waarzonder het sowieso nooit een succes was geworden. Nogmaals bedankt voor het CRISPR avontuur van de afgelopen jaren. Ik heb extreem veel van jou mogen leren! De wereld is klein, en onze interesses hebben veel raakvlakken, dus wie weet komen we elkaar nog wel een keer weer tegen. Ik wens jou en Asiya het allerbeste toe in Weesp! Bovenal wens ik jullie heel veel geluk toe strakjes met z'n drietjes! En als straks iedereen op het punt staat om naar huis te gaan, dan doen we er nog eentje met de jas aan!

Nicky, natuurlijk in de eerste plaats de mamma van Mila, maar daarvoor ook altijd al een



---

beetje de mamma van het MacLab! Ik bewonder jouw doorzettingsvermogen en de drive om zowel de moleculaire als functionele kanten van de projecten willen begrijpen, iets waar ik van hoop dat je nu nog verder kan ontwikkelen. Bedankt voor alles de afgelopen jaren en heel veel succes in Nijmegen!

Lisa! Als jouw hoofd tussen een kier in de tussendeur van het kantoor geklemd zat omdat je met Nicky aan het praten, dan wist je dat je maar beter later terug kon komen. Je verborg nooit je mening en kon ook altijd zo lekker groots verkondigen als je wat fout had gedaan op het lab, om er vervolgens samen hard om te lachen. Bedankt voor alles de afgelopen jaren en veel succes in de toekomst!

Anna! I think we can agree on that we have quite different personalities, but we managed and had great fun in the process. I still have the card you gave me when we were relocated to different offices. I have become impressed by your persistence, eye for detail knowledge of microscopy and of doing things your own way! Your input over the years has been great, and I want to thank you everything. I wish you all the best in Bristol!

Yolanda. Somehow, when you are around people, everyone gets happier! Thank you for everything the last few years. I wish you all the luck in your new job!

Niels, jammer genoeg hebben wij maar een tijdje kunnen samenwerken, maar in die korte tijd heb ik wel kunnen zien hoe jouw doorzettingsvermogen je nu heeft gebracht waar je bent. Ik wens je heel veel succes met het een stapje voor stapje beter begrijpen van Alzheimer! Met jouw interesse voor dat onderwerp zit het in ieder geval wel goed!

Naast het MacLab, heb ik mogen werken op een afdeling vol met geweldige mensen. Hierbij wil ik ook mijn oud stage begeleider Max bedanken! Ik heb de fijne kneepjes van het kloneren van je mogen leren, en niet in de laatste plaats door dat USBtje met de volledige versie van Snapgene, welke tijdens mijn PhD veel gebruikt is. Jouw passie voor de imaging heb je sinds enkele jaren kunnen doorzetten in de VS. Ik hoop dat je het daar nog erg naar je zin hebt! Mocht je toevallig in Nederland zijn sluit gerust aan, al was mijn plan niet om na de promotie Chupitos in te duiken. Ik denk dat ik namelijk nog nooit zo slecht van de drank ben geweest dan na jouw promotiefeestje.

Wilco, de man van alles. Wil je een nieuwe proef opzetten? Vraag Wilco. Wil je een nieuw lab bouwen? Vraag Wilco. Ben je opzoek naar een ongezouten mening? Vraag Wilco. Ik bewonder jouw instelling ten aanzien van het doen van een goede proef en het belang van goede lab-skills! Dankjewel voor alles wat ik de afgelopen jaren van je heb mogen leren! René, dankjewel voor de leuke samenwerking. Gaaf dat we samen de AAV productie hebben kunnen opzetten. Ik weet zeker dat jouw skills nog veel projecten op de afdeling gaan helpen!

Phebe! Als er iemand is waar zonder het lab geheel in elkaar stort, dan ben jij dat wel! Bart, ik ken niemand met zoveel film kennis dan dat jij die bezit. Maar een Colaflesje met een dop van Fanta kan echt niet! Dank jullie wel voor alles de afgelopen jaren!

Ilya, keeping all the microscopes in working order with so many users and run-hours is impressive. Eugene, the first time a saw you present your work in a group meeting during

---

my internship, I really had no clue what it was about, except for the super fancy images that you generated. Over the last year I've become more-and-more impressed by your skills and contribution to many projects within the department! Thanks you both for everything.

Only know, I realize how many people I had the privilege to meet and work with during my PhD. Martin, Wendy, Amelie, Bart, Max, Janine, Joyce, Joshua, Boris, Cynthia, Robin, Fangrui, Hugo, Derk, Emma, Lotte, Malina, Daphne, Giel, Chun Hei, Ha, Nazmiye, Mai Dan, Carlijn, Dipti, Lilian and Klara, thank you for everything! I also would like to thank all people that were part of the neurophotonics consortium, Marijn, Naomi, Pegah, Guilia, Maarten, Ivo, Allard and Hans, thank you for the nice meetings and discussions.

Many whom I have worked with already left the department before me. Roderick, Anne, Sybren, Feline, Dennis, Hai Yin, Dieudonné, Peter-Jan, Yujie, Xingxiu, Robbelien, Jessica, York, thank you!

De afgelopen jaren heb ik het genoeg gehad om meerdere bachelor en master studenten te mogelijk begeleiden in stages. Marc, bedankt voor jouw inzet m.b.t. het AMPAR NTD project, welke contributie een aanzienlijk deel van hoofdstuk 7 is geworden. Naomi, indrukwekkend hoe jij ondanks alles wat er buiten je studie om gebeurde toch wist door te zetten. Ik bewonder jouw doorzettingsvermogen, directheid en openheid. De superresolutie proeven die we als initieel doel in gedachten hadden bleken allemaal toch technisch iets lastiger dan gedacht. Ondanks dat is jouw werk het fundament van hoofdstuk 6, waar veel van jouw bijdrage in verwerkt is! Ik wil jullie nogmaals bedanken en wens jullie beiden het beste toe!

Ik wil ook graag alle mensen bedanken van buiten de afdeling, maar waar ik mee samen heb mogen werken. Fred, Rogier, Joost en Frank, bedankt voor jullie inzet ten aanzien van het ORANGE project.

Het Kruytgebouw, waar ik iets meer dan 6 jaar heb mogen rondlopen. Een beetje nostalgisch is het wel geworden. Van de asbest dat je uit de muren en het plafond kon trekken, de lekkages, het ontbreken van zonnepanelen in de Westwing en warm kraanwater, 40 graden op het lab als de zon erop stond en vleermuizen op de gang in het weekend. Ja, dat ga je dan toch wel een beetje missen....

Naast alle mensen die ik de afgelopen jaren heb mogen ontmoeten zijn er nog meer die ik graag wil bedanken voor mij weg naar deze thesis toe.

Ik wil graag alle docenten van de HBO opleiding Biologie en Medisch laboratorium onderzoek van het Saxion in Deventer bedanken. Sylvia, Rob, Janny, Koop, Peter, Erwin en alle andere mensen van het BML team! Een fantastische (en toen kleinschalige) opleiding waar docenten met voornaam werden aangesproken. Ik wil in het bijzonder Sylvia bedanken als mentor over deze 4 jaren, die er altijd was als het even tegenzat en/of je even kon sparren toen ik geen idee had wat ik nu precies naar mijn HBO studie wilde gaan doen. Rob, u heeft laten zien hoe mooi de moleculaire biologie is en mede daardoor heb ik besloten daarin verder te gaan! Ik hoop dat jullie nog met veel plezier en passie voor het vak, menig studenten kunnen begeleiden in de studie!





---

Koen en Bas, na een dag werken is er dan ook niet zo lekker dan met jullie op dinsdag 'avonds de polder in gaan (of naar de plas) en alle organen een opdonder geven met een intervaltraining. Toch altijd weer met lichte tegenzin beginnen aan een 8x1000m of een leuke piramide gewoon omdat het kan. Breekt zo lekker de week (en het lichaam), en bovendien er goed voor de mentale gezondheid! Ik hoop dat we dat er nog goed in kunnen houden. Zelfs toen mijn eerste paper een soort van geschoopt werd, waren jullie bereid om last-minute op de maandag avond een fiets rondje in te gelasten om het hoofd even helemaal leeg te fietsen (letterlijk en figuurlijk). Twee marathons en talloze triatlons, halve marathons, korter werk, duurlopen waarvoor we de trein namen, lange fietsritten en openwater zwemmen. Wat hebben we niet gedaan? Volgend jaar een Marathon onder de drie uur?

Maik, Amy, Carst, Elske, Kristn, Robin, Jan, Tirza, Koen, Davy, Chiel, het is alweer 10 jaar geleden dat we voor het eerst naar Szigett gingen en al weer 11 jaar sinds we van de HAVO af kwamen, en toch is de groep bij elkaar gebleven. Oude vakantiefoto's worden inmiddels al nostalgisch. Inmiddels echte banen, huizen die worden gekocht en kinderen worden geboren. We worden echte burgers.....! Maar zodra er witte bergen zijn, dan veranderd er elk jaar toch weer iets. Rode wijn of halve liters Weizen alsof het ranja is en als kleine kinderen zo onbenullig van de piste af. Daar kwamen we ons zelf ook wel weer even goed tegen of niet Carst? Gelukkig hebben we de beelden nog! Het doet veel met me dat jullie mijn promotie willen meebeleven. Bedankt!

Robin, enorm trots op wat jij hebt mogen bereiken en dat heb je grotendeels zelf afgedwongen! Zeker de afgelopen jaren heb je kunnen laten zien wat je allemaal wel kan, in plaatst van te horen wat niet. Vaak moest jij ver buiten je comfort-zone stappen. Iets wat voor anderen niet zo zichtbaar is maar des te knapper!

Pap en mam, toen ik aan mijn PhD begon wisten jullie hier net zo weinig van als ik. Op tijden was het voor mij moeilijk om goed te kunnen uitleggen wat ik nu precies deed voor een werk. Desondanks bleven jullie altijd interesse tonen, ondanks dat onze werelden er in dat opzicht zo anders uit zien. In de afgelopen jaren is er voor jullie erg veel veranderd. Opeens, van de een op de andere dag veranderde alles. Ik weet het nog als de dag van gister, dat ma opbelde dat het helemaal mis was, en pa direct moest worden opgenomen vanwege acute nierfalen. Vanaf toen was alles onzeker, pa kwam thuis te en een lange onzekere tijd was aangebroken. Niets was meer zoals daarvoor. Op dat moment realiseerde ik weer even goed dat er belangrijkere dingen zijn om over te stressen over m'n PhD. Ik vind het enorm knap hoe jullie samen deze periode zijn doorgekomen. Pap, altijd keek jij naar wat je nog wel kon. Daar heb ik norm veel bewondering voor! Zelfs toen je vol onder de medicijnen zat blijf jij jezelf vermaken, en probeerde je zo actief te zijn als dat het lichaam dat toeliet. Na een lang traject van ziekenhuis bezoeken, testen en matches was daar misschien wel het mooiste bericht voor jullie ooit. Jullie waren een match en mam mocht jou een nier geven. Een enorme spannende paar weken waren aangebroken, die Robin en ik van dichtbij hebben mogen meemaken. Door de wonderen van de wetenschap werkt de nier nu na anderhalf jaar nog steeds. Er liggen hopelijk nog vele jaren voor jullie en ga er van genieten samen. Steeds vaker trekken jullie er even op-uit, iets wat ik jullie van harte gun! Geniet van het leven!

Jelmer

